Thermoelectric and Ferroelectric Properties of Metal Chalcogenides/ Oxy-chalcogenides and Topological Quantum Materials

A Thesis

Submitted for the Degree of

Doctor of Philosophy

By

MANISHA SAMANTA

New Chemistry Unit
Jawaharlal Nehru Centre for Advanced Scientific Research
(A Deemed University)
Bangalore – 560 064, India

March 2020

Dedicated to my parents

DECLARATION

I hereby declare that this thesis entitled "***Thermoelectric and Ferroelectric Properties of Metal Chalcogenides/ Oxy-chalcogenides and Topological Quantum Materials***" is a result of studies carried out by me at the New Chemistry Unit, Jawaharlal Nehru Centre for Advanced Scientific Research, Bangalore, India, under the supervision of ***Prof. Kanishka Biswas.*** This work has not been submitted elsewhere for the award of any degree or diploma. In keeping with the general practices of reporting scientific observations, due acknowledgements have been made wherever the work described is based on the findings of other investigators in a collaborative pursuit. Any omission which might have occurred by oversight or error in judgment is regretted.

Bangalore, India **Manisha Samanta**

March 31, 2020

CERTIFICATE

I hereby certify that the work described in this thesis titled "***Thermoelectric and Ferroelectric Properties of Metal Chalcogenides/ Oxy-chalcogenides and Topological Quantum Material***" has been carried out by ***Ms. Manisha Samanta*** at New Chemistry Unit, Jawaharlal Nehru Centre for Advanced Scientific Research, Bangalore, India under my supervision and that it has not been submitted elsewhere for the award of any degree or diploma.

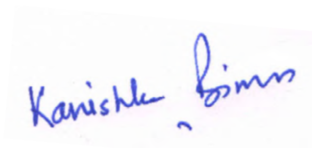

Bangalore, India
March 31, 2020

Prof. Kanishka Biswas
(Research Supervisor)

ACKNOWLEDGEMENTS

Completion of my Ph.D. thesis necessitated a lot of guidance and supports from many people. I take this opportunity to mention a few of them. However, my sincere thanks extend to everyone who has played a role in making this dream a reality.

Firstly, I would like to thank my research supervisor, Prof. Kanishka Biswas for suggesting me research problems and guiding me throughout. His valuable instructions and comments in scientific communications have helped me immensely. I express my hearty gratitude to him for giving me an opportunity to work under his guidance.

I would like to thank Bharat Ratna Prof. C. N. R. Rao, FRS, the chairman of New Chemistry Unit (NCU) for his generous support and encouragement throughout my stay in JNCASR. His presence has given me immense inspiration to indulge in active research. I also thank him for providing the infrastructure and facilities to carry out my research work.

I would like to thank Prof. Umesh V. Waghmare, Prof. Goutam Sheet, Prof. Tanmoy Das, Dr. Shovit Bhattacharyya, Dr. Ajay Singh, Dr. Koushik Pal, Dr. Sandhya Shenoy, Ms. Raagya Arora and Dr. Kapildeb Dolui, for the fruitful scientific collaborations and all the insightful discussions. I have learnt a lot whenever we had meeting or discussion with them.

I am thankful to all my course instructors: Prof. Kanishka Biswas, Prof. A. Sundaresan, Prof. Sebastian C Peter, Prof. Sarit S. Agasti, Prof. Tapas K. Maji, and Prof. Chandrabhas Narayana, whose courses have been extremely helpful.

I thank all my beloved labmates: Dr. S. Roychowdhury, Dr. A. Banik, Dr. S. Guin, Dr. M. Jana, Dr. T. Ghosh, Dr. S. Shidaling, Dr. P. Pal, Dr. S. Perumal, Dr. K. Kundu, Dr. P. Dutta, Ms. E. Rathore, Mr. M. Dutta, Mr. A. Sarkar, Dr. S. Saha, Ms. S. Chandra, Mr. P. Acharyya, Mr. K. Majhi, Mr. D. Sarkar, Mr. A. Bhui, Mr. R. Pathak, and Mr. S. Das for their cheerful company and help in various occasions.

I thank Mr. Premkumar Yanda for his help in measuring low temperature heat capacity and Dr. Jay Ghatak for helping in TEM analysis.

I would like to thank all the funding agencies like UGC, JNCASR, and DST, India. Without these supports, it would have never been possible to conduct research.

Constant assistance and a friendly nature of the technical staff helped me doing my experiments smoothly. Here, I would like to acknowledge Mrs. Usha, Mr. Vasu, Mr. Anil, Ms. Selvi, Dr. Jay Ghatak, Mr. Mahesh, Mr. Shiva, Mr. Kanan, Mr. N. Kishore, Mr. M. Gowda, Mr. Dileep, Mr. Peer, Mr. Srinivas and others. I am thankful to all the

academic, administrative, technical, security, complab and health center staffs for making our campus life smooth and easy.

I express my deep gratitude to all my high school and undergraduate teachers for training me to be disciplined, the basics of science and for growing my interest in research field.

I thank all my colleagues, juniors and friends in JNCASR.

I have been benefited a lot from my JNC friends. Their help and advice made my academic and non-academic life a memorable and comfortable one here at JNC. I am thankful to all of them. A special thanks to Ranjan, Aritra, Sourav, Swagatam, Debashish, Manaswee, Neha, Pradeep, Divya, Brinta, Vijaya, Sumon, Anindita, Anaranya, Manoj, Sudip, Swastika, Rana for all the moments I spent with them and also for supporting me any time I required.

Lastly, I would like to acknowledge the most important people of my life, my parents, younger sister and family. Without their unconditional love and support all my efforts would have gone to vain. I am grateful to you all for whatever you gave me, and I dedicate my thesis to you.

PREFACE

Metal chalcogenides/oxy-chalcogenides present an important platform for exploring various intriguing properties. This Ph.D. thesis presents novel synthesis and investigations of detailed structure-property relationships of various metal chalcogenides/oxy-chalcogenides/topological quantum materials of varied structures and dimensionality for majorly exploring their thermoelectric properties. The thesis also includes results of ferroelectricity in ultra-thin 2D metal oxy-chalcogenides. Thesis work is divided into four parts (1-4), containing one, five, three and two chapters respectively.

Part 1 presents a brief introduction to thermoelectrics and recent advances in designing high-performance materials. Then, I have discussed intriguing crystal structure, lattice dynamics, ferroelectric instability and electronic structure of germanium telluride (GeTe) and addressed the key challenges in the way of optimizing the thermoelectric performance of GeTe. I have also discussed favourable electronic and phonon transport of layered chalcogenides and oxychalcogenides in designing high performance thermoelectrics materials. Further, I have discussed why topological quantum materials are potential candidates for thermoelectrics with detailed discussion about various types of quantum materials. I have presented a brief introduction to ferroelectrics and challenges of 2D-ferroelectrics. Lastly, I have described the experimental details including various synthesis and characterization techniques for metal chalcogenides/oxy-chalcogenides, and thermoelectric techniques.

Part 2 of my thesis is focused on the optimization of the thermoelectric performance of GeTe based materials, an alternative to lead chalcogenide. Recently, GeTe based materials have gained significant attention in terms of designing high performance thermoelectric materials and developing efficient thermoelectric power-generators owing to their favorable electronic –lattice structure as well as superior thermal and mechanical stability. Main constrains in the way of optimizing thermoelectric performance of GeTe are its high thermal conductivity, and low Seebeck-coefficient values. **Chapter 1** reports realization of the significant reduction of lattice thermal conductivity (κ_{lat}) and high average figure of merit (zT_{avg}) in GeTe by alloying with $AgSbSe_2$. $AgSbSe_2$ alloying in GeTe optimizes the carrier concentration and leads to the formation of hierarchical nano-structuring which brings out extremely low κ_{lat} in GeTe near to the theoretical minimum limit, κ_{min}. Successful applications of a thermoelectric material require simultaneous development of compatible n- and p-type counterparts. While the thermoelectric performance of p-type GeTe has been improved tremendously in recent years, it has been a challenge to find compatible n-type GeTe counterpart due to the prevalence of intrinsic Ge vacancies. In **chapter 2**, I have shown that alloying of $AgBiSe_2$ with GeTe results in an evolution in its crystal and electronic structures, resulting in n-type thermoelectric properties in cubic GeTe. I have demonstrated that the ambient rhombohedral structure of pristine GeTe transforms into cubic phase in $(GeTe)_{100-x}(AgBiSe_2)_x$ for $x \geq 25$, with concurrent change from its p-type electronic character to n-type character in electronic transport properties. **Chapter 3** reports a high

thermoelectric performance along with extremely high thermoelectric conversion efficiency in GeTe, enabled by distinct but complementary role of Bi and In co-dopants. In doping significantly enhances the Seebeck coefficient (S) of GeTe through the formation of resonance level, while Bi doping markedly reduces the κ_{lat} of GeTe due to the formation of extensive solid solution point defects and domain variants. In **chapter 4**, I have reported high thermoelectric performance in GeTe-x% BiSe and established the role of BiSe doping on modulating various thermoelectric parameters of GeTe. Further, I have investigated the power generating properties of GeTe-x% BiSe based single leg thermo-element. In all these previous chapters, I have shown that nano-structuring in GeTe shows great promise to minimize κ_{lat} and to improve its thermoelectric performance. However, nano-structuring also affects carrier mobility which is detrimental for electronic transport in GeTe. **Chapter 5** demonstrates an innovative strategy to minimize the κ_{lat} of GeTe by creating entropy driven extensive solid solution point defects with minimal effect on carrier mobility.

Quantum materials (*e*.g. topological insulators, topological crystalline insulators and topological semimetal), characterized by their nontrivial electronic surface states, have recently created a sensation in designing new thermoelectric materials. In **part 3**, I have investigated thermoelectric properties with detailed understanding of structure property relationship of few topological quantum materials from $(Bi_2)_m(Bi_2X_3)_n$ (x = Se/Te; m,n - integer) homologous family. **Chapter 1** reports realization of ultralow κ_{lat} and high *n*-type thermoelectric performance in BiSe, a weak topological insulator (WTI) from $(Bi_2)_m(Bi_2Se_3)_n$ homologous family. Detailed investigations of various aspects of the structure and lattice dynamics through measurements of low temperature heat capacity and first-principles density functional theoretical (DFT) calculations, indicates localized vibrations of Bi-bilayer is responsible for the unusually low κ_{lat} in BiSe. In **chapter 2**, we demonstrate simultaneous occurrence of intrinsically low κ_{lat} and high carrier mobility (μ) in *n*-type BiTe, facilitated by its unique dual topological quantum phases. BiTe being a WTI hosts layered hetero-structure and hence it exhibits low κ_{lat}; while BiTe, being a TCI with metallic surface states, possess high μ. In **chapter 3**, I have developed a general and facile wet chemical procedure for synthesizing ultra-thin 2D-nanosheets of various topological quantum materials with layered heterostructure such as BiSe, Bi_4Se_3 from $(Bi_2)_m(Bi_2Se_3)_n$ homologous family and performed extensive microscopic investigations to characterize their morphology. Further nanosheets of BiSe, Bi_4Se_3 with layered heterostructure, exhibit ultra-low κ_{lat} throughout the measured temperature (300 K -623 K) which is lower than that of Bi_2Se_3 with simple layered structure. Presence of metallic surface states also facilities to obtain high carrier mobility of ~ 100 -200 cm^2/Vs in the synthesized n-type nanosheets of the TQM.

Layered metal oxy-chalcogenides provide unique opportunities to study their transport and ferroelectric properties in nano-dimension because of their better thermal and environmental stability. In **part 4**, I have studied ferroelectric and thermoelectric properties of Bi_2O_2Se and BiCuSeO nanosheets respectively. In **chapter 1**, I have shown the emergence of an ordered ferroelectric ground state in ultrathin (~ 2 nm) single crystalline nanosheet of Bi_2O_2Se at room temperature. Free-standing ferroelectric

nanosheets, in which oppositely charged alternating layers are self-assembled together by electrostatic interactions, are synthesized by a simple, rapid and scalable wet chemical procedure at room temperature. The existence and origin of ferroelectricity in Bi_2O_2Se nanosheets is confirmed by various experiments and density functional theory calculations. **Chapter 2** presents a facile surfactant free low temperature solvothermal synthesis of few layered ultrathin BiCuSeO nanosheets for the first time. Nanosheets of BiCuSeO exhibit nanosheets exhibits a superior power factor and lower lattice thermal conductivity compared to that of the bulk sample.

TABLE OF CONTENTS

DECLARATION III

CERTIFICATE V

ACKNOWLEDGEMENTS VII

PREFACE IX

PART 1: A Brief Introduction to Thermoelectrics, Topological Quantum Materials and Ferroelectrics **1**

Summary... 3
1.1 Introduction to thermoelectrics 5
1.2 Thermoelectric parameters 6
1.3 Recent advnaces in TE materials research 10
1.3.1 Increment of the power factor 10
1.3.2 Reduction of the thermal conductivity 14
1.4 Thermoelectric materials of interest 21
1.4.1 Germanium telluride 21
1.4.2 Layered metal chalcogenides/oxy-chalcogenides 26
1.5 Topological quantum materials and its correlation with thermoelectrics 29
1.5.1 Topological insulators 30
1.5.2 Topological crystalline insulators 33
1.6 A brief introduction to ferroelectrics 35
1.7 Synthesis and characterizations 39
1.7.1 Synthesis 39
1.7.2 Characterizations 42
1.8 Thermoelectric measurements 50
1.8.1 Electronic transport 50
1.8.2 Thermal conductivity 52
1.8.3 Fabrication of thermoelement and measurement of power-conversion efficiency 53
1.9 Scope of the thesis 55
1.10 References 58

PART 2: Thermoelectric Properties of Germanium Telluride........................65

Chapter 1: High Average Thermoelectric Figure of Merit, Low Lattice Thermal Conductivity and Enhanced Micro-hardness in $(GeTe)_x(AgSbSe_2)_{100-x}$................67

Summary 69
1.1 Introduction 71
1.2 Methods 72

1.3 Results & discussion 73
1.4 Conclusions 84
1.5 References 85

Chapter 2: Realization of both *n*- and *p*-type GeTe Thermoelectrics: Electronic Structure Modulation by $AgBiSe_2$ Alloying 87
Summary 89
2.1 Introduction 91
2.2 Methods 93
2.3 Results & discussion 97
2.4 Conclusions 110
2.5 References 110

Chapter 3: Realization of High Thermoelectric Figure of Merit in GeTe by Complementary Co-doping of Bi and In 113
Summary 115
3.1 Introduction 117
3.2 Methods 118
3.3 Results & discussion 124
3.4 Conclusions 141
3.5 References 141

Chapter 4: Realization of High Thermoelectric Performance in GeTe-x%BiSe: Synergistic Effect of Carrier Concentration Optimization and Low Thermal Conductivity 145
Summary... 147
4.1 Introduction 149
4.2 Methods 150
4.3 Results & discussion 153
4.4 Conclusions 165
4.5 References 165

Chapter 5: Low Thermal Conductivity and High Thermoelectric Performance in $(GeTe)_{1-2x}(GeSe)_x(GeS)_x$: Competition between Solid Solution and Phase Separation 167
Summary 169
5.1 Introduction 171
5.2 Methods 172
5.3 Results & discussion 174
5.4 Conclusions 190
5.5 References 191

PART 3: Thermoelectric Properties of Topological Quantum Materials 193

Chapter 1: Localized Vibrations of Bi Bilayer Leading to Ultralow Lattice Thermal Conductivity and High Thermoelectric Performance in Weak Topological Insulator *n*-type BiSe 195
Summary 197
1.1 Introduction 199

1.2 Methods ... 201
1.3 Results & discussion ... 203
1.4 Conclusions ... 215
1.5 References ... 216

Chapter 2: Intrinsically Low Thermal Conductivity and High Carrier Mobility in Dual Topological Quantum Material, *n*-type BiTe ... 219
Summary ... 221
2.1 Introduction ... 223
2.2 Methods ... 224
2.3 Results & discussion ... 227
2.4 Conclusions ... 239
2.5 References ... 240

Chapter 3: 2D Nanosheets of Topological Quantum Materials from Homologous $(Bi_2)_m(Bi_2Se_3)_n$ Heterostructures: Synthesis and Ultralow Thermal Conductivity ... 243
Summary ... 245
3.1 Introduction ... 247
3.2 Methods ... 249
3.3 Results & discussion ... 252
3.4 Conclusions ... 263
3.5 References ... 263

PART 4: Ferroelectric and Transport Properties of Layered Bismuth Oxy-chalcogenides ... 267

Chapter 1: Room Temperature Ferroelectricity in Ultrathin Free-standing 2D-Nanosheets of Bi_2O_2Se ... 269
Summary... ... 271
1.1 Introduction ... 273
1.2 Methods ... 274
1.3 Results & discussion ... 278
1.4 Conclusions ... 288
1.5 References ... 288

Chapter 2: Transport Properties of Ultrathin Few Layer Oxy-chalcogenide BiCuSeO Nanosheets ... 293
Summary... ... 295
2.1 Introduction ... 297
2.2 Methods ... 299
2.3 Results & discussion ... 301
2.4 Conclusions ... 307
2.5 References ... 307

List of Publications ... 309
Biography ... 311

PART 1

A Brief Introduction to Thermoelectrics, Topological Quantum Materials and Ferroelectrics

Chapter 1

A Brief Introduction to Thermoelectrics, Topological Quantum Materials and Ferroelectrics[†]

Summary

Heat dissipation being a natural by-product of every form of utilized energy, thermoelectrics (TE) constitute a viable means of efficient energy management in near future, by converting the untapped heat into electrical energy On the other hand, the discovery of topological quantum materials (TQM) (e.g. topological insulator, topological crystalline insulator, topological semimetal) with unique metallic surface states has added a new dimension in the field of electronics and spintronics. Interestingly, most of the TQM are also good candidates for TE because both demand similar material features such as heavy constituent elements, narrow band gap, and strong spin-orbit coupling. Ferroelectrics, a *vital branch of functional materials with spontaneous switchable electric polarization, are one of the most studied system due to their wide range of applications including TE. Presence of ferroelectric instability in TE materials such as in GeTe are proven to be beneficial in lowering their lattice thermal conductivity and hence tuning their TE performance. Recently, various metal chalcogenides/oxy-chalcogenides are getting attention as potential candidates for 2D-ferroelectrics which are much coveted system due to their broad use in nanodevices. In a nut-shell metal chalcogenides/oxy-chalcogenides present a common platform for exploring thermoelectrics, quantum materials and ferroelectrics. This chapter highlights a brief introduction to (a) thermoelectrics and its recent advances, (b) thermoelectric materials of interest for the thesis, (c) topological quantum materials and its correlation with thermoelectrics and (d) ferroelectricity. In the last part of this chapter is focused on a general discussion of synthesis, characterizations and thermoelectric measurements of metal chalcogenide/oxy-chalcogenides.*

[†]*A part of this chapter has been published/communicated in* (a) *World Scientific Publications* **2019,** 350-375 (Book chapter); (b) *Chem. Mater.* **2018**, *30,* 5799-5813. (Perspective); (c) *J. Solid State. Chem.* **2019**, *275,* 103-123 (Review article) and (c) *J. Mater. Chem. A* **2020**, under review (Review article).

1.1 Introduction to thermoelectrics

Increasing global demand for energy is causing a dramatic rise of social and political unrest. Fossils fuels, the primary source of energy are going to be exhausted in near future; so it is the prime time to think of some alternative, sustainable energy sources. Moreover ~ 70% of the utilized energy is being lost in form of waste heat. One of the effective way to consummate the global need for energy production and management is to utilize the enormous amount of unused waste heat, which is produced in home heating, automotive exhaust, and industrial processes, into useful electrical energy by using thermoelectric (TE).[1–5] Thermoelectric (TE) materials, being capable of direct and reversible conversion of heat into electricity, are thought to be a key solution for future global energy management. Thermoelectric (TE) module consists of both *p*-type and *n*-type semiconductors connected through metallic conducting pad.[6–8] A TE module or device comprises an array of TE couples, which are arranged electrically in series and thermally in parallel. Both power generation and refrigeration can be accomplished as shown in Figure 1.1a. Advances in thermoelectric could similarly enable the replacement of compression-based refrigeration with solid-state Pettier coolers. As thermoelectric generators are all solid state devices without any mobile parts, they are suitable for small-scale power generation and distribution. Exhaust from domestic heating, automobiles and industrial produce a large amount of unused waste heat that could be converted to electricity by using thermoelectric devices. For the past 40 years, thermoelectric generators are consistently providing power in remote terrestrial and extra-terrestrial locations (radioisotope thermoelectric generators, RTGs in Voyager 1, Voyager 2, Galileo, Ulysses, Cassini, and New Horizons spacecraft).[9,10] Efforts are already underway to mount thermoelectric device in exhaust stream of cars to utilize the waste heat, thereby improving fuel efficiency Recently large multinational car companies like BMW, Ford, Renault and Honda have shown their interest in exhaust heat recovery, developing systems that make use of thermoelectric generators.[11] The reliability and stability of thermoelectrics makes them suitable for wider applications such as sub-ambient cooling of infrared detectors and thermal management systems in microprocessors etc.[12,13] More recently, research on the topic of solar-thermoelectrics is gaining attention where the IR-part of the solar spectrum is utilized for thermoelectric-solar power generation.[14]

Thermoelectric phenomena were first discovered at the beginning of the 19th century by the German scientist, Thomas J. Seebeck, who observed the deviation of a compass needle when keeping the two junctions of dissimilar metals at different temperatures.[4,15] However, Seebeck believed it to be a magnetic phenomenon and tried to correlate the Earth's magnetism with the temperature difference between the equator and the Poles. Later, it was realized that a "Thermoelectric Force" induced an electrical current, which deflected the magnet following Ampere's law. More specifically, the temperature difference (ΔT) produces an electric potential (ΔV) which drives an electric current in a closed circuit. The proportionality constant is known as the Seebeck coefficient (S), and frequently referred to "thermopower" even though it is more related to potential than power. Shortly thereafter, in 1834, a complementary effect was discovered by French scientist Jean C. A. Peltier who observed the temperature change in the vicinity of the junction between dissimilar conductors when a current passed.[13] However, he was unable to realize the fundamental nature of his observations or relate the effect to the findings of Seebeck. The true nature of the Peltier effect was explained by the Russian scientist, Lenz in 1838. He stated that heat can be absorbed or generated at a junction between two conductors, depending upon the direction of the current flow. The Peltier coefficient, Π can be described as the ratio of heat flow (Q), to applied current (I), ($\Pi = \frac{Q}{I}$). In 1851 W. Thomson (Lord Kelvin) established the relationship between the Seebeck and Peltier coefficients and predicted the existence of a third thermoelectric effect, the Thomson effect, which describes the heating or cooling in a single homogeneous conductor when a current passes along it in the presence of a temperature gradient.

1.2 Thermoelectric parameters

The possible use of thermoelectric phenomena in electricity generation was first considered in the year of 1885 by Rayleigh who first calculated, although incorrectly, the efficiency of a thermoelectric generator.[2,8,15] In 1909, Altenkirch analysed the efficiency of a thermoelectric generator and derived an expression for the load resistance that yields the highest efficiency in a TE generator. Altenkirch's paper described the role of thermal conductivity, κ, and electrical conductivity, σ on its power conversion efficiency. In 1947, Telkes presented an extensive historical review of TE generators, including consideration

of desirable properties, but with no discussion of a single figure of merit. Later, *Ioffe* introduced the figure of merit, zT as a part of TE efficiency.[8] The thermoelectric conversion efficiency for a material requires both high zT values and a large temperature difference across the thermoelectric materials, as given by the following relation:[3]

$$\eta_{TE} = \eta_c \frac{\left(\sqrt{1+zT} - 1\right)}{\left(\sqrt{1+zT} + \frac{T_C}{T_H}\right)} \tag{1.1}$$

where η_c, T_H and T_C are Carnot Efficiency, the temperatures of the hot and cold ends and zT, the dimensionless figure of merit is expressed as

$$zT = \frac{\sigma S^2}{\kappa} T \tag{1.2}$$

Where σ, S, κ and T are the electrical conductivity, Seebeck coefficient, thermal conductivity and absolute temperature, respectively.[2–4]

Figure 1.1. *(a) Schematic illustrations of a thermoelectric (TE) module for active power generation-Seebeck effect (left) and refrigeration-Peltier effect (right). (b) TE figure-of-merit (zT) as a function of temperature and year illustrating important milestones. (b) Reproduced with permission from ref. 1 © 2016 American Chemical Society.*

To maximize the thermoelectric figure of merit (zT) of a material, high electrical conductivity, a large Seebeck coefficient and a low thermal conductivity are needed. The quantity σS^2 is defined as power factor and is the key to achieve high thermoelectric performance. A large power factor means the generation of large voltage and a high current. For high σS^2, a material is needed to have high electrical conductivity (σ) and large Seebeck coefficient (S). For metals or degenerate semiconductors (parabolic band, energy-

independent scattering approximation),[3] the Seebeck coefficient is proportional to the effective mass (m^*) and temperature, and inversely proportional to the charge carrier concentration (n_H), as seen in equation 1.3.

$$S = \frac{8\pi^2 k_B^2}{3eh^2} m^* T \left(\frac{\pi}{3n_H}\right)^{2/3} \tag{1.3}$$

where k_B is the Boltzmann constant, h is the Planck constant, and e is the electron charge. Thus, a large Seebeck coefficient indicates a large effective mass which is equivalent to a large density-of-states (DOS) or flat bands at the Fermi level. High electrical conductivity requires a large mobility (μ) and a large carrier (electrons or holes) concentration (n_H), as seen in equation 1.4.

$$\sigma = ne\mu \tag{1.4}$$

Where mobility, μ can be defined by the following expression:

$$\mu = \frac{e\tau}{m^*} \tag{1.5}$$

Here τ is the relaxation time and m^* is the carrier effective mass.[1]

On the other hand, thermal conductivity (κ) has two parts: the lattice or phonon contribution (κ_{lat}) and the electronic contribution (κ_{el}) (Equation 1.6).

$$\kappa \quad = \kappa_{el} + \kappa_{lat} \tag{1.6}$$

κ_{el} is proportional to the electrical conductivity through the Wiedemann–Franz law.

$$\kappa_{el} = L\sigma T \tag{1.7}$$

where L is the Lorenz Number. For free electrons, it is 2.45×10^{-8} $W\Omega K^{-2}$. The Lorenz number varies with the material's carrier concentration and can be reduced by as much as 20% from the free-electron value for the materials with low-carrier-concentration.[1,3] From equation 1.7, it is clear that increasing electrical conductivity is detrimental to realize high zT because of simultaneous enhancement in electrical and thermal conductivity.

Since κ_{el} is proportional to σ via Wiedemann–Franz law law (Equation 1.7), the only way to achieve low thermal conductivity (κ) is to manipulate the lattice thermal

conductivity (κ_{lat}). According to the kinetic theory of phonon 'gas', the lattice thermal conductivity of a solid material can be described as[1,16,17]

$$\kappa_{lat} = \frac{1}{3} c_V \vartheta l \tag{1.8}$$

where c_V is the specific heat capacity at constant volume, l is phonon mean free path (MFP, defined as the average distance traveled by phonons between successive scatterings), and ϑ is the average velocity of sound. Unlike c_V and l, the velocity of sound (ϑ) is material-dependent and varies very little with changes in temperature, morphology, or doping. At high temperatures ($T >> \Theta_D$, Debye temperature), since the energy carried by each atom in bulk materials approaches to $3k_BT$, specific heat reaches the Dulong–Petit limit ($3k_B$ per atom), resulting in the difficulty for manipulating the specific heat of thermoelectric materials. Thus, above Debye temperature (Θ_D), κ_{lat} primarily depends on phonon mean free path, l. Phonon mean free path is determined by rate of a) phonon-phonon scattering and (b) scattering with grain-boundaries or static impurities. In case of semiconductors when carrier concentration is lesser than 10^{19} cm^{-3}, κ_{lat} usually dominates the κ. Moreover, acoustic phonons usually dominate κ_{lat} over optical phonons because of their higher group velocities, $\vartheta_i = \frac{\partial \omega}{\partial k}$ (here i refers to polarization of acoustic phonons i.e., longitudinal (LA) or transverse (TA1, TA2)). Since phonon mean free path of any material is limited by inter atomic distance, minimum the lattice thermal conductivity, κ_{min} cannot be reduced lower than that of the amorphous limit, as defined by Cahill[18,19]

$$\kappa_{min} = \frac{1}{2} (\frac{\pi}{6})^{\frac{1}{3}} k_B V^{-(\frac{2}{3})} (2\vartheta_t + \vartheta_l) \tag{1.9}$$

where V is average volume per atom, k_B is the Boltzmann constant, ϑ_t and ϑ_l are the transverse and longitudinal sound velocities.

1.3 Recent advances in TE materials research

Thermoelectric have always been a materials design problem relating complicated tuning of structure-property relationships in inorganic solids through principles of solid state chemistry. Several years ago Slack and thereafter Mahan has portrayed the chemical characteristics of materials those might be proven to be good candidates for a TE application. According to them, narrow-band gap semiconductors (e.g., $E_g \approx 10\ k_BT$ or $\approx$ 0.25 eV at 300 K) with high-mobility carriers are the ideal candidate for TE application.[3,4,20] In semiconductors, the Seebeck coefficient and the electrical conductivity (both in the numerator of zT) depend on the doping level and chemical composition. In addition to this, material's κ_{lat} should be low. Therefore, to design a high performance TE material, these quantities must be optimized. The major obstacle lies in the optimization of all of these parameters together in a single material due to their strong interdependence.[2,3] However, in the last few years, numerous efforts have been devoted to decoupling and synergizing individual TE parameters. Approaches to improve the power factor includes enhancement of the Seebeck coefficient through the formation of resonance level in the electronic bands[21–25] and convergence of degenerate electronic band valleys[26–30] through alloying and carrier engineering. Significantly low lattice thermal conductivity has been achieved via phonon scattering by solid solution point defects,[31–33] second phase nanoprecipitates,[34–37] meso-scale grain boundaries[38,39] and intrinsic bond anharmonicity.[17,40,41] In the following section, I will summarize the most recent approaches of designing high-performance TE materials.

1.3.1 Increment of the power factor

Power factor (σS^2) is a purely electronic property, governed by materials' electronic structure and scattering mechanism. Strategies to enhance power factor include: a) engineering of carrier-concentration (n_H) through chemical doping, b) enhancement of the effective carrier mass (m^*) and Seebeck coefficient (S) via the convergence of multiple valence/conduction band extrema,[26–30] or distortion of the density of states near Fermi level by resonance impurity levels,[21–25] and c) enhancement of carrier mobility (μ) by modulation-doping[1,42]

1.3.1.1 Carrier concentration optimization

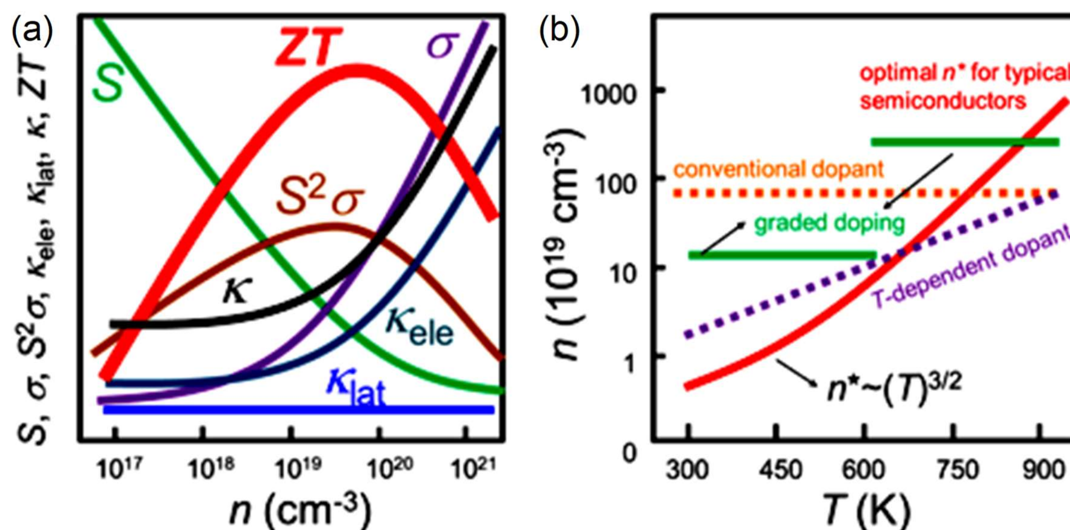

Figure 1.2. *(a) Schematic diagram showing the dependence of ZT (~zT) and its parameters (electrical conductivity σ, Seebeck coefficient S, power factor* $S^2\sigma$*, electronic thermal conductivity* κ_{el}*, lattice thermal conductivity* κ_{lat} *and total thermal conductivity, κ) on carrier concentration n. (b) Strategies for stabilizing the optimal carrier concentration. Reproduced with permission from ref. 1 © 2016 American Chemical Society.*

The fundamental challenge of designing high-*zT* thermoelectric materials is strong interdependence of *σ*, *S* and *κ* through carrier concentration, *n* (Figure 1.2) which can be optimized by controlling the doping level. The maximum *zT* value arises in the carrier concentration range of 10^{19}-10^{21} cm^{-3}, which falls in between metals and semiconductors - that is concentration typically found in heavily doped semiconductors (i.e. degenerate semiconductor).[4] However, carrier concentration (n_H) increases rapidly with rising temperature, following the power law of $T^{3/2}$. Although conventional doping is effective to tune room temperature carrier optimization, it is difficult to achieve optimum carrier concentration at high temperature. Thus the maximum theoretical *zT* cannot be fully realized at every working temperature. An effective solution to this issue is the use of functionally graded doping, by integrating two or multiple segments with dissimilar n_H. The modifications to the conventional doping method to include temperature-dependent doping behaviour are helpful to acquire larger average *zT* values which are especially important for technological applications.

1.3.1.2 Resonance level

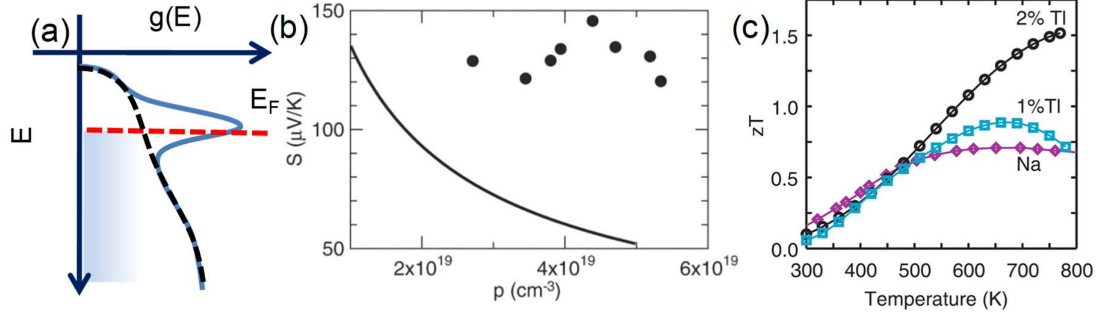

Figure 1.3. *(a) Schematic diagram of resonance level in the valence band. Schematic diagram of density of state (DOS) of the valence band of pristine sample (dotted black line). Tl-doped PbTe shows asymmetric distortion of DOS (blue line) near Fermi level. (b) Pisarenko relation of Seebeck coefficient vs hole concentration, p for PbTe (solid line) at 300 K compared to the results on Tl-PbTe sample. Significantly large S value in Tl-doped PbTe confirmed the presence of resonance level. (c) The temperature dependent zT values for $Tl_{0.02}Pb_{0.98}Te$ (black circles) and $Tl_{0.01}Pb_{0.99}Te$ (blue squares) compared to that of a reference sample of Na-PbTe (purple diamonds). Figure (b) and (c) are reproduced with permission from ref. 21 © 2008 AAAS.*

The concept of resonance level was first proposed in 1950.[43] Resonance level originates from the coupling between electrons of a dilute impurity with those of the valence or conduction band of the host solid near its Fermi level.[44] Thus, resonance dopant creates an excess density of states near the valence or the conduction band edge of the host compound (Figure 1.3a) and results in higher effective mass, m^* and thereby enhances Seebeck coefficient, according to Mott expression (Equation 1.10).[3]

$$S = \frac{\pi^2}{3}\frac{k_B}{q}k_BT\left\{\frac{d[ln(\sigma(E))]}{dE}\right\}_{E\,=\,E_F}$$
$$= \frac{\pi^2}{3}\frac{k_B}{q}k_BT\left\{\frac{1}{n_H}\frac{dn_H(E)}{dE}+\frac{1}{\mu}\frac{d\mu(E)}{dE}\right\}_{E\,=\,E_F} \quad (1.10)$$

Here, $\sigma(E)$ is the electrical conductivity determined as a function of the band filling or Fermi energy, E_F ($\sigma(e) = n_H(E)q\mu(E)$) and $n_H(E)$ ($n_H(E) = g(E)f(E)$), the carrier density at the energy level, E (here q is the carrier charge, and $\mu(E)$ is the mobility as a function of energy, $f(E)$ is the Fermi function, $g(E)$ is density of state).

When electronic scattering is independent of energy, $\sigma(E)$ is just proportional to the density of states (DOS) at E. Based on the above expression it is clear that the system with

rapid change in DOS near E_F is expected to have large Seebeck. Pisarenko plot represents the dependence of Seebeck on carrier concentration. A significantly higher S value than what a Pisarenko plot gives the indication of resonance level formation (Figure 1.3b).[21] Group-III (mainly Al, In and Tl) dopants form resonance level in PbTe.[44] Heremans, *et al*. demonstrated experimentally that Tl doping improves S of PbTe by resonance level formation and thereby achieved the double value of zT, as seen in Figure 1.3c.[21]

1.3.1.3 Convergence of electronic band valleys

Multiple pockets in valence or conduction band extreme give rise to high Seebeck coefficient because these valleys (separate pockets of Fermi surface with the same energy) have the effect of producing large effective mass (m*) without explicitly reducing μ, as seen in equation 1.11.[26–30]

$$m^* = N_V^{2/3} m_b^* \qquad (1.11)$$

Where N_V represents orbital degeneracy and m_b^* represents single valley density of state effective mass of degenerate valleys. Thus, effective doping to energetically align the electronic bands for a higher degree of band degeneracy lies at the core of the band-convergence scheme. The aim is to enhance the Seebeck coefficient without substantially degrading the σ. When the system is heavily doped, overall effective mass can be enhanced through carrier redistribution to multiple valleys, thus results in high Seebeck coefficient. Since carrier mobility will be unaffected in this process, valence band convergence gives rise to significantly high σS^2 and zT in carrier optimized system.

Pei *et al.* have demonstrated the band convergence of at least 12 valleys in doped $PbTe_{1-x}Se_x$ alloys, leading to an extraordinarily high zT value of 1.8 at about 850 K, as seen in Figure 1.4.[26] Alloying Se reduces the energy difference between the L and Σ bands of the PbTe making the two bands effectively converged. Hence enhancement in N_V from 4 (for L band) to 12 (for Σ band) results in an increase in m^* and Seebeck. A similar result was observed in PbTe, after it was alloyed with wide band gap chalcogenides (MgTe, CaTe, BaTe).

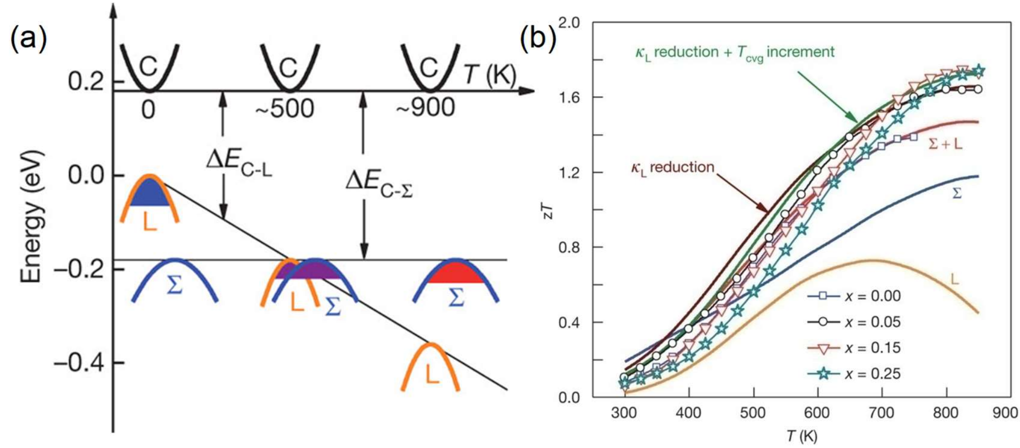

Figure 1.4 *(a) Relative energy of the valence bands in $PbTe_{0.85}Se_{0.15}$. At, 500 K the two valence bands converge, resulting in contributions from both the L and Σ bands in the transport properties. (b) Temperature dependent zT of p-$PbTe_{1-x}Se_x$ materials doped with 2 atom % Na. Adopted with permission from ref. 22 © 2011 Nature Publishing Group.*

Recently, an innovative strategy of slight-symmetry reduction has been adopted to realize band convergence in GeTe. Detailed electronic structure analysis of GeTe demonstrate that rhombohedral distortion of GeTe along the [111] crystallographic direction (along the L point of BZ) splits up the 4 L pockets of cubic GeTe ($Fm\overline{3}m$) into 3 L + 1 Z pockets in rhombohedral GeTe (*R3m)* and 12 Σ pockets of cubic GeTe into 6 Σ + 6 η pockets in rhombohedral GeTe.[45,46] Thus manipulation of the degree of the rhombohedral distortion (also referred as slight symmetry reduction) can result in band convergence of L and Σ bands. In a recent report by Li *et al.*, it has been shown that slight symmetry reduction of cubic GeTe towards rhombohedral symmetry by Pb and Bi doping causes an effective valence band (L and Σ bands) convergence, resulting in a high zT of ~2.4 in rhombohedral phase of Pb and Bi codoped GeTe at 600 K.[45,46]

1.3.2 Reduction of the thermal conductivity

As discussed earlier in Eq^n 1.8, lattice thermal conductivity of bulk materials is provided by $\kappa_{lat} = \frac{1}{3}C_V v_g^2 \tau$.[17] Thus, to minimize the κ_{lat}, one has to engineer materials which decrease the specific heat (C_V), the group velocity (v_g) or the phonon relaxation time (τ).

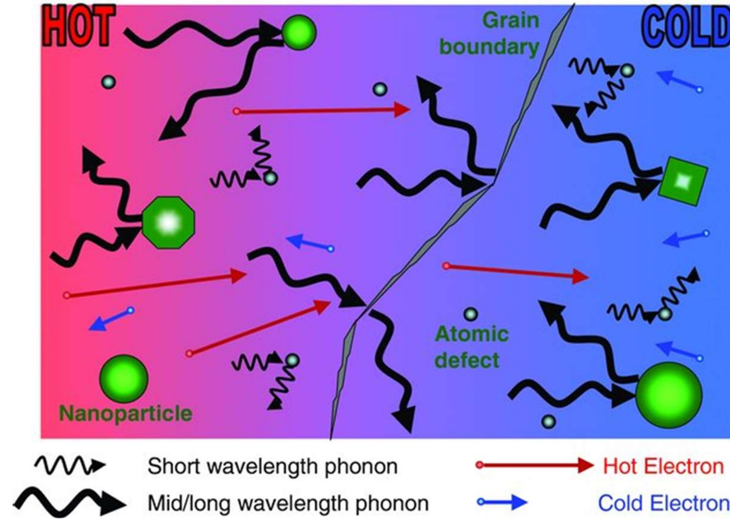

Figure 1.5. *Schematic illustration of phonon-scattering by atomic defects (short wave length phonons), nanoparticles (mid-long wave length phonons) and grain boundaries (long wave length phonons) in a solid (lower panel). Reproduced with permission from ref. 47 © 2010 Wiley.*

Typically in thermoelectrics, the phonon relaxation time is the most focussed variable to tweak and achieve desirable κ_{lat} via extrinsically introducing 0D point defects, 1D dislocations or 2D grain boundaries or fine precipitates (Figure 1.5).[16,47] Each of these defects enhances the phonon-scattering process and decreases the relaxation time (τ) and thereby decreasing the κ_{lat}. Each of the aforementioned processes has their own frequency (ω) dependence. For example, the 0D point defects scatters the high frequency phonons ($\tau_{PD} \sim \omega^{-4}$); 1D dislocation scatters the mid frequency phonons ($\tau_{DC} \sim \omega^{-3}$ for dislocation cores and $\tau_{DS} \sim \omega^{-1}$ for dislocation strains); 2D interface scattering originating from grain boundaries or precipitates are effective for the low frequency phonons ($\tau_{inter} \sim \omega^{0}$). The umklapp process which is ubiquitous has a relaxation time, $\tau_U \sim \omega^{-2}$, thus being effective in scattering the phonons of all frequencies. Callaway devised a phenomenological model considering all the contributions arising from the microstructural effects on phonon scattering at various length scales. The model which is given as [16,47,48]

$$\kappa_{lat} = \frac{k_B}{2\pi^2 v_g}\left(\frac{k_B T}{\hbar}\right)^3 \int_0^{\theta_D/T} \tau_C(x)\,\frac{x^4 e^4}{(e^x-1)^2}\,dx \tag{1.12}$$

acts as a guide to quantitatively access the contributions arising from each micro-structural effects. k_B in equation (7) corresponds to Boltzmann's constant; ђ, T and τ_C denotes Plank's

constant, absolute temperature and total relaxation time respectively. τ_C corresponds to the individual relaxation time via the relation $\tau_C^{-1} = \tau_U^{-1} + \tau_{PD}^{-1} + \tau_{DS}^{-1} + \tau_{DC}^{-1} + \tau_{inter}^{-1} + \ldots$, where τ_U, τ_{PD}, τ_{DS}, τ_{DC} and τ_{inter} corresponds to relaxation times arising from the contributions of Umpklapp scattering, point defects, dislocation strain, dislocation cores and interface scattering respectively.

Apart from the extrinsic approaches to reduce the thermal conductivity, rational unearthing of materials with intrinsically low lattice thermal conductivity is an intriguing and efficient prospect.[17] Since electrons and phonons propagate within the same sublattice, suppressing the phonon transport also handicaps the electron mobility. Thus materials with innate κ_{lat} offer an independent control to achieve high TE performances without having to compromise on the electrical mobility which is beneficial in maintaining high power factor.[17] In this section, we have touched upon several techniques to reduce the κ_{lat} of the materials using extrinsic approaches such as alloying and nano-structuring as well as the intrinsic approaches.

1.3.2.1 Phonon-phonon scattering

There are two types of phonon–phonon scattering process - normal process (N-process), and Umklapp process (U-process). While N-processes don't directly contribute to thermal resistance, U-processes hinder thermal transport. The effectiveness of U-processes in inhibiting heat transfer depends on 1) the scattering cross-section or frequency of collisions and 2) the amount of momentum loss during each collision. Since the U-process depends on the phonons density, it becomes more dominant as the temperature is increased, and the phonon mean free path corresponding to U-process is inversely proportional to temperature, $\sim 1/T$ ($T >> \Theta_D$). For ideal crystal, U-scattering is the dominant process for thermal resistivity at high temperatures.

1.3.2.2 Point defect phonon scattering

Introduction of lattice imperfections (point defects) in the host lattice (doping or alloying) is a well-known strategy of decreasing the κ_{lat} via scattering of short-wavelength phonons.[31–33] According to the thermal conductivity model developed by Callaway[49] and Klemens,[50] reduction of κ_{lat} can be attributed to the combined effect of mass contrast and

strain field fluctuations. The degree of κ_{lat} reduction can be evaluated by the following expression of scattering parameter (Γ):

$$\Gamma = x(1-x)[\left(\frac{\Delta M}{M}\right)^2 + \varepsilon\,(\frac{\Delta a}{xa})^2] \tag{1.13}$$

where ε is a phenomenological parameter related to the material's Grüneisen parameter γ, M and a are the molar mass and lattice constant of the alloy, ΔM and Δa are the differences in mass and lattice constant between the two constituents. From equation 1.13, one can conclude that to maximize Γ and achieve the lowest κ_{lat}, it is necessary to have (1) a high doping fraction x, (2) a large mass difference between the dopant and the host element (ΔM) creating disorder in the lattice, and (3) a significant lattice mismatch (Δa) between the disordered phase and the host phase. Thus, solid solutions of $PbTe_{1-x}Se_x$ has lower κ_{lat} as compared to that of pure PbTe (Figure 1.6a).[51] Although most of the notable binary alloying is governed by enthalpy of the system, Kanatzidis and his co-workers argued that ternary alloying of $(PbTe)_{1-x-y}(PbSe)_x(PbS)_y$ is driven by the configurational entropy.[52] A low κ_{lat} of 0.5 $Wm^{-1}K^{-1}$ have been achieved in $(PbTe)_{1-2x}(PbSe)_x(PbS)_x$ system owing to strong point defect scattering.

1.3.2.3 Nanostructuring

An innovative way to inhibit the transport of phonons having mid and longer wavelength is via introducing nano-scaled defects into the matix.[47] An effective scattering of mid and low frequency phonons would be possible only if the nano-scaled defects are distributed uniformly and are of similar size to these phonons, typically upto to dozens of nanometres. Quite a few approaches have been undertaken to achieve nanoscale in homogeneity viz. external addition of guest phase via chemical of mechanical mixing,[53] and in-situ precipitation of second phase via kinetically or thermodynamically driven processes.[47,54,55] In-situ approach is the widely used due to even dispersion of the nano-precipitates which are also favourable for charge transport. Spinodal decomposition,[35] and nucleation and growth,[56] matrix encapsulation[34,57] are the most common approaches for producing in-situ nanostructures in bulk matrix.

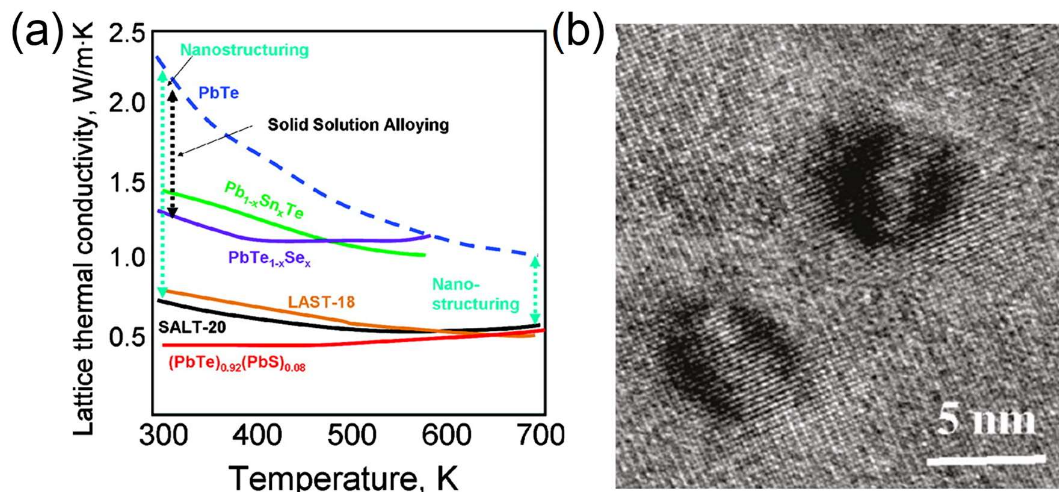

Figure 1.6. *(a) Lattice thermal conductivity (κ_{lat}) as a function of temperature for various PbTe-based alloys and nanostructured samples. (b) High resolution transmission electron microscopy of a LAST-18 sample. Adopted with permission from ref. 51 © 2010 American Chemical Society.*

Since the well-known TE materials such as PbTe, SnTe and GeTe have a wide array of phonons with mean free paths of 1-100 nm, nanostructuring is proved to be effective pathway to reduce the κ_{lat} of these compounds. Replacing Pb in PbTe with two aliovalent atoms (i.e., Ag and Sb) to form $AgPb_mSbTe_{m+2}$ (LAST-m) shows a substantial decrease in the κ_{lat} (Figure 1.6). Particularly LAST-18 shows a significant reduction in the κ_{lat} (0.5 $Wm^{-1}K^{-1}$at 700 K) as compared to PbTe.[55] It has been argued that the very low κ_{lat} of the LAST system was attributed to the spontaneous formation of nanostructured second phases in the PbTe matrix (Figure 1.6b).

1.3.2.4 Mesoscale grain boundaries

So far I have discussed about κ_{lat} reduction by scattering of low- and medium-mean free path phonons, which carry ~75 % of the transported heat. To further reduce κ_{lat} it is necessary to scatter phonons with long mean free path (~0.1-1 μm) (Figure 1.5). Necessary approaches involve the formation of crystal defects at submicrometer length scale (mesoscale, grain size ~0.1-3 μm), which can be engineered into materials through careful powder processing.

Rowe *et al.* investigated the thermal conductivities of SiGe alloys with different grain sizes and compared them with that of their single crystals.[58] They showed that grains

with relatively small sizes (<5 μm) could scatter phonons strongly (~20% reduction of thermal conductivity with respect to the single crystal). This work highlights the importance of mesoscale grains in impeding the phonon transport of bulk materials and points to further research to better understand mesoscale effects.

1.3.2.5 All-scale hierarchical architectures

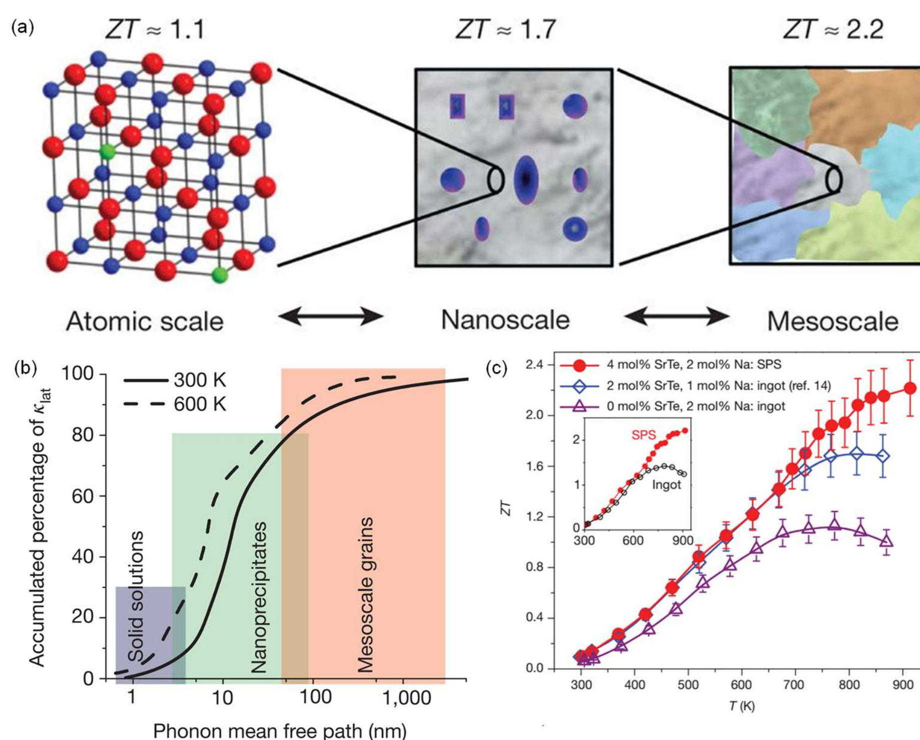

Figure 1.7. *(a) Maximum achievable ZT (~zT) values for the respective length scales: the atomic scale (alloy scattering: red, Te; blue, Pb; green, dopant) the nanoscale (PbTe matrix, grey; SrTe nanocrystals, blue) to the mesoscale (grain-boundary scattering). (b) Contributions of phonons with different mean free paths to the cumulative* κ_{lat} *value for PbTe. (c) Temperature dependent thermoelectric figure-of-merit ZT (~zT) for the all-scale hierarchical architecture PbTe system. Reproduced with permission from ref. 39 © 2012 Nature Publishing Group.*

When point defects, nanostructuring, and meso-structuring are all combined into a single thermoelectric material, it is termed as all-scale hierarchical architectures (Figure 1.7). Thermal conductivity in crystalline materials can be significantly decreased by defects present at different length scales with a broad range of wavelengths and mean free paths. Theoretical calculations suggest that, in PbTe, over 50% of the κ_{lat} value comes from the

contribution by phonons with MFP less than 1 nm, which can be scattered significantly by atomic-scale point defects. The remaining contribution to κ_{lat} is almost equally divided between phonon modes with MFP of 1−10 nm and phonon modes with MFP 10−1000 nm, (Figure 1.7), which can be notably impeded by nanoscale precipitates and mesoscale grains, respectively.[38,39] Biswas and coworkers have demonstrated the substantial suppression of lattice thermal conductivity at high temperature in the PbTe-SrTe system that led to a record high zT of ~2.2 at 915 K in spark plasma sintered samples.[39] This is the result of introducing phonon scattering at all-length scales in a hierarchical fashion from atomic scale doping and endotaxial nanostructuring to mesoscale grain boundary engineering.

1.3.2.6 Intrinsic low thermal conductivity

In addition to the above-mentioned strategies, materials having soft optical phonon modes exhibit low lattice thermal conductivity. In spite of having low phonon group velocity, soft optical phonons can interact with heat carrying acoustic phonons and cause additional scattering of acoustic phonons, indirectly affecting the lattice thermal conductivity.[17] Theoretical and experimental studies demonstrate that the strong anharmonicity in PbTe is closely associated with ferroelectric instability,[59] resulting in a strong acoustic–optical coupling and a significantly reduced phonon relaxation time.

The above strategies for reducing the lattice thermal conductivity give emphasis to the reduction of the phonon relaxation time (τ) through the enhancement of phonon scattering. Besides these conventional approaches, solids with intrinsically low κ_{lat}, arising from complex crystal structures, part-crystalline part-liquid state rattling modes,[60–62] superionic substructures with liquid-like cation disordering,[63,64] resonant bonding,[65] lattice anharmonicity due to lone pair[66,67] and anisotropic layered crystal structure,[68] has drawn huge attention of the thermoelectric community. Ultralow thermal conductivity in these materials arises either from low sound velocity or from low specific heat.

1.4. Thermoelectric materials of interest

1.4.1 Germanium telluride

In recent years, plenty of new TE materials have been identified with satisfactory TE properties. TE materials which are used for mid-temperature (500 – 800 K) power conversion, are particularly interesting since the major share of the waste heat in industry and automobile exhaust is within this range.[9] Lead chalcogenides, such as PbTe and other lead chalcogenides has been raised to the peak *via* synergistic effect of band engineering (resonance levels formation, band convergence and bands alignment)[21,26] and nano/microstructure manipulation in all scaled hierarchical architectures.[39,69,70] However, environmental concern about Pb, has slowed down the progress of its mass-market application. Hence, the solid-state chemist and TE community demand discovery of Pb-free high performance TE materials.

In recent years, germanium telluride (GeTe) and it derivatives from IV-VI semiconducting metal chalcogenides family is recently emerging as potential alternative of PbTe[71–73] Though of GeTe-based thermoelectric is known since 1960,[74] recent years have witnessed tremendous improvement in thermoelectric performance (zT > 2) of various GeTe-based materials which is mainly originating from better under-standing of its crystal-electronic structure as well as lattice dynamics.[71–73] In order to gain a better insight into the structure-properties correlation of GeTe, we must understand the nature of chemical bonding, crystal structure and phase transition of GeTe in-details.

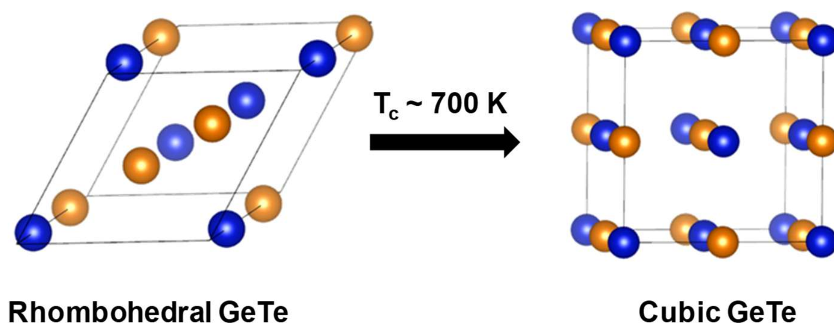

Figure 1.8. *Rhombohedral to a cubic structural phase transition in GeTe (blue and yellow atoms are Ge and Te, respectively).*

1.4.1.1 Crystal structure

GeTe has rocksalt crystal structure (space group $Fm\bar{3}m$ with a lattice constant of a = 6.009 Å, β phase), similar to lead chalcogenides (PbX; X-S/Se/Te) only at high temperature (>700 K).[71–73] Below 700 K, GeTe undergoes a structural distortion along [111] direction of cubic structure and adopts rhombohedral structure ($R3m$ with the lattice parameters of a = b = 4.164 Å and c = 10.690 Å, α phase) (Figure 1.8).[75,76] Although similar structural distortion is also observed in semimetal Sb and Bi, GeTe is ferroelectric because of the presence of two different atoms (Ge and Te) with different electronegativity making the bonding polar.[76] At room temperature, the crystal structure of PbTe and SnTe is cubic, whereas GeTe crystallizes in the less symmetric rhombohedral crystal structure. This anomaly mainly governs by the presence of the ns^2 lone pair on the cation.[2] The role of the lone pair has long been invoked for explaining the off-centering structural distortion. The ns2 lone pair can be either stereochemically active or quenched depending on the local bonding. Interestingly, as the molecular weight of the metal increases, the chance of quenching of ns^2 lone pair increases, which favours the formation of high symmetry structure that is clearly seen in cubic SnTe and PbTe. When comparing the orbital energy levels of GeTe and PbTe, the separation between cation s and anion p electronic band is higher in PbTe than that of GeTe, resulting in weak cation-s and anion-p interaction for PbTe (relativistic effect) which favours the stable rocksalt structure in PbTe, whereas GeTe undergoes a rhombohedral distortion.[2,77]

The relative displacement of Ge and Te sublattice along the [111] direction make GeTe ferroelectric near room temperature.[71–73,78] This distortion changes the angle α = 88.35º from ideal angle of 90º between the axes in the face-centered cubic unit cell. The crystal structure turns into non-centrosymmetric due to the atomic rearrangement, resulting in a spontaneous polarization of ~60 $\mu C/m^2$.[79] Neutron diffraction study by Chattopadhyay *et al.* showed that this ferroelectric structural transition is displacive in nature. Mention must be made that number of atoms (two) and formula unit (one) per primitive unit cell of GeTe for both the phases are same.[80] Moreover, density functional theory (DFT) calculation has indicated that this transition is mainly because of the displacement of Ge and Te.[75] The ferroelectric phase transition in GeTe is identified by softening of transverse optical (TO) phonon modes at zone-center (Γ).[81] Raman scattering on GeTe showed the

presence of two peaks at 98 and 140 cm^{-1} corresponding to E and A_1 modes, respectively which arise due to the vibration of Ge and Te sublattices along and perpendicular to the threefold axis. Softening of these two modes has been observed with increasing temperature.[75,81]

1.4.1.2 Lattice dynamics, ferroelectric instability and thermal transport properties

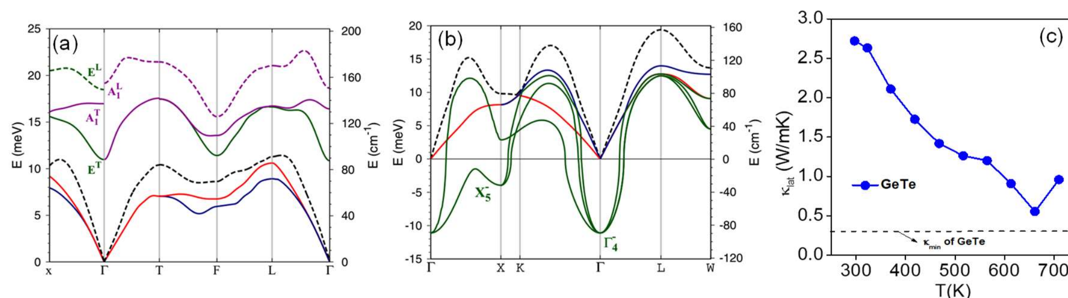

Figure 1.9. *Phonon dispersion plot of (a) rhombohedral and (b) cubic GeTe. Solid and dashed lines represent transverse (T) and longitudinal (L) modes, respectively. (c) Temperature dependent lattice thermal conductivity of GeTe showing sudden drop near the phase transition. Figure (a) and (b) are reproduced with the permission from ref 82. © 2014, American Physical Society.*

Recently, Wdowik *et al* provide clear insight into the lattice dynamics of GeTe (both the phases α & β) together with inelastic neutron scattering experiments and density functional theory calculation.[82] To understand the thermal transport of both rhombohedral and cubic GeTe, it is important to examine phonon dispersions of both the phases. Phonon dispersion for α-GeTe at Γ point exhibits six vibrational modes namely 3 acoustic modes, 2 transverse optical modes (TO) and one longitudinal optical mode (LO) (Figure 1.9a). Both A_1 (non-degenerate) and E (doubly degenerate) modes for rhombohedral GeTe (α-GeTe) are Raman and IR active owing to the absence of inversion symmetry in the structure. Whereas, phonon-dispersion of the high-symmetry rocksalt structure of GeTe (β phase) provide the evidence for the presence of several soft phonon modes mainly TO components which are responsible for the symmetry change at the phase transition (Figure 1.9b).[82] Notably, phonon dispersion of cubic GeTe exhibits several imaginary modes in the Brillouin Zone which is the one of the reason for the absence of cubic GeTe at ambient condition, whereas

rhombohedral phase exhibits real modes. *β* phase exhibits local distortions similar to Peierls distortion, which result in three shorter (2.86 Å) and three longer (3.25 Å) Ge-Te bonds.[83,84]

Generalized phonon density of states display the extension of the acoustic band is from 0 to ~11 eV. The mixed vibration of Ge and Te sublattice contributes to the acoustic and intermediate TO modes.[82] Highest frequency region, composed of the LO-phonon band, is governed by the vibrations of the Ge sublattice, which is also confirmed by the phonon density of state (Ph-DOS) calculation and the ^{125}Te nuclear inelastic scattering experiments.[85] Phonon DOS of cubic GeTe show noticeable red-shift compared to rhombohedral GeTe which can be attributed to the phonon softening in the cubic phase.[86]

GeTe is much more resistant to heat conduction compared to another polycrystalline thermoelectric alloy with a strong mass disorder like InSb (InSb, κ_{lat} ~ 16 W/m.K; GeTe, κ_{lat} ~3 W/ m.K, Figure 1.9c).[65] Here, chemical bonding plays an important role. Softer bonding in GeTe compared to InSb leads to decrease in the speed of sound and the lattice thermal conductivity. Octahedral coordination in GeTe results in softer bonding compared to that of InSb (tetrahedral bonding) which leads to the decrease in the average sound velocity in GeTe (1900 m/s) compared to InSb (2300 m/s), thereby lower lattice thermal conductivity in GeTe. Moreover, the strong anharmonic interaction between soft ferroelectric transverse optic mode and longitudinal acoustic modes cause sudden decrease in lattice thermal conductivity of GeTe near the phase transition (Figure 1.9c).[81,87] This soft-phonon mode mediated phase transition temperature can be decreased to room temperature from 700 K through proper doping/alloying,[88] which can bring down the lattice thermal conductivity of GeTe to its minimum value (κ_{min} ~ 0.3 W/mK), thus can improve thermoelectric performance of GeTe near room temperature. κ_{lat} of GeTe can be further decreased by employing convention strategies like alloying and nanostructuring in order to improve its TE performance.[71–73] These strategies lead to the development of various high performance *p*-type GeTe thermoelectric materials like $Ge_{1-x}Pb_xTe$,[89–92] GeTe-$AgSb(Te/Se)_2$,[37,93] $GeTe_{1-2x}Se_xS_x$[33] and $Ge_{1-x}(Sb/Bi/In/Mn)_xTe$.[27,86,88,94–97]

1.4.1.3 Electronic structure and electronic transport properties

GeTe is rich with naturally formed and thermodynamically stable Ge-vacancies which drives the system to be intrinsically off-stoichiometric along with naturally occurring Ge

precipitations in the matrix.[98] These thermodynamically favourable Ge vacancies makes pristine GeTe to be highly p-type with a very high carrier concentration of $\sim 10^{21}$ cm^{-3}. The high concentration of Ge vacancies results in high electrical conductivity of ~ 8000 S/cm and moderate Seebeck coefficient of ~ 32 μV/K in GeTe at room temperature (Figure 1.10a).[71–73,99] Interesting, GeTe exhibits higher S values compared to that of SnTe although both the materials possesses similar carrier concentration. Further, GeTe exhibits exceptionally high power factor (~ 50 μW/cmK^2) compared to other TE materials from IV-VI family, especially PbTe (~30 μW/cmK^2) and SnTe (~20 μW/cmK^2) which can be understood by analysing their electronic structure.[45,46,100]

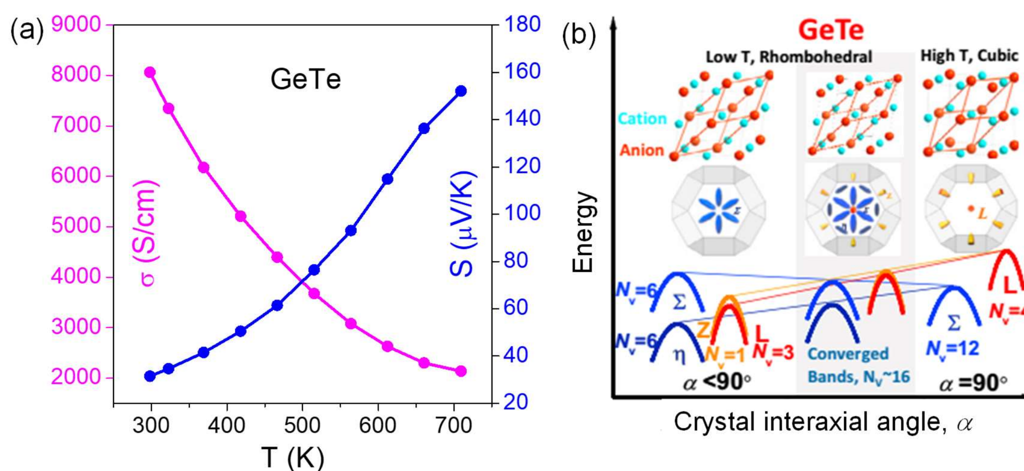

Figure 1.10. *(a) Temperature dependent electrical conductivity and Seebeck Coefficient of GeTe. Schematic energy diagram of the evolution of the electronic structure of GeTe from the rhombohedral phase cubic to depending on interaxial angle. (b) is reproduced with the permission from ref 45. © 2018, Elsevier respectively.*

Both SnTe and PbTe possess rock-salt NaCl structure (*Fm-3m*) with valence band maxima occurring at L in Brillouin zone. Electronic structure calculations of GeTe have been demonstrated that 8 half-valleys at L band (4 equivalent L band) in cubic GeTe (*Fm-3m*) splited into 6 half-valleys at L- point (3 equivalent L band) and 2 half-valleys at Z-point (1 equivalent Z band) in rhombohedral GeTe phase (*R3m*), while 12 full valleys of Σ–band in *Fm-3m* splited into 6 along Σ and rest 6 full valleys along η-line (Figure 1.10b).[45,46,100] Notably, valence band maximum at L-point in cubic GeTe shifts to heavy Σ–band in rhombohedral GeTe during phase-transition. As a result, heavier effective mass carriers of Σ–band are dominated in transport properties in rhombohedral GeTe at room

temperature, which, in fact, led to the unconventional enhancement in power factor in GeTe, unlike PbTe and SnTe. Further, GeTe has relatively low energy difference (~ 0.23 eV) between the heavy hole Σ band and light hole *L* band, and the energy offset decreases with increasing temperature which results in the increasing contribution of the lower lying valance band in electronic transport. [45,94,100] The relatively low energy offset between the two valance bands also lead to several successful chemical doping approaches for the valance band convergence which resulted in high thermoelectric performance.[27,88,89,95,101] Innovative strategies like "slight symmetry reduction" has also been developed to achieve this valance band convergence.[45,46] Further, In doping, which results in the formation of resonance level, has also been shown to be effective in increasing the Seebeck coefficient, and thereby the thermoelectric performance of GeTe.[23,86] A major part of my thesis (**part 2**) is involves understanding structure-property relationship of GeTe and improving its thermoelectric performance.

1.4.2 Layered metal chalcogenides/oxy-chalcogenides

Layered materials have been established as potential candidates for thermal management and TE energy generation due presence of favourable electrical and phonon transport properties.[102–105] In the 1950s, tetradymites (M_2X_3, M=Bi/Sb, X=Te/Se) were identified as the class of semiconductors with the highest TE efficiency and their TE performance has been further improved over decades via materials engineering.[13,106,107] Bi_2Te_3 and its derivatives from the tetradymites family have been explored both as *p*- and *n*-type thermoelectric materials and still today, considered as best TE materials for near room-temperature (RT) power generation applications.[108–110] Recently, SnSe, a layered material, has created sensation as an outstanding thermoelectric material for the mid-temperature range, both as *p*-type[111,112] and *n*-type[113,114] thermoelectric material, and hence SnSe is being considered as potential alternative to PbTe.[115] Moreover, the thermoelectric materials experience high temperature, thereby their thermal and environmental degradation is a major concern. Various oxy-chalcogenides with layered structure such as BiCuSeO,[116,117] Bi_2O_2Se[118,119] provide unique opportunities for their better thermal and environmental stability. Hence, enormous research interest is growing to improve TE performance of many layered metal oxy-chalcogenides such as BiCuSeO, Bi_2O_2Se. In a nutshell, various

chalcogenides and oxy-chalcogenides with layered structure always have aced the field of thermoelectrics because of their high-performance, facilitated by their unusual phonon and electronic transports.

1.4.2.1 Phonon transport in layered materials

Materials with intrinsically low κ_{lat} and understanding the correlation between lattice dynamics and chemical bonding in those materials would enable us to manipulate various intrinsic parameters in order to control phonon transport through bulk medium. As lattice thermal conductivity holds direct proportional to the square of phonon group velocity (v_g), slight change in the sound velocity will have high impact on the phonon transport. Phonon group velocity, which is intrinsic property of each material, is directly proportional to the square root of *(f/m)* where *f* and *m* signify force-constant and mass of the compound of interest, respectively.[17] Materials with weak chemical bonding and heavy constituent elements are ideal for achieving low v_g. Layered materials generally have very weak bonding along stacking direction, which eventually result in low phonon group velocity such in those materials, such as in Bi_2Te_3 (v_g ~ 1750 m/S)[120] and SnSe (v_g ~ 1420 m/S)[68], limiting the lattice thermal conductivity. Further weak interlayer bonding in layered materials also results in soft optical phonons which strongly couple with heat carrying acoustic phonons, such as in natural van der Waals (vdWs) heterostructure, reflecting in their extremely low κ_{lat}. Lattice anharmonicity, renders κ_{lat} to a temperature-dependent finite quantity, plays an important role in manipulating the phonon transport in crystalline solids.[121] Strong lattice anharmonicity amplifies phonon−phonon Umklapp scatterings which cause significant reduction in κ_{lat}. Lattice anharmonicity, a measure of deviation of real crystal from ideal harmonic behavior, is quantified by the Grüneisen parameter, defined by[17]

$$\gamma(\omega) = - d\ln(\omega)/ \ln(V) \tag{1.14}$$

for a given frequency (ω) of the phonon where V is volume of the system. Relation of κ_{lat} with Grüneisen parameter can be seen from the Slack's model:[122]

$$\kappa_{lat} = B.(\overline{M}\, \theta_D^3 \delta)/\gamma^2 T \tag{1.15}$$

considering that the heat transport is governed by acoustic phonons and three-phonon U scattering is the dominant scattering mechanism. In the Slack's model of κ_{lat}, B is a

numerical coefficient and $\bar{M}$ is the average mass of the basis atoms. The average volume per atom is denoted by δ^3 and θ_D is the acoustic Debye temperature. In general, the materials with complex crystal structure and bonding heterogeneity possess strong lattice anharmonicity. Bonding heterogeneity and consequent lattice anharmonicity are common to most of the layered materials because of their strong in-plane covalent bonding while having weak van der Waals bonding for the out-of-plane direction. For example, SnSe shows average Grüneisen parameter[68] of ~ 3.13, which is much higher than that of PbTe (γ ~1.65) or PbSe (γ ~1.69),[68] explaining occurrence of ultra-low κ_{lat} in SnSe. Further, presence of resonant bonding in some of the layered compounds (e.g., Bi_2Te_3, SnSe) with distorted rock-salt-based structures produce soft optical phonons.[65,68] These compounds unable to form six two-center-two-electron (2c−2e) octahedral bonds due to fewer valence electrons available per atom. However, coordination can be satisfied by forming long-range resonance bonds which result in highly polarizable bonds as well as soft phonons, enhancing anharmonic optical-acoustic scattering. Also, Slack's formula describes the general material's feature to realize low κ_{lat} which are the presence heavy atomic mass, weak inter-atomic bonding, complex crystal structure and high anharmonicity, and the layered materials with heavy constituent elements possess all these features, in general. As a result of these favourable materials traits, plenty of layered chalcogenides/oxy-chalcogenides exhibit low-lattice thermal conductivity.

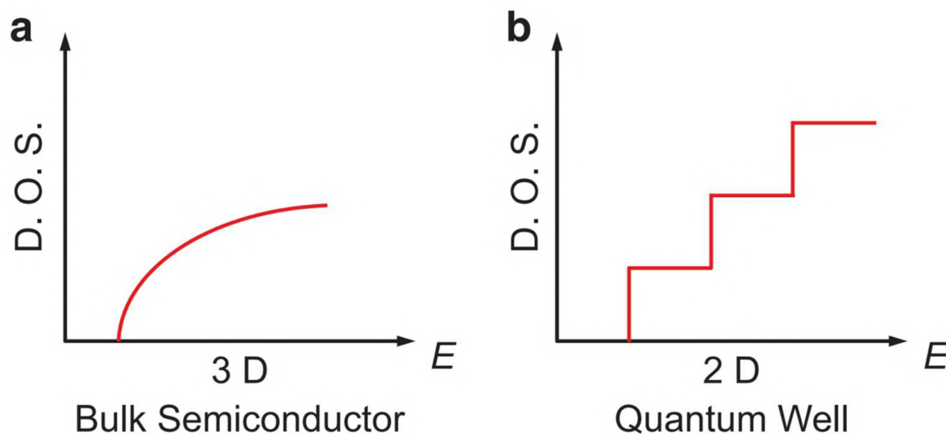

Figure 1.11. *Schematic diagram of electronic density of states (DOS) for (a) 3D bulk semiconductor and (b) 2D quantum well (Adapted with permission from ref. 102).*

1.4.2.2 Electronic transport in layered materials

Layered materials host atomically thin layers bound by weak vdWs interaction, which can be considered as quasi 2D materials and hence free charge carriers within each layer can experience quantum confinement, like 2D.[102–105] Consequently, electronic- DOS of these quasi-2D layered materials exhibits strong anisotropy, deviating from a 3D-bulk material. For instance, DOS in the basal plane can rise sharply, in contrast to smooth change in DOS of 3D materials (Figure 1.11).[104] If Fermi level of quasi-2D layered materials is tuned within rapidly varying DOS, it can result a large asymmetry between hot carriers ($E > E_F$) and cold ($E < E_F$) carriers, hence more effective transportation of entropy per charge, facilitating higher Seebeck coefficient with minimal effect on electrical conductivity.[104] Further, tunability of the position of the E_F is easily accessible in 2D-layered materials, than that in bulk materials by intercalating ions or applying an external electric field which can effectively assist in enhancing the thermopower of the system. Moreover, anisotropic crystal structure of layered materials can individually engineer the phonon-transport and electronic-transport by the changing the sizes of dimensionality close to wavelengths of the phonons and/or electrons.[102–104] Last two part (**part 3 and part 4**) of my thesis is centred around the investing the thermoelectric properties of layered metal-chalcogenides and oxy-chalcogenides, respectively.

1.5 Topological quantum materials and its correlation with thermoelectrics

Recently, topological quantum materials, TQM (*e.*g. topological insulators [TI], topological crystalline insulators [TCI] and topological semimetals), characterized by their nontrivial electronic surface states, have created a sensation in designing new thermoelectric materials.[20,107,123–126] Many TQM such as Bi_2Te_3 (TI), Bi_2Se_3 (TI), SnTe (TCI) have been established as potential thermoelectric materials. Underlying reason for TQM being a source of potential candidates for thermoelectrics is ascribed to the fact that both TQM and TE materials demand similar material features such as the presence of heavy constituent elements, narrow band gap and strong spin-orbit coupling. The robust surface states with linearly dispersed Dirac cones lead to high mobility across the surface of topological materials. Fascinating electronic transport properties of TQM originates from

the presence of metallic surface states, which offers high carrier mobility (μ) and makes them potential candidates for TE applications also. Interestingly, band inversion in TQM generates many local extrema in the valence or conduction bands during the electronic topological transition, resulting in large DOS and asymmetry near the Fermi level which additionally helps to improve σ and S values. Moreover, TQM with heavy constituent elements have soft vibrational (phonon) modes and consequently have low κ_{lat} which is one of the key requirements to achieve high TE performance. However, the optimization of the properties for TM and TE require a different range of carrier concentrations. Targeted bulk carrier concentration range is $<10^{16}$ cm^{-3} for TQM in order to avoid the interference coming from the bulk, while the same is in the range 10^{19}-10^{20} cm^{-3} for TE.[107] Thus, the intersection of these two ongoing research fields may reveal several new and exciting phenomena and new prospects which are not available in conventional materials. Further, topologically nontrivial boundary states also help to improve the thermoelectric performance of a material compared to the trivial phase because boundary states act as conducting channels for carriers with minimal backscattering effect. As a part of my thesis (**part 3**) involves investigations of TE properties of few intriguing TQM such as weak TI, dual 3D-TI, in this sections, I have briefly discussed basic characteristics about topological insulator (strong and weak) and topological crystalline insulators.

1.5.1 Topological insulator

Topological insulators (TIs) behave as the normal insulator/semiconductor in bulk with time-reversal symmetry (TRS) protected non-trivial metallic surface states.[127] A TI can be viewed as the counterpart of QH state without applied magnetic field. Here, spin-orbit coupling (SOC) plays a role similar to the magnetic field in QH state, which has potential applications in different fields including spintronics and thermoelectrics. The simplest way to portray a topological insulator is as a non-trivial insulator with metallic boundary when placed next to an 'ordinary' insulator (vacuum). These metallic boundaries arise from topological invariants. The exotic metallic surface of TI is known as helical metal, where the electron spin is perpendicularly coupled with its orbital angular momentum.[128] Interestingly, crystal defects present in the surface of a topological insulator are not able to change the direction of moving electron (forward/backward) because of the 'locked' nature

of spin and momentum in helical metal. Hence, the presence of defects at the surface will flip the electron spin due to the changes in momentum sign. To obey the law of conservation of angular momentum, 'U-turn' is prohibited for the surface electron, resulting in dissipationless charge transport along the material's surface. However, it is experimentally observed that mobility of the surface electrons is finite. The spin-momentum locking forbids only recoil (180 degrees) scattering whereas small-angle scattering in a plane is perfectly allowed and known to limit the mobility of topological surface states.[129] We can distinguish topological insulator from a trivial insulator by introducing novel Z_2 topological index which is classified as Hamiltonian for time-reversal invariant (T).[130] The value of topological invariant, ν equals to zero (0) and one (1) for existing even and an odd number of Dirac cones in the BZ, respectively for both 2D and 3D topological insulators.

In case of a 2D-topological insulator, topological edge states were first obtained in quantum wells of mercury telluride (HgTe) with a critical thickness (d_c ~6.5 nm) which is sandwiched between two cadmium telluride (CdTe) layers.[131] HgTe crystallizes in zincblende structure with a space group of *F-43m* (lattice parameter, a = 6.460 Å), similar to group IV (Si & Ge), III-V (GaAs &InP) and II-VI (CdSe) semiconductors. The energy gap between the valence band (p orbitals of anion) and conduction band (s orbital of cation) is 1.5 eV for CdTe, a trivial semiconducting material. The band gap is large for CdTe because of favourable bonding interaction between *s* and *p* bands. On the other hand, in HgTe (Hg and Te occupy the Wyckoff sites 4a and 4c, respectively), the presence of heavy elements such as Hg and Te induces significant SOC that splits the *p* bands into two components ($p_{1/2}$ and $p_{3/2}$) and drive the *p*-orbitals above the *s*-orbitals i.e. the bands are inverted compared to lighter CdTe.[132] Quantum well of HgTe can be established by burying HgTe (strong SOC) between two CdTe (weak SOC) layers with a similar lattice constant. Therefore, it is very important to recognize the critical thickness of HgTe layer to realize the optimum strength of SOC for the whole quantum well which finally leads to the band inversion and the realization of topological surface states along the edge of the quantum well.[131]

The next imperative advancement is the recognition of 3D topological insulator. Three dimension topological insulators can be classified into strong and weak topological insulators depending on the nature of the surface states. The 3D weak topological insulator

can be created by stacking 2D TI which is identical to the layered Quantum Hall States. Weak topological insulator (WTI) and strong topological insulator (STI) both are characterized by four Z_2 indexes (ν_0, ν_1,ν_2, ν_3). STI has a nontrivial ν_0 which implies the presence of an odd number of Dirac cones in the surface states. For WTI, ν_0 is 0 and ν_1,ν_2,ν_3 $\neq 0$ and thus it possesses an even number of Dirac cones in the surface states.[133] First 3D strong TI was predicted in $Bi_{1-x}Sb_x$ in 2007 by Fu and Kane which was later experimentally confirmed through angle-resolved photoemission spectroscopy (ARPES) in 2008 by Hsieh *et al*.[134] The surface electronic structure of this alloy is quite complicated which motivates researcher to search for other 3D TI materials with much simpler surface band structure.

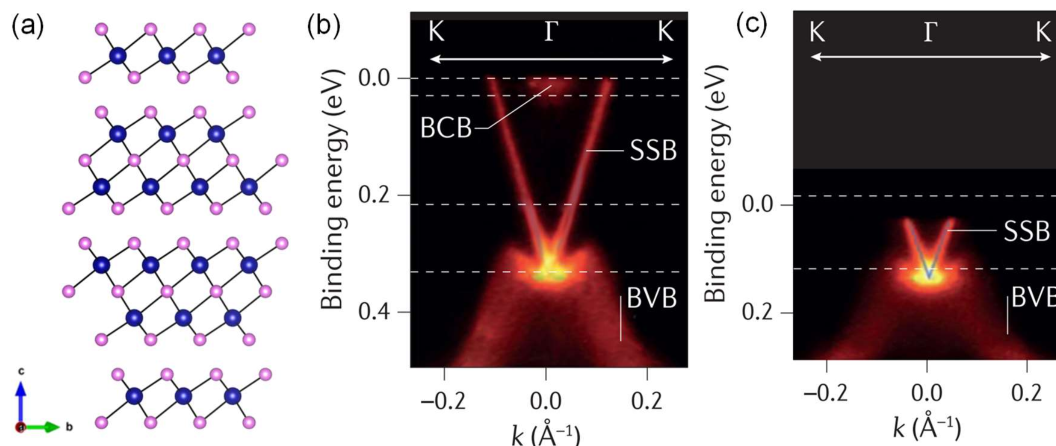

Figure 1.12. *(a) Crystal structure of M_2X_3 (M = Sb/Bi; X = Te/Se), Blue and magenta atom represent M and X, respectively, Energy dispersion for (b) n-type Bi_2Te_3 and (c) p-type Bi_2Te_3 via ARPES study. Figure (b) and (c) Reproduced with the permission from ref 136. © 2009, American Association for the Advancement of Science.*

Layered binary chalcogenides (tetradymite compounds) such as Bi_2Se_3, Bi_2Te_3 and Sb_2Te_3 (Figure 1.12a) are the widely studied compounds as 3D strong TIs (Figure 1.12b-c) because of several enviable properties.[107,135–137] Strong SOC alters the order of two p_z orbitals (Bi and X, X = Se/Te) responsible for the formation of the valence band and conduction band, respectively, thereby band inversion occurs at the Γ point. At room temperature, tetradymite crystallizes in the rhombohedral phase (space group, $R\bar{3}m$) (Figure 1.12a). These 3D TIs have typically a bulk band gap of 0.2 - 0.3 eV. Further, the presence of the anti-site defects makes them conducting in nature. Importantly, exotic surface properties of tetradymite compounds can be accessible even at room temperature

because of the large band gap. However, it is very challenging to distinguish between the bulk and surface conductivity because of the residual conductivity of bulk states coming from the intrinsic doping and anti-site defects. [107]

BiSe and Bi_2Se_3 belong to the same homologous series $(Bi)_m(Bi_2Se_3)_n$.[138] Crystal structure of BiSe consists of a bismuth bilayer (Bi_2), a known quantum spin hall insulator sandwiched between two units of Bi_2Se_3 which are three dimensional strong topological insulators. Recently, BiSe emerges as weak topological insulators which has been verified by experimentally.[139] BiSe belongs to the (0;001) class of Z_2 weak TIs, where the band inversion takes place at C and A points in the Brillouin Zone. In **chapter 1 of part 3**, I have discussed the thermoelectric properties of 3D weak topological insulator, BiSe.

1.5.2 Topological crystalline insulator

Generally, metallic surface states in TI are protected by time-reversal symmetry while the bulk remains insulating. In 3D TI, Dirac point is generally located at the Γ point of the BZ. Motivated by the exciting research on TI, researchers have explored new topologically nontrivial surface states, protected by other symmetries (invariant). Thus, the knowledge of crystal structure and symmetry is essential to understand the electronic properties of materials. In 2011, L. Fu has theoretically predicted a new kind of topological material named as a topological crystalline insulator (TCI).[140] Topological surface states of TCI are protected by crystal symmetries such as rotation, reflection etc. which eventually replace the responsibility of time-reversal symmetry in well studied Z_2 TI. Exploration of new TCI phases both theoretical and experimental investigations are still in their infancy because of the complexity of crystal structure. Unlike Z_2 index for TI, mirror Chern number, N_M helps one to identify the TCI from the library of compounds. Mirror Chern number can be defined as[20]

$$N_M \equiv (N_{+i} - N_{-i})/2 \tag{1.16}$$

Where two integers, N_{+i} and N_{-i} are topological invariants which are the Bloch Eigen states corresponding to Chern numbers. Mirror Chern number must be a nonzero integer for TCI, even if total Chern number is zero, which actually defines mirror symmetry protected TCI phases. In 2012 Hsieh *et al.* have theoretically predicted the TCI phase in SnTe (Figure

1.13a).[141] Till now, the TCI phase is experimentally realized in SnTe, $Pb_{1-x}Sn_xTe$ and $Pb_{1-x}Sn_xSe$ all of which crystallize in rocksalt structure (space group $Fm\bar{3}m$).[142–144]

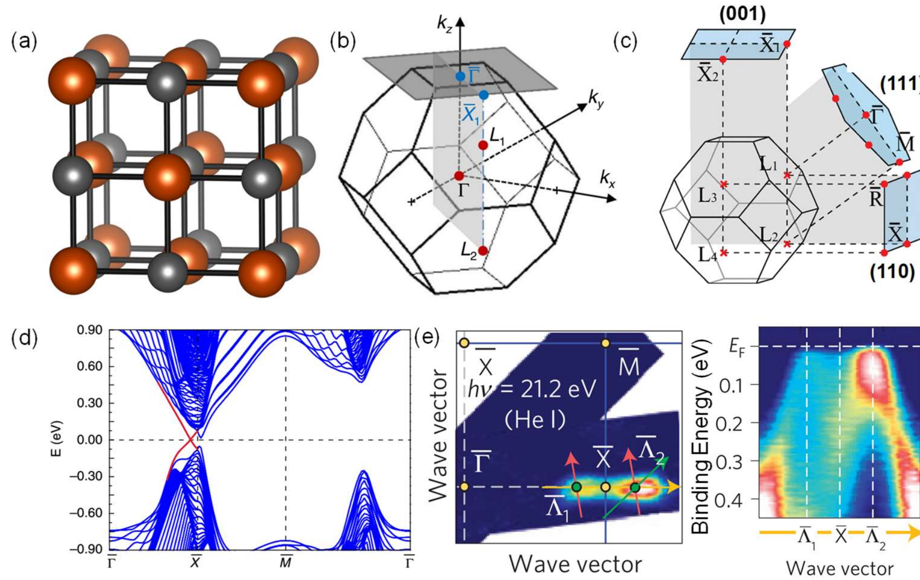

Figure 1.13. *(a) Crystal structure of SnTe (orange and grey atom represent Sn and Te, respectively), (b) the bulk and corresponding surface (001) Brillouin zone of SnTe, (c) Dirac cones in three different surfaces of Brillouin zones, (d) band dispersion of SnTe (e) mapping of the ARPES intensity at the Fermi level, E_F. Figure (b) - (d) Reproduced with the permission from ref 141. © 2012, Springer Nature, (e) Reproduced with the permission from ref 142. © 2012, Springer Nature.*

In SnTe, the existence of nonzero mirror Chern number confirms the presence of topologically protected surface states on the crystal faces which are symmetric with (110) mirror planes (Figure 1.13b-c). Hsieh *et al.* have observed that three surface terminations fulfilling this condition such as (001), (110) and (111) surface (Figure 1.13b).[141] Moreover, surface orientation generates two different types of surface states in TCI like SnTe. One type of surface states exist on the (001) and (110) surface. For the (001) surface, four L (1, 2 & 3, 4) points of the bulk BZ project onto X (1 and 2) point in the surface BZ (Figure 1.13c). The calculated mirror Chern number, $N_M = 2$ confirms the presence of two pairs of spin-polarized surface states with opposite Eigen values which confirms the existence of four Dirac points in the surface states. Another type of surface state exists on the (111) surface in TCI where three L points of bulk BZ project onto $\bar{M}$ point in the surface BZ and another one L point of bulk BZ projects onto $\bar{\Gamma}$ point in the surface BZ (Figure 1.13c).

Interestingly, both types of surface states of SnTe possess even number of Dirac points which make them distinguishable from Z_2 TI with an odd number of Dirac points in the BZ. After the theoretical prediction of topological surface states in SnTe (Figure 1.13d), Tanaka *et al.* have experimentally confirmed the presence of four Dirac cones in the surface states of SnTe by using ARPES experiment (Figure 1.13e).[142] Experimentally the double Dirac cone structure is observed at $\bar{X}$ point of the surface BZ for the (001) surface of SnTe. Interestingly, none of the Dirac points of (001) surface are located at time reversal invariant momentas of the surface BZ, whereas for (111) surface, four Dirac points are located at time reversal invariant momentas ($1\,\bar{\Gamma} + 3\,\bar{M}$).

BiTe is both a WTI and a TCI, and hence a novel type of dual TI .[145] BiTe exhibits a dark surface perpendicular to the stacking direction which is free of time-reversal symmetry-protected surface states at the time-reversal invariant momenta (TRIM) points, due to weak topological Z_2 indices (0;001). Moreover, an additional protection of topological states with crossings at non-TRIM points in the $\overline{\Gamma M}$ mirror plane direction governed by the crystal mirror symmetry with non-zero mirror Chern number n_M = - 2. This dual WTI and TCI character leads to the existence of topological states on every surface of the crystal, which are protected either by time reversal or by mirror symmetries. In **chapter 2** of **part 3**, I have discussed thermoelectric properties of BiTe and its correlation with its different quantum phases.

1.6 A brief introduction to ferroelectricity

Ferroelectricity is exhibited by materials with spontaneous polarization and is reversible through the application of an electric field.[146,147] Ferroelectricity is a subset of pyroelectricity; it exhibits spontaneous polarization below a transition temperature known as the Curie temperature. In ferroelectric materials, this spontaneous polarization can be reoriented by application of an electric field; full reversal of the polarization is called “switching.” Generally, ferroelectric material undergoes a structural phase transition from the paraelectric phase to the ferroelectric phase at the Curie point (ie, the transition temperature, T_c). The paraelectric phase, which is at a higher temperature, is likely to be piezoelectric or non-piezoelectric and is rarely polar. This transition from a high-temperature paraelectric phase to a low-temperature ferroelectric phase usually results in

strong anomalous changes in the dimensions of the crystal unit cell and thermodynamic properties (dielectric, elastic, and thermal properties) of that pyroelectric material. It is well known that in the vicinity of the Curie temperature (T_c) the dielectric constant of the material, ε rises sharply and above this temperature ε follows the Curie-Weiss equation:

$$\varepsilon = \frac{A}{T - T_0} \tag{1.17}$$

where A is the Curie constant and T_o is called the Curie–Weiss temperature. A typical plot for variation of ε with temperature for GeTe thin film has been demonstrated in Figure 1.14b and 1.14c, which shows that T_O is lower than the transition temperature, T_c.[148]

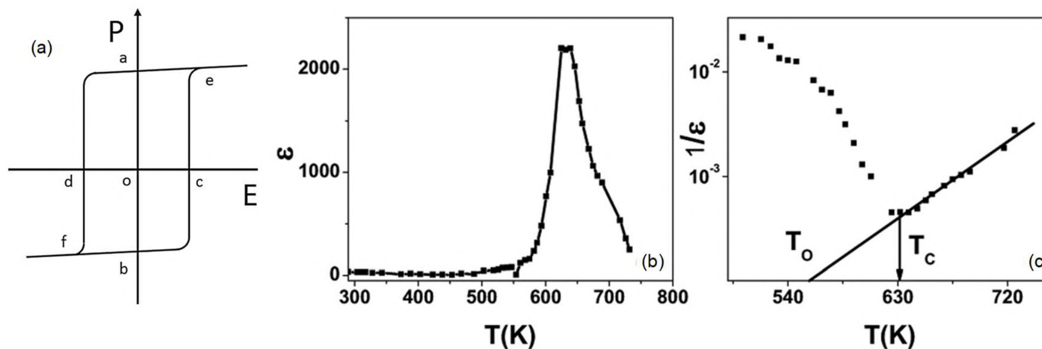

Figure 1.14. *Schematic diagram of (a) typical polarization (P) Vs. Electrical field (E) hysteresis loop.*[147] *Temperature dependencies of (b) dielectric constant and (c) reciprocal dielectric constant (b) for the GeTe film.*[148] *(b) and (c) Reproduced with the permission from ref 148. © 2012, American Physical Society.*

Ferroelectric material can be defined as a material that has a nonlinear relationship with polarization P and applied electrical field E. This relationship is given by a hysteresis loop (as shown in Figure. 1.14a), which was experimentally first observed in Rochelle salts ($NaKC_4H_4O_6.4H_2O$) by Prof. C. B. Sawyer and Prof. C. H. Tower in 1930 (known as Sawyer–Tower circuit method).[149] In the schematic representation of a hysteresis loop which is shown in Figure 1.14a, the lengths of “oa” and “ob” represent the magnitude of spontaneous polarization, and the direction of spontaneous polarization is called the ferroelectric axis.[147] The lengths of “oc” and “od” represent the coercive field strength, which is not a well-defined quantity. The slope of the hysteresis loop in absence of an external field represents the susceptibility of the material. A symmetrical hysteresis loop is the ideal shape of the loop when the positive and negative parts of coercive field and spontaneous polarization are equal. These parameters and the shape of the loop may be

affected by many factors, including temperature, defects, mechanical stress, and electrical measurement conditions imposed on the sample.

The occurrence of a hysteresis loop (Figure 1.14a) is suggested to be a consequence of the changes in the ferroelectric domain, such as the growth of existing antiparallel domains, domain wall motion, and nucleation and growth of new antiparallel domains, whereby ferroelectric domains are the regions with uniformly oriented spontaneous polarization and the domain wall is the region between two domains. By applying an AC electrical field, polarization increases linearly with the amplitude of the electrical field until the direction of the polarization of all domains aligns with the direction of the applied field, which can be observed at point e in Figure 1.14a. When the field starts to decrease, the direction of some domains will switch back. However, the polarization will not become zero by decreasing the applied field to zero; instead, it will become zero at the opposite coercive field. Further increasing the applied field in the reverse direction will cause a new alignment in direction of the domains at point f; again, decreasing the applied field in reverse completes the hysteresis loop. It should be noted that with a particular shape of the hysteresis loop, such as in Figure 1.14a, spontaneous polarization is the point when the applied electrical field is zero. The actual spontaneous polarization is the intercept of the polarization axis with the extrapolated linear segment at point e or f, and the point at the absent applied electrical field is called the remanent polarization.

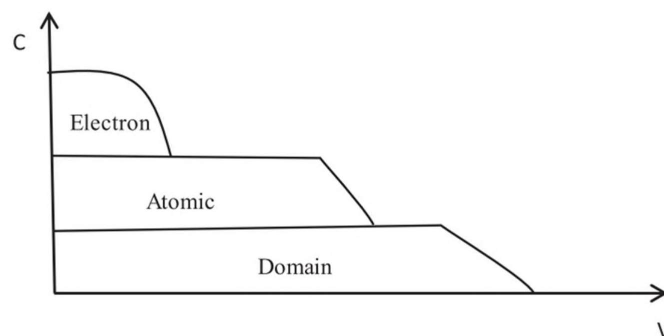

Figure 1.15. *Schematic diagram of capacitance (C) regimes for electronic, atomic and domain polarization in ferroelectrics with respect to applied voltage.*[147]

An understanding of the polarization–electric field (P–E) plot, such as that shown in Figure 1.14a, of the ferroelectric material provides important information regarding the properties of the material. We can relate polarization (P) to voltage (V) by

using their respective derivatives: δP/δV = (δQ/δV)/Area. This is equal to large signal capacitance (C) per unit area. A “large signal” means that the test waveform amplitude is large enough to switch dipoles in the ferroelectric material. In this case, the measurement captures all the changes that the sample experiences, including remanent polarization and parasitics. A capacitance–voltage plot allows conversion of capacitance to its equivalent contribution to each voltage through mathematical integration. This plot also provides an idea of the dynamics of electrons/atoms/domains at different time scales (which can be seen in Figure 1.15). Capacitance provides an indication of the separation of charges: electrons are fast, dynamics on an atomic scale are slow, and domain dynamics are even slower. We can discuss linear capacitance, nonlinear capacitance, and remanent polarization within the context of the ferroelectric hysteresis loop, as previously described in 1.15a. Referring to the hysteresis loop, linear capacitance is observed at low electric fields when the material acts as a normal dielectric because the electric field is not strong enough to align the domains. Thus, at low voltages, polarization is directly proportional to the electric field ($P \propto E$) and the capacitance is correspondingly linear. At higher electric fields, the electric fields can reorient the domains and the polarization increases dramatically, resulting in a nonlinear capacitance. If the electric field is reversed, then the polarization correspondingly reverses in polarity. Remanent polarization is defined as the polarization that remains when the applied electric field is zero.

Ferroelectrics, with spontaneous switchable electric polarization, are a vital branch of functional materials due to their broad use in nanodevices, such as field-effect transistors (FET), random-access memory (RAM), and photovoltaics.[146,147,150] Perovskites (Such as $BaTiO_3$) have been established as very important class of ferroelectric materials that are used in a range of applications.[147] Recently, ferroelectricity has been realized in some of metal chalcogenides such as GeTe,[78,148] SnTe.[151,152], $Pb_{1-x}Ge_xTe$.[153] Presence of ferroelectric instability in TE materials such as in GeTe, SnTe are proven to be beneficial in lowering their κ_{lat} and hence tuning their TE performance.[81,87,88] Added to that the miniaturization of ferroelectricity based devices is suffering from the size limitation due to the internal depolarization field.[146,154] In order to overcome this challenge, significant progress has been made in two-dimensional (2D) ferroelectrics. Differing from perovskite oxides, the ferroelectric polarization (PFE) in 2D materials of atomic thickness can be

strong enough to subsist, offering a natural solution for nanoscale ferroelectric applications. Recently, various layered metal chalcogenides/oxy-chalcogenides are getting attention as potential candidates for 2D-ferroelectrics.[152,155–157]

1.7 Synthesis and characterizations

1.7.1 Synthesis

The successful utilization of thermoelectric devices depends critically on the synthesis techniques. A great majority of chalcogenides known to date have been synthesized by sealed-tube reactions in vacuum (10^{-3} - 10^{-5} Torr) either by employing high-temperature melt cooling or alkali metal polychalcogenide fluxes A_2Q_n (Q = S/Se/Te) at low temperatures. In high temperature vacuum sealed tube melting reaction, appropriate quantities of starting materials (mostly in their elemental form) are heated above the melting point of the desired product in absence of air, followed by cooling of the subsequent reaction mixture at a specific cooling speed depending upon material's nature (congruent/incongruent). Products of the reactions are generally thermodynamically stable polycrystalline or single-crystalline ingots.

The Spark plasma sintering (SPS) is newly developed technique for the syntheses and processing of thermoelectric materials employing ON-OFF pulse DC voltage / current (Figure 1.16).[158,159] This is considered as an energy-saving sintering technology due to its short processing time and a small number of processing steps. The SPS process is based on the electrical spark discharge phenomenon. Application of a high energy, low voltage spark pulse (spark discharge) momentarily produces a local high temperature state (several to ten thousand degree) in the gap between the particles of a material *via* joule heating (Figure 1.16c-d). This results in vaporization and melting of the powder particles' surfaces and formation of constricted shapes or "necks" around the contact area between the particles. These constricted shapes gradually develop, and plastic transformation progresses during sintering, resulting in a sintered material with density of ≥ 99%. By application of voltage and current repeatedly with this ON-OFF, the discharge point and the Joule heating point (locally high-temperature generation field) move throughout the sample, resulting in less power consumption and efficient sintering. Since only the surface temperature of the particles rises rapidly by self-heating, particle growth of the starting powder materials is

controlled. Therefore, a precision sintered compact is manufactured in a shorter time. At the same time, bulk fabrication of particles with an amorphous structure and crystalline nanostructure formation are now possible without changing their characteristics. Vaporization, melting and sintering are completed in short periods of approximately 5-20 minutes, including temperature rise and holding times. SPS sintering temperatures range from low to over 2000 °C which are 200-500 °C lower than with conventional sintering.

In order to prepare high performance thermoelectric materials, we have done spark plasma sintering (SPS) of the melt grown ingots in SPS-211Lx, Fuji Electronic Industrial Co., Ltd (Figure 1.16a). The SPS process and geometrical configuration of the punches, mould and powder are illustrated in Figure 1.16. Powders to be consolidated, are placed in a die and heated by applying the electric current. The melt grown ingots were first ground into fine powders using a mortar and pestle to reduce the grains size in an inert glove box. This powder was then pressed into cylindrical shape by SPS method (SPS-211Lx, Fuji Electronic Industrial Co., Ltd.) at specific temperature and pressure under vacuum (Figure 1.16a). Highly dense (~ ≥ 98% of theoretical density) disk-shaped pellets with ~ 10 mm diameter and ~ 10 mm thickness were obtained.

Innovative metal chalcogenide (MC) nanomaterials synthesized on a large scale with controlled morphology, size, composition, and structure lie at the heart of their practical applications. To achieve this, conventional solid-state strategies are often unsatisfactory. On the other hand, soft-chemical solution phase synthesis has been witnessed to be very powerful for obtaining desired MC functional nanomaterials. In this process, the employed solutions and/or surfactants can be rationally selected based on the target MCs, and the nucleation and growth process of the products can be easily controlled by adjusting the thermodynamic and kinetic parameters of the reaction. Additionally, liquid-based synthetic routes do not involve the use of drastic conditions (e.g., high temperatures, high pressures) and yield products in large amounts. Most commonly used liquid-based methods are solvothermal method and Schlenk line (also vacuum gas manifold) techniques which are often used to synthesize high-quality MCs.

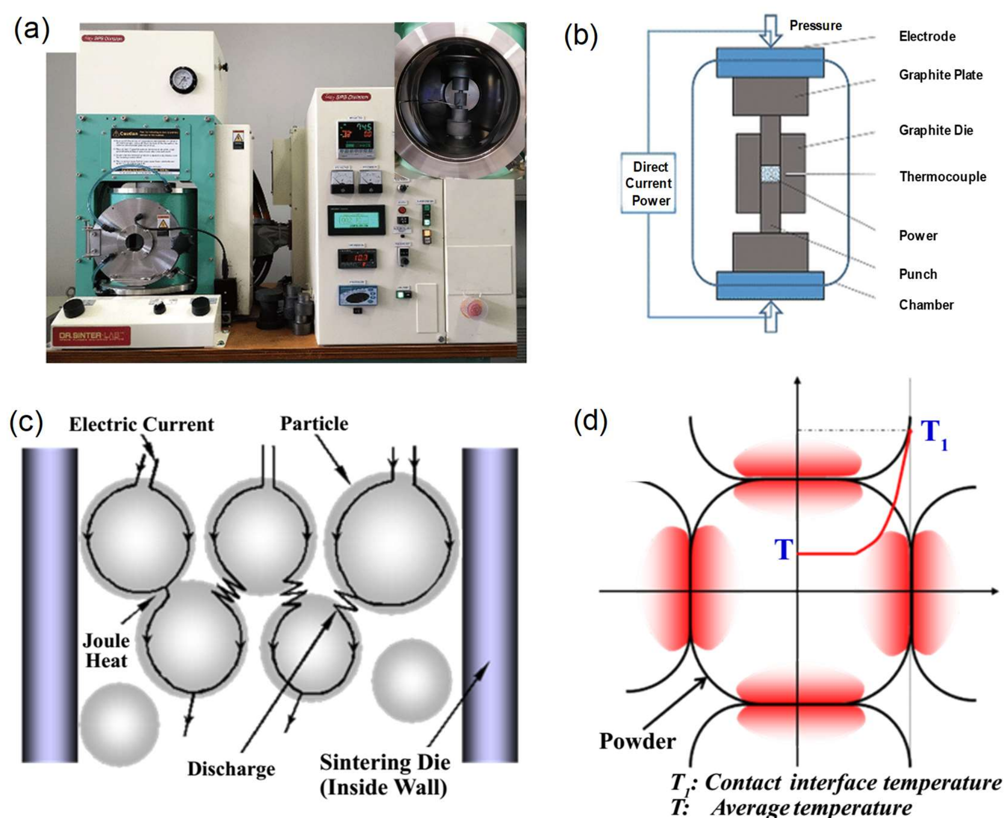

Figure 1.16. *(a) Photograph of SPS-211Lx instrument. The inset image shows sitering chamber. (b) Schematic illustration of a spark plasma sintering equipment. (c) Possible electric current path through powder particles inside the die. (d) The temperature image on powder particles surface. Contact surface temperature (T_1) differs significantly from average temperature (T).*[159]

The solvothermal method involves heating the reactants and solvent in a closed vessel, called autoclave. An autoclave is usually constructed from thick stainless steel to withstand the high pressures, and is fitted with safety valves; it may be lined with nonreactive materials such as teflon. The pressure generated in the vessel due to the solvent vapours elevates the boiling point of the solvent. Typically, solvothermal methods make use of various organic solvents such as ethanol, toluene, long chain organic molecule (oleic acid, octadecene, oleylamine) and water. This method has been widely used to synthesize zeolites, inorganic open-framework structures, and other solid materials. In the past few years, solvothermal synthesis has emerged to become the chosen method to synthesize nanocrystals of inorganic materials. By employing a metal salt, elemental Te/Se/S and a

reducing agent, it is possible to produce metal chalcogenide nanocrystals. Control over size is rendered possible by the slow release of sulfide or selenide ions.

The Schlenk line (also vacuum gas manifold) techniques are very useful to work with air sensitive compounds. It consists of a duplex of glass tubes with several ports connected side-by-side, which together is called a manifold. One manifold is connected to a source of purified inert gas (Ar, N_2), while the other is connected to a vacuum pump. The inert gas line is vented through an oil bubbler. A liquid nitrogen or dry-ice/acetone cold trap generally use in the connector line of pump and manifold to prevent the contamination of the vacuum pump oil from solvent vapours and gaseous reaction products. Special stopcocks or Teflon taps allow vacuum or inert gas to be selected without the need for placing the sample on a separate line.

For my Ph.D. work, I have used both the vacuum sealed melting routes and soft chemical solution phase synthesis.

1.7.2 Characterizations

I have used the following characterization techniques for my thesis works.

1.7.2.1 Powder X-ray diffraction (PXRD)

Powder X-ray diffraction is the most commonly used technique in solid state inorganic chemistry and has many uses from analysis and assessing phase purity to determining the structure. In this thesis, both lab source X- ray and synchrotron X-ray have been used for structural characterization. In the laboratory, X-rays are generated in a cathode tube. In this technique, a tungsten filament was heated to produce electrons and electron beam was then accelerated towards an anode by applying a voltage (~ 30 - 40 kV). When electrons have sufficient energy to dislodge inner shell electrons of the target material, characteristic X-ray spectra are produced. These spectra consist of several components, the most common being $K\alpha$ and $K\beta$. $K\alpha$ consists, in part, of $K\alpha_1$ and $K\alpha_2$. $K\alpha_1$ has a slightly shorter wavelength and twice intensity than $K\alpha_2$. The specific wavelengths are characteristic of the target material (Cu, Fe, Mo, Cr). Cu is the most common target material use for laboratory X-ray. To produce monochromatic X-rays, it is required filtering out K_β radiation by foils or crystal monochromators. For Cu radiation, a sheet of Ni foil is a very effective filter, but

it is difficult to remove Kα_2 from Kα_1 because of close wavelength. The filtering process in laboratory X-ray leads to a reduction in intensity and hence it is difficult to detect low-intensity peaks in laboratory X-ray diffraction. In addition, it is difficult to distinguish peak splitting when peaks appear closely. These limitations can be ruled out in synchrotron X-ray. Synchrotron radiation is emitted when charged particles such as electrons, traveling at relativistic speeds, are forced to change direction on passing through a magnetic field. To generate synchrotron radiation, electrons or positrons are accelerated to speeds close to that of light and circulate in ultra-high vacuum tubes or storage rings, guided by arrays of magnets.

X-ray diffraction obeys Bragg's law, which states that constructive interference would occur if the path difference between the X-rays scattered from parallel planes were an integer number of the wavelength of radiation. If the planes of atoms, separated by a distance d, make an angle θ with the incident beam, then the path difference would be $2d\sin\theta$. So, for constructive interference, the Braggs law must be satisfied

i.e. $n\lambda = 2d\sin\theta, \; n = 1, 2, 3, \ldots\ldots$ (1.18)

λ= wavelength of the X-ray radiation

In this thesis, room-temperature and high-temperature powder X-ray diffraction experiments on the samples are carried out using Bruker D8 Advance diffractometer using Cu-Kα radiation having wavelength 1.5406 Å. Powder or precipitates of the sample were placed on a glass plate sample holder during measurement. To understand the structural evolution, we have also used temperature dependent synchrotron X-ray diffraction measurements under N_2 atm at BL-18B (Indian beamline), Photon Factory, KEK, Tsukuba, Japan. The wavelength of X-ray and temperature ranges for the measurement have been given in the experimental part of the respective chapters. The energy of the beam was set by Si(111) double crystal monochromator, which was cross-checked with Si (640b NIST) standard. All the measurements were carried out in Bragg-Brentano geometry with a divergence slit (300 μm), an anti-scattering slit (350 μm), and a receiving slit (300 μm). High-temperature measurements were carried out with Anton Paar DHS1100 heat cell.

1.7.2.2 Transmission electron microscope (TEM)

TEM is one of the important tools in material science for characterization of the microscopic structure of materials. A TEM image represents a two-dimensional projection of a three-dimensional object. TEM operates on the same basic principles as the light microscope, however, uses electrons as "light source" that makes it possible to get a resolution of about thousand times better than a visible light microscope. Instead of glass lenses focusing the light in the light microscope, the TEM uses electromagnetic lenses to focus the electrons into a very thin beam. The electron beam then travels through the specimen you want to study. When the electron beam passes through an ultra-thin specimen, it gets absorbed or diffracted through the specimen. Some of the electrons are scattered and disappear from the beam depending on the density of the material present on the focused region. A "shadow image" is formed by the interaction of the electrons transmitted through the specimen focused onto a fluorescent screen or a photographic film or by a sensor such as a charge-coupled device (CCD). TEM study allows to focus electron beam to any part of specimen and electron diffraction data from a different area of the specimen can give us more details about the accurate local structure of the sample.

TEM samples for the solid state materials were prepared by conventional mechanical and tripod polishing. Large electron transparent area was obtained by subsequent Ar ion milling in the precision ion polishing system (PIPS) with the ion energy of 4.5 eV and beam angle of 7 deg. The thickness was restricted to 40-50 μm. Bright field imaging, Diffraction pattern, HRTEM imaging is carried out in aberration corrected FEI TITAN3™ 80–300kV transmission electron microscope.

1.7.2.3 Field emission scanning electron microscope (FESEM)

A FESEM is used to visualize topographic details of the sample surface. Similar to TEM, FESEM microscope also uses electrons as a light source. Electrons are ejected from a field emission source and accelerated in a high electrical field gradient. These electrons (termed as primary electrons) produce a narrow scan beam within the high vacuum column, which bombards the sample material. The incident electrons cause emission of electrons from the sample due to elastic and inelastic scattering. The angle and velocity of these secondary electrons produced by inelastic collision of accelerated electrons with sample atoms relate

to the surface structure of the object. High-energy electrons those are produced by an elastic collision of a primary electrons with atom's nucleus of the sample are termed as backscattered electrons (BSE). Larger atoms (with a high atomic number, *Z*) have a higher chances of producing elastic collisions because of their greater cross-sectional area. Thus, a "brighter" BSE intensity correlates with higher average *Z* in the sample, and "dark" areas have lower average *Z*. BSE images are very helpful for obtaining high-resolution compositional maps of a sample.

In my Ph.D. work, I have performed both normal and BSE mode FESEM experiments using NOVA NANO SEM 600 (FEI, Germany) operated at 15 kV to study surface morphology and phase homogeneity. For BSE imaging, I have used a finely polished sample in the back-scattering mode to produce a BSE image of the surface.

1.7.2.4 High-angle annular dark-field scanning transmission electron microscopy (HAADF-STEM)

Scanning transmission electron microscope (STEM) is a special kind of transmission electron microscope, where the electron beam is focused to a fine spot (with the typical spot size of ~0.05-0.2 nm) and then scanned over the sample in such way that at each point, sample illuminated with the beam is parallel to the optical axis. HAADF-STEM is a STEM technique which receives inelastically scattered electrons at high angles using an annular dark-field (ADF) detector (from ～50 mrad to sufficiently high angle, e.g. ～200 mrad). The HAADF image intensity is reported to be proportional to the square of the *Z*-contrast (atomic number). For HAADF-STEM, I have prepared the sample by adopting similar sample preparation technique to that of TEM.

1.7.2.5 Energy dispersive X-ray analysis (EDAX)

EDAX is an analytical technique used for elemental composition analysis of the sample. EDAX makes use of the X-ray spectrum emitted by a solid sample bombarded with a focused beam of electrons. For EDAX analysis, an X-ray detector is generally integrated with FESEM instrument. Its characterization capabilities are due in large part to the fundamental principle that each element has a unique atomic structure allowing a unique

set of peaks on its electromagnetic emission spectrum. I have performed EDAX using EDAX Genesis instrument attached to FESEM column.

1.7.2.6 Atomic Force Microscopy (AFM)

The Atomic Force Microscope (AFM) is a kind of scanning probe microscope in which a topographical image of the sample surface can be achieved based on the interactions between a tip and a sample surface.[160–162] The atomic force microscope was invented by Gerd Binning et al. in 1986 at IBM Zurich based on the STM (Scanning Tunneling Microscope).[160] While the latter depends on the conductive samples, the AFM allows also the use of non-conductive samples. In 1987, the inventors were awarded the Nobel Prize in Physics for the achievements. A typical AFM consists of a cantilever with a small tip (probe) at the free end, a laser, a 4-quadrant photodiode and a scanner. The surface characteristics can be explored with very accurate resolution in a range of 100 μm to less than 1 μm. In AFM, a tip is used for imaging. It is generally made of silicon or silicon nitride (Si_3N_4). It approaches the sample in a range of interatomic distances (around 10 Å). The tip is commonly 3-15 microns in length. It is attached to the end of the spring cantilever. The cantilever is around 100-500 microns in length. When the tip, which is attached to the free end of the cantilever, come very close to the surface attractive and repulsive forces due to the interactions between the tip and the sample surface cause a negative or positive bending of the cantilever. This bending is detected by the help of a laser beam. The cantilever can be thought of as a spring. The quantity of the generated force between the tip and the surface depends on the spring constant (stiffness) of the cantilever and the distance between the tip and the surface. This force can be characterized with Hooke's Law, $F=-kx$; F = Force, k = spring constant and x = cantilever deflection. If the spring constant of the cantilever is less than surface, a bending occurs in the cantilever and this deflection is monitored. As the tip travels across the sample, it moves up and down according to the surface properties of the sample (eg. topography). These fluctuations are sourced by the interactions (electrostatic, magnetic, capillary, Van der Waals) between the tip and the sample. The displacement of the tip is measured, and a topographical image is obtained. In my work, I have performed AFM on nanosheet sample using Bruker Innova microscope in tapping mode with an antimony doped silicon tip.

1.7.2.7 X-ray photoelectron spectroscopy (XPS)

XPS is a surface analysis technique, which measures surface composition, chemical and electronic state of the present elements in a material. This technique is based on Einstein's photoelectric effect. When an X-Ray beam directs to the sample surface, the energy of the X-Ray photon is absorbed completely by core electrons of the atoms presents at the surface. XPS spectra are obtained by irradiating a material with a beam of X-rays while simultaneously measuring the kinetic energy ($E_{kinetic}$) and the number of core electrons of atoms that escape from the top 0-10 nm of the material being analyzed. A typical XPS spectrum is a plot of the number of electrons detected *vs* the binding energy of the detected electrons ($E_{binding}$), as obtained from Einstein relationship ($E_{photon} = E_{binding} + E_{kinetic} + \upsilon$, where υ is threshold frequency). Each element produces a characteristic set of XPS peaks at characteristic $E_{binding}$ values that directly identify each element presents in or on the surface of the material being analyzed. Since core electrons are close to nucleus and have binding energies characteristic of the certain chemical environment, XPS allows determining the atomic compositions of a sample or chemical state of certain elements. From the binding energy and intensity of a photoelectron peak, the elemental identity, chemical state, and quantity of a detected element can be determined. For my research work, XPS measurement has been performed on a powdered sample using Mg-Kα (1253.6 eV) X-ray source with a relative composition detection better than 0.1% on an Omicron Nano-technology spectrometer.

1.7.2.8 Inductively coupled plasma-atomic emission spectroscopy (ICP-AES)

ICP-AES is an analytical technique used to determine the accurate elemental composition of the sample. Through the use of the Inductively Coupled Plasma, an ICP-AES produces excited ions and atoms (by ionization in an intense electromagnetic field) that emit detectable amounts of light at characteristic wavelengths, with intensities proportional to the concentration of the ion. As indicated by the name, the spectra is measured and analyzed by atomic emission spectrometer (AES) using concentration-intensity correlations which are similar to the Beer-Lambert Law. ICP-AES measurements were done in Perkin-Elmer Optima 7000DV instrument. Samples were prepared by dissolved powdered samples in aqua regia (HNO_3:HCl = 1:3) followed by dilution with Millipore water.

1.7.2.9 Optical band gap

In my thesis work, the diffuse reflectance method has been used for the determination of band gap of the solid powdered materials. Diffuse reflectance is an excellent sampling tool for powdered crystalline materials. When light shines onto a powder sample, two types of reflections can occur. Some of the light undergoes specular reflection at the powder surface. Diffuse reflection happens when radiation penetrates into the sample and then emerges at all the angles after suffering multiple reflections and refractions by sample particles. A diffuse reflection accessory is designed to minimize the specular component. To estimate optical energy difference between the valence band and conduction band, optical diffuse reflectance measurements have been done with finely ground powder at room temperature using FT-IR Bruker IFS 66V/S spectrometer and Perkin-Elmer Lambda 900, UV/Vis/NIR spectrometer. Absorption (α/Λ) data were estimated from reflectance data using Kubelka−Munk equation:

$$\alpha/\Lambda = (1-R)^2/(2R) \tag{1.19}$$

where R is the reflectance, α and Λ are the absorption and scattering coefficients, respectively. The energy band gaps were derived from α/Λ vs E (eV) plots.

1.7.2.10 Raman spectroscopy

Raman spectroscopy is one of the vibrational spectroscopic techniques used to provide information on molecular vibrations and crystal structures. This technique is based on inelastic scattering of monochromatic light. A change in the molecular polarizability with respect to the vibronic coordinate is required for a molecule to exhibit Raman effect. Normally, a laser source Nd-YAG with a fixed wavelength of 532 nm, an Argon ion laser source at 514 nm or He-Ne laser at 633 nm is used as light source. The laser light interacts with molecular vibrations, phonons or other excitations in the system, resulting in the energy of the laser photons being shifted up or down. The shift in energy gives information about the vibrational modes in the system. Room temperature Raman spectroscopic measurements were carried out on pellet shaped samples using Horiba HR Evolution spectrometer with 532 nm excitation laser and HORIBA LABRAM HR800 spectrometer with the excitation wavelength of the laser 514 nm.

1.7.2.11 Differential scanning calorimetry (DSC)

DSC is a thermo-analytical technique in which the difference in the amount of heat required to increase the temperature of a sample and reference is measured as a function of temperature. Both the sample and reference are maintained at nearly the same temperature throughout the experiment. The basic principle underlying this technique is that when the sample undergoes any physical transformation such as phase transition, melting etc, amount of heat flow required to maintain both of them at the same temperature will be different. When the amount of heat required for the sample is lesser than the reference, the process is termed as exothermic. Endothermic process requires a higher amount of heat flow to maintain the temperature. By observing the difference in heat flow between the sample and reference, differential scanning calorimeters are able to measure the amount of heat absorbed or released during such transitions.

DSC data were collected using TA INSTRUMENT Differential Scanning Calorimeter (DSC Q2000) in N_2 atmosphere. The temperature range has been given in the relevant chapter.

1.7.2.12 Hall effect

The Hall effect describes the behavior of the free carriers in a semiconductor when applying an electric as well as a magnetic field along the perpendicular direction.[163] Thus, measurement of the Hall voltage is used to determine the type of charge carrier present in the system, the free carrier density and the carrier mobility. When a current-carrying semiconductor is kept in a magnetic field, the charge carriers of the semiconductor experience a force in a direction perpendicular to both the magnetic field and the current. At equilibrium, a voltage appears at the semiconductor edges. The ratio of the induced voltage to the product of the current density (I/t, where I is applied current and t is sample thickness) and the applied magnetic field (B) is defined as Hall coefficient (R_H) (Equation 1.20 and 1.21).

$$R_H = \frac{Vt}{IB} \tag{1.20}$$

$$n_H = \frac{1}{R_H e} \tag{1.21}$$

where, e is the charge of an electron (1.602 x 10^{-19} C). In this thesis Hall measurement has been done in using an ECOPIA HMS 3000 system, PPMS (Physical Property Measurement System, Quantum Design, USA) system and in a Hall equipment developed by Excel instrument. We have used a four-contact Hall-bar geometry and a varying magnetic field up for the measurements.

1.8 Thermoelectric measurements

1.8.1 Electronic transport

The power factor of the zT expression depends on the product of the Seebeck coefficient and the electrical conductivity. The Seebeck coefficient is the ratio of a resulting electric field gradient to an applied temperature gradient. In a typical measurement, the temperature is varied around a constant average temperature and the slope of the voltage (V) *vs.* temperature difference (ΔT) curve gives the Seebeck coefficient (the slope method) or just $V/\Delta T$ is measured (single point measurement). Either a specific temperature difference is stabilized before each measurement (steady-state), which takes longer, or measurements are conducted continuously while the temperature difference is varied slowly (quasi-steady-state). Little difference was found between steady-state and quasi-steady-state measurements when good thermal and electrical contact is ensured. The employed temperature difference should be kept small, but too small will lead to decreased accuracy. Usually, 4 - 20 K (or 2 - 10 K) is appropriate for the full temperature span.

In the present thesis, temperature dependent Seebeck coefficient measurement has been done using the most popular commercial instruments ULVAC ZEM 3 RIKO using off-axis 4-point geometry under low-pressure helium (He) atmosphere (Figure 1.17a). In the off-axis, 4-point geometry, the thermocouples, and voltage leads are pressed against the sides of the sample (Figure 1.17b). The instrument uses slope method to extract the Seebeck coefficient from steady-state measurements. In the slope method, the measured raw data is corrected for constant offset voltages by using the slope of several (ΔT, V) points for extracting the Seebeck coefficient. The typical sample for measurement has a rectangular shape with the dimensions of ~ 2 mm × 2 mm × 8 mm and ΔT values 5, 10, 15 K have been used in the measurement. The error in the measurement is ~ 5%. In a typical measurement,

the sample is set in a vertical position between the upper and lower electrode blocks in the heating furnace. For temperature dependent measurement, the sample was first heated to a specified temperature using an infrared (IR) furnace. Thereafter a temperature gradient across the sample was created by heating the lower part of it by a heater. Seebeck coefficient is measured by measuring the upper and lower temperatures T_1 and T_2 with the thermocouples pressed against the side of the sample, followed by measurement of voltage (ΔV) between the same wires on one side of the thermocouple.[94]

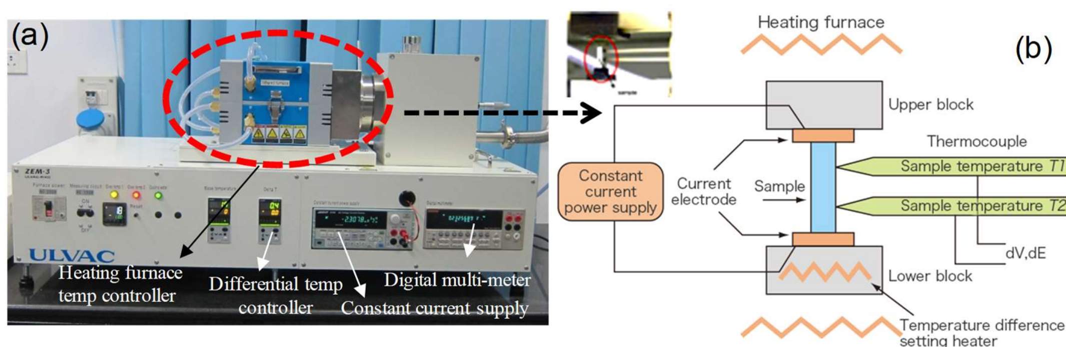

Figure 1.17 *(a) Photograph of sample-chamber in ULVAC-ZEM3 apparatus. (b) Schematic of UlVAC-ZEM 3 four-probe measurement system.*

The electrical conductivity, σ is measured using the four-probe method. Temperature dependent σ has been measured concurrently during Seebeck measurement in ULVAC ZEM 3 RIKO. For the measurement, a constant current I is applied to both ends of the sample to measure the voltage V between the thermocouple. By knowing resistance of sample, R ($R = V/I$), we can calculate σ from resistivity (ρ) of the sample using following equations:

$$\rho = R \times \frac{A}{l} \tag{1.22}$$

$$\sigma = \frac{1}{\rho} \tag{1.23}$$

where A is sample cross section and l is the distance between probes.

1.8.2 Thermal conductivity

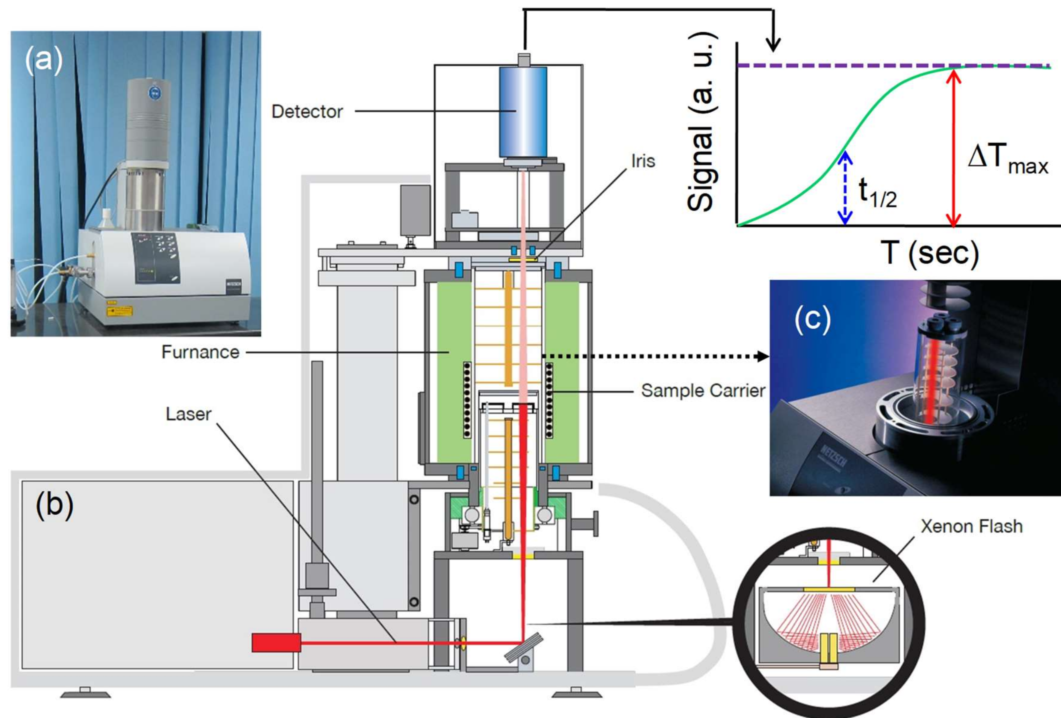

Figure 1.18 *(a) Photograph of NETZSCH LFA-457 instrument. (b) and (c) Schematic of LFA- 457 diffusivity measurement apparatus.*

The flash diffusivity method most frequently is used for the determination of thermal conductivity (κ) of material. Non-contact, non-destructive, easy sample preparation, applicability for a wide range of diffusivity values with excellent accuracy and reproducibility makes this method more advantageous than direct method. In the flash diffusivity method, the thermal conductivity is calculated as $\kappa = DC_p\rho$, where D is thermal diffusivity, ρ is density, and C_p is the constant pressure heat capacity. In this method, the sample is mounted on a carrier system, which is located in a furnace. After the sample reaches a predetermined temperature, a short heat pulse from a pulsed laser is applied to one side of a thin sample, resulting in homogeneous heating. The relative temperature increase on the rear face of the sample is then measured as a function of time by an IR detector. The temperature will rise to a maximum, after which it will decay. The time for

the temperature to increase to half-maximum, $t_{1/2}$, is used to calculated the thermal diffusivity using equation 1.24

$$D = 0.1388 \times \frac{l^2}{t_{1/2}} \tag{1.24}$$

where D is thermal diffusivity in cm^2/sec, l is the thickness.[164]

In this thesis, temperature dependent thermal transport measurement has been done using the most popular NETZSCH LFA-457 instrument in N_2 atmosphere (Figure 1.18). Coins with ~ 8 mm diameter and ~ 2 mm thickness were used for all the measurements. The samples were coated with a thin layer of graphite (~ 5 μm) in order to enhance the absorption of laser energy and emission of IR radiation to the detector. It also increases the signal to noise ratio. The error for the κ_{total} measurement is ~ 5%. The samples were placed inside SiC sample holder to mount on carrier system (Figure 1.18c). A Nd-Glass pulsed laser source of wavelength 1054 nm has been used for all the measurement. To measure the increased temperature on the rear face of the sample a liquid N_2 cooled InSb IR detector has been used. The density (ρ) was determined using the dimensions and mass of the sample and C_p, was derived indirectly using a standard sample (pyroceram). The thermal diffusivity data were analyzed using a Cowan model with pulse correction to account for heat losses on the sample faces.[165]

1.8.3 Fabrication of thermoelement and measurement of power-conversion efficiency

A thermoelectric material can be combined with metal electrodes to form a thermoelectric element to measure its power-generating properties. The thermoelement here were prepared using powder metallurgy processes to create stacked Cu/Fe/powdered TE material/Fe/Cu structures. The powders were charged into a graphite die such that the thickness of each electrode layer was 0.3 mm, and that of the thermoelectric material layer was 7.7 mm. The powder layers were consolidated into thermoelement using Spark Plasma Sintering at ~ 773 K and a pressure of 50 MPa in vacuum for 5 min.

Power generating properties and thermoelectric conversion efficiency of the fabricated thermoelement has been measured using mini-PEM module testing system

(Advance Riko, Figure 1.19a).[166] This system was used to conduct the current load tests of the thermo-elements with large temperature gradients. A schematic of the experimental apparatus is shown in Figure 1.19b. The thermo-element was sandwiched between Cu blocks; the upper block contained a heating element and the lower block functioned as an isothermal heat sink with an integrated flow calorimeter. High temperature part can reach up to 600 °C (standard specifications), while low temperature part is cooled with water flow. Thermocouples were used to monitor the temperatures of the upper (Th) and lower (Tc) Cu foils. A DC supply was connected to either end of the TE element. The conversion efficiency is evaluated from current dependency of power generation measured with four-probe method and heat flow measured with heat flow meter.

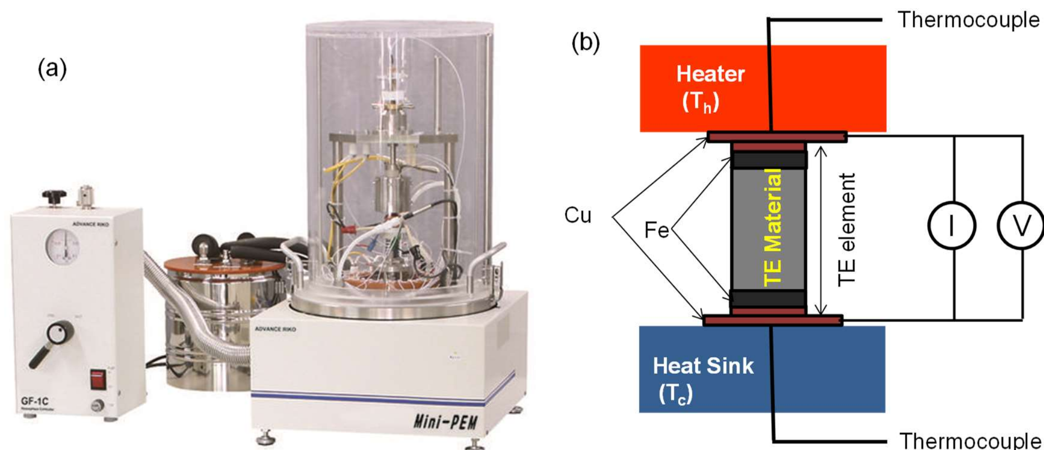

Figure 1.19. *(a) Photograph of Mini-PEM instrument. (b) Schematic diagram of the mounted thermoelement in the Mini-PEM test system.*

1.9 Scope of the thesis

Metal chalcogenides/oxy-chalcogenides present a common platform for exploring thermoelectrics, topological quantum materials and ferroelectricity. In my Ph.D. work, I have synthesized and investigated detailed structure-property relationships of various metal chalcogenides/oxychalcogenides/topological quantum materials of varied structures and dimensionality for exploring their thermoelectric and ferroelectric properties. Apart from the present introductory part (**part 1**), my thesis work is divided into three parts (2-4), containing five, three and two chapters respectively.

Thermoelectric (TE) materials constitute a viable means of efficient energy management in near future, by converting the untapped heat into electrical energy. PbTe and its derivatives from IV-VI metal chalcogenides family have been established as champion thermoelectric materials for mid-temperature power generation.[21,26,39,69,70] However, it is the toxicity of lead which prevents mass market applications for TE power-generation. Recently, GeTe-based TE materials are gaining attention as high performance p-type TE materials and an alternative to PbTe-based TE materials.[71–73] **Part 2** of my thesis work involves the optimization of all the TE parameters and development of high-performance germanium telluride based TE materials. GeTe crystallizes in rhombohedral structure (*R3m*) at room temperature which is ferroelectric in nature and it undergoes a second order displacive phase transition to cubic structure (Fm3m, paraelectric) at high temperature (> 673 K). This ferroelectric -paraelectric phase transition also plays a vital in dictating TE performance of GeTe. However, the main constrains in the way of optimizing TE performance of GeTe is its high p-type carrier concentration driven by Ge-vacancies, high thermal conductivity and low Seebeck-coefficient values. In **Part 2** of the thesis, I have addressed all these issues and developed various high-performance GeTe-based TE materials. I have minimized κ_{lat} of GeTe near to the theoretical minimum limit, κ_{min} by nanostructuring, enabled by alloying it with $AgSbSe_2$ and $AgBiSe_2$. A high average figure of merit, $zT_{avg} \sim 1.4$ and zT of 1.9 is achieved in GeTe by alloying with $AgSbSe_2$. Further, alloying of $AgBiSe_2$ with GeTe results in an intriguing evolution in its crystal and electronic structures, resulting in n-type electronic conduction in cubic-GeTe which is the first instances in GeTe-based TE community. I have demonstrated that the ambient rhombohedral structure of pristine GeTe transforms into cubic phase in $(GeTe)_{100-}$

$_x(AgBiSe_2)_x$ for x ≥ 25, with concurrent change from its p-type electronic character to n-type character in electronic transport properties. I have reported that extremely high TE conversion efficiency of ~ 12.3% and zT of 2.1 in GeTe, enabled by distinct but complementary role of Bi and In co-dopants. In doping significantly enhances the S of GeTe through the formation of resonance level, while Bi doping markedly reduces the κ_{lat} of GeTe due to the formation of extensive solid solution point defects and domain variants. Further, BiSe alloying (4-8%) enables to achieve very high thermoelectric performance (zT ~ 2.2) in GeTe by creating Ge-nanoprecipitates of different sizes and optimizing its carrier concentration. Further, I have investigated the power generating properties of GeTe-x% BiSe based single leg thermo-element. Although Nano-structuring in GeTe shows great promise to minimize κ_{lat} and to improve its thermoelectric performance. However, nano-structuring also affects μ which is detrimental for electronic transport in GeTe. I have shown an innovative strategy to minimize its κ_{lat} of GeTe by creating entropy driven extensive solid solution point defects with minimal effect on μ.

Topological quantum materials, TQM (*e*.g. topological insulators, topological crystalline insulators and topological semimetals), characterized by their nontrivial electronic surface states, have created a sensation in designing new TE materials.[20] Underlying reason for TQM being a source of potential candidates for TE is ascribed to the fact that both TQM and TE materials demand similar material features such as the presence of heavy constituent elements, narrow band gap and strong spin-orbit coupling (SOC). **Part 3** of my thesis discusses investigations of TE properties with detailed understanding of structure property relationship of few intriguing TQM from $(Bi_2)_m(Bi_2X_3)_n$ (x = Se/Te; m,n - integer) homologous family.[138,167,168] I have reported realization of ultralow κ_{lat} and high *n*-type thermoelectric performance in BiSe, a weak topological insulator (WTI) from $(Bi_2)_m(Bi_2Se_3)_n$ homologous family.[139] Detailed investigations of various aspects of the structure and lattice dynamics through measurements of low temperature heat capacity and first-principles density functional theoretical (DFT) calculations, indicates localized vibrations of Bi-bilayer is responsible for the unusually low κ_{lat} of ~ 0.6 W/mK in BiSe. I have demonstrated simultaneous occurrence of intrinsically low κ_{lat} of ~ 0.5-0.8 W/mK and high μ of ~ 500 -707 cm^2/Vs in *n*-type BiTe, facilitated by its unique dual topological quantum phases.[145] BiTe being a WTI hosts layered hetero-structure and hence it exhibits

low κ_{lat}; while BiTe, being a TCI with metallic surface states, possess high μ. I have developed a general and facile wet chemical procedure for synthesizing ultra-thin 2D-nanosheets of various topological quantum materials with layered heterostructure such as BiSe, Bi_4Se_3 from $(Bi_2)_m(Bi_2Se_3)_n$ homologous family.[138,167] Further BiSe, Bi_4Se_3 nanosheets exhibit ultra-low κ_{lat} throughput the measured temperature (300 K -623 K) which is lower than that of Bi_2Se_3 with simple layered structure. Presence of metallic surface states also facilities to obtain high carrier mobility of ~ 100 -200 cm^2/Vs in the synthesized nanosheets of the TQM.

Moreover, ferroelectrics, with spontaneous switchable electric polarization, are a vital branch of functional materials due to their broad use in nanodevices, such as field-effect transistors (FET), random-access memory (RAM), and photovoltaics.[155] Layered metal chalcogenides or oxy-chalcogenides are potential candidates for exploring ferroelectricity in nano-dimension.[152,154–156] **Part 4** of my thesis involves investigations of transport and ferroelectric properties of few bismuth oxy-chalcogenides based materials because of their better thermal and environmental stability. Nanosheets of BiCuSeO exhibit nanosheets exhibits a superior power factor and lower κ_{lat} compared to that of the bulk sample. Ultrathin ferroelectric semiconductors with high charge carrier mobility are much coveted systems for the advancement of various electronic and optoelectronic devices. I have shown the emergence of an ordered ferroelectric ground state in ultrathin (~ 2 nm) single crystalline nanosheet of Bi_2O_2Se at room temperature. Free-standing ferroelectric nanosheets, in which oppositely charged alternating layers are self-assembled together by electrostatic interactions, are synthesized by a simple, rapid and scalable wet chemical procedure at room temperature. The existence and origin of ferroelectricity in Bi_2O_2Se nanosheets is confirmed by various experiments such as piezoforce microscopy, DSC, dielectric measurements and density functional theory calculations.

To summarize, in the initial part of my thesis (**Part 2**), I have examined the thermoelectric properties of germanium telluride based materials. My research work involves implications of the recent state-of-art strategies modulation of crystal and electronic structure, point defects and nanostructure induced phonon scattering to reduce κ_{lat} for designing high-performance p- and n-type GeTe-based TE materials which can guide in developing efficient GeTe-based TE power-generators for mid-temperature

applications. I have also strived to understand the correlation between crystal structure, bonding, electronic structure, phonon dispersion to explain observed thermoelectric properties of various intriguing topological quantum materials (**Part 3**) and ferroelectric properties of layered metal oxy-chalcogenides (**Part 4**).

1.10 References

(1) Tan, G.; Zhao, L. D.; Kanatzidis, M. G. *Chem. Rev.* **2016**, *116*, 12123.
(2) Zeier, W. G.; Zevalkink, A.; Gibbs, Z. M.; Hautier, G.; Kanatzidis, M. G.; Snyder, G. J. *Angew. Chemie Int. Ed.* **2016**, *55*, 6826.
(3) Sootsman, J. R.; Chung, D. Y.; Kanatzidis, M. G. *Angew. Chemie Int. Ed.* **2009**, *48*, 8616.
(4) Snyder, G. J.; Toberer, E. S. *Nat. Mater.* **2008**, *7*, 105.
(5) Samanta, M.; Dutta, M.; Biswas, K. *Advances in the Chemistry and Physics of Materials*; WORLD SCIENTIFIC, **2019**, 350.
(6) Snyder, G. J.; Ursell, T. S. *Phys. Rev. Lett.* **2003**, *91*, 148301.
(7) Liu, W.; Jie, Q.; Kim, H. S.; Ren, Z. *Acta Mater.* **2015**, *87*, 357.
(8) Kim, H. S.; Liu, W.; Chen, G.; Chu, C.-W.; Ren, Z. *Proc. Natl. Acad. Sci.* **2015**, *112*, 8205.
(9) Yang, J.; Caillat, T. *MRS Bull.* **2006**, *31*, 224.
(10) Fleurial, J.-P. *JOM* **2009**, *61*, 79.
(11) Orr, B.; Akbarzadeh, A.; Mochizuki, M.; Singh, R. *Appl. Therm. Eng.* **2016**, *101*, 490.
(12) Ge, Z. H.; Zhao, L. D.; Wu, D.; Liu, X.; Zhang, B. P.; Li, J. F.; He, J. *Mater. Today* **2016**, *19*, 227.
(13) Goldsmid, H. J.; Douglas, R. W. T. *J. Appl. Phys.* **1954**, *5*, 386.
(14) Kraemer, D.; Poudel, B.; Feng, H.-P.; Caylor, J. C.; Yu, B.; Yan, X.; Ma, Y.; Wang, X.; Wang, D.; Muto, A.; McEnaney, K.; Chiesa, M.; Ren, Z.; Chen, G. *Nat. Mater.* **2011**, *10*, 532.
(15) Beretta, D.; Neophytou, N.; Hodges, J. M.; Kanatzidis, M. G.; Narducci, D.; Martin-Gonzalez, M.; Beekman, M.; Balke, B.; Cerretti, G.; Tremel, W.; Zevalkink, A.; Hofmann, A. I.; Müller, C.; Dörling, B.; Campoy-Quiles, M.; Caironi, M. *Mater. Sci. Eng. R Reports* **2019**, *138*, 100501.
(16) Chen, Z.; Zhang, X.; Pei, Y. *Adv. Mater.* **2018**, *30*, 1705617.
(17) Jana, M. K.; Biswas, K. *ACS Energy Lett.* **2018**, *3*, 1315.
(18) Cahill, David G. Watson, S. K., Pohl, R. O. *Phys. Rev. B* **1992**, *46*, 6131.
(19) Agne, M. T.; Hanus, R.; Snyder, G. J. *Energy Environ. Sci.* **2018**, *11*, 609.
(20) Roychowdhury, S.; Samanta, M.; Banik, A.; Biswas, K. *J. Solid State Chem.* **2019**, *275*, 103.
(21) Heremans, J. P.; Jovovic, V.; Toberer, E. S.; Saramat, A.; Kurosaki, K.; Charoenphakdee, A.; Yamanaka, S.; Snyder, G. J. *Science* **2008**, *321*, 554.
(22) Jaworski, C. M.; Kulbachinskii, V.; Heremans, J. P. *Phys. Rev. B* **2009**, *80*, 233201.
(23) Wu, L.; Li, X.; Wang, S.; Zhang, T.; Yang, J.; Zhang, W.; Chen, L.; Yang, J. *NPG Asia Mater.* **2017**, *9*, e343.
(24) Zhang, Q.; Liao, B.; Lan, Y.; Lukas, K.; Liu, W.; Esfarjani, K.; Opeil, C.; Broido, D.; Chen, G.; Ren, Z. *Proc. Natl. Acad. Sci.* **2013**, *110*, 13261.
(25) Heremans, J. P.; Wiendlocha, B.; Chamoire, A. M. *Energy Environ. Sci.* **2012**, *5*, 5510.
(26) Pei, Y.; Shi, X.; LaLonde, A.; Wang, H.; Chen, L.; Snyder, G. J. *Nature* **2011**, *473*, 66.
(27) Zheng, Z.; Su, X.; Deng, R.; Stoumpos, C.; Xie, H.; Liu, W.; Yan, Y.; Hao, S.; Uher, C.; Wolverton, C.; Kanatzidis, M. G.; Tang, X. *J. Am. Chem. Soc.* **2018**, *140*, 2673.
(28) Banik, A.; Shenoy, U. S.; Saha, S.; Waghmare, U. V.; Biswas, K. *J. Am. Chem. Soc.* **2016**,

138, 13068.
(29) Banik, A.; Shenoy, U. S.; Anand, S.; Waghmare, U. V.; Biswas, *Chem. Mater.* **2015**, *27*, 581.
(30) Nshimyimana, E.; Hao, S.; Su, X.; Zhang, C.; Liu, W.; Yan, Y.; Uher, C.; Wolverton, C.; Kanatzidis, M. G.; Tang, X. *J. Mater. Chem. A* **2020**, *8*, 1193.
(31) Roychowdhury, S.; Shenoy, U. S.; Waghmare, U. V.; Biswas, K. *Angew. Chemie - Int. Ed.* **2015**, *54*, 15241.
(32) Xiao, Y.; Wang, D.; Qin, B.; Wang, J.; Wang, G.; Zhao, L.-D. *J. Am. Chem. Soc.* **2018**, *140*, 13097.
(33) Samanta, M.; Biswas, K. *J. Am. Chem. Soc.* **2017**, *139*, 9382.
(34) Banik, A.; Vishal, B.; Perumal, S.; Datta, R.; Biswas, K. *Energy Environ. Sci.* **2016**, *9*, 2011.
(35) Androulakis, J.; Lin, C.-H.; Kong, H.-J.; Uher, C.; Wu, C.-I.; Hogan, T.; Cook, B. A.; Caillat, T.; Paraskevopoulos, K. M.; Kanatzidis, M. G. *J. Am. Chem. Soc.* **2007**, *129*, 9780.
(36) Pei, Y.; Heinz, N. a.; LaLonde, A.; Snyder, G. J. *Energy Environ. Sci.* **2011**, *4*, 3640.
(37) Samanta, M.; Roychowdhury, S.; Ghatak, J.; Perumal, S.; Biswas, K. *Chem. - A Eur. J.* **2017**, *23*, 7438.
(38) Zhao, L. D.; Wu, H. J.; Hao, S. Q.; Wu, C. I.; Zhou, X. Y.; Biswas, K.; He, J. Q.; Hogan, T. P.; Uher, C.; Wolverton, C.; Dravid, V. P.; Kanatzidis, M. G. *Energy Environ. Sci.* **2013**, *6*, 3346.
(39) Biswas, K.; He, J.; Blum, I. D.; Wu, C.-I.; Hogan, T. P.; Seidman, D. N.; Dravid, V. P.; Kanatzidis, M. G. *Nature* **2012**, *489*, 414.
(40) Dutta, M.; Pal, K.; Waghmare, U. V.; Biswas, K. *Chem. Sci.* **2019**, *10*, 4905.
(41) Jana, M. K.; Pal, K.; Warankar, A.; Mandal, P.; Waghmare, U. V; Biswas, K. *J. Am. Chem. Soc.* **2017**, *139*, 4350.
(42) Berry, T.; Fu, C.; Auffermann, G.; Fecher, G. H.; Schnelle, W.; Serrano-Sanchez, F.; Yue, Y.; Liang, H.; Felser, C. *Chem. Mater.* **2017**, *29*, 7042.
(43) Korringa, J.; Gerritsen, A. N. *Physica* **1953**, *19*, 457.
(44) Ravich, Y. I.; Nemov, S. A. *Semiconductors* **2002**, *36*, 1.
(45) Li, J.; Zhang, X.; Chen, Z.; Lin, S.; Li, W.; Shen, J.; Witting, I. T.; Faghaninia, A.; Chen, Y.; Jain, A.; Chen, L.; Snyder, G. J.; Pei, Y. *Joule* **2018**, *2*, 976.
(46) Roychowdhury, S.; Biswas, K. *Chem* **2018**, *4*, 939.
(47) Vineis, C. J.; Shakouri, A.; Majumdar, A.; Kanatzidis, M. G. *Adv. Mater.* **2010**, *22*, 3970.
(48) Callaway, J.; von Baeyer, H. *Phys. Rev.* **1960**, *120*, 1149.
(49) Callaway, J. Summary for Policymakers. *Phy. Rev* **1960**, *120*, 1149.
(50) Klemens, P. G. *Phys. Rev.* **1960**, *119*, 507.
(51) Kanatzidis, M. G. *Chem. Mater.* **2010**, *22*, 648.
(52) Korkosz, R. J.; Chasapis, T. C.; Lo, S.; Doak, J. W.; Kim, Y. J.; Wu, C.-I.; Hatzikraniotis, E.; Hogan, T. P.; Seidman, D. N.; Wolverton, C.; Dravid, V. P.; Kanatzidis, M. G. *J. Am. Chem. Soc.* **2014**, *136*, 3225.
(53) Min, Y.; Roh, J. W.; Yang, H.; Park, M.; Kim, S. Il; Hwang, S.; Lee, S. M.; Lee, K. H.; Jeong, U. *Adv. Mater.* **2013**, *25*, 1425.
(54) Biswas, K.; He, J.; Zhang, Q.; Wang, G.; Uher, C.; Dravid, V. P.; Kanatzidis, M. G. *Nat. Chem.* **2011**, *3*, 160.
(55) Hsu, K. F.; Loo, S.; Guo, F.; Chen, W.; Dyck, J. S.; Uher, C.; Hogan, T.; Polychroniadis, E. K.; Kanatzidis, M. G. *Science* **2004**, *303*, 818.
(56) Ke, X.; Chen, C.; Yang, J.; Wu, L.; Zhou, J.; Li, Q.; Zhu, Y.; Kent, P. R. C. *Phys. Rev. Lett.* **2009**, *103*, 145502.
(57) Sootsman, J. R.; Pcionek, R. J.; Kong, H.; Uher, C.; Kanatzidis, M. G. *Chem. Mater.* **2006**, *18*, 4993.
(58) Rowe, D. M.; Shukla, V. S.; Savvides, N. *Nature* **1981**, *290*, 765.
(59) Delaire, O.; Ma, J.; Marty, K.; May, A. F.; McGuire, M. A.; Du, M.-H.; Singh, D. J.;

Podlesnyak, A.; Ehlers, G.; Lumsden, M. D.; Sales, B. C. *Nat. Mater.* **2011**, *10*, 614.
(60) Qiu, W.; Xi, L.; Wei, P.; Ke, X.; Yang, J.; Zhang, W. *Proc. Natl. Acad. Sci. U. S. A.* **2014**, *111*, 15031.
(61) Snyder, G. J.; Christensen, M.; Nishibori, E.; Caillat, T.; Iversen, B. B. *Nat. Mater.* **2004**, *3*, 458.
(62) Jana, M. K.; Pal, K.; Waghmare, U. V; Biswas, K. *Angew. Chemie - Int. Ed.* **2016**, *55*, 7792.
(63) Li, B.; Wang, H.; Kawakita, Y.; Zhang, Q.; Feygenson, M.; Yu, H. L.; Wu, D.; Ohara, K.; Kikuchi, T.; Shibata, K.; Yamada, T.; Ning, X. K.; Chen, Y.; He, J. Q.; Vaknin, D.; Wu, R. Q.; Nakajima, K.; Kanatzidis, M. G. *Nat. Mater.* **2018**, *17*, 226.
(64) Liu, H.; Shi, X.; Xu, F.; Zhang, L.; Zhang, W.; Chen, L.; Li, Q.; Uher, C.; Day, T.; Snyder, G. J.
Nat. Mater. **2012**, *11*, 422.
(65) Lee, S.; Esfarjani, K.; Luo, T.; Zhou, J.; Tian, Z.; Chen, G. *Nat. Commun.* **2014**, *5*, 3525.
(66) Nielsen, M. D.; Ozolins, V.; Heremans, J. P. *Energy Environ. Sci.* **2013**, *6*, 570.
(67) Skoug, E. J.; Morelli, D. T. *Phys. Rev. Lett.* **2011**, *107*, 235901.
(68) Xiao, Y.; Chang, C.; Pei, Y.; Wu, D.; Peng, K.; Zhou, X.; Gong, S.; He, J.; Zhang, Y.; Zeng, Z.; Zhao, L.-D. *Phys. Rev. B* **2016**, *94*, 125203.
(69) Wu, H. J.; Zhao, L.-D.; Zheng, F. S.; Wu, D.; Pei, Y. L.; Tong, X.; Kanatzidis, M. G.; He, J. Q. *Nat. Commun.* **2014**, *5*, 4515.
(70) Chen, Z.; Ge, B.; Li, W.; Lin, S.; Shen, J.; Chang, Y.; Hanus, R.; Snyder, G. J.; Pei, Y. *Nat. Commun.* **2017**, *8*, 13828
(71) Perumal, S.; Roychowdhury, S.; Biswas, K. *J. Mater. Chem. C* **2016**, *4*, 7520.
(72) Roychowdhury, S.; Samanta, M.; Perumal, S.; Biswas, K. *Chem. Mater.* **2018**, *30*, 5799.
(73) Hong, M.; Zou, J.; Chen, Z. *Adv. Mater.* **2019**, *31*, 1807071.
(74) Rosi, F. D.; Dismukes, J. P.; Hockings, E. F. *Electr. Eng.* **1960**, *79*, 450.
(75) Rabe, K. M.; Joannopoulos, J. D. *Phys. Rev. B* **1987**, *36*, 6631.
(76) Shaltaf, R.; Gonze, X.; Cardona, M.; Kremer, R. K.; Siegle, G. *Phys. Rev. B* **2009**, *79*, 075204.
(77) Waghmare, U. V; Spaldin, N. A.; Kandpal, H. C.; Seshadri, R. F *Phys. Rev. B* **2003**, *67*, 125111.
(78) Polking, M. J.; Han, M.-G.; Yourdkhani, A.; Petkov, V.; Kisielowski, C. F.; Volkov, V. V; Zhu, Y.; Caruntu, G.; Paul Alivisatos, A.; Ramesh, R. *Nat. Mater.* **2012**, *11*, 700.
(79) Shaltaf, R.; Durgun, E.; Raty, J. Y.; Ghosez, P.; Gonze, X. *Phys. Rev. B - Condens. Matter Mater. Phys.* **2008**, *78*, 205203.
(80) Balagurov, A. M.; Kozlova, E. P.; Mironova, G. M.; Jacyna-Onyszkiewicz, I. *Phys. Status Solidi* **1993**, *136*, 57.
(81) Steigmeier, E. .; Harbeke, G. *Solid State Commun.* **1970**, *8*, 1275.
(82) Wdowik, U. D.; Parlinski, K.; Rols, S.; Chatterji, T. *Phys. Rev. B - Condens. Matter Mater. Phys.* **2014**, *89*, 224306.
(83) Chatterji, T.; Kumar, C. M. N.; Wdowik, U. D. *Phys. Rev. B - Condens. Matter Mater. Phys.* **2015**, *91*, 054110.
(84) Sun, Z.; Zhou, J.; Mao, H.; Ahuja, R. *Proc. Natl. Acad. Sci. U. S. A.* **2012**, *109*, 5948.
(85) Bauer Pereira, P.; Sergueev, I.; Gorsse, S.; Dadda, J.; M??ller, E.; Hermann, R. P. *Phys. Status Solidi Basic Res.* **2013**, *250*, 1300.
(86) Hong, M.; Chen, Z.-G.; Yang, L.; Zou, Y.-C.; Dargusch, M. S.; Wang, H.; Zou, J. *Adv. Mater.* **2018**, *30*, 1705942.
(87) Banik, A.; Ghosh, T.; Arora, R.; Dutta, M.; Pandey, J.; Acharya, S.; Soni, A.; Waghmare, U. V.; Biswas, K. *Energy Environ. Sci.* **2019**, *12*, 589.
(88) Liu, Z.; Sun, J.; Mao, J.; Zhu, H.; Ren, W.; Zhou, J.; Wang, Z.; Singh, D. J.; Sui, J.; Chu, C.-W.; Ren, Z. *Proc. Natl. Acad. Sci.* **2018**, *115*, 5332.
(89) Wu, D.; Zhao, L.-D.; Hao, S.; Jiang, Q.; Zheng, F.; Doak, J. W.; Wu, H.; Chi, H.; Gelbstein,

Y.; Uher, C.; Wolverton, C.; Kanatzidis, M.; He, J. *J. Am. Chem. Soc.* **2014**, *136*, 11412.
(90) Davidow, J.; Gelbstein, Y. *J. Electron. Mater.* **2013**, *42*, 1542.
(91) Gelbstein, Y.; Davidow, J. *Phys. Chem. Chem. Phys.* **2014**, *16*, 20120.
(92) Hazan, E.; Ben-Yehuda, O.; Madar, N.; Gelbstein, Y. *Adv. Energy Mater.* **2015**, *5*, 1500272.
(93) Salvador, J. R.; Yang, J.; Shi, X.; Wang, H.; Wereszczak, A. A. *J. Solid State Chem.* **2009**, *182*, 2088.
(94) Perumal, S.; Roychowdhury, S.; Negi, D. S.; Datta, R.; Biswas, K. *Chem. Mater.* **2015**, *27*, 7171.
(95) Perumal, S.; Bellare, P.; Shenoy, U. S.; Waghmare, U. V.; Biswas, K. *Chem. Mater.* **2017**, *29*, 10426.
(96) Perumal, S.; Roychowdhury, S.; Biswas, K. *Inorg. Chem. Front.* **2016**, *3*, 125.
(97) Li, J.; Zhang, X.; Lin, S.; Chen, Z.; Pei, Y. *Chem. Mater.* **2017**, *29*, 605.
(98) Zhang, X.; Li, J.; Wang, X.; Chen, Z.; Mao, J.; Chen, Y.; Pei, Y. *J. Am. Chem. Soc.* **2018**, *140*, 15883.
(99) Levin, E. M.; Besser, M. F.; Hanus, R. *J. Appl. Phys.* **2013**, *114*, 083713.
(100) Li, J.; Chen, Z.; Zhang, X.; Sun, Y.; Yang, J.; Pei, Y. *NPG Asia Mater.* **2017**, *9*, e353-8.
(101) Hong, M.; Wang, Y.; Liu, W.; Matsumura, S.; Wang, H.; Zou, J.; Chen, Z.-G. *Adv. Energy Mater.* **2018**, *8*, 1801837.
(102) Mao, J.; Liu, Z.; Ren, Z. *npj Quantum Mater.* **2016**, *1*, 16028.
(103) Zhou, Y.; Zhao, L. D. *Adv. Mater.* **2017**, *29*, 1702676.
(104) Wu, J.; Chen, Y.; Wu, J.; Hippalgaonkar, K. *Adv. Electron. Mater.* **2018***, 4, 1800248*.
(105) Dresselhaus, M. S.; Chen, G.; Tang, M. Y.; Yang, R.; Lee, H.; Wang, D.; Ren, Z.; Fleurial, J. P.; Gogna, P. *Adv. Mater.* **2007**, *19*, 1043.
(106) Yim, W. M.; Rosi, F. D. *Solid. State. Electron.* **1972**, *15*, 1121.
(107) Heremans, J. P.; Cava, R. J.; Samarth, N. *Nat. Rev. Mater.* **2017**, *2*, 17049.
(108) Hao, F.; Qiu, P.; Tang, Y.; Bai, S.; Xing, T.; Chu, H. S.; Zhang, Q.; Lu, P.; Zhang, T.; Ren, D.; Chen, J.; Shi, X.; Chen, L. *Energy Environ. Sci.* **2016**, *9*, 3120.
(109) Poudel, B.; Hao, Q.; Ma, Y.; Lan, Y.; Minnich, A.; Yu, B.; Yan, X.; Wang, D.; Muto, A.; Vashaee, D.; Chen, X.; Liu, J.; Dresselaus; Chen, G.; Ren, Z. *Science* **2008**, *320*, 634.
(110) Kim, S. Il; Lee, K. H.; Mun, H. A.; Kim, H. S.; Hwang, S. W.; Roh, J. W.; Yang, D. J.; Shin, W. H.; Li, X. S.; Lee, Y. H.; Snyder, G. J.; Kim, S. W. *Science* **2015**, *348*, 109.
(111) Zhao, L.-D.; Tan, G.; Hao, S.; He, J.; Pei, Y.; Chi, H.; Wang, H.; Gong, S.; Xu, H.; Dravid, V. P.; Uher, C.; Snyder, G. J.; Wolverton, C.; Kanatzidis, M. G. *Science* **2016**, *351*, 141.
(112) Zhao, L.-D.; Lo, S.-H.; Zhang, Y.; Sun, H.; Tan, G.; Uher, C.; Wolverton, C.; Dravid, V. P.; Kanatzidis, M. G. *Nature* **2014**, *508*, 373.
(113) Chang, C.; Wu, M.; He, D.; Pei, Y.; Wu, C.-F.; Wu, X.; Yu, H.; Zhu, F.; Wang, K.; Chen, Y.; Huang, L.; Li, J.-F.; He, J.; Zhao, L.-D. *Science* **2018**, *360*, 778.
(114) Duong, A. T.; Nguyen, V. Q.; Duvjir, G.; Duong, V. T.; Kwon, S.; Song, J. Y.; Lee, J. K.; Lee, J. E.; Park, S.; Min, T.; Lee, J.; Kim, J.; Cho, S. *Nat. Commun.* **2016**, *7*, 13713.
(115) Zhao, L. D.; Chang, C.; Tan, G.; Kanatzidis, M. G. *Energy Environ. Sci.* **2016**, *9*, 3044.
(116) Samanta, M.; Guin, S. N.; Biswas, K. *Inorg. Chem. Front.* **2017**, *4*, 84.
(117) Zhao, L.-D.; He, J.; Berardan, D.; Lin, Y.; Li, J.-F.; Nan, C.; Dragoe, N. *Energy Environ. Sci.* **2014**, *7*, 2900.
(118) Ghosh, T.; Samanta, M.; Vasdev, A.; Dolui, K.; Ghatak, J.; Das, T.; Sheet, G.; Biswas, K. *Nano Lett.* **2019**, *19*, 5703.
(119) Ruleova, P.; Drasar, C.; Lostak, P.; Li, C. P.; Ballikaya, S.; Uher, C. *Mater. Chem. Phys.* **2010**, *119*, 299.
(120) Bessas, D.; Sergueev, I.; Wille, H. C.; Peron, J.; Ebling, D.; Hermann, R. P. *Phys. Rev. B* **2012**, *86*, 224301.
(121) Heremans, J. P. *Nat. Phys.* **2015**, *11*, 990.
(122) Slack, G. A. *J. Phys. Chem. Solids* **1973**, *34*, 321.

(123) Gooth, J.; Schierning, G.; Felser, C.; Nielsch, K. *MRS Bull.* **2018**, *43*, 187.
(124) Xu, N.; Xu, Y.; Zhu, J. *npj Quantum Mater.* **2017**, *2*, 51.
(125) Banik, A.; Roychowdhury, S.; Biswas, K. *Chem. Commun.* **2018**, *54*, 6573.
(126) Müchler, L.; Zhang, H.; Chadov, S.; Yan, B.; Casper, F.; Kübler, J.; Zhang, S. C.; Felser, C. *Angew. Chemie - Int. Ed.* **2012**, *51*, 7221.
(127) Moore, J. E. *Nature* **2010**, *464*, 194.
(128) Kong, D.; Cui, Y. *Nat. Chem.* **2011**, *3*, 845.
(129) Seo, J.; Roushan, P.; Beidenkopf, H.; Hor, Y. S.; Cava, R. J.; Yazdani, A. *Nature* **2010**, *466*, 343.
(130) Hasan, M. Z.; Kane, C. L. *Rev. Mod. Phys.* **2010**, *82*, 3045.
(131) Bernevig, B. A.; Hughes, T. L.; Zhang, S.-C. *Science* **2006**, *314*, 1757.
(132) Müchler, L.; Casper, F.; Yan, B.; Chadov, S.; Felser, C. *Phys. status solidi - Rapid Res. Lett.* **2013**, *7*, 91.
(133) Ringel, Z.; Kraus, Y. E.; Stern, *Phys. Rev. B* **2012**, *86*, 045102.
(134) Hsieh, D.; Qian, D.; Wray, L.; Xia, Y.; Hor, Y. S.; Cava, R. J.; Hasan, M. Z. *Nature* **2008**, *452*, 970–974.
(135) Kim, D.; Cho, S.; Butch, N. P.; Syers, P.; Kirshenbaum, K.; Adam, S.; Paglione, J.; Fuhrer, M. S. *Nat. Phys.* **2012**, *8*, 459.
(136) Chen, Y. L.; Analytis, J. G.; Chu, J.-H.; Liu, Z. K.; Mo, S.-K.; Qi, X. L.; Zhang, H. J.; Lu, D. H.; Dai, X.; Fang, Z.; Zhang, S. C.; Fisher, I. R.; Hussain, Z.; Shen, Z.-X. *Science* **2009**, *325*, 178.
(137) Zhang, H.; Liu, C. X.; Qi, X. L.; Dai, X.; Fang, Z.; Zhang, S. C. *Nat. Phys.* **2009**, *5*, 438.
(138) Lind, H.; Lidin, S.; Häussermann, U. *Phys. Rev. B - Condens. Matter Mater. Phys.* **2005**, *72*, 184101.
(139) Majhi, K.; Pal, K.; Lohani, H.; Banerjee, A.; Mishra, P.; Yadav, A. K.; Ganesan, R.; Sekhar, B. R.; Waghmare, U. V; Anil Kumar, P. S. *Appl. Phys. Lett.* **2017**, *110*, 162102.
(140) Fu, L. *Phys. Rev. Lett.* **2011**, *106*, 106802.
(141) Hsieh, T. H.; Lin, H.; Liu, J.; Duan, W.; Bansil, A.; Fu, L. *Nat. Commun.* **2012**, *3*, 982.
(142) Tanaka, Y.; Ren, Z.; Sato, T.; Nakayama, K.; Souma, S.; Takahashi, T.; Segawa, K.; Ando, Y. *Nat. Phys.* **2012**, *8*, 800.
(143) Xu, S.-Y.; Liu, C.; Alidoust, N.; Neupane, M.; Qian, D.; Belopolski, I.; Denlinger, J. D.; Wang, Y. J.; Lin, H.; Wray, L. A.; Landolt, G.; Slomski, B.; Dil, J. H.; Marcinkova, A.; Morosan, E.; Gibson, Q.; Sankar, R.; Chou, F. C.; Cava, R. J.; Bansil, A.; Hasan, M. Z. *Nat. Commun.* **2012**, *3*, 1192.
(144) Dziawa, P.; Kowalski, B. J.; Dybko, K.; Buczko, R.; Szczerbakow, A.; Szot, M.; Łusakowska, E.; Balasubramanian, T.; Wojek, B. M.; Berntsen, M. H.; Tjernberg, O.; Story, T. *Nat. Mater.* **2012**, *11*, 1023.
(145) Eschbach, M.; Lanius, M.; Niu, C.; Młyńczak, E.; Gospodarič, P.; Kellner, J.; Schüffelgen, P.; Gehlmann, M.; Döring, S.; Neumann, E.; Luysberg, M.; Mussler, G.; Plucinski, L.; Morgenstern, M.; Grützmacher, D.; Bihlmayer, G.; Blügel, S.; Schneider, C. M. *Nat. Commun.* **2017**, *8*, 14976.
(146) Martin, L. W.; Rappe, A. M. *Nat. Rev. Mater.* **2017**, *2*, 16087.
(147) Said, S. M.; Sabri, M. F. M.; Salleh, F. Ferroelectrics and Their Applications. In *Reference Module in Materials Science and Materials Engineering*; Elsevier, **2017**, 1–12.
(148) Prokhorov, E.; Trapaga, G. *J. Appl. Phys.* **2016**, *112*, *052018*.
(149) Sawyer, C. B.; Tower, C. H. *Phys. Rev.* **1930**, *35*, 269.
(150) Scott, J. F. *Science* **2007**, *315*, 954.
(151) Aggarwal, L.; Banik, A.; Anand, S.; Waghmare, U. V.; Biswas, K.; Sheet, G. *J. Materiomics* **2016**, *2*, 196.
(152) Chang, K.; Liu, J.; Lin, H.; Wang, N.; Zhao, K.; Zhang, A.; Jin, F.; Zhong, Y.; Hu, X.; Duan, W.; Zhang, Q.; Fu, L.; Xue, Q. K.; Chen, X.; Ji, S. H. *Science* **2016**, *353*, 274.

(153) Murphy, R. M.; Murray, É. D.; Fahy, S.; Savić, I. *Phys. Rev. B* **2017**, *95*, 144302.
(154) Cui, C.; Xue, F.; Hu, W.-J.; Li, L.-J. T *npj 2D Mater. Appl.* **2018**, *2*, 18.
(155) Zhang, J. J.; Guan, J.; Dong, S.; Yakobson, B. I. *J. Am. Chem. Soc.* **2019**, *141*, 15040.
(156) Shirodkar, S. N.; Waghmare, U. V. *Phys. Rev. Lett.* **2014**, *112*, 157601.
(157) Yu, H.; Gao, D.; Wang, X.; Du, X.; Lin, X.; Guo, W.; Zou, R.; Jin, C.; Li, K.; Chen, Y. *NPG Asia Mater.* **2018**, *10*, 882.
(158) Munir, Z. A.; Anselmi-Tamburini, U.; Ohyanagi, M. *J. Mater. Sci.* **2006**, *41*, 763.
(159) Xie, G. *J. Powder Metall. Min.* **2013**, *2*, e109.
(160) Binnig, G.; Quate, C. F.; Gerber, C. *Phys. Rev. Lett.* **1986**, *56*, 930.
(161) Tersoff, J.; Hamann, D. R. *Phys. Rev. Lett.* **1983**, *50*, 1998.
(162) Binnig, G.; Rohrer, H.; Gerber, C.; Weibel, E. *Phys. Rev. Lett.* **1982**, *49*, 57.
(163) Hall, E. H. *Am. J. Math.* **1879**, *2*, 287.
(164) Parker, W. J.; Jenkins, R. J.; Butler, C. P.; Abbott, G. L. *J. Appl. Phys.* **1961**, *32*, 1679.
(165) Cowan, R. D. Pulse Method of Measuring Thermal Diffusivity at High Temperatures. *J. Appl. Phys.* **1963**, *34* (4), 926–927.
(166) Kunioka, H.; Yamamoto, A.; Iida, T.; Obara, H. *Appl. Phys. Express* **2017**, *10*, 095801.
(167) Zhang, J.; Liu, X.; Huang, G. *Phys. status solidi* **2015**, *252*, 2090.
(168) Sharma, P. A.; Sharma, A. L. L.; Medlin, D. L.; Morales, A. M.; Yang, N.; Barney, M.; He, J.; Drymiotis, F.; Turner, J.; Tritt, T. M. *Phys. Rev. B - Condens. Matter Mater. Phys.* **2011**, *83*, 235209.

PART 2

Thermoelectric Properties of Germanium Telluride

Chapter 1

High Average Thermoelectric Figure of Merit, Low Lattice Thermal Conductivity and Enhanced Micro-hardness in Nanostructured $(GeTe)_x(AgSbSe_2)_{100-x}$

Chapter 1

High Average Thermoelectric Figure of Merit, Low Lattice Thermal Conductivity and Enhanced Micro-hardness in Nanostructured $(GeTe)_x(AgSbSe_2)_{100-x}$†

Summary

Waste heat sources are generally diffused and provide a range of temperatures rather than a particular temperature. Thus, thermoelectric 'waste heat to electricity conversion' requires high average thermoelectric figure of merit (zT_{avg}) of materials over the entire working temperature along with high peak thermoelectric figure of merit (zT_{max}). Herein, we report an ultrahigh zT_{avg} of 1.4 for $(GeTe)_{80}(AgSbSe_2)_{20}$ [TAGSSe-80, T – Tellurium, A - Antimony, G – Germanium, S – Silver, Se – Selenium] in the temperature range of 300–700K, which is one of the highest value measured among the state-of-art Pb-free polycrystalline thermoelectric materials.Moreover, TAGSSe-80 exhibits high zT_{max} of 1.9 at 660K, which isreversible and reproducible with respect to several heating-cooling cycles. High thermoelectric performance of TAGSSe-x is attributed to extremely low lattice thermal conductivity (κ_{lat}), which mainly arises due toextensive phonon scattering by hierarchical nano/meso-structuresin the TAGSSe-x matrix. Addition of $AgSbSe_2$ in GeTe results in κ_{lat} of ~ 0.4 W/mK in the 300-700 K range, approachingto the theoretical minimum limitof lattice thermal conductivity (κ_{min}) of GeTe. Additionally, $(GeTe)_{80}(AgSbSe_2)_{20}$ exhibits higher Vickers microhardness (mechanical stability) value of ~ 209 kgf/mm^2 compared to the other the state-of-art metal chalcogenides, making it an important material for thermoelectrics.

†*Paper based on this study has been published in Chem. Eur. J.* **2017**, *23,* 7438-7443.

1.1 Introduction

The broad-based implementation of thermoelectric materials in converting heat to electricity hinges on the achievement of high conversion efficiency. Considering the diffused nature of waste heat resources, effective thermoelectric 'waste heat to electricity conversion' requires high thermoelectric performace over the entire working temperature, i.e., high average thermoelectric figure of merit, zT_{avg} of the materials are desired for device applications. Further, the efficiency of a thermoelectric device depends on the materials' zT_{avg} over the entire working temperature range, rather than it's zT_{max}.[1-4] However, most of the inorganic solid exhibits the maximum figure of merit (zT_{max}) at a particular temperature. Therefore, it is essential to improve the zT_{avg} of the thermoelectric materials over the whole temperature range of interest.

Although GeTe based alloys have been known for their promising thermoelectric properties since 1960,[5,6] pristine GeTe was not popular enough due to its high *p*-type carrier concentration of ~ 8.7 x 10^{20}/cm^3 because of the intrinsic Ge vacancies,[6-9] which gives rise to high σ of ~ 8000 S/cm, high electrical thermal conductivity (κ_{el}) and a low *S* of ~34 μV/K at room temperature.[10] Pseudo-binary solid solution compositions $(GeTe)_x(AgSbTe_2)_{100-x}$, commonly known as TAGS-x, are one of the best traditional thermoelectric materials since its discovery in 1960.[5,11-13] TAGS materials have been widely used in deep space mission by NASA for radioisotope thermoelectric generator.[13] TAGS-85 possess high zT (~1.5 at 750 K), low lattice thermal conductivity and good mechanical stability.[11,12] Other GeTe based materials such as $Ge_{1-x}Pb_xTe$,[14,15] $Ge_{1-x}(Sb/Bi)_xTe$[16,17] and $(CoGe_2)_{0.22}(GeTe)_{19}Sb_2Te_3$[18,19] recently exhibited high zT_{max} at ~750 K. Although, most of these GeTe based materials exhibit high zT_{max}, but a high zT over a wide range of temperature i.e. high zT_{avg}, with good mechanical stability are desirable for real application.

Herein, we report ultra-high zT_{avg} of 1.4 between 300-700 K with a high zT_{max} value of 1.9 at 660 K in $(GeTe)_{80}(AgSbSe_2)_{20}$ which belongs to new pseudo binary solid solution composition $(GeTe)_x(AgSbSe_2)_{100-x}$ [x = 75 - 100], termed as TAGSSe-x (T – Tellurium, A - Antimony, G – Germanium, S – Silver, Se – Selenium and x represents the percentage of GeTe). Moreover, κ_{lat} value of ~ 0.4 W/mK in the 300-700 K range was achieved for TAGSSe-80, which is indeed close the theoretical minimum limit (κ_{min}) of GeTe. This is the lowest κ_{lat} value measured so far among GeTe based materials. Transmission electron

microscopy (TEM) reveals the formation of hierarchical nano/mesostructures of different dimensions and compositions in GeTe matrix, which provide significant phonon scattering of different wave-lengths to result in ultralow κ_{lat} in TAGSSe-x. Additionally, TAGSSe-80 exhibits high Vickers microhardness (H_v) (mechanical stability) value of ~ 209 kgf/mm^2, which is higher than that of the state-of-art metal chalcogenide based thermoelectric material.

1.2 Methods

1.2.1 Reagents. Germanium (Aldrich 99.999%), tellurium (Alfa Aesar 99.999+ %), silver (Alfa Aesar 99.9999%), antimony (Alfa Aesar 99.9999%) and selenium (Alfa Aeser 99.9999%) were used for synthesis without any further purification.

1.2.2 Synthesis. Polycrystalline ingots (~6 g) of $(GeTe)_x(AgSbSe_2)_{100-x}$ (x= 10, 15, 20, 25) were synthesized by mixing stoichiometric amounts of high purity starting materials of Ge, Te, Ag, Sb, and Se in a quartz ampoule, which then sealed under vacuum (10^{-6} Torr). The tubes were slowly heated to 723 K and then to 1223 K over a time period of 12 h and 5 h respectively, then annealed for 6 h, and cooled slowly to room temperature over 10 h. For electrical and thermal properties measurement of the samples, they are cut in the shape of bar and coin respectively and finely polished.

1.2.3 Powder X-ray diffraction. Powder X-ray diffraction (PXRD) for all synthesized samples were recorded using a Cu K_α (λ = 1.5406 Å) radiation source on a Bruker D8 diffractometer.

1.2.4 Electrical Transport. Electrical conductivity and Seebeck coefficients were measured simultaneously under a helium atmosphere from room temperature to 723 K on a ULVAC-RIKO ZEM-3 instrument. For measurement, the typical dimension of the parallelepiped shaped sample was ~2×2×8 mm^3. The longer direction coincides with the direction in which the thermal conductivity was measured. Heating and cooling cycles provide reversible electrical properties for the synthesized samples.

1.2.5 Hall measurement. Hall measurement was carried out at room temperature in the setup develop by Excel instrument, where fixed magnetic field and dc-current were used to be 0.57 T and 100 mA, respectively.

1.2.6 Thermal conductivity. Thermal diffusivity, D, of the samples were directly measured in the range 300−723K by using the laser flash diffusivity method in a Netzsch LFA-457 under a nitrogen atmosphere. Coins with ∼8 mm diameter and ∼2 mm thickness were used for the measurements. Coins were coated with a thin layer of graphite to avoid errors coming from thermal emissivity of the materials. Temperature dependent heat capacity, C_p, of GeTe were derived using standard sample (pyroceram) in LFA-457, which is in good agreement with Dulong-Petit C_p value. The total thermal conductivity, κ, was calculated using the formula $\kappa = DC_p\rho$, where ρ is the density (~ 97% of theoretical density). C_p values of GeTe are used for deriving κ for all the samples. Electronic thermal conductivity (κ_{el}) of TAGSSe samples is estimated from Wiedemann-Franz law, $\kappa_{el} = L.\sigma.T$, where, L is the Lorenz number, σ is the electrical conductivity at temperature T. Temperature dependent Lorenz number was calculated based on the fitting of temperature dependent of Seebeck values assuming single parabolic band model.[16]

1.2.7 TEM measurements. TEM imaging was performed using an aberration corrected FEI TITAN cubed 80–300 kV transmission electron microscopes,operating at 300 kV.

1.2.8 Mechanical properties. Measurement of microhardness of all the samples was done in Zwick Roellzhu 2.5 microhardness machine using the diamond indenter on the Vickers hardness scale, where the force was used to be 2 N and the indent was kept for 10s. Vickers hardness (kgf/mm^2) values were determined by the equation of $H_v = 1.854xL/(2d)^2$, where 2d is the diagonal length of the indentation and L is the indentation load. In ths case, applied L is 0.1kg and the 2d value of $(GeTe)_{80}(AgSbSe_2)_{20}$ is 29.78 µm. The error in microhardness measurement is about 5%

1.3 Results & discussion

Pristine GeTe exhibits κ_{lat} of ~2.7 W/mK at room temperature,[16] whereas the theoretical limit of minimum lattice thermal conductivity (κ_{min}) of GeTe is ~ 0.3 W/mK. This hints that the presence of enormous room to decrease the κ_{lat} of GeTe. To minimize the κ_{lat} of GeTe, we have particularly chosen the combination of GeTe and $AgSbSe_2$ considering the fact that $AgSbSe_2$ has ultralow κ_{lat} of ~ 0.35 W/mK in the 300-700 K range due to Sb lone pair induced bond anharmonicity.[20,21] Furthermore, addition of $AgSbSe_2$ in GeTe may

result in formation of second phase nanostructures in the GeTe matrix due to lattice parameter mismatch of GeTe and $AgSbSe_2$, which may result in low κ_{lat} in GeTe. With this motivation we have synthesized different GeTe rich composition of TAGSSe crystalline ingots and studied the structural, microscopic and thermoelectric properties in details.

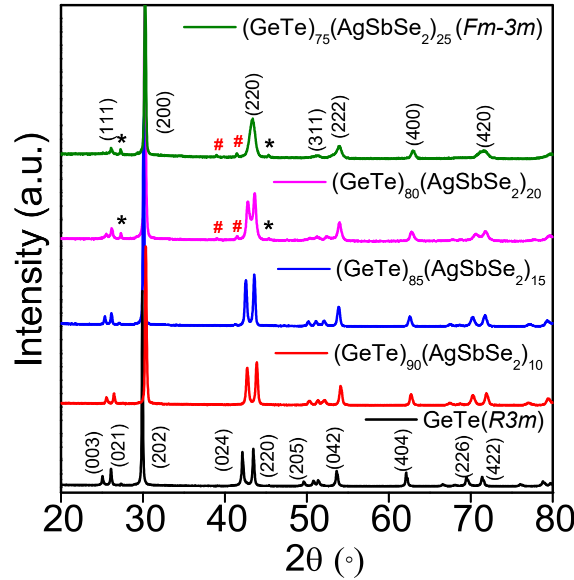

Figure 1.1. *Powder XRD pattern of* $(GeTe)_x(AgSbSe_2)_{100-x}$ *(x = 75-100). "*" and "#" sign signifies the presence of second phase of Ge and of* $Ag_{4.53}Te_3$ *rich phase respectively.*

The powder X-ray diffraction (PXRD) patterns of $(GeTe)_x(AgSbSe_2)_{100-x}$ (x = 75-100) at room temperature are presented in Figure 1.1. All samples except $(GeTe)_{75}(AgSbSe_2)_{25}$ could be indexed based on rhombohedral structure of GeTe (space group *R3m*), whereas $(GeTe)_{75}(AgSbSe_2)_{25}$ could be indexed based on cubic structure of GeTe (space group $Fm\bar{3}m$). With the increase in the percentage of $AgSbSe_2$ in $(GeTe)_x(AgSbSe_2)_{100-x}$, the double peaks at (024) and (220) between 2θ = 41 - 45° approach closer and ultimately converge to a single peak in $(GeTe)_{75}(AgSbSe_2)_{25}$, suggests that cubic nature of samples increases with increase in $AgSbSe_2$ concentration. In the PXRD pattern of $(GeTe)_x(AgSbSe_2)_{100-x}$ additional reflections due to second phases are also being observed for x = 75 and 80. These low intensity reflections occur due to the existence of second phases of Ge (space group, $Fd\bar{3}m$) and of $Ag_{4.53}Te_3$ (space group $P\bar{6}2m$) (Figure 1.1).

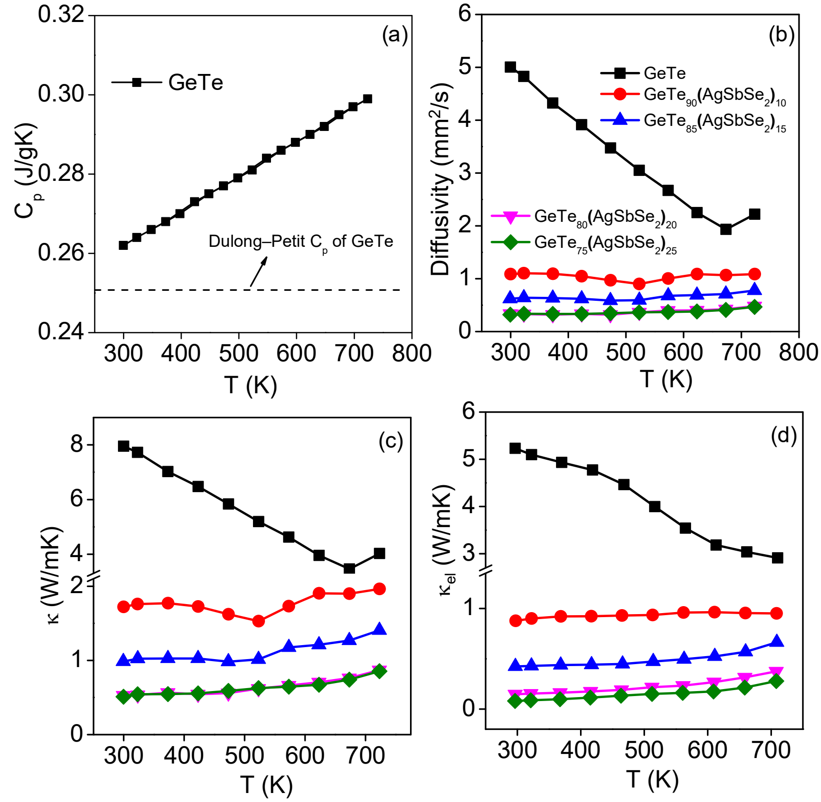

Figure 1.2. *(a) Heat capacity (C_p) of GeTe. Temperature dependent (b) thermal diffusivity, (c) total thermal conductivity (κ) and (d) electrical thermal conductivity (κ_{el}) of $(GeTe)_x(AgSbSe_2)_{100-x}$ (x = 100-75) samples.*

Figure 1.2c shows the temperature dependent total thermal conductivity (κ) of $(GeTe)_x(AgSbSe_2)_{100-x}$ (x = 100-75) samples. A significant reduction of κ is observed with increasing the $AgSbSe_2$ in TAGSSe. At room temperature, GeTe exhibits a κ of ~ 8 W/mK, which is suppressed to a value of ~ 0.51 W/mK in $(GeTe)_{75}(AgSbSe_2)_{25}$, which is the lowest κ value measured among all the GeTe based thermoelectric materials. For $(GeTe)_x(AgSbSe_2)_{100-x}$ (x = 90, 85) , the temperature dependent κ shows an anomaly at ~ 525 K, which is due the structural phase transition (rhombohedral to cubic) of GeTe. The transition temperature is significantly decreased in TAGSSe compared to pristine GeTe (~700 K). Temperature dependent electronic thermal conductivity (κ_{el}) (Figure 1.2d) shows significantly reduced κ_{el} values in TAGSSe samples compared to pristine GeTe sample, originating from reduced electrical conductivity of the TAGSSe samples (discussed in details in later section).

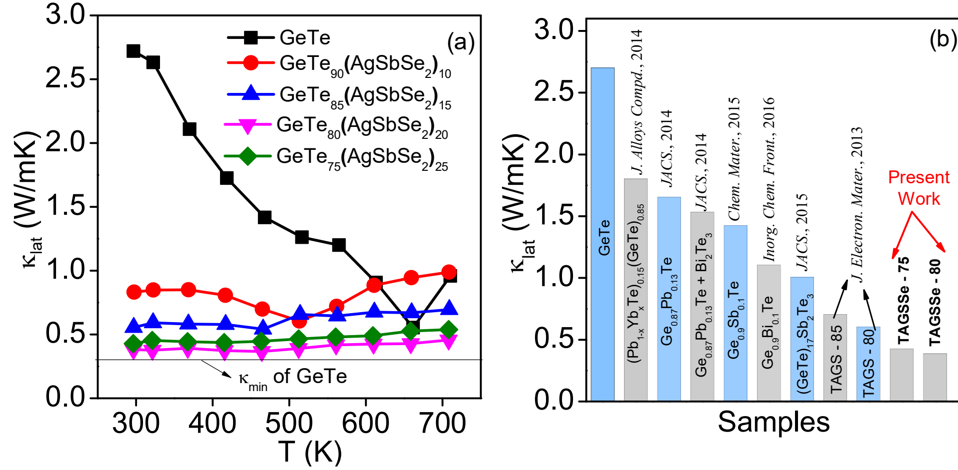

Figure 1.3. *(a) Temperature dependent lattice thermal conductivity (κ_{lat}) of $(GeTe)_x(AgSbSe_2)_{100-x}$ (x = 100-75) samples. Black line represents the minimum lattice thermal conductivity (κ_{min}) of GeTe. (b) Histogram shows κ_{lat} values for TAGSSe-x (x = 80, 75) and different GeTe based thermoelectric materials.*[11,15-18,25]

Lattice thermal conductivities (κ_{lat}) of the all samples are shown in Figure 1.3a, which are obtained by subtracting the κ_{el} from κ. κ_{lat} for all the samples is decreased significantly compared to that of the pristine GeTe samples. TAGSSe-80 exhibits κ_{lat} of ~ 0.4 W/mK at 300 K, which remains nearly flat throughout the measured temperature range (Figure 1.3a). κ_{lat} of TAGSSe is ultra-low which is indeed approaching close to the theoretical minimum limit of thermal conductivity (κ_{min}) of ~ 0.3 W/mK in GeTe, which has been calculated using Cahill's formulation[22]

$$\kappa_{min} = \frac{1}{2}\left(\frac{\pi}{6}\right)^{1/3} k_B V^{-2/3}(2v_t + v_l)$$

where, k_B is the Boltzmann constant, V is the average volume per atom; v_t and v_l are the transverse and longitudinal sound velocities. Average sound velocity (v_a) and Poisson ratio (P) are directly related to the v_l and v_t by the following equation[23]

$$v_a = \left(\frac{1}{3}\left[\frac{1}{v_l^3} + \frac{2}{v_t^3}\right]\right)^{-1/3} \text{and } P = \frac{1-2\left(\frac{v_t}{v_l}\right)^2}{2-2\left(\frac{v_t}{v_l}\right)^2}$$

By using v_a ~ 1900m/S[24] and P ~ 0.24 of GeTe,[12] v_l and v_t are calculated using the above two equation. In Figure 1.3b, we have compared the κ_{lat} of the present TAGSSe samples with other state of art GeTe based thermoelectric material[11,15-18,25] and found that the κ_{lat} of TAGSSe-75 and TAGSSe-80 are the lowest among all.

In order to understand the origin of the observed ultralow κ_{lat} of $(GeTe)_x(AgSbSe_2)_{100-x}$ (x = 80, 75), we have performed detailed transmission electron microscopic (TEM) study for both the samples. TAGSSe-80 and TAGSSe-75 both the samples undergo phase separation leading to the formation of hierarchical nano/mesostructures which causes extensive scattering of heat carrying phonon of different wavelengths. Figure 1.4 and Figure 1.5 depict the observed nano/mesostructures of TAGSSe-80 and TAGSSe-75, respectively. Low magnification TEM image of TAGSSe-80 illustrates formation of different phase separated nanoprecipitates of irregular sizes and meso-scale grains (Figure 1.4a). Corresponding high resolution TEM (HRTEM) image (highlighted area of Figure 1.4a) which is presented in Figure 1.4b, represents a crystalline nanoprecipiate with relatively darker contrast situating near the grain boundary. Another Low magnification TEM image of TAGSSe-80 and representative HRTEM of one of the dark contrast nanoprecipitate are presented in Figure 1.4c and Figure 1.4d, respectively. Calculated *d* spacing of both the dark contrast precipitates (obtained from HRTEM image in Figure 1.4b & Figure 1.4d) is found to be 0.305 nm, which is best attributed to the (214) planes of $Ag_{4.53}Te_3$ phase (space group $P\bar{6}2m$).[26] This finding is further supported by the observation of $Ag_{4.53}Te_3$ phase as low intensity second phase in PXRD pattern (Figure 1.1). In order to find out the composition of different nanoprecipitates, energy dispersive of X-rays analysis (EDAX) has been performed (Figure 1.4e). Nanoprecipitates of relatively darker contrast are consisting of Ag-Te rich phases, whereas precipitates of lighter contrast are to be Ge rich phases (Figure 1.4e). We could not able to quantitatively determine the exact composition of individual nanoprecipitates by EDAX analysis, as these nanoprecipitates overlap with matrix as well as with other nanoprecipitate. Figure 1.4f shows HRTEM image of TAGSSe-80 consisting of very small (2-6 nm) nanodots of Ag_2Te (space group, $P2_1/c$), which is much more prominent in the case of TAGSSe-75 sample.

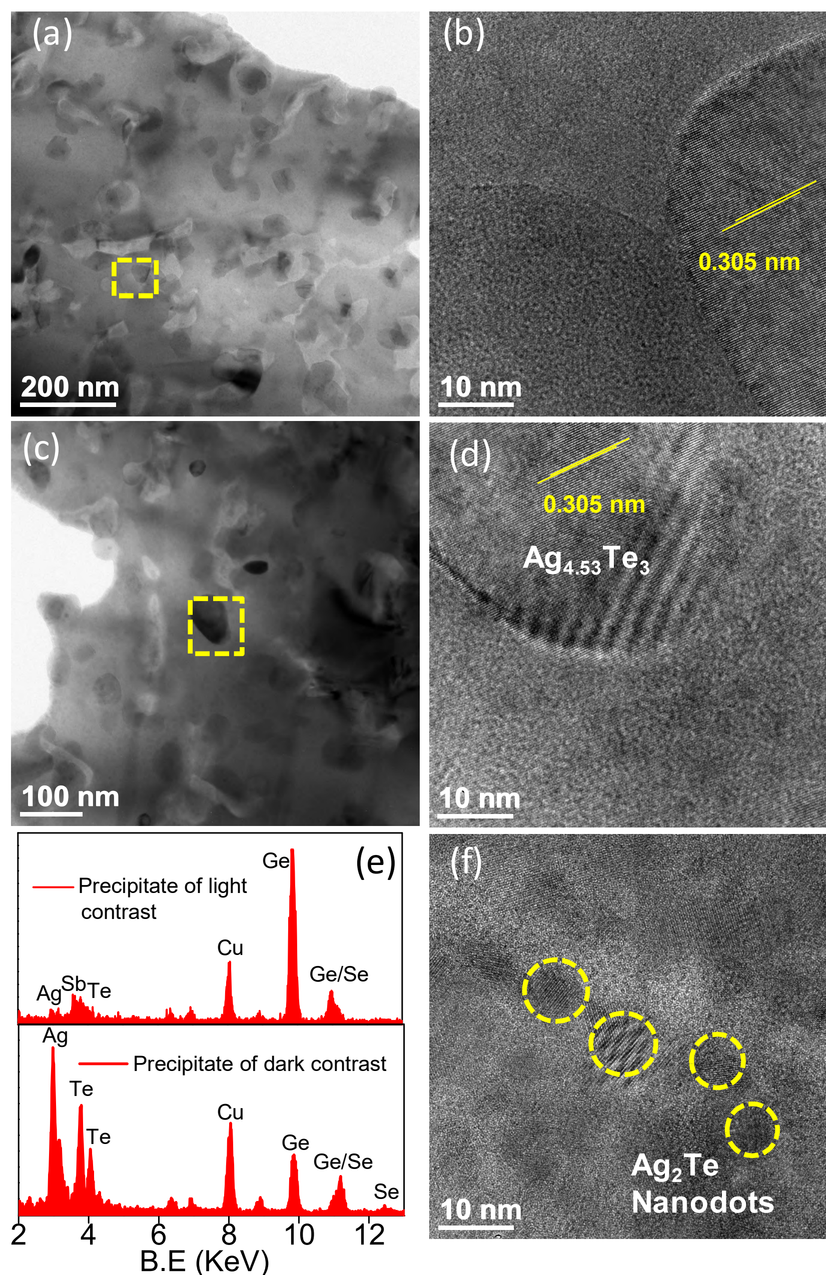

***Figure 1.4**. (a) Low magnification TEM image of $(GeTe)_{80}(AgSbSe_2)_{20}$. (b) HRTEM of the highlighted area in figure (a) representing overlap of different types of nanoprecipitates. (c) Another Low magnification TEM image of $(GeTe)_{80}(AgSbSe_2)_{20}$. (d) HRTEM of the black precipitate, highlighted in figure (c). (e) EDAX of the dark and light contrast region. (f) HRTEM image of $(GeTe)_{80}(AgsbSe_2)_{20}$ from another region showing presence of Ag_2Te nanodots.*

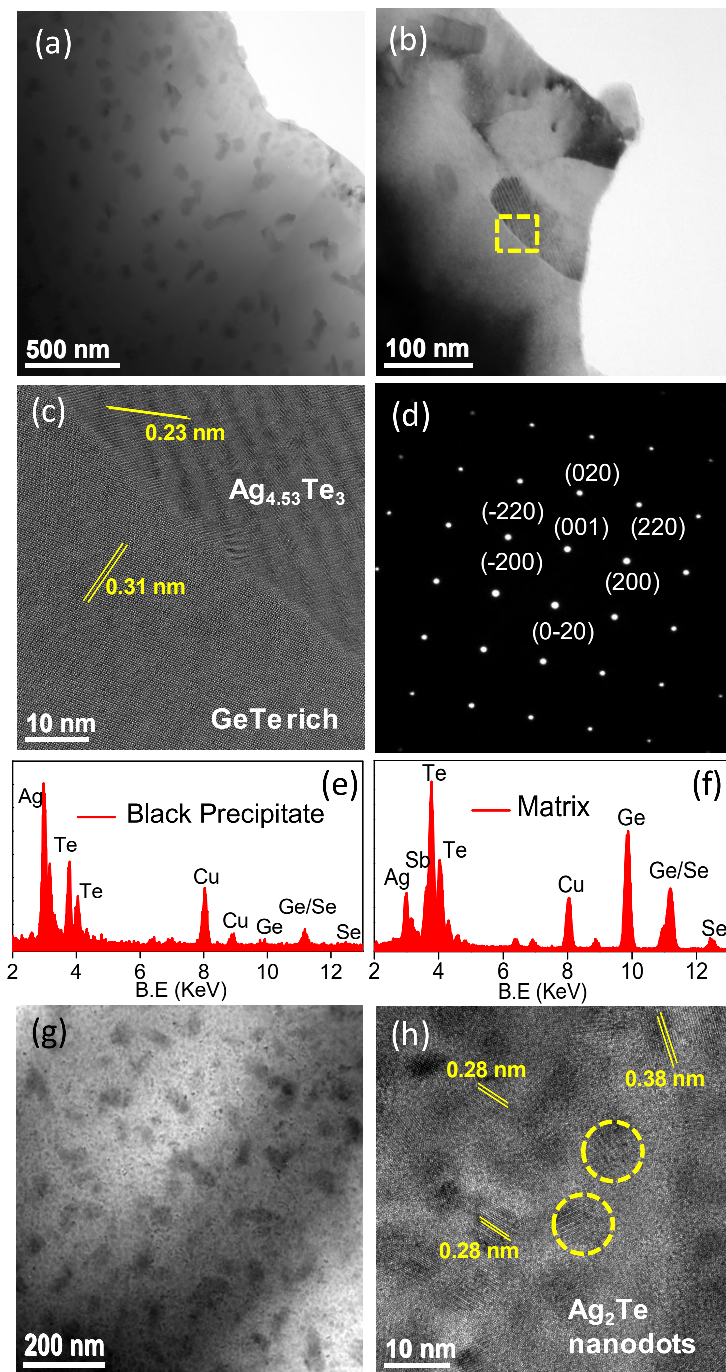

Figure 1.5. *(a) Low magnification TEM image of TAGSSe-75.(b)Zoomed version of TEM micrograph of a nanoprecipitate. (c) HRTEM of the highlighted area in figure (b). (d) ED pattern of the matrix. (e) & (f) EDAX of the black precipitate and matrix respectively. (g) Low magnification TEM image and corresponding (h) HRTEM images of TAGSSe-75 from another region, showing presence of Ag-Te rich nanodots.*

Figure 1.5 represents low magnification TEM image of TAGSSe-75, which shows presence of dark contrast precipitates of irregular sizes in the range 20-80 nm distributed uniformly in GeTe matrix. Zoomed TEM micrograph of the nanoprecipiate and HRTEM image of that nanoprecipiate (highlighted in Figure 1.5b) are shown in Figure 1.5b and Figure 1.5c, respectively. HRTEM image shows a lattice spacing of the matrix 0.31 nm which corresponds to (200) planes of cubic GeTe, whereas *d* spacing of 0.23 nm of the precipitate is best attributed to (500) planes of $Ag_{4.53}Te_3$ (space group, $P\bar{6}2m$). The measured PXRD pattern of TAGSSe-75 further corroborates the observed findings (Figure 1.1). Selected area diffraction pattern (SAED) pattern obtained from the matrix (Figure 1.5d) further confirms the occurrence of cubic phase of GeTe when the concentration of $AgSbSe_2$ in the alloy as high as 25%. In order to understand the composition, EDAX has been performed on both the matrix and the precipitate (Figure 1.5e and f). While the matrix is cubic $Ge_{1-x}Sb_xTe_{1-y'}Se_y$, the darker contrast nanoprecipitates (20-80 nm) are $Ag_{4.53}Te_3$ rich phases. Figure 1.5g and h show low magnification TEM image and the corresponding HRTEM image of TAGSSe-75 from a different region, which illustrate presence of numerous small nanodots (2-6 nm). Calculation of *d* spacing of the nanodots confirms the presence of Ag_2Te phase (space group, $P2_1/c$). Measured *d* spacing of the nanodots is 0.28 nm which is best attributed to the ($\bar{2}12$) planes of Ag_2Te having highest intensity of reflection in PXRD, whereas *d* spacing of 0.38 nm corresponds to (011) planes of Ag_2Te. Presence of nanoscale dots/precipitates along with mesoscale grain boundaries gives rise to hierarchical nano/mesostructuring in TAGSSe in different length scale, which cause significant scattering of heat carrying phonons of different wavelengths, thereby results in ultralow lattice thermal conductivity in $(GeTe)_x(AgSbSe_2)_{100-x}$ (x = 80, 75).

Carrier concentration (p) of all the $(GeTe)_x(AgSbSe_2)_{100-x}$ (x = 100-75) samples are estimated using the formula: $p = 1/(eR_H)$; where e is the electronic charge and R_H is the Hall coefficient. R_H values measured at room temperature for all the samples are found to be positive indicating *p*-type carriers (see Table 1.1). *p*-type carrier concentrations decrease from 8.72 x 10^{20} cm^{-3} in pristine GeTe to 2.6 x 10^{19} cm^{-3} in $(GeTe)_{75}(AgSbSe_2)_{25}$.

Temperature dependent electrical conductivity (σ) of all the $(GeTe)_x(AgSbSe_2)_{100-x}$ (x = 100-75) samples, measured in the range of 300-723 K , are presented in Figure 1.6a. Alloying of $AgSbSe_2$ with GeTe suppresses the carrier concentration because of donor

dopant nature of Sb (Table 1.1), thereby decreases the σ according to the equation, $\sigma = ne\mu$. GeTe has a very high electrical conductivity of ~7584 S/cm at room temperature due to high carrier concentration, which decreases to ~2329 S/cm at 710 K, indicating degenerate semiconductor behaviour. Room temperature electrical conductivity of TAGSSe-90 is to be ~1408 S/cm, which decreases to ~170 S/cm for TAGSSe-75 as we increase the concentration of $AgSbSe_2$ in the TAGSSe-x (Figure 1.6a).

Table 1.1. *Carrier concentration of $(GeTe)_x(AgSbSe_2)_{100-x}$ (x = 100 - 75) samples at room temperature.*

Samples	Carrier concentration, *n*, ($\times10^{20}$/cm^3)
GeTe	8.72
$(GeTe)_{90}(AgSbSe_2)_{10}$	2.14
$(GeTe)_{85}(AgSbSe_2)_{15}$	1.39
$(GeTe)_{80}(AgSbSe_2)_{20}$	0.46
$(GeTe)_{75}(AgSbSe_2)_{25}$	0.26

In Figure 1.6b, temperature dependent Seebeck coefficients (*S*) of the $(GeTe)_x(AgSbSe_2)_{100-x}$ (x = 100-75) are presented, which are positive for all the samples indicating *p*-type conduction. Significant increase in Seebeck coefficient is observed with increase in the $AgSbSe_2$ concentration in GeTe. Typically *S* increases from ~ 34 μV/K for GeTe to ~ 248 μV/K for the TAGSSe-75 at 300K, which reaches up to ~ 264 μV/K at 709 K for TAGSSe-75. In order to understand the mechanism of significant increment of *S* in TAGSSe-x, we compare *S* vs. *n* data for different $(GeTe)_x(AgSbSe_2)_{100-x}$ samples with previously reported Pisarenko plot for GeTe[15] along with different GeTe based samples[15-17] at room temperature (see Figure 1.6c). All the points corresponding to the present TAGSSe-x samples fall on or close to the Pisarenko curve of GeTe, suggesting the increase in *S* is solely due to the decrease in *p*-type carrier concentration (see Table 1.1).

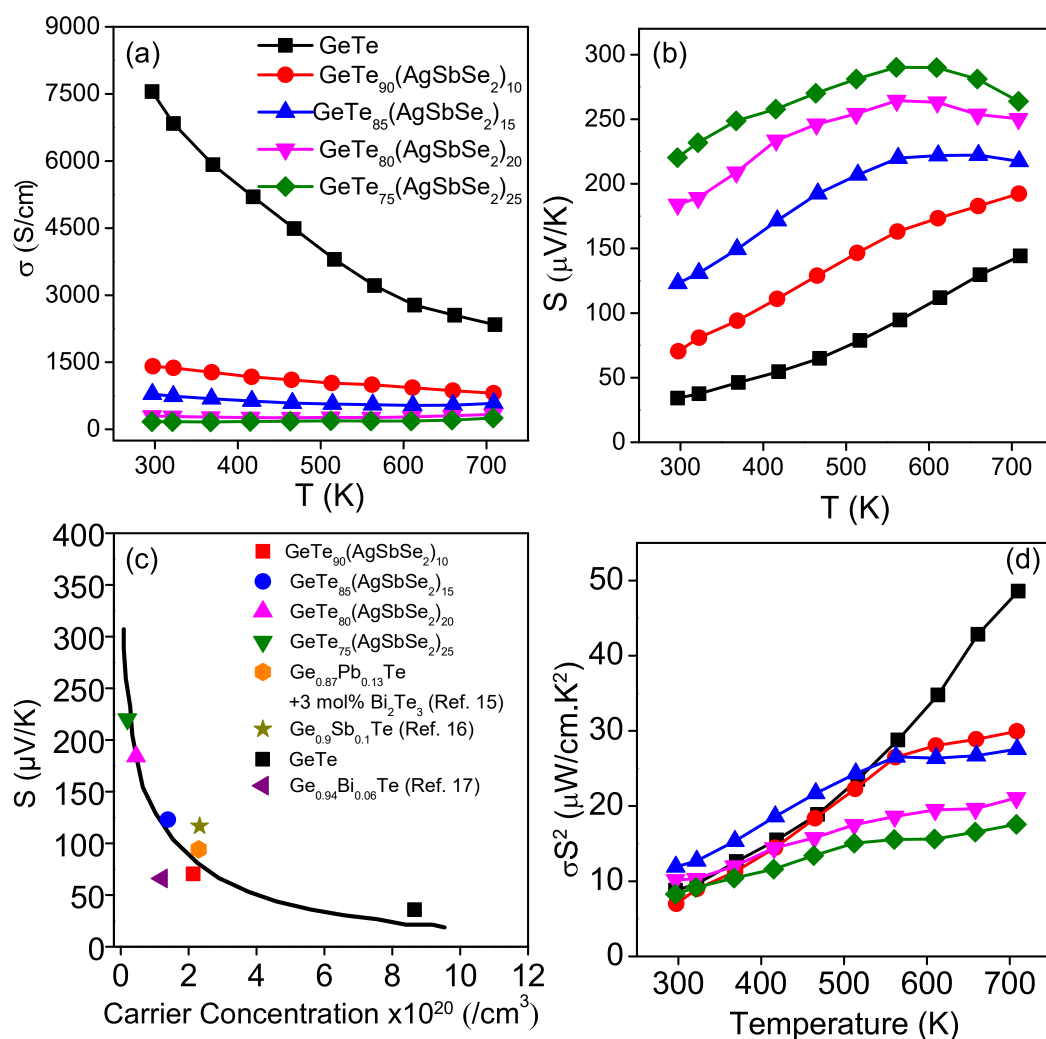

Figure 1.6. *Temperature dependent (a) electrical conductivity (σ) ; (b) Seebeck coefficient (S) and (d) power factor (σS^2) of $(GeTe)_x(AgSbSe_2)_{100-x}$ (x = 100-75) samples. (c) S Vs p data for $(GeTe)_x(AgSbSe_2)_{100-x}$ (x = 100-75) samples along with previously reported Pisarenko plot of GeTe and GeTe based samples.*[15-17]

Temperature dependent power factor ($S^2\sigma$) of all the $(GeTe)_x(AgSbSe_2)_{100-x}$ (x = 100-75) samples is presented in Figure 1.6d. $(GeTe)_{85}(AgSbSe_2)_{15}$ has the $S^2\sigma$ of ~12 μW/cmK^2 at room temperature which rises up to ~28 μW/cmK^2 at 708 K, whereas $(GeTe)_{90}(AgSbSe_2)_{10}$ has $S^2\sigma$ of ~ 7 μW/cm.K^2 at room temperature which reaches to high value of ~ 30 μW/cmK^2 at 710 K. Mention must be made that all TAGSSe-x samples exhibit lower $S^2\sigma$ compared to pristine GeTe at higher temperature due to significant

decrease in the σ. In terms of overall thermoelectric performance TAGSSe-x gains over GeTe due to significant reduction of thermal conductivity.

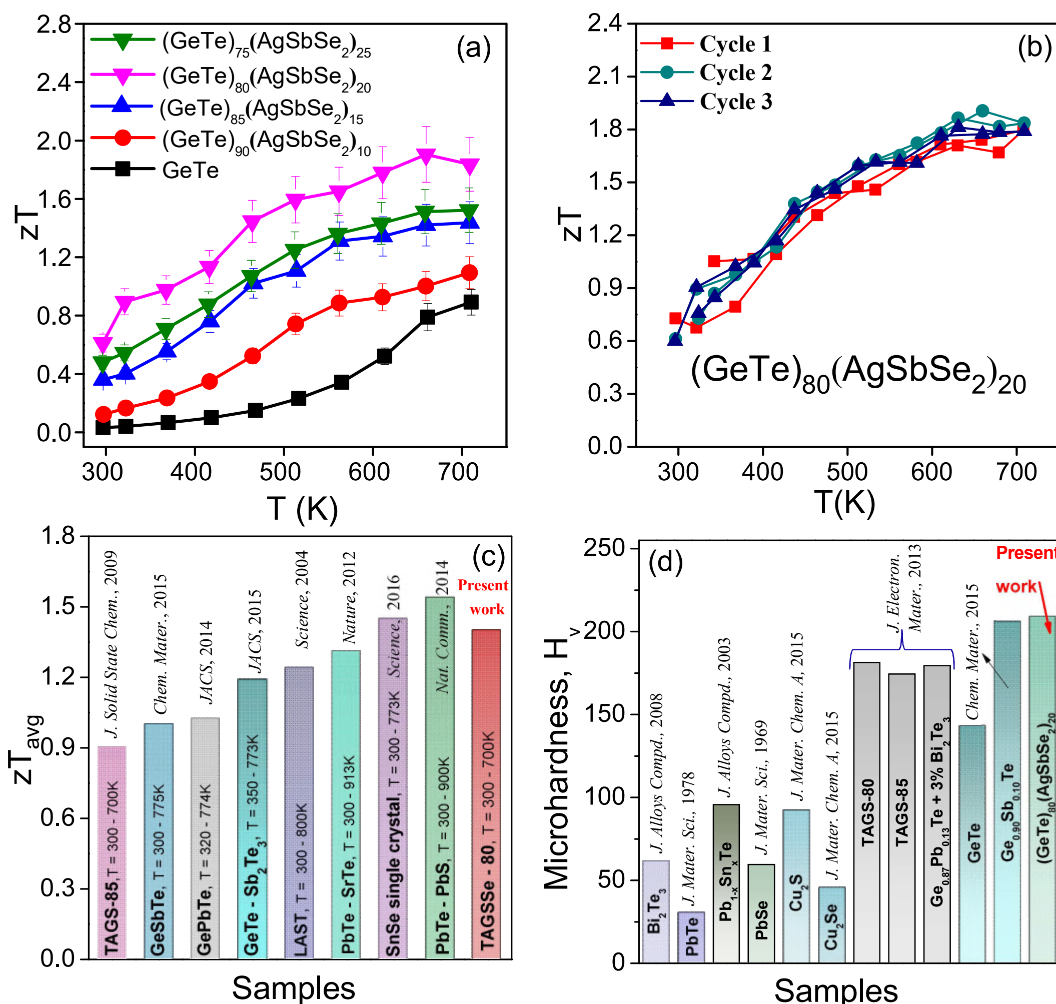

Figure 1.7. *(a)Temperature dependent figure of merit (zT) of* $(GeTe)_x(AgSbSe_2)_{100-x}$ *(x = 100-75) samples. (b)Reversibility and reproducibility of zT of* $(GeTe)_{80}(AgSbSe_2)_{20}$*. (c) Histogram comparing average zT of* $(GeTe)_{80}(AgSbSe_2)_{20}$ *with different state of art thermoelectric materials.*[4,12,15,16,18,27-29] *(d) Vickers microhardness value* (H_v) *of GeTe and* $(GeTe)_{80}(AgSbSe_2)_{20}$ *along with other state of art thermoelectric materials.*[11,16,30-35]

Temperature dependent zT of all the $(GeTe)_x(AgSbSe_2)_{100-x}$ (x = 100-75) samples are illustrated in Figure 1.7a. As a result of ultra-low thermal conductivity, zT_{max} reaches the highest value of 1.9 at 660 K for $(GeTe)_{80}(AgSbSe_2)_{20}$. $(GeTe)_{75}(AgSbSe_2)_{25}$ and $(GeTe)_{85}(AgSbSe_2)_{15}$ also exhibit high zT_{max} of 1.5 and 1.43 at 710 K, respectively. Three

cycle heating-cooling data of zT vs. T of $(GeTe)_{80}(AgSbSe_2)_{20}$ reveals the temperature stability and reversibility of the high zT (see Figure 1.7b).

To implement the thermoelectric technology commercially, thermoelectric materials should have high efficiency, which is directly related to average thermoelectric figure of merit (zT_{avg}) of a material.[3] This is essential because the temperature of heat sources ranges from medium to high, without having a fixed temperature. Thus, a thermoelectric material must have high zT_{avg} over the entire working temperature range in addition to high zT_{max} at a particular temperature. TAGSSe-80 has zT of 0.6 at 300 K and 1.9 at 660 K respectively. As a result, TAGSSe-80 exhibits high zT_{avg} of 1.4 in the temperature range 300–700K, which is one of the highest zT_{avg} obtained among all the state-of-art Pb-free polycrystalline thermoelectric materials. Figure 1.7c represents a histogram showing the ZT_{avg} of $(GeTe)_{80}(AgSbSe_2)_{20}$ along with different state-of-art thermoelectric material.[4,12,15,16,18,27-29] This result indicates that TAGSSe-x materials are one of the desired candidate for thermoelectric module fabrication and power generation application in mid temperature range.

A thermoelectric material should have good mechanical stability, but it is rare for metal chalcogenides. Measured Vickers microhardness for $(GeTe)_{80}(AgSbSe_2)_{20}$ is to be ~ 209 Hv (kgf/mm^2), whereas pristine GeTe and $AgSbSe_2$ have H_v value of ~ 165 and ~183 Hv respectively. We have compared the H_v value of $(GeTe)_{80}(AgSbSe_2)_{20}$ with different state of art metal chalcogenide based thermoelectric materials in Figure 1.7d.[11,16,30-35] Present TAGSSe-x exhibits highest Vickers microhardness value among all the state of the art metal chalcogenides thermoelectric materials.

1.4 Conclusions

In conclusion, alloying of GeTe with $AgSbSe_2$ leads to an ultralow κ_{lat} of ~ 0.4 W/mK for TAGSSe-80 in 300-700 K temperature range, which is indeed approaching to the κ_{min} (~ 0.3 W/mK) in GeTe. Detailed transmission electron microscopic study reveals thatboththe TAGSSe-80 and TAGSSe-75 samples exhibit all-scale hierarchical architecturing starting from mesoscale grain boundaries to nanoscale precipitate to nanodots, which in turn lead to the significant scattering of heat carrying phonons of different wave-length. Such an ultralow thermal conductivity leads to a high figure of merit, zT of ~1.9 at 660 K for

TAGSSe-80. More interestingly, an ultrahigh zT_{avg} of 1.4 for TAGSSe-80 is obtained in the temperature range 300 K- 700K, which provides another dimension of importance to this material. In addition to that, this material possesses a high mechanical stability compared to other leading metal chalcogenide thermoelectric materials making it desirable for thermoelectric exploration and further studies.

1.5 References

(1) Tan, G.; Zhao, L. D.; Kanatzidis, M. G. *Chem. Rev.* **2016**, *116*, 12123−12149.

(2) Snyder, G. J; Toberer, E. S. *Nat. Mater.* **2008**, *7*, 105 – 114.

(3) Zhao, L. D., Dravid, V. P.; Kanatzidis, M. G. *Energy Environ. Sci.* **2014,** *7*, 251-268.

(4) Wu, H. J.; Zhao, L. D.; Zheng, F. S.; Wu, D.; Pei, Y. L.; Tong, X., Kanatzidis, M.G.; He, J.Q. *Nature Commun.* **2014,** *5*, 4515.

(5) Rosi, F.D.; Dismukes, J. P.; Hockings, E.F. *Electrical Engineering,* **1960**, *79*, 450.

(6) Perumal, S., Roychowdhury, S. & Biswas, K. *J. Mater. Chem. C* **2016**, **4**, 7520-7536.

(7) Christakudi, T. A.; Plachkova, S. K.; Christakudis, G. Ch. *Phys. Status Solidi A* **1995**, *147*, 211-220.

(8) Lewis, J. E. *Phys. Status Solid A.* **1970**, *38*, 131-140.

(9) Damon, D. H.; Lubell, M. S.; Mazelsky, R. *J. Phys. Chem. Solids* **1967**, *28*, 520-522.

(10) Levin, E. M.; Besser, M. F.; Hanus, R. *J. Appl. Phys*. **2013**, *114*, 083713.

(11) Davidow, J.; Gelbstein, Y. *J. Eelectron. Mater.* **2013**, *42*, 1542-1549.

(12) Salvador, J. R.; Yang, J.; Shi, X.; Wang, H.; Wereszczak, A. *J. Solid State Chem*. **2009**, *182*, 2088-2095.

(13) Chen, Y.; Jaworski, C. M.; Gao, Y. B.; Wang, H.; Zhu, T. J.*;* Snyder, G. J.; Heremans, J. P.; Zhao, X. B. *New J. Phys.* **2014***, 16*, 013057.

(14) Gelbstein, Y.; Davidow, J.; Girard, S. N.; Chung, D. Y.; Kanatzidis, M. G. *Adv. Energy Mater.* **2013**, *3*, 815-820.

(15) Wu, D.; Zhao, L-D.; Hao, S.; Jiang, Q.; Zheng, F.; Doak, J. W.; Wu, H.; Chi, H.; Gelbstein, Y.; Uher, C.; Wolverton, C.; Kanatzidis, M. G.; He, J. *J. Am. Chem. Soc*. **2014**, *136*, 11412-11419.

(16) Perumal, S.; Roychowdhury, S.; Negi, D. V.; Datta R.; Biswas, K. *Chem. Mater.* **2015**, *27*, 7171 - 7178.

(17) Perumal, S.; Roychowdhury, S.; Biswas, K. *Inorg. Chem. Front.* **2016,** *3*, 125-132.

(18) Fahrnbauer, F.; Souchay, D.; Wagner, G.; Oeckler, O. *J. Am. Chem. Soc.* **2015**, *137*, 12633−12638.

(19) Rosenthal,T.; Schneider, M. N.; Stiewe, C., Doblinger, M.; Oeckler, O. *Chem. Mater.* **2011**, *23*, 4349-4356.

(20) Morelli, D. T.; Jovovic, V.; Heremans, J. P. *Phys. Rev. Lett.* **2008**, *101*, 035901.

(21) Guin, S. N.; Chatterjee, A.; Negi, D. S.; Datta, R.; Biswas, K. *Energy Environ. Sci.* **2013**, *6*, 2603-2608.

(22) Cahill, D.; Watson, S.; Pohl, R. *Phys.Rev.B.***1992**, *46*, 6131−6140.

(23) Pei, Y.; He, J.; Li, J.-F.; Li, F.; Liu, Q.; Pan, W.; Barreteau, C.; Berardan, D.; Dragoe N.; Zhao, L. D. *NPG Asia Mater.* **2013**, *5*, e47.

(24) Pereira, P. B.; Sergueev, I.; Gorsse, S.; Dadda, J.; Muller, E.; Hermann, R. P. *Phys. Status Solidi B* **2013**, *250*, 1300-1307.
(25) Deng, J. F.; Li, J.Q.; Ye, R.F.; Liu, X. Y.; Liu, S.; Ao, W. Q. *J. Alloys Compd.* **2014**, *585*, 173–177.
(26) Peters, J., Conrad, Bremer, O., B. & Krebs, B. *Z. anorg. allg. Chem.* **1996**, *622*, 1823-1832.
(27) Biswas, K.; He, J.; Blum, I. D.; Wu, C. I.; Hogan, T. P.; Seidman, D. N.; Dravid, V. P.; Kanatzidis, M. G. *Nature* **2012**, *489*, 414-418.
(28) Zhao, L. D.; Tan, G.; Hao, S.; He, J.; Pei, Y.; Chi, H.; Wang, H.; Gong, S.; Xu, H.; Dravid, V. P.; Uher, C.; Snyder,G. J.; Wolverton, C.;Kanatzidis, M. G. *Science* **2016**, *351*, 141-144.
(29) Hsu, K. F., Loo, S., Guo, F., Chen, W., Dyck, J. S., Uher, C., Hogan, T., Polychroniadis, E. K. & Kanatzidis, M. G. *Science.* **2004**, *303*, 818-821.
(30) Zhao, L.-D.; Zhang, B.-P.; Li, J.-F.; Zhou, M.; Liu,W.-S.; Liu, J. *J. Alloys Compd.* **2008**, *455*, 259-264.
(31) Gelbstein, Y.; Gotesman, G.; Lishzinker, Y.; Dashevsky, Z.; Dariel, M. P. *Scripta Materialia* **2008**, *58*, 251-254.
(32) Crocker, A. J.; Wilson, *J. Mater. Sci*. **1978**, *13*, 833-842.
(33) Cui, J. L.; Qian, X.; Zhao, X. B. *J. Alloy. Compd*. **2003**, *358*, 228-234.
(34) Darrow, W. B. W. M. S.; Roy, R. *J. Mater. Sci.* **1969**, *4*, 313-319.
(35) Zhao, L.; Wang, X.; Fei, F. Y.; Wang, J.; Cheng, Z.; Dou, S.; Wanga, J.; Snyder, G. J. *J. Mater. Chem. A* **2015**, *3*, 9432-9437.

Chapter 2

Realization of both *n*- and *p*-type GeTe Thermoelectrics: Electronic Structure Modulation by $AgBiSe_2$ Alloying

Chapter 2

Realization of both *n*- and *p*-type GeTe Thermoelectrics: Electronic Structure Modulation by $AgBiSe_2$ Alloying†

Summary

Successful applications of a thermoelectric material require simultaneous development of compatible n- and p-type counterparts. While the thermoelectric performance of p-type GeTe has been improved tremendously in recent years, it has been a challenge to find compatible n-type GeTe counterpart due to the prevalence of intrinsic Ge vacancies. Herein, we have shown that alloying of $AgBiSe_2$ *with GeTe results in an intriguing evolution in its crystal and electronic structures, resulting in n-type thermoelectric properties. We have demonstrated that the ambient rhombohedral structure of pristine GeTe transforms into cubic phase in* $(GeTe)_{100-x}(AgBiSe_2)_x$ *for* $x \geq 25$*, with concurrent change from its p-type electronic character to n-type character in electronic transport properties. Such change in structural and electronic properties is confirmed from the non-monotonous variation of band gap, unit cell volume, electrical conductivity and Seebeck coefficient, all of which show an inflection point around* $x \sim 20$*, as well as from the temperature variations of synchrotron powder X-ray diffractions and differential scanning calorimetry. First principles density functional theoretical (DFT) calculations explain that the shift towards n-type electronic character with increasing* $AgBiSe_2$ *concentration arises due to increasing contribution of Bi-p orbitals in the conduction band edge of* $(GeTe)_{100-x}(AgBiSe_2)_x$*. This cubic n-type phase has promising thermoelectric properties with a band gap of ~ 0.25 eV and ultralow lattice thermal conductivity which ranges between 0.3 – 0.6 W/mK. Further, we have shown that* $(GeTe)_{100-x}(AgBiSe_2)_x$ *has promising thermoelectric performance in the mid-temperature range (400-500 K) with maximum thermoelectric figure of merit, zT, reaching ~ 1.3 in p-type* $(GeTe)_{80}(AgBiSe_2)_{20}$ *at 467 K and ~ 0.6 in n-type* $(GeTe)_{50}(AgBiSe_2)_{50}$ *at 500 K.*

†*Paper based on this study has been published in* J. Am. Chem. Soc. **2019**, *141,* 19505−19512.

2.1 Introduction

GeTe and its derivatives are being used as promising *p*-type Pb-free thermoelectric materials for mid-temperature power generation for a long time. However thermoelectric performance of GeTe based materials has been improved tremendously in the last few years, stemming from improved understanding on the optimization of various thermoelectric parameters.[1–4] In ambient conditions, GeTe crystallizes in rhombohedral phase (space group *R3m*) and undergoes a ferroelectric phase transition to a cubic rock-salt structure (space group $Fm\overline{3}m$) at ~ 700 K (Figure 2.1).[2,5] Intrinsic Ge-vacancies in GeTe drive the Fermi level deep inside the valance band so that the system becomes highly *p*-type with high electrical conductivity of σ ~ 8000 S/cm and low Seebeck coefficient of ~ 32 μV/K at room temperature.[6,7] GeTe has relatively low energy difference (~ 0.23 eV) between the heavy hole Σ and light hole *L* valence bands, and the energy offset decreases with increasing temperature which results in the increasing contribution of the lower lying valance band in electronic transport.[6–8] The relatively low energy offset between the two valance bands also lead to several successful chemical doping approaches for the valance band convergence which resulted in high thermoelectric performance.[9–13] Innovative strategies like "slight symmetry reduction" has also been developed to achieve this valance band convergence.[8,14] Further, In doping, which results in the formation of resonance level, has also been shown to be effective in increasing the Seebeck coefficient, and thereby the thermoelectric performance of GeTe.[15–17] The high κ_{lat} of GeTe has been optimized via various techniques such as conventional alloying[6,10–12,15,16,18–20] and nanostructuring[9,21–26] in order to increase the thermoelectric performance.[2] These strategies lead to the development of various high performance *p*-type GeTe thermoelectric materials like $Ge_{1-x}Pb_xTe$,[9,21–23] GeTe-$AgSb(Te/Se)_2$,[24,25] $GeTe_{1-2x}Se_xS_x$[20] and $Ge_{1-x}(Sb/Bi/In/Mn)_xTe$.[13,17–19,22-26]

Although GeTe and its solid solutions have been established as one of the best performing *p*-type Pb-free thermoelectric materials, the continued challenges are to find a compatible *n*-type counterpart. Better compatibility of a thermoelectric module demands that both *p*- and *n*-type thermoelectric performance should be realized in materials having similarity in their chemical compositions.[27] GeTe have intrinsic Ge vacancies which lead to their *p*-type electronic nature and makes the realization of *n*-type thermoelectric

performance a mounting task.[2] Recently, *n*-type electronic conduction has been realized in the other Ge chalcogenides like in layered GeSe based $(GeSe)_{100-x}(AgBiSe_2)_x$[28] which instigates us to look into the structure-property relationships of $AgBiSe_2$ alloyed GeTe. Here, we are curious to answer the following questions: (a) cubic phase of GeTe generally show high performance but it is only stable above 700 K. Will it be possible to stabilize the cubic phase of GeTe at ambient conditions by alloying with $AgBiSe_2$? and (b) Will it be possible to realize *n*-type electronic conduction in polycrystalline GeTe (which is not found before)?

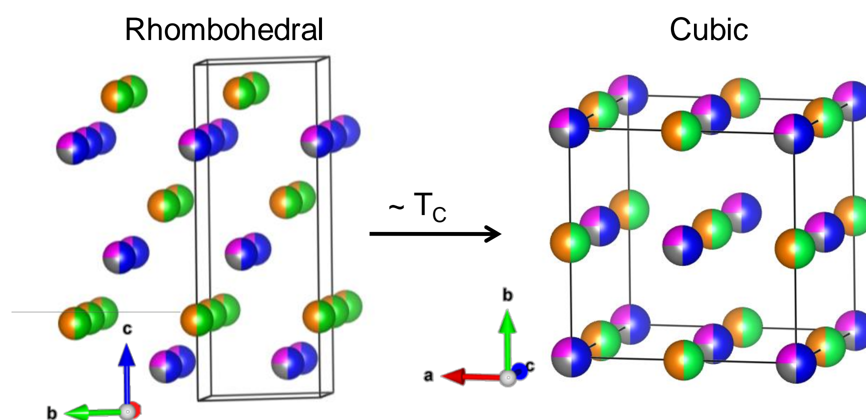

Figure 2.1. *Crystal structure of different phases of $(GeTe)_{100-x}(AgBiSe_2)_x$ (Blue, pink, grey, green and orange atoms are Ge, Ag, Bi, Te and Se respectively). It undergoes rhombohedral to cubic structural phase transition at T_C.*

Herein, we have demonstrated the realization of both *n*- and *p*-type electronic transport in GeTe when alloyed with varied concentrations of $AgBiSe_2$. The room temperature rhombohedral phase of pristine GeTe transforms into cubic rocksalt structure when alloyed with $AgBiSe_2$ with the concentration ≥ 25 mol%. Temperature dependent synchrotron powder X-ray diffraction (PXRD) and differential scanning calorimetry (DSC) further demonstrated the decrease in rhombohedral to cubic phase transition temperature with increasing $AgBiSe_2$ concentration and the cubic phase of $(GeTe)_{100-x}(AgBiSe_2)_x$ finally stabilizes in ambient conditions for x ≥ 25. The band gap, unit cell volume, electrical conductivity and Seebeck coefficient all changes non-monotonously with $AgBiSe_2$ concentration and have an inflection point around x = 20. Importantly, the electronic character of $(GeTe)_{100-x}(AgBiSe_2)_x$ changes from *p*- to *n*-type with increasing $AgBiSe_2$ concentration and the dominant *n*-type electronic transport becomes evident for x > 25.

Using first principal density functional theoretical (DFT) calculations, we showed that the *p*- to *n*-type electronic evolution occurs due to the increasing presence of Bi-p electronic states on the conduction band edge with increasing $AgBiSe_2$ concentration. Further, the alloying of GeTe with $AgBiSe_2$ leads to a significant reduction in κ_{lat} due to increased phonon scattering by enhanced point defects and nanostructures. Both *p*- and *n*-type $(GeTe)_{100-x}(AgBiSe_2)_x$ compositions have promising mid-temperature (400-500 K) thermoelectric performance with the maximum *zT* reaching ~ 1.3 at 467 K in *p*-type $(GeTe)_{80}(AgBiSe_2)_{20}$ and ~ 0.6 at 500 K in *n*-type $(GeTe)_{50}(AgBiSe_2)_{50}$.

2.2 Methods

2.2.1 Reagents. Germanium (Strategy Elements, 99.999%), tellurium (Strategy Elements, 99.999 %), silver (Alfa Aesar 99.9999%), bismuth (SRL chemicals, 99.99 %) and selenium (Alfa Aeser 99.9999%) were used for synthesis without any further purification.

2.2.2 Synthesis. High quality polycrystalline ingots (~ 6 g) of $(GeTe)_{100-x}(AgBiSe_2)_x$ (x = 0 - 50) were synthesized using stoichiometric amounts of high purity starting elements Ge, Te, Ag, Bi, and Se. The constituent elements were sealed in a quartz ampoule under vacuum (10^{-6} Torr). The quartz ampoules were slowly heated to 723 K and then to 1223 K over a time period of 12 hours and 5 hours, respectively. At 1223 K the composition mixtures were soaked for 8 hours which was then slowly cooled down to room temperature over 10 h. The quartz tubes were shaken several times during soaking at 1223 K to achieve compositional homogeneity. The obtained ingots were cut in the shape of bar and coin for electrical and thermal properties measurement, respectively.

2.2.3 Powder X-ray Diffraction (PXRD). Room temperature PXRD patterns of all synthesized samples were collected using Cu Kα (λ = 1.5406 Å) radiation source in a Bruker D8 diffractometer. The temperature dependent PXRD patterns were collected in the 300 – 623 K temperature range under N_2 flow in the BL-18B synchrotron beam line (λ = 0.7749 Å) at Photon Factory, KEK, Tsukuba, Japan.

2.2.4 Band Gap Measurement. To determine the optical band gap of $(GeTe)_{100-x}(AgBiSe_2)_x$ (x = 0 - 50), diffuse reflectance from finely ground powder was measured

using a FT-IR Bruker IFS 66V/S spectrometer in the wavenumber range 4000 - 400 cm^{-1}. Absorption (α/Λ) data were then calculated from measured reflectance data using Kubelka-Munk equation: $\alpha/\Lambda = (1-R)^2/(2R)$, where α and Λ are the absorption and scattering coefficients, respectively and R is the reflectance.

2.2.5 Transmission Electron Microscopy (TEM). The TEM images of $(GeTe)_{80}(AgBiSe_2)_{20}$ were collected using a FEI TECNAI G2 20 STWIN TEM instrument operating at 200 kV.

2.2.6 Field Emission Scanning Electron Microscopy (FESEM). FESEM experiments of $(GeTe)_{80}(AgBiSe_2)_{20}$ were performed using NOVA NANO SEM 600 (FEI, Germany) equipment operated at 15 KV.

2.2.7 Differential Scanning Calorimetry (DSC). DSC data of $(GeTe)_{100-x}(AgBiSe_2)_x$ were collected in the temperature range of 290 – 700 K using a DSC Q2000 with heating/cooling rate of 5 K/min under N_2 atmosphere.

2.2.8 Electrical Transport. Temperature variation of electrical conductivity (σ) and Seebeck coefficient (S) of $(GeTe)_{100-x}(AgBiSe_2)_x$ were measured simultaneously using a ULVAC-RIKO ZEM-3 instrument under helium atmosphere in the 300 - 723 K temperature range. The typical dimension of sample used for this measurement was ~ 2×2×8 mm^3. We observed that heating and cooling cycles have reversible electrical properties in all the synthesized samples.

2.2.9 Hall Measurement. Room temperature hall measurements of $(GeTe)_{100-x}(AgBiSe_2)_x$ were carried out at in a setup developed by Excel instrument with a maximum magnetic field of 0.55 T and a fixed applied dc-current of 100 mA.

2.2.10 Thermal Conductivity. Thermal diffusivity, D, of $(GeTe)_{100-x}(AgBiSe_2)_x$ were measured by laser flash diffusivity method using a Netzsch LFA-457 in the 300 − 723 K temperature range under N_2 atmosphere. Coins with typical dimension of ~8 mm diameter and ~2 mm thickness were used for the measurements. Coins were coated with a thin layer of graphite to avoid errors coming from thermal emissivity of the materials. Temperature dependent heat capacity, C_p, of GeTe and $(GeTe)_{50}AgBiSe_2)_{50}$ were determined by comparing with a standard sample (pyroceram) in LFA-457. The total thermal conductivity,

κ_{tot}, was then estimated using the formula $\kappa_{tot} = D\rho C_p$, where ρ is the density of the samples which were found to be ~ 97% of theoretical density in all the $(GeTe)_{100-x}(AgBiSe_2)_x$ compositions. Electrical and thermal transports were measured in the same direction. Electronic thermal conductivity, κ_{el}, was then estimated from Wiedemann-Franz law $\kappa_{el} = L.\sigma.T$, where L is the Lorenz number and σ is the electrical conductivity at temperature T. Temperature dependent Lorenz number was calculated by fitting the temperature dependent Seebeck values assuming single parabolic band model and acoustic phonon scattering.[6]

2.2.11 Computational Details. This part of the work has been performed in collaboration with Prof. Umesh V. Waghmare's group in JNCASR, India. We used first-principles density functional theory (DFT) based computational methods as implemented in QUANTUM ESPRESSO (QE) code.[29] We used a generalized gradient approximation (GGA)[30] to the exchange-correlation energy functional as parametrized by Perdew, Burke, and Ernzerhof (PBE)[31] and Projected Augmented–Wave (PAW) potentials. Electronic wave functions and charge density were represented in plane wave basis sets truncated with cut-off energies of 45 Ry and 360 Ry, respectively. The discontinuity in occupation numbers of the electronic states at the Fermi level was smeared with an energy width of $k_BT = 0.003$ Ry in the Fermi Dirac distribution function. We determined electronic structure of GeTe, $(GeTe)_{90}(AgBiSe_2)_{10}$, $(GeTe)_{80}(AgBiSe_2)_{20}$ and $(GeTe)_{60}(AgBiSe_2)_{40}$ at their optimized lattice parameters. At ambient conditions, GeTe stabilizes in the rhombohedral phase containing two and six atoms in its primitive and conventional unit cells, respectively. Integrations over Brillouin Zone (BZ) were sampled on a uniform 8x8x8 and 8x8x4 mesh of k-points in simulations with primitive and conventional unit cells, respectively. Electronic structure was determined at Bloch wave vectors along high symmetry lines W – L – Γ – U – X – W – K (primitive unit cell) and Γ - M - K - Γ -A - L - H - A - L - M - K – H (hexagonal conventional unit cell) in the Brillouin zone. $(GeTe)_{90}(AgBiSe_2)_{10}$ and $(GeTe)_{80}(AgBiSe_2)_{20}$ also have rhombohedral phase, and we need a 2x2x1supercell to simulate the desired concentration. Brillouin Zone (BZ) integrations were sampled on uniform 8x8x8 mesh of k-points, and electronic bands were determined at Bloch vectors along high symmetry lines (Γ - M - K - Γ -A - L - H - A - L - M - K - H) in the Brillouin zone of the rhombohedral lattice. With further increase in concentration of

$AgBiSe_2$, an FCC phase is stabilized. $(GeTe)_{60}(AgBiSe_2)_{40}$ exists in the cubic structure consisting of 8 atoms in the unit cell. To simulate this composition, 8 atoms unit cell and a 1x1x2 supercell were used and Brillouin Zone (BZ) integrations were sampled on a uniform 8x8x8 and 8x8x6 mesh of k-points, respectively. Electronic spectrum was determined at Bloch vectors along high symmetry lines Γ - X - M - Γ -R - X - M – R and Γ - X - M - Γ - Z - R - A–Z – X – R – M - A in the Brillouin zones of the cubic cell and 1x1x2 supercell, respectively. We compared electronic structures calculated with and without spin-orbit coupling (SOC) using fully relativistic and scalar relativistic potentials, respectively. Since the electronic structure near the gap is more strongly influenced by disorder and large SOC is associated with heavy atoms in these materials, we do not adopt more accurate methods (like hybrid functional or self-interaction corrected methods) in estimation of band gap here. Our optimized lattice parameters for conventional unit cell of pristine GeTe in the rhombohedral structure are a = b = 4.22 Å, c = 10.75 Å, which agree within the typical GGA errors with experimental lattice parameters (a = b = 4.23 Å, c = 10.89 Å). Our estimated lattice parameters of $(GeTe)_{90}(AgBiSe_2)_{10}$ in the rhombohedral structure are a = b = 4.20 Å and c = 10.71 Å, which agree well with the experimental values of a = b = 4.17 Å and c = 10.62 Å. The ambient crystal structure of $(GeTe)_{100-x}(AgBiSe_2)_x$ with x = 20 is rhombohedral with experimental lattice parameters a = b = 4.18 Å and c = 10.54 Å. We found that the optimized lattice parameters are a = b = 4.20 Å and c = 10.78 Å in agreement with the experimental lattice parameters. The crystal structure of $(GeTe)_{100-x}(AgBiSe_2)_x$ with x = 40 is cubic in ambient conditions with experimental lattice parameters a = b = c = 5.91 Å and the obtained optimized lattice parameters are a = b = c = 5.94 Å, which shows good agreement between experimentally and theoretically determined lattice parameters.

2.3 Results & discussion

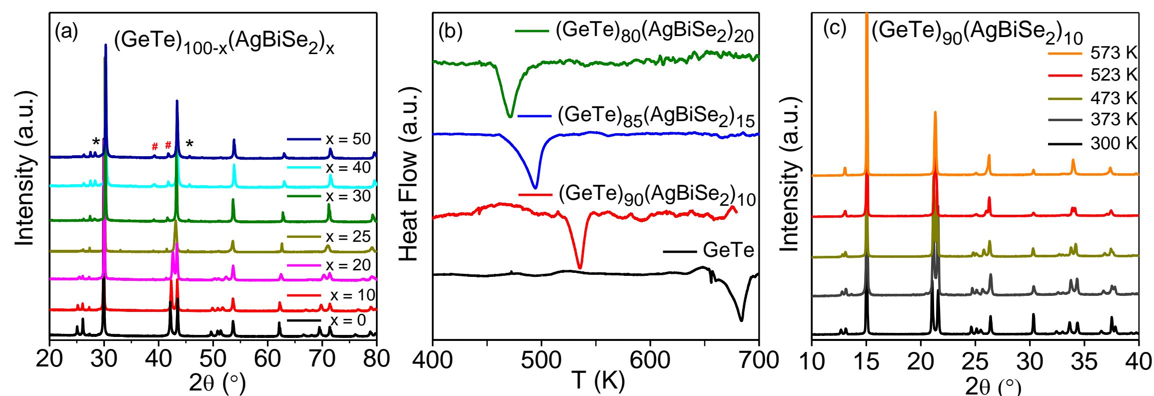

Figure 2.2. *(a) Room temperature PXRD patterns (laboratory source, Cu Kα, λ = 1.5406 Å) of $(GeTe)_{100-x}(AgBiSe_2)_x$ (x = 0 - 50) exhibiting the structural phase evolution from rhombohedral (space group, R3m) to cubic (space group, $Fm\bar{3}m$) phase with increasing $AgBiSe_2$ concentration at ambient conditions. "*" and "#" sign refers the peak corresponding to the Ge (space group, $Fd\bar{3}m$) and Ag_2Te (space group, P21/c) minority phases, respectively. (b) Temperature variation of DSC signal of $(GeTe)_{100-x}(AgBiSe_2)_x$ (x = 0 - 20) exhibits the rhombohedral to cubic structural phase transition which decreases with increasing $AgBiSe_2$ concentration. (c) Temperature dependent synchrotron (λ = 0.7749 Å) PXRD patterns of $(GeTe)_{90}(AgBiSe_2)_{10}$ showing the structural phase evolution from the rhombohedral to cubic phase with increasing temperature.*

The room temperature powder X-ray diffraction (PXRD) patterns of $(GeTe)_{100-x}(AgBiSe_2)_x$ (x = 0 - 50) (Figure 2.2a) measured in lab diffractometer show the structural phase evolution from rhombohedral (space group *R3m*) to cubic (space group *Fm-3m*) phase with increasing $AgBiSe_2$ content in GeTe. The room-temperature PXRD patterns of $(GeTe)_{100-x}(AgBiSe_2)_x$ could be indexed based on the rhombohedral phase of pristine GeTe up to x ≤ 20. However, the gap between the doublet (024) and (220) peaks of rhombohedral phase present in the range 2θ = 41° - 45° gradually decreases with increasing $AgBiSe_2$ concentration. For x ≥ 25, these two peaks completely merged together which results in the single (220) peak of cubic $Fm\bar{3}m$ phase. GeTe based systems are known to possess intrinsic Ge vacancies and the corresponding small amount of Ge second phase (space group $Fd\bar{3}m$) peaks in their PXRD patterns, which is also evident in the present $(GeTe)_{100-x}(AgBiSe_2)_x$ (x = 0 – 50) system (Figure 2.2a; * marked peaks).[2] Additionally, we observed the presence of small additional peaks (Figure 2.2a; # marked peaks) corresponding to Ag_2Te (space group *P21/c*) which appears after the addition of $AgBiSe_2$ in GeTe. The concentration of both of

these minor second phases slightly increase with increasing $AgBiSe_2$ concentration.[24] The structural parameters obtained from Rietveld refinements of the room temperature PXRD patterns of $(GeTe)_{100-x}(AgBiSe_2)_x$ (x = 0, 20 and 40) (Figure 2.3) are listed in Table 2.1-2.3. After the addition of $AgBiSe_2$ in GeTe, Ag and Bi atoms preferentially occupy the Ge sites while Se atoms occupy the Te sites, which creates substitutional disorder. Thus, the consequent excess configurational entropy increases with increasing $AgBiSe_2$ content in GeTe. The stabilization of the high-temperature cubic phase of GeTe in ambient conditions in $(GeTe)_{100-x}(AgBiSe_2)_x$ (x ≥25) might be because of this increased configurational entropy in the system.[28]

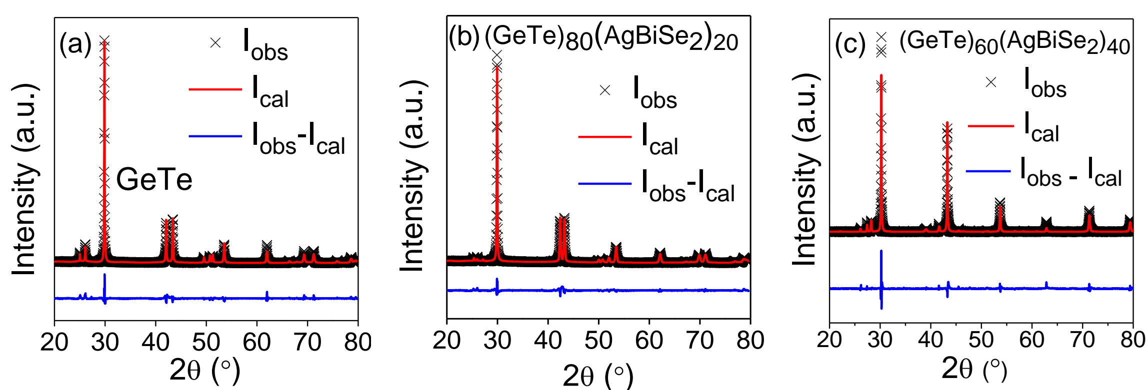

Figure 2.3. *Rietveld refinements of room-temperature PXRD patterns of $(GeTe)_{100-x}(AgBiSe_2)_x$ (x = 0, 20 and 40); (a) x = 0, rhombohedral phase (space group R3m), (b) x = 20, rhombohedral phase (space group R3m), and (c) x = 40, cubic phase (space group Fm-3m).*

Table 2.1. *Structural parameters of pristine GeTe obtained from Rietveld refinement of room temperature PXRD pattern.*

GeTe : Space group: *R3m*; a = b = 4.17352(6) Å, c = 10.6923(3) Å, α = β = 90º, γ = 120º

Constituent elements	x/a	y/b	z/c	U_{iso} (Å^2)	Occupancy	GOF
Ge	0	0	0.7611(2)	0.119(1)	1	2.78
Te	0	0	0.2389(2)	0.135(1)	1	

Table 2.2. *Structural parameters of* $(GeTe)_{80}(AgBiSe_2)_{20}$ *obtained from Rietveld refinement of room temperature PXRD pattern.*

- $(GeTe)_{80}(AgBiSe_2)_{20}$: Space group: *R3m*; a = 4.18249(7) Å, b = 4.18249(7) Å, c = 10.5405(3) Å, α = β = 90°, γ = 120°

Constituent elements	x/a	y/b	z/c	Occupancy	U_{iso} (Å^2)	GOF
Ge	0	0	0.7618(3)	0.667	0.136(2)	
Te	0	0	0.2406(3)	0.667	0.128(1)	
Ag	0	0	0.7618(3)	0.167	0.136(2)	2.22
Bi	0	0	0.7618(3)	0.167	0.136(2)	
Se	0	0	0.2406(2)	0.333	0.128(1)	

- Ge: Space group: *Fd-3m*; a = b = c = 5.682(3) Å, α = β = γ = 90°

Constituent elements	x/a	y/b	z/c	Occupancy	U_{iso} (Å^2)	GOF
Ge	0	0	0	1	0.39(3)	2.22

- Weight Fraction: $(GeTe)_{80}(AgBiSe_2)_{20}$ = 0.971 and Ge = 0.029

Table 2.3. *Structural parameters of* $(GeTe)_{60}(AgBiSe_2)_{40}$ *obtained from Rietveld refinement of room temperature PXRD pattern.*

- $(GeTe)_{60}(AgBiSe_2)_{40}$:Space group: *Fm-3m*; a = b = c = 5.90898(4) Å, α = β = γ = 90°

Constituent elements	x/a	y/b	z/c	Occupancy	U_{iso} (Å^2)	GOF
Ge	0	0	0	0.429	0.205(1)	
Te	0.5	0.5	0.5	0.429	0.189(1)	
Ag	0	0	0	0.286	0.205(1)	2.82
Bi	0	0	0	0.286	0.205(1)	
Se	0.5	0.5	0.5	0.571	0.189(1)	

- Ge: Space group: *Fd-3m*; a = b = c = 5.6293(6) Å, α = β = γ = 90°

Constituent elements	x/a	y/b	z/c	Occupancy	U_{iso} (Å^2)	GOF
Ge	0	0	0	1	0.25(2)	2.82

- Ag_2Te: Space group: *P2₁/c*; a = 7.5729 (20) Å, b = 4.893(1) Å, c = 8.274(2) Å, α = 90º, β = 120.89º(2), γ = 90º

Constituent elements	x/a	y/b	z/c	Occupancy	U_{iso} (Å^2)	GOF
Ag	0.025(3)	0.063(3)	0.293(4)	1	0.220(6)	2.82
Ag	0.332(3)	0.818(5)	0.988(4)	1	0.220(6)	
Te	0.291(2)	0.228(3)	0.267(4)	1	0.200(8)	

- Weight Fraction: $(GeTe)_{60}(AgBiSe_2)_{40}$ = 0.848; Ge = 0.055; Ag_2Te = 0.097

The rhombohedral to cubic phase transition in GeTe is evident from the temperature variation of DSC signal (Figure 2.2b). As the $AgBiSe_2$ concentration increases in $(GeTe)_{100-x}(AgBiSe_2)_x$, the phase transition temperature gradually decreases (Figure 2.2b) and finally, the cubic phase stabilizes at room temperature at x = 25. T_c reduces to 535, 495, and 471 K in $(GeTe)_{90}(AgBiSe_2)_{10}$, $(GeTe)_{85}(AgBiSe_2)_{15}$ and $(GeTe)_{80}(AgBiSe_2)_{20}$, respectively. The temperature dependent rhombohedral to cubic structural phase evolution is further evident from the temperature dependent synchrotron PXRD (λ = 0.7749 Å) of $(GeTe)_{100-x}(AgBiSe_2)_x$ (x = 10, 20) (Figure 2.2c).

Intriguing electronic properties emerge in $(GeTe)_{100-x}(AgBiSe_2)_x$ with the structural phase evolution as can be seen from the room temperature electronic properties vs. $AgBiSe_2$ concentration plots displayed in Figure 2.4. The notable observations are: (a) nearly zero band gap for x = 20 and (b) the n-type electronic conduc-tion for x > 25 in $(GeTe)_{100-x}(AgBiSe_2)_x$. Two distinct re-gions are evident in the compositional variation of room temperature band gap (Figure 2.4a), unit cell volume (Figure 2.4b), electrical conductivity (Figure 2.4c), Seebeck coefficient (Figure 2.4d) plots and carrier concentration table (Table 2.4). The compositional variations of all these parameters with $AgBiSe_2$ concentration show an inflection point around x ~ 20 where the ambient crystal structure of $(GeTe)_{100-x}(AgBiSe_2)_x$ transforms from rhombohedral to cubic. The $AgBiSe_2$ concentration dependent optical band gap of $(GeTe)_{100-x}(AgBiSe_2)_x$ (x = 0 - 50) (Figure 2.4a), exhibits a gradual decrease in band gap with increasing $AgBiSe_2$ concentration up to x ~ 20. With increasing the $AgBiSe_2$, the band gap decreases from ~ 0.18 eV for pristine GeTe to nearly zero at x = 20. With further increase of $AgBiSe_2$ content above x = 20, band gap starts increasing and reaches to ~ 0.25 eV at x = 50. Further, we observed that unit cell

volume of $(GeTe)_{100-x}(AgBiSe_2)_x$ decreases with increasing $AgBiSe_2$ concentration up to x ~ 20 in the rhombohedral phase (Figure 2.4b). The unit cell volume decreases from 161.24 $Å^3$ for pristine GeTe to 157.17 $Å^3$ at x = 20. Above x = 20, the ambient structure of $(GeTe)_{100-x}(AgBiSe_2)_x$ transform to cubic phase and the unit cell volume increases to 207.47 $Å^3$ at x = 25. With further increasing the $AgBiSe_2$ concentration above x > 25, the unit cell volume gradually decreases and reaches to 202.26 $Å^3$ at x = 50. This fascinating correlation between the compositional dependent electronic band gap and unit cell volume indicates a possible role of chemical pressure in tuning the electronic structure in $(GeTe)_{100-x}(AgBiSe_2)_x$.

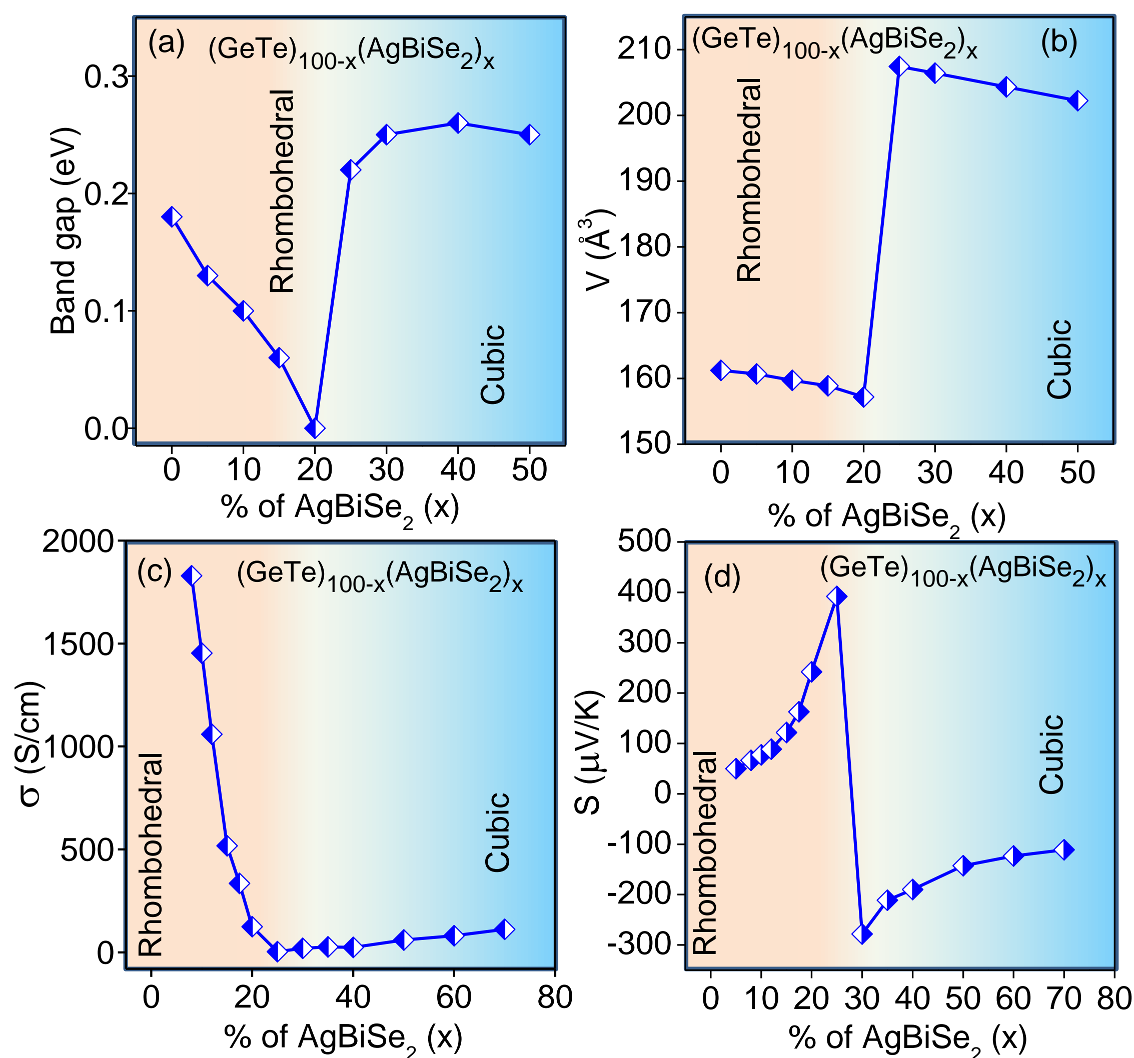

Figure 2.4. *Compositional variation of (a) band gap, (b) unit cell volume (V), (c) room temperature electrical conductivity (σ), and (d) room temperature Seebeck coefficient (S) with $AgBiSe_2$ concentration in $(GeTe)_{100-x}(AgBiSe_2)_x$ (x = 0 - 50) exhibits a non-monotonous variation with an inflection point around x ~ 20.*

Table 2.4. *Room temperature carrier concentration and mobility of* $(GeTe)_{100-x}(AgBiSe_2)_x$ *(x = 0 - 50) obtained from Hall measurement.*

Sample	Carrier concentration (x $10^{20}/cm^3$)	Mobility (cm^2/Vs)
GeTe	8.75 (*p*-type)	57.3
$(GeTe)_{90}(AgBiSe_2)_{10}$	2.74 (*p*-type)	33.1
$(GeTe)_{80}(AgBiSe_2)_{20}$	0.22 (*p*-type)	35.2
$(GeTe)_{70}(AgBiSe_2)_{30}$	0.033 (*n*-type)	36.6
$(GeTe)_{50}(AgBiSe_2)_{50}$	0.87 (*n*-type)	43.2

The room temperature electrical conductivity (σ) also changes non-monotonously with $AgBiSe_2$ concentration; initially it decreases up to x = 25 where it reaches to a minimum value of 3.3 S/cm and then it starts increasing with further increase in $AgBiSe_2$ concentration (Figure 2.4c). This initial sharp drop in room temperature electrical conductivity followed by gradual increase with increasing $AgBiSe_2$ concentration can be understood in terms of variation in charge carrier concentration as obtained from Hall effect measurements (Table 2.4). Pristine GeTe is a heavily doped *p*-type semiconductor because of intrinsic Ge vacancies (carrier concentration 8.75×10^{20} cm^{-3}). As the $AgBiSe_2$ concentration increases, the majority charge carriers in $(GeTe)_{100-x}(AgBiSe_2)_x$ gradually changes from *p*- to *n*-type (Table 2.4). The *p*-type carrier concentration drops to a value of 2.2×10^{19} cm^{-3} at x = 20. Subsequently, the majority charge carriers become *n*-type at x = 30 with carrier concentration of 3.3×10^{18} cm^{-3} and starts increasing with further increase in $AgBiSe_2$ content which reaches to a value of 8.76×10^{19} cm^{-3} at x = 50. The tuning of *p*- to *n*-type electronic transport with variation in $AgBiSe_2$ concentration is also reflected from the compositional variation of room temperature Seebeck coefficient (*S*) (Figure 2.4d). The room temperature Seebeck coefficient is initially positive with a value of ~ 34 μV/K in pristine GeTe. As $AgBiSe_2$ concentration increases, room temperature Seebeck coefficient also increases gradually to a maximum value of ~ 392 μV/K up to x = 25, which further corroborates to the gradual drop in *p*-type carrier concentration obtained from the Hall effect measurement with initial increase of $AgBiSe_2$ concentration. At x = 30, the room temperature Seebeck coefficient suddenly becomes negative with a value of ~ -278 μV/K

signifying the change in majority carrier in the system from *p*- to *n*-type. Further increase in $AgBiSe_2$ concentration results in gradual decrease in room temperature Seebeck coefficient due to increase in *n*-type carrier concentration in the system.

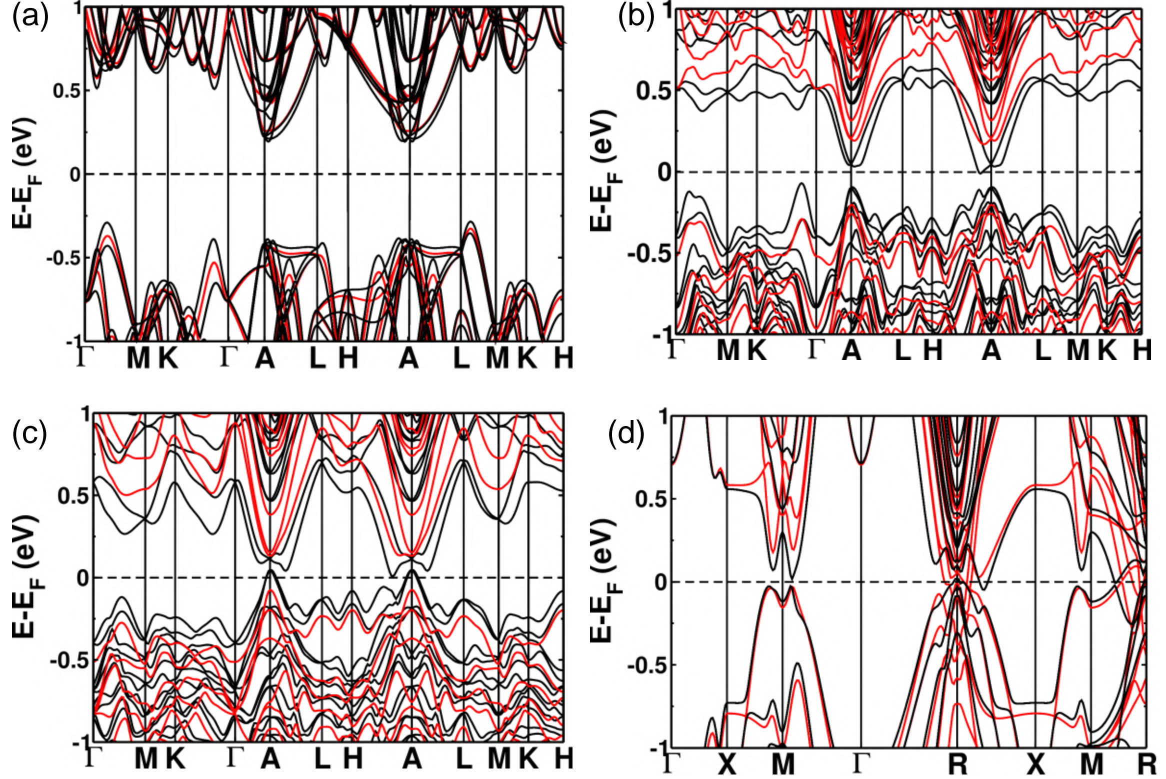

Figure 2.5. *Electronic structure of (a) rhombohedral GeTe, (b) rhombohedral* $(GeTe)_{90}(AgBiSe_2)_{10}$*, (c) rhombohedral* $(GeTe)_{80}(AgBiSe_2)_{20}$*, and (d) cubic* $(GeTe)_{60}(AgBiSe_2)_{40}$ *calculated with (black colour lines) and without (red colour lines) the inclusion of spin-orbit coupling (SOC).*

We now present the results of DFT based electronic structure calculations of $(GeTe)_{100-x}(AgBiSe_2)_x$ with and without the inclusion of spin orbit coupling to understand the evolution of band gap and the crossover from *p*- to *n*-type electronic transport. Electronic structure has been calculated at selected compositions: Pristine GeTe (rhombohedral, Figure 2.5a), $(GeTe)_{90}(AgBiSe_2)_{10}$ (rhombohedral, Figure 2.5b), $(GeTe)_{80}(AgBiSe_2)_{20}$ (rhombohedral, Figure 2.5c) and $(GeTe)_{60}(AgBiSe_2)_{40}$ (cubic, Figure 2.5d). Electronic structure calculation reveals a clear reduction in electronic band gap with initial increase of $AgBiSe_2$ concentration in rhombohedral GeTe, consistent with the observed composition dependent band gap estimated from diffuse reflectance

spectroscopy. Our calculated band gap of rhombohedral GeTe is 0.47 eV (with SOC), which agrees well with the previous reports.[14,15] As the $AgBiSe_2$ concentration increases, band gap decreases to ~ 0.07 eV in $(GeTe)_{90}(AgBiSe_2)_{10}$ (with SOC) (Figure 2.5b) and becomes semi-metallic in nature in rhombohedral $(GeTe)_{80}(AgBiSe_2)_{20}$ with valence bands crossing the Fermi Level at A point (Figure 2.5c). While the experimental band gap of cubic $(GeTe)_{100-x}(AgBiSe_2)_x$ increases with increasing $AgBiSe_2$ concentration, the calculated electronic structure indicates that the material remains semi-metallic even at x = 40. A similar observation is reported earlier also in case of $(GeSe)_{100-x}(AgBiSe_2)_x$ where it was found that chemical disorder strongly alters the electronic structure near Fermi level opening up a band gap.[28]

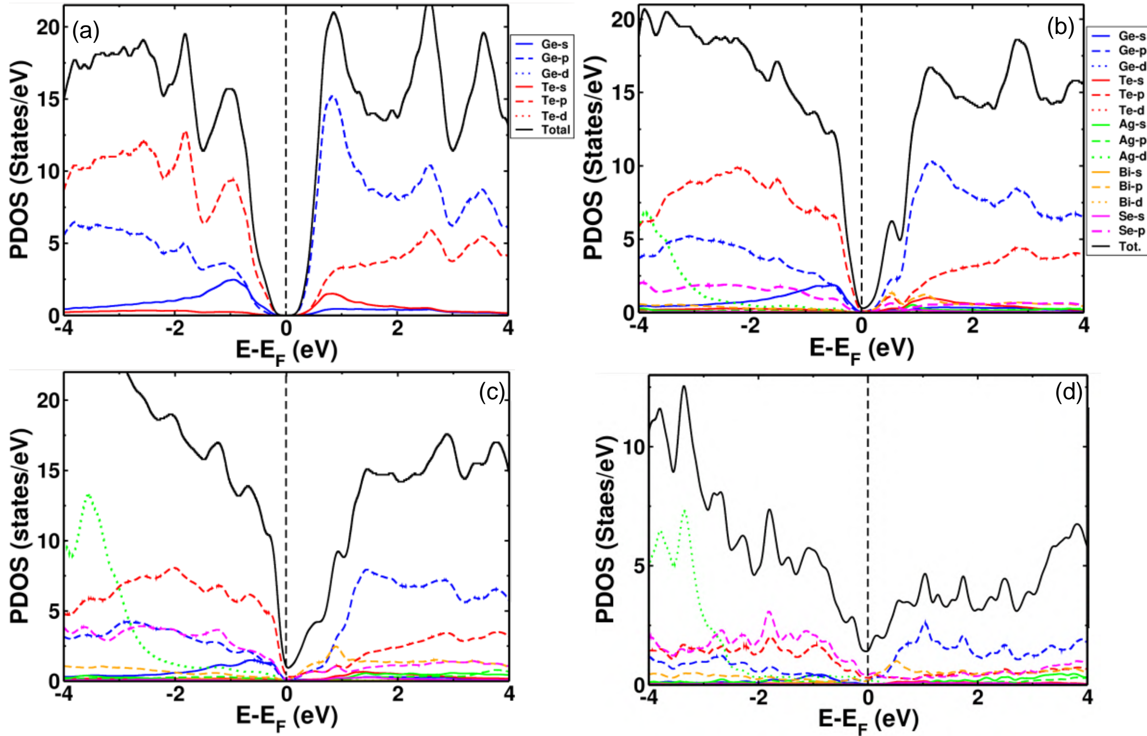

Figure 2.6. *Electronic density of states (DOS) and projected density of states (PDOS) of (a) rhombohedral GeTe, (b) rhombohedral* $(GeTe)_{90}(AgBiSe_2)_{10}$*, (c) rhombohedral* $(GeTe)_{80}(AgBiSe_2)_{20}$ *and (d) cubic* $(GeTe)_{60}(AgBiSe_2)_{40}$ *calculated with the inclusion of spin-orbit coupling (SOC).*

We have calculated the atom projected density of states (PDOS) (Figure 2.6) to understand the transition from *p*- to *n*-type electronic transport with increasing $AgBiSe_2$ concentration. The rhombohedral phase exhibits *p*-type electronic transport while the cubic phase has *n*-type electronic transport at room temperature. In pristine GeTe, valence band

edge is dominated by Te-p orbitals while Ge-p orbitals have the dominant contribution in conduction band edge (Figure 2.6a). The inclusion of $AgBiSe_2$ in GeTe causes change in the orbital contributions to electronic states near the valance and conduction band edges. The states near the valance band edge get additional contributions from Ag-d and Se-p orbitals, while Se-p and Bi-p orbitals contribute to the states at the conduction band edge (Figure 2.6b-c). The isoelectronic substitution of Se in place of Te does not play any significant role in driving the system from *n*- to *p*-type. However, the Bi^{3+} substitution in place of Ge^{2+} has a much stronger influence on the conduction band edge states compared to the Ag^+ contribution to the valence band edge, resulting in crossover in electronic character of $(GeTe)_{100-x}(AgBiSe_2)_x$ from *p*- to *n*-type. Further, Bi-p orbital contribution to the conduction band increases in the cubic phase (Figure 2.6d) relative to that of rhombohedral phase (Figure 2.6b) with increasing the concentration of $AgBiSe_2$, making the cubic phase *n*-type.

Temperature variation of electrical conductivity of $(GeTe)_{100-x}(AgBiSe_2)_x$ is shown in Figure 2.7a . σ of $(GeTe)_{100-x}(AgBiSe_2)_x$ (x = 0 - 15) decreases systematically with increase in $AgBiSe_2$ concentration and it decreases with increase in temperature, depicting the degenerate semiconductor behavior. Typically, σ of $(GeTe)_{90}(AgBiSe_2)_{10}$ decreases from 1453 S/cm at 295 K to 718 S/cm at 710 K. The main reason for the decrease of σ with increase in $AgBiSe_2$ content is the decrease in *p*-type carrier concentrations (Table 2.4). For x ≥30, σ increases with the increase in $AgBiSe_2$ concentration due to the increase in *n*-type carrier concentration. Typically, σ of $(GeTe)_{50}(AgBiSe_2)_{50}$ increases from 60 S/cm at 295 K to 219 S/cm at 721 K. Moreover, σ of all the $(GeTe)_{100-x}(AgBiSe_2)_x$ with x ≥ 30 increases with increase in temperature indicating the semiconducting electronic transport. Further, we have doped Br (0.5 mol %) in $(GeTe)_{50}(AgBiSe_2)_{50}$ in order to optimize its *n*-type electronic transport, but we do not see significant difference compared to the undoped sample.

Temperature dependent Seebeck coefficient (*S*) of $(GeTe)_{100-x}(AgBiSe_2)_x$ are presented in Figure 2.7b. *S* is positive for the entire temperature range of 300 – 723 K for x ≤ 25 indicating *p*-type electronic transport (Figure 2.5b). While *S* is positive in the entire measured temperature range for x ≤ 25, bipolar nature of the samples becomes increasingly prominent at lower temperatures with increase in *x*, which is due to the decrease in band

gap of the sample with the increase in $AgBiSe_2$ concentration. However, when x ≥ 30, $(GeTe)_{100-x}(AgBiSe_2)_x$ shows *n*-type electronic conduction as is evident from the negative *S* values in the entire temperature range of 300 – 723 K. Typically, $(GeTe)_{50}(AgBiSe_2)_{50}$ exhibits *S* value of -141μV/K at 300 K which decreases to -123μV/K at 723 K.

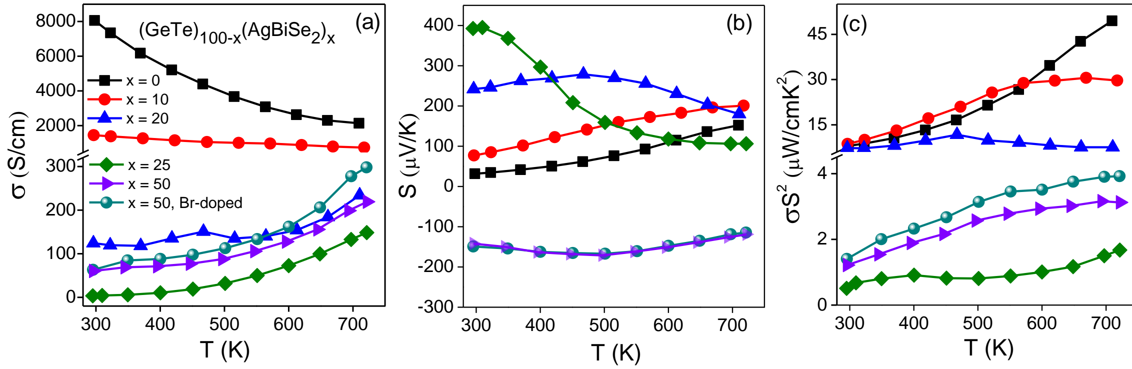

Figure 2.7. *Temperature-dependent (a) electrical conductivity (σ), (b) Seebeck coefficient (S) and (c) power factor (σS^2) of $(GeTe)_{100-x}(AgBiSe_2)_x$ (x = 0 - 50) samples.*

Temperature variation of power factor ($S^2\sigma$) of $(GeTe)_{100-x}(AgBiSe_2)_x$ is shown in Figure 2.7c. The maximum achieved power factor in rhombohedral *p*-type $(GeTe)_{80}(AgBiSe_2)_{20}$ is ~ 12 μW/cmK^2 at 467 K, whereas the maximum *n*-type power factor is obtained in cubic $(GeTe)_{50}(AgBiSe_2)_{50}$ which is ~ 3.2 μW/cmK^2 at 693 K. Further, the optimization of thermoelectric properties of *n*-type $(GeTe)_{50}(AgBiSe_2)_{50}$ through Br doping resulted in an improved power factor ~ 4 μW/cmK^2 at 721 K, which is mainly ascribed to improved electrical conductivity of the system.

Temperature variation of total thermal conductivity (κ_{tot}) of $(GeTe)_{100-x}(AgBiSe_2)_x$ is shown in Figure 2.8c. $AgBiSe_2$ alloying with GeTe drastically decrease κ_{tot} in $(GeTe)_{100-x}(AgBiSe_2)_x$. Typically, $(GeTe)_{50}(AgBiSe_2)_{50}$ exhibits κ_{tot} of ~ 0.33 W/mK at 300 K which increases to 0.91 W/mK at 726 K. The increase in κ_{tot} at higher temperature could be due to the enhanced bipolar thermo-diffusion as a result of small band gap. Temperature dependent lattice thermal conductivity (κ_{lat}) of $(GeTe)_{100-x}(AgBiSe_2)_x$ (x = 0 - 50) is obtained by subtracting the electronic thermal conductivity (κ_{el}) from the total thermal conductivity (κ_{tot}). κ_{lat} for all the $AgBiSe_2$ alloyed GeTe decreases drastically compared to that of the pristine GeTe. For example, room temperature κ_{lat} ~ 2.78 W/mK of pristine GeTe

decreases to 0.35 W/mK and 0.3 W/mK in $(GeTe)_{80}(AgBiSe_2)_{20}$ and $(GeTe)_{50}(AgBiSe_2)_{50}$, respectively (Figure 2.8d).

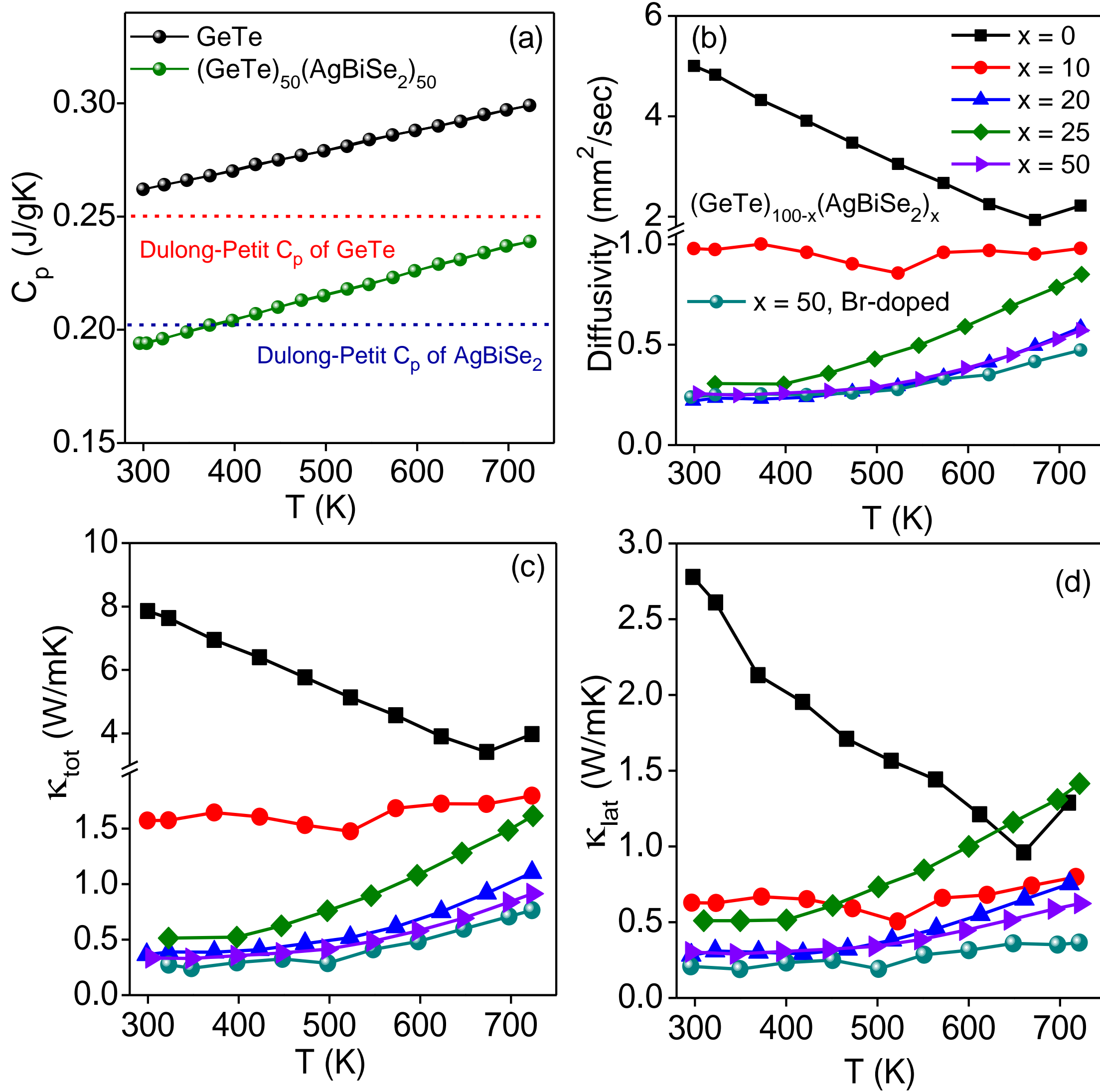

Figure 2.8. *(a) Temperature variations of heat capacity (C_p) of GeTe and $(GeTe)_{50}(AgBiSe_2)_{50}$ samples. Temperature dependent (b) Diffusivity (D), (c) total thermal conductivity (κ_{tot}) and (d) lattice thermal conductivity (κ_{lat}) of $(GeTe)_{100-x}(AgBiSe_2)_x$ (x = 0 - 50).*

To further understand the ultralow κ_{lat}, backscattered electron (BSE) mode-FESEM, energy dispersive X-ray spectroscopy (EDAX) and transmission electron microscopy (TEM) were performed on $(GeTe)_{80}(AgBiSe_2)_{20}$. The BSE-FESEM image of $(GeTe)_{80}(AgBiSe_2)_{20}$ (Figure 2.9a) shows the presence of dark precipitates of ~ 20-200 nm size (encircled with yellow dotted lines in Figure 2.9a). EDAX analysis confirms that the precipitates as Ge (Figure 2.9b).

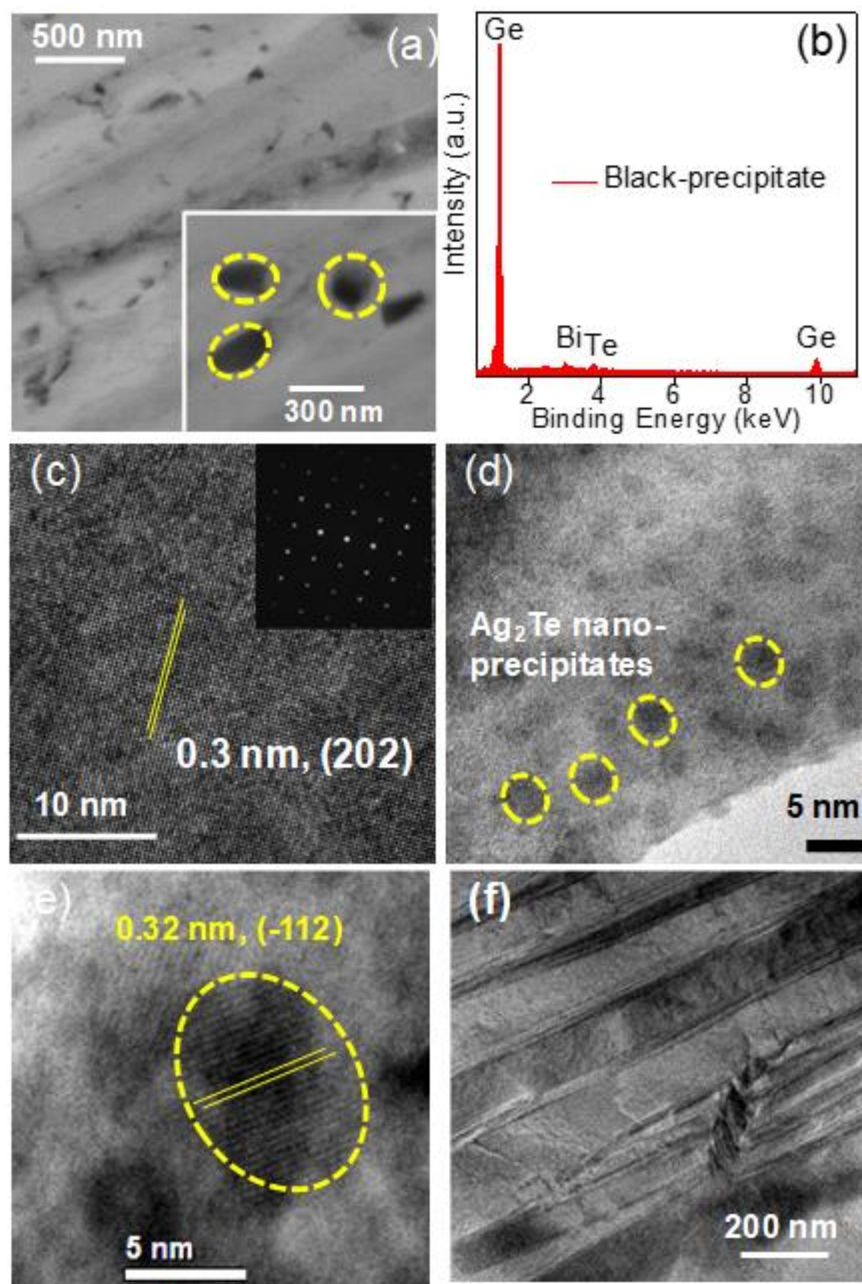

Figure 2.9. *(a) BSE-FESEM image of $(GeTe)_{80}(AgBiSe_2)_{20}$. Inset shows the black precipitates (encircled in yellow dotted lines) of Ge (space group $Fd\bar{3}m$) and the corresponding (b) EDAX spectra of the precipitates. (c) HRTEM micrograph of $(GeTe)_{80}(AgBiSe_2)_{20}$ exhibiting an interplanar spacing of 0.3 nm corresponding to the (202) planes of rhombohedral GeTe (space group R3m). Inset shows the SAED pattern. (d) and (e) HRTEM image of $(GeTe)_{80}(AgBiSe_2)_{20}$ showing the presence of nano precipitates (encircled in yellow dotted lines) of Ag_2Te phase. The interplanar spacing of 0.32 nm in figure (e) corresponds to the (-112) plane of Ag_2Te (space group P21/c). (f) Low magnification TEM micrograph of $(GeTe)_{80}(AgBiSe_2)_{20}$ exhibiting the ordered domain variants with dark and bight contrast difference.*

Figure 2.9c exhibits the high resolution TEM (HRTEM) micrograph of the $(GeTe)_{80}(AgBiSe_2)_{20}$ matrix with interplanar distance of d = 0.3 nm which corresponds to (202) planes of the rhombohedral phase. Selected area electron diffraction pattern (SAED) along <001> zone axis (Inset of Figure 2.9c) indicates the single crystalline domains of rhombohedral phase of $(GeTe)_{80}(AgBiSe_2)_{20}$ at room temperature. Further, HRTEM images show the presence of nanoprecipitates of Ag_2Te phase (Figures 2.9d and 2.9e) in the rhombohedral $(GeTe)_{80}(AgBiSe_2)_{20}$ matrix. Low magnification TEM images of $(GeTe)_{80}(AgBiSe_2)_{20}$ also reveal the presence of ordered domain variants with successive bright and dark contrasts due to the breakdown of Friedel symmetry in rhombohedral GeTe (Figure 2.9f).[6,9] The formation of domain structure and grain boundaries along with the presence of Ge and Ag_2Te nano-precipitates play an important role in the reduction of κ_{lat} by scattering the mid to long wavelength phonons.

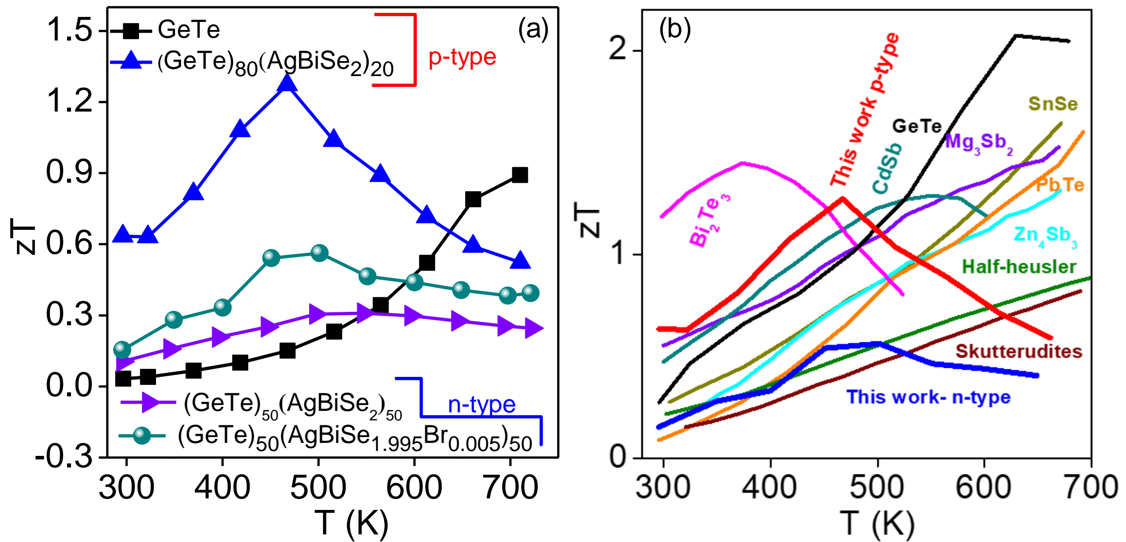

Figure 2.10. *(a) Temperature dependent thermoelectric figure of merit (zT) of selective p- and n-type $(GeTe)_{100-x}(AgBiSe_2)_x$ samples. (b) Comparison of the temperature dependent (300-700 K) thermoelectric figure of merit (zT) of our best p- and n- type $(GeTe)_{100-x}(AgBiSe_2)_x$ samples with other state-of-the-art thermoelectric materials such as Bi_2Te_3,[32] PbTe,[33] SnSe,[34] CdSb,[35] GeTe,[36] Mg_3Sb_2,[37] Zn_4Sb_3,[38] Half-heusler[39] and Skutterudites.[40]*

Temperature dependent zT of p-type $(GeTe)_{100-x}(AgBiSe_2)_x$ ($x \leq 25$) and n-type $(GeTe)_{100-x}(AgBiSe_2)_x$ ($x \geq 30$) samples are presented in Figure 2.10a. The maximum obtained p-type zT is ~ 1.3 at 467 K in $(GeTe)_{80}(AgBiSe_2)_{20}$. This zT value is significant

for TE applications in the 400-500 K range (Figure 2.10b). More importantly, the obtained maximum *n*-type *zT* is ~ 0.6 in $(GeTe)_{50}(AgBiSe_{1.995}Br_{0.005})_{50}$ at 500 K, which is the only promising *n*-type GeTe based thermoelectrics, to the best our knowledge.

2.4 Conclusions

In conclusion, we have demonstrated both *n* and *p*-type thermoelectric properties in $(GeTe)_{100-x}(AgBiSe_2)_x$. A room temperature structural phase evolution from rhombohedral to cubic phase in GeTe was evidenced via alloying with $AgBiSe_2$. This structural change accompanies an electronic structure modulation which triggers the change of the *p*-type nature of (GeTe) to a rare *n*-type character in $(GeTe)_{100-x}(AgBiSe_2)_x$ with increasing $AgBiSe_2$ concentration. The crystal and electronic structure modulations of $(GeTe)_{100-x}(AgBiSe_2)_x$ with $AgBiSe_2$ composition has been confirmed from the non-monotonous variation of unit cell volume, band gap, room temperature electrical conductivity and Seebeck coefficient. DFT calculations of the electronic structure further corroborated that the *n*-type electronic transport of $(GeTe)_{100-x}(AgBiSe_2)_x$ arises due to the increasing contribution of Bi-p orbitals at the conduction band edge with increasing $AgBiSe_2$ concentration. We achieved a promising *p*- and *n*-type thermoelectric figure of merit, *zT*, ~ 1.3 at 467 K and 0.6 at 500 K in $(GeTe)_{80}(AgBiSe_2)_{20}$ and $(GeTe)_{50}(AgBiSe_2)_{50}$, respectively. The demonstration of both *n*- and *p*-type thermoelectric performance in GeTe in the mid-temperature range (400-500 K) opens new opportunities for GeTe based thermoelectric materials.

2.5 References

(1) Rosi, F. D.; Dismukes, J. P.; Hockings, E. F. *Electr. Eng.* **1960**, *79*, 450–459.
(2) Roychowdhury, S.; Samanta, M.; Perumal, S.; Biswas, K. *Chem. Mater.* **2018**, *30*, 5799–5813.
(3) Perumal, S.; Roychowdhury, S.; Biswas, K. *J. Mater. Chem. C* **2016**, *4*, 7520–7536.
(4) Hong, M.; Zou, J.; Chen, Z. *Adv. Mater.* **2019**, *31*, 1807071.
(5) Polking, M. J.; Han, M.-G.; Yourdkhani, A.; Petkov, V.; Kisielowski, C. F.; Volkov, V. V; Zhu, Y.; Caruntu, G.; Alivisatos, a P.; Ramesh, R. *Nat. Mater.* **2012**, *11*, 700–709.
(6) Perumal, S.; Roychowdhury, S.; Negi, D. S.; Datta, R.; Biswas, K. *Chem. Mater.* **2015**, *27*, 7171–7178.
(7) Li, J.; Chen, Z.; Zhang, X.; Sun, Y.; Yang, J.; Pei, Y. *NPG Asia Mater.* **2017**, *9*,

e353.
(8) Li, J.; Zhang, X.; Chen, Z.; Lin, S.; Li, W.; Shen, J.; Witting, I. T.; Faghaninia, A.; Chen, Y.; Jain, A.; Chen, L.; Snyder, G. J.; Pei, Y. *Joule* **2018**, *2*, 976–987.
(9) Wu, D.; Zhao, L.-D.; Hao, S.; Jiang, Q.; Zheng, F.; Doak, J. W.; Wu, H.; Chi, H.; Gelbstein, Y.; Uher, C.; Wolverton, C.; Kanatzidis, M.; He, J. *J. Am. Chem. Soc.* **2014**, *136*, 11412–11419.
(10) Perumal, S.; Bellare, P.; Shenoy, U. S.; Waghmare, U. V.; Biswas, K. *Chem. Mater.* **2017**, *29*, 10426–10435.
(11) Liu, Z.; Sun, J.; Mao, J.; Zhu, H.; Ren, W.; Zhou, J.; Wang, Z.; Singh, D. J.; Sui, J.; Chu, C.-W.; Ren, Z. *Proc. Natl. Acad. Sci.* **2018**, *115*, 5332–5337.
(12) Zheng, Z.; Su, X.; Deng, R.; Stoumpos, C.; Xie, H.; Liu, W.; Yan, Y.; Hao, S.; Uher, C.; Wolverton, C.; Kanatzidis, M. G.; Tang, X. *J. Am. Chem. Soc.* **2018**, *140*, 2673–2686.
(13) Hong, M.; Wang, Y.; Liu, W.; Matsumura, S.; Wang, H.; Zou, J.; Chen, Z.-G. *Adv. Energy Mater.* **2018**, *8*, 1801837.
(14) Roychowdhury, S.; Biswas, K. *Chem* **2018**, *4*, 939–942.
(15) Wu, L.; Li, X.; Wang, S.; Zhang, T.; Yang, J.; Zhang, W.; Chen, L.; Yang, J. *NPG Asia Mater.* **2017**, *9*, e343.
(16) Hong, M.; Chen, Z.-G.; Yang, L.; Zou, Y.-C.; Dargusch, M. S.; Wang, H.; Zou, J. *Adv. Mater.* **2018**, *30*, 1705942.
(17) Perumal, S.; Samanta, M.; Ghosh, T.; Shenoy, U. S.; Bohra, A. K.; Bhattacharya, S.; Singh, A.; Waghmare, U. V.; Biswas, K. *Joule* **2019**, *3*, 2565–2580.
(18) Perumal, S.; Roychowdhury, S.; Biswas, K. *Inorg. Chem. Front.* **2016**, *3*, 125–132.
(19) Li, J.; Zhang, X.; Lin, S.; Chen, Z.; Pei, Y. *Chem. Mater.* **2017**, *29*, 605–611.
(20) Samanta, M.; Biswas, K. *J. Am. Chem. Soc.* **2017**, *139*, 9382–9391.
(21) Davidow, J.; Gelbstein, Y. *J. Electron. Mater.* **2013**, *42*, 1542–1549.
(22) Gelbstein, Y.; Davidow, J. *Phys. Chem. Chem. Phys.* **2014**, *16*, 20120.
(23) Hazan, E.; Ben-Yehuda, O.; Madar, N.; Gelbstein, Y. *Adv. Energy Mater.* **2015**, *5*, 1500272.
(24) Samanta, M.; Roychowdhury, S.; Ghatak, J.; Perumal, S.; Biswas, K. *Chem. - A Eur. J.* **2017**, *23*, 7438–7443.
(25) Salvador, J. R.; Yang, J.; Shi, X.; Wang, H.; Wereszczak, A. A. *J. Solid State Chem.* **2009**, *182*, 2088–2095.
(26) Fahrnbauer, F.; Souchay, D.; Wagner, G.; Oeckler, O. *J. Am. Chem. Soc.* **2015**, *137*, 12633–12638.
(27) Snyder, G. J.; Ursell, T. S. *Phys. Rev. Lett.* **2003**, *91*, 148301.
(28) Roychowdhury, S.; Ghosh, T.; Arora, R.; Waghmare, U. V.; Biswas, K. *Angew. Chemie - Int. Ed.* **2018**, *57*, 15167–15171.
(29) Giannozzi, P.; Baroni, S.; Bonini, N.; Calandra, M.; Car, R.; Cavazzoni, C.; Ceresoli, D.; Chiarotti, G. L.; Cococcioni, M.; Dabo, I.; Dal Corso, A.; De Gironcoli, S.; Fabris, S.; Fratesi, G.; Gebauer, R.; Gerstmann, U.; Gougoussis, C.; Kokalj, A.; Lazzeri, M.; Martin-Samos, L.; Marzari, N.; Mauri, F.; Mazzarello, R.; Paolini, S.; Pasquarello, A.; Paulatto, L.; Sbraccia, C.; Scandolo, S.; Sclauzero, G.; Seitsonen, A. P.; Smogunov, A.; Umari, P.; Wentzcovitch, R. M. *J. Phys. Condens. Matter* **2009**, *21*, 395502.
(30) Hua, X.; Chen, X.; Goddard, W. A. *Phys. Rev. B* **1997**, *55*, 16103–16109.
(31) Perdew, J. P.; Burke, K.; Ernzerhof, M. *Phys. Rev. Lett.* **1996**, *77*, 3865–3868.

(32) Poudel, B.; Hao, Q.; Ma, Y.; Lan, Y.; Minnich, A.; Yu, B.; Yan, X.; Wang, D.; Muto, A.; Vashaee, D.; Chen, X.; Liu, J.; Dresselaus; Chen, G.; Ren, Z. *Science* **2008**, *320*, 634–638.

(33) Biswas, K.; He, J.; Blum, I. D.; Wu, C.-I.; Hogan, T. P.; Seidman, D. N.; Dravid, V. P.; Kanatzidis, M. G. *Nature* **2012**, *489*, 414–418.

(34) Chang, C.; Wu, M.; He, D.; Pei, Y.; Wu, C.-F.; Wu, X.; Yu, H.; Zhu, F.; Wang, K.; Chen, Y.; Huang, L.; Li, J.-F.; He, J.; Zhao, L.-D. *Science* **2018**, *360*, 778–783.

(35) Wang, S.; Yang, J.; Wu, L.; Wei, P.; Yang, J.; Zhang, W.; Grin, Y. *Chem. Mater.* **2015**, *27*, 1071–1081.

(36) Samanta, M.; Biswas, K. *J. Am. Chem. Soc.* **2017**, *139*, 9382–9391.

(37) Zhang, J.; Song, L.; Pedersen, S. H.; Yin, H.; Hung, L. T.; Iversen, B. B. *Nat. Commun.* **2017**, *8*, 13901.

(38) Snyder, G. J.; Christensen, M.; Nishibori, E.; Caillat, T.; Iversen, B. B. *Nat. Mater.* **2004**, *3*, 458–463.

(39) Chen, S.; Lukas, K. C.; Liu, W.; Opeil, C. P.; Chen, G.; Ren, Z. *Adv. Energy Mater.* **2013**, *3*, 1210–1214.

(40) Sale, B. C.; Mandrus, D.; Williams, R. K. *Science* **1996**, *272*, 1325–1328.

Chapter 3

Realization of High Thermoelectric Figure of Merit in GeTe by Complementary Co-doping of Bi and In

Chapter 3

Realization of High Thermoelectric Figure of Merit in GeTe by Complementary Co-doping of Bi and In†

Summary

The principle challenge in optimizing the thermoelectric figure of merit, zT, of GeTe is the low Seebeck coefficient (S) and high thermal conductivity of GeTe. Here, we report a high zT ~ 2.1 at 723 K in In and Bi co-doped GeTe along with extremely high estimated TE conversion efficiency ~ 12.3% in single-leg thermoelectric generator for the temperature difference of 445 K. In and Bi play distinct but complementary role. In doping significantly enhances the Seebeck coefficient (S) through the formation of resonance level, which is confirmed with first-principles density functional theory calculations and Pisarenko plot considering two valance band model. On the other hand, Bi doping markedly reduces the lattice thermal conductivity due to the formation of extensive solid solution point defects and domain variants. Moreover, a high value of Vickers microhardness (~ 200 H_v, H_v = kgf/mm^2) reveals excellent mechanical stability.

---

†*Paper based on this study has been published in* Joule (Cell Press) **2019**, *3*, 2565–2580.

3.1 Introduction

PbTe and its derivatives are well-known for their superior thermoelectric performance in the mid-temperature operational range of 600 - 900 K.[1–4] However, the toxicity of Pb limits their large-scale applications necessitating the research for alternative thermoelectric materials. In recent years GeTe-based thermoelectric materials have emerged as potential alternatives to PbTe-based thermoelectric materials.[5–7] Better ubderstanding of electronic structure, lattice dyanmics, structure-properties correlation along with several innovative strategies lead to development of various high-perfoemance *p*-type GeTe-based thermoelectric materials[8,9,18–20,10–17] Inspite of significant improvement in *zT*, the experimental power conversion efficiency (η), especially for the GeTe-based single-leg TE generator, has been limited in the range of 8 – 9 %.[21,22]

Substitution of Bi in GeTe is known to result in low κ_{lat} ~ 1 W/mK due to phonon scattering by solid solution point defects for Bi < 6 mol%.[10,12,13] When Bi concentration is ≥ 10 mol%, the reduction of κ_{lat} is mainly attributed to the formation of nanoprecipitates and nanoscale cation defect layer.[12] Further, the aliovalent doping of Bi^{3+} at Ge^{2+} site in GeTe drastically reduces the *p*-type carrier density from ~ 10^{21} cm^{-3} to ~ 10^{20} cm^{-3}.[10,12,13] On the other hand, the formation of resonant states close to Fermi level in the valence band of GeTe has been realized upon In doping,[15] which alters the density of states (DOS) near Fermi level leading to a significant enhancement in Seebeck coefficient. Therefore, In and Bi have different but complementary roles in the enhancement of the thermoelectric performance of GeTe. Thus, co-doping of In and Bi in GeTe may synergistically enhance the overall thermoelectric performance due to their complementary effects. Further, for practical applications, it is important to study the micro-hardness (mechanical stability) and investigate the experimental thermoelectric efficiency of single-leg TE devices based on high performance Bi and In co-doped GeTe.

Herein, we demonstrate a significantly high thermoelectric performance in Bi and In co-doped GeTe, ascribed to distinct but complementary roles of In and Bi in terms of modulating the electronic structure and scattering of heat carrying phonons, respectively. The enhanced Seebeck coefficient (~ 120 μV/K at 300 K) with In doping is shown to be due to the formation of resonance level in valence band and the reduced κ_{lat} (~ 0.5 W/mK at 300 K) is due to significant scattering of phonons at point defects associated with Bi

substitution in GeTe. Their synergy results in a high thermoelectric figure of merit, zT, of 2.1 at 723 K and a high average TE figure of merit, zT_{avg}, of 1.3 in the temperature range of 300 - 723 K in the composition $Ge_{0.93}In_{0.01}Bi_{0.06}Te$. Fundamental understanding of the enhancement of Seebeck coefficient in In and Bi co-doped GeTe has been realized via first principles density functional theoretical (DFT) calculations of electronic structure and Pisarenko plot considering two band model, which reveals that In and Bi co-doping not only results in the formation of resonance level, it also facilitates the valence band convergence by decreasing the energy difference between the light and heavy hole valence bands. Further, the measured Vickers microhardness of the $Ge_{0.93}In_{0.01}Bi_{0.06}Te$ sample (~ 200 H_v) reveals its high mechanical stability. High thermoelectric figure of merit and enhanced mechanical stability motivates us to measure the power conversion efficiency of single-leg TE devices based on In and Bi co-doped GeTe. We obtained extremely high estimated thermoelectric conversion efficiency (η) of ~ 12.3% in single-leg $Ge_{0.93}In_{0.01}Bi_{0.06}Te$ TE generator for the temperature difference of 445 K. The obtained power conversion efficiency is the highest among the single-leg based thermo-element (non-segmented) in the ΔT range of 400 - 600 K.

3.2 Methods

3.2.1 Reagents. Highly pure germanium (Sigma Aldrich, 99.995%), bismuth (Sigma Aldrich, 99.9999%), indium (Alfa Aesar, 99.99%) and tellurium (Alfa Aesar, 99.999%) were used for synthesis without further purification.

3.2.2 Synthesis. Samples (~ 10 g scale) of $Ge_{1-x-y}Bi_xIn_yTe$ (x = 0.06; y = 0.005, 0.01 and 0.02) were prepared by vacuum sealed quartz tube melting reaction followed by hot-pressing. The stoichiometric amounts of starting elements of Ge, Bi, In and Te were taken in quartz tubes and sealed under vacuum pressure of 10^{-6} Torr. These sealed tubes were heated to 1223 K for 10 h, then dwelled at 6 h, and slowly cooled down to room temperature over 10 h. Further, ingots thus obtained were crushed into fine powers and powders were hot-pressed at 873 K for 7 min with pressure of 42 MPa under Ar atmosphere. The compacted pellets were cut into coins and bars by using low speed diamond saw and then used for thermoelectric measurements. The density of the all compacted pellets was measured by Archimedes' methods and found to be ~ 97% of theoretical density.

3.2.3 Powder X-ray diffraction. Powder X-ray diffraction patterns were recorded for the finely ground samples using a Cu-Kα (λ = 1.5406 Å) source on a Bruker D8 diffractometer.

3.2.4 Band gap measurement. Optical band gaps of finely ground $Ge_{1-x-y}Bi_xIn_yTe$ (x = 0.06; y = 0.005, 0.01 and 0.02) samples were estimated by diffuse reflectance method using FT-IR Bruker IFS 66V/S spectrometer in the wave number range 4000 - 400 cm^{-1} with 2 cm^{-1} resolution and 50 scans. The absorption (α/Λ) data were calculated from reflectance data using Kubelka-Munk equation: $\alpha/\Lambda = (1-R)^2/(2R)$, where R is the reflectance, α and Λ are the absorption and scattering coefficient, respectively. The energy band gaps of all the samples were determined from α/Λ vs. E (eV) plot.

3.2.5 Transmission electron microscopy. Aberration corrected FEI TITAN 3^{TM} 80 - 300 KV transmission electron microscope was used to analyze the structure morphologies of $Ge_{1-x-y}Bi_xIn_yTe$ sample. TEM samples were prepared by mechanical polishing and followed by the ion beam polishing/milling to achieve thin foil of ~ 20 - 80 nm. Bright field imaging, high resolution TEM imaging and selected area electron diffraction (SAED) were performed on the prepared samples.

3.2.6 Electrical transport. Electrical conductivity (σ) and Seebeck coefficients (S) were measured concurrently under He atmosphere in the temperature range 300 K to 723 K on a ULVAC-RIKO ZEM-3 instrument system. The typical sample for measurement had a parallelepiped shape with the dimensions of ~ 2×2×8 mm^3. Electrical and thermal transport properties are measured along pressing direction.

3.2.7 Hall measurement. Hall measurements were carried out at room temperature in the home made setup, where variable magnetic field with a maximum field of 0.7 T and fixed dc-current of 10 mA were used. The carrier concentration (n) of the samples was derived from the equations of $n = 1/(eR_H)$, where R_H and e are the Hall coefficient and the electron charge, respectively.

3.2.8 Thermal conductivity. Thermal diffusivity, D, was directly measured in the range 300 − 723 K by using laser flash analyzer in a Netzsch LFA-457. Coins with 8 mm diameter and less than 2 mm thickness were used in all the measurements. Temperature dependent heat capacity, C_p, of GeTe was derived using standard sample (pyroceram) in LFA-457,

which is slightly higher than Dulong-Petit C_p value of GeTe. The total thermal conductivity, κ_{total}, was calculated using the formula $\kappa_{total} = DC_p\rho$, where ρ is the density. The measured densities of all the samples were about 97% of theoretical density.

3.2.9 Microhardness. Microhardness of $Ge_{0.93}Bi_{0.06}In_{0.01}Te$ was measured in Zwick Roell Zhu 2.5 microhardness testing instrument using diamond indenter on the Vickers hardness scale. Vickers hardness (kgf/mm^2) value of the sample was obtained from the equation of $H_v = 1.854xL/(2d)^2$, where L is the indentation load and 2d is the diagonal length of the indentation. For the measurement, applied force was 2 N and the indent was kept for 10s. The error in microhardness measurement is about 5%.

3.2.10 Computational details. This part has been done in collaboration with Prof. Umesh V. Waghmare's group in JNCASR, India. Electronic structure of GeTe, Bi-doped, In-doped and Bi-In co-doped GeTe were determined within density functional theory (DFT) using Quantum Espresso package.[23] Here, fully relativistic ultra-soft pseudo potentials were used to model interaction between valence electrons and ionic cores, and to include the spin orbit coupling (SOC). Valence and semicore electronic states of Ge Te, Bi and In as $3d^{10}\,4s^2\,4p^2$, $4d^{10}\,5s^2\,5p^4$, $5d^{10}\,6s^2\,6p^3$ and $4d^{10}\,5s^2\,5p^1$ reference configurations were considered through these pseudopotentials. A Generalized Gradient Approximation (GGA) to exchange-correlation energy was employed with a functional parametrized by Perdew, Burke, and Erzenhoff (PBE).[24] Pristine, singly doped and co-doped samples of GeTe were simulated with a $(\sqrt{2} \times \sqrt{2} \times 2)a_0$ tetragonal supercell of GeTe containing 32 atoms, a_0 being the cubic lattice constant. Plane wave basis used in representing Kohn-Sham wave functions was truncated with an energy cutoff of 40 Ry, and that for charge density with energy cutoff of 320 Ry. Uniform 8x8x6 mesh of k points was used in sampling Brillouin zone integrations. The discontinuity in occupation numbers of electronic states across the gap or Fermi energy was smeared with Fermi-Dirac distribution function with a width (k_BT) of 0.04 eV. Electronic structure was determined along Γ - X - M - Γ - Z - R - A - Z lines of high symmetry in the Brillouin zone.

3.2.11 Calculation for ZT_{eng} and η (ZT_{eng}). Material's thermoelectric figure of merit, zT, is not very accurate for determining the conventional TE conversion efficiency because one always assumes the temperature-independent behaviour of S, $\rho = 1/\sigma$, and κ_{total} in the

calculations. Recently, H. S. Kim *et al.*[25] have proposed the engineering figure of merit, ZT_{eng}, based TE conversion efficiency which accounts for the cumulative temperature-dependent TE properties, which is useful for exactly determining the TE efficiency for a given material at a large temperature difference between the cold and hot ends of the TE legs. The expressions for ZT_{eng} and $\eta(ZT_{eng})$ are,[25]

$$(ZT)_{eng} = Z_{eng}\Delta T = \frac{(\int_{T_C}^{T_H} S(T)dT)^2}{\int_{T_C}^{T_H} \rho(T)dT \int_{T_C}^{T_H} \kappa(T)dT}\Delta T = \frac{(PF)_{eng}}{\int_{T_C}^{T_H} \kappa(T)dT} \qquad (3.1)$$

$$\eta_{max} = \eta_C \cdot \frac{\sqrt{1 + (ZT)_{eng}(\alpha/\eta_C - 1/2)} - 1}{\alpha\sqrt{1 + (ZT)_{eng}(\alpha/\eta_C - 1/2)} - \eta_C} \qquad (3.2)$$

Where $\rho(T)$, $S(T)$, $\kappa(T)$, η_C, and α represent the resistivity, Seebeck coefficient, total thermal conductivity, Carnot efficiency and a dimensionless intensity factor of Thomson coefficient, respectively. The engineering power density (P_d) was calculated using the following expression,

$$P_d = \frac{(PF)_{eng}\Delta T}{L}\frac{m_{opt}}{(1 + m_{0pt})^2} \qquad (3.3)$$

Where $(PF)_{eng}$ and m_{opt} are the engineering power factor and optimum ratio of external electrical load (R_L) and internal resistance (R_{int}).

3.2.12 Fabrication of single-leg TE devices and measurement of thermoelectric efficiency (η). This part has been done in collaboration with Dr. Shovit Bhattacharya's group in BARC, India. Typically, fabrication of the single-leg thermoelement involves two step processes. Firstly, the melt grown In and Bi co-doped GeTe powder was consolidated along with the end layers of Ag/Fe using spark plasma sintering at 450 ºC with 40 MPa for 5 min under vacuum. The view of layers in the fabricated single-leg In and Bi co-doped GeTe based thermoelement can be described as Ag/Fe/Ge(BiIn)Te/Fe/Ag. The introduction of Fe/Ag layers at the ends of the thermoelement creates a sharp interface due to immiscibility of Fe and Ag.[26] The second step is metallization process, where Ag contact leads (stripes) were attached with compacted thermoelement by diffusion bonding at high temperature and pressures. In

particular, during metallization, thermoelement was placed in a zirconia (thermal and electrical insulator) housing with Ag stripes (thickness: 0.5 mm, width: 8 mm, length ~ 18 mm) at ends of the thermoelements and subsequently subjected to vacuum hot-pressing at ~ 400 °C with load ~ 50 kg. To estimate the output electrical power and conversion efficiency, the fabricated device was sandwiched between an electrical heater and water-cooled copper block wherein a steady-state temperature difference ΔT was maintained using home-made TE performance setup.

In order to measure a load voltage (V_L), a load resistance (R_L) of 2 mΩ (i.e. equivalent to the four probe resistance of the thermoelement at room temperature) was soldered at the output leads (silver stripes) of the device. The ratio of load voltage and load resistance gives the estimation of load current (I_L) generated by the device. The uncertainty in the measurement of output electrical power is around 2% and it arises due to small error in the measurement of load resistance that has been put across the device.

Further, TE conversion efficiency, η, of single-leg based In and Bi co-doped GeTe TE generator at highest temperature is obtained from the measured electrical output power (P_W) divided by the input heat flowing (Q_H) through the thermoelement. For estimation of input heat flowing (Q_H) through the device, the correction of heat losses from the electrical power given to the heater is done in a systematic way. To carry out corrections of heat losses for correct estimation of actual working efficiency of the device, following measurements were carried out by thermally insulating the device from the atmosphere: (i) Heater assembly was insulated from outside and electrical power was given to the heater to reach ~ 500 °C. (ii) A zirconia sheet (the similar size used to hold single element device) was placed in between the hot surface and water-cooled sink. The entire assembly is covered with a glass wool based thermal insulation. In this case, the heat required to reach a particular temperature was estimated. This measurement gives an estimate of heat flowing through the zirconia housing holding the thermoelement. (iii) The single element device (with zirconia housing) was placed in between the hot surface and water-cooled sink. In this case, the heat required to reach a particular temperature was estimated. (iv) By subtracting the heat obtained in step (i) and (ii) from the heat input required in step (iii), we could estimate the actual heat flowing through thermoelement. The hot end (T_h) and cold end (T_c) temperatures of the device was measured using thin wire (~ 25 μm) K-type

thermocouples placed at the hot/cold ends of the device. The small diameter of thermocouples ensures the negligible heat loss through it. The uncertainty in the estimated input heat flow is around 10% due to radiation and convection losses. Further, to test the reliability of our home made set up for estimation of input heat flowing through the device, the thermal conductivity (κ) of a fused quartz sample (purity ~ 99.9%) was measured at three different average temperatures 40 °C, 250 °C and 500 °C and the respective values were found out to be 1.45, 1.64 and 2.03 W/mK. These values are in good agreement (uncertainty ±10%) with the literature reported values.[27]

From the measured open circuit voltage of the device and measured ΔT, we have estimated the average S of GeBiInTe device as ~ 126µV/K. The average S of the device is lower than the average S (~ 172 µV/K) of GeBiInTe sample without any electrical contact. The difference between the average S estimated for the device and sample could be due to actual temperature difference across the thermoelements (used in the device). The actual temperature difference across the active part of the thermoelements (i.e., GeBiInTe) being lower due to the temperature drop across the Ag stripes and the interfacial Ag/Fe layers at both ends of the thermoelement. From the correction of heat losses and actual power supplied to the heater for maintaining a constant hot end temperature, we have estimated the heat supplied to the device as ~ 4.37 W for T_h ~ 500 ºC and ΔT of ~ 445 K. With this, TE conversion efficiency, η, of single-leg GeBiInTe TE generator is calculated from the ratio of electrical output power (P_W) to the input heat flowing (Q_H) across the thermoelement. Considering the uncertainty in output electrical power measurement and input heat flow measurement the combined uncertainty in the efficiency measurement is around 10.2%.

3.2.12 Kelvin probe force microscopy (KPFM). The relative position of the Fermi level in Bi,In co-doped GeTe samples was probed by KPFM at room temperature using Bruker's dimension icon atomic force microscopy (AFM) system. For this measurement, Pt-Ir coated Si cantilever (SCM-PIT-V2 from Bruker) with 25 nm radius was used.

3.3 Results & discussion

Samples of $Ge_{1-x-y}Bi_xIn_yTe$ (x = 0.06, y = 0.005, 0.01 and 0.02) were synthesized by vacuum sealed tube melting reaction and their structures are initially analyzed by powder X-ray diffraction (PXRD). Figure 3.1a shows the PXRD patterns of $Ge_{1-x-y}Bi_xIn_yTe$ and all the obtained patterns could be matched with the rhombohedral structure (α-GeTe, space group *R3m*). Low intensity peaks corresponding to excess Ge were identified in all the patterns which often arise due to the presence of thermodynamically driven cation (Ge) vacancies in GeTe, agreeing with the previous reports.[9,11,13] The high intensity peak at 2θ = 29.88˚ in pristine GeTe gradually shifts towards lower angle with increasing Bi and In concentration due to the replacement of smaller Ge (1.25Å) atoms by larger Bi (1.43Å) and In (1.56Å).

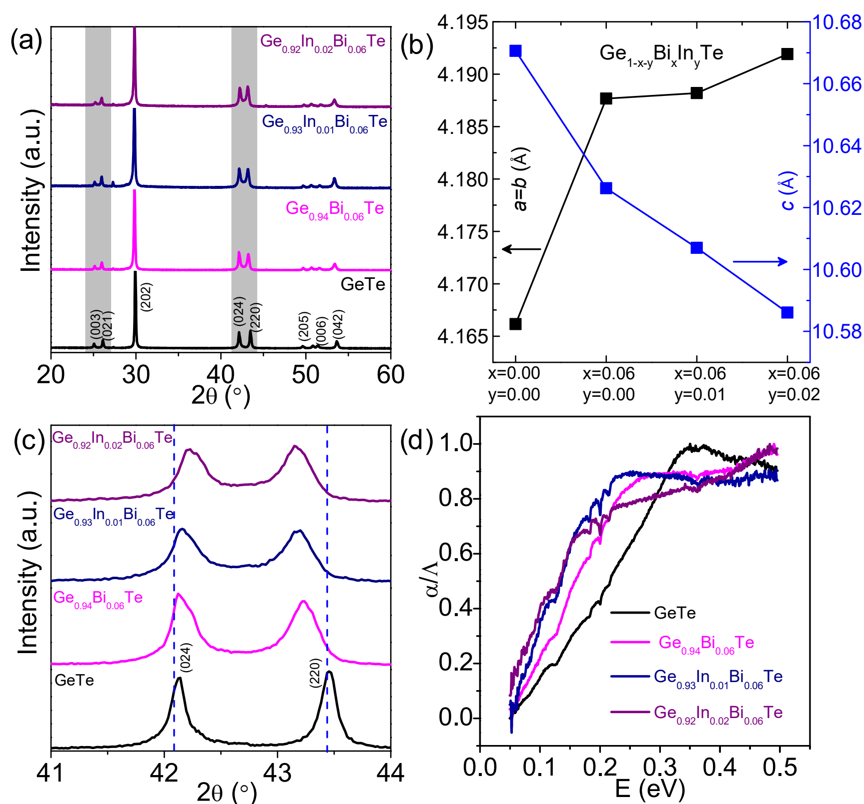

Figure 3.1. *(a) Powder XRD patterns of $Ge_{1-x-y}Bi_xIn_yTe$ (x = 0.06; y = 0, 0.01 and 0.02) samples. (b) the lattice constants of $Ge_{1-x-y}Bi_xIn_yTe$ as a function of the composition. (c) Zoomed in version of PXRD pattern of Figure 3.1(a) in the angles (2Θ) between 40˚ and 45˚, indicating the evolution of (024) and (220) peaks with co-doping of In and Bi. (d) Electronic absorption spectra of $Ge_{1-x-y}Bi_xIn_yTe$ samples.*

Figure 3.1b shows the calculated lattice constants of $Ge_{1-x-y}Bi_xIn_yTe$. The lattice parameters of pristine GeTe are $a = b = 4.1664(2)$ Å, $c = 10.\ 6707(4)$ Å, whereas $Ge_{0.94}Bi_{0.06}Te$ exhibits the lattice constants of $a = b = 4.1876\ (8)$ Å, $c = 10.6262\ (5)$ Å indicating that addition of Bi increases *a* and *b* axes with the contraction along the *c*-axis, which conforms with the previous reports of Bi and Bi-Sb co-doped GeTe.[12,13] Moreover, the substitution of In in $Ge_{0.94}Bi_{0.06}Te$ further increases *a* and *b* axes and reduces *c* axis, as seen in Figure 3.1b. Figure 3.1c illustrates the zoomed in version of the double peaks present between the 2θ angles of 41° and 45° which further confirms the rhombohedral structure (*α*-GeTe) at room temperature. The double peaks from (024) and (220) planes get closer upon Bi and In co-doping in GeTe. This is a clear indication that co-doping of Bi and In in GeTe drives the system towards cubic (space group $Fm\bar{3}m$) structure by relaxing the structure along [111] direction.

Figure 3.1d presents the electronic absorption spectra of $Ge_{1-x-y}Bi_xIn_yTe$ samples as a function of energy (*E*). Pristine GeTe has a band gap of ~ 0.21 eV, which is consistent with the previous reports.[11–13] The addition of Bi notably reduces the band gap of GeTe from 0.21 eV to 0.12 eV and In doping further decreases the band gap to 0.08 eV. Due to the higher electronegativity ($\chi_{Te} = 2.10$ in Pauling scale), Te orbitals predominantly constitutes the valence band of GeTe, whereas Ge orbitals predominately contribute to the conduction band because of its lower electronegativity ($\chi_{Ge} = 2.01$). The reduction in band gap is mainly due to the formation of impurity states of Bi and In just below the conduction band because of their donor dopant nature and the slightly higher electronegativity of Bi (~ 2.02) than Ge. Electronic structure of Bi and In doped GeTe calculated from density functional theory (DFT) further confirms the formation of Bi and In induced states below the conduction band of GeTe which we have discussed later.

Figure 3.2 depicts the TEM micrographs of $Ge_{0.93}Bi_{0.06}In_{0.01}Te$ samples, investigated using an aberration corrected TEM. Figure 3.2a shows the low magnification TEM micrograph of $Ge_{0.93}Bi_{0.06}In_{0.01}Te$ exhibiting the ordered domain variants of bright and dark contrast in the <110> direction. Generally, the consecutive contrast difference with a regular interval arises due to the breakdown of Friedel symmetry in non-centrosymetric crystals. [9,11,13] Doping of Bi alone in GeTe does not introduce any such domain variants,[12] however, the addition of 1 mol% of In in $Ge_{0.94}Bi_{0.06}Te$ results in the

formation of ordered domain variants. A clear selected area electron diffraction (SAED) pattern is shown in inset Figure 3.2a, which confirms the highly crystalline nature. High resolution TEM micrograph of a region from Figure 3.2a is shown in Figure 3.2b, which depicts the lattice spacing of ~ 0.3 nm that corresponds to the (202) plane in rhombohedral GeTe. The presence of reflection twins along <110> direction with distinguishable ordered domains variants in the form of herringbone structure is observed in $Ge_{0.93}Bi_{0.06}In_{0.01}Te$ (see Figure 3.2c). The corresponding SAED pattern (Figure 3.2d) along the zone axis of <110> exhibits spot splitting, which further confirms the existence of twins. These domain variants along with solid solution point defects would be expected to scatter large amounts of mid-wavelength phonons and thereby reduce the κ_{lat} (discussed later).

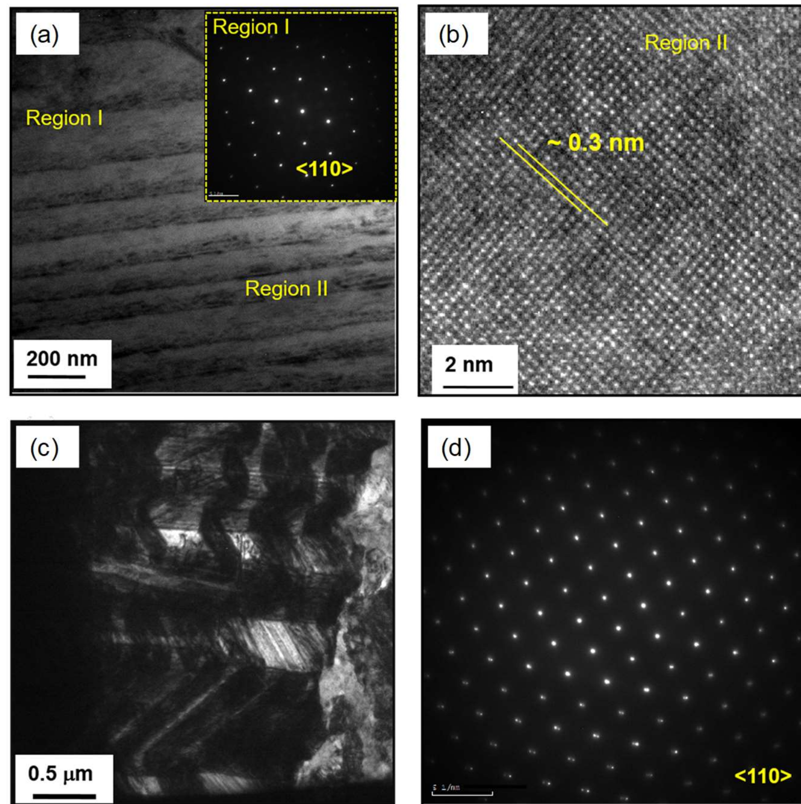

Figure 3.2. *(a) Low magnification TEM micrograph of $Ge_{0.93}Bi_{0.06}In_{0.01}Te$ with ordered domain variants of dark and bight contrast difference. Inset of (a) shows the corresponding SAED, indicating high quality single crystalline nature. (b) HRTEM micrograph of $Ge_{0.93}Bi_{0.06}In_{0.01}Te$ depicts an interplanar spacing of 0.3 nm corresponding to (202) plane of α-GeTe (R3m). (c) The existence of reflection twins with herringbone structure along <110> zone axis and (d) SAED pattern with spot splitting confirms the presence of twins.*

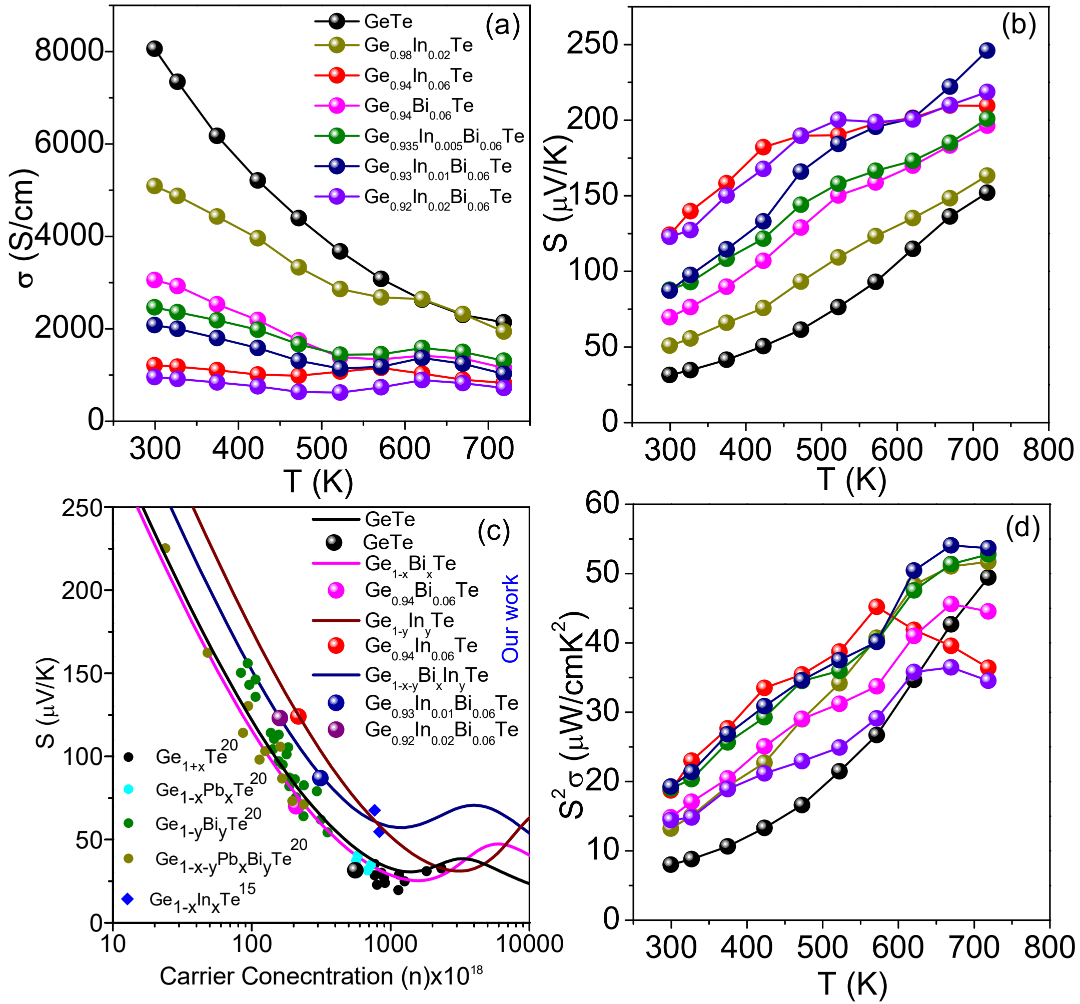

Figure 3.3.*Temperature-dependent (a) electrical conductivity (σ) and (b) Seebeck coefficient (S) of $Ge_{1-x-y}Bi_xIn_yTe$ samples. (c) Calculated Pisarenko plots considering two valance band model (solid lines) and the experimental S vs. n data points of the In and Bi co-doped GeTe compared with previously reported S vs. n data of different GeTe based samples.*[15,20] *(d) Temperature-dependent power factor ($S^2\sigma$) of $Ge_{1-x-y}Bi_xIn_yTe$ samples.*

The temperature dependence of electrical conductivity, σ, of $Ge_{1-x-y}Bi_xIn_yTe$ (x = 0.06, y = 0.005, 0.01 and 0.02) is presented in Figure 3.3a. The σ of all the samples decreases with increasing temperature, indicating the degenerate semiconductor behaviour. At 300 K, pristine GeTe shows the σ value of 8067 S/cm, which reduces to 2158 S/cm at 708 K. Above 675 K, σ starts increasing due to the second order structural transition (*R3m* → $Fm\bar{3}m$). Co-doping of In and Bi in GeTe drastically reduces the σ values throughout the measured temperature range due to the suppression of Ge vacancies and the donor dopant

nature of In^{3+} and Bi^{3+} at Ge^{2+} sites, which decreases the hole density by offering excess electrons. In particular, the room temperature σ value of ~ 8067 S/cm in GeTe decreases to ~ 970 S/cm in $Ge_{0.92}Bi_{0.06}In_{0.02}Te$. The substitution of Bi and In in GeTe gradually decreases the structural transition temperature from 675 K in GeTe to 525 K in $Ge_{0.92}Bi_{0.06}In_{0.02}Te$ which is evident from the change in slope near the phase transition temperature in σ vs. T data (Figure 3.3a).

To examine the reduction in σ values in the Bi and In co-doped GeTe, room temperature Hall measurements were performed for all the samples of $Ge_{1-x-y}Bi_xIn_yTe$. *p*-type carrier density (*n*) of undoped GeTe is 5.87 x 10^{20} cm^{-3}, which reduces to 2.1 x 10^{20} cm^{-3}, 2.17 x10^{20} cm^{-3}, 3.13 x 10^{20} cm^{-3} and 1.59 x 10^{20} cm^{-3} in $Ge_{0.94}Bi_{0.06}Te$, $Ge_{0.94}In_{0.06}Te$, $Ge_{0.93}Bi_{0.06}In_{0.01}Te$ and $Ge_{0.92}Bi_{0.06}In_{0.02}Te$, respectively (Table 3.1). The suppression of *p*-type carrier density is due to the aliovalent dopants of In^{3+} and Bi^{3+} at Ge^{2+} site in GeTe as they provide excess electron to the system. Further, the estimated carrier mobility (μ) of different $Ge_{1-x-y}BixIn_yTe$ samples (Table 3.1) shows that while Bi doped GeTe samples retains the high mobility, while In doped and Bi,In co-doped samples have significantly lower mobility than that of the pristine GeTe. In doping in GeTe is known to create resonance level near the Fermi energy. The observed reduced mobility of the present In doped samples corroborates with such resonant scattering scenario of charge carriers.[15]

Table 3.1. *Variation of carrier concentration, electrical conductivity and carrier mobility with In and Bi doping in GeTe.*

Composition	**Carrier Concentration (n) x $10^{20}/cm^3$**	**Electrical conductivity (σ) in S/cm**	**Carrier mobility (μ) in cm^2/Vs**
GeTe	5.87	8062	85.7
$Ge_{0.94}In_{0.06}Te$	2.17	1212	34.9
$Ge_{0.94}Bi_{0.06}Te$	2.1	3053	91.1
$Ge_{0.93}In_{0.01}Bi_{0.06}Te$	3.13	2081	41.5
$Ge_{0.92}In_{0.02}Bi_{0.06}Te$	1.59	955	37.5

Temperature dependence of Seebeck coefficient, *S*, of $Ge_{1-x-y}Bi_xIn_yTe$ is presented in Figure 3.3b. The *S* values of all the measured samples are of positive sign which implies that holes are the majority carries in $Ge_{1-x-y}Bi_xIn_yTe$, supporting the Hall coefficient data. The *S* values of all the samples increase with rise in temperature in the measured temperature range. Typically, the *S* value of pristine GeTe is ~ 34 μV/K at 300 K, which substantially increases to ~ 153 μV/K at 720 K. The inverse relation of *S* and *n* leads to increase in *S* values as doping of In and Bi in GeTe leads to significant suppression of *p*-type carrier density. In particular, doping of 6 mol % Bi in GeTe increases *S* value from 32 μV/K in pristine GeTe to ~ 70 μV/K at 300 K, whereas 6 mol% of In doping shows drastic enhancement in *S* value to 125 μV/K which is about 290% improvement in *S* value than that of pristine GeTe. This large enhancement in *S* upon In doping is associated with distortion of density of states (DOS) of GeTe due to the formation of resonant states close to Fermi level, E_F, and is discussed in a later section.[15] Moreover, it is clearly seen that increase in In concentration in $Ge_{0.94}Bi_{0.06}Te$ substantially enhances the S values. Typically, the S value of $Ge_{0.94}Bi_{0.06}Te$ is ~ 70 μV/K at 300 K which increases to ~ 86 μV/K, ~ 89 μV/K and ~ 122 μV/K in $Ge_{0.935}Bi_{0.06}In_{0.005}Te$, $Ge_{0.93}Bi_{0.06}In_{0.01}Te$, $Ge_{0.92}Bi_{0.06}In_{0.02}Te$, respectively. The obtained maximum *S* value is ~ 246 μV/K at 720 K in the $Ge_{0.93}Bi_{0.06}In_{0.01}Te$ sample.

Table 3.2. *Variation of band gap (E_g), energy difference between the heavy and light hole valence bands (Δ) and effective mass (m*) with In and Bi doping in GeTe.*

Composition	E_g (eV)	Δ (eV)	m_{hh}*	m_{lh}*
GeTe	0.21	0.23	1.3 m_0	0.24 m_0
$Ge_{0.94}In_{0.06}Te$	0.11	0.23	2.4 m_0	0.24 m_0
$Ge_{0.94}Bi_{0.06}Te$	0.12	0.23	1.3 m_0	0.24 m_0
$Ge_{0.93}In_{0.01}Bi_{0.06}Te$	0.09	0.16	1.9 m_0	0.24 m_0

Table 3.3. *Variation of band gap (E_g), work function, carrier concentration with In and Bi doping in GeTe.*

Composition	**Work function (eV)**	**Carrier Concentration (n) x $10^{20}/cm^3$**
$Ge_{0.93}In_{0.01}Bi_{0.06}Te$	4.65	3.13
$Ge_{0.92}In_{0.02}Bi_{0.06}Te$	4.59	1.59

To understand the carrier concentration dependent Seebeck coefficient of individual and Bi and In co-doped GeTe, the experimental room temperature *S* values were compared with calculated Pisarenko plot (*S* vs. *n*) considering two valance band model[15,31,40] (Figure 3.3c and Table 3.2). In the two valance band model, the total Seebeck coefficient has the contribution from both the heavy hole valance band (S_{hh}) and light hole valance band (S_{lh}). The heavy hole valance band is considered as a non-parabolic with a non-parabolicity factor k_BT/E_g (E_g is the band gap), while the light hole valance band far below the Fermi level is considered as parabolic. The values of acoustic deformation potentials are taken from the literatures.[10] The calculated Pisarenko plot for pristine GeTe matches well with the previously reported data as well as with the present data (Figure 3.3c). At room temperature, the contribution of S_{lh} to the total Seebeck coefficient is, however, negligible in pristine GeTe owing to the large energy gap between the heavy and light hole valance band (Δ = 0.23 eV).[9,10] From the Pisarenko analysis, we find that although Bi doped GeTe has higher room temperature Seebeck coefficient, the enhancement is entirely due to the decrease in carrier concentration caused by Bi^{3+} doping in place of Ge^{2+}. The large enhancement in the Seebeck coefficient in the In doped GeTe samples, on the other hand, can only be accounted by drastic increase in the effective mass of the heavy hole valance band (m_{hh} = 2.4 m_0). Such drastic increase in effective mass of the heavy hole valance band upon In doping indicates distortion in the electronic density of states by the formation of resonance level close to the Fermi energy.[15] While the band gap, E_g, decrease in both cases of individual In and Bi doping, Δ remains unaltered. In case of In and Bi co-doping, the Pisarenko analysis of the room temperature Seebeck coefficient exhibits that along with increase in effective mass of the heavy hole valance band (m_{hh} = 1.9 m_0), gap between two valence band (Δ) also decreases to 0.16 eV (Table 3.2). The decrease in Δ indicates the

presence of valance band convergence effect between the heavy and light hole valance band at room temperature in Bi and In coped GeTe.

We used DFT calculations to determine the electronic structures of doped and undoped GeTe compositions for further understanding the experimentally observed thermoelectric transport behaviors. Electronic structure of valence and conduction bands of rocksalt GeTe is similar to that of SnTe and PbTe, with 4 extrema at L point and 12 extrema along Σ line in the Brillion zone (BZ). GeTe undergoes a cubic to rhombohedral phase transition at ~ 700 K, breaking the inversion symmetry in the low temperature rhombohedral phase. Since the rhombohedral phase of GeTe is nearly cubic with minor lattice distortions and the cubic phase is relevant to the thermoelectric performance at high temperatures, we analyze the electronic structure of doped and undoped GeTe in the cubic phase, similar to the earlier works.[9,13] Due to the Brillouin zone folding associated with the ($\sqrt{2} \times \sqrt{2} \times 2$) supercell used in the calculations here, the principal valence band maximum (VBM) occurring normally at L point of the cubic cell, occurs at Γ point, and the conduction band minimum (CBM) also folds back to Γ point. The heavy hole valence band maximum occurring along Σ line of the cubic BZ, appears at Z + δ along Z→R direction in the Brillouin zone of ($\sqrt{2} \times \sqrt{2} \times 2$) tetragonal supercell.[9] Electronic structure of $Ge_{16}Te_{16}$ (Figure 3.4a) exhibits a band gap of ~ 0.19 eV at Γ point, which is in good agreement with the previous electronic structure calculations.[9,13] The energy difference between the light and heavy hole valence bands, Δ ~ 0.20 eV. Although, in the DFT calculated electronic structure, the Fermi level resides in the middle of the band gap between VBM and CBM in pristine GeTe, large amount of Ge vacancies in the experimentally synthesized GeTe samples cause the Fermi level to move deep inside the valance band resulting its *p*-type thermoelectric transport behavior.[10,15]

In pristine GeTe, the Ge-*p* orbitals form the CBM, while the Te-*p* orbitals dominate the VBM. In 6.25 mol% Bi substituted GeTe, a new impurity band associated with the Bi-*p* orbital forms in the energy gap between VBM and CBM (Figure 3.4b). The more electronegative character of Bi compared to Ge and the donor dopant nature of Bi results in the shift of CBM downward in energy. This is reflected in the lower band gap in Bi doped GeTe compositions. The energy difference between the light hole and heavy hole valence band, however, remains essentially unchanged ~ 0.201 eV in Bi doped GeTe.

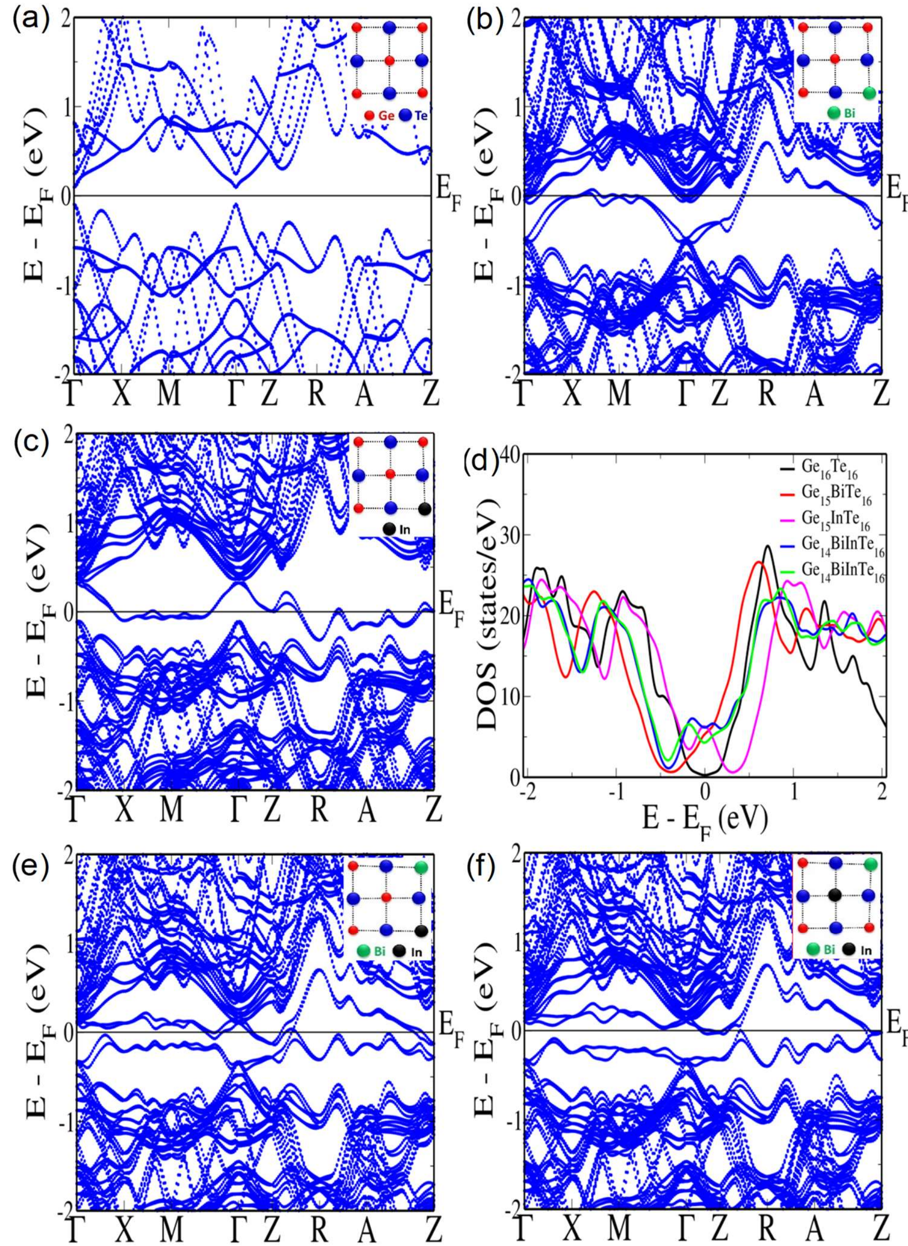

Figure 3.4. *Electronic structures of (a)* $Ge_{16}Te_{16}$*, (b)* $Ge_{15}BiTe_{16}$ *and (c)* $Ge_{15}InTe_{16}$*.(d) Density of electronic states of pure GeTe and Bi-, In- and co-doped (Bi and In) GeTe samples. Solid blue line and green lines represent the cases where Bi and In atoms are far and close to each other, respectively. Electronic structures of (e)* $Ge_{14}BiInTe_{16}$ *(Bi and In atoms close to each other) and (f)* $Ge_{14}BiInTe_{16}$ *(Bi and In atoms far from each other).*

This observation further corroborates to the Pisarenko plot analysis of the room temperature Seebeck coefficient. Indium (In) substitution in GeTe also introduces impurity band in the energy gap between VBM and CBM similar to the Bi doping, however, the salient feature

of the electronic structure is very different. In case of In doping, the impurity band is much weakly dispersed near the Fermi energy, leading to the formation of resonance level close to the Fermi level, as seen in Figure 3.4c and d. The formation of resonance level with weakly dispersed band near the Fermi energy results in increased effective mass which is reflected in the increased room temperature Seebeck coefficient and further supports the increased effective mass of the heavy hole valance band obtained from the Pisarenko analysis. As reported in the earlier investigations,[15] we also found that the deep defect states of pristine GeTe move upward towards Fermi energy due to the hybridization of In-*p* orbital with the host.

DFT calculation of electronic structures for the individual doping of In and Bi in GeTe indicates their distinct roles: while Bi doping results in the formation of impurity bands close to the CBM, In doping causes the formation of resonance level close to the Fermi energy. Therefore, to understand the modulation of electronic structure in case of Bi and In co-doped GeTe, we considered various configurations of their co-doping. Here we have shown two particular interesting configurations: (i) one with Bi and In atoms close to each other (Figure 3.4f) and (ii) another with Bi and In atoms far from each other (Figure 3.4e). We find that two almost parallel bands forms in the gap between VBM and CBM and resides on the two sides of E_F. Interestingly, these bands mix with each other between Z and R points of the BZ and their interaction gives rise to multiple minima and maxima in both valence and conduction bands at closely spaced energies. Although the resonance level form in this co-doping case also, as can be seen from Figure 3.4d, the resonance level moves away from the Fermi energy and deeper towards the valance band. Consequently, the distortion in the electronic density of states decreases and this is further reflected in the Pisarenko analysis of the room temperature Seebeck coefficient which indicates the lower effective mass of the heavy hole valance band in case In and Bi co-doped GeTe compared to individual In doped GeTe. With increasing the Bi concentration in this Bi and In co-doped GeTe, the impurity bands hybridizes more strongly with the host, which further pushes the resonance level deeper inside the valance band. Surprisingly, we observed that co-doping of Bi and In results in decreasing energy difference between the heavy and light hole valance band to 0.10 eV compared to 0.20 eV in case of pristine GeTe. We have observed similar valance band convergence effect in the Pisarenko analysis of the room

temperature Seebeck coefficient in In and Bi co-doped GeTe. As can be seen from Figure 3.4, In impurity states hybridizes much more effectively with the host valance states in case of Bi and In co-doped GeTe compared to individual In doping, which results in the observed decrease in energy difference between heavy and light hole valance band. The increased interaction of In with the host valance states is also probed using Kelvin probe force microscopy (KPFM). With increasing In concentration in the In and Bi co-doped system, the increased interaction between the impurity and host decreases the *p*-type carrier concentration which is evident from the decreased work function as obtained from KPFM (Table 3.3).

Figure 3.3d presents the power factor, $S^2\sigma$, of $Ge_{1-x-y}Bi_xIn_yTe$ (x = 0.06, y = 0.005, 0.01 and 0.02) as a function of temperature, which exhibits that power factor increases with rise in temperature. Typically, undoped GeTe has the $S^2\sigma$ value of ~ 8.1 $\mu Wcm^{-1}K^{-2}$ at 300 K and it reaches to the maximum value of ~ 49.2 $\mu Wcm^{-1}K^{-2}$ at 720 K. Additionally, the 6 mol% of Bi doped GeTe sample shows the $S^2\sigma$ values of ~ 14.8 and ~ 45.4 $\mu Wcm^{-1}K^{-2}$ at 300 K and 675 K, respectively, whereas $S^2\sigma$ values of $Ge_{0.98}In_{0.02}Te$ are ~ 13.2 and ~ 51.6 $\mu Wcm^{-1}K^{-2}$ at 300 K and 675 K, respectively. Further, the addition of In in $Ge_{0.94}Bi_{0.06}Te$ substantially increases the values of $S^2\sigma$ in the measured temperature range of 300 - 725 K. In particular, the $S^2\sigma$ value of $Ge_{0.93}Bi_{0.06}In_{0.01}Te$ is ~ 19.3 $\mu Wcm^{-1}K^{-2}$ at 300 K, which increases with temperature and reaches to the maximum value of ~ 53.7 $\mu Wcm^{-1}K^{-2}$ at 720 K. This large enhancement in $S^2\sigma$ value is due to the formation of In induced resonant states and Bi driven suppression in *p*-type carrier concentration.

Temperature-dependent total thermal conductivity, κ_{total}, of $Ge_{1-x-y}Bi_xIn_yTe$ (x = 0.06, y = 0.005, 0.01 and 0.02) is shown in Figure 3.5c, which exhibits that κ_{total} substantially reduces with increase in temperature, as often seen in typical degenerate semiconducting solids. κ_{total} of pristine GeTe is ~ 8.3 W/mK at 300 K, which gradually reduces to the minimum value of ~ 3.4 W/mK at 673 K. Above 675 K, κ_{total} starts increasing due to Ge translation along <111> direction induced second order structural transition ($R3m \rightarrow Fm\bar{3}m$), which is also observed in σ vs. *T* data in Figure 3.3a. The addition of individual dopants of In and Bi in GeTe rapidly reduces κ_{total} to ~ 3.8 and ~ 2.28 W/mK at 300 K for the compositions of $Ge_{0.98}In_{0.02}Te$ and $Ge_{0.94}Bi_{0.06}Te$, respectively. In addition, co-doping of In and Bi in GeTe further decreases the κ_{total} to ~ 1.68 W/mK at 300 K which

moderately comes down with temperature and reaches the minimum value of ~ 1.55 W/mK at 500 K in the composition of $Ge_{0.92}In_{0.02}Bi_{0.06}Te$.

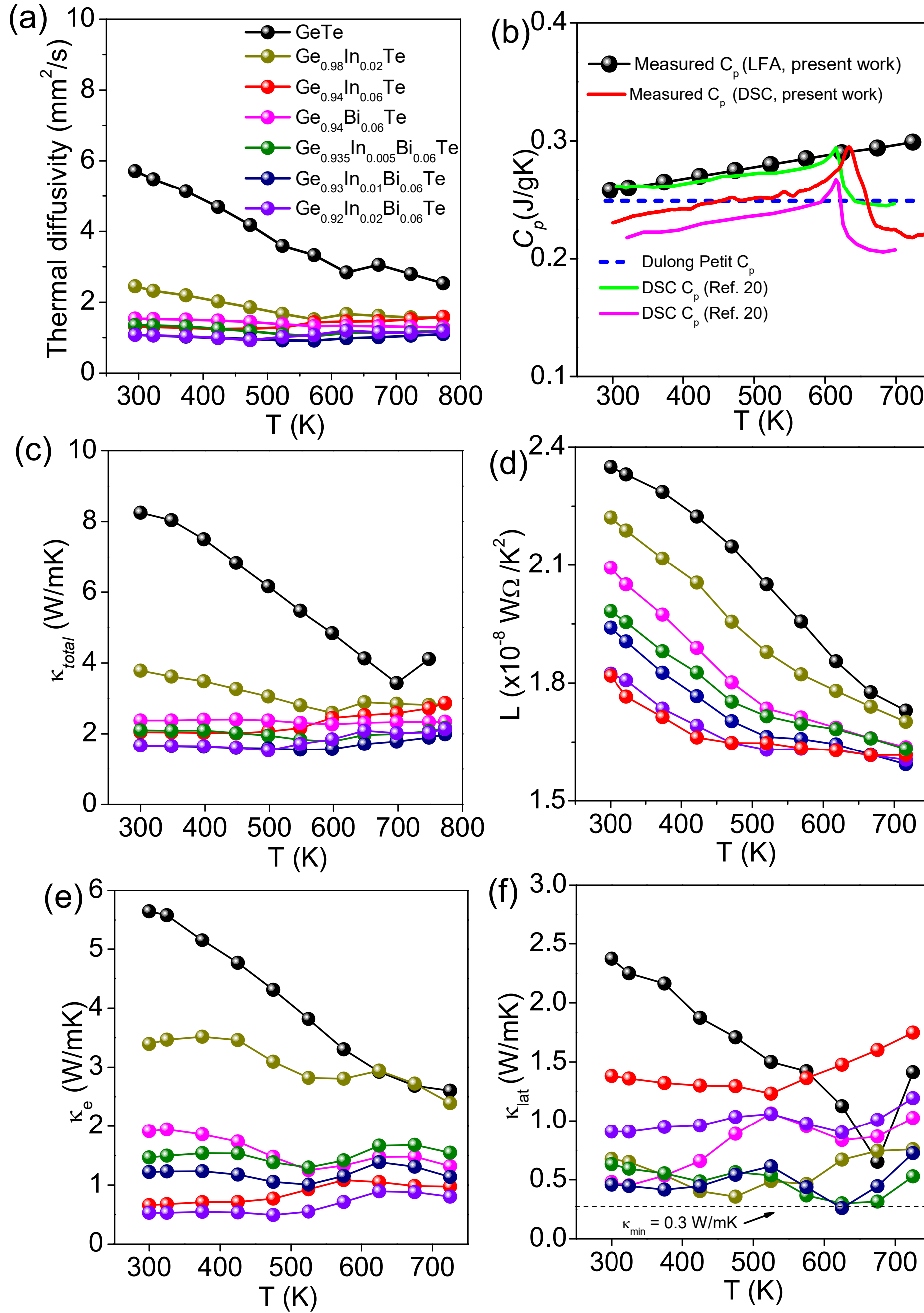

Figure 3.5. *The temperature-dependent (a) thermal diffusivity of $Ge_{1-x-y}Bi_xIn_yTe$ samples and (b) heat capacity (C_p) of GeTe. Temperature-dependent (c) total thermal conductivity (κ_{total}), (d) Lorenz number (L), (e) electronic thermal conductivity (κ_e) and (f) lattice thermal conductivity (κ_{lat}) of $Ge_{1-x-y}Bi_xIn_yTe$ samples.*

Figure 3.5e presents the electronic contribution to thermal conductivity, κ_e, of $Ge_{1-x-y}Bi_xIn_yTe$ (x = 0.06, y = 0.005, 0.01 and 0.02) as a function of temperature. κ_e is calculated form Wiedemann-Franz law, $\kappa_e = \sigma \cdot L \cdot T$, where L_0 is the Lorenz number. The temperature-dependent L is obtained by estimating the reduced chemical potential from temperature dependent Seebeck coefficient considering a single parabolic band model[9,11,13] (Figure 3.5d). The κ_e of GeTe is ~ 5.65 W/mK at 300 K which shows that *p*-type carriers have a dominant contribution to $\kappa_{total.}$ Co-doping of In and Bi in place of Ge in GeTe largely suppresses the Ge vacancies and reduces the hole density, thereby significantly decreases the κ_e values to ~ 0.55 W/mK at 300 K for the composition of $Ge_{0.92}In_{0.02}Bi_{0.06}Te$.

The κ_{lat} of $Ge_{1-x-y}Bi_xIn_yTe$ (x = 0.06, y = 0.005, 0.01 and 0.02) samples are estimated by subtracting the κ_e from κ_{total} and temperature dependent κ_{lat} is shown in Figure 3.5f. The κ_{lat} of GeTe is ~ 2.4 W/mK at 300 K which subsequently decreases with increasing temperature and reaches the minimum value of ~ 0.67 W/mK near the phase transition temperature (~ 675 K) and above 675 K, the κ_{lat} of GeTe starts increasing. This fact is mainly ascribed to the ferroelectric instability near phase transition temperature as it induces soft optical phonon modes which strongly scatter the heat carrying acoustic phonons. Addition of 6 mol% of Bi in GeTe decreases the κ_{lat} value to ~ 0.67 W/mK at 300 K, whereas 6 mol% of In doping results in κ_{lat} ~ 1.38 W/mK at 300 K. This indicates the effective role of Bi doping in reducing κ_{lat} of GeTe. Interestingly, $Ge_{0.93}In_{0.01}Bi_{0.06}Te$ has κ_{lat} ~ 0.27 W/mK at 625 K, which is very close to the theoretical κ_{min} (~ 0.3 W/mK) of GeTe.[16,17] This large reduction in κ_{lat} could be attributed to the strong phonon scattering by the collection of (i) solid solution point defects, (ii) domain variants, and (iii) twin boundaries with herringbone structures, which were observed in the TEM micrographs (Figure 3.2a and c).

Figure 3.6a illustrates the dimensionless figure of merit, *zT*, of $Ge_{1-x-y}Bi_xIn_yTe$ (x = 0.06, y = 0.005, 0.01 and 0.02) as a function of temperature. Pristine GeTe exhibits maximum *zT* of 0.9 at 675 K.[11] Further, the maximum *zT* of 1.31 and 1.38 at 725 K are achieved in the controlled compositions $Ge_{0.98}In_{0.02}Te$ and $Ge_{0.94}Bi_{0.06}Te$, respectively, consistent with the previous reports.[12,15] Interestingly, In and Bi co-doping in GeTe remarkably increases the *zT*. Specifically, the *zT* of $Ge_{0.93}In_{0.01}Bi_{0.06}Te$ reaches the maximum value of 2.1 at 723 K which is ~ 233% higher than that of the pristine GeTe.

High zT samples were re-measured and taken for cyclic measurement (heating and cooling cycle), which exhibits good heating-cooling reversibility and reproducibility (see Figure 3.6b).

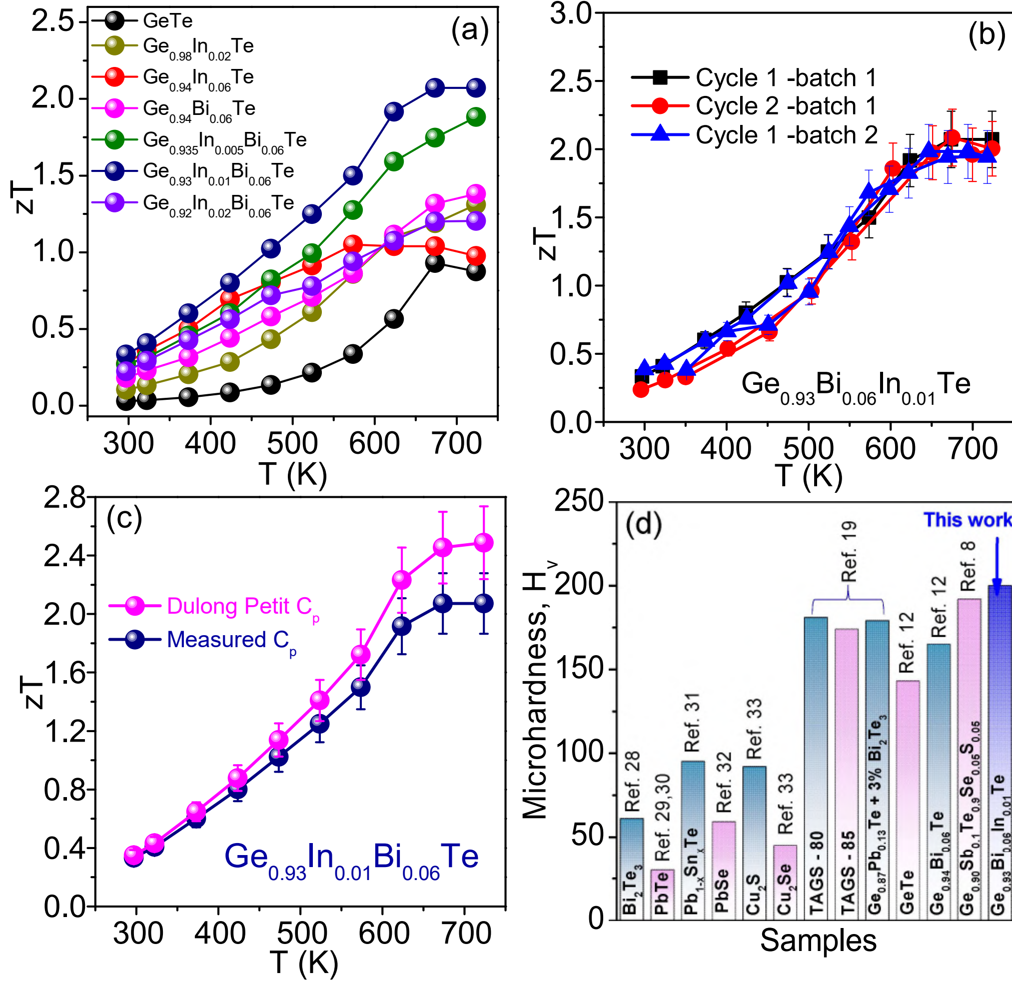

Figure 3.6. *(a) Temperature dependent thermoelectric figure of merit (zT) of* $Ge_{1-x-y}Bi_xIn_yTe$ *system. (b) The reversibility (heating-cooling cycles) and reproducibility (two different batches) of zT of* $Ge_{0.93}Bi_{0.06}In_{0.01}Te$ *as function of temperature (error bar ~ 10%). (c) Comparison of the temperature dependent zT of* $Ge_{0.93}Bi_{0.06}In_{0.01}Te$ *sample estimated based on measured* C_p *value (LFA-457) and using Dulong-Petit* C_p *value. (d) Histogram representing Vickers microhardness value of* $Ge_{0.93}In_{0.01}Bi_{0.06}Te$ *along with other state-of-the-art metal chalcogenides.*[8,12,19,28–33]

We would like to point out that if we calculate zT based on the thermal conductivity obtained using Dulong-Petit heat capacity (C_p, Figure 3.5b) value, the maximum zT in $Ge_{0.93}In_{0.01}Bi_{0.06}Te$ would be ~ 2.5 at 723 K (Figure 3.6c). Although in few recent reports

zT has been calculated based on the Dulong-Petit C_p value,[10,14,15,20,34] we believe it is better to use measured C_p for the estimation of thermal conductivity and *zT*, which will reduce the error in zT estimation. Thus, we have used maximum *zT* of 2.1 for further calculation of zT_{avg} and ZT_{eng} (see later). The composition of $Ge_{0.93}In_{0.01}Bi_{0.06}Te$ possess the zT_{avg} of ~ 1.3 which is significantly high as compared to the recently reported GeTe based materials, such as $Ge_{0.94}Bi_{0.06}Te$, $Ge_{0.9}Sb_{0.1}Te$, 3% Bi_2Te_3 added $Ge_{0.87}Pb_{0.13}Te$, TAGS80, TAGS85, $Ge_{0.98}In_{0.02}Te$, $Ge_{0.86}Sb_{0.04}Mn_{0.1}Te$ and so on.[9,11,12,15,17–19]

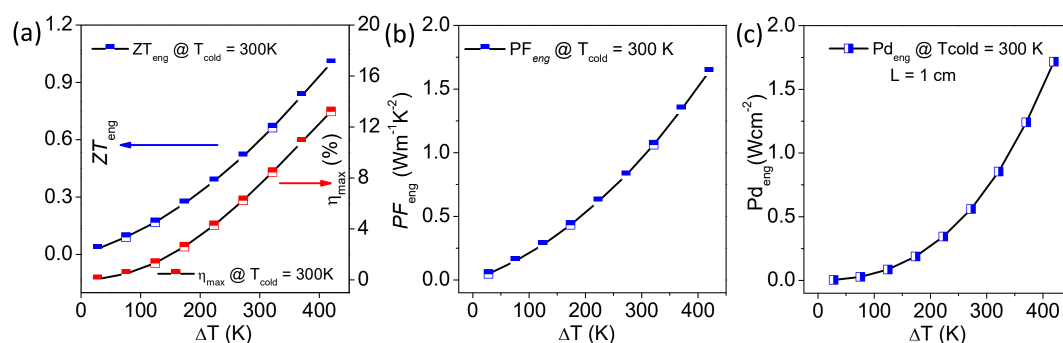

Figure 3.7. *(a) Calculated engineering figure of merit (ZT_{eng}) and efficiency (η_{max}) (b) power factor (PF_{eng}) and (c) output power density (P_d) of $Ge_{0.93}Bi_{0.06}In_{0.01}Te$ as function of temperature difference, respectively, with cold side temperature of 300 K.*

As the calculation of TE conversion efficiency (η) based on the materials figure of merit, *zT*, is not very reliable due to the major assumption of temperature-independence of *S*, *σ*, and κ_{total}, Kim *et al.*[25] have recently introduced the engineering figure of merit, ZT_{eng}, and the maximum efficiency, η (ZT_{eng}), based on the cumulative temperature-dependent properties which has been used here to reliably calculate the η with large temperature difference. Here, we have calculated the ZT_{eng} and η (ZT_{eng}) of $Ge_{0.93}In_{0.01}Bi_{0.06}Te$ as a function of temperature difference of the cold and hot sides (see Figure 3.7a), in which T_C is assumed as 300 K in the calculation. The maximum ZT_{eng} of $Ge_{0.93}In_{0.01}Bi_{0.06}Te$ is calculated to be ~ 1, whereas the highest η (ZT_{eng}) is determined as ~13.3 % for the temperature difference ΔT = 420 K (see Figure 3.7a).

Further, in order to check the mechanical stability of the high performance Bi and In co-doped GeTe, Vickers microhardness of $Ge_{0.93}Bi_{0.06}In_{0.01}Te$ is measured and it is found to be ~ 200 H_v (kgf/mm^2), which is comparatively higher than that of the un-doped GeTe

(H_v ~ 143). Reduced Ge-vacancies and enhanced atomic mixing in In and Bi co-doped GeTe inhibits the propagation of nano/micro-cracks and thus increases the mechanical stability of the material compared to pristine GeTe. A comparison of H_v values of different state-of-the-art metal chalcogenides and $Ge_{0.93}Bi_{0.06}In_{0.01}Te$ are presented in Figure 3.6d.[8,12,19,28–33]

Motivated by the calculated high η (ZT_{eng}) and enhanced microhardness of the Bi and In co-doped GeTe samples, we have successfully fabricated single-leg based TE devices with the high zT p-type $Ge_{0.93}In_{0.01}Bi_{0.06}Te$ sample. A schematic diagram of the $Ge_{0.93}In_{0.01}Bi_{0.06}Te$ based single-leg thermoelement with diffusion barrier (Fe) and contact layers (Ag) connected with load resistance is depicted in Figure 3.8a. The open circuit voltage (V_{OC}) of the device as a function of hot end temperature (T_h) is shown in Figure 3.8b. We find that the experimental V_{OC} of the device enhances with increasing T_h due to increasing temperature difference (ΔT) and enhanced S of the TE material at higher temperatures and the V_{OC} reaches the maximum value of 55 mV at 773 K. A plot of load voltage (V_L), load current (I_L) and generated output power (i.e. $P_W = I_L \times V_L$) as a function of T_h is shown in Figure 3.8c and d. P_W increases with increasing T_h and the maximum P_W of ~ 538 mW is obtained for the maximum T_h of 773K. To check the thermal stability of the device, the V_{OC} was continuously monitored for 16 h at T_h of 500 °C (Figure 3.8e) and it can be seen that we do not observe any noticeable change (a degradation of ~2.8% over a period of 16 hrs) in the V_{OC} when device is maintained for long time at the highest ΔT. we have estimated the heat supplied to the device as ~ 4.37 W for T_h ~ 500 ºC and ΔT of ~ 445 K from the correction of heat losses and actual power supplied to the heater for maintaining a constant hot end temperature (discussed in details in experimental section). With this, TE conversion efficiency, η, of single-leg $Ge_{0.93}In_{0.01}Bi_{0.06}Te$ TE generator is estimated by taking the ratio of experimental electrical output power (P_W) to estimated input heat flowing (Q_H) across the thermoelement and the maximum η of ~ 12.3% was obtained for the temperature difference of ΔT = 445 K (see Figure 3.7f).

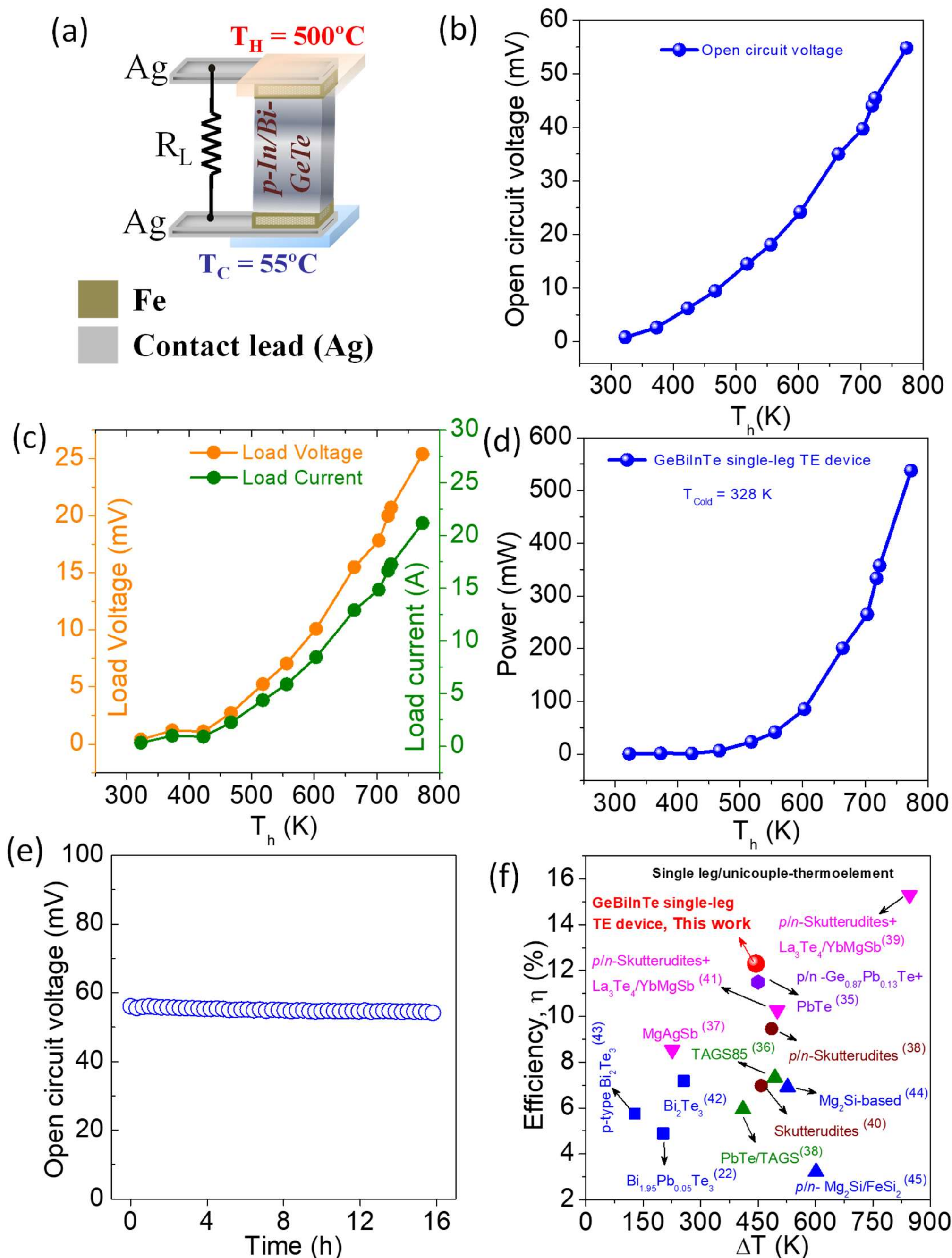

Figure 3.8. *(a) The schematic diagram of single-leg p-type $Ge_{0.93}Bi_{0.06}In_{0.01}Te$ based single-leg TE device. (b) Open circuit voltage (V_{OC}), (c) load voltage (V_L) and load current (I_L) and (d) output power (P_w) as a function of T_h of single-leg p-type $Ge_{0.93}Bi_{0.06}In_{0.01}Te$ based TE device. (e) The open circuit voltage of the device as a function of time representing the stability of the device.. (f) Comparison of the efficiency of the present single-leg based In and Bi co-doped GeTe thermoelement with other state-of-the-art single-leg/unicouple based thermoelectric device (non-segmented based).*[22,35,44,45,36–43]

We have compared this remarkable high efficiency of single leg based $Ge_{0.93}In_{0.01}Bi_{0.06}Te$ TE device with other reported single leg or unicouple based device (non-segmented), which shows that the present single leg $Ge_{0.93}In_{0.01}Bi_{0.06}Te$ TE device shows highest η in the ΔT range of 450 - 600 K (see Figure 3.7f).[22,35,44,45,36–43] Mention must be made that, at ΔT = 445 K, the measured values of output power density (P_d) and estimated efficiency (η) are ~ 1.1 W/ cm^2 and 12.3 %, respectively, which are comparatively lower than the respective simulated values (P_{deng} = 1.7 W/cm^2 and η (ZT_{eng}) = 13.3 % for ΔT = 420 K, Figure 3.8) which can be partly attributed to the added electrical resistance at different material interfaces in the fabricated device.[46–48]

3.4 Conclusions

In conclusion, we have demonstrated a very high zT of 2.1 at 723 K along with high zT_{avg} of ~ 1.3 in the temperature range of 300 - 723 K in In and Bi co-doped GeTe. Aliovalent Bi doping in GeTe effectively optimized the *p*-type carrier density and reduced the lattice thermal conductivity by the formation of extensive point defects and domain variants. On the other hand, In doping in GeTe leads to the formation of resonant states close to Fermi level which consequently distorts DOS and accounts for the huge enhancement in Seebeck coefficient. The co-doping of In and Bi in GeTe leads to distinct but complementary contributions to modulate the electronic structure and thermal transport of GeTe, and hence results in high thermoelectric performance. Moreover, the measured Vickers microhardness of $Ge_{0.93}In_{0.01}Bi_{0.06}Te$ of 200 H_v (kgf/mm^2) reflects the high mechanical stability of the material. The fabricated single-leg TE devices based on In and Bi co-doped GeTe shows high output power of ~ 538 mW and extremely high estimated thermoelectric efficiency of 12.3% for the temperature difference of 445 K.

3.5 References

(1) Biswas, K.; He, J.; Blum, I. D.; Wu, C.-I.; Hogan, T. P.; Seidman, D. N.; Dravid, V. P.; Kanatzidis, M. G. *Nature* **2012**, *489*, 414–418.
(2) Heremans, J. P.; Jovovic, V.; Toberer, E. S.; Saramat, A.; Kurosaki, K.; Charoenphakdee, A.; Yamanaka, S.; Snyder, G. J. *Science* **2008**, *321*, 554–557.
(3) Pei, Y.; Shi, X.; Lalonde, A.; Wang, H.; Chen, L.; Snyder, G. J. *Nature* **2011**, *473*, 66–69.
(4) Zhao, L. D.; Wu, H. J.; Hao, S. Q.; Wu, C. I.; Zhou, X. Y.; Biswas, K.; He, J. Q.;

Hogan, T. P.; Uher, C.; Wolverton, C.; Dravid, V. P.; Kanatzidis, M. G. *Energy Environ. Sci.* **2013**, *6*, 3346–3355.
(5) Perumal, S.; Roychowdhury, S.; Biswas, K. *J. Mater. Chem. C* **2016**, *4*, 7520–7536.
(6) Hong, M.; Zou, J.; Chen, Z. *Adv. Mater.* **2019**, *31*, 1807071.
(7) Roychowdhury, S.; Samanta, M.; Perumal, S.; Biswas, K. *Chem. Mater.* **2018**, *30*, 5799–5813.
(8) Samanta, M.; Biswas, K. *J. Am. Chem. Soc.* **2017**, *139*, 9382–9391.
(9) Wu, D.; Zhao, L.-D.; Hao, S.; Jiang, Q.; Zheng, F.; Doak, J. W.; Wu, H.; Chi, H.; Gelbstein, Y.; Uher, C.; Wolverton, C.; Kanatzidis, M.; He, J. *J. Am. Chem. Soc.* **2014**, *136*, 11412–11419.
(10) Li, J.; Chen, Z.; Zhang, X.; Sun, Y.; Yang, J.; Pei, Y. *NPG Asia Mater.* **2017**, *9*, e353.
(11) Perumal, S.; Roychowdhury, S.; Negi, D. S.; Datta, R.; Biswas, K. *Chem. Mater.* **2015**, *27*, 7171–7178.
(12) Perumal, S.; Roychowdhury, S.; Biswas, K. *Inorg. Chem. Front.* **2016**, *3*, 125–132.
(13) Perumal, S.; Bellare, P.; Shenoy, U. S.; Waghmare, U. V.; Biswas, K. *Chem. Mater.* **2017**, *29*, 10426–10435.
(14) Hong, M.; Chen, Z.-G.; Yang, L.; Zou, Y.-C.; Dargusch, M. S.; Wang, H.; Zou, J. *Adv. Mater.* **2018**, *30*, 1705942.
(15) Wu, L.; Li, X.; Wang, S.; Zhang, T.; Yang, J.; Zhang, W.; Chen, L.; Yang, J. *NPG Asia Mater.* **2017**, *9*, e343–e343.
(16) Samanta, M.; Roychowdhury, S.; Ghatak, J.; Perumal, S.; Biswas, K. *Chem. - A Eur. J.* **2017**, *23*, 7438–7443.
(17) Zheng, Z.; Su, X.; Deng, R.; Stoumpos, C.; Xie, H.; Liu, W.; Yan, Y.; Hao, S.; Uher, C.; Wolverton, C.; Kanatzidis, M. G.; Tang, X. *J. Am. Chem. Soc.* **2018**, *140*, 2673–2686.
(18) Liu, Z.; Sun, J.; Mao, J.; Zhu, H.; Ren, W.; Zhou, J.; Wang, Z.; Singh, D. J.; Sui, J.; Chu, C.-W.; Ren, Z. *Proc. Natl. Acad. Sci.* **2018**, *115*, 5332–5337.
(19) Davidow, J.; Gelbstein, Y. *J. Electron. Mater.* **2013**, *42*, 1542–1549.
(20) Li, J.; Zhang, X.; Chen, Z.; Lin, S.; Li, W.; Shen, J.; Witting, I. T.; Faghaninia, A.; Chen, Y.; Jain, A.; Chen, L.; Snyder, G. J.; Pei, Y. *Joule* **2018**, *2*, 976–987.
(21) Hazan, E.; Ben-Yehuda, O.; Madar, N.; Gelbstein, Y. *Adv. Energy Mater.* **2015**, *5*, 1500272.
(22) Bohra, A. K.; Bhatt, R.; Singh, A.; Bhattacharya, S.; Basu, R.; Meshram, K. N.; Sarkar, S. K.; Bhatt, P.; Patro, P. K.; Aswal, D. K.; Muthe, K. P.; Gadkari, S. C. *Mater. Des.* **2018**, *159*, 127–137.
(23) Giannozzi, P.; Baroni, S.; Bonini, N.; Calandra, M.; Car, R.; Cavazzoni, C.; Ceresoli, D.; Chiarotti, G. L.; Cococcioni, M.; Dabo, I.; Dal Corso, A.; De Gironcoli, S.; Fabris, S.; Fratesi, G.; Gebauer, R.; Gerstmann, U.; Gougoussis, C.; Kokalj, A.; Lazzeri, M.; Martin-Samos, L.; Marzari, N.; Mauri, F.; Mazzarello, R.; Paolini, S.; Pasquarello, A.; Paulatto, L.; Sbraccia, C.; Scandolo, S.; Sclauzero, G.; Seitsonen, A. P.; Smogunov, A.; Umari, P.; Wentzcovitch, R. M. *J. Phys. Condens. Matter* **2009**, *21*, 395502.
(24) Perdew, J. P.; Burke, K.; Ernzerhof, M. *Phys. Rev. Lett.* **1996**, *77*, 3865–3868.
(25) Kim, H. S.; Liu, W.; Chen, G.; Chu, C.-W.; Ren, Z. *Proc. Natl. Acad. Sci.* **2015**, *112*, 8205–8210.
(26) Gupta, R.; Weisheit, M.; Krebs, H. U.; Schaaf, P. *Phys. Rev. B - Condens. Matter*

Mater. Phys. **2003**, *67*, 1–7.
(27) Sugawara, A. *J. Appl. Phys.* **1968**, *39*, 5994–5997.
(28) Zhao, L. D.; Zhang, B. P.; Li, J. F.; Zhou, M.; Liu, W. S.; Liu, J. *J. Alloys Compd.* **2008**, *455*, 259–264.
(29) Gelbstein, Y.; Gotesman, G.; Lishzinker, Y.; Dashevsky, Z.; Dariel, M. P. *Scr. Mater.* **2008**, *58*, 251–254.
(30) Crocker, A. J.; Wilson, M. *J. Mater. Sci.* **1978**, *13*, 833–842.
(31) Cui, J. .; Qian, X.; Zhao, X. . *J. Alloys Compd.* **2003**, *358*, 228–234.
(32) Darrow, M. S.; White, W. B.; Roy, R. *J. Mater. Sci.* **1969**, *4*, 313–319.
(33) Zhao, L.; Wang, X.; Fei, F. Y.; Wang, J.; Cheng, Z.; Dou, S.; Wang, J.; Snyder, G. J. *J. Mater. Chem. A* **2015**, *3*, 9432–9437.
(34) Li, J.; Zhang, X.; Lin, S.; Chen, Z.; Pei, Y. *Chem. Mater.* **2017**, *29*, 605–611.
(35) Gelbstein, Y.; Davidow, J.; Girard, S. N.; Chung, D. Y.; Kanatzidis, M. *Adv. Energy Mater.* **2013**, *3*, 815–820.
(36) Singh, A.; Bhattacharya, S.; Thinaharan, C.; Aswal, D. K.; Gupta, S. K.; Yakhmi, J. V.; Bhanumurthy, K. *J. Phys. D. Appl. Phys.* **2009**, *42*, 015502.
(37) Kraemer, D.; Sui, J.; McEnaney, K.; Zhao, H.; Jie, Q.; Ren, Z. F.; Chen, G. *Energy Environ. Sci.* **2015**, *8*, 1299–1308.
(38) Muto, A.; Yang, J.; Poudel, B.; Ren, Z.; Chen, G. *Adv. Energy Mater.* **2013**, *3*, 245–251.
(39) T. Caillat, S. Firdosy, B. C- Y. Li, C. –K. Huang, B. Cheng, J. Paik, J. Chase, T. Arakelian, L. Lara, and J.-P. F. *Nucl. Emerg. Technol. Sp.* **2012**, 3077.
(40) Salvador, J. R.; Cho, J. Y.; Ye, Z.; Moczygemba, J. E.; Thompson, A. J.; Sharp, J. W.; Koenig, J. D.; Maloney, R.; Thompson, T.; Sakamoto, J.; Wang, H.; Wereszczak, A. A. *Phys. Chem. Chem. Phys.* **2014**, *16*, 12510–12520.
(41) Caillat, T.; Fleurial, J.-P.; Snyder, G. J.; Borshchevsky, A. In *Proceedings ICT2001. 20 International Conference on Thermoelectrics (Cat. No.01TH8589)*; IEEE, 2001, 282–285.
(42) Anatychuk, L. I.; Vikhor, L. N.; Strutynska, L. T.; Termena, I. S. *J. Electron. Mater.* **2011**, *40*, 957–961.
(43) Liu, W.; Jie, Q.; Kim, H. S.; Ren, Z. *Acta Mater.* **2015**, *87*, 357–376.
(44) Aoyama, I.; Kaibe, H.; Rauscher, L.; Kanda, T.; Mukoujima, M.; Sano, S.; Tsuji, T. *Jpn. J. Appl. Phys.* **2005**, *44*, 4275–4281.
(45) GroB, E.; Riffel, M. *J. Mater. Res.* **1995**, *10*, 34–40.
(46) Hu, X.; Jood, P.; Ohta, M.; Kunii, M.; Nagase, K.; Nishiate, H.; Kanatzidis, M. G.; Yamamoto, A. *Energy Environ. Sci.* **2016**, *9*, 517–529.
(47) Chetty, R.; Kikuchi, Y.; Bouyrie, Y.; Jood, P.; Yamamoto, A.; Suekuni, K.; Ohta, M. *J. Mater. Chem. C* **2019**, *7*, 5184–5192.
(48) Kim, H. S.; Ren, Z. *Energy Environ. Sci.* **2017**, *10*, 69–85.

Chapter 4

Realization of High Thermoelectric Performance in GeTe- x% BiSe: Synergistic Effect of Carrier Concentration Optimization and Low Thermal Conductivity

Chapter 4

Realization of High Thermoelectric Performance in GeTe-x% BiSe: Synergistic Effect of Carrier Concentration Optimization and Low Thermal Conductivity†

Summary

Thermoelectric (TE) performance of GeTe is driven by its thermodynamically stable Ge-vacancies which make the system highly p-type in nature. Optimization of carrier concentration of the GeTe paves way to achieve high TE performance. Herein, we report high zT of ~ 1.7 at 720 K in GeTe, enabled by alloying with BiSe, an n-type system with intrinsically ultralow lattice thermal conductivity (κ_{lat}). Detailed structure-property analysis reveals several roles of BiSe in optimizing TE property of GeTe: (a) Occupation of Bi^{+3} in Ge^{+2} positions increases Ge-precipitates with size distribution from 10 nm to 1µm; (b) Extensive point defects aroused by Ge/Bi and Te/Se disorders as well as presence of Ge-precipitates cause significant reduction in κ_{lat} of the system; and (c) Donor dopant nature of Bi optimizes carrier concentration of the system enhancing the Seebeck coefficient. Further optimization of TE properties of GeTe-4% BiSe, by Ge self-compensation and Pb doing, results in record high zT of ~ 2.2 in $Ge_{0.98}Pb_{0.05}Te$-4% BiSe at 652 K. Fabricated single leg thermoelement based on $Ge_{0.98}Pb_{0.05}Te$-4% BiSe shows promising output power of ~ 170 mW for temperature difference of 475 K, imposing great technological importance of the material.

---

†*Manuscript under preparation.*

4.1 Introduction

GeTe is rich with naturally formed Ge-vacancies which drives the system to be intrinsically off-stoichiometric along with Ge precipitations in the matrix.[1–4] These thermodynamically favorable Ge vacancies makes pristine GeTe to be highly *p*-type with a very high carrier concentration of $\sim 10^{21}$ cm^{-3} . The high concentration of Ge vacancies results in high electrical and thermal conductivity and low Seebeck coefficient in GeTe, which limits its thermoelectric performance and hence needed to be optimized. Carrier concentration optimization in GeTe is generally performed via aliovalent cation doping.[5–13] Bismuth (Bi) has been established as effective dopant for IV-VI semiconductor family of chalcogenides for carrier concentration optimizations and reducing κ_{lat} of the system. Substitution of Bi^{+3} in place of M^{+2} ions in IV-VI facilitates to attain desired carrier concentration. Bi doping in PbTe/PbSe/SnSe makes the system *n*-type with high thermoelectric performance, facilitated by donor dopant nature of Bi.[14–16] On the other hand, Bi doping in highly *p*-type system such as GeTe,[7,17] SnTe [18] simultaneously optimizes the carrier concentration and reduces the κ_{lat} of the system by creating Bi-based nanostructures.[7,19] Interestingly, recently BiSe, a weak topological insulator, has been reported to exhibit ultralow κ_{lat} and high *n*-type thermoelectric performance.[20] Hence, we thought it would be interesting to unveil the role of BiSe alloying on thermoelectric properties of GeTe.

In this work, we report high thermoelectric performance (zT of ~ 1.7) in GeTe facilitated by alloying with BiSe, an *n*-type system with intrinsically ultralow κ_{lat}. Detailed structure-property analysis reveals role of BiSe in optimizing TE property of GeTe. Addition of BiSe in GeTe, leads to increase in Ge precipitates and enhanced disorder in the system. Detailed microscopic analysis reveals presence of Ge-precipitates of various sizes ranging from nano-meter to micro-meter. These Ge-nanoprecipiates and extensive point defects aroused by Ge/Bi and Te/Se disorders provide an effective path for phonon scattering centers and results in ultra-low κ_{lat} of ~ 0.23 W/mK in GeTe + 4% BiSe at 500 K. On the other hand, substitution of Bi^{+3} in place of Ge^{+2} leads to carrier concentration optimization which increases the Seebeck coefficient of the System. Further optimization of TE properties of GeTe-4% BiSe, by self-compensation of Ge and Pb doing, results in zT of ~ 2.2 in $Ge_{0.98}Pb_{0.05}Te$-4% BiSe at 652 K. Fabricated single leg thermoelement based on

$Ge_{0.98}Pb_{0.05}Te$-4% BiSe shows promising output power of ~ 170 mW for temperature difference of 475 K, imposing great technological importance of the material.

4.2 Methods

4.2.1 Reagents. Germanium (Strategy Elements, 99.999%), tellurium (Strategy Elements, 99.99 %), bismuth (SRL chemicals, 99.99 %), selenium (Alfa Aesar 99.9999%) and lead (Alfa Aesar, 99.999 %) were used for synthesis of all the compounds.

4.2.2 Synthesis. High quality polycrystalline ingots were synthesized by weighing stoichiometric amounts of high purity starting elements Ge, Te, Bi, Pb and Se in quartz tubes which were then sealed under vacuum (10^{-6} Torr). The quartz tubes were slowly heated to 1223 K and soaked at 1223 K for 8 hours, followed by slow cooling to room temperature over 10 h. To ensure phase homogeneity, the quartz tubes were shaken for several times during soaking at high temperature. The obtained ingots were crushed into fine powders which then consolidated into cylinder by Spark plasma Sintering (Dr. Sinter Lab, 211-LX) at 773 K and 50 MPa for 5 minutes.

4.2.3 Powder X-ray Diffraction (PXRD). Room temperature PXRD patterns of all synthesized samples were recorded using Cu Kα (λ = 1.5406 Å) radiation source in a Bruker D8 diffractometer. For Rietveld refinement of the samples, we have collected the PXRD data using Panalytical XRD machine.

4.2.4 Band Gap Measurement. Optical band gap of GeTe-x% BiSe (x= 0-6) were measured using FT-IR Bruker IFS 66V/S spectrometer in the wave number range 4000-400 cm^{-1}. Absorption (α/Λ) data were derived from measured reflectance data of GeTe-x% BiSe (x= 0-6) using Kubelka-Munk equation: $\alpha/\Lambda = (1-R)^2/(2R)$, where α, Λ and R are the absorption coefficient, scattering coefficient, and reflectance respectively.

4.2.5 Transmission Electron Microscopy (TEM). TEM micrographs of GeTe-4% BiSe were collected using an aberration corrected FEI TITAN cubed 80–300 kV transmission electron microscopes, operating at 300 kV.

4.2.6 Field Emission Scanning Electron Microscopy (FESEM). FESEM experiments of GeTe-4% BiSe were performed using NOVA NANO SEM 600 (FEI, Germany) equipment operated at 15 KV.

4.2.7 Electrical Transport. Temperature variation of electrical conductivity (σ) and Seebeck coefficient (*S*) of GeTe-x% BiSe (x= 0-8) were measured simultaneously using a ULVAC-RIKO ZEM-3 instrument under helium atmosphere in the 300-723 K temperature range. The typical dimension of sample used for this measurement was ~2×2×8 mm^3. We observed that heating and cooling cycles give reversible electrical properties in all the synthesized samples.

4.2.8 Hall Measurement. Room temperature hall measurements of GeTe-x% BiSe (x= 0-8) were carried out at in a setup developed by Excel instrument with a maximum magnetic field of 0.55 T and a fixed applied dc-current of 100 mA.

4.2.9 Thermal Conductivity. Thermal diffusivity, D, of GeTe-x% BiSe (x= 0-8) were measured by laser flash diffusivity method using a Netzsch LFA-457 in the 300−750 K temperature range under N_2 atmosphere. Coins with typical dimension of ~10 mm diameter and ~2 mm thickness were used for the measurements. Coins were coated with a thin layer of graphite to avoid errors coming from thermal emissivity of the materials. Temperature dependent heat capacity, C_p, of GeTe was determined by comparing with a standard sample (pyroceram) in LFA-457.[21] The total thermal conductivity, κ_{tot}, was then estimated using the formula $\kappa_{tot} = D\rho C_p$, where ρ is the density of the samples which were found to be ~ 97% of theoretical density in the entire GeTe-x% BiSe (x= 0-8) compositions.

4.2.10 Calculation for zT_{eng} and η_{eng}. The engineering figure of merit, zT_{eng} and corresponding TE conversion efficiency, η_{eng} of the thermoelectric material which are calculated based on cumulative temperature-dependent TE properties, is helpful for exactly determining the TE efficiency for a given material at a large temperature difference between the cold and hot ends of the TE legs.[22] The expressions for zT_{eng} and $\eta(zT_{eng})$ are as follows

$$(zT)_{eng} = z_{eng}\Delta T = \frac{\left(\int_{T_C}^{T_H} S(T)dT\right)^2}{\int_{T_C}^{T_H} \rho(T)dT \int_{T_C}^{T_H} \kappa(T)dT}\Delta T = \frac{(PF)_{eng}}{\int_{T_C}^{T_H} \kappa(T)dT} \qquad (4.1)$$

$$\eta_{max} = \eta_C \cdot \frac{\sqrt{1 + (ZT)_{eng}(\alpha/\eta_C - 1/2)} - 1}{\alpha\sqrt{1 + (ZT)_{eng}(\alpha/\eta_C - 1/2)} - \eta_C} \qquad (4.2)$$

Where $\rho(T)$, $S(T)$,$\kappa(T)$, η_C, and α represent the resistivity, Seebeck coefficient, total thermal conductivity, Carnot efficiency and a dimensionless intensity factor of Thomson coefficient, respectively. The engineering power density (P_d) was calculated using the following expression,

$$P_d = \frac{(PF)_{eng}\Delta T}{L}\frac{m_{opt}}{(1+m_{0pt})^2} \qquad (4.3)$$

Where $(PF)_{eng}$ and m_{opt} are the engineering power factor and optimum ratio of external electrical load (R_L) and internal resistance (R_{int}). Here we have considered l = 10 mm and $m_{opt} = 1$ for calculation of P_d.

4.2.11 Device Fabrication. Typically, fabrication of the single-leg thermoelement involves consolidation of the melt grown $Ge_{0.98}Pb_{0.05}Te$-4% BiSe powder along with the end layers of Cu/Fe using spark plasma sintering at 500ºC with 50 MPa for 5 min under vacuum. The arrangement of different layers in the fabricated single-leg $Ge_{0.98}Pb_{0.05}Te$-4% BiSe based thermoelement can be described as Cu/Fe/$Ge_{0.98}Pb_{0.05}Te$-4% BiSe/Fe/Cu. Typical dimension of the fabricated thermoelement is 8 mm in diameter and 9 mm in length. Power generating properties of the fabricated $Ge_{0.98}Pb_{0.05}Te$-4% BiSe thermoelement was estimated by mini-PEM module testing system (Advance Riko).[23–25]

4.3 Results & discussion

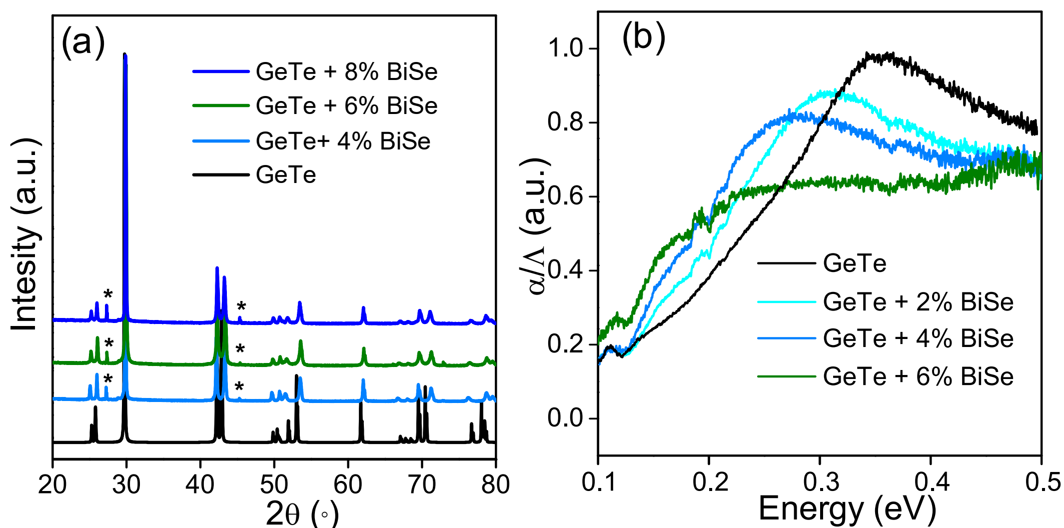

Figure 4.1. *(a) Powder X-ray diffraction pattern and (b) optical absorption spectra of GeTe + x% BiSe samples. "*" sign in the PXRD pattern signifies presence of Ge as minority phase.*

Powder X-ray diffraction (PXRD) pattern of all the samples of GeTe-x% BiSe (x = 0-8) samples are presented in Figure 4.1a. The room-temperature PXRD patterns of GeTe-x% BiSe (x = 0-8) can be indexed based on the rhombohedral phase of pristine GeTe (*R3m*). Moreover, additional reflections for Ge-impurity (Figure 4.1a; * marked peaks, space group $Fd\bar{3}m$) are being observed in all the PXRD patterns.[7,9] It is interesting to note that with increase in content of BiSe in the system, relative intensity of the impurity peak for Ge in PXRD pattern increases. In GeTe- x% BiSe samples, Bi occupies Ge-site and Se occupies Te site which increase the Ge precipitaes in the system and creates enhanced substitutional disorder in the system with consequent effect on transport properties.

Optical absorption spectra of GeTe-x% BiSe (x = 0-6) samples as a function of energy (eV) (Figure 4.1b) shows that band gap of pristine GeTe decreases from ~0.2 eV to ~ 0.14 eV in GeTe-6% BiSe. In pristine GeTe, valence band edge is dominated by Te-p orbitals while Ge-p orbitals have the dominant contribution in conduction band edge. As Bi occupies Ge-site and Bi (χ_{Bi} = 2.02) is slightly electropositive than Ge (χ_{Ge} = 2.01), Bi forms an impurity state just below the conduction band which has been established by both experimentally and theoretically in earlier reports.[7,9]

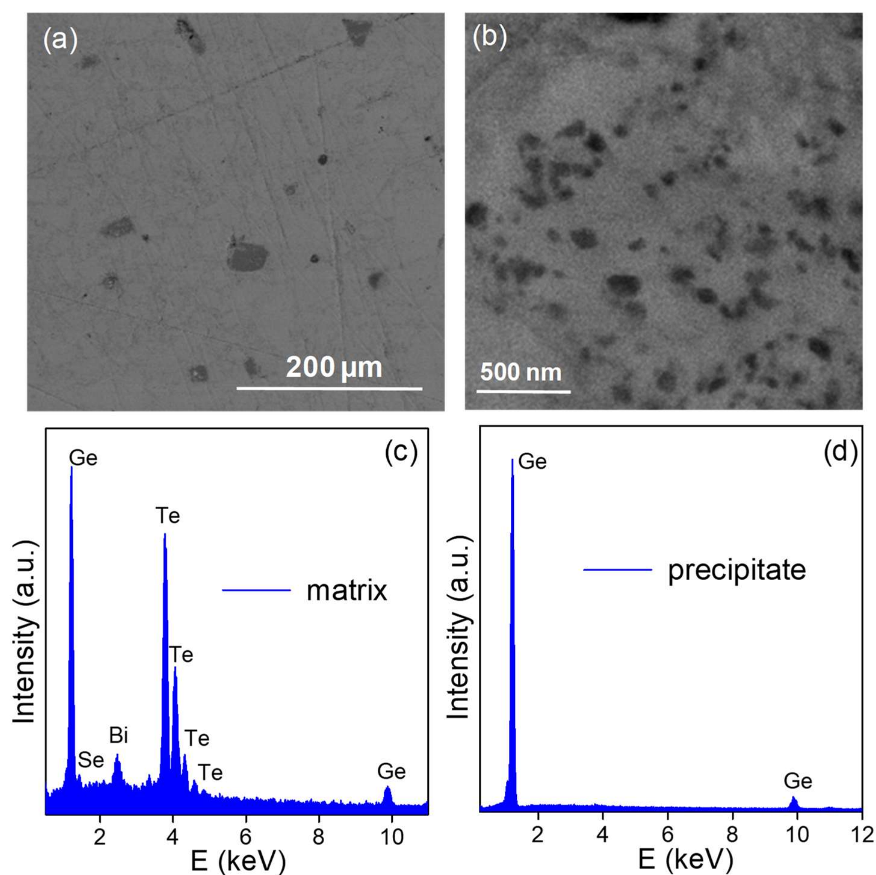

Figure 4.2. *(a) and (b) Back scattered FESEM images of GeTe + 4% BiSe samples which shows presence of different sizes of precipitates (dark contrast) throughout the matrix (light contrast). (c) and (d) EDAX spectra of the matrix and black precipitates respectively.*

Backscattered electron imaging (BSE) has been performed on GeTe-4% BiSe during FESEM to understand micro/nano-structure of the system (Figure 4.2). Low magnification BSE-FESEM images of GeTe-4% BiSe shows presence of micrometer size Ge-precipitates (dark precipitates, Figure 4.2a), while high magnification BSE image shows the presence of nanometer size Ge precipitates (dark precipitates in Figure 4.2b). EDAX analysis of the matrix (Figure 4.2c) and the black precipitates (Figure 4.2d) confirms the composition darker precipitates as Ge phase.

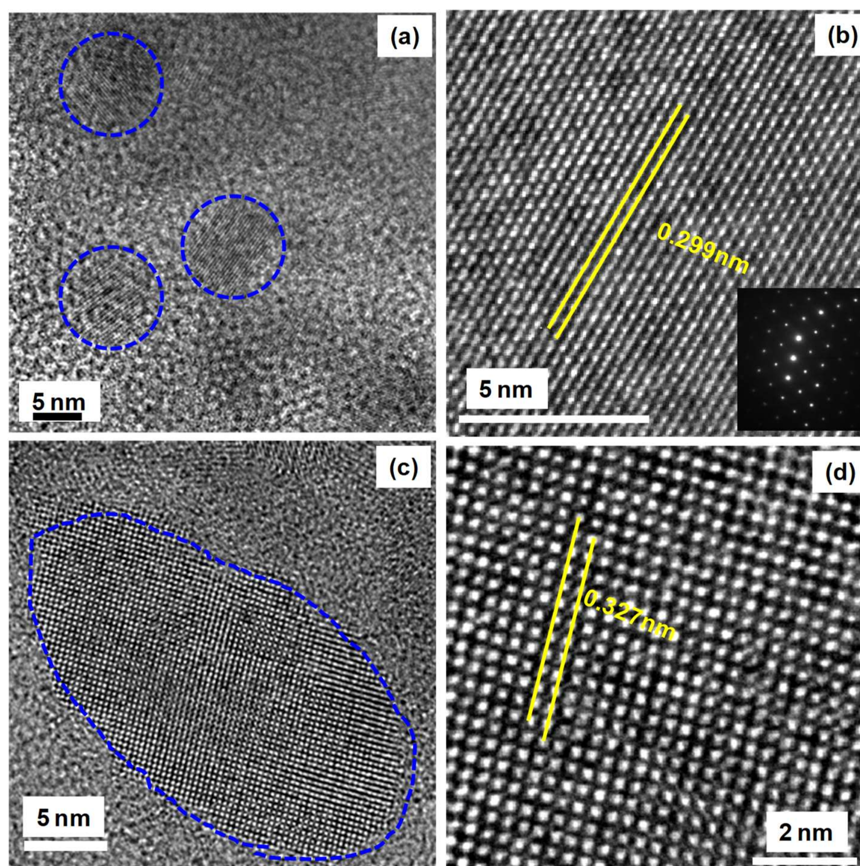

Figure 4.3. *(a) Low magnification TEM micrograph of GeTe+ 4% BiSe showing precipitates of 10-30 nm sizes (encircled with blue lines). (b) HRTEM micrograph of matrix with an interplannar spacing of 0.299 nm, corresponding to (202) planes of α-GeTe (R3m). Inset shows ED pattern of the matrix confirming single crystalline nature of the system. (c) Zoomed TEM micrograph of single precipitates and (d) corresponding HRTEM image with an interplannar spacing of 0.327 nm, corresponding to (111) planes of Ge (Fd$\bar{3}$m) confirming presence of Ge -nanoprecipitates.*

Further to confirm the presence of Ge nanoprecipitates in the matrix, transmission electron microscopy of GeTe-4% BiSe has been investigated. Low magnification TEM micrograph of GeTe-4% BiSe shows presence of small precipitates of 10-30 nm sizes (Encircled in blue dotted lines, Figure 4.3a. Figure 4.3b shows the high resolution TEM micrographs (HRTEM) of matrix with interplannar spacing of d = 0.299 nm, corresponding to (202) planes of the rhombohedral phase of GeTe. Selected area electron diffraction (SAED) pattern of the matrix (insets of Figure 4.3b indicates single crystalline nature of rhombohedral GeTe-4% BiSe. Figure 4.3c and 4.3d shows zoomed TEM micrograph and

corresponding HRTEM image of a single nano-precipitate respectively. Calculated d-spacing from the HRTEM images of the precipitate is ~ 0.327 nm which best attributed to the (111) planes of Ge (Space group $Fd\bar{3}m$) confirming presence of Ge-nanoprecipitates.

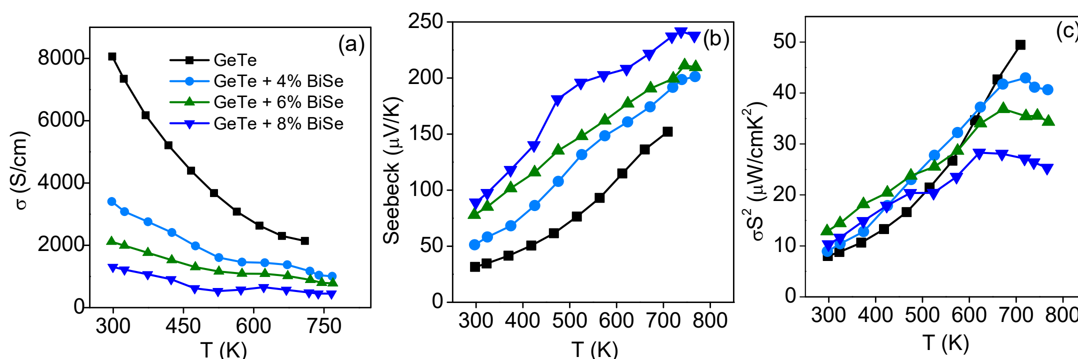

Figure 4.4. *Temperature dependent (a) electrical conductivity (σ), (b) Seebeck coefficient (S) and (c) power factor (σS^2) of GeTe + x% BiSe (x = 0 - 8) samples.*

Electronic transport properties of GeTe-x% BiSe (x = 0-8) has demonstrated in Figure 4.4. Electrical conductivity (σ) of all the samples decreases with temperature depicting degenerate semiconductor nature of GeTe-x% BiSe samples (Figure 4.4a). Electrical conductivity of GeTe-x% BiSe systematically decreases with increase in BiSe concentration. Typically, σ of GeTe decreases from ~ 8067 S/cm to 3422 S/cm in GeTe-4% BiSe at room temperature. Measured carrier concentration (n) of the GeTe-x% BiSe samples which has been presented in Table 5.4, clearly shows that both the carrier concentration and mobility of the charge carrier decreases with increase in BiSe concentration in the system. Decrease in carrier concentration can be understood from the donor dopant nature of the Bi,[7–9,13] whereas reduced mobility is mainly attributed to the added disorders such as Ge/Bi and Te/Se in the system.

Seebeck coefficient (S) of GeTe-x% BiSe (x= 0-8) samples has been presented in Figure 4.4b, which shows systematic enhancement with increase in BiSe concentration in the system. Typically, S value increases from ~ 32 μV/K in GeTe to ~ 89 μV/K in GeTe-8%BiSe at 300 K. This systematic increase in S with increase in BiSe concentration is mainly ascribed to reduced carrier concentration of the system (Table 4.1). Further, Seebeck coefficient of all the samples increases with temperature. For example, S value of GeTe-4% BiSe increases from 51 μV/K at 295 K to 202 μV/K at 769 K.

Table 4.1. *Room temperature carrier concentration, electrical conductivity and mobility of the GeTe-x% BiSe (x= 0-8) system.*

Sample	Carrier concentration (n) × 10^{20}/cm^3	Electrical conductivity (σ) in S/cm	Mobility (μ) in cm^2/Vs
GeTe	7.3	8067	68.98
GeTe + 4% BiSe	3.2	3422	66.75
GeTe + 6% BiSe	2.45	2102	53.5
GeTe + 8% BiSe	1.65	1330	50.3

Temperature dependent power factor (σS^2) of all GeTe-x% BiSe (x= 0-8) samples are shown in Figure 4.4c. At room temperature, power factor of all BiSe alloyed GeTe samples exhibit higher power factor compared to pristine GeTe and this fact is mainly ascribed to the enhanced Seebeck coefficient of GeTe-BiSe systems at room temperature. However, at high temperature pristine GeTe has the higher power factor compared to GeTe-x% BiSe (x= 4-8) samples because of bipolar conduction. Among GeTe-x% BiSe (x= 4-8) samples, GeTe-4% BiSe has the highest power factor of ~ 43 μW/cmK^2 at 720 K.

Temperature dependent total thermal conductivity (κ_{tot}) of GeTe-x% BiSe (x = 0 - 8) samples is presented in Figure 4.5b. Measurement of κ_{tot} shows decreasing trend with increase in BiSe concentration in GeTe-x% BiSe samples. Typically, κ_{tot} of GeTe decreases from ~ 8 W/mK to 1.45 W/mK in GeTe-8% BiSe at 300 K. Pristine GeTe and BiSe alloyed GeTe samples show an anomaly in κ_{tot} near 700 K and 600 K respectively. This anomaly in κ_{tot} is associated with the ferroelectric instability during phase transition of samples from rhombohedral structure to cubic structure.[26,27] We have derived the electrical thermal conductivity (κ_{el}) by using Wiedemann-Franz law which is given by $\kappa_{el} = L \times \sigma \times T$, where L is the Lorenz number. T-dependent Lorenz number was obtained by fitting the T-dependent S values considering single parabolic band conduction and only acoustic phonon scattering.[5] κ_{el} of GeTe-x% BiSe (x = 0 - 8) (Figure 4.5c) decreases with increase in BiSe concentration in the system which can be understood by analyzing the electrical conductivity data of the samples.

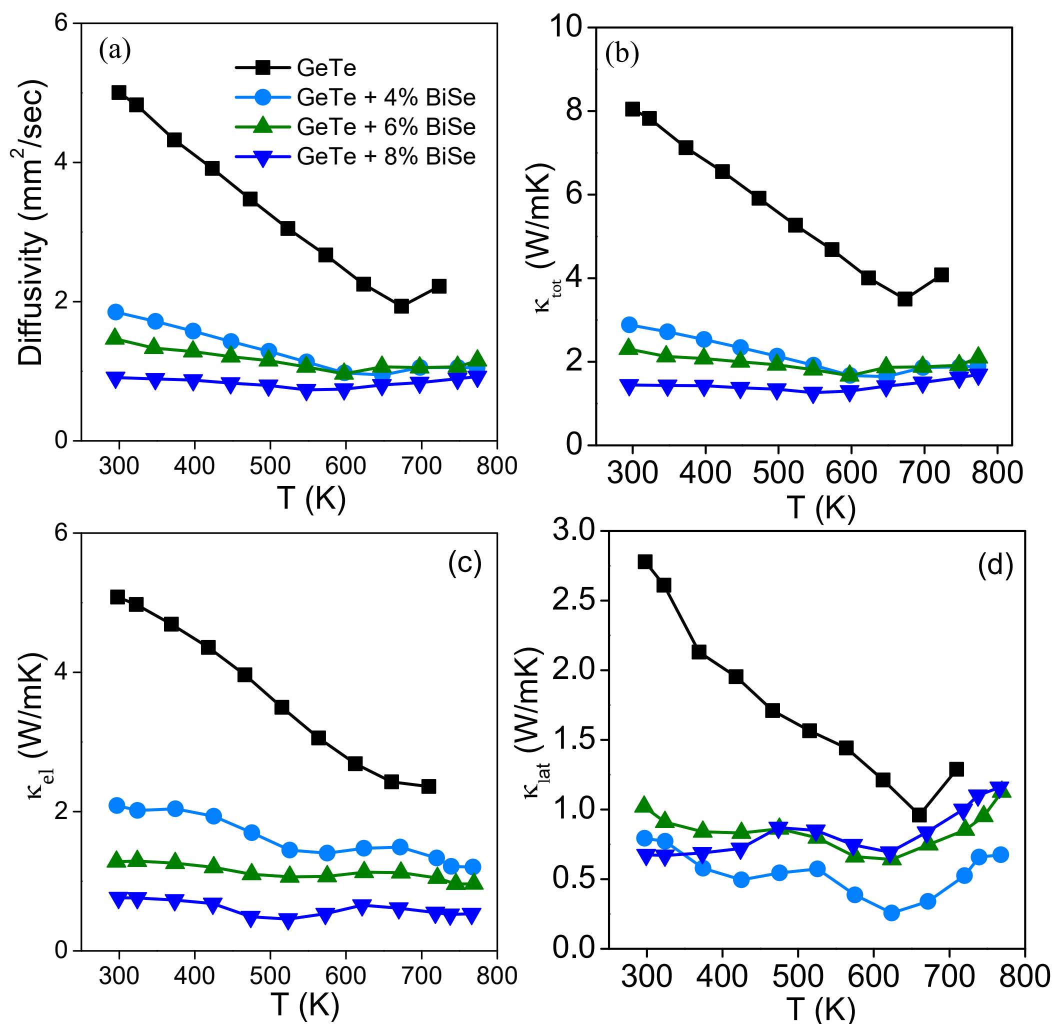

Figure 4.5. *Temperature dependent (a) thermal diffusivity, (b) total thermal conductivity (κ_{tot}), (c) electronic thermal conductivity (κ_{el}) and (b) lattice thermal conductivity (κ_{lat}) of of GeTe + x% BiSe (x = 0 - 8) samples.*

Lattice thermal conductivity (κ_{lat}) of GeTe-x% BiSe (x = 0 - 8) which has been derived by subtracting κ_{el} from $\kappa_{lat,}$ has been demonstrated in Figure 4.5d. All the BiSe alloyed GeTe samples exhibit significantly reduced κ_{lat} compared to pristine GeTe at room temperature. Typically, room temperature κ_{lat} of GeTe is reduced from ~ 2.78 W/mK to 0.8 W/mK in GeTe-4% BiSe. This huge reduction in κ_{lat} in GeTe-4% BiSe samples compared to pristine GeTe is mainly ascribed to strengthened phonon scattering by extensive point defects in the system arouse by Ge/Bi and Te/Se disorders and Ge-nanoprecipiates. Further, κ_{lat} of GeTe-4% BiSe decreases to a very low value of ~ 0.26 W/mK 623 K and afterwards

it again starts increasing. This ultralow κ_{lat} of GeTe-4% BiSe near the phase transition temperature is associated with the ferroelectric instability during the phase transition.[26,27]

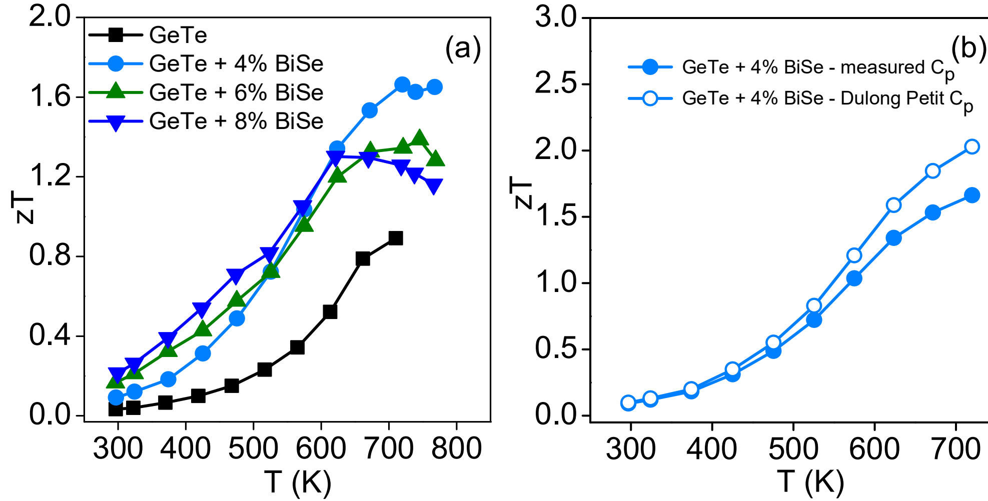

Figure 4.6. *(a) Temperature dependent thermoelectric figure of merit (zT) of GeTe + x% BiSe (x = 0 - 8) samples. (b) Comparison of the temperature dependent thermoelectric figure of merit (zT) of GeTe -4% BiSe sample estimated based on measured C_p value (solid symbols) and using Dulong-Petit C_p value (open symbols).*

T-dependent thermoelectric figure of merit (zT) of GeTe-x% BiSe sample are presented in Figure 4.6(a). As a result of synergistic effect of optimization of carrier concentration and reduced κ_{lat}, all the BiSe alloyed samples demonstrate higher thermoelectric figure of merit compared to pristine GeTe. Among all the BiSe alloyed GeTe samples, GeTe-4%BiSe sample shows highest zT of ~ 1.7 at 720 K. Moreover, in order to compare the thermoelectric performance of GeTe-4% BiSe with recently reported GeTe-based thermoelectric materials,[2,28–30] we have calculated zT of GeTe-4% BiSe using Dulong-Petit C_p which is ~ 2 at 720 K (Figure 4.6b).

Further to optimize thermoelectric performance of GeTe-4% BiSe, the strategy of self-compensation of Ge[31] and Pb-doping has been employed.[28] PXRD pattern of $Ge_{1.03-y}Pb_yTe$-4% BiSe (y = 0.04-0.07) samples (Figure 4.7a) shows that all the peaks can be indexed based on rhombohedral phase of GeTe (*R3m*) with minor Ge-impurity as second phase (marked with * symbol in the PXRD). Investigation of TEM of $Ge_{0.98}Pb_{0.05}Te$-4% BiSe further confirms presence of Ge-nanoprecipitates (Figure 4.7b-c).

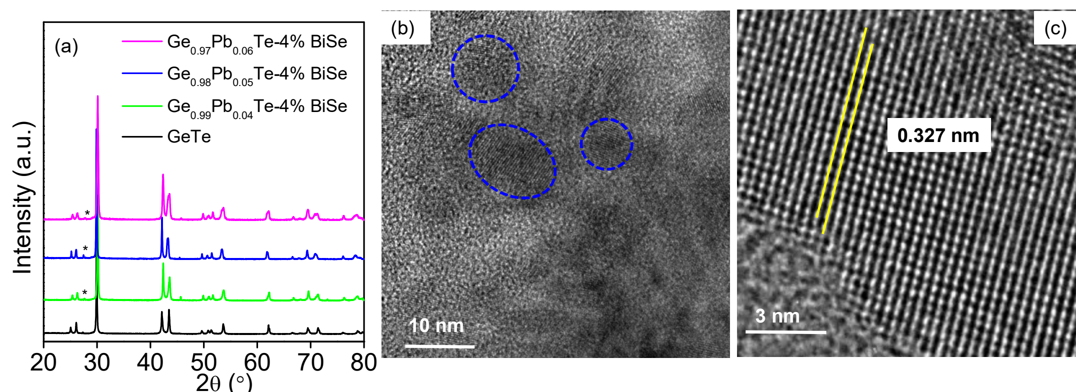

Figure 4.7. *(a) PXRD patterns of $Ge_{1.03-y}Pb_yTe$ –4% BiSe (y = 0.04-0.06) samples. "*" sign in the PXRD pattern signifies presence of Ge as minority phase. (b) Low magnification TEM micrograph of $Ge_{0.98}Pb_{0.05}Te$+ 4% BiSe showing precipitates of 10 -30 nm sizes (encircled with blue lines). (c) HRTEM image of a nano-precipitates shows an interplannar spacing of 0.327 nm, corresponding to (111) planes of Ge (Fd-3m).*

Transport properties of $Ge_{1.03-y}Pb_yTe$-4% BiSe (y = 0.04-0.06) samples are presented in Figure 4.8. Electrical conductivity of all the $Ge_{1.03-y}Pb_yTe$-4%BiSe samples show reduced electrical conductivity compared to the GeTe-4% BiSe, arising from reduced carrier concentration (*n*) in $Ge_{1.03-y}Pb_yTe$-4% BiSe (For example, *n* of $Ge_{0.98}Pb_{0.05}Te$-4% BiSe ~ 2.4 $x10^{20}/cm^3$). All the $Ge_{1.03-y}Pb_yTe$-4% BiSe samples have higher *S* values compared to GeTe-4% BiSe. Typically, Seebeck value of $Ge_{0.98}Pb_{0.05}Te$-4% BiSe is ~ 79 μV/K at 300 K and it increases to 250 μV/K at 725 K; while GeTe-4% BiSe has *S* of ~ 51 μV/K at 300 K which increases to 192 μV/K at 720 K. This enhanced *S* of $Ge_{1.03-y}Pb_yTe$-4% BiSe samples is stemming from reduced carrier concentration and implications of slight symmetry reduction technique which has been established in Pb, Bi co-doped GeTe samples.[28,32] As a result of reduced σ and enhanced *S* values, the entire $Ge_{1.03-y}Pb_yTe$-4% BiSe (y = 0.04-0.06) shows high power factor in the range of ~ 43-45 $\mu W/cmK^2$ at 652 K. All the $Ge_{1.03-y}Pb_yTe$-4% BiSe samples show significantly low κ_{lat} (Figure 4.9d), derived by subtracting the κ_{el} from κ_{tot} (Figure 4.9 b and c), throughout the measured temperature. This huge reduction in κ_{lat} is manifestation of high degree of disorders in the system such as Ge/Bi/Pb and Te/Se and presence of Ge-nanoprecipitates in the GeTe matrix.

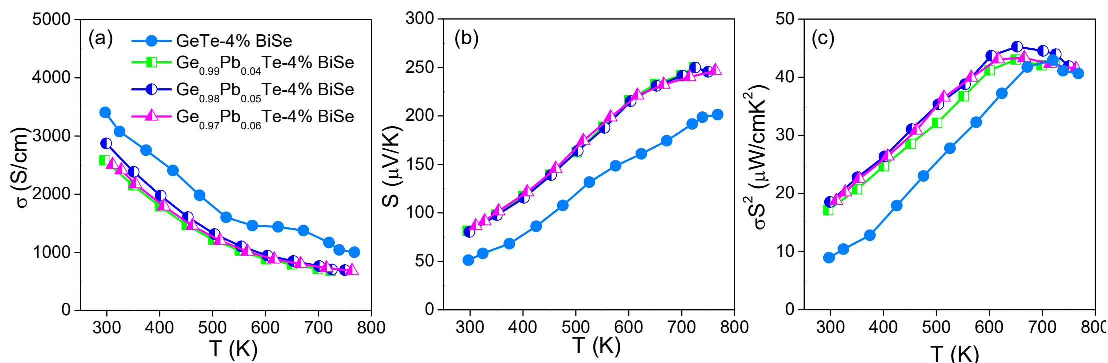

Figure 4.8. *Temperature dependent (a) electrical conductivity (σ), (b) Seebeck coefficient (S), and (c) power factor (σS^2) of $Ge_{1.03-y}Pb_yTe$ + 4% BiSe (y = 0 – 0.06) samples.*

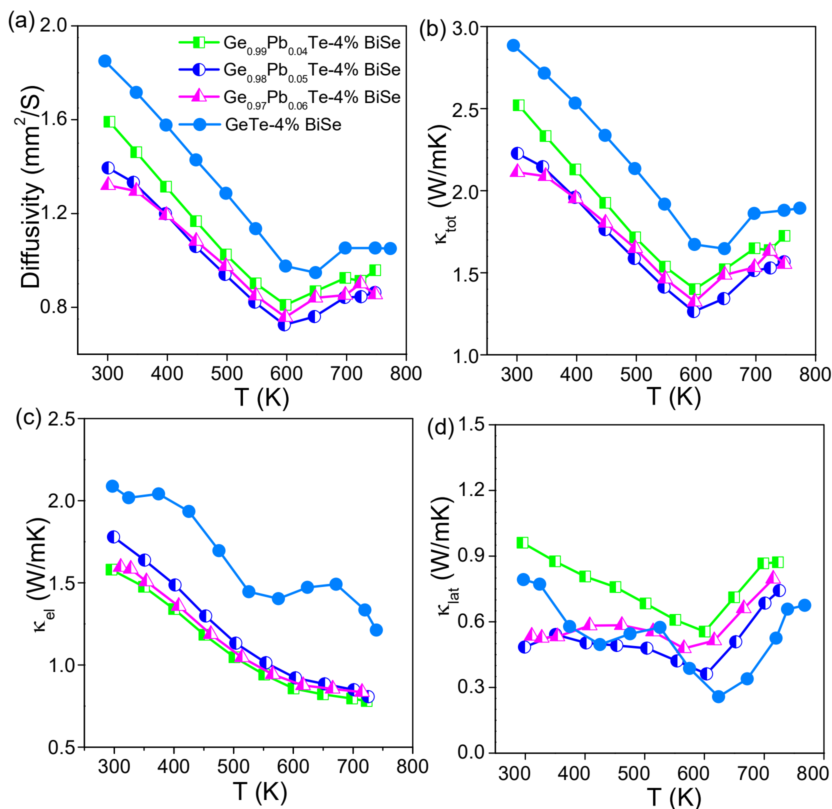

Figure 4.9. *Temperature dependent (a) thermal diffusivity, (b) total thermal conductivity (κ_{tot}), (c) electronic thermal conductivity (κ_{el}) and (d) lattice thermal conductivity (κ_{lat}) of $Ge_{1.03-y}Pb_yTe$ + 4% BiSe (y = 0 – 0.06) samples.*

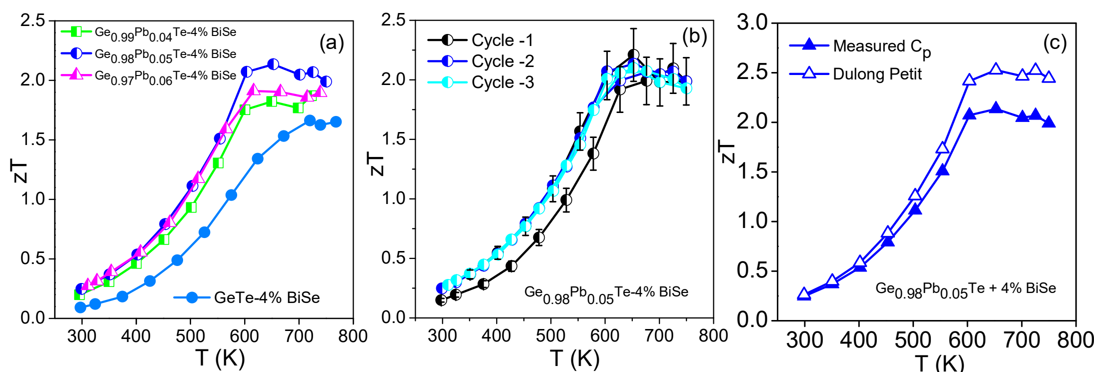

Figure 4.10. *(a) Temperature dependent thermoelectric figure of merit of $Ge_{1.03-y}Pb_yTe$ + 4% BiSe (y = 0.04 – 0.06) samples. (b) The reversibility (three heating-cooling cycles) of thermoelectric figure of merit of $Ge_{0.98}Pb_{0.05}Te$ + 4% BiSe as function of temperature (error bar ~ 10%).(c) Comparison of the temperature dependent thermoelectric figure of merit (zT) of $Ge_{0.98}Pb_{0.05}Te$ -4% BiSe sample estimated based on measured C_p value (solid symbols) and using Dulong-Petit C_p value (open symbols).*

Temperature dependent zT of $Ge_{1.03-y}Pb_yTe$-4% BiSe (y = 0.04-0.06) samples (Figure 4.10a) demonstrates promising zT values. A highest zT of ~ 2.2 is achieved in $Ge_{0.98}Pb_{0.05}Te$-4% BiSe at 652 K which is ~ 244 % higher compared to pristine GeTe (zT of ~ 0.9 at 723 K). Further, *zT* of $Ge_{0.98}Pb_{0.05}Te$-4% BiSe sample is re-measured for several heating and cooling cycles, which shows good heating-cooling reversibility of the zT (see Figure 4.10b). Moreover, estimation of zT of $Ge_{0.98}Pb_{0.05}Te$-4% BiSe using Dulong-Petit C_p shows a record-high zT of ~ 2.5 at 652 K in (Figure 4.10c), which shows thermoelectric performance of $Ge_{0.98}Pb_{0.05}Te$-4% BiSe outperforms many state of art thermoelectric materials.[2,28–30]

In order to have quantitative estimation of maximum obtainable efficiency η_{eng}, Kim *et al.*[22] have introduced the concept of engineering figure of merit, zT_{eng} based on the cumulative temperature-dependent thermoelectric properties. Hence, we have derived the PF_{eng}, output power density (P_d), zT_{eng} and η_{eng} of $Ge_{0.98}Pb_{0.05}Te$-4% BiSe as a function of temperature difference (ΔT) of the cold (T_C) and hot sides (T_H) (Figure 4.11) with T_C = 300K. The maximum zT_{eng} of $Ge_{0.98}Pb_{0.05}Te$-4% BiSe is calculated to be ~ 0.95, whereas the highest P_d *and* η_{eng} is determined as 1.7 W/cm^2 and ~13 % for the ΔT= 450K.

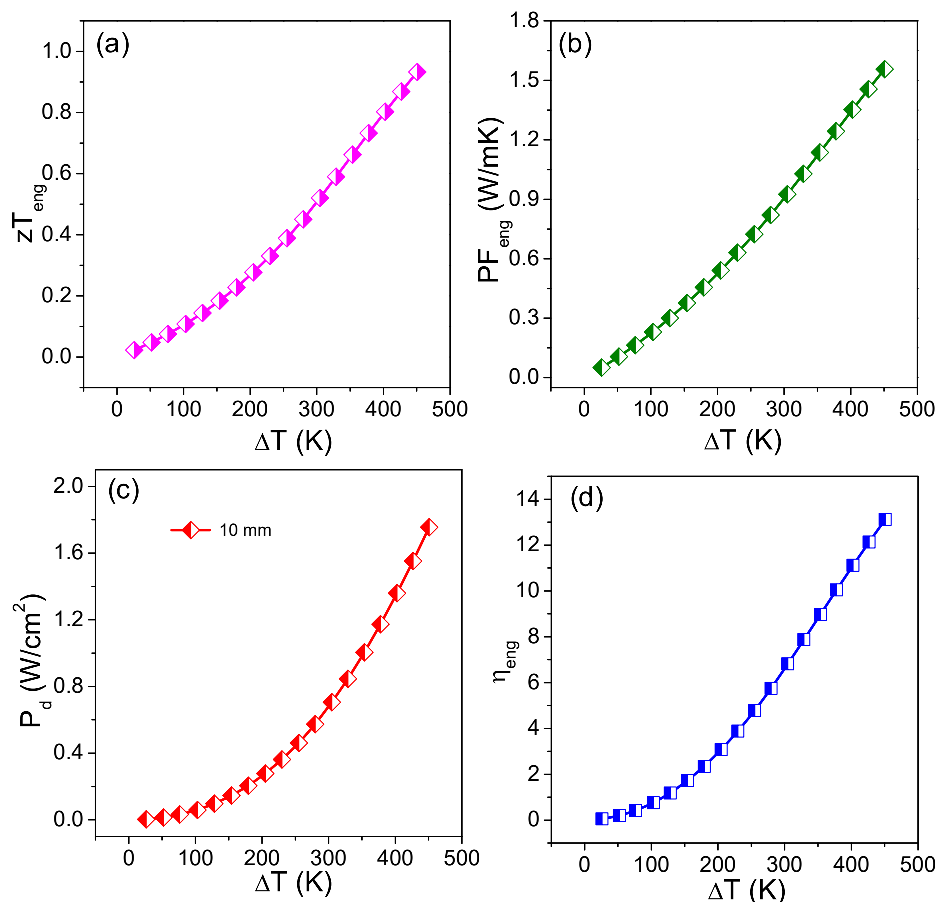

Figure 4.11. *Calculated engineering (a) figure of merit (zT_{eng}), (b) power factor (PF_{eng}), (c) output power density (P_d) and (d) efficiency (η_{eng}) of $Ge_{0.98}Pb_{0.05}Te$ – 4%BiSe samples as a function of temperature difference.*

Further, we have fabricated a single leg thermoelement using highest zT sample which is *p*-type $Ge_{0.98}Pb_{0.05}Te$-4% BiSe material (Figure 4.12a) and investigated it's power generation characteristics by using mini-PEM test system.[23–25] Internal resistance (R) of the thermoelement (Figure 4.12b) increases with increase in the temperature of the hot-side which is the characteristic of the material, a degenerate semiconductor. Moreover, the resistance of the fabricated device is higher than that of $Ge_{0.98}Pb_{0.05}Te$-4% BiSe, because of the interfacial resistance which is common in TE-device community.[33–37] Variation of terminal voltage (V) and output power (P) of $Ge_{0.98}Pb_{0.05}Te$-4% BiSe-based single-leg thermoelement as a function of electrical current (I) are presented in Figure 4.12 c and d. The maximum obtainable output power, P_{max} from the device is ~ 170 mW for ΔT = 475 K, which is quite significant for device applications.

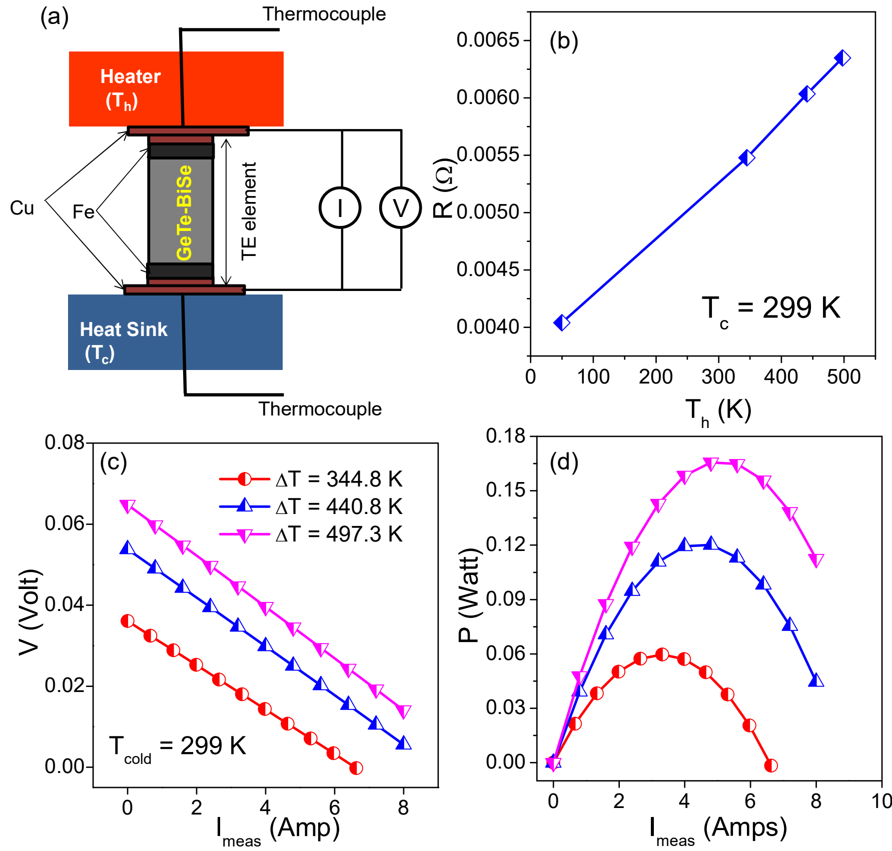

Figure 4.12. *(a) Schematic diagram of the mounted thermoelement in the mini-PEM test system. (b) Variation of internal resistance (R) of the $Ge_{0.98}Pb_{0.05}Te – 4\%BiSe$ -based single thermoelement as a function T_h. Variation of (b) terminal voltage (V) and (c) output power (P) as a function of electrical current (I_{meas}) of the $Ge_{0.98}Pb_{0.05}Te – 4\%BiSe$ -based single thermoelement.*

Further, we have estimated the heat flow (Q_c) through the thermoelement by using, Fourier's Law,[24] which is as follows,

$$Q_c = \frac{k\left(T_{avg}\right) \times A \times \Delta T}{L}$$

where A is the cross-sectional area and L is the length of the fabricated thermoelement. In addition, $\kappa(T_{avg})$ is the thermal conductivity of $Ge_{0.98}Pb_{0.05}Te$-4% BiSe at $T_{avg} = (T_h + T_c)/2$, and $\Delta T = T_h – T_c$. We have estimated the heat supplied to the device as ~ 3.4 W for ΔT of ~ 495 K. With this, TE conversion efficiency, η of single-leg $Ge_{0.98}Pb_{0.05}Te$-4% BiSe based TE generator is estimated to be ~ 5%, calculated by taking the ratio of electrical output

power (P_{max}) to input heat flowing (Q_c) across the thermoelement. The uncertainty in the conversion efficiency evaluation was approximately 10–12%.

4.4 Conclusions

In conclusion, BiSe alloying enables high thermoelectric performance (zT ~ 1.7 at 720 K) in GeTe, facilitated by (a) successful optimizations of the carrier concentration and (b) low thermal conductivity due to nano to micro meter size Ge-precipitates throughout the matrix and extensive Ge/Bi and Te/Se disorders. Further optimizations of thermoelectric performance of GeTe-4% BiSe is performed by self-compensation of Ge and Pb-doping, which results in enhanced Seebeck coefficient and significantly reduced the lattice thermal conductivity in the system. As a result of optimizations of all the thermoelectric parameters, an ultra-high zT of ~ 2.2 is achieved in $Ge_{0.98}Pb_{0.05}Te$-4% BiSe at 652 K. Motivated by the high thermoelectric performance of $Ge_{0.98}Pb_{0.05}Te$-4% BiSe, a single leg thermoelement has been fabricated which shows significantly high output power of ~ 170 mW and power conversion efficiency, η of ~ 5% for ΔT = 475K.

4.5 References

(1) Roychowdhury, S.; Samanta, M.; Perumal, S.; Biswas, K. *Chem. Mater.* **2018**, *30*, 5799–5813.
(2) Zhang, X.; Li, J.; Wang, X.; Chen, Z.; Mao, J.; Chen, Y.; Pei, Y. *J. Am. Chem. Soc.* **2018**, *140*, 15883–15888.
(3) Hong, M.; Zou, J.; Chen, Z. *Adv. Mater.* **2019**, *31*, 1807071.
(4) Perumal, S.; Roychowdhury, S.; Biswas, K. *J. Mater. Chem. C* **2016**, *4*, 7520–7536.
(5) Perumal, S.; Roychowdhury, S.; Negi, D. S.; Datta, R.; Biswas, K. *Chem. Mater.* **2015**, *27*, 7171–7178.
(6) Wu, L.; Li, X.; Wang, S.; Zhang, T.; Yang, J.; Zhang, W.; Chen, L.; Yang, J. *NPG Asia Mater.* **2017**, *9*, e343–e343.
(7) Perumal, S.; Roychowdhury, S.; Biswas, K. *Inorg. Chem. Front.* **2016**, *3*, 125–132.
(8) Li, J.; Chen, Z.; Zhang, X.; Sun, Y.; Yang, J.; Pei, Y. *NPG Asia Mater.* **2017**, *9*, e353.
(9) Perumal, S.; Samanta, M.; Ghosh, T.; Shenoy, U. S.; Bohra, A. K.; Bhattacharya, S.; Singh, A.; Waghmare, U. V.; Biswas, K. *Joule* **2019**, *3*, 2565–2580.
(10) Samanta, M.; Biswas, K. *J. Am. Chem. Soc.* **2017**, *139*, 9382–9391.
(11) Wu, D.; Zhao, L.-D.; Hao, S.; Jiang, Q.; Zheng, F.; Doak, J. W.; Wu, H.; Chi, H.; Gelbstein, Y.; Uher, C.; *et al. J. Am. Chem. Soc.* **2014**, *136*, 11412–11419.
(12) Wu, D.; Feng, D.; Xu, X.; He, M.; Xu, J.; He, J. *J. Alloys Compd.* **2019**, *805*, 831–839.

(13) Jin, Y.; Xiao, Y.; Wang, D.; Huang, Z.; Qiu, Y.; Zhao, L. D. *ACS Appl. Energy Mater.* **2019**, *2*, 7594–7601.
(14) Lee, M. H.; Park, S.; Lee, J. K.; Chung, J.; Ryu, B.; Park, S. D.; Rhyee, J. S. *J. Mater. Chem. A* **2019**, *7*, 16488–16500.
(15) Lee, Y.; Lo, S.-H.; Chen, C.; Sun, H.; Chung, D.-Y.; Chasapis, T. C.; Uher, C.; Dravid, V. P.; Kanatzidis, M. G. *Nat. Commun.* **2014**, *5*, 3640.
(16) Duong, A. T.; Nguyen, V. Q.; Duvjir, G.; Duong, V. T.; Kwon, S.; Song, J. Y.; Lee, J. K.; Lee, J. E.; Park, S.; Min, T.; *et al. Nat. Commun.* **2016**, *7*, 13713.
(17) Jin, Y.; Xiao, Y.; Wang, D.; Huang, Z.; Qiu, Y.; Zhao, L.-D. *ACS Appl. Energy Mater.* **2019**, *2*, 7594–7601.
(18) Banik, A.; Roychowdhury, S.; Biswas, K. *Chem. Commun.* **2018**, *54*, 6573–6590.
(19) Zhou, Z.; Yang, J.; Jiang, Q.; Luo, Y.; Zhang, D.; Ren, Y.; He, X.; Xin, J. *J. Mater. Chem. A* **2016**, *4*, 13171–13175.
(20) Samanta, M.; Pal, K.; Pal, P.; Waghmare, U. V.; Biswas, K. *J. Am. Chem. Soc.* **2018**, *140*, 5866–5872.
(21) Samanta, M.; Ghosh, T.; Arora, R.; Waghmare, U. V; Biswas, K. *J. Am. Chem. Soc.* **2019**, *141*, 19505–19512.
(22) Kim, H. S.; Liu, W.; Chen, G.; Chu, C.-W.; Ren, Z. *Proc. Natl. Acad. Sci.* **2015**, *112*, 8205–8210.
(23) Kunioka, H.; Yamamoto, A.; Iida, T.; Obara, H. *Appl. Phys. Express* **2017**, *10*, 095801.
(24) Chetty, R.; Kikuchi, Y.; Bouyrie, Y.; Jood, P.; Yamamoto, A.; Suekuni, K.; Ohta, M. *J. Mater. Chem. C* **2019**, *7*, 5184–5192.
(25) Hu, X.; Barnett, M. R.; Yamamoto, A. *J. Alloys Compd.* **2015**, *649*, 1060–1065.
(26) Banik, A.; Ghosh, T.; Arora, R.; Dutta, M.; Pandey, J.; Acharya, S.; Soni, A.; Waghmare, U. V.; Biswas, K. *Energy Environ. Sci.* **2019**, *12*, 589–595.
(27) Steigmeier, E. .; Harbeke, G. S. *Solid State Commun.* **1970**, *8*, 1275–1279.
(28) Li, J.; Zhang, X.; Chen, Z.; Lin, S.; Li, W.; Shen, J.; Witting, I. T.; Faghaninia, A.; Chen, Y.; Jain, A.; *et al. Joule* **2018**, *2*, 976–987.
(29) Hong, M.; Chen, Z.-G.; Yang, L.; Zou, Y.-C.; Dargusch, M. S.; Wang, H.; Zou, J. *Adv. Mater.* **2018**, *30*, 1705942.
(30) Hong, M.; Wang, Y.; Liu, W.; Matsumura, S.; Wang, H.; Zou, J.; Chen, Z.-G. *Adv. Energy Mater.* **2018**, *8*, 1801837.
(31) Banik, A.; Biswas, K. *J. Mater. Chem. A* **2014**, *2*, 9620.
(32) Roychowdhury, S.; Biswas, K. *Chem* **2018**, *4*, 939–942.
(33) Zebarjadi, M.; Esfarjani, K.; Dresselhaus, M. S.; Ren, Z. F.; Chen, G. *Energy Environ. Sci.* **2012**, *5*, 5147–5162.
(34) Liu, W.; Jie, Q.; Kim, H. S.; Ren, Z. *Acta Mater.* **2015**, *87*, 357–376.
(35) Hazan, E.; Ben-Yehuda, O.; Madar, N.; Gelbstein, Y. *Adv. Energy Mater.* **2015**, *5*, 1500272.
(36) Singh, A.; Bhattacharya, S.; Thinaharan, C.; Aswal, D. K.; Gupta, S. K.; Yakhmi, J. V.; Bhanumurthy, K. *J. Phys. D. Appl. Phys.* **2009**, *42*, 015502.
(37) Bohra, A. K.; Bhatt, R.; Singh, A.; Bhattacharya, S.; Basu, R.; Meshram, K. N.; Sarkar, S. K.; Bhatt, P.; Patro, P. K.; Aswal, D. K.; *et al. Mater. Des.* **2018**, *159*, 127–137.

Chapter 5

Low Thermal Conductivity and High Thermoelectric Performance in $(GeTe)_{1-2x}(GeSe)_x(GeS)_x$: Competition between Solid Solution and Phase Separation

Chapter 5

Low Thermal Conductivity and High Thermoelectric Performance in $(GeTe)_{1-2x}(GeSe)_x(GeS)_x$: Competition between Solid Solution and Phase Separation†

Summary

High lattice thermal conductivity (κ_{lat}) is one of the main constrain in the way of optimizing thermoelectric performance of GeTe. Herein, we demonstrate low κ_{lat} (~0.7 W/mK) and significantly high thermoelectric figure of merit (zT = 2.1 at 630 K) in Sb doped pseudo-ternary $(GeTe)_{1-2x}(GeSe)_x(GeS)_x$ system by two step strategies. $(GeTe)_{1-2x}(GeSe)_x(GeS)_x$ system provides an excellent podium to investigate competition between entropy driven solid solution and enthalpy driven phase separation. In first step, small concentration of Se and S were substituted simultaneously in the position of Te in GeTe to reduce the κ_{lat} by phonon scattering due to mass fluctuations and point defects. When the Se/S concentration increases significantly the system deviates from solid solution, and phase separation of the $GeS_{1-x}Se_x$ (5-20 μm) precipitates in the $GeTe_{1-x}Se_x$ matrix occur, which do not participate in phonon scattering. In second stage, κ_{lat} of the optimized sample is further reduced to 0.7 W/mK by Sb alloying and spark plasma sintering (SPS), which introduces additional phonon scattering centers such as excess solid solution point defects and grain boundaries. The low κ_{lat} in Sb doped $(GeTe)_{1-2x}(GeSe)_x(GeS)_x$ is attributed to phonon scattering by entropically driven solid solution point defects rather than conventional endotaxial nanostructuring. As a consequence SPS processed $Ge_{0.9}Sb_{0.1}Te_{0.9}Se_{0.05}S_{0.05}$ sample exhibits a remarkably high zT of 2.1 at 630 K, which is reproducible and stable over temperature cycles. Moreover, Sb doped $(GeTe)_{1-2x}(GeSe)_x(GeS)_x$ exhibits significantly higher Vickers micro-hardness (mechanical stability) compared to that of pristine GeTe.

†*Paper based on this study has been published in J. Am. Chem. Soc.* **2017**, *139*, 9382–9391.

5.1 Introduction

Pristine GeTe possess lattice thermal conductivity, κ_{lat} of ~ 3 W/mK at room temperature, whereas the theoretical limit of minimum lattice thermal conductivity (κ_{min}) of GeTe is ~ 0.3 W/mK.[1–5] This hints to the presence of enormous room to decrease the κ_{lat} of GeTe. Recently, significant reduction of κ_{lat} in $(PbTe)_{1-2x}(PbSe)_x(PbS)_x$ was achieved by the scattering of heat carrying phonons mainly by point defects, mass fluctuations and grain boundaries.[6,7] In this case, nanostructuring does not seems to be a dominant mechanism for phonon scattering. Thus, it would be interesting to study the consequences of alloying of GeSe and GeS with GeTe on the thermal conductivity and zT of GeTe. While pseudo-ternary $(GeTe)_{1-x-y}(GeSe)_x(GeS)_y$ [i.e. $GeTe_{1-x-y}Se_xS_y$] system exhibits large compositional scope, we restricted our study to the compositions that feature equal fractions of GeSe and GeS in GeTe i.e. $GeTe_{1-2x}Se_xS_x$. Several important questions can appear easily while studying complex system such as $GeTe_{1-2x}Se_xS_x$. For example, is the $GeTe_{1-2x}Se_xS_x$ a solid solution or a phase separated system or co-existence of both the solid solution and phase separation? Can lower κ_{lat} and higher thermoelectric performance be achieved in $GeTe_{1-2x}Se_xS_x$ compared to pseudobinary and pristine GeTe systems?

Herein, we demonstrate the excellent thermoelectric performance in GeTe rich pseudoternary $GeTe_{1-2x}Se_xS_x$ system which is achieved by modulating κ_{lat} in two step strategies. In first stage, GeS and GeSe alloying in GeTe reduces the κ_{lat} to 0.91 W/mK at 710 K. Callaway's model fitting of temperature dependent κ_{lat} indicates that the reduction of κ_{lat} is due to the phonon scattering by mainly mass fluctuations and point defects in $GeTe_{1-2x}Se_xS_x$. When the concentration of GeS/GeSe in GeTe increases over x = 5 mol%, big size (5–20 μm) precipitates of $GeS_{1-x}Se_x$ phase separates in $GeTe_{1-x}Se_x$ matrix, which is confirmed by powder X-ray diffraction, back scattered FESEM and detailed EDAX analysis. $GeS_{1-x}Se_x$ precipitates do not play significant role in phonon scattering because of its larger size compared to the mean free path of heat carrying phonon. In the second stage, to further decrease the κ_{lat} of optimized $GeTe_{0.9}Se_{0.05}S_{0.05}$ sample, it was alloyed with Sb (2-10 mol%) and ingot samples were processed by spark plasma sintering (SPS). This leads to significant reduction of κ_{lat} to 0.7 W/mK at 730 K due to phonon scattering by additional point defect (effect of Sb alloying) and grain boundaries (effect of SPS). The low κ_{lat} in Sb doped $(GeTe)_{1-2x}(GeSe)_x(GeS)_x$ is accounted for essentially phonon scattering by

entropically driven solid solution point defects rather than conventional endotaxial nanostructuring. As a consequence SPS processed $Ge_{0.9}Sb_{0.1}Te_{0.9}Se_{0.05}S_{0.05}$ sample exhibits a high zT of 2.1 at 630 K, which is thermally stable over cycling. Further, Vickers microhardness (mechanical stability) for $Ge_{0.9}Sb_{0.1}Te_{0.9}Se_{0.05}S_{0.05}$ is measured to be 186 Hv, which is higher than that of pristine GeTe.

5.2 Methods

5.2.1 Reagents. Germanium (Aldrich 99.999%), tellurium (Alfa Aesar 99.999+ %), sulphur (Alfa Aesar 99.9999%), antimony (Alfa Aesar 99.9999%) and selenium (Alfa Aeser 99.9999%) were used for synthesis without further purification.

5.2.2 Synthesis. First, polycrystalline ingots (~ 6 g) of $GeTe_{1-2x}Se_xS_x$ were synthesized by mixing stoichiometric amounts of high purity starting materials of Ge, Te, Se and S in quartz ampoule. The tubes were sealed under vacuum (10^{-6} Torr) and were slowly heated to 723 K and then to 1223 K over a time period of 12 h and 5 h, respectively, then kept for 6 h, and cooled slowly to room temperature over 10 h. Sb (2-10 mol%) doped $GeTe_{1-2x}Se_xS_x$ (x = 0.05) were synthesized by following similar procedure. In order to measure the electrical and thermal transport properties, ingots were cut in the shape of bar and coin respectively and finely polished. In order to improve the thermoelectric performance further, spark plasma sintering (SPS) was done with the ingot samples with highest performance. The as synthesized ingots were crushed and grounded to fine powders using a mortar and pestle. The powders were then loaded into a graphite die of ~10 mm diameter and compacted before placing the die assembly into a spark plasma sintering system (SPS 211-LX, Dr. Sinter Lab). The sintering-system was first evacuated to 10^{-3}. For the first 1 minute, temperature of the SPS chamber was held at room temperature and axial pressure was increased to 50 MPa. Then the temperature was increased to 350 °C in 5 minutes, followed by 450 °C in 2 minutes with a constant pressure of 50 MPa. For the next 5 minutes, temperature and pressure were held at 450 °C and 50 MPa, respectively, and then slowly decreased to ambient condition in 10 minutes. The SPS processed cylindrical shaped sample is further cut and polished for electrical and thermal transport measurement.

5.2.3 Powder X-ray diffraction. Powder X-ray diffraction for all synthesized samples were recorded using a Cu K_α ($\lambda = 1.5406$ Å) radiation source on a Bruker D8 diffractometer.

5.2.4 Band gap measurement. The optical band gap of all the samples were measured with finely grounded powder using diffuse reflectance mode in FT-IR Bruker IFS 66V/S spectrometer in the wave number range 4000-400 cm^{-1}. Absorption (α/Λ) data of the samples were calculated from measured reflectance data using Kubelka-Munk equation: $\alpha/\Lambda = (1-R)^2/(2R)$, where α and Λ are the absorption and scattering coefficient, R is the reflectance, respectively.

5.2.5 Electrical transport. Measurements of electrical conductivity and Seebeck coefficients of all the samples were carried out simultaneously in ULVAC-RIKO ZEM-3 instrument under a helium atmosphere from room temperature to 723 K. The typical dimension of sample for measurement is of ~2×2×8 mm^3. The longer direction coincides with the direction in which the thermal conductivity was measured. Heating and cooling cycles provide reversible electrical properties for the synthesized samples.

5.2.6 Hall measurement. Hall measurement of all the samples was carried out in the setup developed by Excel instrument, where a variable magnetic field of 0 - 0.57 Tesla and dc-current of 100 mA were used at room temperature.

5.2.7 Transmission electron microscopy (TEM). The TEM images of $GeTe_{1-2x}Se_xS_x$ were taken using a JEOL (JEM3010) TEM instrument (300 kV accelerating voltage) fitted with a Gatan CCD camera and also using a FEI TECNAI G2 20 STWIN TEM instrument (operating at 200 kV).

5.2.8 Thermal conductivity. Thermal diffusivity, D, of the samples was directly measured in Netzsch LFA-457 instrument in the temperature range 300−723 K by using the laser flash diffusivity method under nitrogen atmosphere. Coins with ~8 mm diameter and ~2 mm thickness were used for this purpose. Coins were coated with a thin layer of graphite in order to avoid errors coming from thermal emissivity of the materials. Temperature dependent heat capacity, C_p of GeTe was derived using standard sample (pyroceram) in LFA-457, which is in good agreement with Dulong-Petit C_p value. The total thermal conductivity, κ, was calculated using the formula $\kappa_{total} = DC_p\rho$, where ρ is the ensity

of the samples. To determine of total thermal conductivity of the other samples, C_p of GeTe was used.[4,8]

5.2.9 Mechanical properties. Microhardness of all the samples was measured in Zwick Roell zhu 2.5 microhardness instrument using the diamond indenter on the Vickers hardness scale. Vickers hardness (kgf/mm^2) values of the samples were determined by the equation of H_v = 1. 854xL/(2d)^2, where L is the indentation load and 2d is the diagonal length of the indentation. Here, the applied L is 0.1kg and the indent was kept for 10s. The obtained 2d value of $Ge_{0.9}Sb_{0.1}Te_{0.9}Se_{0.05}S_{0.05}$ is 31.5 µm. The error in microhardness measurement is about 5%.

5.3 Results & discussion

Though there are few reports on GeTe-GeSe system,[9,10] pseudoternary GeTe-GeSe-GeS system has not been explored hitherto due to the complexity in the structural chemistry. Microstructures analyzed in GeTe-GeSe-GeS system are similar to that in the previously reported PbTe-PbSe-PbS system.[6,7] Significant miscibility gap between GeTe and GeS is evidenced because of large differences in size between Te and S, which is characterized by XRD and back scattered FESEM analysis. Herein, we report detailed structural analysis and thermoelectric properties of $GeTe_{1-2x}Se_xS_x$ system.

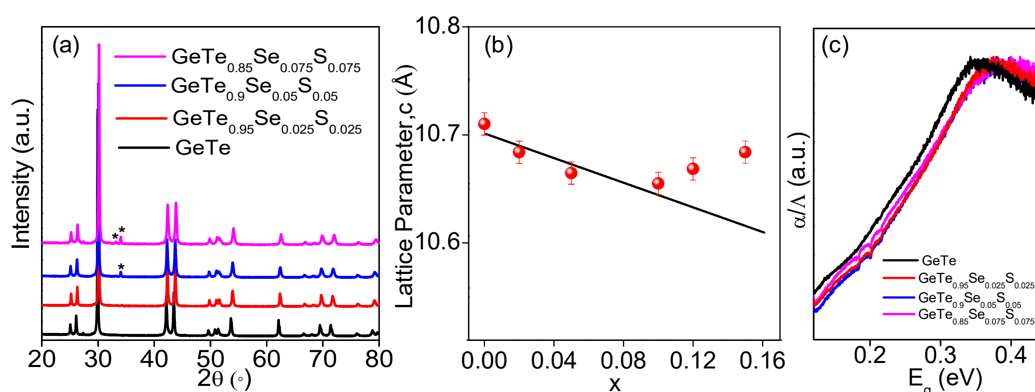

Figure 5.1. *(a) Powder X-ray diffraction pattern of $GeTe_{1-2x}Se_xS_x$ (x = 0 - 0.075) samples.* Sign signifies the presence of second phase of $GeS_{1-x}Se_x$. (b) The lattice parameter, c of $GeTe_{1-2x}Se_xS_x$ as function of the doping fraction x. The solid line is the trend of the data which reflects the deviation of the data point for x = 0.15. (c) Optical absorption spectra of $GeTe_{1-2x}Se_xS_x$ (x = 0 - 0.075) samples.*

PXRD patterns recorded at room temperature for the $GeTe_{1-2x}Se_xS_x$ (x = 0 – 0.075) samples are shown in Figure 5.1a, which could be indexed based on rhombohedral GeTe (space group, *R3m)*. With the increase in Se and S concentration up to 5 mol% in GeTe, *2Θ* values of PXRD peaks of GeTe are shifted towards right side indicating the decrease in the lattice parameters, which further verified by plotting the lattice parameter with respect to the concentration of Se/S (Figure 5.1b). This observation is consistent with the fact that the incorporation of smaller size Se and S with lower concentration in place of Te in GeTe leads to decrease in lattice parameter. However, PXRD patterns of $GeTe_{1-2x}Se_xS_x$ for higher Se/S concentration (x = 0.05 and 0.075) show additional weak reflections due to phase separation of $GeS_{1-x}Se_x$ (space group, *Pnam*) which is further verified by back scattered scanning electron microscopy. The linear decrease in lattice parameter with increasing the Se/S concentration discontinued due the phase separation of of $GeS_{1-x}Se_x$, when the concentration of Se/S is high enough in GeTe. These results indicate that initially the system $GeTe_{1-2x}Se_xS_x$ is solid solution (rich in point defects) with lower concentration of Se/S in GeTe, but with the higher Se/S concentration solid solution and phase separation coexist in $GeTe_{1-2x}Se_xS_x$.

To understand the surface morphology and microstructure compositions of $GeTe_{1-2x}Se_xS_x$, backscattered electron imaging (BSE) during FESEM and energy dispersive X-ray spectroscopy (EDAX) are performed on $GeTe_{1-2x}Se_xS_x$. The BSE images of different magnifications of $GeTe_{0.90}Se_{0.05}S_{0.05}$ are presented in Figure 5.2a-c, which show presences of the precipitates of ~5-20 μm size. Precipitates are of darker contrast compared to light contrast matrix. In order to understand the composition of the matrix and the precipitate, EDAX have been performed both on precipitate and matrix (Figure 5.2d and e). Elemental compositions of the matrix and the precipitate, which are determined by EDAX analysis, have been given in the inset of Figure 5.2d and 6.2e respectively. Matrix is $GeTe_{1-x}Se_x$ rich while the precipitate is to be $GeS_{1-x}Se_x$. To further confirm the phase composition, line scanning on a precipitate along with matrix (highlighted by a white line in Figure 5.2c) was performed, which clearly shows that the matrix is $GeTe_{1-x}Se_x$ rich, whereas precipitate is $GeS_{1-x}Se_x$ (Figure 5.2f). These results indicate that solubility of GeSe in GeTe is higher than that of GeS in GeTe matrix, which is mainly attributed to the smaller size of S compared to bigger Te.

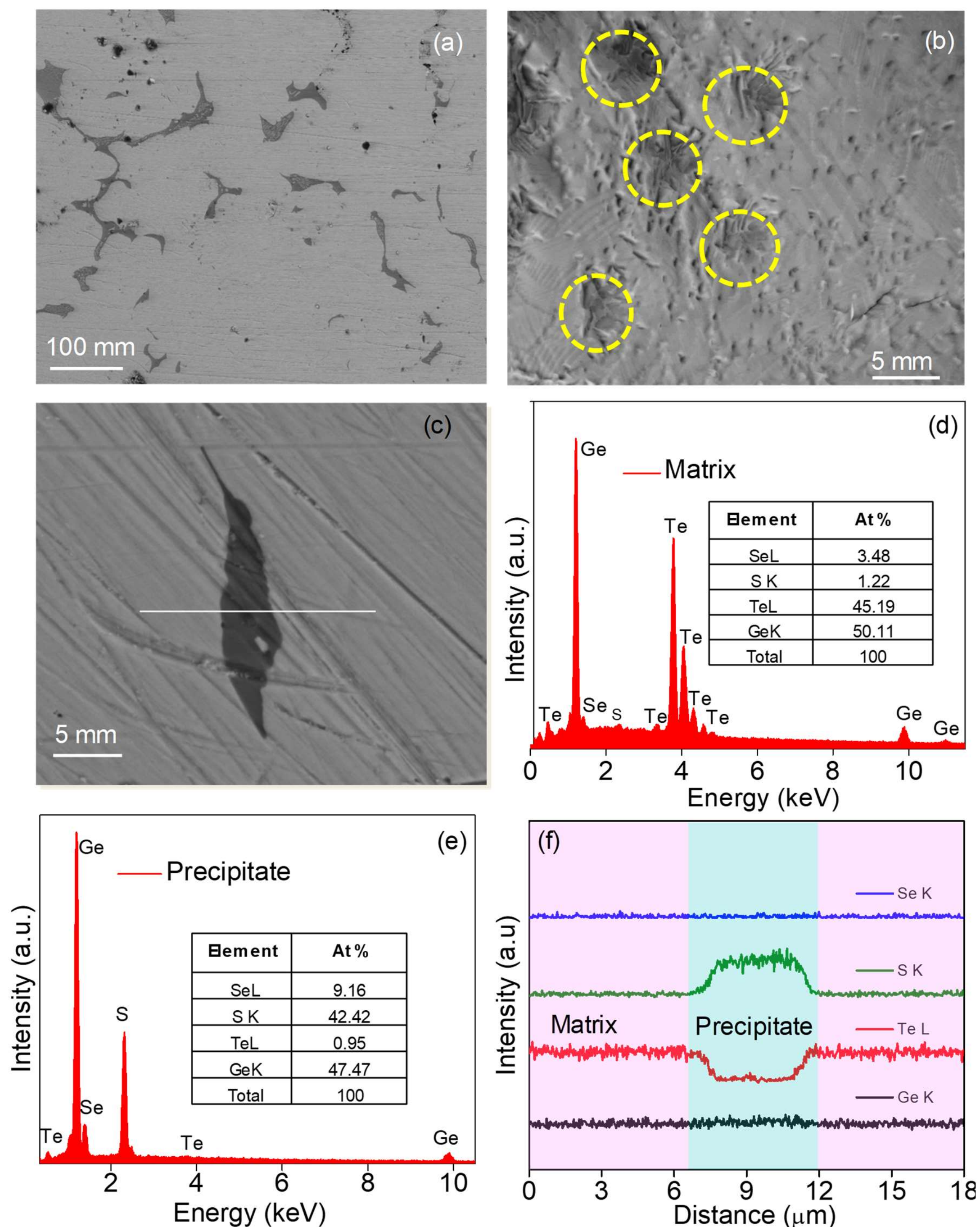

Figure 5.2. *(a)-(c) Back scattered FESEM images of different magnification from polished and rough surfaces of* $GeTe_{0.9}Se_{0.05}S_{0.05}$*, which show presence of precipitates of relatively dark contrast and large size (dotted yellow circles in image (b)). (d) & (e) EDAX of matrix and precipitate, respectively. (f) EDAX line scan along the precipitate (highlighted in image c).*

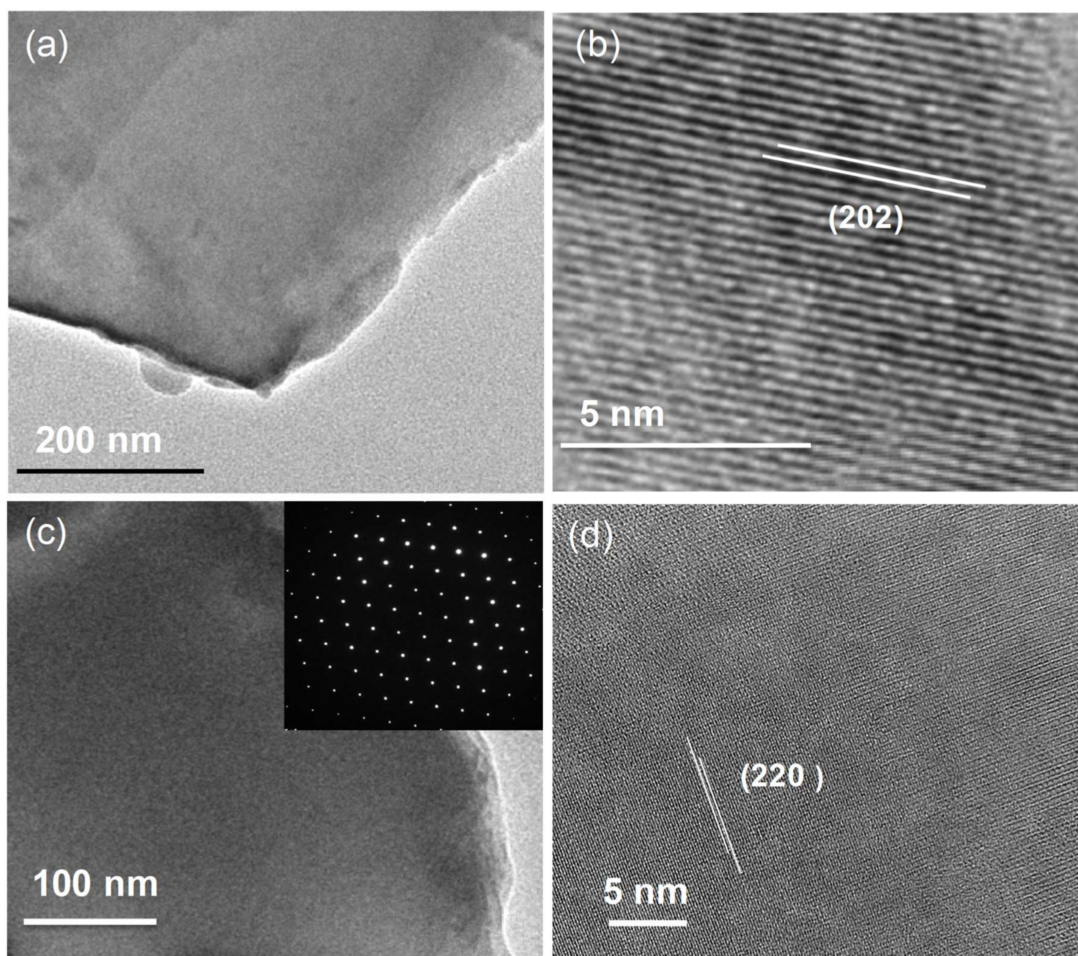

Figure 5.3. *(a) Low magnification TEM and (b) HRTEM images of* $GeTe_{0.95}Se_{0.025}S_{0.025}$ *respectively. (c) Low magnification TEM and (d) HRTEM images of* $GeTe_{0.9}Se_{0.05}S_{0.05}$ *respectively. Corresponding SAED pattern is given in the inset of (c).*

We have also performed TEM/HRTEM experiments on $GeTe_{1-2x}Se_xS_x$ (x= 0.025, 0.05) samples in order to check whether any small nanoscale precipitate present in the matrix or not. Figure 5.3a and 6.3b show representative low magnification TEM and HRTEM images of $GeTe_{0.95}Se_{0.025}S_{0.025}$, while, Figure 5.3c and 5.3d show representative low magnification TEM and HRTEM images of $GeTe_{0.9}Se_{0.05}S_{0.05}$. Calculated *d* spacing from HRTEM in Figure 5.3b is ~ 0.29 nm which corresponds to (202) planes of GeTe (*R*3*m*). Similarly calculated *d* spacing of ~ 0.2 nm from the HRTEM in Figure 5.3d is best attributed to (220) planes of GeTe. TEM images of both samples do not show presence of any small size nanoprecipitates of $GeS_{1-x}Se_x$. Selected area diffraction pattern (inset of

Figure 5.3c from the matrix does not show any additional spots which further clarifies absence of small nanoprecipitates present in the matrix when the concentration of Se/S is below x = 0.05. Thus, we believe pseudo-ternary system forms relatively bigger (5-20 μm) precipitates of $GeS_{1-x}Se_x$ in the matrix when the Se/S concentration is high in GeTe, rather than the formation of small nanoprecipitates, which are generally seen in pseudo-binary systems.

Table 5.1. *Carrier concentration and mobility values of $GeTe_{1-2x}Se_xS_x$ samples at room temperature.*

Sample	Carrier concentration (n) $\times 10^{20}$ /cm^3	Mobility (cm^2/Vs)
GeTe	8.6	58.5
$GeTe_{0.95}Se_{0.025}S_{0.025}$	7.23	49.3
$GeTe_{0.9}Se_{0.05}S_{0.05}$	7.19	48.7
$GeTe_{0.85}Se_{0.075}S_{0.075}$	7.25	40

We have estimated carrier concentration of $GeTe_{1-2x}Se_xS_x$ at room temperature by Hall measurement. Assuming single parabolic band model, carrier concentration (n) of the samples are calculated using the formula, $n = 1/eR_H$; where e is the electronic charge and R_H is the Hall coefficient. R_H for all the samples is found to be positive suggesting p-type conduction. Calculated carrier concentrations of $GeTe_{1-2x}Se_xS_x$ samples are given in Table 5.1, which suggests that carrier concentration of all the $GeTe_{1-2x}Se_xS_x$ samples are similar at room temperature because Se/S substitutes isovalently in GeTe. We have measured the band gap of $GeTe_{1-2x}Se_xS_x$ samples and found out that $GeTe_{0.95}Se_{0.025}S_{0.025}$ and $GeTe_{0.9}Se_{0.05}S_{0.05}$ samples have slightly higher band gap (Eg ~ 0.22 eV) compared to that of of GeTe (Eg ~ 0.2 eV) (Figure 5.1c). However, this small difference in band gap across the composition range is almost negligible. Considering band gap remains unaltered much for $GeTe_{1-2x}Se_xS_x$ samples studied here, it is expected that the carrier concentrations might be unaffected across the composition range at higher temperatures, which was further supported by temperature dependent Seebeck data (see below).

Temperature dependent electrical transport data of $GeTe_{1-2x}Se_xS_x$ ingot samples are shown in Figure 5.4. Electrical conductivity (σ) of the $GeTe_{1-2x}Se_xS_x$ (Figure 5.4a)

decreases with temperature depicting the behavior of degenerate semiconductor. With increase in proportions of Se and S in the GeTe, electrical conductivity of GeTe decreases. At room temperature, σ of pristine GeTe is ~ 8007 S/cm, whereas $GeTe_{0.9}Se_{0.05}S_{0.05}$ sample has σ of ~ 5600 S/cm at room temperature. On the other hand, all the samples have Seebeck coefficient of ~ 30 μV/K at room temperature (Figure 5.4b). All the $GeTe_{1-2x}Se_xS_x$ samples exhibit similar Seebeck coefficient values from room temperature to 625 K (Figure 5.4b), which further validate the occurrence of similar carrier concentration for $GeTe_{1-2x}Se_xS_x$ samples up to 625 K. With increasing the Se and S concentration in GeTe, electrical conductivities of the samples decrease originating from reduced carrier mobility due to point defect carrier scattering (Table 5.1).

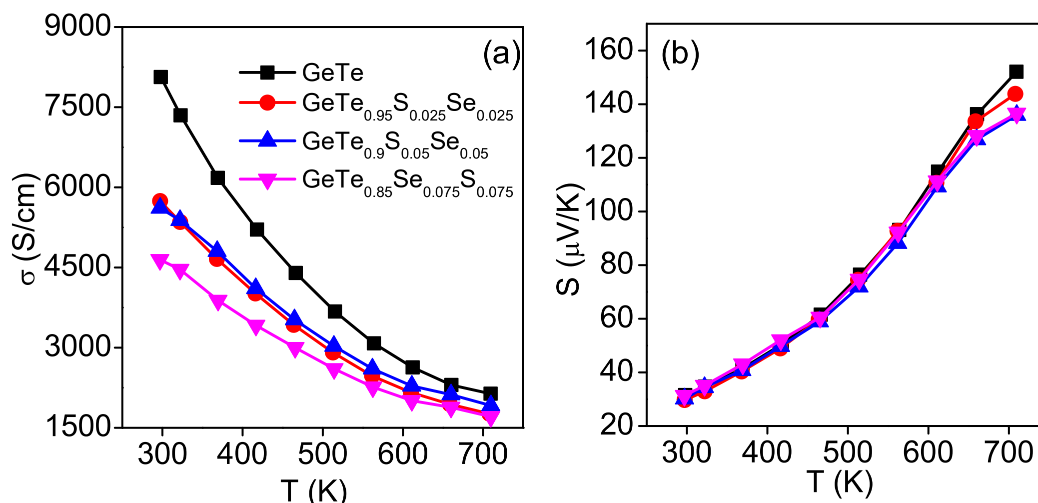

Figure 5.4. *Temperature dependent (a) electrical conductivity (σ) and (b) Seebeck coefficients (S) of $GeTe_{1-2x}Se_xS_x$ (x = 0 - 0.075) samples.*

Temperature dependent thermal transport data of $GeTe_{1-2x}Se_xS_x$ (x = 0–0.075) are illustrated in Figure 5.5. Total thermal conductivity, κ of the samples decreases with increase in Se and S content in GeTe (Figure 5.5b). For example, pristine GeTe exhibits κ of ~ 8 W/mK which decreases to 5.2 W/mK in $GeTe_{0.9}Se_{0.05}S_{0.05}$ at room temperature. Electrical thermal conductivity, κ_{el} (Figure 5.5c) was determined using Wiedemann-Franz Law, i.e. $\kappa_{el} = L\sigma T$, where L is Lorenz number. Lorenz numbers of all the samples were calculated based on fitting of respective Seebeck *vs* temperature data which was discussed elsewhere.[11] κ_{lat} of the samples were estimated by subtracting κ_{el} from κ. For all the samples, κ and κ_{lat} initially decrease with increasing in temperature and at ~ 625 K κ and κ_{lat} values

take an upward turn with the further increase in temperature. This is due to the rhombohedral to cubic structural phase transition of GeTe. With increase in Se and S concentration up to x = 0.05, κ_{lat} of $GeTe_{1-2x}Se_xS_x$ decrease, but further increase in the Se and S concentration, κ_{lat} does not decrease. At room temperature, $GeTe_{0.9}Se_{0.05}S_{0.05}$ exhibit κ_{lat} ~ 1.3 W/mK, which reaches to ~ 0.91 W/mK at 710 K.

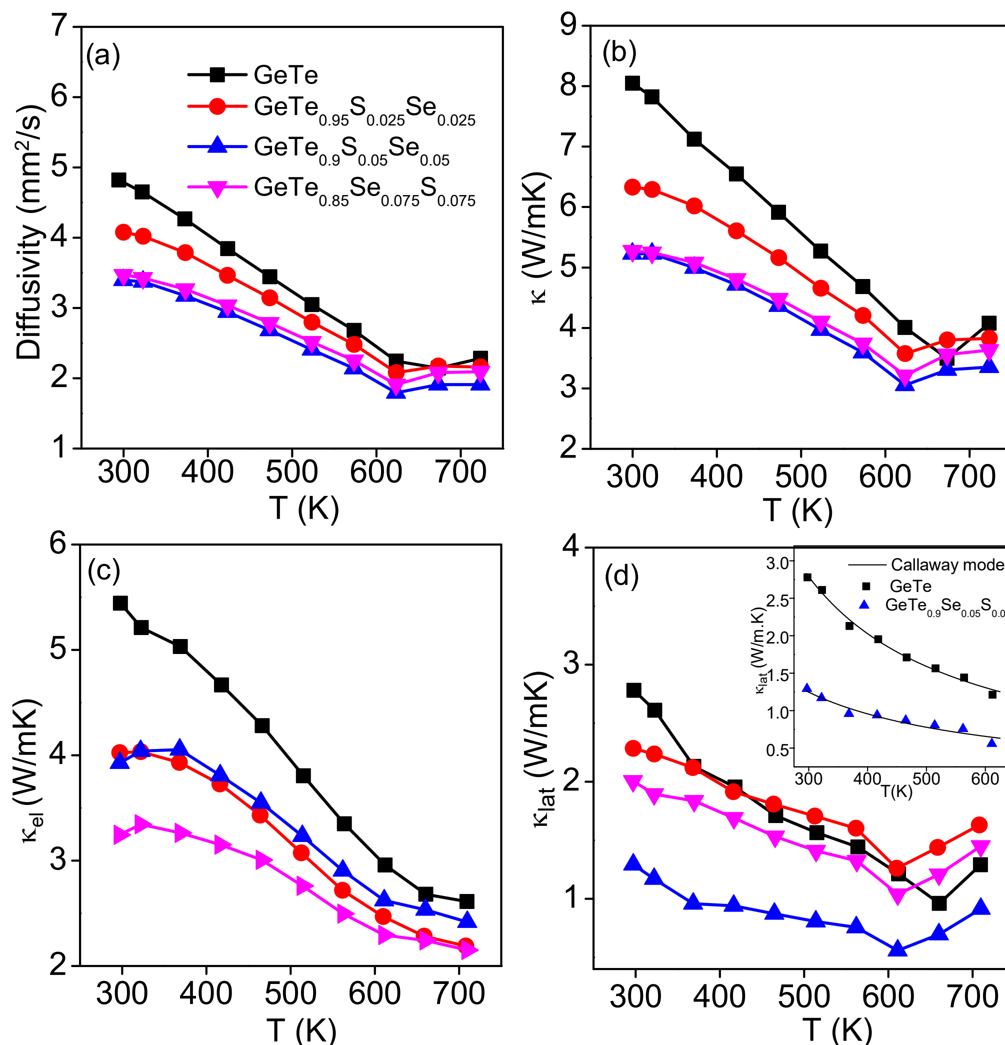

Figure 5.5. *Temperature dependent (a) thermal diffusivity, (b) total thermal conductivity (κ), (c) electrical thermal conductivity (κ_{el}) and (d) lattice thermal conductivity (κ_{lat}) of GeTe_{1-2x}Se_xS_x (x = 0-0.075) samples. Callaway model fitting of κ_{lat} of GeTe and GeTe_{0.9}Se_{0.05}S_{0.05} are given in the inset of Figure (d).*

Phonons with mean free paths smaller than 10 nm comprise ~90% of the κ_{lat} for IV-VI metal tellurides.[12] As the size of the $GeS_{1-x}Se_x$ precipitates (5-20 μm) in $GeTe_{1-x}Se_x$

matrix are much larger than heat carrying phonon's mean free path in IV-VI metal tellurides, such precipitates would not take part in phonon scattering significantly. Thus, reduction of κ_{lat} in $GeTe_{0.9}Se_{0.05}S_{0.05}$ ingot sample is mainly attributed to phonon scattering due to mass fluctuations and point defects. In order to provide further insight, we have used Callaway's model to investigate the lattice thermal conductivity in details. Thermal conductivity due to the heat transport by phonons is given by[13,14]

$$k_{lat} = \frac{k_B}{2v\pi^2}\left(\frac{2\pi k_B T}{h}\right)^3 \int_0^{\frac{\theta_D}{T}} \frac{\tau_C(x,T)x^4 e^x}{(e^x-1)^2}dx$$

Where $x = h\omega/2\pi k_B T$, ω is the phonon frequency, h is the Planck constant, θ_D is the Debye temperature, v is the velocity of sound, and τ_c is a combined relaxation time. Usually, the phonon scattering relaxation rates can be written as:

$$\tau_C^{-1} = \tau_B^{-1} + \tau_{PD}^{-1} + \tau_U^{-1} + \tau_{ep}^{-1} = \frac{v}{L} + A\omega^4 + B\omega^2 T exp\left(-\frac{\theta_D}{3T}\right) + C\omega^2$$

where L is the grain size; the coefficients A, B and C are fitting parameters; τ_B grain boundary scattering; τ_{PD} is point defect scattering; τ_U is phonon-phonon Umklapp scattering and τ_{ep} is electron–phonon scattering. At the high temperatures, the grain boundary and the electron–phonon scattering are generally ignored as they are usually effective at low temperatures.[13,14,15] Thus, we have modeled the κ_{lat} data of GeTe and $GeTe_{0.9}Se_{0.05}S_{0.05}$ considering point defect scattering and Umklapp phonon scattering, and the relaxation time can be expressed as: $\tau_C^{-1} = \tau_{PD}^{-1} + \tau_U^{-1}$. The fitted κ_{lat} data of GeTe and $GeTe_{0.9}Se_{0.05}S_{0.05}$ are plotted in the inset of Figure 3d, and the A and B parameter, derived from fitting, are provided in Table 5.2.

Table 5.2. *Callaway model fitted point defect prefactor A and Umklapp scattering prefactor B of GeTe and $GeTe_{0.9}Se_{0.05}S_{0.05}$.*

Sample	A [10^{-42} s^3]	B [10^{-17} s K^{-1}]
GeTe	1.002	1.18
$GeTe_{0.9}Se_{0.05}S_{0.05}$	13.9	2.03

As relaxation time of phonon is inversely proportional to A and B parameter, higher value of A and B will lead to shorter relaxation time and more scattering. Thus, significantly higher value of A parameter in case of $GeTe_{0.9}Se_{0.05}S_{0.05}$ compared to that of GeTe reflects that enhanced point defects scattering in $GeTe_{0.9}Se_{0.05}S_{0.05}$ is mainly responsible for the

significant reduction of κ_{lat} of $GeTe_{0.9}Se_{0.05}S_{0.05}$ compared to that of GeTe. Further, calculated phonon relaxation time due to point defects (τ_{PD}) for both GeTe and $GeTe_{0.9}Se_{0.05}S_{0.05}$ (Figure 5.6) reflects that point defects cause strong mid-high frequency phonon scattering in $GeTe_{0.9}Se_{0.05}S_{0.05}$ compared to that of pristine GeTe. This further provides a comprehensive account of the consistency between experimental observations and Callaway κ_{lat} modelling of the point defects induced phonon scattering in $GeTe_{1-2x}Se_xS_x$ system.

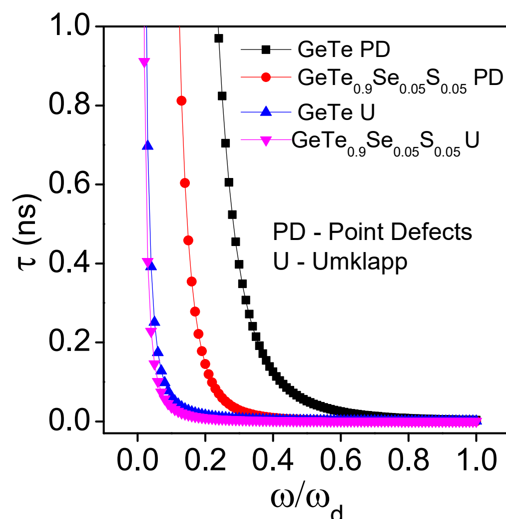

Figure 5.6. *Relaxation time versus the normalized phonon frequency of GeTe and $GeTe_{0.9}Se_{0.05}S_{0.05}$ at 300 K. The phonon frequency (ω) is normalized with respect to the Debye frequency (ω_D).*

In the second step, κ_{lat} optimized sample, $GeTe_{0.}Se_{0.05}S_{0.05}$, was alloyed with various concentration of Sb (2-10 mol %) to further improve the overall thermoelectric properties. PXRD patterns of all the Sb doped $GeTe_{0.9}Se_{0.05}S_{0.05}$ samples are shown in Figure 5.7a. All the major peaks of $Ge_{1-y}Sb_yTe_{0.9}Se_{0.05}S_{0.05}$ (y = 0-0.15) could be indexed based on rhombohedral GeTe (space group, *R3m*). Additional weak reflections in PXRD could be indexed based on the second phase of $GeS_{1-x}Se_x$ (space group, *Pnam*). With the increase in Sb concentration, cubic nature of the $Ge_{1-y}Sb_yTe_{0.9}Se_{0.05}S_{0.05}$ samples increases, which is indicated in y = 0.15 sample, where the two rhombohedral peaks of (024) and (220) between *2Θ = 41-45°* starts merging to single peak (220) of cubic phase. Similar phenomenon has earlier observed in Sb doped GeTe samples.[5]

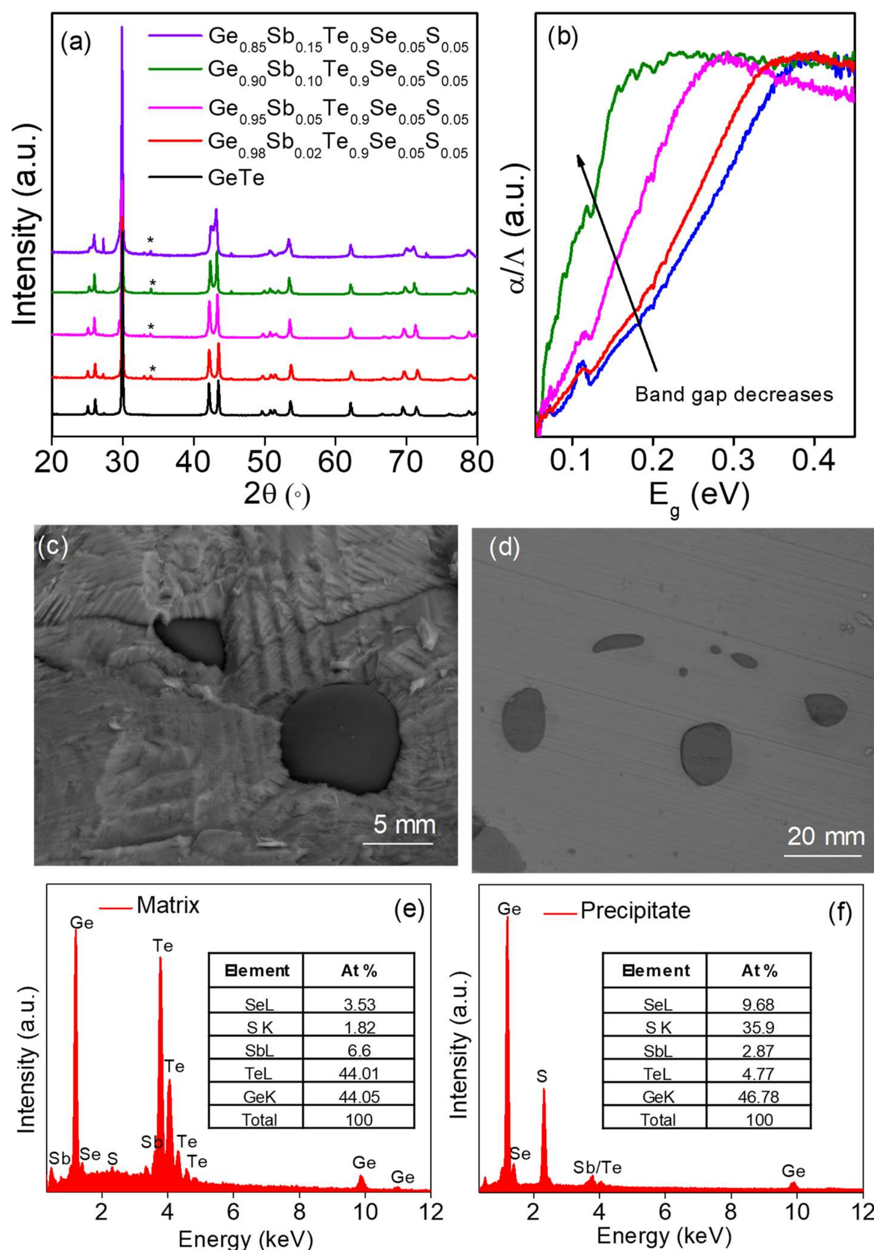

Element	At %
SeL	3.53
S K	1.82
SbL	6.6
TeL	44.01
GeK	44.05
Total	100

Element	At %
SeL	9.68
S K	35.9
SbL	2.87
TeL	4.77
GeK	46.78
Total	100

Figure 5.7. *(a) Powder XRD patterns and (b) optical absorption spectra of of $Ge_{1-y}Sb_yTe_{0.9}Se_{0.05}S_{0.05}$ (y = 0-0.15) samples. (*) Sign in PXRD signifies the presence of second phase of $GeS_{1-x}Se_x$. (c) & (d) Back scattered FESEM images of ingot $Ge_{0.9}Sb_{0.1}Te_{0.9}Se_{0.05}S_{0.05}$ from rough and polished surface. (e) & (f) EDAX spectra from matrix and precipitate, respectively.*

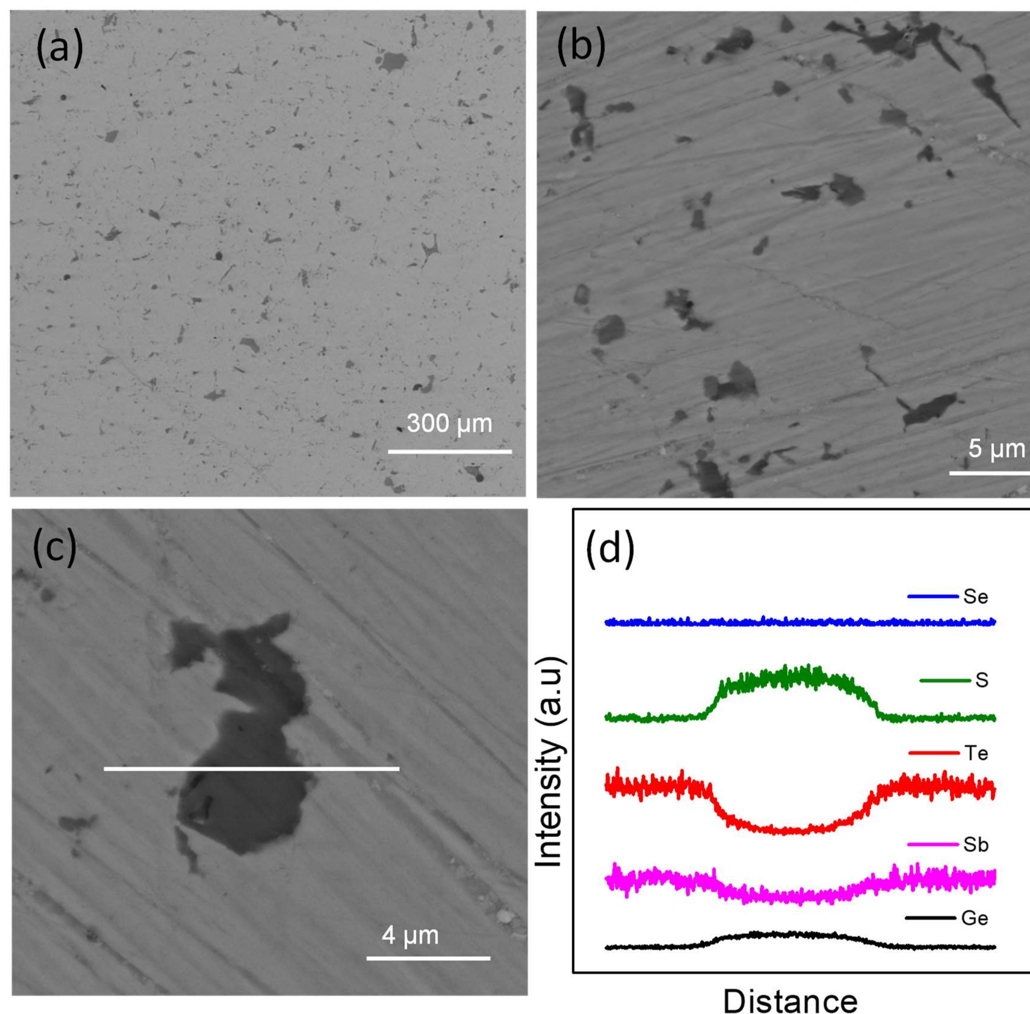

Figure 5.8. *(a)-(c) Back scattered FESEM images of different magnification from the polished surface of SPS processed* $Ge_{0.9}Sb_{0.1}Te_{0.9}Se_{0.05}S_{0.05}$ *sample, which shows presence of precipitates of relatively dark contrast. (d) EDAX line scan along the precipitate (highlighted in image c). It is evident from line scan that matrix is* $Ge_{1-y}Sb_yTe_{1-x}Se_x$ *whereas precipitate is* $GeS_{1-x}Se_x$*.*

BSE images of ingot $Ge_{0.9}Sb_{0.1}Te_{0.9}Se_{0.05}S_{0.05}$ and spark plasma sintered (SPS) $Ge_{0.9}Sb_{0.1}Te_{0.9}Se_{0.05}S_{0.05}$ samples are given Figure 5.7(c-f) and Figure 5.8, respectively. We have observed the presence of precipitates with size of 5-10 μm with darker contrast relative to that of matrix. EDAX has been performed both on precipitates and matrix, which indicates that the matrix is $Ge_{1-y}Sb_yTe_{1-x}Se_x$ (Figure 5.7e), whereas precipitate is $GeS_{1-x}Se_x$ rich (Figure 5.7f). Elemental composition of precipitates and matrix are given in the inset of Figure 5.7e and 5.7f respectively. EDAX line scanning further confirms the Sb doping

in the $GeTe_{1-x}Se_x$ matrix (Figure 5.8d) which has important role in electronic transport and thermal conductivity. As the sizes of the precipitates are comparatively larger (in the order of μm) with respect to mean free path of heat carrying phonons (in the order of nm), such precipitates would not participate significantly in phonon scattering.

Table 5.3. *Carrier concentration of $Ge_{1-y}Sb_yTe_{0.9}Se_{0.05}S_{0.05}$ samples at room temperature.*

Sample	**Carrier concentration (*n*) ×10^{20}/cm^3**
$Ge_{0.98}Sb_{0.02}Te_{0.9}Se_{0.05}S_{0.05}$	5.18
$Ge_{0.95}Sb_{0.05}Te_{0.9}Se_{0.05}S_{0.05}$	2.39
$Ge_{0.90}Sb_{0.1}Te_{0.9}Se_{0.05}S_{0.05}$	1.16
$Ge_{0.90}Sb_{0.1}Te_{0.9}Se_{0.05}S_{0.05}$ (**SPS**)	1.02
$Ge_{0.85}Sb_{0.15}Te_{0.9}Se_{0.05}S_{0.05}$	0.96

Measured carrier concentrations of $Ge_{1-y}Sb_yTe_{0.9}Se_{0.05}S_{0.05}$ samples are given in Table 5.3, which indicates that the *p*-type carrier concentration decreases with increasing the Sb concentration in $GeTe_{1-x}Se_x$. Substitution of Sb^{3+} in place of Ge^{2+} in GeTe generates one extra electron, from simple valence counting, which decreases the carrier concentration of GeTe.[5,16] Detailed EDAX study, clearly indicates that the matrix is $Ge_{1-y}Sb_yTe_{1-x}Se_x$ rich phase, which means that Sb^{+3} effectively substitutes Ge^{2+} which gives rise to reduced carrier concentration. We have observed lower carrier concentration in SPS processed samples compared to that in ingot sample with same composition (Table 5.3). This result indicates that solubility of Sb in $GeTe_{1-x}Se_x$ matrix increases after mechanical grinding and SPS processing, which may further decrease the κ_{lat} due to enhanced solid solution point defect phonon scattering.

Temperature dependent electrical transport data for both ingot and SPS samples of $Ge_{1-y}Sb_yTe_{0.9}Se_{0.05}S_{0.05}$ (y=0-0.15) are shown in Figure 5.9. With increase in concentration of Sb, electrical conductivity of the samples decreases drastically (Figure 5.9a) because of significant decrease in carrier concentration (Table 5.3). $GeTe_{0.9}Se_{0.05}S_{0.05}$ has σ of 5600 S/cm at 300 K, which reaches to 1915 S/cm at 715 K ; whereas $Ge_{0.9}Sb_{0.1}Te_{0.9}Se_{0.05}S_{0.05}$ has σ of 1000 S/cm at 300K, which decreases to ~ 550 S/cm at 709K. In addition, SPS

processed $Ge_{0.9}Sb_{0.1}Te_{0.9}Se_{0.05}S_{0.05}$ sample exhibits lower σ ~ 684 S/cm (at 300 K) compared to that of ingot because of lower *p*-type carrier concentration in SPS sample.

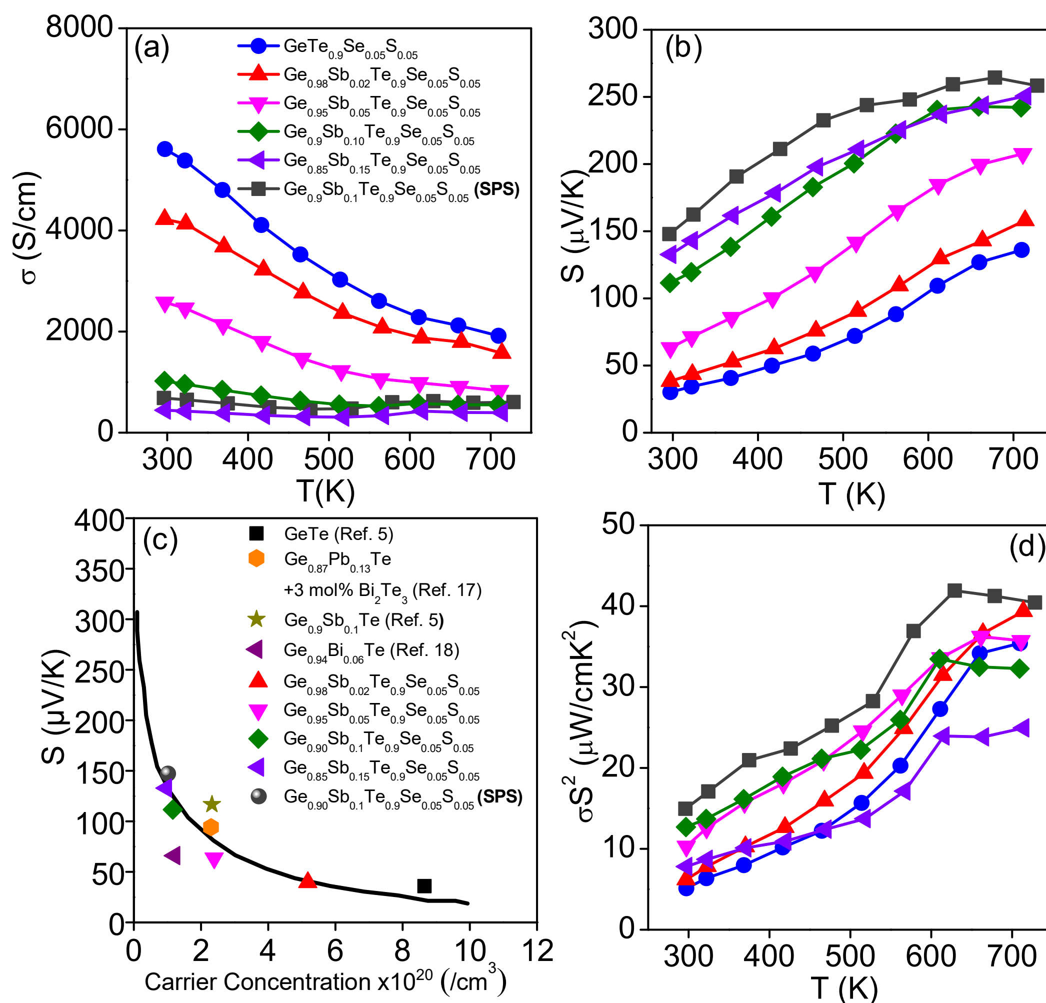

Figure 5.9. *Temperature dependent (a) electrical conductivity (σ) and (b) Seebeck coefficient (S) of* $Ge_{1-y}Sb_yTe_{0.9}Se_{0.05}S_{0.05}$ *(y = 0-0.15) samples. (c) Room temperature S vs n data of* $Ge_{1-y}Sb_yTe_{0.9}Se_{0.05}S_{0.05}$ *along with the Pisarenko plot of GeTe.*[5,17,18] *(d) Variation of power factor* (σS^2) *with temperature of the* $Ge_{1-y}Sb_yTe_{0.9}Se_{0.05}S_{0.05}$ *(y = 0-0.15) samples.*

Temperature dependent Seebeck coefficients of the $Ge_{1-y}Sb_yTe_{0.9}Se_{0.05}S_{0.05}$ (x = 0-0.15) samples are shown in Figure 5.9b. Seebeck coefficients of the $Ge_{1-y}Sb_yTe_{0.9}Se_{0.05}S_{0.05}$ samples gradually increase with increase in Sb concentration. The enhancement of Seebeck with increase in Sb concentration could be attributed due to reduced carrier density (Table 5.3), which is further verified by plotting Pisarenko relation.[5,17,18] For all the samples, at room temperature, Seebeck values fall close to the Pisarenko line (Figure 5.9c) which

actually ruling out the possibility of valence band convergence as reason of enhancement of Seebeck coefficient. Ingot of $Ge_{0.9}Sb_{0.1}Te_{0.9}Se_{0.05}S_{0.05}$ and SPS processed $Ge_{0.9}Sb_{0.1}Te_{0.9}Se_{0.05}S_{0.05}$ exhibit Seebeck values of 113 μV/K and 148 μV/K at 300 K, which increases to 242 μV/K at 709 K and 259 μV/K at 728K, respectively. SPS processed sample exhibit higher Seebeck compared to ingot because of lower *p*-type carrier concentration in SPS sample. Higher concentration of Sb doping shows the effect of bipolar conduction in the Seebeck data at high temperatures (Figure 5.9b), which is mainly due to the decrease in the band gap of $GeTe_{0.}Se_{0.05}S_{0.05}$ after Sb alloying (Figure 5.7b).[5]

Temperature dependent power factor, σS^2 of the $Ge_{1-y}Sb_yTe_{0.9}Se_{0.05}S_{0.05}$ (y = 0-0.15) samples are presented in Figure 5.9d. Ingot of $Ge_{0.9}Sb_{0.1}Te_{0.9}Se_{0.05}S_{0.05}$ has power factor ~ 13 $\mu W/cmK^2$ at 300 K which increases to ~32 $\mu W/cm.K^2$ at 709 K, but SPS processed $Ge_{0.9}Sb_{0.1}Te_{0.9}Se_{0.05}S_{0.05}$ sample exhibits power factor of ~ 15 $\mu W/cmK^2$ at 300 K which reaches to ~ 40.5 $\mu W/cm.K^2$ at 728 K. The reason of enhancement of power factor of SPS processed $Ge_{0.9}Sb_{0.1}Te_{0.9}Se_{0.05}S_{0.05}$ sample compared to ingot is solely attributed to the enhanced Seebeck coefficient of SPS processed $Ge_{0.9}Sb_{0.1}Te_{0.9}Se_{0.05}S_{0.05}$ sample.

Figure 5.10a shows temperature dependent total thermal conductivity (κ) of $Ge_{1-y}Sb_yTe_{0.9}Se_{0.05}S_{0.05}$ (y = 0-0.15) samples. A significant reduction in κ is achieved by Sb alloying in $GeTe_{0.9}Se_{0.05}S_{0.05}$. κ value of $GeTe_{0.9}Se_{0.05}S_{0.05}$ is ~ 5.2 W/mK which is suppressed to ~ 1.29 W/mK in $Ge_{0.85}Sb_{0.15}Te_{0.9}Se_{0.05}S_{0.05}$ at room temperature, which remains almost same in 300 –700 K temperature range. κ of the all samples shows an anomaly at 620 K, which is due to structural phase transition of GeTe. Lattice thermal conductivity (κ_{lat}) of all the samples are obtained by subtracting the κ_{el} (Figure 5.10b) from total κ (Figure 5.10a). Among all the ingot samples, $Ge_{0.9}Sb_{0.1}Te_{0.9}Se_{0.05}S_{0.05}$ shows lowest κ_{lat} ~ 0.9 W/mK at room temperature (Figure 5.10c). Sb doping in $GeTe_{0.9}Se_{0.05}S_{0.05}$ further increases the point defect concentration, thereby decreases the κ_{at} compared to the undoped $GeTe_{0.9}Se_{0.05}S_{0.05}$. SPS processed $Ge_{0.9}Sb_{0.1}Te_{0.9}Se_{0.05}S_{0.05}$ sample shows further decreased κ_{lat} (0.7 W/mK at 728 K) compared to that of the ingot of $Ge_{0.9}Sb_{0.1}Te_{0.9}Se_{0.05}S_{0.05}$ sample (inset of Figure 5.10c). κ_{lat} of SPS processed $Ge_{0.9}Sb_{0.1}Te_{0.9}Se_{0.05}S_{0.05}$ sample remains flat throughout the temperature range of 300 -730K.

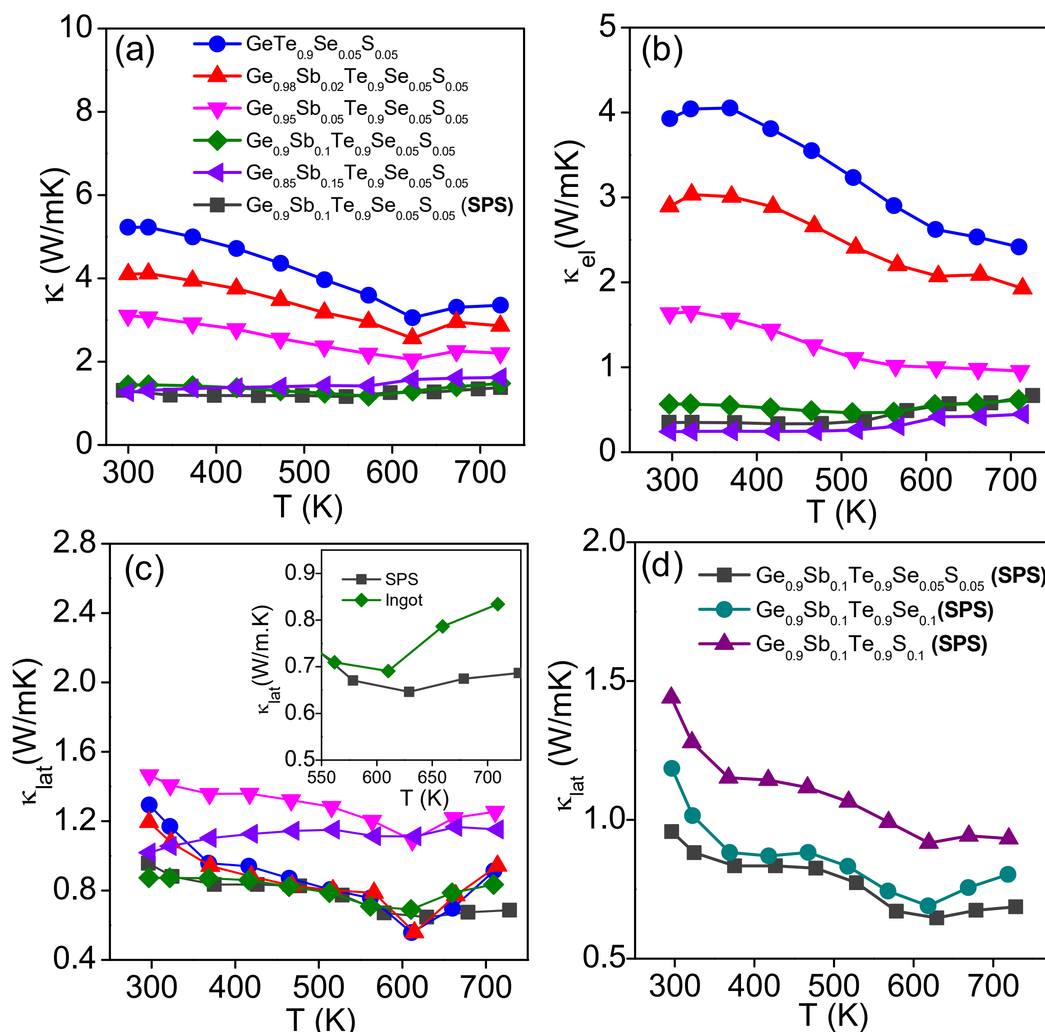

***Figure 5.10**. Temperature dependent (a) total thermal conductivity (κ), (b) electrical thermal conductivity (κ_{el}) and (c) lattice thermal conductivity (κ_{lat}) of $Ge_{1-y}Sb_yTe_{0.9}Se_{0.05}S_{0.05}$ (y = 0-0.15) samples. Inset shows decrease of κ_{lat} for SPS processed $Ge_{0.9}Sb_{0.1}Te_{0.9}Se_{0.05}S_{0.05}$ sample compared to ingot $Ge_{0.9}Sb_{0.1}Te_{0.9}Se_{0.05}S_{0.05}$ sample. (d) Comparison plot of the κ_{lat} for SPS processed $Ge_{0.9}Sb_{0.1}Te_{0.9}Se_{0.05}S_{0.05}$, $Ge_{0.9}Sb_{0.1}Te_{0.9}Se_{0.1}$ and $Ge_{0.9}Sb_{0.1}Te_{0.9}S_{0.1}$ samples.*

In order to compare the κ_{lat} between pseudo-ternary (GeTe-GeSe-GeS) and pseudo-binary (GeTe-GeSe and GeTe-GeS) systems, we have measured κ_{lat} of SPS processed $Ge_{0.9}Sb_{0.1}Te_{0.9}Se_{0.05}S_{0.05}$, $Ge_{0.9}Sb_{0.1}Te_{0.9}Se_{0.1}$ and $Ge_{0.9}Sb_{0.1}Te_{0.9}S_{0.1}$ samples (Figure 5.10d). $Ge_{0.9}Sb_{0.1}Te_{0.9}Se_{0.05}S_{0.05}$ exhibits lowest κ_{lat} among them. Thus, lower κ_{lat} in SPS processed $Ge_{0.9}Sb_{0.1}Te_{0.9}Se_{0.05}S_{0.05}$ sample can be accounted due to significant phonon scattering by enhanced point defects involving a broad set of multiple types of mass

fluctuations both in cation and anion sites of GeTe such as Ge/Sb, Te/Se, Te/S and Se/S. Undoubtedly, the GeTe-GeSe-GeS system is important to study the competition between entropically driven atomic mixing (solid solution) and enthalpy driven phase separation.

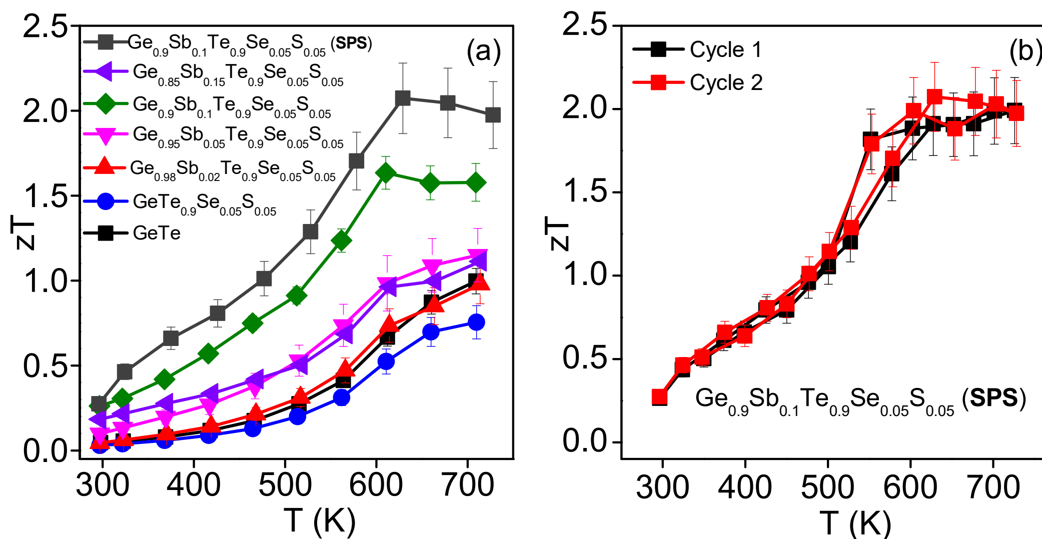

***Figure 5.11**. (a) Thermoelectric figure of merit (zT) of $Ge_{1-y}Sb_yTe_{0.9}Se_{0.05}S_{0.05}$ (y = 0-0.15) samples. (b) zT of $Ge_{0.9}Sb_{0.1}Te_{0.9}Se_{0.05}S_{0.05}$ (SPS) sample is reversible and reproducible over temperature cycles.*

Temperature dependent figure of merit (zT) of all the samples $Ge_{1-y}Sb_yTe_{0.9}Se_{0.05}S_{0.05}$ (y = 0-0.15) are presented in Figure 5.11a. Ingot sample of $Ge_{0.9}Sb_{0.1}Te_{0.9}Se_{0.05}S_{0.05}$ exhibits highest zT ~ 1.65 at 610 K which is 180% higher compared to pristine GeTe. Moreover, SPS processed $Ge_{0.9}Sb_{0.1}Te_{0.9}Se_{0.05}S_{0.05}$ sample exhibit significantly high zT of 2.1 at 630 K. This enhancement of zT of $Ge_{0.9}Sb_{0.1}Te_{0.9}Se_{0.05}S_{0.05}$ is attributed to the significant reduction of lattice thermal conductivity compared to pristine GeTe. zT of SPS processed $Ge_{0.9}Sb_{0.1}Te_{0.9}Se_{0.05}S_{0.05}$ shows reversibility and temperature stability after two heating-cooling cycle (Figure 5.11b).

A thermoelectric material should possess good mechanical stability along with high zT. In order to have essence of mechanical stability, Vickers microhardness of $Ge_{0.9}Sb_{0.1}Te_{0.9}Se_{0.05}S_{0.05}$ is measured which is found to be ~ 186 Hv (kgf/mm^2), which is higher than that of pristine GeTe (H_v value of ~ 143). Sb doping in $GeTe_{1-2x}Se_xS_x$ reduces Ge- vacancies, thus increases the mechanical stability of the material. Moreover, formation of GeS-rich micro-precipitates and enhanced atomic mixing in Sb doped $GeTe_{1-2x}Se_xS_x$

inhibit the propagation of micro/nano-cracks, which in turn helps to improve the mechanical stability of Sb doped $GeTe_{1-2x}Se_xS_x$ compared to pristine GeTe. A comparison of H_v value of $Ge_{0.9}Sb_{0.1}Te_{0.9}Se_{0.05}S_{0.05}$ along with different state of art thermoelectric materials are presented in Figure 5.12. [5,18–25]

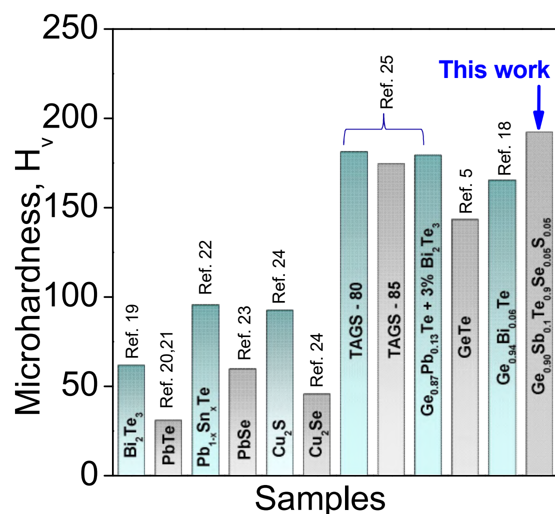

***Figure 5.12**. Histogram representing Vickers microhardness value of $Ge_{0.9}Sb_{0.1}Te_{0.9}Se_{0.05}S_{0.05}$ along with other state of art thermoelectric materials.* [5,18–25]

5.4 Conclusions

Although the extent of any investigation of the $(GeTe)_{1-2x}(GeSe)_x(GeS)_x$ system is huge due to vast compositional scope; here, we have demonstrated an initial exploration and analysis of thermoelectric properties of *p*-type GeTe rich compositions with equimolar fraction of GeSe and GeS. While with lower concentration of Se and S in GeTe, the system is solid solution, but with higher concentration of Se and S, the system becomes phase separated with occurrence of $GeS_{1-x}Se_x$ big precipices (5-20 μm) in $GeTe_{1-x}Se_x$ matrix. Solubility of Se is much higher compared to S in GeTe due to large mismatch in size between Te and S. The pseudoternary system's assumed higher entropy may favor a disordered solid solution rather than conventional nanostructuring. Our study uncovered a very low lattice thermal conductivity (0.7 W/mK at 730K) in SPS processed $Ge_{0.9}Sb_{0.1}Te_{0.9}Se_{0.05}S_{0.05}$, where phonon scattering mainly occurs due to effective point defect scattering involving a broad set of multiple types of mass fluctuations such as Ge/Sb, Te/Se, Te/S and Se/S. As a result a remarkably high zT of 2.1 is achieved in SPS processed

$Ge_{0.9}Sb_{0.1}Te_{0.9}Se_{0.05}S_{0.05}$ sample at 630 K. Moreover, Sb doped $(GeTe)_{1-2x}(GeSe)_x(GeS)_x$ samples exhibit higher mechanical stability than that of pristine GeTe.

5.5 References

(1) Roychowdhury, S.; Samanta, M.; Perumal, S.; Biswas, K. *Chem. Mater.* **2018**, *30*, 5799–5813.
(2) Perumal, S.; Roychowdhury, S.; Biswas, K. *J. Mater. Chem. C* **2016**, *4*, 7520–7536.
(3) Hong, M.; Zou, J.; Chen, Z. *Adv. Mater.* **2019**, *31*, 1807071.
(4) Samanta, M.; Roychowdhury, S.; Ghatak, J.; Perumal, S.; Biswas, K. *Chem. - A Eur. J.* **2017**, *23*, 7438–7443.
(5) Perumal, S.; Roychowdhury, S.; Negi, D. S.; Datta, R.; Biswas, K. *Chem. Mater.* **2015**, *27*, 7171–7178.
(6) Korkosz, R. J.; Chasapis, T. C.; Lo, S.; Doak, J. W.; Kim, Y. J.; Wu, C.-I.; Hatzikraniotis, E.; Hogan, T. P.; Seidman, D. N.; Wolverton, C.; Dravid, V. P.; Kanatzidis, M. G. *J. Am. Chem. Soc.* **2014**, *136*, 3225–3237.
(7) Yamini, S. A.; Mitchell, D. R. G.; Gibbs, Z. M.; Santos, R.; Patterson, V.; Li, S.; Pei, Y. Z.; Dou, S. X.; Jeffrey Snyder, G. *Adv. Energy Mater.* **2015**, *5*, 1501047.
(8) Perumal, S.; Samanta, M.; Ghosh, T.; Shenoy, U. S.; Bohra, A. K.; Bhattacharya, S.; Singh, A.; Waghmare, U. V.; Biswas, K. *Joule* **2019**, *3*, 2565–2580.
(9) Li, J.; Zhang, X.; Lin, S.; Chen, Z.; Pei, Y. *Chem. Mater.* **2017**, *29*, 605–611.
(10) Yang, L.; Li, J. Q.; Chen, R.; Li, Y.; Liu, F. S.; Ao, W. Q. *J. Electron. Mater.* **2016**, *45*, 5533–5539.
(11) Biswas, K.; He, J.; Blum, I. D.; Wu, C.-I.; Hogan, T. P.; Seidman, D. N.; Dravid, V. P.; Kanatzidis, M. G. *Nature* **2012**, *489*, 414–418.
(12) Lee, S.; Esfarjani, K.; Luo, T.; Zhou, J.; Tian, Z.; Chen, G. *Nat. Commun.* **2014**, *5*, 3525.
(13) Shi, X.; Pei, Y.; Snyder, G. J.; Chen, L. *Energy Environ. Sci.* **2011**, *4*, 4086.
(14) Callaway, J. *Phy. Rev.* **1960,** *120*, 1149–1154.
(15) Glassbrenner, C. J.; Slack, G. A. *Phys. Rev.* **1964**, *134*, A1058–A1069.
(16) Hoang, K.; Mahanti, S. D.; Kanatzidis, M. G. *Phys. Rev. B* **2010**, *81*, 115106.
(17) Wu, D.; Zhao, L.-D.; Hao, S.; Jiang, Q.; Zheng, F.; Doak, J. W.; Wu, H.; Chi, H.; Gelbstein, Y.; Uher, C.; Wolverton, C.; Kanatzidis, M.; He, J. *J. Am. Chem. Soc.* **2014**, *136*, 11412–11419.
(18) Perumal, S.; Roychowdhury, S.; Biswas, K. *Inorg. Chem. Front.* **2016**, *3*, 125–132.
(19) Zhao, L. D.; Zhang, B. P.; Li, J. F.; Zhou, M.; Liu, W. S.; Liu, J. *J. Alloys Compd.* **2008**, *455*, 259–264.
(20) Gelbstein, Y.; Gotesman, G.; Lishzinker, Y.; Dashevsky, Z.; Dariel, M. P. *Scr. Mater.* **2008**, *58*, 251–254.
(21) Crocker, A. J.; Wilson, M. *J. Mater. Sci.* **1978**, *13*, 833–842.
(22) Cui, J. .; Qian, X.; Zhao, X. . *J. Alloys Compd.* **2003**, *358*, 228–234.
(23) Darrow, M. S.; White, W. B.; Roy, R. *J. Mater. Sci.* **1969**, *4*, 313–319.
(24) Zhao, L.; Wang, X.; Fei, F. Y.; Wang, J.; Cheng, Z.; Dou, S.; Wang, J.; Snyder, G. J. *J. Mater. Chem. A* **2015**, *3*, 9432–9437.
(25) Davidow, J.; Gelbstein, Y. *J. Electron. Mater.* **2013**, *42*, 1542–1549.

PART 3

Thermoelectric Properties of Topological Quantum Materials

Chapter 1

Localized Vibrations of Bi Bilayer Leading to Ultralow Lattice Thermal Conductivity and High Thermoelectric Performance in Weak Topological Insulator *n*-type BiSe

Chapter 1

Localized Vibrations of Bi Bilayer Leading to Ultralow Lattice Thermal Conductivity and High Thermoelectric Performance in Weak Topological Insulator *n*-type BiSe†

Summary

Realization of high thermoelectric performance in n-type semiconductors is of imperative need on account of the dearth of efficient n-type thermoelectric materials compared to the p-type counterpart. Moreover, development of efficient thermoelectric materials based on Te-free compound is desirable because of the scarcity of Te in the earth crust. Herein, we report the intrinsic ultralow thermal conductivity and high thermoelectric performance near room temperature in n-type BiSe, a Te-free solid, which recently has emerged as a weak topological insulator. BiSe possesses a layered structure consisting of a bismuth bilayer (Bi_2) sandwiched between two Bi_2Se_3 quintuple layers [Se-Bi-Se-Bi-Se], resembling natural heterostructure. High thermoelectric performances of BiSe is realized through the ultralow lattice thermal conductivity (κ_{lat} of ~ 0.6 W/mK at 300 K), which is significantly lower than that of Bi_2Se_3 (κ_{lat} of ~ 1.8 W/mK at 300 K), although both of them belong to the same layered homologous family $(Bi_2)_m(Bi_2Se_3)_n$. Phonon dispersion calculated from first principles and the experimental low-temperature specific heat data indicate that soft localized vibrations of bismuth bilayer in BiSe are responsible for its ultralow κ_{lat}. These low energy optical phonon branches couple strongly with the heat carrying acoustic phonons, and consequently suppress the phonon mean free path leading to low κ_{lat}. Further optimization of thermoelectric properties of BiSe through Sb substitution and spark plasma sintering (SPS) results in high zT ~ 0.8 at 425 K along the pressing direction, which is indeed remarkable among Te-free n-type thermoelectric materials near room temperature.

†*Paper based on this study has been published in J. Am. Chem. Soc.* **2018**, *140,* 5866-5872.

1.1 Introduction

Minimization of the thermal conductivity and understanding the governing phonon-transport mechanism in solids are of paramount importance for the improvement of performance of thermoelectric materials.[1–3] Conflicting interdependency among the Seebeck coefficient (S), electrical conductivity (σ) and electrical thermal conductivity (κ_{el}) leave the only choice of tuning of the lattice thermal conductivity (κ_{lat}) independently to enhance the material's thermoelectric figure of merit. While the traditional approaches such as extrinsic solid solution alloying and nano/meso-structuring have been proven to effectively reduce κ_{lat},[4–6] but these approaches are detrimental to the electrical mobility. Thus, materials with *intrinsically* low κ_{lat} are practically desirable as they offer nearly independent control over the electronic transport.[7]

Exploring new solids with *intrinsic* low κ_{lat} and uncovering its origin are essential to design, engineer and improve the performance of thermoelectric materials. Random rattling of a guest atom in the hollow cage of skutterudites and clathrates, are effective in scattering phonons, thereby lowering the κ_{lat}.[8,9] Zintl compounds with partly rigid covalent and weakly bound ionic sub-structures,[10] along with intrinsic rattling of selective sub-lattice yield a low κ_{lat}.[11,12] Thermal damping effects due to liquid-like cation dynamics in Cu_3SbSe_3, Cu_2Se and $AgCrSe_2$ also resulted in low κ_{lat}.[13–16] High degree of lattice anharmonicity arising from ns^2 lone pair of group V element in I-V-VI_2 chalcogenides[17,18] and layered structure in SnSe[19] give rise to ultra-low κ_{lat}. To design new materials with unique structural attributes and intrinsically low lattice thermal conductivity, identification of the correlations between thermal transports, lattice dynamics and chemical bonding has remained an important and challenging problem in chemistry.

Conventional 3D topological insulator (TI, like Bi_2Se_3 and Bi_2Te_3)[20,21] and topological crystalline insulator (TCI, e.g. SnTe)[22,23] are considered as potential thermoelectric materials due to their superior electronic transport properties.[24–33] Weak topological insulator is a new quantum state of matter which arises in a stack of 2D TI layers with even number of Dirac cones on the side surfaces.[34,35] Weak topological insulators generally form layered structure consisting of the stacks of topologically nontrivial quantum spin Hall layers, possibly separated by topologically trivial normal insulating layers. Thus they can be potentially good thermoelectric material with minimum

lattice thermal conductivity.[36,37] BiSe, a member of the homologous series $(Bi_2)_m(Bi_2Se_3)_n$ (where m:n = 1:2),[38] is recently discovered to be a weak topological insulator.[39]

BiSe possesses a layered crystal structure consisting of a bismuth bilayer (Bi_2) sandwiched between two Bi_2Se_3 quintuple [Se-Bi-Se-Bi-Se] layers (Figure 1.1a): essentially a natural heterostructure. Unlike other weak topological insulators (eg. $Bi_{14}Rh_3I_9$ and Bi_2TeI),[36,40,41] the spacer layer (i.e. the bismuth bilayer) in BiSe, which separates the quantum spin Hall layers (i.e. Bi_2Se_3 quintuple layers), is topologically nontrivial.[39] Although Bi_2Se_3, a strong topological insulator, is recognized as a decent thermoelectric material,[24,25,30] the additional anisotropy in BiSe arising from the presence of extra bismuth bilayer (Bi_2 layer, Figure 1a) is expected to play an important role in lattice thermal conduction.

Herein, we establish the ultralow κ_{lat} of ~0.6 W/mK in a wide temperature range of 300-650 K and high thermoelectric performance in *n*-type BiSe, a Te-free weak topological insulator. Although BiSe (m:n = 1:2) and Bi_2Se_3 (m:n = 0:1) belongs to the same layered homologous series $(Bi_2)_m(Bi_2Se_3)_n$ (Figure 1a), crystalline ingot of BiSe exhibits significantly lower κ_{lat} compared to that of the ingot of Bi_2Se_3; indicating the role of topologically nontrivial Bi bilayer in BiSe in reducing the κ_{lat} down to its theoretical minimum (κ_{min}). We have investigated the aspects of the structure and lattice dynamics that are responsible for the unusually low κ_{lat} in BiSe through measurements of low temperature heat capacity and first-principles density functional theoretical (DFT) calculations of its phonon dispersion. Localized vibrations of Bi_2 layers in BiSe constitute low-lying optical phonon branches which couple with heat carrying acoustic phonons leading to suppressed phonon group velocities as well as mean free path, thereby giving an ultra-low κ_{lat} of BiSe. Interestingly, BiSe exhibits *n*-type electronic conduction and superior electronic transport properties compared to Bi_2Se_3, which are further supported by the electronic structure obtained from first-principles calculation. We have optimized and measured the anisotropic thermoelectric properties of Sb substituted and spark plasma sintered (SPS) $Bi_{1-x}Sb_xSe$, which demonstrates significantly high zT of 0.8 at 425 K in *n*-type $Bi_{0.7}Sb_{0.3}Se$ (along the SPS pressing direction), which marks a remarkable advance in the development of the Te-free *n*-type thermoelectrics for near room temperature applications.

1.2 Methods

1.2.1 Reagents. Bismuth (SRL chemicals, 99.99%), antimony (Alfa Aesar 99.9999%) and selenium (Alfa Aeser 99.9999%) were used for synthesis without further purification.

1.2.2 Synthesis. First, ingots (~6 g) of BiSe and $Bi_{1-x}Sb_xSe$ (x= 0-0.3) were synthesized by mixing stoichiometric amounts of high purity starting materials of Bi, Sb and Se in quartz ampoules. The tubes were sealed under vacuum (10^{-6} Torr) and were slowly heated to 723 K and then to 1123 K over a time period of 12 hours and 5 hours respectively, then soaked for 6 h, and cooled slowly to 893 K and annealed it for 6 hours and then cooled to room temperature over 8 h. In order to measure the electrical and thermal transport properties, ingots were cut in the shape of bar and coin respectively and polished. As BiSe possesses anisotropic layered rhombohedral structure (Figure 1a), we have measured the directional thermoelectric properties of spark plasma sintered (SPS) samples. The as-synthesized ingots were powder crushed and grounded using a mortar and pestle. The powders were then loaded into a graphite die of 10 mm diameter and compacted before placing the die assembly into a SPS system (SPS211-LX, Dr. Sinter Lab). The sintering-system was first evacuated to 10^{-3} Torr and then the powders were consolidated by pulsed electric current sintering at 723 K for 5 minutes under an axial pressure of 40 MPa. The SPS processed cylindrical shaped sample is cut and polished for further electrical and thermal transport measurement.

1.2.3 Powder X-ray diffraction. Powder X-ray diffractions for all synthesized samples were recorded using a Cu K_α (λ = 1.5406 Å) radiation source on a Bruker D8 diffractometer.

1.2.4 Electrical transport. Electrical conductivity and Seebeck coefficients were measured simultaneously under a helium atmosphere from room temperature to 650 K on a ULVAC-RIKO ZEM-3 instrument system. The typical sample for measurement had a parallelepiped shape with the dimensions of ~2×2×8 mm^3. Electrical and thermal properties are always measured in the same direction for all the samples.

1.2.5 Hall measurement. Hall measurement of all the samples was carried out in a setup developed by Excel instrument, where the variable magnetic field of 0-0.55 T and dc-current of 100 mA were used at room temperature.

1.2.6 Thermal conductivity. Thermal diffusivity, *D*, was directly measured in the range 300−650 K by using the laser flash diffusivity method in a Netzsch LFA-457 under nitrogen atmosphere. Coin/square shaped samples were coated with a thin layer of graphite to avoid errors coming from thermal emissivity of the materials. Temperature dependent (300-650) heat capacity, C_p of BiSe is derived using the standard sample (pyroceram) in LFA-457, which is in good agreement with Dulong-Petit C_p value. The total thermal conductivity, κ, was estimated using the formula $\kappa = DC_p\rho$, where D is thermal diffusivity of the sample, ρ is the density (~97 % theoretical density).

1.2.7 Heat capacity. Low temperature (2-200K) specific heat of BiSe is measured in Physical Property Measurement System (PPMS).

1.2.8 Computational methods. This part of the work has been perfomed in collaboration with Prof. Umesh V. Waghmare's group in JNCASR, India. Our first-principles calculations are based on density functional theory (DFT) as implemented in Quantum Espresso (QE),[42] that employs the pseudo-potential model for the interaction between ionic core (nucleus and core electrons) and valence electrons in an atom. We used norm-conserving pseudopotentials here treating exchange and correlation energy of the electrons with a generalized gradient approximated (GGA)[43] functional parameterized by Perdew, Burke and Ernzerhof.[44] Expansions of electronic wave functions and charge density inplane wave basis were truncated with cut-off energies of 60 Ry and 240 Ry respectively. Integrations over Brillouin Zone (BZ) of rhombohedral and hexagonal crystal structures were sampled on the uniform meshes of 8×8×8 and 12×12×2 k-points respectively. The discontinuity in occupations number of electronic states across the gap was smeared with Fermi-Dirac distribution function with a broadening of $k_BT = 0.003$ Ry. We determined the electronic structure and phonon dispersion properties of BiSe (a = 4.212 Å and c = 22.942Å) and Bi_2Se_3 (a=4.135 Å and c=28.64 Å) at their experimental lattice constants.[45] We used density functional perturbation theory (DFPT)[46] to obtain phonon dispersion of these compounds. In this, the interatomic force constant matrices were first obtained within DFPT on a 2×2×2 and 4×4×1 meshes of q-points for Bi_2Se_3 and BiSe, respectively. These were Fourier interpolated to obtain those at an arbitrary q-vector. Gruneisen parameter (γ) measures the degree of anharmonic interaction of phonons with acoustic modes of a material. We estimated the mode Gruneisen parameters (γ_{qv}) of BiSe

using a finite difference formula, taking phonon frequencies calculated at two volumes (V_0 and $0.98V_0$, V_0 being the cell volume of the experimental structure). While we included the spin-orbit coupling(SOC) in determination of the electronic structure through the use of fully relativistic pseudopotentials, phonon frequencies were obtained using scalar relativistic pseudopotentials (SOC = 0).

1.3 Results & discussion

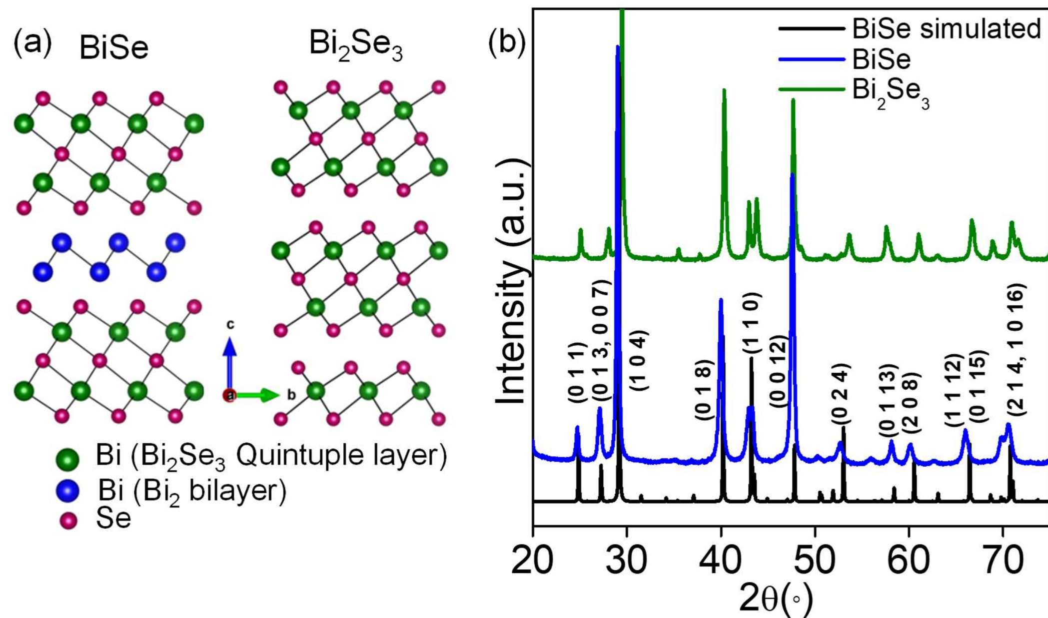

Figure 1.1. *(a) Crystal structures and (b) powder XRD patterns of BiSe and Bi_2Se_3.*

High quality crystalline ingots of BiSe and $Bi_{1-x}Sb_xSe$ (x = 0-0.3) have been synthesized by vacuum (10^{-6} Torr) sealed tube melting reaction at 1123 K and subsequent annealing at 893 K. Powder X-ray diffraction (PXRD) patterns of as-synthesized BiSe could be indexed as pure layered BiSe structure (space group $P\bar{3}m1$; Figure 1.1b). First, we present a comparison between the thermoelectric properties (measured along the ingot growth direction) of BiSe and Bi_2Se_3, which reveals the intriguing role of Bi-bilayer in BiSe for its superior thermoelectric properties compared to Bi_2Se_3. To further improve the thermoelectric properties of BiSe, we have substituted Sb in place of Bi in BiSe and performed spark plasma sintering (SPS) and measured anisotropic thermoelectric properties.

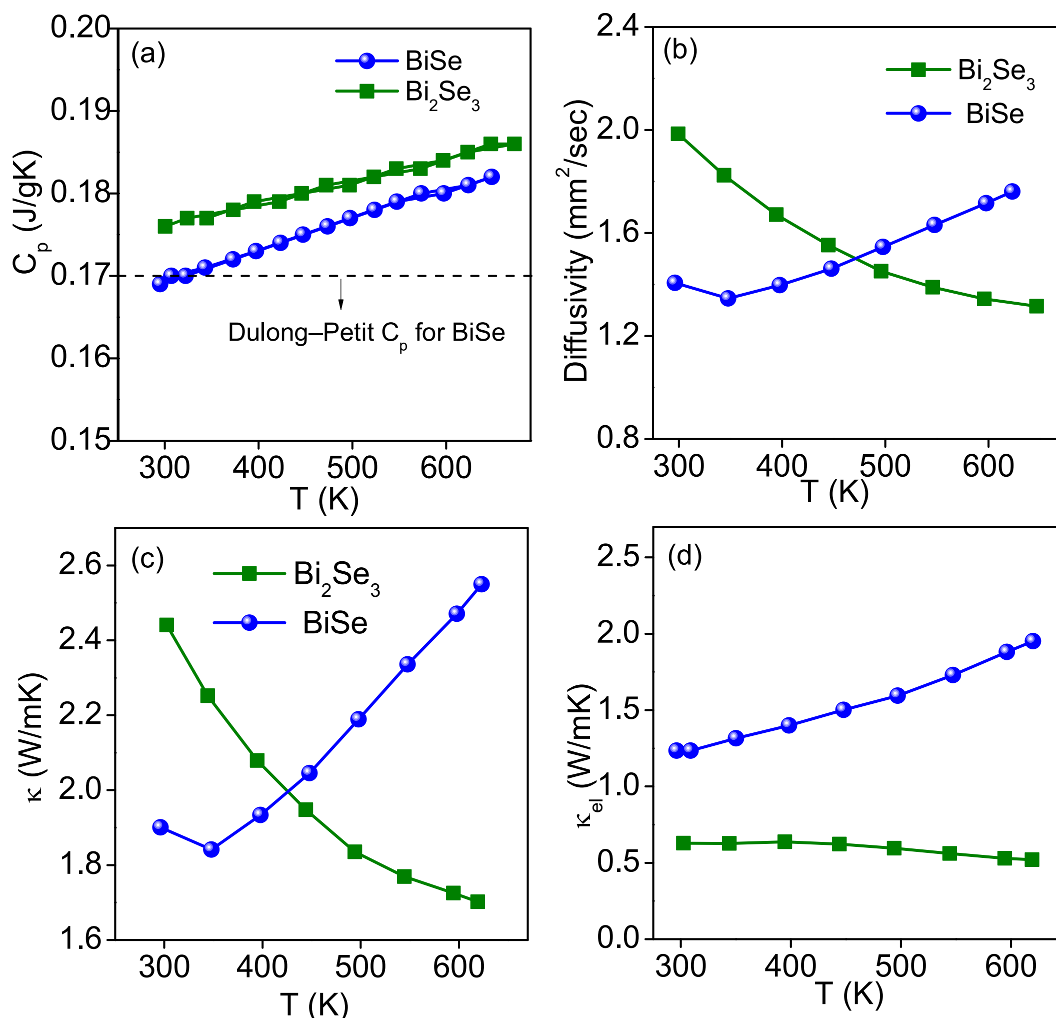

Figure 1.2. *Temperature dependent (a) heat capacity (C_p), (b) Thermal diffusivity, (c) total thermal conductivity (κ) and (d) electronic thermal conductivity (κ_{el}) of BiSe and Bi_2Se_3.*

Temperature dependent total thermal conductivity (κ) of Bi_2Se_3 and BiSe are presented in figure 1.2c. κ of BiSe increases with temperature, whereas κ of Bi_2Se_3 decreases with temperature. This fact is mainly attributed to the bipolar conduction in BiSe which is having a lower band gap compared to Bi_2Se_3 (discussed later). Electronic thermal conductivity (κ_{el}) of BiSe (Figure 1.2d) is estimated from Wiedemann-Franz law, $\kappa_{el} = L.\sigma.T$, where, L is the Lorenz number, σ is the electrical conductivity at temperature T. Temperature dependent L was calculated based on the fitting of temperature dependent on Seebeck values assuming single parabolic band model (discussed elsewhere).[28] Lattice thermal conductivities (κ_{lat}) of all samples are obtained by subtracting the κ_{el} from κ.

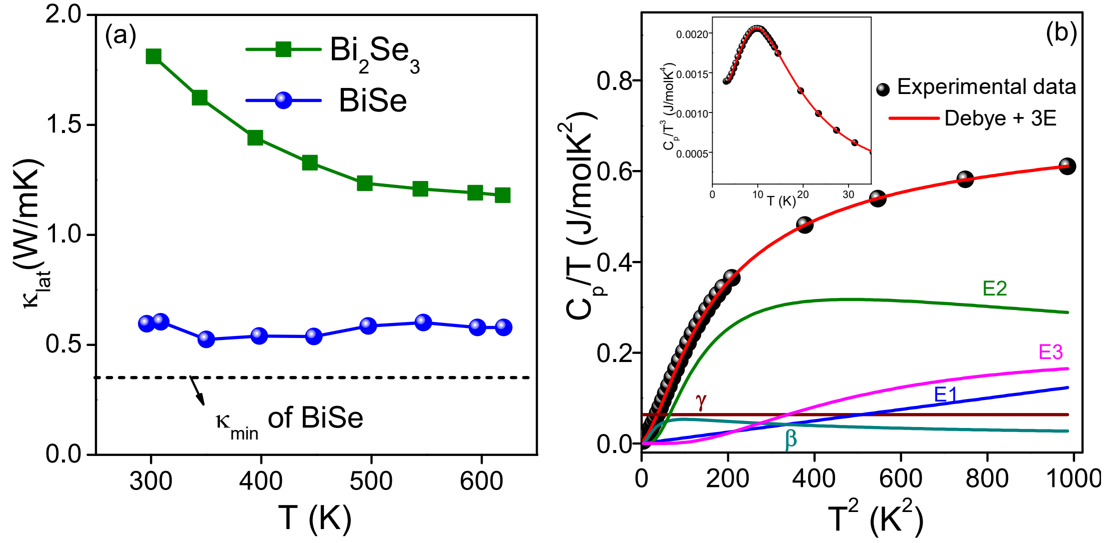

Figure 1.3. *(a) Lattice thermal conductivity (κ_{lat}) of Bi_2Se_3 and BiSe ingots measured along the ingot growth direction. (b) C_p/T vs T^2 plot of BiSe. Solid lines are obtained by fitting of experimental C_p/T vs. T^2 data using combined Debye-Einstein model (red line), with individual contributions from electronic (γ), Debye (β) and three Einstein modes (E_1, E_2, E_3). Inset shows C_p/T^3 vs. T plot with Boson-peak like feature.*

Figure 1.3a. represents temperature dependent lattice thermal conductivity of BiSe and Bi_2Se_3 ingots measured along the ingot growth direction in the 300-650 K range. BiSe ingot exhibits a very low κ_{lat} of ~ 0.6 W/mK at 300 K, which remains nearly flat throughout the 300-650 K range. κ_{lat} of BiSe lies close to its calculated theoretical minimum of lattice thermal conductivity (κ_{min} ~ 0.35 W/mK), estimated using Cahill's formulation,[11,47]

$$\kappa_{min} = \frac{1}{2}\left(\frac{\pi}{6}\right)^{1/3} k_B V^{-2/3}(2v_t + v_l) \qquad (1.1)$$

where, k_B is the Boltzmann constant, V is the average volume per atom, v_t (1762.67 & 2083.33 m/s) and v_l (2073.33 m/s) are the average transverse and longitudinal sound velocities respectively, Table 1.2. Although BiSe and Bi_2Se_3 belong to the same homologous family $(Bi_2)_m(Bi_2Se_3)_n$, Bi_2Se_3 shows a κ_{lat} of ~ 1.8 W/mK at 300 K which decreases to 1.2 W/mK at 650 K, which is significantly higher than that of BiSe (Figure 2a). The fundamental structural difference between BiSe (weak TI) and Bi_2Se_3 (strong TI) is the sandwiched Bi_2 layer in BiSe, which may have significant role in lowering κ_{lat} in BiSe.

In order to find out the underlying mechanism for such low κ_{lat} of BiSe and to check the presence of independent Einstein oscillator modes (like rattling atoms or localized vibrations), we have measured low temperature C_p of BiSe from 1.9 K to 200 K and fit the C_p/T vs. T^2 graph (Figure 1.3b) of BiSe to a combined Debye-Einstein model[8,11] which is as follows :

$$\frac{C_p}{T} = \gamma + \beta T^2 + \sum_n \left(A_n\left(\Theta_{E_n}\right)^2 . (T^2)^{-\frac{3}{2}} . \frac{e^{\frac{\Theta_{E_n}}{T}}}{\left(e^{\frac{\Theta_{E_n}}{T}} - 1\right)^2} \right) \tag{1.2}$$

In Eq. 1.2, first term, γ represents electronic contribution, whereas the second term provides the contribution from the Debye modes, in which $\beta = B.\left(12\pi^4 N_A \kappa_B / 5\right).(\Theta_D)^{-3}$; and N_A, k_B and Θ_D are Avogadro number, Boltzmann constant and Debye Temperature, respectively. B is given by $B = 1 - \Sigma_n A_n/3NR$, where N is the number of atoms per formula unit and R is universal gas constant (8.314 J/mole.K). The third term in Eq. 1.2 denotes the contribution arising from Einstein oscillator modes and A_n is the prefactor of nth Einstein mode, Θ_{En}. The low temperature C_p data of BiSe is well fitted by using three Einstein modes with characteristics temperatures Θ_{E1}= 25.9 K (i.e. 18 cm^{-1}), Θ_{E2}= 56.7 K (i.e. 39 cm^{-1}) and Θ_{E3}= 111.1 K (i.e.77 cm^{-1}). The various fitting parameters are provided in Table 1.1. The derived Debye temperature (Θ_D) for BiSe is 195 K. Interestingly, low temperature C_p data of BiSe shows a broad peak which becomes even more prominent in C_p/T^3 vs. T plot (Inset of Figure 1.3b), which can only be fitted with a combined Debye-Einstein model confirming the contribution from Einstein oscillators. Such a broad peak in C_p/T^3 vs. T resembles the Boson-peak like hump observed in the disordered glasses, skutterudites and clatharates,[9] which indicates the excess phonon density of states that may result in from the low-energy optical modes generated by localized vibrations of Bi bilayer, sandwiched between Bi_2Se_3 quintuple layers in BiSe (further discussed later). These low-lying optical modes (Einstein modes) in BiSe strongly couple with heat carrying acoustic phonons leading to suppressed phonon group velocities as well as mean free path, and thereby reducing κ_{lat} to an ultra-low value.

Table 1.1. *Derived parameters obtained by modeling low temperature C_p/T vs T^2 data of BiSe by using combined Debye-Einstein equation*.

Parameters	Derived Values
$\gamma/10^{-3}$(J mol^{-1}K^{-2})	6.37 ± 0.44
B/10^{-4}(J mol^{-1}K^{-4})	1.25 ± 0.15
A_1(J mol^{-1}K^{-1})	0.9 ± 0.08
Θ_{E1} (K)	25.92 ± 0.72 (~ 18 cm^{-1})
A_2(J mol^{-1}K^{-1})	11.8 ± 0.55
Θ_{E2} (K)	56.71 ± 0.93 (~ 39 cm^{-1})
A_3(J mol^{-1}K^{-1})	13.42 ± 1.3
Θ_{E3} (K)	111.1 ± .14 (~ 77 cm^{-1})
Θ_D (K)	195
R^2	0.99999
χ^2	4.49026 x 10^{-7}

To unravel the role of Bi bilayer in BiSe in lowering its κ_{lat}, we present a comparative analysis of phonon spectra of BiSe and Bi_2Se_3, determined from first-principles. In the phonon dispersions of BiSe and Bi_2Se_3 (shown in Figures 1.4a and 1.4b, respectively) the branches have been coloured based on fractional amplitudes of vibration of each inequivalent atoms multiplying by their weighs. Atom projected phonon dispersion of BiSe (Figure 1.4a) reveals that two of the lowest frequency optical branches (26 cm^{-1} and 37 cm^{-1}, coloured with pink dots) involve essentially the localized vibrations of the atoms in the Bi bilayer. Atom-projected phonon density of states (phDOS) (Figure 1.4c) of BiSe clearly confirms the dominant character in the low-energy phonon modes to be localized vibrations of the Bi atom of Bi bilayer (Figure 1.4d). The optical phonon modes at 26 cm^{-1} and 37 cm^{-1} are associated with localized vibration of Bi bilayer (Figure 1.4d), which are in close agreement with the two Einstein modes (Θ_{E1} = 25.9 K, Θ_{E2} = 56.7 K) inferred from experimental C_p data of BiSe at low-T. These localized phonon modes effectively scatter the heat carrying acoustic phonons through coupling that is evident in the avoided crossing (see inset of Figure 1.4a) between branches of longitudinal acoustic

(highlighted with red dashed line) and optical branches (highlighted with blue dashed lines). Low cut-off frequencies of acoustic modes are signature to low lattice thermal conductivity of any material.

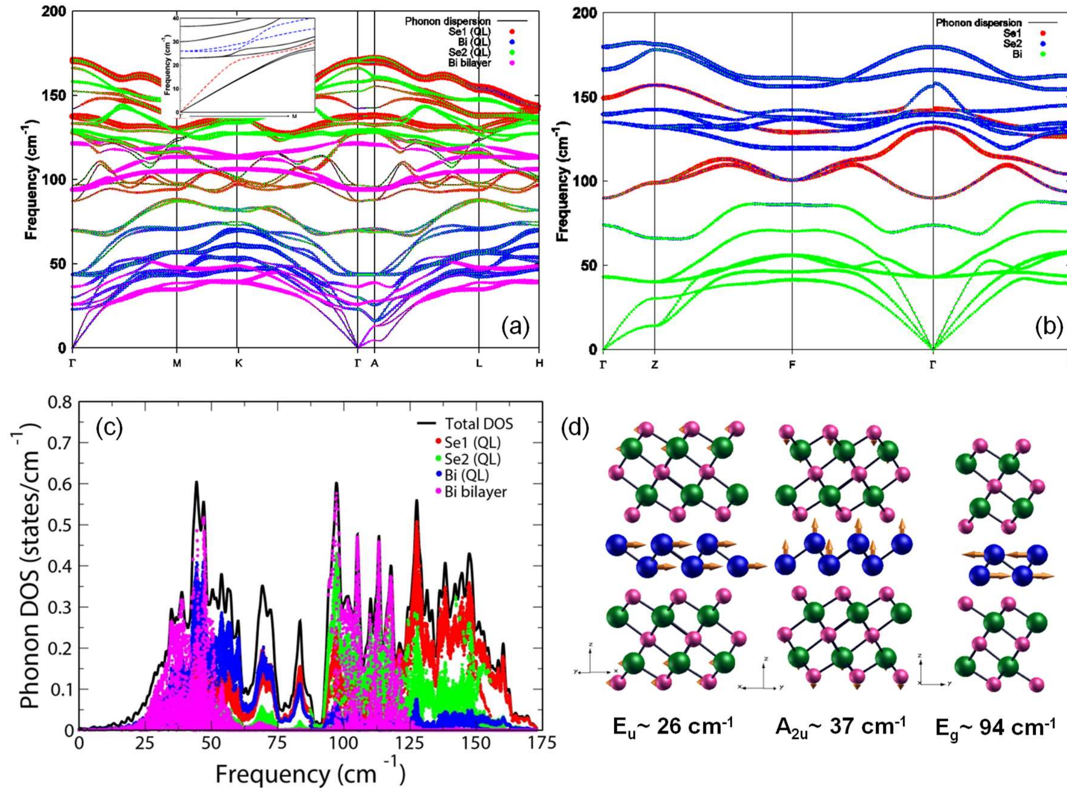

Figure 1.4. *Calculated phonon dispersion of (a) BiSe and (b) Bi_2Se_3 in which bands are colored based on atomic character (fractional amplitudes of vibration of each inequivalent atom multiplied by their weighs). The thickness of a band represents relative contribution of vibration of a particular type of atom to that phonon. BiSe consists of a Bi bilayer sandwiched between two Bi_2Se_3 quintuple layers (QLs). A Bi_2Se_3 QL consists of two inequivalent Se and one inequivalent Bi atom. Inset of (a) shows the avoided crossing between longitudinal acoustic band (red dashed line) and low-lying optical modes (blue dashed lines). (c) Phonon DOS of BiSe exhibiting dominant contribution of Bi atoms from Bi_2 bilayer in the low frequency region. (d) Normal modes with localized vibrations of Bi bilayer in BiSe which constitute low energy optical modes. Green, blue and pink colors represent Bi of Bi_2Se_3 layer, Bi of Bi_2 layer and Se respectively.*

We have also calculated the cut-off frequencies of the acoustic branches of BiSe (see Table 1.3) reaching an extremely low value of 4 cm^{-1} for the longitudinal acoustic (LA) mode in Γ-A direction (i.e. the stacking direction of the layers). Weak bonding

between the Bi bilayer and the adjacent Bi_2Se_3 quintuple layers as well as between neighbouring Bi_2Se_3 quintuple layers gives rise to weak force constant, hence the low cut-off frequencies particularly along stacking direction. Moreover, heavy constituent atoms and lower cut-off frequencies of the acoustic branches in BiSe give rise to lower sound velocities in BiSe compared to that of Bi_2Se_3 (Table 1.2). As κ_{lat} depends quadratically on the velocity of sound through $\kappa_{lat} \sim 1/3Cv^2\tau$, where v is the average velocity of sound and τ is the relaxation time of the phonons, κ_{lat} of BiSe is lower than the κ_{lat} of Bi_2Se_3.

Table 1.2. *Comparison of calculated sound velocities of BiSe and Bi_2Se_3 in different high symmetric directions.*

BiSe (ω in cm^{-1})				Bi_2Se_3 (ω in cm^{-1})			
Direction	TA1	TA2	LA	Direction	TA1	TA2	LA
Γ-M	Γ-M	1820	1862	2424	Γ-L	2112	2976
Γ-K	Γ-K	1397	2317	2963	Γ-F	2170	3296
Γ-A	Γ-A	2071	2071	833	Γ-Z	1257	1257

Table 1.3. *Comparison of cut-off frequencies of the acoustic phonon branches of BiSe and Bi_2Se_3 in different high symmetric directions.*

BiSe (ω in cm^{-1})				Bi_2Se_3 (ω in cm^{-1})			
Direction	TA1	TA2	LA	Direction	TA1	TA2	LA
Γ-M	24	24	20	Γ-L	43	51	32
Γ-K	27	24	22	Γ-F	45	51	41
Γ-A	13	13	4	Γ-Z	13	13	29

To assess the strength and effects of lattice anharmonicity, we determined the mode Gruneisen parameters (γ_{qv}) of a few low lying phonon branches (see Figure 1.5). The low-frequency optical modes including the localized phonons of the bismuth bilayer in BiSe are strongly anharmonic with $\gamma_{qv} > 2$. Among the three branches of acoustic phonons, the longitudinal acoustic (LA) exhibits the strongest anharmonicity with $\gamma_{qv} > 40$ (see along Γ-A direction in Figure 1.5a) because of anisotropic layered structure and weak bonding between different layers (Bi_2 layer and Bi_2Se_3 quintuple layers). Large γ_{qv} of LA modes

and its strong q-dependence is reminiscent of nonlinear elastic behaviour dependence of BiSe. Thus, low sound velocities and strong anharmonic interaction between soft localized vibrations of Bi atoms in the Bi bilayer and acoustic phonons are mainly responsible for the low κ_{lat} in BiSe.

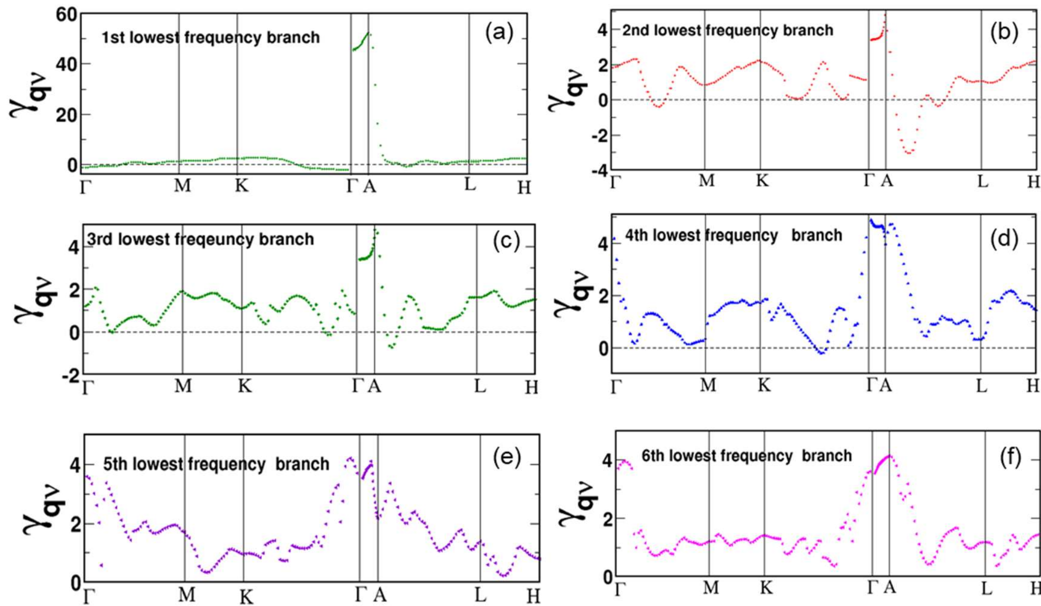

Figure 1.5. *Plot of mode Gruneisen parameter (γ_q) along high symmetric directions in the reciprocal space for the six lowest frequency phonon branches of BiSe. Although all of these branches show quite significant anharmonicity, the longitudinal acoustic (LA) mode exhibits the strongest anharmonicity with its γ_q> 40 (along Γ-A line in (a)).*

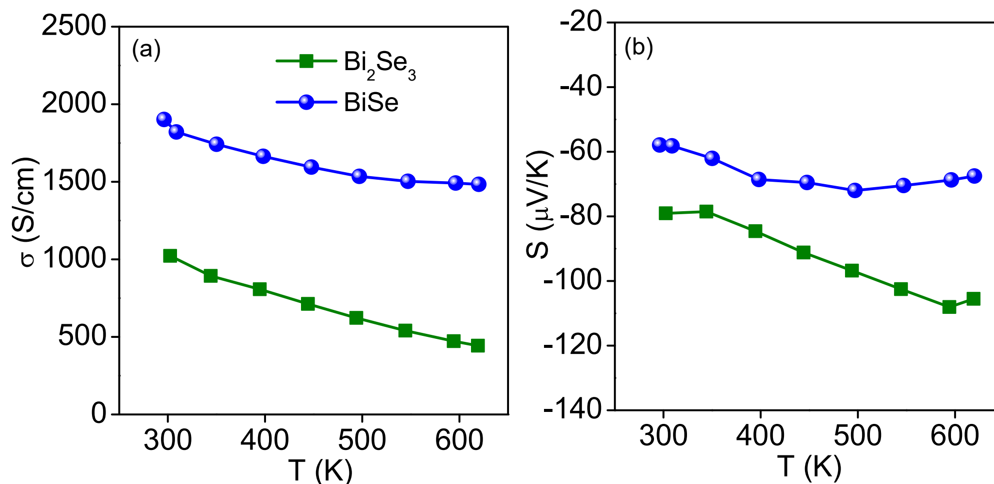

Figure 1.6. *(a) Electrical conductivity (σ) and (b) Seebeck Coefficient (S) of BiSe and Bi_2Se_3 ingots measured along the ingot growth direction.*

Electrical transport properties of crystalline ingots of BiSe and Bi_2Se_3 measured along the ingot growth direction are presented in Figure 1.6. BiSe exhibits a higher electrical conductivity (σ) of ~ 1900 S/cm compared to Bi_2Se_3 (σ of ~ 1000 S/cm) at 300 K (Figure 1.6a). BiSe and Bi_2Se_3 exhibit negative Seebeck coefficient values (*S*) confirming n-type conduction in both these materials, but the absolute value of Seebeck coefficient ($|S|$) of BiSe is 60 μV/K which is smaller than that of Bi_2Se_3 ($|S|$~ 80 μV/K) (Figure 1.6b). This is attributed mainly to higher n-type carrier density ($n \sim 3.15 \times 10^{19}/cm^3$) in BiSe compared to that of Bi_2Se_3 ($n \sim 4.24 \times 10^{18}/cm^3$).

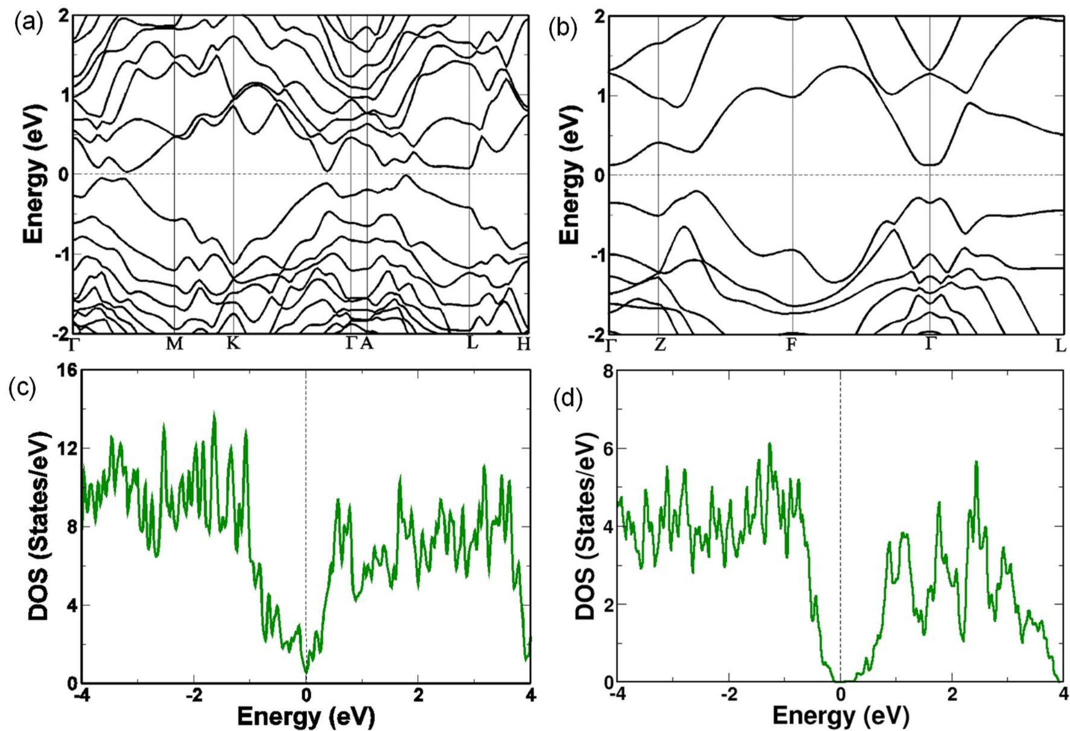

Figure 1.7. *Electronic structures of (a) BiSe and (b)* Bi_2Se_3*, calculated at their experimental lattice parameters with inclusion of spin-orbit coupling (SOC) effects. Total electronic density of states (DOS) of (c) BiSe and (d)* Bi_2Se_3 *at energies near* $E_F = 0$ *eV.*

Electronic structures of BiSe and Bi_2Se_3 (Figure 1.7a and 1.7b), calculated by including the effects of spin-orbit coupling reveal that BiSe possesses a band gap (E_g) of 20 meV which is smaller than that of Bi_2Se_3 (E_g = 0.35 eV). Due to the smaller band gap and high carrier concentration, electrical conductivity (σ) of BiSe is higher than that of

Bi_2Se_3. Moreover, the electronic density of states (DOS) of BiSe (Figure 1.7c) is highly asymmetric near the Fermi level than that of Bi_2Se_3 (Figure 1.7d), which generates a considerably high Seebeck coefficient in BiSe inspite of having high carrier concentration. This is because the Seebeck coefficient depends linearly on the variation in density of states (D(E)) with respect to energy (i.e. dD(E)/dE) at the E_F.[28]

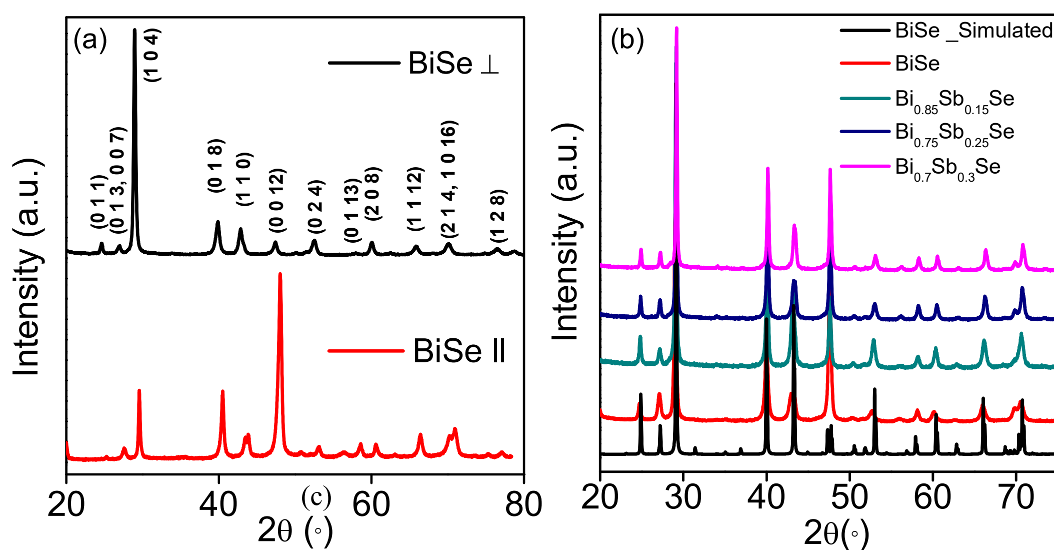

Figure 1.8. *(a) XRD pattern of BiSe sample along parallel and perpendicular to SPS pressing directions. Strong anisotropy of the bulk sample is prominent from significant difference in the relative peak intensity of (104) and (0012) planes. (b) PXRD pattern of* $Bi_{1-x}Sb_xSe$ *ingot samples.*

Because of the anisotropic layered structure (Figure 1.1a), BiSe is expected to exhibit directional properties. To probe anisotropic thermoelectric properties, we have performed SPS processing of the ingot samples and measured transport properties along directions parallel to SPS pressing direction, $SPS_{\parallel}$ (i.e. perpendicular to BiSe layer stacks) and perpendicular to SPS pressing direction, $SPS_{\perp}$ (i.e. parallel to BiSe layer stacks). The PXRD pattern of BiSe along parallel and perpendicular to SPS pressing direction reflects strong anisotropy, evident from the significant difference in the relative peak intensities of (104) and (0012) planes (Figure 1.8a). Electronic and thermal transport properties of BiSe along different SPS directions are presented in Figure 1.9. BiSe exhibits higher electrical and thermal conductivity and reduced Seebeck coefficient in the direction perpendicular to

SPS pressing direction compared to that of along parallel to SPS pressing direction. This originates from weak bonding between layers of BiSe. Lower value of κ_{lat} was measured along $SPS_{||}$ (i.e. perpendicular to BiSe layer stacks) compared to $SPS_{\perp}$ (i.e. parallel to BiSe layer stacks). As a result of reduced κ_{lat} of ~ 0.5 W/mK at 425 K, BiSe has a higher zT of 0.36 at 425 K along $SPS_{||}$ compared to that of (zT of 0.26 at 425 K) $SPS_{\perp}$ (Figure 1.9f).

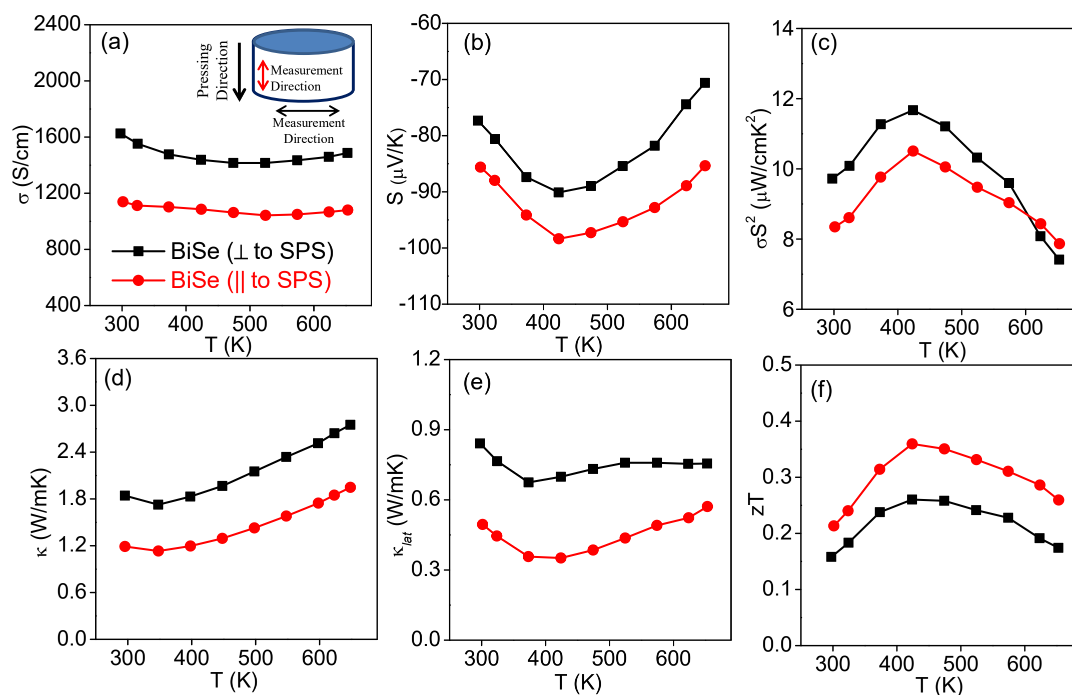

Figure 1.9. *Temperature dependent (a) electrical conductivity (σ), (b) Seebeck Coefficient (S), (c) power factor (σS^2), (d) total thermal conductivity (κ), (e) lattice thermal conductivity (κ_{lat}) and (f) thermoelectric figure of merit (zT) of BiSe measured parallel and perpendicular to SPS pressing directions. Inset in (a) shows schematic of thermoelectric measurement directions, along the pressing direction (red, ||) and perpendicular to pressing direction (black, ⊥).*

In order to optimize the thermoelectric performance of BiSe, we substituted Sb in place of Bi in BiSe and processed all the samples using SPS. PXRD patterns of as-synthesized $Bi_{1-x}Sb_xSe$ (x = 0-0.3) samples could be indexed based on the hexagonal BiSe (Space group $P\bar{3}m1$) without any additional peaks being observed within the detection limits of XRD (Figure 1.8b). Thermoelectric properties of all the $Bi_{1-x}Sb_xSe$ (x=0-0.3) samples have been measured parallel to the SPS pressing direction (Figure 1.10) as pristine BiSe shows superior thermoelectric performances parallel to the SPS-pressing direction.

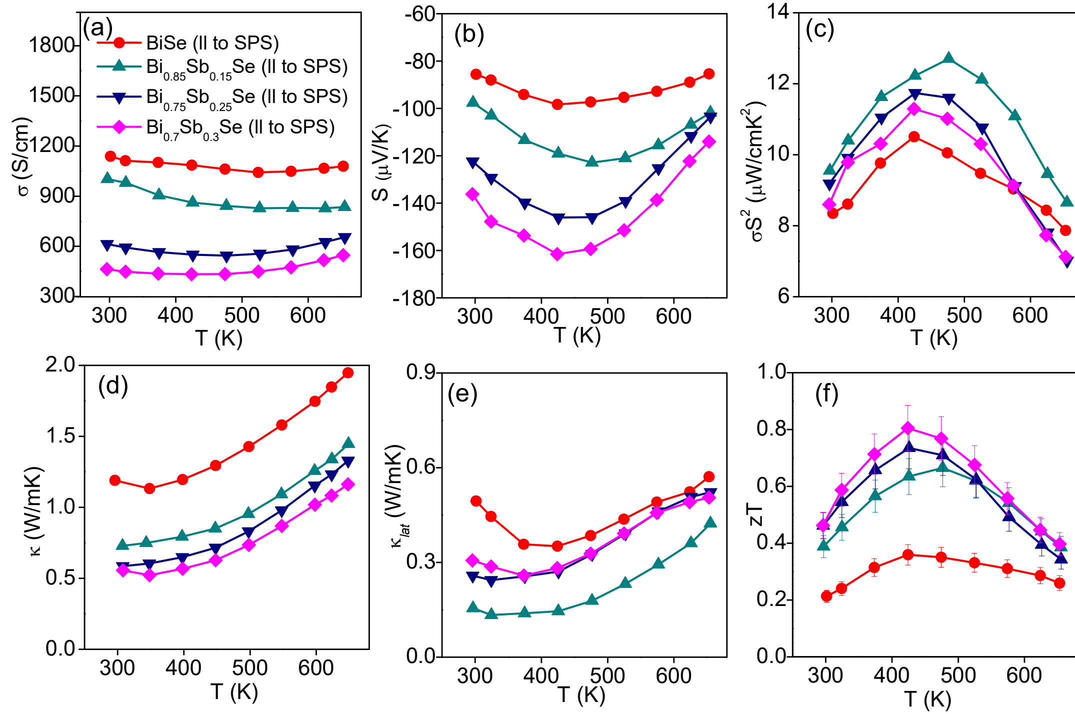

Figure 1.10. *Temperature dependent (a) electrical conductivity (σ), (b) Seebeck Coefficient (S), (c) power factor (σS^2), (d) total thermal conductivity (κ), (e) lattice thermal conductivity (κ_{lat}) and (f) thermoelectric figure of merit (zT) of of $Bi_{1-x}Sb_xSe$ (x = 0-0.3) measured parallel to the SPS pressing direction.*

Electrical conductivity (σ) of $Bi_{1-x}Sb_xSe$ samples decreases with increasing x. σ of BiSe decreases from 1140 S/cm to 462 S/cm in $Bi_{0.7}Sb_{0.3}Se$ at 300 K (Figure 1.10a). Seebeck coefficient of the samples shows negative values depicting the *n*-type carrier conduction. Absolute value of the Seebeck coefficient (|S|) increases from 85.4 μV/K in BiSe to 136 μV/K in $Bi_{0.7}Sb_{0.3}Se$ at 300 K (Figure 1.10b) which mainly attributes to reduced carrier concentration upon Sb alloying (Table 1.4). Among all the $Bi_{1-x}Sb_xSe$ samples, $Bi_{0.85}Sb_{0.15}Se$ exhibits highest power factor (σS^2) of ~12.71 μW/cmK^2 at 477 K (Figure 1.10c). On the other hand, κ of the $Bi_{1-x}Sb_xSe$ samples exhibits decreasing trend upon increasing Sb concentration in $Bi_{1-x}Sb_xSe$ (Figure 1.10d). κ of BiSe is ~ 1.2 W/m.K at room temperature, which decreases to ~ 0.55 W/mK in $Bi_{0.7}Sb_{0.3}Se$ (Figure 1.10d). All the Sb alloyed $Bi_{1-x}Sb_xSe$ samples show reduced κ_{lat} compared to the pristine BiSe (Figure 1.10e) e.g.; κ_{lat} of BiSe is ~ 0.5 W/mK at 300 K whereas κ_{lat} of $Bi_{0.7}Sb_{0.3}Se$ is ~ 0.3 W/mK at 300 K. This decrease can be attributed to effective solid solution point defect scattering due to Sb alloying in BiSe. With the enhanced power factor value and reduced thermal

conductivity, *n*-type $Bi_{0.7}Sb_{0.3}Se$ shows significantly high zT of ~ 0.8 at 425 K (parallel to the SPS pressing direction, Figure 1.10f) which makes $Bi_{0.7}Sb_{0.3}Se$ a potential candidate for being a *n*-type Te-free material for near room temperature thermoelectric applications.

Table 1.4. *Carrier concentration of $Bi_{1-x}Sb_xSe$ (x= 0-0.3) samples.*

Sample	**Carrier Concentration (*n*) $x10^{19}/cm^3$**
BiSe	3.15
$Bi_{0.85}Sb_{0.15}Se$	2.24
$Bi_{0.75}Sb_{0.25}Se$	1.92
$Bi_{0.7}Sb_{0.3}Se$	1

1.4 Conclusions

In conclusion, BiSe, a weak topological insulator, exhibits ultralow κ_{lat} of ~ 0.6 W/mK at 300 K, which is significantly lower than that of Bi_2Se_3, a strong 3D topological insulator (κ_{lat} of ~ 1.8 W/mK) belonging to the same layered homologous family $(Bi_2)_m(Bi_2Se_3)_n$. Low temperature heat capacity measurements and first-principles theoretical analysis of phonon dispersion of BiSe unravelled the key role of the soft modes of localized vibrations of Bi bilayer in reducing its κ_{lat}. These low-energy optical phonons inhibit the propagation of heat-carrying acoustic phonons (optical-acoustic coupling), thereby reducing the κ_{lat} of BiSe. Low cut-off frequencies of acoustic branches and strong anharmonicity in phonon-phonon interactions further cause ultralow κ_{lat} in BiSe. BiSe exhibits n-type electrical conduction and superior electronic transport properties that are further supported by theoretical analysis of electronic structure of BiSe which has a low band gap and highly asymmetric DOS near the Fermi level. We have optimized and measured the anisotropic thermoelectric properties of Sb alloyed and SPS processed $Bi_{1-x}Sb_xSe$ samples, which shows further low κ_{lat} of 0.3 W/mK at 300 K and high zT of 0.8 at 425 K in *n*-type $Bi_{0.7}Sb_{0.3}Se$ (parallel to the SPS pressing direction), which is indeed remarkable among the Te-free *n*-type thermoelectric materials, opening up application possibilities near room temperature.

1.5 References

(1) Tan, G.; Zhao, L. D.; Kanatzidis, M. G. *Chem. Rev.* **2016**, *116*, 12123–12149.

(2) Zhao, L.-D.; Dravid, V. P.; Kanatzidis, M. G. *Energy Environ. Sci.* **2014**, *7*, 251–268.

(3) Ge, Z. H.; Zhao, L. D.; Wu, D.; Liu, X.; Zhang, B. P.; Li, J. F.; He, J. *Mater. Today* **2016**, *19*, 227–239.

(4) Biswas, K.; He, J.; Blum, I. D.; Wu, C.-I.; Hogan, T. P.; Seidman, D. N.; Dravid, V. P.; Kanatzidis, M. G. *Nature* **2012**, *489*, 414–418.

(5) Poudel, B.; Hao, Q.; Ma, Y.; Lan, Y.; Minnich, A.; Yu, B.; Yan, X.; Wang, D.; Muto, A.; Vashaee, D.; Chen, X.; Liu, J.; Dresselaus; Chen, G.; Ren, Z. *Science* **2008**, *320*, 634–638.

(6) Samanta, M.; Biswas, K. *J. Am. Chem. Soc.* **2017**, *139*, 9382–9391.

(7) Jana, M. K.; Biswas, K. *ACS Energy Lett.* **2018**, *3*, 1315–1324.

(8) Shi, X.; Yang, J.; Salvador, J. R.; Chi, M.; Cho, J. Y.; Wang, H.; Bai, S.; Yang, J.; Zhang, W.; Chen, L. *J. Am. Chem. Soc.* **2011**, *133*, 7837–7846.

(9) Takabatake, T.; Suekuni, K.; Nakayama, T.; Kaneshita, E. *Rev. Mod. Phys.* **2014**, *86*, 669–716.

(10) Kauzlarich, S. M.; Brown, S. R.; Jeffrey Snyder, G. *Dalt. Trans.* **2007**, *21*, 2099.

(11) Jana, M. K.; Pal, K.; Warankar, A.; Mandal, P.; Waghmare, U. V.; Biswas, K. *J. Am. Chem. Soc.* **2017**, *139*, 4350–4353.

(12) Jana, M. K.; Pal, K.; Waghmare, U. V; Biswas, K. *Angew. Chemie - Int. Ed.* **2016**, *55*, 7792–7796.

(13) Qiu, W.; Xi, L.; Wei, P.; Ke, X.; Yang, J.; Zhang, W. *Proc. Natl. Acad. Sci. U. S. A.* **2014**, *111*, 15031–15035.

(14) Liu, H.; Shi, X.; Xu, F.; Zhang, L.; Zhang, W.; Chen, L.; Li, Q.; Uher, C.; Day, T.; Snyder, G. J. *Nat. Mater.* **2012**, *11*, 422–425.

(15) Liu, H.; Yang, J.; Shi, X.; Danilkin, S. A.; Yu, D.; Wang, C.; Zhang, W.; Chen, L. *J. Mater.* **2016**, *2*, 187–195.

(16) Li, B.; Wang, H.; Kawakita, Y.; Zhang, Q.; Feygenson, M.; Yu, H. L.; Wu, D.; Ohara, K.; Kikuchi, T.; Shibata, K.; Yamada, T.; Ning, X. K.; Chen, Y.; He, J. Q.; Vaknin, D.; Wu, R. Q.; Nakajima, K.; Kanatzidis, M. G. *Nat. Mater.* **2018**, *17*, 226–230.

(17) Guin, S. N.; Chatterjee, A.; Negi, D. S.; Datta, R.; Biswas, K. *Energy Environ. Sci.* **2013**, *6*, 2603–2608.

(18) Morelli, D. T.; Jovovic, V.; Heremans, J. P. *Phys. Rev. Lett.* **2008**, *101*, 035901.

(19) Zhao, L. D.; Lo, S. H.; Zhang, Y.; Sun, H.; Tan, G.; Uher, C.; Wolverton, C.; Dravid, V. P.; Kanatzidis, M. G. *Nature* **2014**, *508*, 373–377.

(20) Hasan, M. Z.; Kane, C. L. *Rev. Mod. Phys.* **2010**, *82*, 3045–3067.

(21) Zhang, S.; Dai, X.; Qi, X.; Liu, C.; Zhang, H.; Fang, Z. *Nat. Phys.* **2009**, *5*, 438–442.

(22) Hsieh, T. H.; Lin, H.; Liu, J.; Duan, W.; Bansil, A.; Fu, L. *Nat. Commun.* **2012**, *3*, 982.

(23) Dziawa, P.; Kowalski, B. J.; Dybko, K.; Buczko, R.; Szczerbakow, A.; Szot, M.; Łusakowska, E.; Balasubramanian, T.; Wojek, B. M.; Berntsen, M. H.; Tjernberg, O.; Story, T. *Nat. Mater.* **2012**, *11*, 1023–1027.

(24) Roychowdhury, S.; Samanta, M.; Banik, A.; Biswas, K. *J. Solid State Chem.* **2019**,

275, 103–123.
(25) Hor, Y. S.; Richardella, A.; Roushan, P.; Xia, Y.; Checkelsky, J. G.; Yazdani, A.; Hasan, M. Z.; Ong, N. P.; Cava, R. J. *Phys. Rev. B - Condens. Matter Mater. Phys.* **2009**, *79*, 195208.
(26) Li, W.; Wu, Y.; Lin, S.; Chen, Z.; Li, J.; Zhang, X.; Zheng, L.; Pei, Y. *ACS Energy Lett.* **2017**, *2*, 2349–2355.
(27) Tan, G.; Shi, F.; Hao, S.; Chi, H.; Bailey, T. P.; Zhao, L. D.; Uher, C.; Wolverton, C.; Dravid, V. P.; Kanatzidis, M. G. *J. Am. Chem. Soc.* **2015**, *137*, 11507–11516.
(28) Banik, A.; Shenoy, U. S.; Saha, S.; Waghmare, U. V.; Biswas, K. *J. Am. Chem. Soc.* **2016**, *138*, 13068–13075.
(29) Roychowdhury, S.; Shenoy, U. S.; Waghmare, U. V; Biswas, K. *Angew. Chemie Int. Ed.* **2015**, *127*, 15456–15460.
(30) Sun, Y.; Cheng, H.; Gao, S.; Liu, Q.; Sun, Z.; Xiao, C.; Wu, C.; Wei, S.; Xie, Y. *J. Am. Chem. Soc.* **2012**, *134*, 20294–20297.
(31) Kim, S. Il; Lee, K. H.; Mun, H. A.; Kim, H. S.; Hwang, S. W.; Roh, J. W.; Yang, D. J.; Shin, W. H.; Li, X. S.; Lee, Y. H.; Snyder, G. J.; Kim, S. W. *Science* **2015**, *348*, 109–114.
(32) Park, K.; Ahn, K.; Cha, J.; Lee, S.; Chae, S. I.; Cho, S. P.; Ryee, S.; Im, J.; Lee, J.; Park, S. D.; Han, M. J.; Chung, I.; Hyeon, T. *J. Am. Chem. Soc.* **2016**, *138*, 14458–14468.
(33) Ma, Y.; Hao, Q.; Poudel, B.; Lan, Y.; Yu, B.; Wang, D.; Chen, G.; Ren, Z. *Nano Lett.* **2008**, *8*, 2580–2584.
(34) Ringel, Z.; Kraus, Y. E.; Stern, *Phys. Rev. B - Condens. Matter Mater. Phys.* **2012**, *86*, 045102.
(35) Yan, B.; Müchler, L.; Felser, C. *Phys. Rev. Lett.* **2012**, *109*, 116406.
(36) Wei, P.; Yang, J.; Guo, L.; Wang, S.; Wu, L.; Xu, X.; Zhao, W.; Zhang, Q.; Zhang, W.; Dresselhaus, M. S.; Yang, J. *Adv. Funct. Mater.* **2016**, *26*, 5360–5367.
(37) Pal, K.; Anand, S.; Waghmare, U. V. *J. Mater. Chem. C* **2015**, *3*, 12130–12139.
(38) Lind, H.; Lidin, S.; Häussermann, U. *Phys. Rev. B - Condens. Matter Mater. Phys.* **2005**, *72*, 184101.
(39) Majhi, K.; Pal, K.; Lohani, H.; Banerjee, A.; Mishra, P.; Yadav, A. K.; Ganesan, R.; Sekhar, B. R.; Waghmare, U. V; Anil Kumar, P. S. *Appl. Phys. Lett.* **2017**, *110*, 162102.
(40) Rasche, B.; Isaeva, A.; Ruck, M.; Borisenko, S.; Zabolotnyy, V.; Büchner, B.; Koepernik, K.; Ortix, C.; Richter, M.; Van Den Brink, J. *Nat. Mater.* **2013**, *12*, 422–425.
(41) Zeugner, A.; Kaiser, M.; Schmidt, P.; Menshchikova, T. V; Rusinov, I. P.; Markelov, A. V; Van den Broek, W.; Chulkov, E. V; Doert, T.; Ruck, M.; Isaeva, A. *Chem. Mater.* **2017**, *29*, 1321–1337.
(42) Giannozzi, P.; Baroni, S.; Bonini, N.; Calandra, M.; Car, R.; Cavazzoni, C.; Ceresoli, D.; Chiarotti, G. L.; Cococcioni, M.; Dabo, I.; Dal Corso, A.; De Gironcoli, S.; Fabris, S.; Fratesi, G.; Gebauer, R.; Gerstmann, U.; Gougoussis, C.; Kokalj, A.; Lazzeri, M.; Martin-Samos, L.; Marzari, N.; Mauri, F.; Mazzarello, R.; Paolini, S.; Pasquarello, A.; Paulatto, L.; Sbraccia, C.; Scandolo, S.; Sclauzero, G.; Seitsonen, A. P.; Smogunov, A.; Umari, P.; Wentzcovitch, R. M. *J. Phys. Condens. Matter* **2009**, *21*, 395502.
(43) Hua, X.; Chen, X.; Goddard, W. A. *Phys. Rev. B* **1997**, *55*, 16103–16109.

(44) Perdew, J. P.; Burke, K.; Ernzerhof, M. *Phys. Rev. Lett.* **1996**, *77*, 3865–3868.
(45) Belsky, A.; Hellenbrandt, M.; Karen, V. L.; Luksch, P. *Acta Crystallogr. Sect. B* **2002**, *58*, 364–369.
(46) Karsch, F.; Patkós, A.; Petreczky, P. *Rev. Mod. Phys.* **2001**, *73*, 515–561.
(47) Cahill, David G. Watson, S. K., Pohl, R. O. *Phys. Rev. B* **1992**, *46*, 6131–6140.

Chapter 2

Intrinsically Low Thermal Conductivity and High Carrier Mobility in Dual Topological Quantum Material, *n*-type BiTe

Chapter 2

Intrinsically Low Thermal Conductivity and High Carrier Mobility in Dual Topological Quantum Material, *n*-type BiTe[†]

Summary

The grand challenge in thermoelectrics is to achieve the intrinsically low thermal conductivity in crystalline solids while maintaining the high carrier mobility (μ). While topological quantum materials such as topological insulator (TI) or topological crystalline insulator (TCI) can exhibit high μ, weak topological insulators (WTI) are of interest due to their layered hetero-structural nature which is intriguing for exhibiting low lattice thermal conductivity (κ_{lat}). BiTe, a unique member of the $(Bi_2)_m(Bi_2Te_3)_n$ homologous series (where m:n = 1:2), possesses both the quantum states, TCI and WTI, which is distinct from the conventional TI, Bi_2Te_3 (where m:n = 0:1). In BiTe, Bi-Bi zigzag bilayer is sandwiched between the Te-Bi-Te-Bi-Te quintuple layers bonded via weak van der Waals interactions. Here, we report intrinsically low κ_{lat} of 0.47- 0.8 W/mK in the 300-650 K range in BiTe due to the presence of low energy optical phonon branches which originate primarily from the localized vibrations of Bi-bilayer. These soft optical modes couple strongly with the acoustic modes, hindering the propagation of acoustic phonons, resulting in a low κ_{lat}. BiTe exhibits negative Seebeck coefficients attributing to n-type electronic conduction. BiTe possess high μ of ~ 516 cm^2/Vs and 707 cm^2/Vs along parallel and perpendicular to spark plasma sintering (SPS) directions, respectively, at room temperature. Electronic structure of BiTe reveals that multiple band extrema in the conduction bands with nearly linear dispersion in a narrow energy window (~25 meV) corresponding to the thermal energy at room temperature, resulting in a facile conduction channel; hence supports manifestation of high μ.

[†]*A paper based on this work has been published in Angew. Chem. Int. Ed.* **2020**, *59*, 4822-4829

2.1 Introduction

Quantum materials (*e.*g. topological insulators, topological crystalline insulators and Weyl semimetal), characterized by their nontrivial electronic surface states, have recently created a sensation in designing new thermoelectric materials.[1–3] Semiconducting crystalline solids with narrow band gap and heavy constituent elements are desired to facilitate strong spin orbit-coupling to realize the band inversion in topological materials.[2] Interestingly, strong spin-orbit coupling in topological materials (TM) facilitates high band degeneracy (N_V), thus high carrier mobility (μ) while heavy constituent elements cause slow acoustic waves needed to achieve low κ_{lat}. Conventional topological insulators (TI, where metallic surface states are protected by time reversal symmetry)[2–4] such as Bi_2Te_3 and Bi_2Se_3 and topological crystalline insulators (TCI, where metallic surface states are protected by crystal mirror symmetry)[5–8] such as SnTe are some of the best known TE materials. A weak topological insulator (WTI, *e.g.* BiSe) arises from stacking of 2D TI layers and exhibits even number of Dirac cones on the side surfaces; its layered hetero-structure is important to exhibit low κ_{lat}.[9,10]

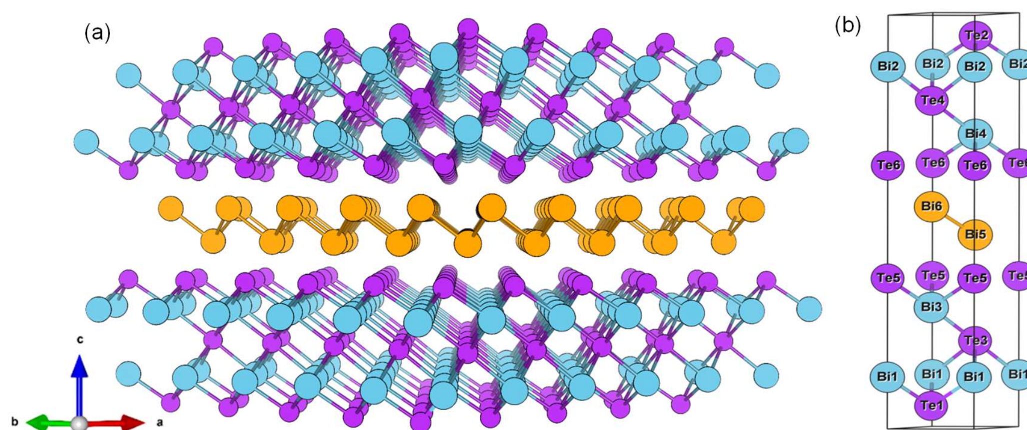

Figure 2.1. *(a) Crystal structure and (b) unit cell of BiTe. Pink, cyan and yellow color represent Te, Bi atom of Bi_2Te_3 layer and Bi atom of Bi_2 layer respectively.*

BiTe, a unique member of the $(Bi_2)_m(Bi_2Te_3)_n$ (where m:n = 1:2) homologous series,[11,12] possesses natural van der Waals hetero-structure (space group $P\bar{3}m1$), where zigzag Bi-Bi bilayer is sandwiched between the Te-Bi-Te-Bi-Te quintuple layers (QL) via weak van der Waals interaction (Figure 2.1). Recently, BiTe has emerged as a dual

topological insulator, which is a fascinating new quantum material.[13] Here, both the weak topological insulator (WTI) and topological crystalline insulator (TCI) phases coexist. WTI phase with the layered van der Waals hetero-structure will be promising to possess low κ_{lat}, whereas, TCI phase with the metallic surface states protected by crystal mirror symmetry and low carrier effective mass may provide high carrier mobility. Such unique crystal and electronic structure of BiTe stimulate enough interest to investigate its thermal conductivity and electronic properties. Although, both Bi_2Te_3 and BiTe belong to the same $(Bi_2)_m(Bi_2Te_3)_n$ homologous series,[11,12] Bi_2Te_3 is a well-known 3D TI and TE materials,[2,4,14–20] but BiTe is a dual topological insulator[13] with no detailed fundamental understanding of its TE properties.

Herein, we demonstrate intrinsically low κ_{lat} of 0.47- 0.8 W/mK in the 300-650 K range and high carrier mobility (μ) of ~ 516 cm^2/Vs (along SPS$_{\parallel}$) and 707 cm^2/Vs (along SPS$_{\perp}$) at room temperature in *n*-type dual topological insulator, BiTe. Measurement of low temperature heat capacity and detailed analysis of phonon dispersion by density functional theory (DFT) confirm the presence of low-lying optical phonon branches, originating mostly from the localized vibrations of zigzag Bi-bilayers in BiTe. These low energy optical modes effectively interact with the acoustic phonon modes, which results in intrinsically low κ_{lat} in BiTe. First-principles electronic structure calculation shows the presence of multiple nearly linearly dispersing conduction band valleys with significant anti-bonding states close vicinity of the Fermi level, resulting in a conductive network which supports the high μ in BiTe.

2.2 Methods

2.2.1 Reagents. Bismuth (SRL chemicals, 99.9%), selenium (Alfa Aeser 99.999%) and tellurium (Strategic Metal, >99.99%) were used for synthesis of BiTe and $BiTe_{1-x}Se_x$ without any further purification.

2.2.2 Synthesis. Ingots (~8 g) of BiTe and $BiTe_{1-x}Se_x$ (x = 0.3-0.5) were synthesized by weighing stoichiometric amounts of starting materials of Bi, Se and Te in quartz tubes and subsequently the quartz tubes were sealed under high vacuum (10^{-6}Torr). All the elements in the vacuum sealed tubes were then melted at 1123 K over a period of 6 h, followed by a rapid cooling to 893K and annealed at 893 K for 6 hours and then slowly cooled to room

temperature over 8 hours. Obtained shiny high quality polycrystalline ingots of BiTe and $BiTe_{1-x}Se_x$ (x = 0.3-0.5) were grounded into fine powders which were then loaded into a 10 mm diameter-graphite die. The graphite die loaded with samples were placed between the two electrodes in spark plasma sintering system (SPS211-LX, Dr. Sinter Lab). The chamber of the sintering-system was evacuated to 10^{-3} Torr prior to proving temperature and pressure. After vacuum, the powders were consolidated into the forms of cylinder at 650 K for 5 minutes under an axial pressure of 50 MPa. The SPS processed cylindrical shaped sample were then cut into the shapes of coin and bar which were are then polished for further thermal and electrical transport measurement respectively.

2.2.3 Powder X-ray diffraction. PXRD pattern for all synthesized BiTe and $BiTe_{1-x}Se_x$ samples were recorded using Bruker D8 diffractometer where Cu K_α (λ = 1.5406 Å) radiation source was being used.

2.2.4 Band gap measurement. The optical band gap of all the samples were measured with finely grounded powder using diffuse reflectance mode in FT-IR Bruker IFS 66V/S spectrometer in the wave number range 4000-400 cm^{-1}. Absorption (α/Λ) data of the samples were calculated from measured reflectance data using Kubelka-Munk equation: $\alpha/\Lambda = (1-R)^2/(2R)$, where α and Λ are the absorption and scattering coefficient, R is the reflectance, respectively.

2.2.5 Electrical transport. Electrical conductivity and Seebeck coefficients were measured simultaneously under a helium atmosphere from room temperature to 650 K on a ULVAC-RIKO ZEM-3 instrument system. The typical sample for measurement had a parallelepiped shape with the dimensions of ~2×2×8 mm^3. Electrical and thermal properties are always measured in the same direction for all the samples.

2.2.6 Hall measurement. Hall measurement of all the samples was carried out in the setup developed by Excel instrument, where the variable magnetic field of 0-0.55 T and dc-current of 100 mA were used at room temperature.

2.2.7 Thermal conductivity. Thermal diffusivity, D, was directly measured in the range 300−650K by using the laser flash diffusivity method in a Netzsch LFA-457 under nitrogen atmosphere. Coin/square shaped samples were coated with a thin layer of graphite to avoid errors coming from thermal emissivity of the materials. Temperature dependent heat

capacity, C_p of BiTe was derived using the standard sample (pyroceram) in LFA-457, which is in good agreement with Dulong-Petit C_p value. The total thermal conductivity, κ_{tot}, was estimated using the formula $\kappa_{tot} = DC_p\rho$, where D is thermal diffusivity of the sample, ρ is the density and C_p is the heat capacity of the sample. Obtained density of all the samples is ~ 8 g/cm^3 which is ~97% of the theoretical density. Electronic thermal conductivity of BiTe is estimated from Wiedemann-Franz law, $\kappa_{el} = L.\sigma.T$, where L is the Lorenz number, σ is the electrical conductivity at temperature T. Temperature-dependent Lorentz number was calculated based on the fitting of temperature dependent of Seebeck values assuming single parabolic band model (discussed elsewhere).[14,21–23] Lattice thermal conductivities (κ_{lat}) of all samples are obtained by subtracting the κ_{el} from κ_{tot}.

2.2.8 Heat Capacity Measurement. Low temperature (2-200K) specific heat of BiTe is measured in Physical Property Measurement System (PPMS).

2.2.9 Computational method. This part of the work has been performed in collaboration with Prof. Umesh V. Waghmare's group in JNCASR, India. Density functional theory (DFT) calculations have been performed using the Vienna Ab-initio Simulation Package (VASP)[24,25] employing the projector augmented wave (PAW)[26] method and the PBEsol[27] generalized gradient approximated (GGA)[28] exchange-correlation functional. We used the pseudo-potentials for Bi and Te supplied by VASP with valence configurations of $5d^{10}6s^26p^3$ and $6s^26p^4$, respectively. We used a kinetic energy cut-off of 520 eV and k-point mesh of 8 × 8 × 4 for all calculations. The lattice parameters of BiTe were fully optimized using energy and force convergence criteria of 10^{-8} eV and 10^{-3} eV/Å, respectively. The calculated lattice parameters agree very well the experimentally reported values. To analyze the chemical bonding, we have performed the crystal orbital Hamiltonian population (COHP) analysis for different pairs of nearest-neighbor atoms in the crystal structure of BiTe using the LOBSTER code.[29] We determined the phonon dispersion of BiTe utilizing the supercell method using Phonopy[30] with VASP as the DFT calculator taking a 2×2×1 supercell containing 48 atoms. To assess the degree of anharmonicity in BiTe, we determined the mode Gruneisen parameters employing a central difference formula taking phonon frequencies calculated at two different volumes ($1.02V_0$ and $0.98V_0$, V_0 being the optimized unit cell volume). Electronic structure of BiTe was calculated with the inclusion of spin-orbit coupling.

2.3 Results & discussion

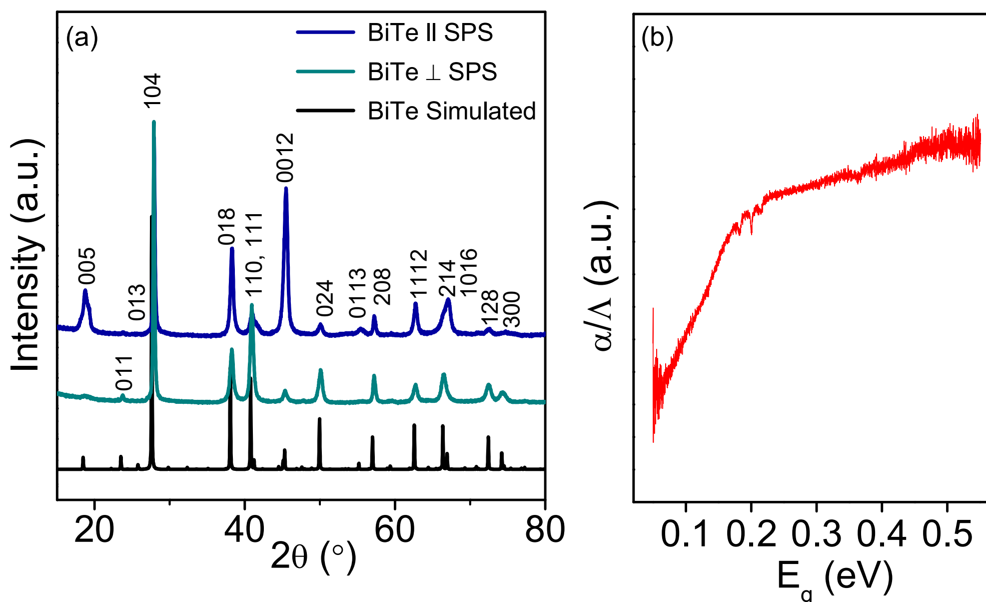

Figure 2.2. *(a) X-ray diffraction pattern of BiTe along different SPS-pressing directions. (b) Optical absorption spectra of powdered BiTe sample.*

BiTe, being a natural van der Waals hetero-structure, is expected to show anisotropic thermoelectric properties along different directions of measurements. Hence, sample preparation for the anisotropic measurement of TE properties of BiTe involvesseveral steps. Initially, high-quality polycrystalline ingot of BiTe has been synthesized by vacuum sealed tube melting reaction and the as-synthesized ingots are then grounded into fine powders. In the following steps, we have performed spark plasma sintering (SPS) on finely powdered BiTe sample and measured the transport properties along parallel to the SPS pressing direction, $SPS_{\|}$ (i.e. perpendicular to the stacking of different layers in BiTe) and perpendicular to SPS pressing direction, $SPS_{\perp}$ (i.e. parallel to the stacking of different layers in BiTe). All the reflections in the X-ray diffraction (XRD) patterns of the spark plasma sintered samples can be indexed based on phase pure BiTe structure (space group $P\overline{3}m1$; Figure 2.2a). However, significant difference in the relative intensities of (00l) and (hk0) planes in the XRD pattern of BiTe along $SPS_{\|}$ and $SPS_{\perp}$ can be observed which reflects strong anisotropy.

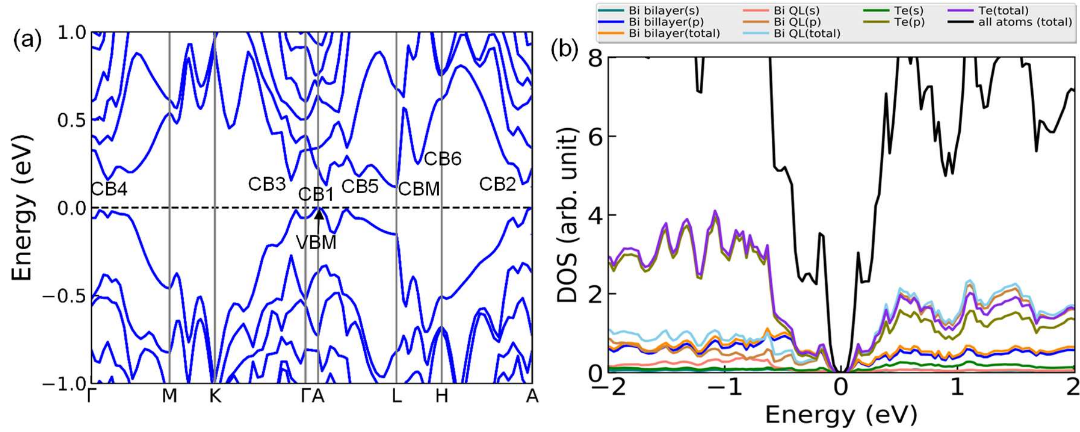

Figure 2.3. *(a) Electronic structure of BiTe at equilibrium. (b) Electrical density of states of BiTe.*

We have measured the optical absorption spectra of finely powdered BiTe sample (Figure 2.2b), which shows band gap of ~ 0.1 eV in BiTe. Electronic structure analysis (Figure 2.3a) of BiTe, calculated with the inclusion of spin-orbit coupling (SOC) in density functional theory (DFT), reveals an indirect band gap (E_g) of 0.12 eV which is in good agreement with the experimentally measured value. The valence band maximum (VBM) and conduction band minimum (CBM) appear at the A and L points, respectively, along with several near-edge band extrema (Figure 2.3a). It is quite interesting to note that band gap of BiTe is higher than the iso-structural compound BiSe (E_g ~ 0.02-0.04 eV)[9,31] despite a smaller electronegativity difference between the elements (i.e., Bi and Te) in the former compound. This observed difference in band gap probably originates from the topology of the electronic band structure of these compounds. BiTe, like its topological cousin BiSe, exhibits inverted a band structure between the valence band (which consisted majorly by 5p orbitals of Te, Figure 2.3b) and conduction bands (mainly consisting of 6p orbitals of Bi QL) around the Fermi level along the Γ-A line in the Brillouin zone. This band inversion is induced by the SOC[13]. Due to the relatively stronger SOC in BiTe (Te being heavier than Se), the energy difference between the inverted bands increases, giving rise to a larger band gap in BiTe.

BiTe exhibits high electrical conductivity (Figure 2.4a) in both the directions which decreases with temperature, depicting its semi-metallic nature. However, BiTe exhibits higher electrical conductivity along $SPS_{\perp}$ ($\sigma_{\perp}$~ 3340 S/cm at room temperature) compared to that of $SPS_{\parallel}$ ($\sigma_{\parallel}$ ~ 2192 S/cm at room temperature). Higher electrical conductivity in the

$SPS_{\perp}$ (measurement parallel to the layers) is attributed to the high anisotropic stacking of layers (QL of Bi_2Te_3 and sandwiched Bi-bilayer). Moreover, the measured *n*-type carrier concentrations (negative Hall coefficient) are ~ 2.65x10^{19}/cm^3 along $SPS_{||}$ and ~ 2.95 x10^{19}/cm^3 along $SPS_{\perp}$, showing little difference. Interestingly, BiTe possesses notably high carrier mobility of ~ 516 cm^2/Vs along $SPS_{||}$ and 707 cm^2/Vs along $SPS_{\perp}$, mainly originating from the metallic surface states of the dual topological insulator.[4,5,13,32–35] Such high carrier mobility of BiTe mainly contributes to the high electrical conductivity of the system. Mention must be made that the carrier mobility of BiTe is significantly higher than that of BiSe (~ 321 cm^2/Vs along $SPS_{\perp}$ and ~ 225 cm^2/Vs along $SPS_{||}$).[9]

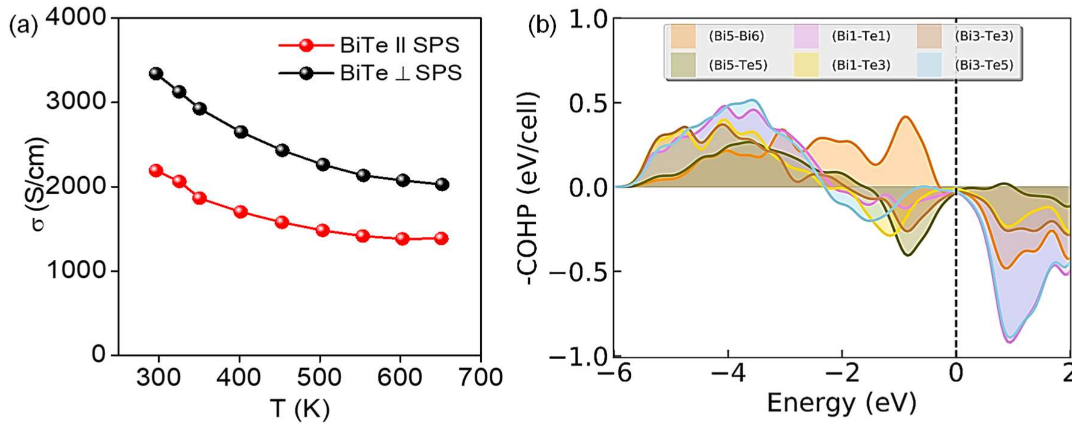

Figure 2.4. *(a) Temperature dependent electrical conductivity of pristine BiTe along the different SPS-pressing directions. (b) Crystal orbital Hamilton population (COHP) analysis of BiTe.*

Further, the origin of high electrical mobility of BiTe, can be understood from analysis of its electronic structure near the gap separating conduction band minimum (CBM) and valence band maximum (VBM). As the BiTe is *n*-type, evident from negative Seebeck coefficient as well (Figure 2.5a), we focus on electronic states at the band edge(s) of its the conduction band manifold. Band inversion usually gives rise to multiples peaks in conduction and valence bands near the Fermi level which are beneficial to thermoelectric transport properties.[36] In the electronic structure (Figure 2.3a) of BiTe, we see sharp Dirac-cone like features in the conduction band along the A-L (CB1) and Γ-K (CB3) directions which are just 2 meV and 7 meV above the CBM (at the L point) respectively, resulting from the inverted band structure. In addition to these, similar sharp conical features also

occur along the H-A (CB2), Γ-M (CB4), A-L (CB5) and L-H (CB6) directions which lie 3 meV, 8 meV, 11 meV and 24 meV, respectively above the CBM. On the other hand, CBM at the L point exhibits parabolic dispersion along L-A but it has linear dispersion along the L-H direction. Interestingly, all the band edges of the CB (i.e., CB1, CB2, CB3, CB4, CB5 and CB6) lie in the close energy proximity of CBM, which is much smaller than the thermal energy scale of the room temperature ($k_BT \sim 25$ meV), signifying that these states in bands extrema contribute to the electrical transport properties of BiTe even at room temperature, which helps in retaining high carrier mobility. As the compounds with linearly dispersing electronic bands (e.g, Dirac semimetals)[33,35] are known to exhibit high carrier mobility, further enhancement in carrier mobility and electrical conductivity of BiTe is caused by its sharp Dirac-cone like features near the conduction band edge.

Chemical origin of the enhanced electrical conductivity in BiTe can also be rationalized from the analysis of its chemical bonding based the crystal orbital Hamilton population (COHP) analysis (Figure 2.4b). It was recently shown[37] that the anti-bonding states near the Fermi level constitute a conductive network, yielding high electrical conductivity. Calculated COHP curves for different pair of nearest-neighbor atoms in BiTe reveal anti-bonding states (i.e., negative values of COHP in Figure 2.4b) near the Fermi level, uncovering clearly the chemical origin of the observed high electrical conductivity in BiTe.

BiTe exhibits reasonably high negative Seebeck coefficient (S) values, depicting *n*-type electronic conduction (Figure 2.5a). BiTe exhibits higher S along SPS-pressing direction ($S \sim$ -42.3 μV/K at 297 K) compared to that of perpendicular to SPS-pressing direction ($S \sim$ -37.8 μV/K at 297 K) which is mainly ascribed to slightly reduced carrier concentrations along SPS-pressing directions.[38–40] The absolute value of the Seebeck coefficient ($|S|$) of BiTe increases with temperature up to ~ 600 K, then it starts to decrease because of bipolar conduction. Typically, S of BiTe along $SPS_{||}$ increases from - 42.3 μV/K at 297 K to -74.9 μV/K at 600 K, then, S value decreases to -72.2 μV/K at 650 K.

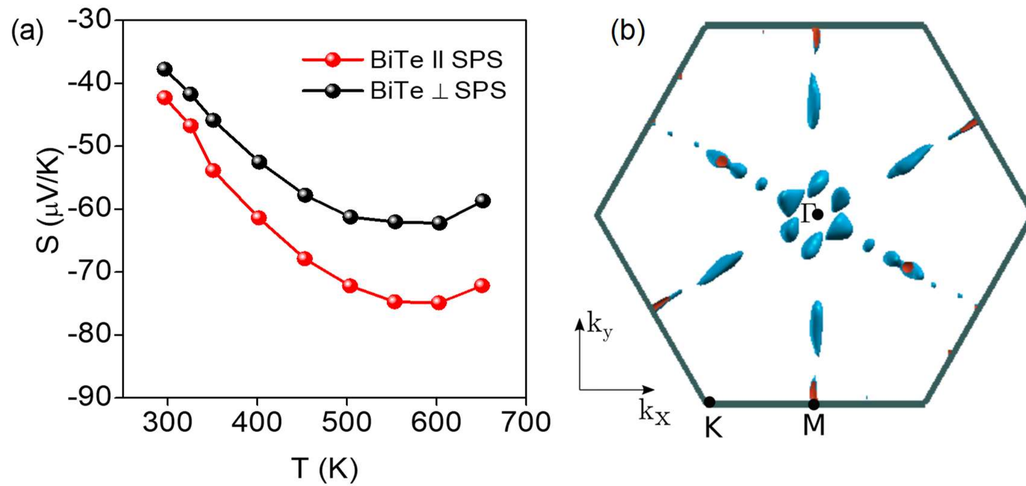

Figure 2.5. *(a) Temperature dependent Seebeck coefficient (S) of pristine BiTe along the different SPS-pressing directions. (b) Fermi surface of BiTe.*

The presence of wiggly bands, characterized by the multiple band extrema and valley degeneracies in the electronic bands near the Fermi level significantly enhances the Seebeck coefficients of materials.[4,41,42] The spin-orbit coupled electronic structure (Figure 2.3a) of BiTe exhibits multiple pockets in its conduction band, as discussed in the previous section. Several band-edges appear just within 10 meV above the CBM (L point), which is smaller than the thermal broadening (~ k_BT = 25 meV at 300 K) of the Fermi-Dirac distribution even at room temperature. Hence all the conduction band pockets (i.e., CB1, CB2, CB3, CB4, CB6, CB6) get populated differentially with temperature gradient and contribute to the electronic transport in BiTe. Further, bands at CB1 (along A-L), CB2 (along H-A) and CB3 (along Γ-K) possesses high valley degeneracies of 3, 3 and 6 respectively. On the other hand, CB4 and CB5 which appear along the Γ-M and A-L directions have valley degeneracy of 6 and 3, respectively. Another near-band-edge is seen along the L-H (CB6) line at E =24 meV above the CBM with valley degeneracy of 3. Visualization of the Fermi surface corresponding to *n*-type doping confirms the presence of multiple carrier pockets in the conduction band (Figure 2.5b). The Seebeck coefficient is reasonably high in BiTe due to these multitude near-edge band extrema of different energies while maintaining large carrier concentration as well as linearly dispersing bands.

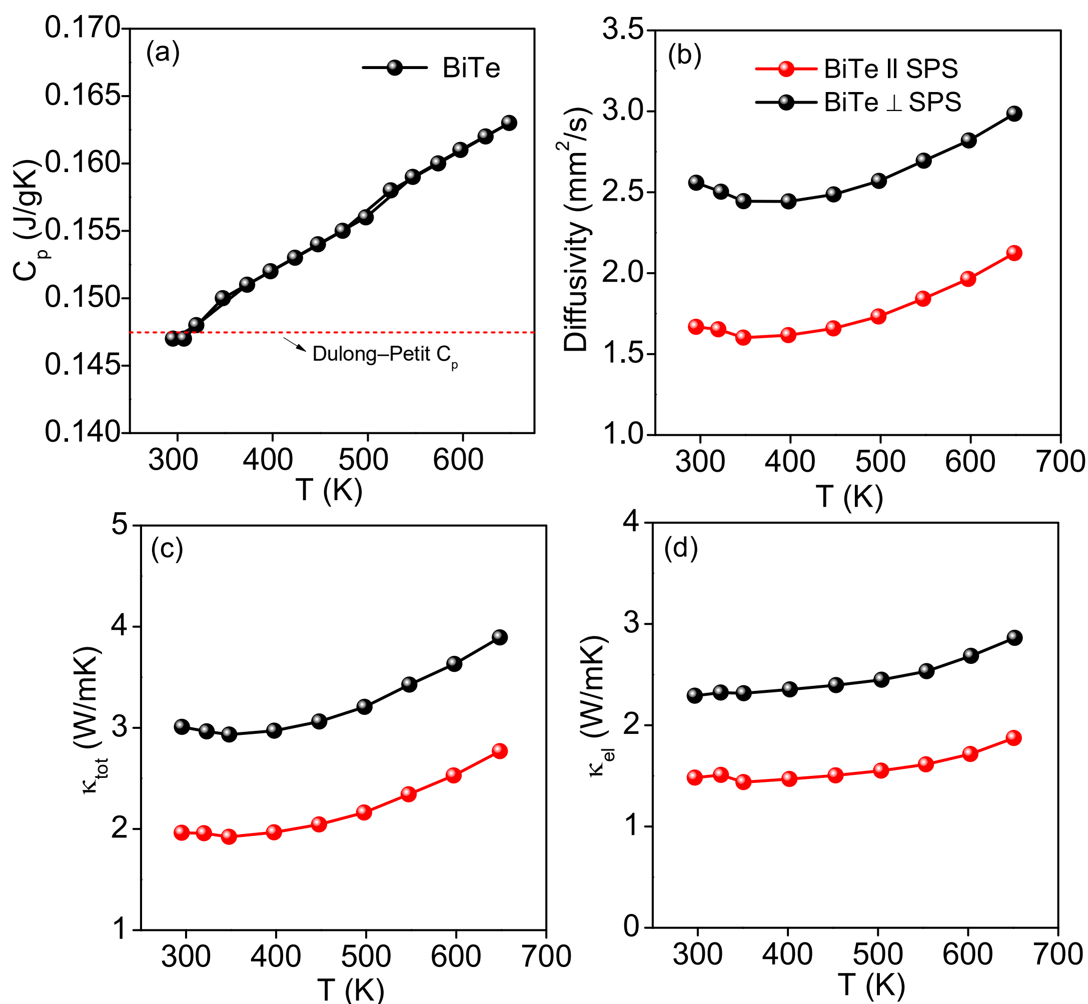

Figure 2.6. *(a) Temperature dependent heat capacity of BiTe. Temperature dependent (b) thermal diffusivity, (c) total thermal conductivity (κ_{tot}) and (d) electronic thermal conductivity (κ_{el}) of BiTe along parallel and perpendicular to SPS-pressing directions.*

Temperature dependent total thermal conductivity (κ_{tot}) of BiTe is measured along both $SPS_{\parallel}$ and $SPS_{\perp}$ directions (Figure 2.6c) in the 300-650K range κ_{tot} of BiTe along $SPS_{\parallel}$ increases from 1.96W/mK at 300 K to 2.76 W/mK at 650 K, whereas κ_{tot} of BiTe along $SPS_{\perp}$ increases from 3 W/mK to 3.89 W/mK at 650 K. Increase in the κ_{tot} at elevated temperature is mainly attributed to the bipolar thermo-diffusion. We have derived lattice thermal conductivity of BiTe by subtracting the electrical thermal conductivity (κ_{el}, Figure 2.6d) from κ_{tot}. BiTe exhibits intrinsically low κ_{lat} along both the $SPS_{\parallel}$ and $SPS_{\perp}$ directions (Figure 2.7a), which is close to its theoretical minimum ($\kappa_{min} \sim 0.25$ *W/mK*) calculated by

Cahill's formula along layer stacking direction (Γ-A direction).[43,44] However, BiTe exhibits lower κ_{lat} (~ 0.47 W/mK at 300 K) along $SPS_{\parallel}$ compared to that of $SPS_{\perp}$ (~ 0.72 W/mK at 300K) which mainly ascribed to weak bonding interactions between the adjacent layers.

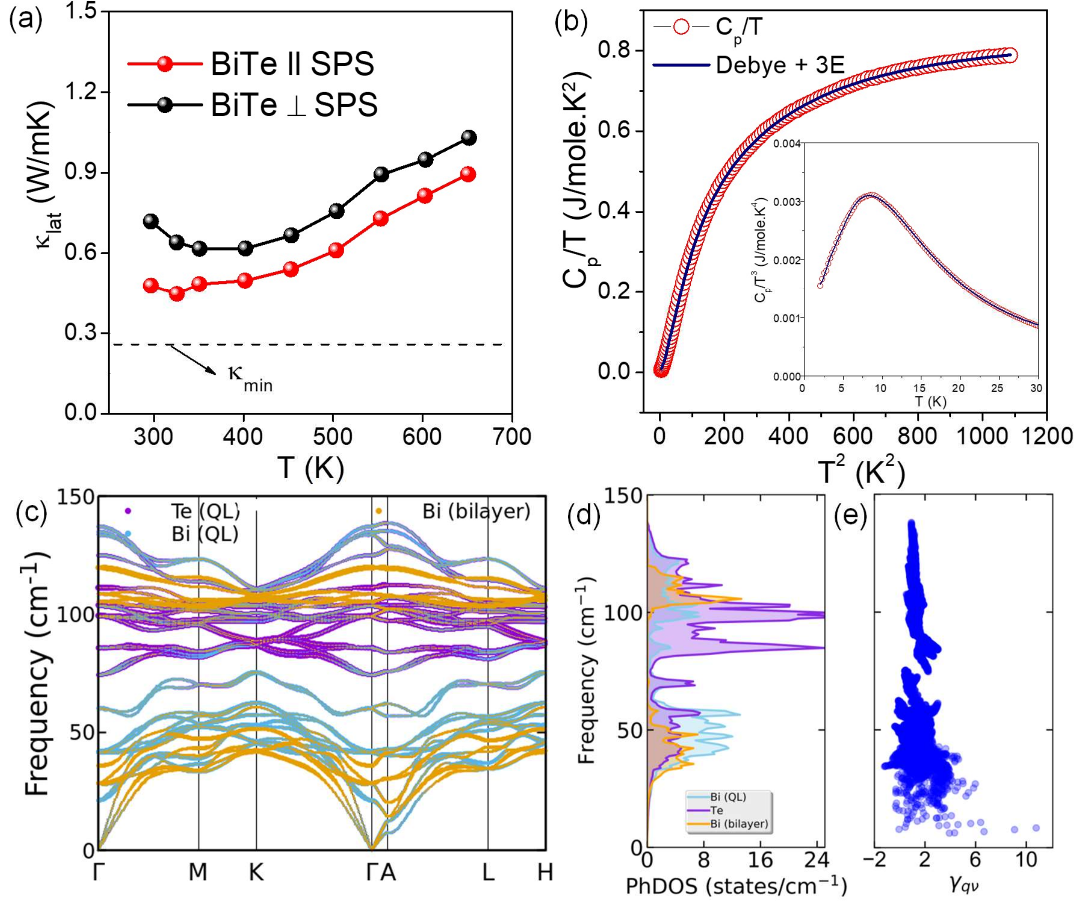

Figure 2.7. *(a) Temperature dependent lattice thermal conductivity (κ_{lat}) of BiTe. (b) Low temperature C_p/T vs T^2 plot of BiTe. Inset shows C_p/T^3 vs T plot. (c) Atom projected phonon dispersion of BiTe. (d) Atom projected phonon-DOS and (e) mode average Grüneisen parameter of BiTe.*

To understand the origin of intrinsically low κ_{lat} of BiTe and to find out the presence of distinguished soft optical modes, low temperature heat capacity (C_p) of BiTe from 1.9 to 200K has been measured. Figure 2.7b represents the fitted data points of C_p/T *vs.* T^2 of BiTe using Debye-Einstein model[9,45] which is as follows:

$$\frac{C_p}{T} = \gamma + \beta T^2 + \sum_n \left(A_n \left(\Theta_{E_n}\right)^2 . \left(T^2\right)^{\frac{-3}{2}} . \frac{e^{\frac{\Theta_{E_n}}{T}}}{\left(e^{\frac{\Theta_{E_n}}{T}} - 1\right)^2} \right) \quad (2.1),$$

where electronic contribution in heat capacity is given by the first term, γ of the equation, the contribution from the Debye modes is represented by the second term, βT^2, in which $\beta = B.\left(\frac{12\pi^4 N_A \kappa_B}{5}\right).(\Theta_D)^{-3}$; and N_A, k_B and Θ_D are Avogadro number, Boltzmann constant and Debye Temperature, respectively. B is given by $B = 1 - \Sigma_n A_n / 3N_f R$, where N_f is the number of atoms per formula unit and R is universal gas constant (8.314 J/molK). The third term in equation (1) represents the contributions from Einstein oscillators and A_n being the Einstein prefactor of nth Einstein mode, Θ_{En}. Low-T specific heat capacity, C_p of BiTe fits quite well by using three Einstein modes with characteristics temperatures Θ_{E1} = 26.47 K (i.e. ~18.4 cm^{-1}),Θ_{E2} = 54.65K (i.e. ~38 cm^{-1}) and Θ_{E3} = 114.97K (i.e. ~78 cm^{-1}), indicating the presence of low frequency optical modes. Interestingly, the derived Debye temperature (Θ_D) for BiTe is 162 K which also indicates a low cut-off frequency of the acoustic phonons of BiTe. Further, low temperature (2-30K) C_p/T^3 *vs.* T behaviour of BiTe (inset of Figure 2.7b) shows broad peak which resembles the Boson-peak like hump observed in the disordered glasses, skutterudites[46] and clatherates.[47] This phenomenon also confirms the presence of excess low-frequency optical phonon density of states which interact with acoustic phonons, resulting in suppressed phonon group velocities and hence ultra-low κ_{lat}. Further we have derived average sound velocity (ν_a) of BiTe which is ~ 1760 m/s using the equation of $\Theta_D = \frac{h}{k_B}\left[\frac{3N}{4\pi V}\right]^{1/3} \upsilon_a$, where h is plank constant, k_B is Boltzmann constant, N is number of atoms per unit cell and V is volume of the unit cell.[48] Low sound velocity of BiTe partly explains the low κ_{lat} of BiTe. In-order to unveil the origin of such low-frequency of optical modes in BiTe, we have examined lattice dynamics of BiTe.

Calculated phonon dispersion (Figure 2.7c) of BiTe shows low (< 40 cm^{-1}) cut-off frequencies of the acoustic phonon modes that limit the phonon group velocity below 3000 m/s in different crystallographic directions (see Table 2.1) of the Brillouin zone, resulting in a low κ_{lat}. Along the stacking direction (i.e., Γ-A), the average sound velocity (1539 m/s) is lower than the other two directions (Γ-M: 1922 m/s, Γ-K: 1986 m/s) which supports the

Table 2.1. *Sound velocities of BiTe in different high symmetric directions.*

Directions	Velocity (m/s)			
	LA	TA1	TA2	Average
Γ- M	2700	1403	1660	1922
Γ- K	2774	1408	1775	1986
Γ- A	1067	1775	1775	1539

experimental finding of notably lower κ_{lat} ($\propto \nu_a^2$) along the SPS$_\parallel$ direction. It is seen from the phonon dispersion (Figure 2.7c) as well as the atom projected phonon density of states (Figure 2.7d) that the frequencies of the vibrations associated with the Bi bilayer remain localized in two regions: (a) a low energy range of 25-50 cm^{-1} that mainly participate in the thermal scattering and conduction processes and (b) a high energy range of 100-125 cm^{-1}. Visualizations of atomic displacements of some of the low frequency (e.g., 36 and 41 cm^{-1} at Γ point; 42 and 46 cm^{-1} at K point) optical phonons (Figure 2.8 and Figure 2.9) clearly show the localization of theses vibrations in the Bi bilayer in BiTe. Figure 2.7c furthers reveals that Bi and Te atoms of the Bi_2Te_3 quintuple layer also contribute to the low frequency optical phonons (< 60 cm-1) in addition to those in the Bi-bilayer. The lattice thermal conductivity of BiTe is lower along the stacking direction (i.e. $\kappa_{lat}^{\parallel}$ along SPS$_\parallel$) due to the weaker bonding and weak force-constants and lower group velocities of sound waves compared to those in the plane of layer direction (i.e. $\kappa_{lat}^{\perp}$ along SPS$_\perp$).[9,49,50]

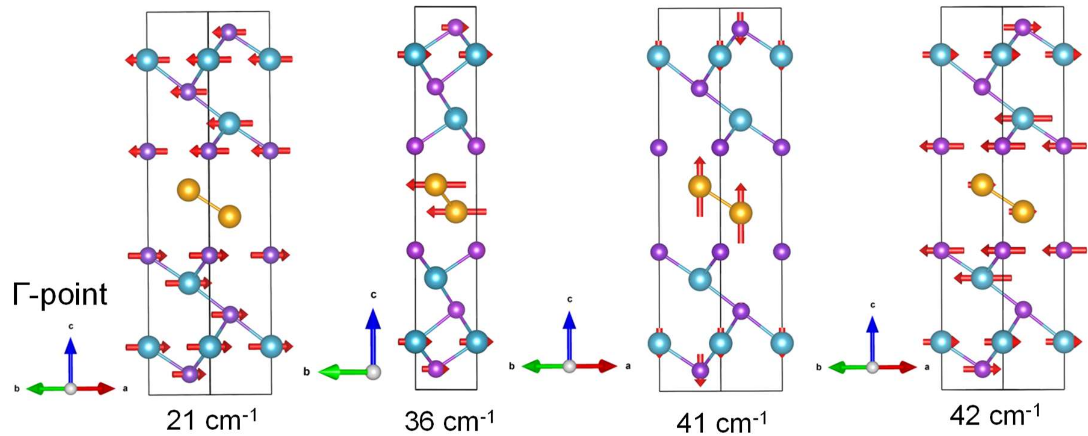

Figure 2.8. *Few low frequency phonon modes at Γ point of BiTe. Pink, cyan and yellow color represent Te, Bi atom of Bi_2Te_3 layer and Bi atom of Bi_2 layer respectively.*

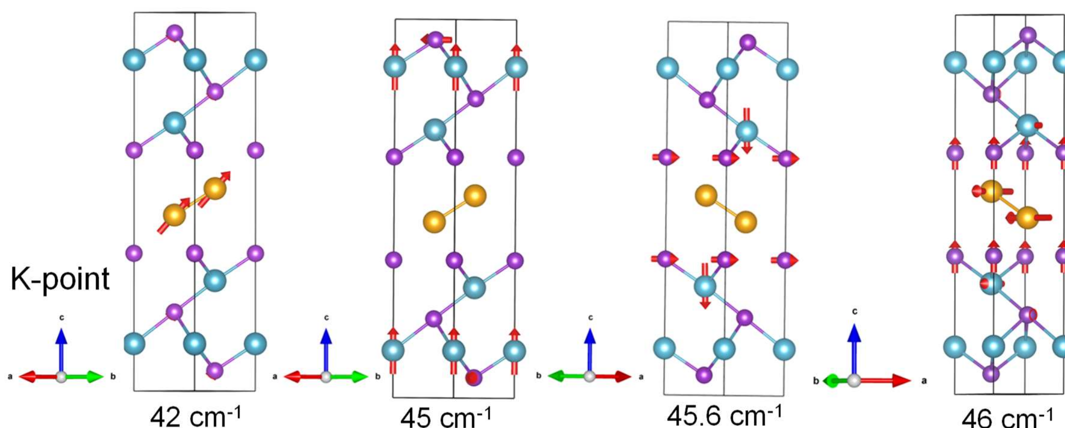

Figure 2.9. *Few low frequency phonon modes at K point of BiTe. Pink, cyan and yellow color represent Te, Bi atom of Bi_2Te_3 layer and Bi atom of Bi_2 layer respectively.*

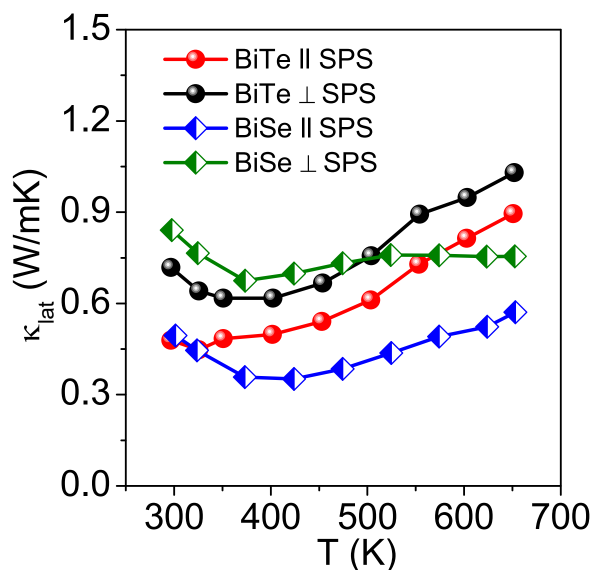

Figure 2.10. *Comparison of lattice thermal conductivity (κ_{lat}) of BiTe and BiSe along parallel and perpendicular to SPS-pressing directions.*[9]

Interestingly although both BiSe and BiTe possess very low κ_{lat} with similar directional dependence, the difference between $\kappa_{lat}^{\parallel}$ and $\kappa_{lat}^{\perp}$ is relatively smaller in BiTe (Figure 2.10).[9] The low frequency vibrations of Bi-bilayer in BiTe are relatively less localized compared to those in BiSe. The lowest frequency modes in the optical phonon branch in BiSe involve vibrations of only the Bi-bilayer,[9] whereas in the case of BiTe, the low energy phonon branch has mixed contributions from Bi-bilayer as well as from Bi of

Bi_2Te_3 QL (Figure 2.7c). Such mixing of vibrations of the bilayer and the QL indicates that their interaction is relatively stronger in BiTe than in BiSe, resulting in a smaller difference between $\kappa_{lat}^{\parallel}$ and $\kappa_{lat}^{\perp}$ in BiTe compared to that of BiSe.

A strong coupling between the acoustic and low-energy optical phonon modes in BiTe is evident in Figure 2.7d where the phonon DOS of Te, Bi of the QL and Bi of bi-layer overlap over a reasonably broad energy range of frequencies (~ 25 – 60 cm^{-1}). This acoustic- optical phonon mode-coupling increases the scattering phase-space of phonons leading to reduced phonon lifetime and hence, a low κ_{lat}. The anharmonicity of a material plays an important role in enhancing the phonon-scattering rates and thereby inducing a low κ_{lat} in the material.[9,43,51,52] The degree of intrinsic anharmonicity in BiTe has been assessed by evaluating the mode Grüneisen parameters ($\gamma_{q\upsilon}$) at each q point and for every phonon mode υ as function of phonon frequency (ω) (Figure 2.7e). It reveals very high $\gamma_{q\upsilon}$ for the acoustic (maximum $\gamma_{q\upsilon}$ ~ 11) and the low frequency optical ($\gamma_{q\upsilon}$ ~ 5) phonon branches.

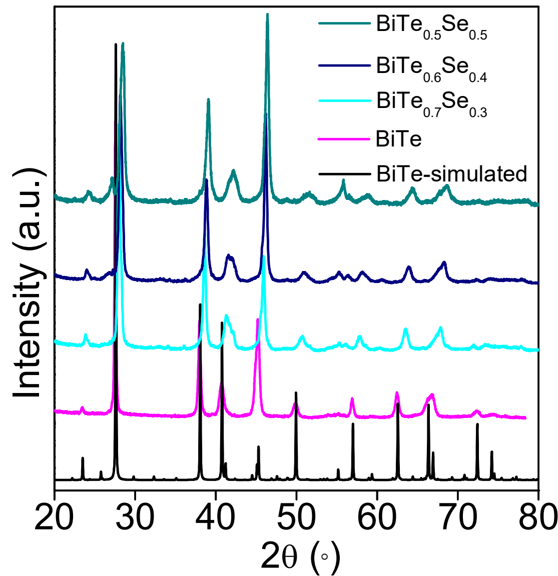

Figure 2.11. *Powder X-ray diffraction patterns of* $BiTe_{1-x}Se_x$.

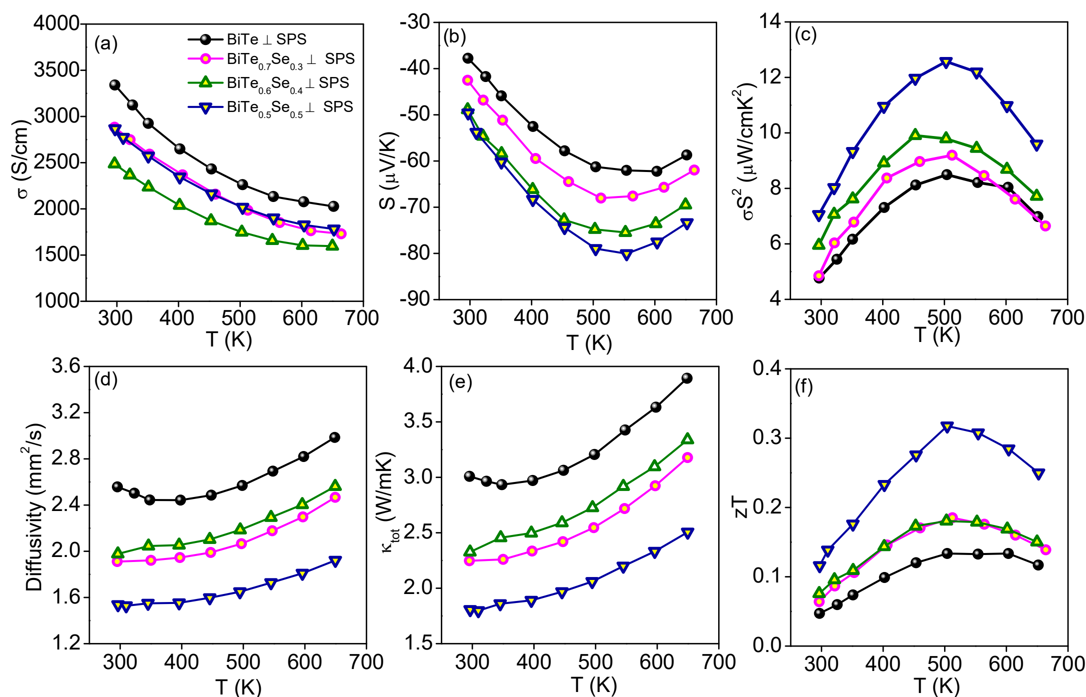

Figure 2.12. *Temperature dependent (a) electrical conductivity (σ), (b) Seebeck coefficient (S), (c) power factor (σS^2), (d) thermal diffusivity (D), (e) total thermal conductivity (κ_{tot}) and (f) zT of $BiTe_{1-x}Se_x$ perpendicular to SPS-pressing direction ($SPS_{\perp}$).*

Thermoelectric performance of BiTe is further optimized by substituting Se in place of Te in BiTe. PXRD patterns of as-synthesized powdered $BiTe_{1-x}Se_x$ (x = 0.3-0.5) samples could be indexed based on the hexagonal BiTe ($P\bar{3}m1$) without any additional peaks being observed within the detection limits of XRD (Figure 2.11). Electrical and thermal transport properties of all the $BiTe_{1-x}Se_x$ (x = 0.3-0.5) are measured in both directions, i.e.; along $SPS_{\perp}$ (Figure 2.12) and $SPS_{||}$ (Figure 2.13). Se substitution in $BiTe_{1-x}Se_x$ decreases the electrical conductivity but increases the Seebeck coefficient. Because of an improved Seebeck coefficient (-80 μV/K at 555 K, Figure 2.12b), $BiTe_{0.5}Se_{0.5}$ exhibits highest power factor of ~ 12.6 $\mu W/cmK^2$ at 500 K along $SPS_{\perp}$ (Figure 2.12c). Further, Se substitution decreases the thermal conductivity effectively by enhanced point defect scattering and results in low κ_{tot} of ~ 1.8 W/mK and ~ 1.5 W/mK in $BiTe_{0.5}Se_{0.5}$ along $SPS_{\perp}$ and $SPS_{||}$ respectively at room temperature. As a result of enhanced power factor and reduced thermal conductivity, $BiTe_{0.5}Se_{0.5}$ exhibits maximum zT of ~ 0.32 at 500 K along $SPS_{\perp}$ (Figure 2.12f) which makes BiTe a promising system to explore as an *n*-type thermoelectric

material near room temperatures. Further optimization of thermoelectric properties of $BiTe_{0.5}Se_{0.5}$ can be achieved by reducing its bipolar conduction.

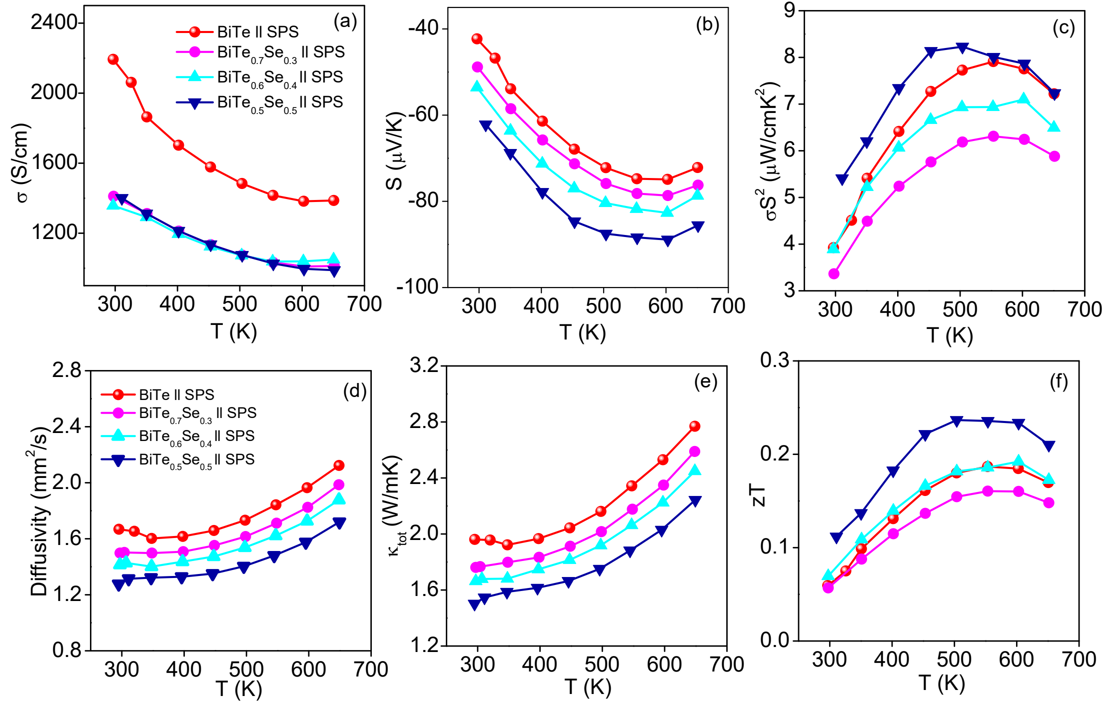

***Figure 2.13.**. Temperature dependent (a) electrical conductivity (σ), (b) Seebeck coefficient (S), (c) power factor (σS^2), (d) thermal diffusivity (D), (e) total thermal conductivity (κ_{tot}) and (f) zT of $BiTe_{1-x}Se_x$ parallel to SPS-pressing directions.*

2.4 Conclusions

In conclusion, the challenging concurrence of intrinsically low lattice thermal conductivity and high carrier mobility in a crystalline solid has been achieved in BiTe, as facilitated by its unique *dual* topological quantum phases. BiTe possesses both the quantum phases, TCI and WTI, which is distinct from the well-known TI, Bi_2Te_3 (where m:n = 0:1). BiTe being a WTI hosts layered hetero-structure and hence it exhibits low κ_{lat} of 0.47- 0.8 W/mK in the 300-650 K. Measurement of its low temperature heat capacity and detailed analysis of phonon dispersion confirm the presence of low-lying optical phonon branches, originating largely from the localized vibrations of zigzag Bi-bilayers of BiTe. These low energy optical modes effectively interact with the acoustic phonon modes, resulting in intrinsically low κ_{lat} in BiTe. BiTe exhibits a negative Seebeck coefficient attributing to *n*-type

electronic conduction. BiTe, being a TCI with metallic surface states, possess high carrier mobility (μ) of ~ 516 cm^2/Vs and 707 cm^2/Vs along parallel and perpendicular to spark plasma sintering (SPS) directions, respectively, at room temperature. First-principles theoretical analysis of electronic structure shows the presence of multiple valleys of nearly linearly dispersing conduction bands with significant anti-bonding states close to the Fermi level, resulting in a facile conductive network; hence supports manifestation of high μ. Co-existence of distinct topological quantum phases in BiTe which is responsible for the simultaneous ultra-low κ_{lat} and high μ, holds the promise for innovative design of new crystalline solids with decoupled thermal and electronic transport properties, which are fundamentals to the efficient thermoelectrics.

2.5 References

(1) Gooth, J.; Schierning, G.; Felser, C.; Nielsch, K. *MRS Bull.* **2018**, *43*, 187–192.
(2) Roychowdhury, S.; Samanta, M.; Banik, A.; Biswas, K. *J. Solid State Chem.* **2019**, *275*, 103–123.
(3) Müchler, L.; Zhang, H.; Chadov, S.; Yan, B.; Casper, F.; Kübler, J.; Zhang, S. C.; Felser, C. *Angew. Chemie - Int. Ed.* **2012**, *51*, 7221–7225.
(4) Heremans, J. P.; Cava, R. J.; Samarth, N. *Nat. Rev. Mater.* **2017**, *2*, 17049.
(5) Banik, A.; Roychowdhury, S.; Biswas, K. *Chem. Commun.* **2018**, *54*, 6573–6590.
(6) Tan, G.; Zhao, L.-D.; Shi, F.; Doak, J. W.; Lo, S.-H.; Sun, H.; Wolverton, C.; Dravid, V. P.; Uher, C.; Kanatzidis, M. G. *J. Am. Chem. Soc.* **2014**, *136*, 7006–7017.
(7) Roychowdhury, S.; Shenoy, U. S.; Waghmare, U. V; Biswas, K. *Angew. Chemie Int. Ed.* **2015**, *127*, 15456–15460.
(8) Chen, L.-C.; Chen, P.-Q.; Li, W.-J.; Zhang, Q.; Struzhkin, V. V.; Goncharov, A. F.; Ren, Z.; Chen, X.-J. *Nat. Mater.* **2019**, *18*, 1321–1326.
(9) Samanta, M.; Pal, K.; Pal, P.; Waghmare, U. V.; Biswas, K. *J. Am. Chem. Soc.* **2018**, *140*, 5866–5872.
(10) Wei, P.; Yang, J.; Guo, L.; Wang, S.; Wu, L.; Xu, X.; Zhao, W.; Zhang, Q.; Zhang, W.; Dresselhaus, M. S.; Yang, J. *Adv. Funct. Mater.* **2016**, *26*, 5360–5367.
(11) Sharma, P. A.; Sharma, A. L. L.; Medlin, D. L.; Morales, A. M.; Yang, N.; Barney, M.; He, J.; Drymiotis, F.; Turner, J.; Tritt, T. M. *Phys. Rev. B* **2011**, *83*, 235209.
(12) Bos, J. W. G.; Faucheux, F.; Downie, R. A.; Marcinkova, A. *AIP Conference Proceedings* **2012**, *1449*, 83–86.
(13) Eschbach, M.; Lanius, M.; Niu, C.; Młyńczak, E.; Gospodarič, P.; Kellner, J.; Schüffelgen, P.; Gehlmann, M.; Döring, S.; Neumann, E.; , E.; Luysberg, M.; Mussler, G.; Plucinski, L.; Morgenstern, M.; Grützmacher, D.; Bihlmayer, G.; Blügel, S.; Schneider, C. *Nat. Commun.* **2017**, *8*, 14976.
(14) Poudel, B.; Hao, Q.; Ma, Y.; Lan, Y.; Minnich, A.; Yu, B.; Yan, X.; Wang, D.; Muto, A.; Vashaee, D.; Chen, X.; Liu, J.; Dresselaus; Chen, G.; Ren, Z. *Science* **2008**, *320*, 634–638.

(15) Kim, S. Il; Lee, K. H.; Mun, H. A.; Kim, H. S.; Hwang, S. W.; Roh, J. W.; Yang, D. J.; Shin, W. H.; Li, X. S.; Lee, Y. H.; Snyder, G. J.; Kim, S. W. *Science* **2015**, *348*, 109–114.

(16) Pan, Y.; Wei, T.-R.; Wu, C.-F.; Li, J.-F. *J. Mater. Chem. C* **2015**, *3*, 10583–10589.

(17) Liu, W. S.; Zhang, Q.; Lan, Y.; Chen, S.; Yan, X.; Zhang, Q.; Wang, H.; Wang, D.; Chen, G.; Ren, Z. *Adv. Energy Mater.* **2011**, *1*, 577–587.

(18) Zhang, H.; Liu, C. X.; Qi, X. L.; Dai, X.; Fang, Z.; Zhang, S. C. *Nat. Phys.* **2009**, *5*, 438–442.

(19) Zhang, T.; Cheng, P.; Chen, X.; Jia, J.-F.; Ma, X.; He, K.; Wang, L.; Zhang, H.; Dai, X.; Fang, Z.; Xie, X.; Xue, Q.-K. *Phys. Rev. Lett.* **2009**, *103*, 266803.

(20) Chen, Y. L.; Analytis, J. G.; Chu, J.-H.; Liu, Z. K.; Mo, S.-K.; Qi, X. L.; Zhang, H. J.; Lu, D. H.; Dai, X.; Fang, Z.; Xie, X.; Xue, Q.-K. *Science* **2009**, *325*, 178–181.

(21) Biswas, K.; He, J.; Blum, I. D.; Wu, C.-I.; Hogan, T. P.; Seidman, D. N.; Dravid, V. P.; Kanatzidis, M. G. *Nature* **2012**, *489*, 414–418.

(22) Samanta, M.; Biswas, K. *J. Am. Chem. Soc.* **2017**, *139*, 9382–9391.

(23) Wu, H. J.; Zhao, L.-D.; Zheng, F. S.; Wu, D.; Pei, Y. L.; Tong, X.; Kanatzidis, M. G.; He, J. Q. *Nat. Commun.* **2014**, *5*, 4515.

(24) Kresse, G.; Furthmüller, J. *Comput. Mater. Sci.* **1996**, *6*, 15–50.

(25) Kresse, G.; Furthmüller, J. *Phys. Rev. B* **1996**, *54*, 11169–11186.

(26) Blochl, P. E. *Physical Review B* **1994**, *54*, 17953.

(27) Perdew, J. P.; Burke, K.; Ernzerhof, M. *Phys. Rev. Lett.* **1996**, *77*, 3865–3868.

(28) Perdew, J. P.; Ruzsinszky, A.; Csonka, G. I.; Vydrov, O. A.; Scuseria, G. E.; Constantin, L. A.; Zhou, X.; Burke, K. *Phys. Rev. Lett.* **2008**, *100*, 136406.

(29) Deringer, V. L.; Tchougréeff, A. L.; Dronskowski, R. *J. Phys. Chem. A* **2011**, *115*, 5461–5466.

(30) Togo, A.; Tanaka, I. *Scr. Mater.* **2015**, *108*, 1–5.

(31) Majhi, K.; Pal, K.; Lohani, H.; Banerjee, A.; Mishra, P.; Yadav, A. K.; Ganesan, R.; Sekhar, B. R.; Waghmare, U. V; Anil Kumar, *Appl. Phys. Lett.* **2017**, *110*, 162102.

(32) Lin, C. C.; Kim, G.; Ginting, D.; Ahn, K.; Rhyee, J. S. *ACS Appl. Mater. Interfaces* **2018**, *10*, 10927–10934.

(33) Liang, T.; Gibson, Q.; Ali, M. N.; Liu, M.; Cava, R. J.; Ong, N. P. *Nat. Mater.* **2015**, *14*, 280–284.

(34) Xiao, Y.; Wang, D.; Qin, B.; Wang, J.; Wang, G.; Zhao, L.-D. *J. Am. Chem. Soc.* **2018**, *140*, 13097–13102.

(35) Khoury, J. F.; Rettie, A. J. E.; Khan, M. A.; Ghimire, N. J.; Robredo, I.; Pfluger, J. E.; Pal, K.; Wolverton, C.; Bergara, A.; Jiang, J. S.; Schoop, L. M.; Vergniory, M. G.; Mitchell, J. F.; Chung, D. Y.; Kanatzidis, M. G. *J. Am. Chem. Soc.* **2019**, *141*, 19130–19137.

(36) Pal, K.; Anand, S.; Waghmare, U. V. *J. Mater. Chem. C* **2015**, *3*, 12130–12139.

(37) Xi, L.; Pan, S.; Li, X.; Xu, Y.; Ni, J.; Sun, X.; Yang, J.; Luo, J.; Xi, J.; Zhu, W.; W.; Li, X.; Jiang, D.; Dronskowski, R.; Shi, X.; Snyder, G. J.; Zhang, W. *J. Am. Chem. Soc.* **2018**, *140*, 10785–10793.

(38) Rhyee, J.-S.; Lee, K. H.; Lee, S. M.; Cho, E.; Kim, S. Il; Lee, E.; Kwon, Y. S.; Shim, J. H.; Kotliar, G. *Nature* **2009**, *459*, 965–968.

(39) Zhao, L.-D.; Lo, S.-H.; Zhang, Y.; Sun, H.; Tan, G.; Uher, C.; Wolverton, C.; Dravid, V. P.; Kanatzidis, *Nature* **2014**, *508*, 373–377.

(40) Li, Y.; Shi, X.; Ren, D.; Chen, J.; Chen, L. *Energies* **2015**, *8*, 6275–6285.

(41) Wang, S.; Sun, Y.; Yang, J.; Duan, B.; Wu, L.; Zhang, W.; Yang, J. *Energy Environ. Sci.* **2016**, *9*, 3436–3447.
(42) Tan, G.; Zhao, L. D.; Shi, F.; Doak, J. W.; Lo, S. H.; Sun, H.; Wolverton, C.; Dravid, V. P.; Uher, C.; Kanatzidis, M. G. *J. Am. Chem. Soc.* **2014**, *136*, 7006–7017.
(43) Dutta, M.; Matteppanavar, S.; Prasad, M. V. D.; Pandey, J.; Warankar, A.; Mandal, P.; Soni, A.; Waghmare, U. V.; Biswas, K. *J. Am. Chem. Soc.* **2019**, *141*, 20293–20299.
(44) Cahill, David G. Watson, S. K., Pohl, R. O. *Phys. Rev. B* **1992**, *46*, 6131–6140.
(45) Jana, M. K.; Biswas, K. *ACS Energy Lett.* **2018**, *3*, 1315–1324.
(46) Shi, X.; Yang, J.; Salvador, J. R.; Chi, M.; Cho, J. Y.; Wang, H.; Bai, S.; Yang, J.; Zhang, W.; Chen, L. *J. Am. Chem. Soc.* **2011**, *133*, 7837–7846.
(47) Takabatake, T.; Suekuni, K.; Nakayama, T.; Kaneshita, E. *Rev. Mod. Phys.* **2014**, *86*, 669–716.
(48) Xiao, Y.; Chang, C.; Pei, Y.; Wu, D.; Peng, K.; Zhou, X.; Gong, S.; He, J.; Zhang, Y.; Zeng, Z.; Zhao, L.-D. *Phys. Rev. B* **2016**, *94*, 125203.
(49) Pal, K.; He, J.; Wolverton, C. *Chem. Mater.* **2018**, *30*, 7760–7768.
(50) Pal, K.; Xia, Y.; He, J.; Wolverton, C. *Phys. Rev. Mater.* **2019**, *3*, 085402.
(51) Jana, M. K.; Pal, K.; Waghmare, U. V.; Biswas, K. *Angew. Chemie Int. Ed.* **2016**, *55*, 7792–7796.
(52) Nielsen, M. D.; Ozolins, V.; Heremans, J. P. *Energy Environ. Sci.* **2013**, *6*, 570–578.

Chapter 3

2D Nanosheets of Topological Quantum Materials from Homologous $(Bi_2)_m(Bi_2Se_3)_n$ Heterostructures: Synthesis and Ultralow Thermal Conductivity

Chapter 3

2D Nanosheets of Topological Quantum Materials from Homologous $(Bi_2)_m(Bi_2Se_3)_n$ Heterostructures: Synthesis and Ultralow Thermal Conductivity[†]

Summary

Topological quantum materials with layered heterostructure hold great promise to exhibit low thermal conductivity. Homologous $(Bi_2)_m(Bi_2Se_3)_n$ (m, n: integers) series hosts different types of topological quantum materials with layered structure such as Bi_4Se_3 (m = 1, n = 1; a topological semimetal), BiSe (m = 1, n= 2; a weak topological insulator) and well known Bi_2Se_3 (m= 0, n=1; a strong topological insulator). In BiSe, Bi-Bi bilayer is sandwiched between the Se-Bi-Se-Bi-Se quintuple layers via weak van der Waals (vdWs) interaction, while in Bi_4Se_3, Bi-Bi bilayer and the Se-Bi-Se-Bi-Se quintuple layer stack alternatively via weak vdWs interactions, thereby forming natural vdWs heterostructure. Synthesis of ultrathin two-dimensional (2D) nanosheets of these quantum materials with natural heterostructure is of high significance in terms low lattice thermal conductivity (κ_{lat}) and good carrier mobility (μ). Herein, we report a low temperature simple solution phase synthesis of ultrathin 2D nanosheets of BiSe and Bi_4Se_3 from the $(Bi_2)_m(Bi_2Se_3)_n$ homologous series. Ultralow κ_{lat} values in the range of ~ 0.24-0.27 W/mK in these 2D nanosheets has been achieved after spark plasma sintering. BiSe and Bi_4Se_3 (both, layered heterostructure) nanosheets exhibit lower κ_{lat} compared to that of the Bi_2Se_3 (κ_{lat} of ~ 0.35 W/mK) nanosheets (simple layered structure) because of significant phonon scattering at various interfaces of heterostructured BiSe and Bi_4Se_3. Solutions grown few-layers ultrathin nanosheets exhibit good carrier mobility.

[†]*Manuscript submitted for publication*

3.1 Introduction

Discovery of graphene and its exotic electronic structure and properties[1–3] have further intensified research in two-dimensional (2D) materials.[4–11] Recently, topological quantum materials, identified by presence of non-trivial metallic surface states, have been at the forefront of materials research due to their prospect for various applications such as in thermoelectrics (TE), spinotronics and catalysis.[12-24] Plethora of interesting phenomena may arise by combining the 2D-nanosheets of quantum materials with the other trivial 2D materials via weak van der Waals (vdWs) forces, known as van der Waals heterostructures.[4,25–27] Recently, natural vdW heterostructure like compounds demonstrated ultra-low thermal conductivity (κ), making them interesting for thermoelectrics.[23,24,28] However, synthesis of 2D vdWs heterostructure often involves complex and expensive physical techniques like molecular beam epitaxy, chemical vapour deposition, which restricts their applications. Hence, scalable and simple chemical synthetic techniques for 2D layered quantum heterostructures are desirable.

Homologous series can serve as magic toolbox[29,30] for predicting new layered heterostructures. The name "homologous series" is envisioned to feature a chemical series that are often expressed by a general formula and built based on the same structural principles where certain modules/building blocks expand in different dimensions by regular increments. Binary/multinary homologous series based on heavy metal chalcogenides such as $M_x^{IV}N_{2y}^{V}Te_{x+3y}$ (M^{IV}= Ge/Sn/Pb; N^{V}=Sb/Bi, where x and y represent stoichiometry of MTe and N_2Te_3 respectively) have been emerged as excellent platform in quest of efficient materials for thermoelectrics.[28,31–34] Interestingly, $M_x^{IV}N_{2y}^{V}Te_{x+3y}$ homologous series hosts several layered intergrowth compounds,[28,32] resembling to the vdWs heterostructures and some of them are identified as topological insulators.[35] Thus, finding a proper homologous series with mixed layered structure and providing general chemical synthetic routes will serve the purpose of finding new 2D vdWs heterostructured nanosheets.

$(Bi_2)_m(Bi_2Se_3)_n$ (m, n: integer numbers), a fascinating homologous series,[36–40] hosts variety of layered heterostructured compounds (except Bi_2Se_3, repetition of the same quintuple layer) depending on the various stacking sequence of Bi-Bi zigzag bilayer and the Se-Bi-Se-Bi-Se quintuple layers via vdWs interaction. Several members from $(Bi_2)_m(Bi_2Se_3)_n$ series are identified as topological quantum materials,[39,41] namely Bi_2Se_3

(m=0, n=1) – a well-known strong topological insulator,[20,42] BiSe (m=1, n=2) – weak topological insulator,[15,43] Bi_4Se_3 (m=1, n=1) – topological semimetal.[44,45] In BiSe, Bi-Bi bilayer is sandwiched between the Se-Bi-Se-Bi-Se quintuple layers bonded via weak van der Waals (vdWs) interaction (Figure 3.1b), while in Bi_4Se_3 Bi-Bi bilayer and the Se-Bi-Se-Bi-Se quintuple layers stack alternatively by weak vdWs interactions (Figure 3.1c). Interestingly, crystal structure of BiSe and Bi_4Se_3 resembles to natural superlattice which are likely to exhibit low κ and hence can be proved to be potential candidates for TE.[38,44,45] Recently, bulk phase of BiSe, synthesized by high temperature solid state route, showed ultra-low lattice thermal conductivity (κ_{lat}) and high n-type thermoelectric performance near room temperature.[24] However, it is quite challenging to synthesize different compounds from the $(Bi_2)_m(Bi_2Se_3)_n$ homologous series in pure form via high-temperature solid-state techniques, mainly ascribed to their incongruent melting points.[37] Further, 2D nanosheets of these natural vdWs heterostructures from $(Bi_2)_m(Bi_2Se_3)_n$ homologous series, such as BiSe and Bi_4Se_3, have not been synthesized previously. Thus, it is worthy to find a general and simple method to synthesize heterostructured compounds in the form of 2D nanosheets from $(Bi_2)_m(Bi_2Se_3)_n$ series and to investigate their transport properties.

Here, we demonstrate a general and facile one-pot colloidal synthesis of few-layer ultrathin 2D nanosheets of natural heterostructured topological quantum materials (BiSe and Bi_4Se_3) from the $(Bi_2)_m(Bi_2Se_3)_n$ homologous series. The ultra-thin 2D-nanosheet morphology of the synthesized samples is confirmed by detailed microscopic measurements, such as transmission electron microscopy (TEM), scanning electron microscopy (SEM) and atomic force microscopy (AFM). The difference in stacking sequence of Bi-Bi zigzag bilayer and the Se-Bi-Se-Bi-Se quintuple layers in BiSe and Bi_4Se_3 nanosheets has been clearly demonstrated by high-angle annular dark field scanning transmission electron microscopy (HAADF-STEM), which also confirms the natural vdWs heterostructure nature. Further presences of topologically nontrivial surface states and heavy constituent elements of BiSe, Bi_4Se_3 and Bi_2Se_3 have motivated us to look into their transport properties. BiSe and Bi_4Se_3 nanosheets exhibit lower κ_{lat} in the 300-600 K range compared to that of the Bi_2Se_3 nanosheets (simple layered structure) due to the significant phonon scattering via layered vdWs heterostructure of BiSe and Bi_4Se_3.

3.2 Methods

3.2.1 Reagents. Bismuth nitrate ($Bi(NO_3)_3 \cdot 5H_2O$, Alfa Aesar, 99.9%), Selenium dioxide (SeO_2, 99.9%, Sigma Aldrich), Oleylamine (OA, 90%, Sigma Aldrich) and 1,10-phenanthroline (Phen, $C_{12}H_8N_2$, 90%, Alfa Aesar) were used without any further purification.

3.2.2 Synthesis.

BiSe. 100 mg of $Bi(NO_3)_2.5H_2O$ (0.21 mmol), 40 mg of 1,10 Phenanthroline, 22.9 mg SeO_2 (0.21 mmol) were dissolved in 10 ml Oleylamine in 3-necked round bottom flask. The entire reaction is carried out in a Nitrogen atmosphere. The temperature of the solution was slowly increased to 120 ºC, kept at that temperature for 1.5 hours, obtained as synthesized black coloured product is then washed with hexane and ethanol for several times and purified product is dried in vacuum oven at 100ºC.

Bi_4Se_3. 100 mg of $Bi(NO_3)_2.5H_2O$ (0.21 mmol), 40 mg of 1,10 Phenanthroline, 17.1 mg SeO_2 (0.16 mmol) were dissolved in 10 ml Oleyl amine in 3-necked round bottom flask. The entire reaction is carried out in Nitrogen atmosphere. The temperature of the solution was slowly increased to 120 ºC, kept at that temperature for 1.5 hours, obtained as synthesized black coloured product is then washed with hexane and ethanol for several times and purified product is dried in vacuum oven at 100ºC.

Bi_2Se_3. 100 mg of $Bi(NO_3)_2.5H_2O$ (0.21 mmol), 40 mg of 1,10 Phenanthroline, 34 mg SeO_2 (0.31 mmol) were dissolved in 15 ml Oleyl amine in 3-necked round bottom flask. The entire reaction is carried out in Nitrogen atmosphere The temperature of the solution was slowly increased to 120 ºC, kept at that temperature for 1.5 hours, obtained as synthesized black coloured product is then washed with hexane and ethanol for several times and purified product is dried in vacuum oven at 100ºC.

3.2.3 X-ray diffraction (XRD). Powder X-ray diffraction were recorded using a Cu K_α (λ = 1.5406 Å) radiation on a Bruker D8 diffractometer.

3.2.4 X-ray photoelectron spectroscopy (XPS). XPS measurement was carried out using an Omicron nanotechnology spectrometer with an Mg-K_α (1253.6 eV) X-ray source.

3.2.5 Field emission scanning electron microscopy (FESEM). FESEM imaging was carried out using a FEI NOVA NANO SEM 600 with operating energy of 15 kV. Energy dispersive spectroscopy (EDAX) analysis was carried out with an attached EDAX genesis instrument.

3.2.6 Transmission electron microscopy (TEM). TEM studies were carried out using a FEI TECNAI G^2 20 STWIN TEM operated at 200 keV and an aberration corrected FEI TITAN3 operating at 300 keV. EDAX compositional analysis and elemental mapping were carried in STEM imaging mode. Very dilute solution of $(Bi_2)_m(Bi_2Se_3)_n$ nanosheets dispersed in ethanol was drop casted on holey carbon coated Cu grid and used for the TEM studies.

3.2.7 Inductively coupled plasma atomic emission spectroscopy (ICP-AES). ICP-AES was carried out for compositional analysis in a Perkin-Elmer Optima 7000DV instrument. For ICP-AES study, powdered nanosheets were dissolved in auqa regia (HNO_3:HCL = 3:1) and then this solution was further diluted using milipore water.

3.2.8 Atomic force microscopy (AFM). Bruker Innova microscope in tapping mode was used to carry out AFM studies using an antimony doped silicon tip.

3.2.9 Removal of capping ligands. In order to remove the organic capping ligands, the material (as prepared nanosheets) collected from few syntheses (~1.5 g) were taken in a quartz tube and was vacuum (10^{-5} torr) sealed. The samples in the sealed quartzed tube was annealed at 250 °C for 24 hours and slowly cooled down to room temperature. The same procedure was repeated thrice to ensure complete removal of the capping agents. Due to this heat treatment, the surface capping ligand oleylamine get detached from the nanosheets surface and after cooling get condensed and remain as liquid droplets at the top part of the inner wall of the tube. The surfactant free nanosheets were collected from the tube.

3.2.10 Thermogravimetric analysis. TGA was performed using a TGA/DSC 2STAR instrument in the temperature range of 300–773 K under nitrogen atmosphere with a ramp rate of 5 K min^{-1}.

3.2.11 Fourier transform infrared spectroscopy. FTIR spectra was recorded using a Bruker IFS 66v/S spectrometer.

3.2.12 Thermoelectric properties. In order to measure thermoelectric properties, scaled up powder of $(Bi_2)_m(Bi_2Se_3)_n$ nanosheets were loaded into graphite die and spark plasma sintered (SPS211-LX, Dr. Sinter Lab) at temperature of 573 K (for Bi_4Se_3) and 623 K (for BiSe and Bi_2Se_3) and pressure of 50 MPa under vacuum (10^{-3} Torr) with a holding time of 5 min. Density of the SPS processed samples was ~ 95% of theoretical density. Cylindrical SPS sample was further cut to parallelepiped shaped bar (2 mm ×3 mm ×8 mm) for the simultaneous electrical conductivity (σ) and Seebeck coefficients (S) measurement. The electronic transport properties were measured by ULVAC-RIKO ZEM-3 instrument under He gas. The longer direction of the bar coincides to the SPS pressing (parallel) direction and we maintained the same direction for thermal conductivity measurement.

Coin shaped sample was cut from SPS'ed cylinder. Thermal diffusivity, D, was measured using laser flash diffusivity method in Netzsch LFA-457 instrument on the sample of the dimension of 10 mm diameter and thickness of 2 mm. Temperature dependent heat capacity, C_p, was obtained using standard sample (pyroceram) in LFA-457.The total thermal conductivity, κ, was calculated using the equation, $\kappa = DC_p.\rho$, where ρ is the density of the sample. Both, the electrical and thermal transports were measured along the parallel to the SPS direction.

The lattice thermal conductivity, κ_{lat} of $(Bi_2)_m(Bi_2Se_3)_n$ nanosheets are obtained by subtracting electrical thermal conductivity (κ_{el}) from total thermal conductivity (κ), whereas κ_{el} is calculated using the Wiedemann-Franz law, $\kappa_{el} = \sigma LT$, where L is the Lorenz number, σ is electrical conductivity at temperature T . L is derived by fitting of the respective Seebeck coefficients which estimate the reduced chemical potential assuming a single parabolic band.

3.2.13 Hall measurement. Carrier concentrations (n) of $(Bi_2)_m(Bi_2Se_3)_n$ nanosheets were calculated using the formula, $n = 1/eR_H$, where e is the electronic charge and R_H is hall coefficient. Hall coefficient of the samples were measured using four-contact geometry in Excel instrument Hall measurement system at room temperature. A variable magnetic field of of 0.1 to 0.55 Tesla and a current of ~ 100 mA were applied during the measurements.

3.3 Results & discussion

Bi_2Se_3, (m:n =0:1) a member of $(Bi_2)_m(Bi_2Se_3)_n$ homologous series[36–40] is widely studied as strong topological insulator and thermoelectric material.[15,18–20,42] It possesses anisotropic layered structure (space group of $R\bar{3}m$, a = b = 0.41 nm, c = 2.86 nm) where quintuple layers (QL) of Se-Bi-Se-Bi-Se (unit length of ~ 0.72 nm) are stacked along crystallographic *c*-axis via weak vdWs interaction with a vdWs gap of ~ 0.2 nm (Figure 3.1a). BiSe (m:n =1:2), from $(Bi_2)_m(Bi_2Se_3)_n$ homologous series, is recently emerged as weak topological insulator.[43] BiSe crystallizes in trigonal structure ($P\bar{3}m1$ space group, a=b=0.42 nm, c = 2.28 nm) where Bi-Bi bilayers (unit length of ~ 0.23 nm) is sandwiched between two Se-Bi-Se-Bi-Se QL (unit length of ~ 0.72 nm) along the *c*-axis via vdWs interactions (Figure 3.1b). Bi_4Se_3 (m:n =1:1) is recently identified as topological semimetal.[44,45] The structure of Bi_4Se_3 also shows resemblance to natural vdWs heterostructure (Figure 3.1c), where Bi-Bi bilayer and the Se-Bi-Se-Bi-Se quintuple layers stack alternatively along c axis (space group of $R\bar{3}m$, a = b = 0.43 nm; c = 4.06 nm). BiSe and Bi_4Se_3 both exhibit large unit cell with natural super lattice structure.[36–40]

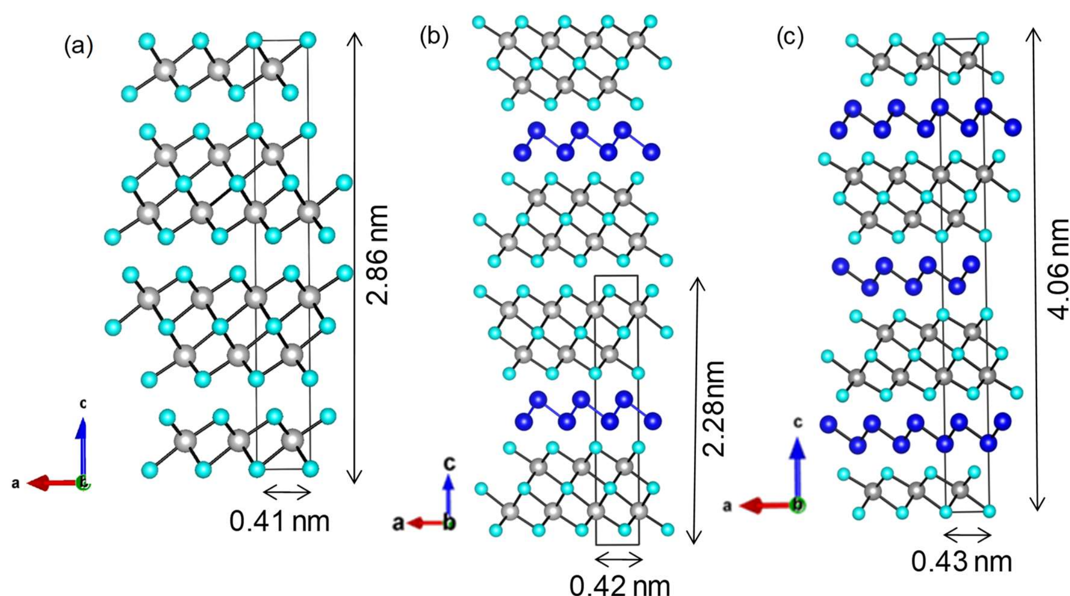

Figure 3.1. *Crystal structure of (a)Bi_2Se_3 (b) BiSe and (c) Bi_4Se_3. Blue, cyan and grey atoms represent Bi of Bi_2 layer, Bi of Bi_2Se_3 layer and Se, respectively.*

Incongruent melting point of different members from $(Bi_2)_m(Bi_2Se_3)_n$ homologous series makes it quite tricky to obtain phase pure compounds by traditional solid state vacuum sealed tube melting reaction. On the contrary, solution based low temperature synthesis techniques are often found to be very effective to arrest such incongruently melting compounds in nano-dimensions through kinetic stabilization.[28,31–34] Here, we have demonstrated a general low temperature one-pot colloidal synthesis of 2D nanosheets of different topological quantum materials (BiSe, Bi_4Se_3 and Bi_2Se_3) from $(Bi_2)_m(Bi_2Se_3)_n$ homologous series by varying the nominal composition of the precursors which are bismuth nitrate pentahydtrate, ($Bi(NO_3)_3.5H_2O$) and anhydrous selenium oxide (SeO_2) along with 1,10 phenanthroline, and oleylamine (OA). In this reaction, OA functions as solvent, reducing agent as well as capping ligand in cooperation with 1,10- phenanthroline[46,47] In a typical synthesis of few-layer nanosheets Bi_4Se_3, 100 mg of $Bi(NO_3)_3.5H_2O$ (0.21 mmol)), 17.2 mg SeO_2 (0.16 mmol), ~ 40 mg of 1,10-phenanthroline, and 10 ml oleylamine were added in 3-necked round bottom flask under the nitrogen atmosphere. The temperature of the solution is slowly raised to 120°C, kept at that temperature for 1.5 hours. The reaction was then cooled to room temperature and as obtained black colored product is then washed with hexane and ethanol mixture (1:1 ratio) for 4-5 times and purified product is dried in vacuum oven at 100ºC. Similarly, we have synthesized the nanosheets of BiSe and Bi_2Se_3 by changing the ratio of $Bi(NO_3)_3.5H_2O$ and SeO_2.

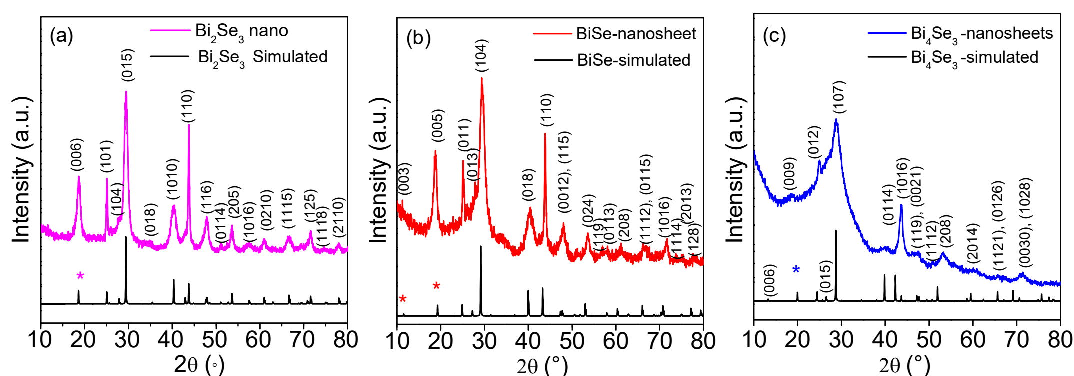

Figure 3.2. *PXRD of as-synthesized (a) Bi_2Se_3 (b) BiSe and (c) Bi_4Se_3 nanosheets. Low angle (00l) peak is identified by * mark.*

Phase purity of the as synthesized samples is confirmed by the powder X-ray diffraction (PXRD) patterns. PXRD patterns of the as synthesized can be indexed based

on pure Bi_2Se_3(space group $R\bar{3}m$; Figure 3.2a), BiSe (space group $P\bar{3}m1$; Figure 3.2b) and Bi_4Se_3 (space group $R\bar{3}m$; Figure 3.2c). Inspite of having similarity in PRXD pattern of different members of $(Bi_2)_m(Bi_2Se_3)_n$ homologous series due the basic building blocks of QL of the Bi_2Se_3, they can be differentiated from low-angle peaks originating from (00l) reflections (highlighted by asterisk marks). To investigate the actual compositions of synthesized nanosheet samples, ICP-AES and EDAX have been performed and the derived compositions are quite close to the nominal compositions of the samples (Table 3.1). These findings further confirm precise control over the composition in the present synthetic technique.

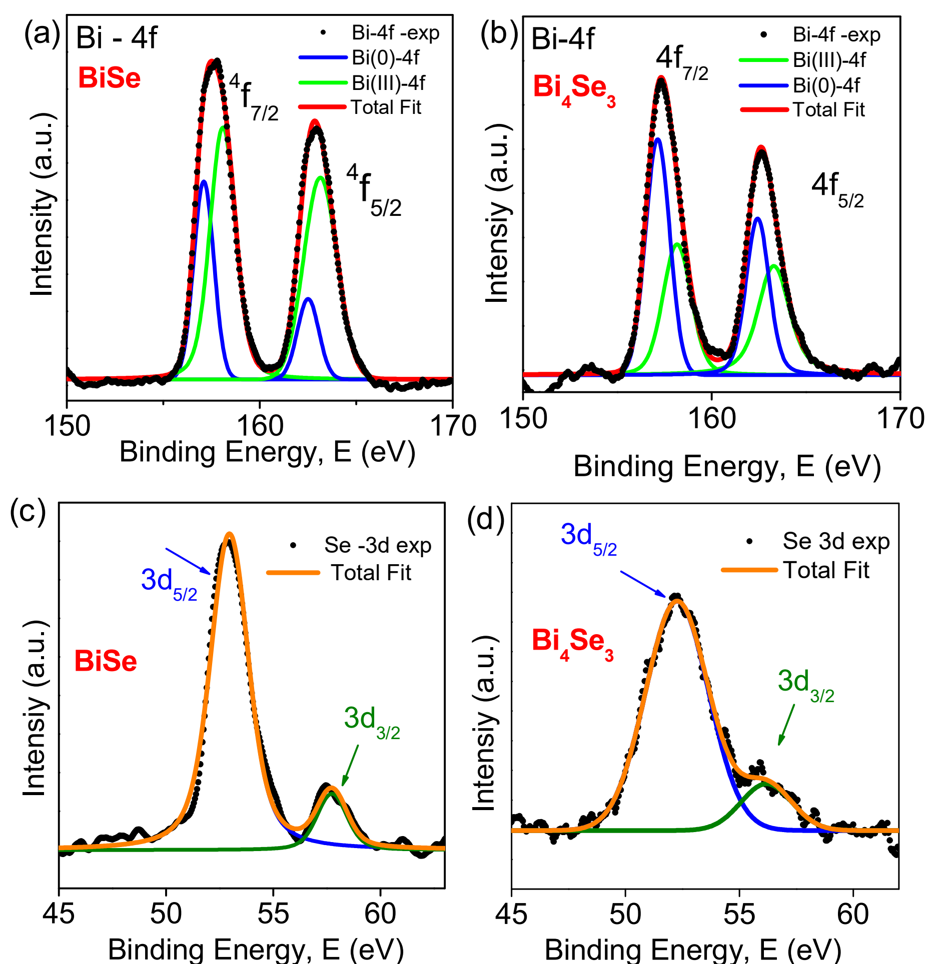

Figure 3.3. *XPS-spectrums of Bi – 4f of (a) BiSe and (b) Bi_4Se_3. De-convolution of Bi-4f doublet peak of BiSe and Bi_4Se_3 clearly shows presence of Bi(III) (green curvature) and Bi(0) (blue curvature) in BiSe and Bi_4Se_3. XPS-spectrums of Se -3d of (c) BiSe and (d) Bi_4Se_3.*

Further, X-ray photoelectron spectroscopy (XPS) has been performed on BiSe and Bi_4Se_3 samples to confirm their oxidation states (Figure 3.3). In case of BiSe, Bi 4f spin-orbit doublet peaks appear at 157.54 eV and 162.89 eV (Figure 3.3a), which can be best assigned to Bi $4f_{7/2}$ and Bi $4f_{5/2}$ respectively. For Bi_4Se_3, Bi $4f_{7/2}$ and Bi $4f_{5/2}$ doublet peaks appear at 157.3 eV and 162.6 eV (Figure 3.3b). Further de-convolution of each of the Bi 4f doublet peaks for both the BiSe and Bi_4Se_3 confirms presence of Bi(0) (from the Bi-Bi bilayer) and Bi(III) (from QL of Bi_2Se_3) oxidation states.[48,49] XPS spectrum due to Se $3d_{5/2}$ and $3d_{3/2}$ are observed at 52.86 eV and 57.6 eV respectively in case of BiSe (Figure 3.3c), whereas $3d_{5/2}$ and $3d_{3/2}$ doublet peaks of Bi_4Se_3 appear at 52.25 eV and 56.23 eV respectively (Figure 3.3d). Further these values are well corroborated with -2 oxidation state of selenium.

Table 3.1 *Nominal compositions and measured compositions of the as-synthesized $(Bi_2)_m(Bi_2Se_3)_n$ nanosheets determined by ICP-AES and EDAX.*

Nominal Composition	ICP-AES Composition	EDAX Composition
Bi_2Se_3	$Bi_{2.1}Se_3$	$Bi_{1.86}Se_3$
BiSe	$Bi_{1.05}Se_1$	$Bi_{0.98}Se_1$
Bi_4Se_3	$Bi_{4.14}Se_3$	$Bi_{4.5}Se_3$

Ultrathin nature of the nanosheets and the stacking sequence of different layers such as Bi-Bi bilayer and the Se-Bi-Se-Bi-Se QL in different $(Bi_2)_m(Bi_2Se_3)_n$ nanosheets have been probed by various microscopic techniques (Figure 3.4, Figure 3.5 and Figure 3.6). FESEM and TEM micrographs of BiSe show formation of ultrathin nanosheets of BiSe (Figure 3.4a & b). High-resolution TEM (HRTEM) micrograph of BiSe nanosheet clearly demonstrates lattice spacing of 0.204 nm, which corresponds to the (110) plane of BiSe (Figure 3.4b). The single-phase homogeneity is confirmed by EDAX elemental mapping on BiSe nanosheet (Figure 3.4c) during scanning TEM (STEM). AFM image demonstrates the freestanding BiSe nanosheets with the thickness of ~ 2.5 nm which corresponds to one layer of BiSe, formed by one layer of Bi_2 sandwiched between two QL layers of Bi_2Se_3 (Figure 3.4d). The lateral dimension of the BiSe nanosheets ranges from 1 to 2 μm.

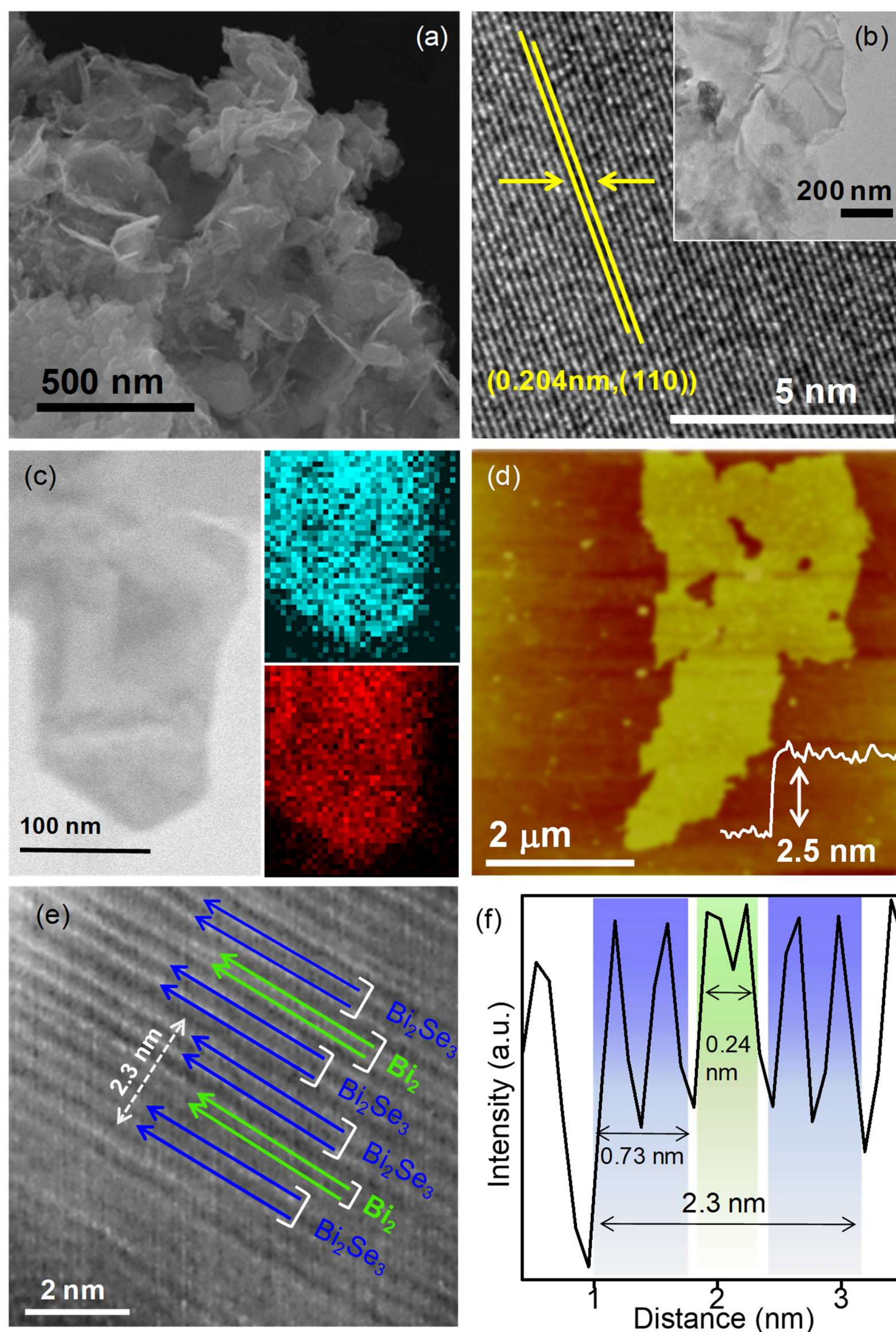

Figure 3.4. *(a) FESEM and (b) HRTEM images of BiSe nanosheets. Inset of figure (b) shows low-magnification TEM micrograph of BiSe nanosheets. (c) EDAX color mapping for Bi and Se of a BiSe nanosheet during STEM imaging. (d) AFM image of BiSe nanosheets. (e) HAADF-STEM image of BiSe nanosheet showing long-range stacking sequence of Se-Bi-Se-Bi-Se and Bi-Bi subunits along c- direction in BiSe nanosheets. (f) HAADF-STEM line scan intensity profile from figure (e).*

Stacking sequence of Bi-Bi bilayer and the Se-Bi-Se-Bi-Se QL in BiSe is confirmed by performing HAADF-STEM of a folded edge of few-layer BiSe 2D nanosheets. Since HAADF-STEM technique is highly sensitive to variations in the atomic number (Z-contrast images), the equally spaced darkest lines in HAADF-STEM image represent the vdWs gap while the brightest lines corresponds to positions of Bi-atoms (high atomic weight) in $(Bi_2)_m(Bi_2Se_3)_n$ nanosheets. Hence, HAADF-STEM image (Figure 3.4e) of BiSe nanosheets clearly shows that BiSe is built from stacking of two types of modules or subunits which are separated via vdWs gap as similar to the crystal structure shown in Figure 3.1b. Analysis of the intensity profile (Figure 3.4f) extracted from HAADF-STEM image (Figure 2e) reveals that the thickness of the two subunits are 0.73 nm and 0.24 nm which corresponds to the Se-Bi-Se-Bi-Se QL and Bi-Bi BL respectively, (Figure 3.4f). Further HAADF-STEM image and corresponding intensity profile of BiSe confirm that Bi_2 layer (0.24 nm) is sandwiched between Bi_2Se_3 layers (0.73 nm) with a stacking thickness of 2.3 nm (Figure 3.4f). The above analysis demonstrates the vdW heterostructure nature of BiSe nanosheets.

2D nanosheet morphology of as synthesized Bi_4Se_3 is evidenced from FESEM (Figure 3.5a) and TEM (Figure 3.5b) images. Lattice spacing obtained from HRTEM image of Bi_4Se_3 is ~ 0.206 nm which is best corroborated with (1016) planes of Bi_4Se_3. EDAX elemental mapping has been performed on Bi_4Se_3 nanosheets in STEM mode and it confirms the single phase homogeneity of Bi_4Se_3 nanosheets (Figure 3.5c). Thickness of as synthesized Bi_4Se_3 nanosheets determined by AFM, is ~ 4.1 nm, corresponding to three layers of Bi_4Se_3 built by alternative stacking of bilayers of Bi_2 and QLs of Bi_2Se_3 (Figure 3.5d). HAADF-STEM image of the folded edge a of few-layer thick Bi_4Se_3 nanosheets clearly shows that Bi_4Se_3 nanosheet is built up from alternative stacking of two different types of modules separated by vdWs gap (dark lines), shown in Figure 3.5e. The corresponding intensity profile obtained from HAADF-STEM image of Bi_4Se_3 nanosheet (Figure 3.5f) confirms that two different modules are Bi-Bi bilayer (thickness ~ 0.26 nm) and Se-Bi-Se-Bi-Se QL layers (thickness ~ 0.73 nm) which are alternatively stacked along *c*-axis to form Bi_4Se_3 (as shown in crystal structure in Figure 3.1c). HAADF-STEM clearly denotes that the stacking sequence is different in Bi_4Se_3 compared to that of the BiSe (Figure 3.4e and 3.5e). HAADF-STEM image of Bi_4Se_3 also verifies the vdWs heterostructure nature of as synthesized Bi_4Se_3 nanosheets.

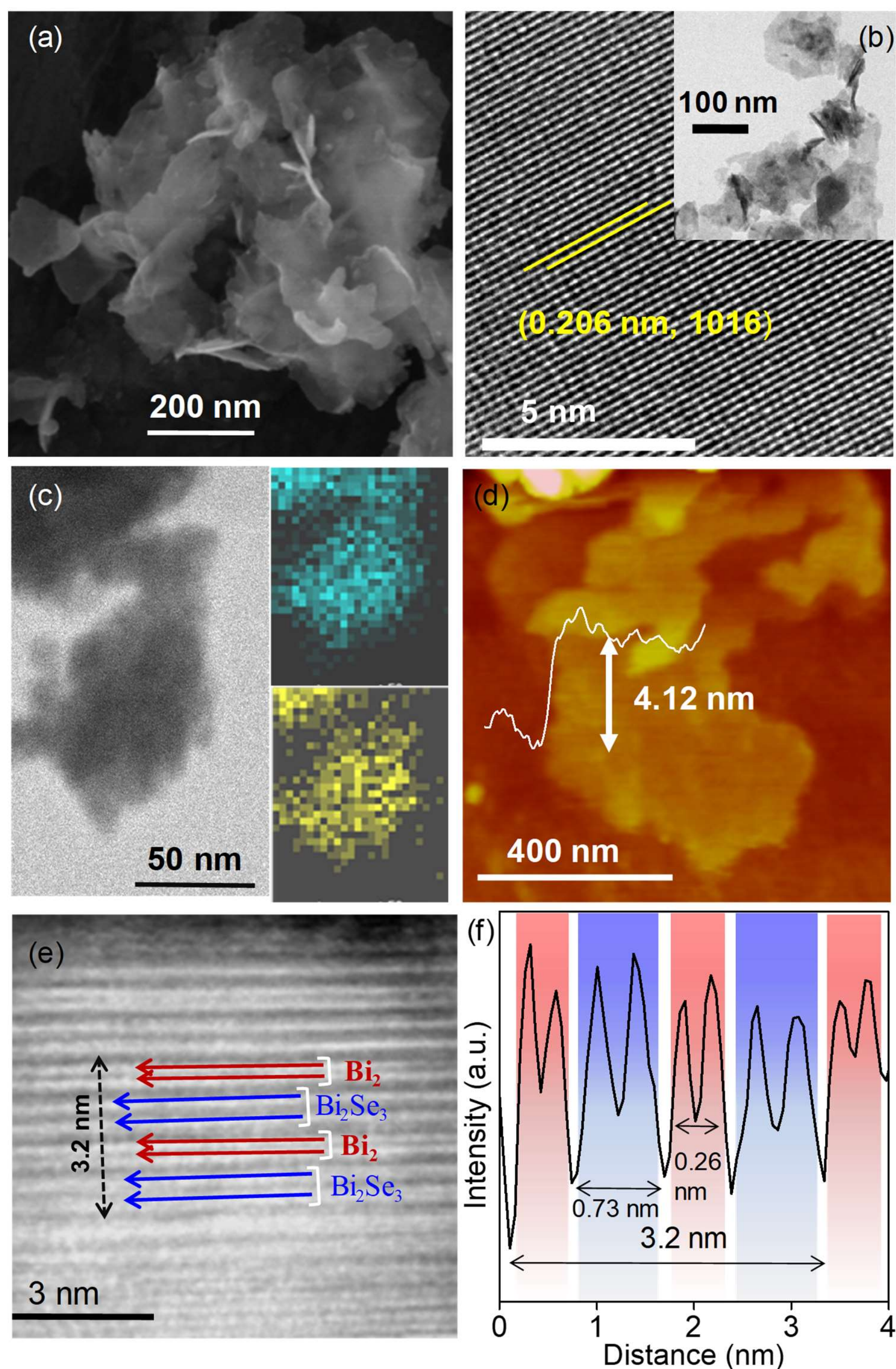

Figure 3.5. *(a) FESEM and (b) HRTEM images of Bi_4Se_3 nanosheets. Inset of figure (b) shows low-magnification TEM micrograph of Bi_4Se_3 nanosheets. (c) EDAX color mapping for Bi and Se of Bi_4Se_3 nanosheet during STEM imaging. (d) AFM image of Bi_4Se_3 nanosheets. (e) HAADF-STEM image of Bi_4Se_3 nanosheet shows long-range stacking sequence of Se-Bi-Se-Bi-Se and Bi-Bi subunits along c-direction in Bi_4Se_3 nanosheets. (f) HAADF-STEM line scan intensity profile from figure (e).*

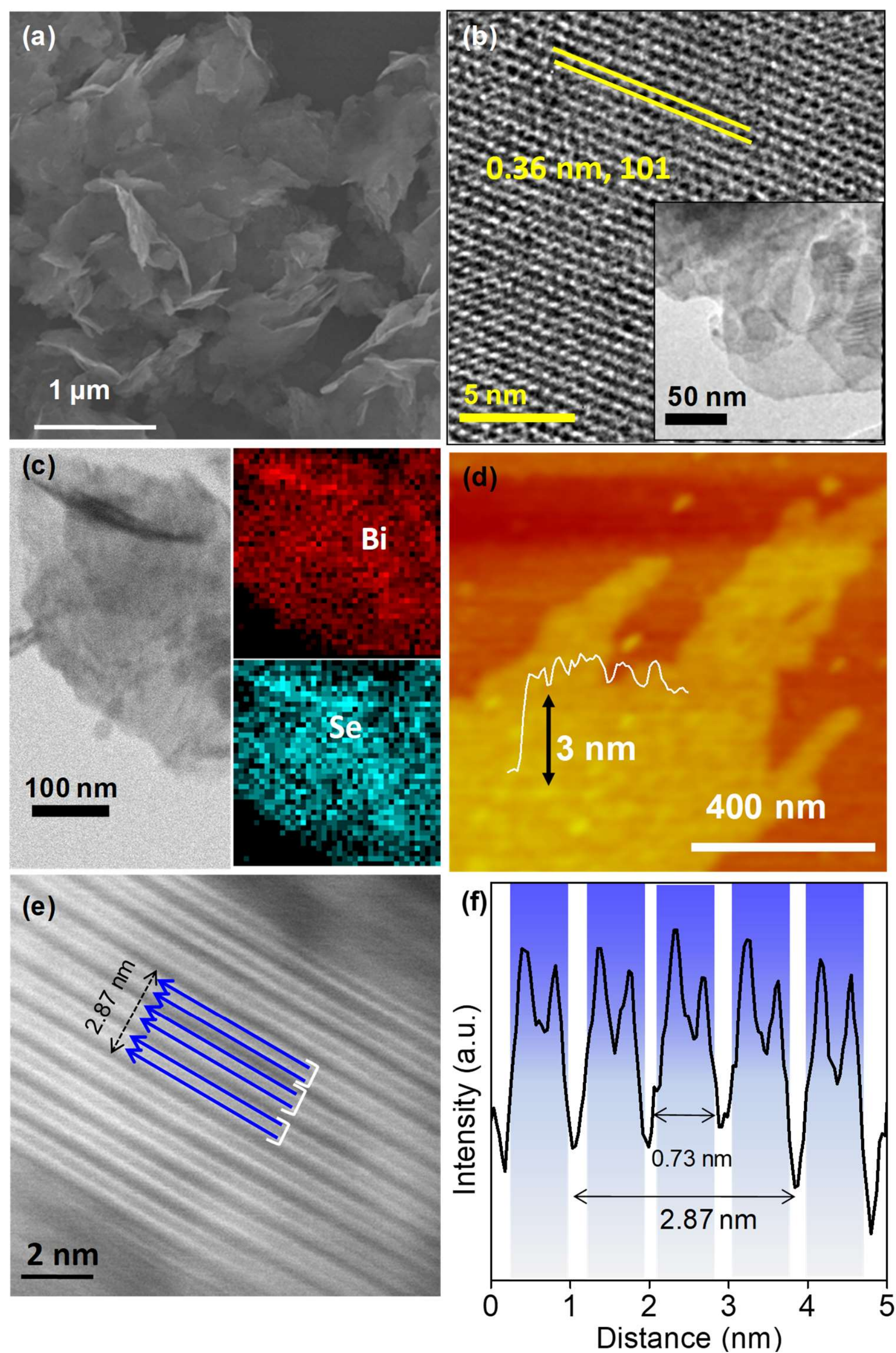

Figure 3.6. *(a) FESEM and (b) HRTEM images of Bi_2Se_3 nanosheets. Inset of figure (b) shows low-magnification TEM micrograph of Bi_2Se_3 nanosheets. (c) EDAX color mapping for Bi and Se of Bi_2Se_3 nanosheet during STEM imaging. (d) AFM image of Bi_2Se_3 nanosheets. (e) HAADF-STEM image shows long-range stacking sequence of Se-Bi-Se-Bi-Se units along c-direction in Bi_2Se_3 nanosheets. (f) HAADF-STEM line scan intensity profile from figure 3.6(e).*

Similraly, FESEM (Figure 3.6a) and TEM images of Bi_2Se_3 (Inset of Figure 3.6b) show formation of ultrathin nanosheet morphology of synthesized Bi_2Se_3 samples. HRTEM image (Figure 3.6b) of Bi_2Se_3 nanosheet clearly demonstrates lattice spacing of 0.36 nm, which corresponds to the (101) plane of Bi_2Se_3. The single-phase homogeneity is confirmed by EDAX elemental mapping on Bi_2Se_3 nanosheet (Figure 3.6c) during STEM. AFM demonstrates the freestanding Bi_2Se_3 nanosheets with the thickness of ~ 3 nm which corresponds to three layers of Bi_2Se_3 (Figure 3.6d). Further HAADF-STEM image (Figure 3.6e) of Bi_2Se_3 nanosheets visibly shows long-range stacking sequence of Se-Bi-Se-Bi-Se units (~ 0.73 nm) along c- direction, separated via van der Waals gap (~ 0.3 nm) which has been further verified by the analysis of the intensity profile (Figure 3.6f) extracted from the corresponding HAADF-STEM image (Figure 3.6e).

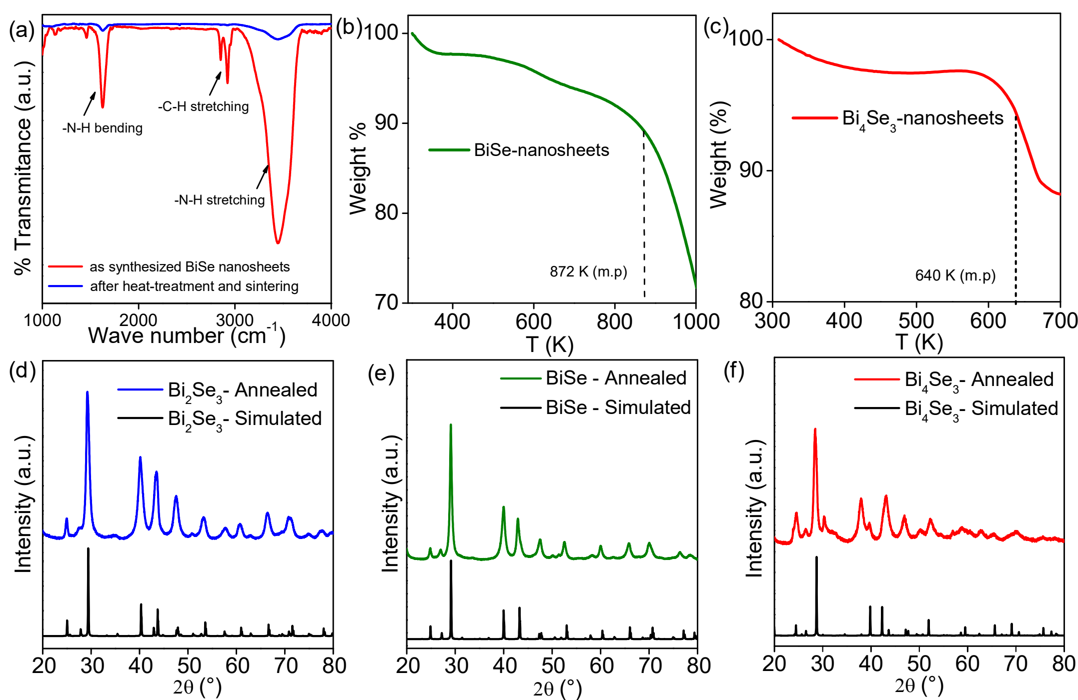

Figure 3.7. *(a) FT-IR spectra of as synthesized BiSe nanosheets, before and after the heat-treatment, showing disappearance of N-H and C-H frequency vibrational modes after heat treatment. Thermo-gravimetric analysis (TGA) of (b) BiSe and (c) Bi_4Se_3, after removal of capping agent depicting their melting point. Powder X-ray diffraction of heat-treated samples of (d) Bi_2Se_3, (e) BiSe and (f) Bi_4Se_3, depicting their phase purity after heat treatment.*

Presence of heavy constituent elements and unique anisotropic layered structure (resembling to vdWs heterostructure) of the members from $(Bi_2)_m(Bi_2Se_3)_n$ homologous

series have encouraged us to investigate the thermal transport properties of these 2D nanosheets. Further, metallic surface states in topological insulators and Dirac cone in bulk electronic structure of topological semimetal makes us curious to look into the electrical transport properties of the 2D nanosheets of $(Bi_2)_m(Bi_2Se_3)_n$ compounds. Prior to the measurement of the thermoelectric properties of the synthesized nanosheets, the organic ligands/capping agents on $(Bi_2)_m(Bi_2Se_3)_n$ nanosheets are removed by heat-treatment of synthesized nanosheets in a vacuum-sealed (10^{-6} torr) quartz tube at 250^0C. The removal of the organic capping agents from the synthesized is further verified by the infra-red (FT-IR) spectra of samples before and after heat treatment (Figure 3.7a).[50] Further, thermo-gravimetric analysis (TGA) of annealed BiSe and Bi_4Se_3 samples (Figure 3.7b-c) enable us to decide the temperature range (300 K to 623 K) for the measurement of transport properties. PXRD pattern of annealed samples also confirms retained phase purity of the samples after heat treatment (Figure 3.7 d-f). The powder samples of nanosheets were pelletized by quick spark plasma sintering (SPS211-LX, Dr. Sinter Lab) at 573 K for Bi_4Se_3 and 623 K for BiSe and Bi_2Se_3 and 50 MPa uni-axial pressure under high vacuum (10^{-5} Torr). Both the electrical and thermal transport properties are measured along the SPS-pressing direction (SPS_{II}).

Electronic and thermal transport properties of BiSe, Bi_4Se_3 and Bi_2Se_3 along spark plasma pressing (SPS_{II}) direction are demonstrated in Figure 3.8. All the synthesized $(Bi_2)_m(Bi_2Se_3)_n$ nanosheets show high electrical conductivity (σ) (Figure 3.8a). Among all the $(Bi_2)_m(Bi_2Se_3)_n$ nanosheets, Bi_4Se_3 nanosheets (which is topological semimetal) shows highest σ of ~ 777 S/cm at 293 K which decreases with temperature indicating metal like conduction. Measured carrier concentration (n) values of BiSe, Bi_4Se_3 and Bi_2Se_3 are to be ~ 1.16×10^{19}, 2.62×10^{19} and 4.06×10^{19} /cm^3 respectively. The measured carrier mobility (μ) values are to be ~ 178, 184 and 102 cm^2/Vs for the 2D nanosheets BiSe, Bi_4Se_3 and Bi_2Se_3, respectively, at room temperature. The reasonably high μ in these 2D nanosheets could be attributed to the metallic surface states of the topological quantum materials. All the samples show negative Seebeck coefficient (S) which reveals n-type conduction in those materials (Figure 3.8b). The S values for BiSe, Bi_4Se_3 and Bi_2Se_3 nanosheets are to be - 66 μV/K, -20 μV/K and - 40μV/K respectively, at room temperature. Among all the samples, BiSe-nanosheets exhibit highest S of ~ -75 μV/K at 400 K which then decreases

with increase in temperature due to bipolar conduction, typical for narrow band-gap semiconductors.

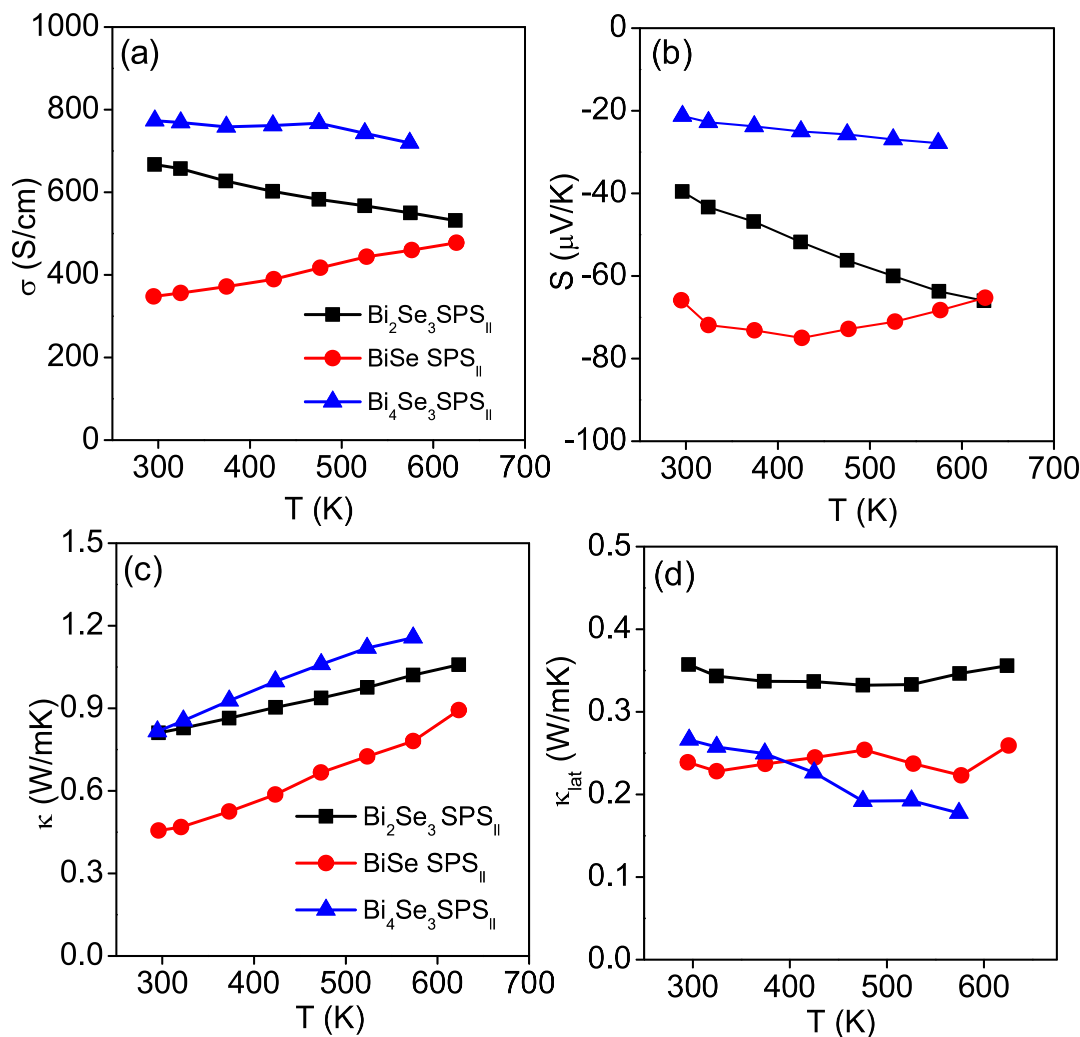

Figure 3.8. *Temperature-dependent (a) electrical conductivity (σ), (b) Seebeck coefficient (S), (c) total thermal conductivity (κ) and (d) lattice thermal conductivity ($κ_{lat}$) of Bi_2Se_3, BiSe and Bi_4Se_3 nanosheets.*

Total thermal conductivity (*κ*) and lattice thermal conductivity ($κ_{lat}$) of synthesized $(Bi_2)_m(Bi_2Se_3)_n$ nanosheets are presented in Figure 3.8c and 3.8d, respectively. All the $(Bi_2)_m(Bi_2Se_3)_n$ nanosheets exhibit ultralow $κ_{lat}$ values of ~ 0.24, 0.27 and 0.35 W/mK for BiSe, Bi_4Se_3 and Bi_2Se_3, respectively, at room temperature (Figure 3.8d). This observed low $κ_{lat}$ values of synthesized $(Bi_2)_m(Bi_2Se_3)_n$ nanosheets are mainly

ascribed to presence of low energy optical modes phonon and additional phonon scattering by various surfaces/interfaces between the layers.[24,38] Interestingly, BiSe and Bi_4Se_3, which are having natural layered heterostructure, exhibit lower κ_{lat} compared to that of Bi_2Se_3 (simple layered structure) throughout the measured temperature range, due to the additional phonon scattering at the corrugated structure with large unit cell and low energy vibrations of Bi-Bi bilayer in BiSe[24] and Bi_4Se_3 samples.[38]

3.4 Conclusions

In conclusions, few-layer 2D nanosheets of different topological quantum materials from $(Bi_2)_m(Bi_2Se_3)_n$ homologous series are successfully synthesized by a general and facile solution based synthesis at low temperatures. Nanosheets of $(Bi_2)_m(Bi_2Se_3)_n$ are ultrathin with 1-3 layers of thickness and 1-2 μm of lateral dimension. HAADF-STEM analysis indicates the detailed structural stacking sequence of the Bi-Bi bilayers and the Se-Bi-Se-Bi-Se quintuple layers in the $(Bi_2)_m(Bi_2Se_3)_n$ nanosheets, revealing their structural resemblance to natural van der Waals heterostructure. Electrical transport properties show that all the synthesized $(Bi_2)_m(Bi_2Se_3)_n$ nanosheets are *n*-type in nature and exhibit good mobility, probably arising from their metallic surface states. Significant phonon scattering due to the layered heterostructured surface/interfaces and soft optical phonon modes in BiSe and Bi_4Se_3 nanosheets have resulted in ultralow κ_{lat} which is lower than that of the Bi_2Se_3 nanosheets. Demonstration of general and simple synthesis of heterostructured 2D nanosheets of different topological quantum materials holds great promise for low thermal conductivity applications.

3.5 References

(1) Novoselov, K. S.; Fal′ko, V. I.; Colombo, L.; Gellert, P. R.; Schwab, M. G.; Kim, K. *Nature* **2012**, *490*, 192.
(2) Novoselov, K. S.; Geim, A. K.; Morozov, S. V.; Jiang, D.; Katsnelson, M. I.; Grigorieva, I. V.; Dubonos, S. V.; Firsov, A. A. *Nature* **2005**, *438*, 197.
(3) Geim, A. K.; Novoselov, K. S. *Nat. Mater.* **2007**, *6*, 183.
(4) Novoselov, K. S.; Mishchenko, A.; Carvalho, A.; Neto, A. H. C. *Science* **2016**, *353*, 461.
(5) Li, L.-J.; Eda, G.; Zhang, H.; Loh, K. P.; Shin, H. S.; Chhowalla, M. *Nat. Chem.* **2013**, *5*, 263.
(6) Huang, X.; Zeng, Z.; Zhang, H. *Chem. Soc. Rev.* **2013**, *42*, 1934.

(7) Nicolosi, V.; Chhowalla, M.; Kanatzidis, M. G.; Strano, M. S.; Coleman, J. N. *Science* **2013**, *340*, 1226419.
(8) Chhowalla, M.; Shin, H. S.; Eda, G.; Li, L.-J.; Loh, K. P.; Zhang, H. *Nat. Chem.* **2013**, *5*, 263.
(9) Chhowalla, M.; Liu, Z.; Zhang, H. *Chem. Soc. Rev.* **2015**, *44*, 2584.
(10) Rao, C. N. R.; Sood, A. K.; Subrahmanyam, K. S.; Govindaraj, A. *Angew. Chemie Int. Ed.* **2009**, *48*, 7752.
(11) Rao, C. N. R.; Ramakrishna Matte, H. S. S.; Maitra, U. *Angew. Chemie - Int. Ed.* **2013**, *52*, 13162.
(12) Gooth, J.; Schierning, G.; Felser, C.; Nielsch, K. *MRS Bull.* **2018**, *43*, 187.
(13) Müchler, L.; Casper, F.; Yan, B.; Chadov, S.; Felser, C. *Phys. Status Solidi - Rapid Res. Lett.* **2013**, *7*, 91.
(14) Müchler, L.; Zhang, H.; Chadov, S.; Yan, B.; Casper, F.; Kübler, J.; Zhang, S. C.; Felser, C. *Angew. Chemie - Int. Ed.* **2012**, *51*, 722.
(15) Roychowdhury, S.; Samanta, M.; Banik, A.; Biswas, K. *J. Solid State Chem.* **2019**, *275*, 103.
(16) Wang, Y.; Zhu, D.; Wu, Y.; Yang, Y.; Yu, J.; Ramaswamy, R.; Mishra, R.; Shi, S.; Elyasi, M.; Teo, K. L.; Wu, Y.; Yang, H. *Nat. Commun.* **2017**, *8*, 6.
(17) Mellnik, A. R.; Lee, J. S.; Richardella, A.; Grab, J. L.; Mintun, P. J.; Fischer, M. H.; Vaezi, A.; Manchon, A.; Kim, E.-A.; Samarth, N.; Ralph, D. C. *Nature* **2014**, *511*, 449.
(18) Heremans, J. P.; Cava, R. J.; Samarth, N. *Nat. Rev. Mater.* **2017**, *2*, 17049.
(19) Sun, Y.; Cheng, H.; Gao, S.; Liu, Q.; Sun, Z.; Xiao, C.; Wu, C.; Wei, S.; Xie, Y. *J. Am. Chem. Soc.* **2012**, *134*, 20294.
(20) Zhang, S.; Dai, X.; Qi, X.; Liu, C.; Zhang, H.; Fang, Z. *Nat. Phys.* **2009**, *5*, 438–442.
(21) Rajamathi, C. R.; Gupta, U.; Kumar, N.; Yang, H.; Sun, Y.; Süß, V.; Shekhar, C.; Schmidt, M.; Blumtritt, H.; Werner, P.; Yan, B.; Parkin, S.; Felser, C.; Rao, C. N. R. *Adv. Mater.* **2017**, *29*, 1606202.
(22) Son, J. S.; Choi, M. K.; Han, M.-K.; Park, K.; Kim, J.-Y.; Lim, S. J.; Oh, M.; Kuk, Y.; Park, C.; Kim, S.-J.; Hyeon, T. *Nano Lett.* **2012**, *12*, 640.
(23) Samanta, M.; Pal, K.; Waghmare, U. V.; Biswas, K. *Angew. Chemie Int. Ed.* **2020**, 59, 4822.
(24) Samanta, M.; Pal, K.; Pal, P.; Waghmare, U. V.; Biswas, K. *J. Am. Chem. Soc.* **2018**, *140*, 5866.
(25) Geim, A. K.; Grigorieva, I. V. *Nature* **2013**, *499*, 419.
(26) Yankowitz, M.; Ma, Q.; Jarillo-Herrero, P.; LeRoy, B. J. *Nat. Rev. Phys.* **2019**, *1*, 112.
(27) Jariwala, D.; Marks, T. J.; Hersam, M. C. *Nat. Mater.* **2017**, *16*, 170.
(28) Banik, A.; Biswas, K. *Angew. Chemie Int. Ed.* **2017**, *56*, 14561.
(29) Kanatzidis, M. G. *Acc. Chem. Res.* **2005**, *38*, 359.
(30) Kanatzidis, M. G. *Inorg. Chem.* **2017**, *56*, 3158.
(31) Sharma, P. A.; Sharma, A. L. L.; Medlin, D. L.; Morales, A. M.; Yang, N.; Barney, M.; He, J.; Drymiotis, F.; Turner, J.; Tritt, T. M. *Phys. Rev. B - Condens. Matter Mater. Phys.* **2011**, *83*, 235209.
(32) Chatterjee, A.; Biswas, K. *Angew. Chemie Int. Ed.* **2015**, *54*, 5623.
(33) Soriano, R. B.; Arachchige, I. U.; Malliakas, C. D.; Wu, J.; Kanatzidis, M. G. *J. Am. Chem. Soc.* **2013**, *135*, 768.

(34) Shelimova, L. E.; Karpinskii, O. G.; Konstantinov, P. P.; Avilov, E. S.; Kretova, M. A.; Zemskov, V. S. *Inorg. Mater.* **2004**, *40*, 451.
(35) Yang, K.; Setyawan, W.; Wang, S.; Buongiorno Nardelli, M.; Curtarolo, S. *Nat. Mater.* **2012**, *11*, 614.
(36) Gaudin, E.; Jobic, S.; Evain, M.; Brec, R.; Rouxel, J. *Mater. Res. Bull.* **1995**, *30*, 549–561.
(37) Lind, H.; Lidin, S.; Häussermann, U. *Phys. Rev. B - Condens. Matter Mater. Phys.* **2005**, *72*, 184101.
(38) Zhang, J.; Huang, G. P. *Solid State Commun.* **2014**, *197*, 34.
(39) Zhang, J.; Liu, X.; Huang, G. *Phys. status solidi* **2015**, *252*, 2090.
(40) Lind, H.; Lidin, S. *Solid State Sci.* **2003**, *5*, 47.
(41) Cava, R. J.; Ji, H.; Fuccillo, M. K.; Gibson, Q. D.; Hor, Y. S. *J. Mater. Chem. C* **2013**, *1*, 3176.
(42) Xia, Y.; Qian, D.; Hsieh, D.; Wray, L.; Pal, A.; Lin, H.; Bansil, A.; Grauer, D.; Hor, Y. S.; Cava, R. J.; Hasan, M. Z. *Nat. Phys.* **2009**, *5*, 398.
(43) Majhi, K.; Pal, K.; Lohani, H.; Banerjee, A.; Mishra, P.; Yadav, A. K.; Ganesan, R.; Sekhar, B. R.; Waghmare, U. V; Anil Kumar, P. S. *Appl. Phys. Lett.* **2017**, *110*, 162102.
(44) Gibson, Q. D.; Schoop, L. M.; Weber, A. P.; Ji, H.; Nadj-Perge, S.; Drozdov, I. K.; Beidenkopf, H.; Sadowski, J. T.; Fedorov, A.; Yazdani, A.; Valla, T.; Cava, R. J. *Phys. Rev. B* **2013**, *88*, 081108.
(45) Valla, T.; Ji, H.; Schoop, L. M.; Weber, A. P.; Pan, Z.-H.; Sadowski, J. T.; Vescovo, E.; Fedorov, A. V.; Caruso, A. N.; Gibson, Q. D.; Müchler, L.; Felser, C.; Cava, R. J. *Phys. Rev. B* **2012**, *86*, 241101.
(46) Li, L.; Chen, Z.; Hu, Y.; Wang, X.; Zhang, T.; Chen, W.; Wang, Q. *J. Am. Chem. Soc.* **2013**, *135*, 1213.
(47) Chandra, S.; Banik, A.; Biswas, K. *ACS Energy Lett.* **2018**, *3*, 1153–1158.
(48) Zatsepin, D. A.; Boukhvalov, D. W.; Gavrilov, N. V.; Kurmaev, E. Z.; Zhidkov, I. S. *Appl. Surf. Sci.* **2016**, *387*, 1093.
(49) Zhang, G.; Qin, H.; Teng, J.; Guo, J.; Guo, Q.; Dai, X.; Fang, Z.; Wu, K. *Appl. Phys. Lett.* **2009**, *95*, 95.
(50) Saha, S.; Banik, A.; Biswas, K. *Chem. Eur. J.* **2016**, *22*, 15634.

PART 4

Ferroelectric and Transport Properties of Layered Bismuth Oxy-chalcogenides

Chapter 1

Room Temperature Ferroelectricity in Ultrathin Free-standing 2D-Nanosheets of Bi_2O_2Se

Chapter 1

Room Temperature Ferroelectricity in Ultrathin Free-standing 2D-Nanosheets of Bi_2O_2Se[†]

Summary

Ultrathin ferroelectric semiconductors with high charge carrier mobility are much coveted systems for the advancement of various electronic and optoelectronic devices. However, in traditional oxide ferroelectric insulators, the ferroelectric transition temperature decreases drastically with decreasing material thickness and ceases to exist below certain critical thickness owing to depolarizing field. Herein, we show the emergence of an ordered ferroelectric ground state in ultrathin (~2 nm) single crystalline nanosheet of Bi_2O_2Se at room temperature. Free-standing ferroelectric nanosheets, in which oppositely charged alternating layers are self-assembled together by electrostatic interactions, are synthesized by a simple, rapid and scalable wet chemical procedure at room temperature. The existence of ferroelectricity in Bi_2O_2Se nanosheets is confirmed by dielectric measurements and piezoresponse force spectroscopy. The spontaneous orthorhombic distortion in the ultrathin nanosheets breaks the local inversion symmetry, thereby results in ferroelectricity. The local structural distortion and the formation of spontaneous dipole moment were directly probed by atomic resolution scanning transmission electron microscopy and density functional theory calculations.

[†]*A Paper based on this study has been published in Nano Lett.* **2019**, *19*, 5703−5709.

1.1 Introduction

Ultrathin two dimensional (2D) materials play a crucial role in the future advancement of electronic, optoelectronic, energy conversion and storage, and numerous other fields with their superior properties.[1-4] They are also known to exhibit many emerging and novel phenomena in quantum materials.[5,6] The experimental realization of cooperative states with long-range ordering such as ferroelectricity, however, has been proved to be increasingly difficult as the materials are gradually thinned down to their monolayer limits. The realization of ferroelectric state in the monolayer limits is not only of fundamental interest, but they also hold immense potential for various electronic and optoelectronic applications such as in random access memory.[7] The ferroelectric transition temperature, however, reduces drastically in traditional 3D ferroelectric insulators like $PbTiO_3$, $BaTiO_3$ etc. when they are gradually thinned down owing to depolarization field[8-12] and ferroelectricity ceases to exist below certain critical thickness.[13] Many layered materials, on the other hand, have been predicted to host ferroelectric state even in their monolayer limits[14-19] and such layered materials are also preferred in device applications for their weak interlayer interactions which minimize interfacial coupling. Room temperature ferroelectricity in ultrathin layered van der Waal (vdW) materials has been experimentally realized in $CuInP_2S_6$ down to 4 nm[20] and so far, the only other layered materials in which ferroelectricity has been experimentally realized in the atomically thin geometry are SnTe,[21] In_2Se_3[22-25] and $MoTe_2$,[26] despite numerous theoretical predictions.

Following the sensation of graphene, many other layered 2D materials like phosphorene, transition-metal dichalcogenides (TMDs), MXenes etc. have been successfully synthesized in their ultrathin form.[27-31] The discovery of new 2D materials in their ultrathin geometry is, in fact, one of the major thrust areas to mitigate the various impediments with the current candidate 2D materials. Recently, vdW heterostructures, either the assembly of different atomically thin 2D materials forming a new heterostructure[32,33] or the synthesis of naturally occurring layered heterostructure materials in their ultrathin form,[34,35] has gained wide attention as they offer manipulation of a wide range of functionalities. Recently, the layered oxy-chalcogenide material Bi_2O_2Se has emerged as a compelling 2D material for their extremely high carrier mobility (>20000 $cm^2V^{-1}s^{-1}$ at 2 K) with very low effective mass (0.14 m_0),[36] indirect size tuneable band gap

(bulk band gap ~0.8 eV)[36,37] which is excellent for electronic and optoelectronic applications,[38-42] and air stability. Moreover, recent density functional theory (DFT) calculations predict that bulk Bi_2O_2Se may possess ferroelectric state under an in-plane biaxial strain and exhibit piezoelectric response an order of magnitude higher than that of monolayer MoS_2.[43] Most of the ferroelectric materials, including the recently discovered layered $CuInP_2S_6$, are insulators with large band gap. Therefore, it is worthwhile to stabilize a ferroelectric state in the atomically thin Bi_2O_2Se for its semiconducting nature and high charge carrier mobility. The robust surface states of Bi_2O_2Se[38,44] against defects is also much desirable in ultrathin ferroelectrics for minimizing the interfacial effects.[45]

Herein, we demonstrate a simple, rapid and scalable synthesis of ultrathin single crystalline Bi_2O_2Se nanosheets by solution-based self-assembly of oppositely charged layers at room temperature. Atomic force microscopy (AFM) reveals that the obtained nanosheets are ~2 nm thick with a smooth surface. Field emission scanning electron microscopy (FESEM) and scanning transmission electron microscopy (STEM) images confirm that the synthesized nanosheets have lateral dimension in the range of 100 – 200 nm. The measurement of temperature dependent dielectric constant reveals that the ferroelectric transition occurs ~235 °C. The piezoresponse force microscopy (PFM) further confirms the presence of spontaneous polarization and 180° polarization switching under an external field at room temperature. To understand the origin of ferroelectricity in ultrathin Bi_2O_2Se nanosheets, we have carried out atomic resolution STEM and corroborated the results with DFT calculations. We found that these free-standing nanosheets have spontaneous orthorhombic distortion which breaks the inversion symmetry locally in the tetragonal crystal structure. Thus, dipole moment develops spontaneously and becomes aligned ferroelectrically.

1.2 Methods

1.2.1 Reagents. Bismuth nitrate ($Bi(NO_3)_3{\cdot}5H_2O$, Alfa Aesar, 99.9%), selenourea ($SeC(NH_2)_2$, Alfa Aesar, 99.9%), potassium hydroxide (KOH, S D Fine-Chem Limited (SDFCL)), sodium hydroxide (NaOH, SDFCL), Disodium EDTA ($C_{10}H_{14}O_8Na_2N_2{\cdot}H_2O$, SDFCL) and ethanol were used without any further purification.

1.2.2 Synthesis procedure. 100 mg (0.206 mmol) of $Bi(NO_3)_3{\cdot}5H_2O$, 12.7 mg (0.103 mmol) of $SeC(NH_2)_2$ and 306.8 mg (0.824 mmol) of disodium EDTA were sequentially added at a 5 minutes interval into 20 ml water in a glass beaker. The solution was stirred continuously. The addition of $Bi(NO_3)_3{\cdot}5H_2O$ into water results in a milky white color solution which turns into an orange color solution after the addition of $SeC(NH_2)_2$. The solution becomes clear after the addition of disodium EDTA. Finally, 120 mg (2.14 mmol) of KOH and 320 mg (8 mmol) of NaOH were added into the solution which turns the solution color black. After 10 minutes of stirring, the solution was put to rest which results in precipitation of the dark brown color nanosheets. We observed that nanosheets of similar morphology and thickness can also be obtained without using disodium EDTA, however, in that case, the required amount of water solvent is much higher, 200 ml. These were then washed with alcohol and water and centrifuged to remove disodium EDTA. The purified product was then dried in a vacuum oven at 150 °C.

Step I: In water, $Bi(NO_3)_3$ undergoes hydrolysis to produce $BiONO_3$ and the process of hydrolysis is expedites in alkaline medium:

$$Bi(NO_3)_3 + H_2O \rightarrow BiONO_3 + 2H^+ + 2NO_3^-$$

Step II: Selenourea $SeC(NH_2)_2$ undergoes decomposition in alkaline medium to generate selenide ions (Se^{2-}) along with cyanamide (H_2NCN):

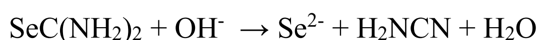

$$SeC(NH_2)_2 + OH^- \rightarrow Se^{2-} + H_2NCN + H_2O$$

Step III: In the final step, Se^{2-} interacts with $BiONO_3$ to form Bi_2O_2Se which is precipitated as dark brown color product in the aqueous medium.

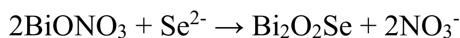

$$2BiONO_3 + Se^{2-} \rightarrow Bi_2O_2Se + 2NO_3^-$$

1.2.3 X-ray diffraction (XRD). Powder XRD patterns were collected in a Panalytical diffractometer with Cu Kα radiation (λ = 1.5406 Å) at room temperature. XRD data of the as synthesized nanosheets were collected after dispersing the nanosheets in ethanol and drop casting on to a glass slide.

1.2.4 Band gap measurement. Diffuse reflectance spectroscopy was carried out using a Perkin Elmer Lambda 900, UV/VIS/NIR spectrometer from which absorption data was calculated using Kubelka-Munk equation: $\alpha/S = (1 - R)^2/2R$ where α, S and R are the

absorption coefficient, scattering coefficient and reflectance, respectively. The optical band gap was then determined from the energy variation of α/S.

1.2.5 X-ray photoelectron spectroscopy (XPS). XPS measurement was carried out using an Omicron nanotechnology spectrometer with an Mg-Kα (1253.6 eV) x-ray source.

1.2.6 Field emission scanning electron microscopy (FESEM). FESEM imaging was carried out using a FEI NOVA NANO SEM 600 with operating energy of 15 kV. Energy dispersive spectroscopy (EDX) analysis was carried out with an attached EDX genesis instrument.

1.2.7 Transmission electron microscopy (TEM). TEM studies were carried out using a FEI TECNAI G^2 20 STWIN TEM operated at 200 keV and an aberration corrected FEI TITAN3 operating at 300 keV. EDX compositional analysis and elemental mapping were carried in STEM imaging mode. Very dilute solution of Bi_2O_2Se nanosheets dispersed in ethanol was drop casted on holey carbon coated Cu grid and used for the TEM studies.

1.2.8 Inductively coupled plasma atomic emission spectroscopy (ICP-AES). ICP-AES was carried out for compositional analysis in a Perkin-Elmer Optima 7000DV instrument. For ICP-AES study, powdered nanosheets were dissolved in aqua regia (HNO_3:HCL = 3:1) and then this solution was further diluted using Millipore water.

1.2.9 Atomic force microscopy (AFM). Bruker Innova microscope in tapping mode was used to carry out AFM studies using an antimony doped silicon tip.

1.2.10 Raman Spectra. Room temperature Raman spectra of Bi_2O_2Se bulk and nanosheet samples were collected on a Horiba Jobin Yvon LabRAM HR800 spectrometer using a He-Ne laser (631.8 nm).

1.2.11 Differential Scanning Calorimetry (DSC). A METTLER-TOLEDO differential scanning calorimeter (DSC 822 e) was used to collet DSC data with a ramp rate of 1 K/min in N_2 atmosphere.

1.2.12 Piezoresponse force microscopy (PFM). This part of the work has been performed in collaboration with Prof. Goutam Sheet's Group in IISER Mohali, India. The measurements were done using an Asylum research AFM (MFP–3D) with an additional high voltage amplifier. The sample was mounted on a conducting sample holder which was

directly connected to the ground of the amplifier. The conductive AFM cantilever having a Pt-Ir tip on it was brought in contact with the sample (nanosheets). An AC excitation of 4V riding on a dc bias voltage (V_{dc}) was applied between the tip and the amplifier ground. The response of the sample to the electrical stimulus was detected through the reflection of the laser beam from the end of the cantilever onto a position sensitive photo diode. In order to ensure that the hysteretic effects are due to ferroelectricity which may otherwise arise from electrostatic and electrochemical effect, all the measurements were performed following SS-PFM (switching spectroscopy piezoresponse force microscopy) initiated by Jesse et al.[46,47] In this method, instead of sweeping V_{dc} continuously, bias is applied in sequence of pulses where the phase and amplitude measurements are done in the "off" states and an appreciable change is observed in the "off-state" results as compared to the "on-state" measurements which is a clear evidence of the minimization of electrostatic effects. We further performed the topographic imaging after the spectroscopic measurements, where no topographic modification was observed which usually occurs due to the electrochemical reaction between the tip and sample.

1.2.13 Dielectric measurements. For dielectric measurements, Bi_2O_2Se nanosheets were pressed into a pellet. Dielectric properties were then measured in the temperature range from room temperature to 573 K and in the frequency range 50 Hz to 2 MHz with an ac excitation of 20 mV using a Solartron 1260A impedance analyzer.

1.2.14 Density functional theory (DFT) calculations. This part of the work has been performed in collaboration with Prof. Tanmoy Das's Group in IISc, India. The first principles electronic structure calculations are performed within the framework of density functional theory (DFT) using generalized gradient approximation (GGA) of the Perdew-Burke-Ernzerhof (PBE)[48] form for the exchange-correlation functional as implemented in the Vinea Ab-initio Simulation Package (VASP).[49] The projector augmented wave (PAW)[50] pseudo-potentials are used to describe the core electrons. Electronic wave-functions are expanded using plane waves up to a cut-off energy of 600 eV. Periodic boundary conditions are employed and at least of 15 Å slab is used on the surface of few layers to eliminate the interaction between consecutive periodic images. The Monkhorst-Pack *k*-mesh is set to 11 × 11 (11 × 11 × 4) in the Brillouin zone for the self-consistent calculation of few layer cases (bulk), and all atoms are relaxed in each optimization cycle

until atomic forces on each atom are smaller than 0.01 eV/Å. As it is well-known that GGA functional underestimates the band gap, all the band structures are computed by using hybrid Heyd-Scuseria-Ernzerhof (HSE06)[51] functional and the GGA-relaxed crystal structure. It should be noted here that we did not include any effect of exciton binding energy in our DFT calculations to estimate the optical band gap. Biaxial strain is simulated by changing the lattice constant *a*, whereas the space group *I4/mmm* is fixed. The symmetric structure represents the equilibrium positions of the atoms at a given strain value. The distorted structure is obtained by diagonally displacing both the Bi and the Se atoms, but in opposite directions from their equilibrium positions. In what follows, if $\mathbf{R}_{Bi}$, and $\mathbf{R}_{Se}$ are the equilibrium planer positions of the Bi and Se atoms respectively in a symmetric structure, then in the distorted structure, they assume positions at $\mathbf{R}_{Bi} + \delta$, and $\mathbf{R}_{Se} - \delta$, respectively. The outermost Se layers are passivated with hydrogen atoms in order to balance the non-stoichiometry due to the additional Se layer.

1.3 Results & discussion

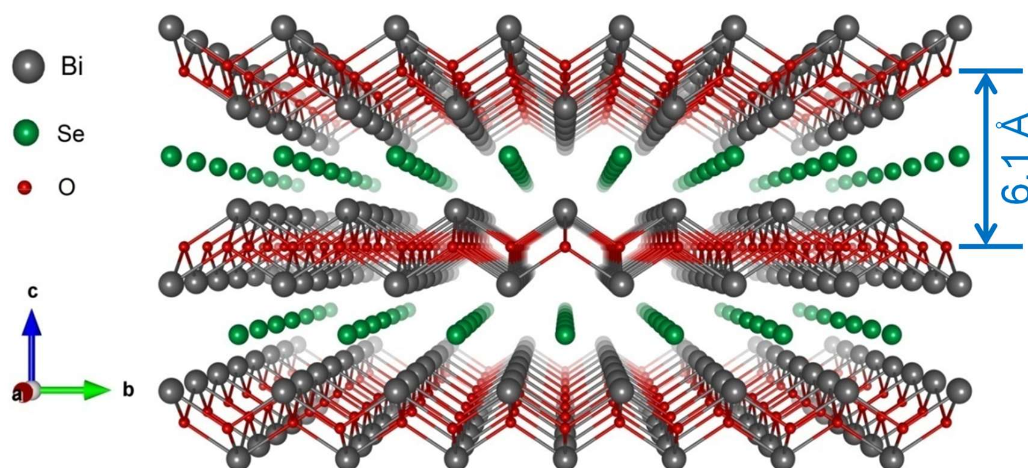

Figure 1.1 *Layered crystal structure of Bi_2O_2Se showing alternative stacks of $[Bi_2O_2]^{2+}$ and Se^{2-} layers and an interlayer separation of 6.1 Å.*

Bi_2O_2Se, with the absence of a well-defined vdW gap, however, intrinsically distinguishes itself from the family of vdW solids. The tetragonal structure (*I4/mmm* space group, a = 3.88 Å, c = 12.16 Å) of Bi_2O_2Se is formed by the alternate stacking of *positively* charged $[Bi_2O_2]^{2+}$ and *negatively* charged Se^{2-} layers along the crystallographic *c*-direction (Figure

1.1).[36,52] Although Bi_2O_2Se has a layered crystal structure, the interlayer interaction is of electrostatic type which arises out of *positively* charged $[Bi_2O_2]^{2+}$ and *negatively* charged Se^{2-} stacking layers and is stronger than vdW interaction.[36]

A pivotal part of the success of any 2D materials in practical applications is the development of a rapid, scalable and simple synthesis process. Various methods of preparation have been developed for the established candidate 2D materials like graphene and TMDCs which often exploit the weak nature of the interlayer vdW force.[27-30] The strong interlayer electrostatic force in Bi_2O_2Se, however, renders such traditional top-down synthesis process, like exfoliation of producing atomically thin vdW materials, unfeasible here. The bottom-up approaches also face considerable challenges as the topmost layer always attracts the oppositely charged next layer and results in vertical growth. So far, ultrathin Bi_2O_2Se nanosheets were grown using chemical vapour deposition (CVD) mostly on freshly cleaved fluorophlogopite mica[36-38,41] where the electrostatic interaction between the substrate and epitaxial nanosheet layer facilitate the lateral growth. Recently, Tan *et al*. has also been successful in growing wafer scale single crystalline Bi_2O_2Se films on lattice matched perovskite oxide substrates such as $SrTiO_3$, $LaAlO_3$ and their derivatives using CVD.[53] However, atomically thin nanosheets were obtained only in few cases so far.[36,37,53] Furthermore, the realization of ferroelectricity requires careful selection of lattice matched substrate to minimize misfit strain[54] and interfacial coupling.[45] The use of charged substrate like fluorophlogopite mica[36-38,41] or chemical etching used for substrate transfer[41] can have severe effects on the ferroelectric state.

Here, we have synthesized free-standing, single crystalline nanosheets of Bi_2O_2Se in a simple solution based method by the reaction of bismuth nitrate ($Bi(NO_3)_3$) and selenourea ($SeC(NH_2)_2$) in alkaline medium at room temperature (see details in Methods, supplementary information). This is a one-pot synthesis method which can be carried out in a glass beaker in ambient conditions. The reaction process is also very fast in which pure and ultrathin nanosheets with high crystalline quality grow within 10 minutes. The reaction is easily scalable up to ~1 g in laboratory conditions. In aqueous medium, $Bi(NO_3)_3$ undergoes hydrolysis to produce $BiONO_3$ and this hydrolysis process further expedites in the alkaline medium after the addition of NaOH and KOH. In alkaline medium, $SeC(NH_2)_2$ also decomposes and produces selenide ions (Se^{2-}). These Se^{2-} ions then interact with

$BiONO_3$ to produce Bi_2O_2Se which precipitates as a dark brown colour product. Thus, *positively* charged $[Bi_2O_2]^{2+}$ and *negatively* charged Se^{2-} layers generated from two different precursors in alkaline medium self-assembled electrostatically to form ultrathin Bi_2O_2Se nanosheets.

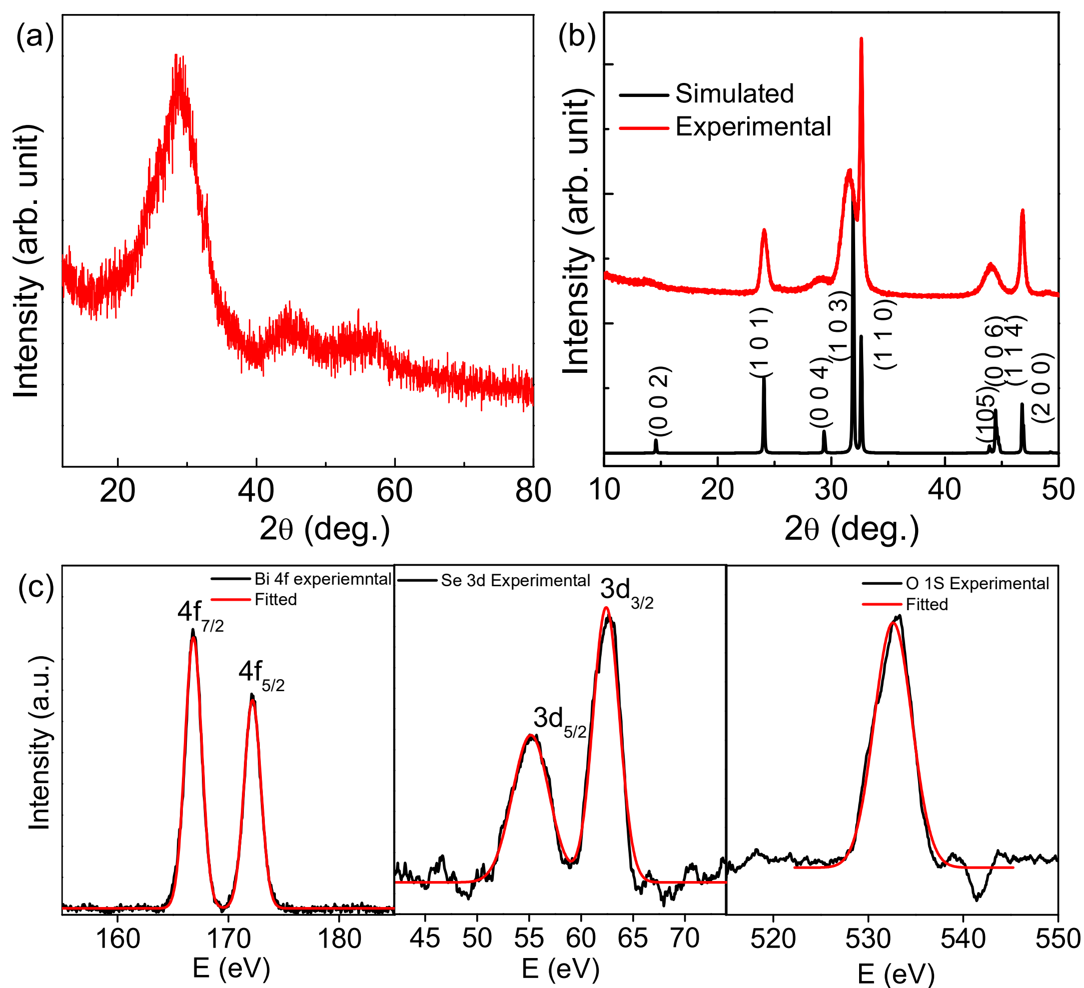

Figure 1.2. *Room temperature XRD pattern of (a) the as synthesized nanosheets and (b) the synthesized Bi_2O_2Se nanosheets after vacuum drying measured with Cu Kα X-ray. (c) X-ray photoelectron spectra of Bi_2O_2Se nanosheet showing the Bi 4f, Se 3d and O 1s peaks.*

The room temperature powder X-ray diffraction (XRD) pattern of the as synthesized nanosheets shows only a broad hump (Figure 1.2a) which indicate towards the ultrathin nature of the synthesized nanosheets. After vacuum drying the nanosheets, the XRD pattern (Figure 1.2b) could be indexed with the pristine Bi_2O_2Se tetragonal structure

(space group *I4/mmm*). The agglomeration of the nanosheets during vacuum drying results in such a clear depiction of the XRD pattern. Energy dispersive X-ray spectroscopy (EDX) (Table 1.1) and inductively coupled plasma atomic emission spectroscopy (ICP-AES) (Table 1.2) confirm that elemental composition of the nanosheets is close to the nominal composition. X-ray photoelectron spectroscopy (XPS) (Figure 1.2c) further confirms the expected Bi(III), O(II) and Se(II) oxidation states of the elements.

Table 1.1. *Elemental compositions as obtained from EDX analysis.*

Element	Wt %	At %
O	6.18	40.8
Bi	79.66	40.26
Se	14.16	18.94
Total	100	100

Table 1.2. *Elemental compositions as obtained from ICP-AES measurement.*

Element	Wt %	At %
Bi	139.5 mg/lit	66
Se	23.81 mg/lit	31

The morphological studies using FESEM, AFM and transmission electron microscopy (TEM) corroborate to the nanosheets ultrathin nature. FESEM (Inset of Figure 1.3), STEM (Figure 1.3a) and low magnification TEM micrographs (Figure 1.3b) clearly demonstrate the ultrathin morphology of the nanosheets with lateral dimensions of the individual nanosheets ranges in between 100 to 200 nm. AFM images (Figure 1.3c) reveal the thickness of most of the individual nanosheets is ~2 nm which consists of 2-3 heterostructure layers. Furthermore, selected area electron diffraction (SAED) pattern (Figure 1.3b, Inset) indicates the single crystalline nature of the as synthesized nanosheets. The layered arrangement along the crystallographic *c*-axis with a spacing of ~0.68 nm is clearly seen from the high resolution TEM (HRTEM) image (Figure 1.3d). The slightly higher spacing of 0.68 nm between two $[Bi_2O_2]^{2+}$ layers compared to the expected value of 0.61 nm from its bulk counterpart might be because of structural relaxation in these free-standing thin nanosheets. Similar, structural relaxation was observed earlier also in chemical vapor deposition (CVD) grown Bi_2O_2Se nanosheets.[37]

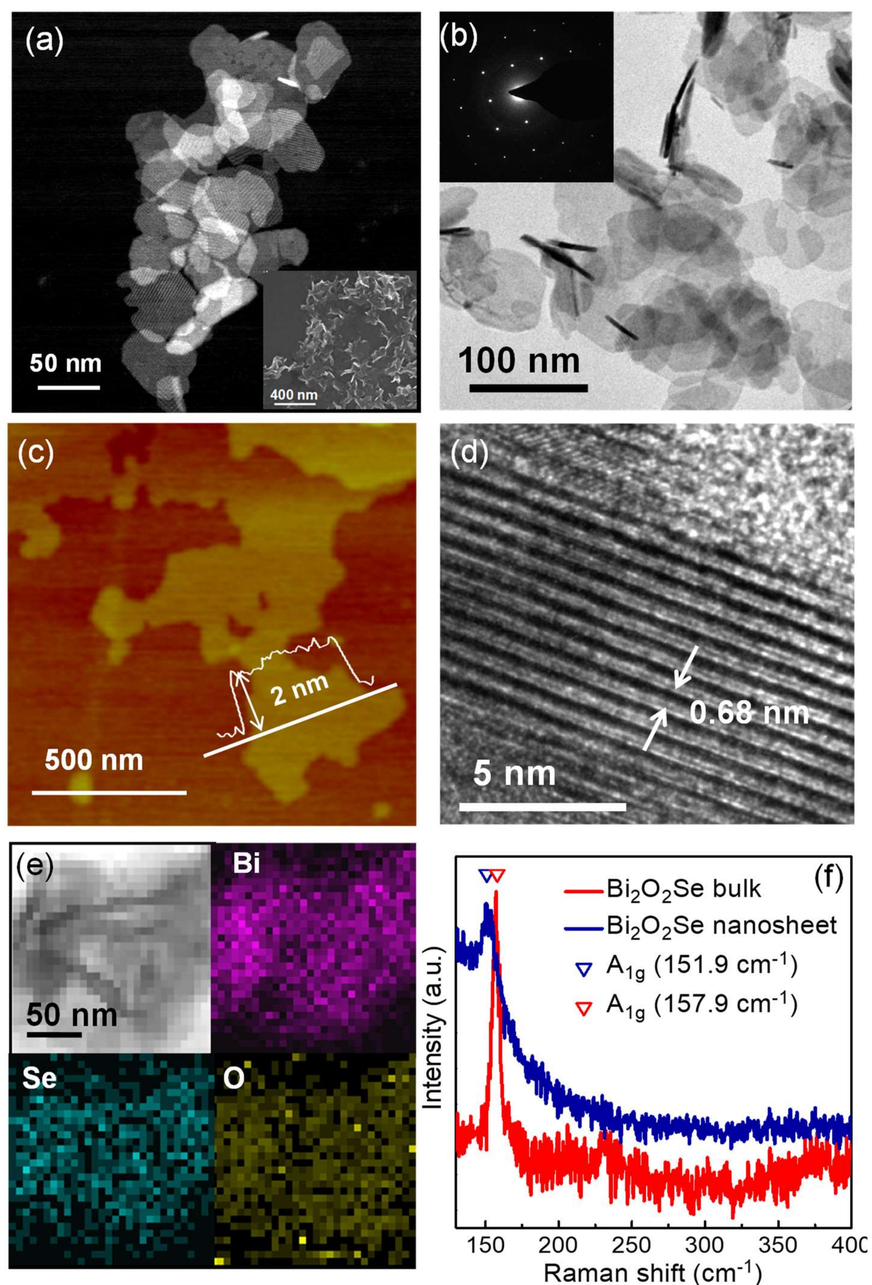

Figure 1.3. *(a) STEM-HAADF image of Bi_2O_2Se nanosheets. Inset show FESEM images of the Bi_2O_2Se nanosheets. (b) Bight field low magnification TEM image of Bi_2O_2Se nanosheets. Inset shows the SAED pattern demonstrating single crystalline nature of the nanosheet. (c) AFM image and the height profile showing Bi_2O_2Se nanosheets of thickness 2 nm which corresponds to approximately 3 layers. (d) HRTEM image of Bi_2O_2Se nanosheet showing the layer by layer arrangement with separation of 6.8 Å. (e) Elemental color mapping exhibiting a homogeneous distribution of Bi, O and Se in the Bi_2O_2Se nanosheet. (f) Room temperature Raman spectra of Bi_2O_2Se bulk and nanosheet.*

EDX elemental color mapping (Figure 1.3e) during STEM exhibits a homogeneous distribution of the elements Bi, O and Se in the nanosheets. Theoretical analysis of *Γ* point phonon modes of Bi_2O_2Se yields four Raman active modes: A_{1g} and B_{1g} modes corresponding to the out of plane vibration of Bi and O atoms, respectively and E_g^1 and E_g^2 modes corresponding to the in-plane vibration of Bi and O atoms, respectively.[55-57] Previous studies indicate that out of these four Raman active modes, only the A_{1g} mode is observable in the backscattering configuration.[37,49,50] Figure 1.3f exhibits the room temperature Raman spectra of the Bi_2O_2Se nanosheets in which the A_{1g} mode is evident around ~151.9 cm^{-1}. A comparison between the Raman spectra of bulk and nanosheet Bi_2O_2Se samples indicates low energy shift of the A_{1g} mode in the nanosheet (Figure 1.3f) due to phonon softening corresponding to weakened interlayer coupling in the ultrathin nanosheets.[55]

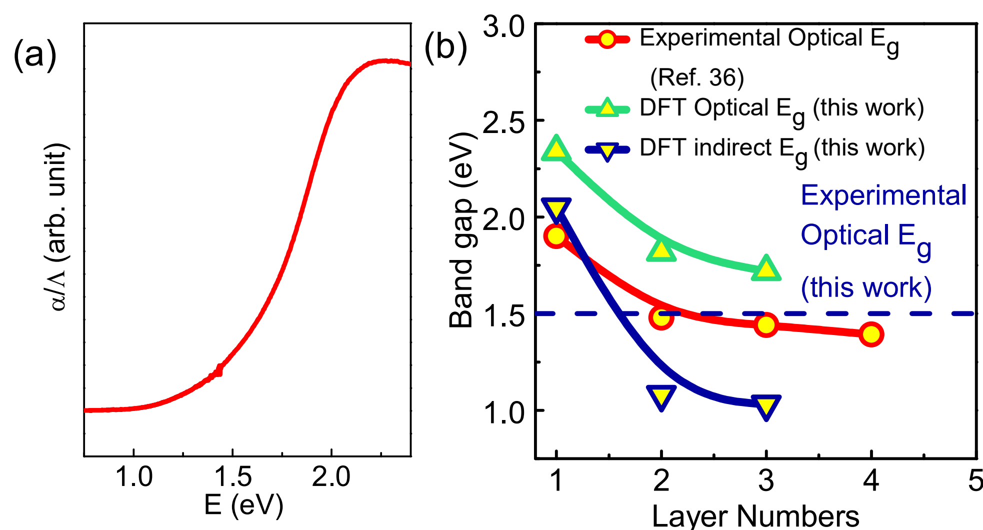

Figure 1.4. *(a) Optical absorption spectrum of Bi_2O_2Se nanosheets showing band gap of 1.5 eV. (b) Experimental and theoretical optical band gap variation with layer numbers for Bi_2O_2Se nanosheet.*

The optical band gap of the as synthesized nanosheets measured using diffuse reflectance spectroscopy was found to be ~1.5 eV (Figure 1.4a). The previous report[37] on CVD grown nanosheet indicated for the thickness tunability of band gap, where optical band gap increases with decreasing layer thickness due to quantum confinement effect. Our DFT calculations (Figure 1.4b and Figure 1.5) also indicate a similar enhancement in

optical band gap at the Γ point due to quantum confinements as the thickness decreases with a maximum optical band gap of 2.34 eV for the monolayer nanosheet. The comparison of experimentally obtained optical band gap for our solution synthesized nanosheets (dashed line in Figure 1.4b) with the reported optical band gap of CVD grown nanosheets further indicates that the synthesized nanosheets are only ~2-3 layer thick. Additionally, an indirect band gap also exists between the Γ and X points. While Se-*p* orbital mainly contributes to the valance band maxima at X point, the conduction band minima at the Γ point originates from the Bi-*p* orbital resulting an indirect band gap along the Γ-X direction (Figure 1.5). Although the band topology does not change from the monolayer to the bulk, the dispersion of the valance band decreases with the decrease in thickness with a corresponding increase in their effective mass (Figure 1.5).

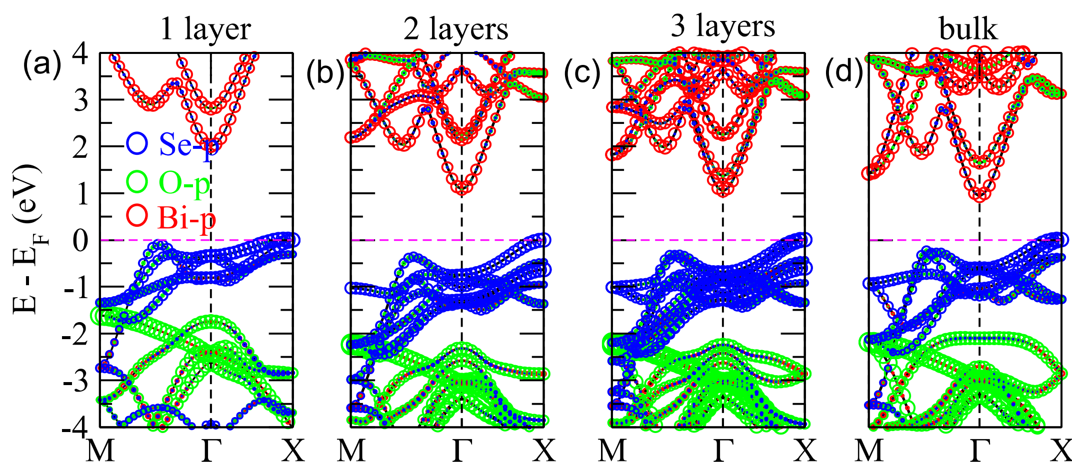

Figure 1.5. *Thickness-dependent and orbital-decomposed bandstructure of (a) monolayer, (b) bilayer, (c) trilayer and (d) bulk of* Bi_2O_2Se*, respectively. Red, green and blue circles indicate the fat-bandstructure, respectively for Bi-p, O-p and Se-p orbitals. Magenta dashed line indicates the Fermi level.*

The temperature dependent dielectric property of the nanosheets at different frequencies is shown in Figure 1.6a. The temperature variation of relative permittivity, $\varepsilon'(T)$, shows a clear maximum at T_c ~235 °C without any observable frequency dependence elucidating a ferroelectric like transition (Figure 1.6a). ε' decreases as frequency increases with the maximum values of ε' are being 64.2, 87.7 and 141.5 at frequencies 2 MHz, 500 kHz and 50 kHz, respectively. The differential scanning calorimetric (DSC) signal of

Bi_2O_2Se nanosheets also shows a transition around the same temperature region where we observed ferroelectric transition in the temperature variation of ε′ (Figure 1.6b).

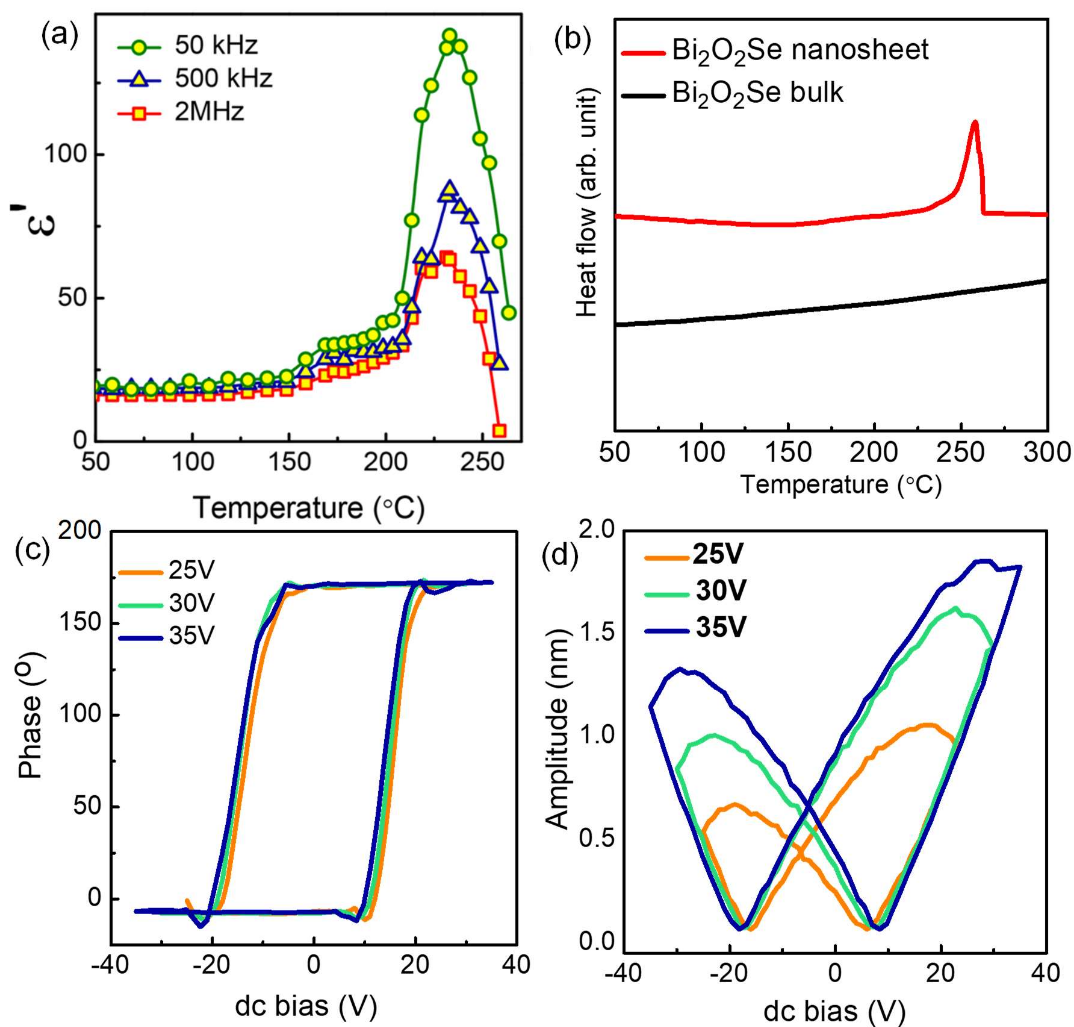

Figure 1.6. *(a) Temperature variation of the real part of relative permittivity (ε′) at different frequencies for Bi_2O_2Se nanosheet. (b) DSC signal of Bi_2O_2Se bulk and nanosheet samples. While the nanosheet sample shows the transition, the bulk does not. "Off-state" (c) phase and (d) amplitude of SS-PFM signal from Bi_2O_2Se nanosheet at room temperature exhibiting ferroelectricity with 180° polarization switching.*

To further ascertain the ferroelectric state, we carried out switching spectroscopy by piezoresponse force microscopy (PFM)[46,47] to show the existence of a spontaneous polarization state and its switching behavior under an externally applied electric field. Figure 1.6c and 2.6d exhibit the observed hysteric behavior in the "off-state" piezoresponse signal at room temperature. The phase of the PFM response signal is correlated with the

domain's polarization direction and for ferroelectric sample, the electrical polarization, and thus the phase of the PFM response signal, should show hysteresis behavior with 180° polarization switching. Figure 1.6d clearly exhibits the hysteresis behavior with a sharp 180° switching of electrical polarization at different applied dc bias (V_{dc}). The coercive field is ~ 14 V which is large indicating a strong energy barrier between the two opposite polarization states. The amplitude of the PFM response signal is related to the magnitude of the local electromechanical response experienced by the PFM cantilever and exhibits hysteresis behavior with expected butterfly-shaped hysteresis loop (Figure 1.6d).

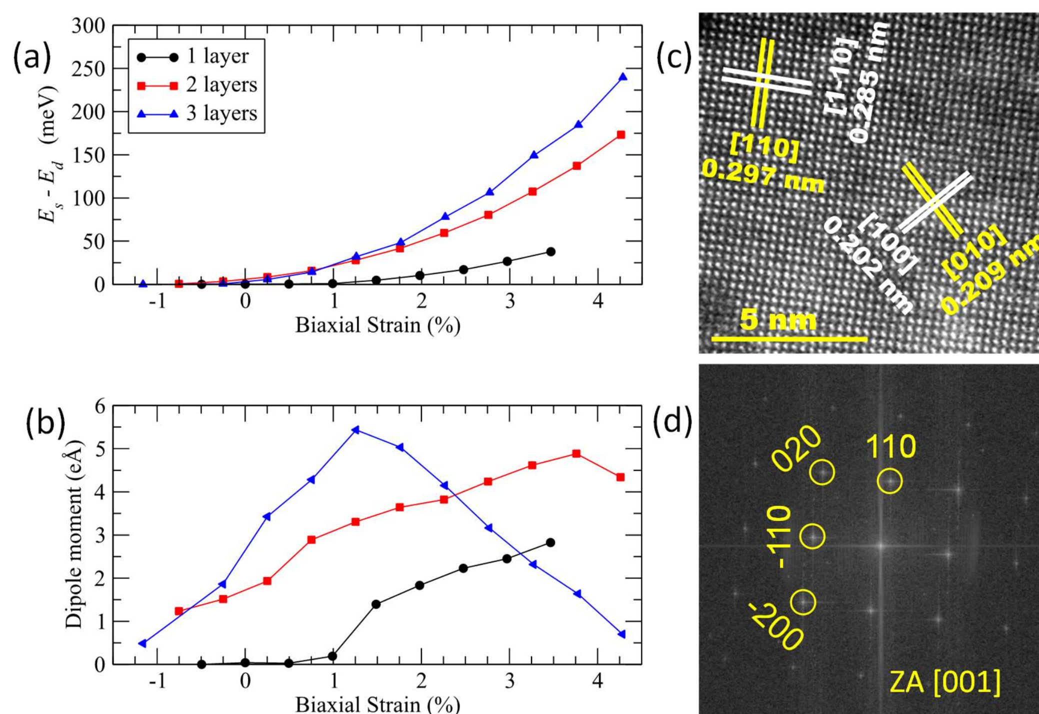

Figure 1.7. *(a) Variation of $\Delta E = E_s - E_d$ and (b) total dipole moment under strain for monolayer, bilayer and tri-layer Bi_2O_2Se nanosheets. E_s and E_d denote the total energy for symmetrical and distorted structures, respectively. (c) Atomic resolution HAADF-STEM image projected along the [001] direction exhibiting deviation between interatomic distances along [110] and [1-10] directions, and along [100] and [010] directions. (d) Fast Fourier transformation (FFT) of the atomic resolution STEM image shown in (c).*

The appearance of room temperature ferroelectricity in ultrathin Bi_2O_2Se nanosheets is rather surprising, considering its known centrosymmetric crystal structure in the bulk phase. Therefore, to further understand the origin of the observed ferroelectric

behavior in the nanosheets, we performed DFT calculations for symmetric structure as well as distorted structure in which Bi and O/Se atoms were displaced diagonally from their equilibrium positions in opposite directions. To investigate the effect of strain in the appearance of ferroelectricity, we have carried out further simulations onto the system by applying both compressive and tensile planar biaxial strains. The strain magnitude has been quantified as $\zeta = (a - a_0)/a_0$, where a, and a_0 are the in-plane lattice constants for the strained and pristine nanosheet, respectively. Figure 1.7a,b show the energetics between symmetric and distorted structure and dipole moments, respectively, at different biaxial strains applied in various nanosheets, in which thicknesses range from monolayer to trilayer. Likewise the ferroelectricity in bulk Bi_2O_2Se predicted previously by theoretical calculations,[43] our calculations show that the ferroelectricity persists in the monolayer nanosheet only for $\zeta >$ 1% (Figure 1.7b). In the ferroelectric phase, the structural inversion symmetry gets broken by atomic displacement of Bi and O atoms. In bulk Bi_2O_2Se, the $[Bi_2O_2]^{2+}$ layer is made by $(BiO)_2$ rhombic network. The atomic displacement of Bi and O atoms distorts this rhombic network in the nanosheet. Interestingly, we find that both the distorted bilayer and trilayer nanosheets exhibit spontaneous dipole moment even in the unstrained phase, unlike the bulk and monolayer cases where certain strains are required to induce the ferroelectricity. For bilayer and trilayer nanosheets, the dipole moments increase initially with tensile strain; and subsequently reach a maximum value at 1.2 % and 3.8 % strain, respectively; producing a dome shape behavior (Figure 1.7b). For the compressive strain, the dipole moment decreases monotonically, and seems to vanish by $\zeta \sim 1.5$ % in the few-layer cases. At various ζ values we compare the energy difference $\Delta E = E_s - E_d$ where E_s and E_d are the total energies for the symmetric and distorted structure. We find that ΔE remains nearly zero for monolayer nanosheets for both compressive and tensile strain up to 1% which indicates that such spontaneous structural distortion is an energetically possible scenario (Figure 1.7a). Furthermore, our results indicate that structural distortion is energetically more favorable for compressive strains than for tensile strains. In the case of tensile strain, we find that structural distortions gradually cost more energy as the strain magnitude ζ or the nanosheet thickness increases (Figure 1.7a).

To experimentally verify the presence of spontaneous distortion in the nanosheets, we carried out atomic resolution high-angle annular dark-field (HAADF)-STEM imaging

of the Bi_2O_2Se nanosheets (Figure 1.7c). The tetragonal *I*4/*mmm* symmetry demands the interplaner spacing d_{h00} for the (h 0 0) and d_{0k0} for the (0 k 0) family of lattice planes to be identical. However, from the electron diffraction pattern (Figure 1.7d) obtained by Fast Fourier transformation of atomic resolution STEM images we found that d_{200} and d_{020} are non-equivalent by ~ 0.11 Å. Correspondingly, in real space, from the atomic resolution STEM images, we find that deviation between interatomic distances along [110] and [1-10] directions is ~ 0.12 Å. This indicates the presence of diagonal distortion in the Bi_2O_2Se nanosheets. The interatomic distances along the [100] and [010] directions are also unequal by ~ 0.07 Å which means that lattice parameters *a* and *b* are no more equal. The distorted scenario is well supported by the DFT calculations which predict the distortion of Bi-O bond-length is about 0.05 Å along [100] and [010] direction for bilayer and trilayer nanosheets under zero strain. The presence of these spontaneous distortions thus changes the system from tetragonal (D_{4h}) (which is the symmetry for the bulk phase) to an orthorhombic (C_{2v}) nanosheet system along with a local inversion symmetry breaking, which supports the presence of room temperature ferroelectricity in the free-standing ultrathin Bi_2O_2Se nanosheets.

1.4 Conclusions

In conclusion, we demonstrated a simple and scalable solution based synthesis to prepare self-assembled charged layered heterostructure nanosheets of Bi_2O_2Se. The obtained nanosheets are ultrathin (~2 nm), single crystalline and free-standing in nature. We found that an intriguing ferroelectric order emerges, which is stable even at room temperature, due to spontaneous orthorhombic distortion in the nanosheets. The distortion is created by atomic displacement of Bi and O atoms which breaks the local inversion symmetry and facilitates the formation of spontaneous dipole moments. The development of room temperature ferroelectricity in the semiconducting nanosheets of this high-mobility Bi_2O_2Se semiconductor is an important advancement for the electronic and opto-electronic devices.

1.5 References

(1) Akinwande, D.; Petrone, N.; Hone, J. *Nat. Commun.* **2014**, *5*, 5678.

(2) Wang, Q. H.; Kalantar-Zadeh, K.; Kis, A.; Coleman, J. N.; Strano, M. S. *Nat. Nanotechnol.* **2012**, *7*, 699–712.
(3) Deng, D.; Novoselov, K. S.; Fu, Q.; Zheng, N.; Tian, Z.; Bao, X. *Nat. Nanotechnol.* **2016**, *11*, 218–230.
(4) Bonaccorso, F.; Colombo, L.; Yu, G.; Stoller, M.; Tozzini, V.; Ferrari, A. C.; Ruoff, R. S.; Pellegrini, V. *Science* **2015**, *347*, 1246501.
(5) Xu, X.; Yao, W.; Xiao, D.; Heinz, T. F. *Nat. Phys.* **2014**, *10*, 343–350.
(6) Basov, D. N.; Averitt, R. D.; Hsieh, D. *Nat. Mater.* **2017**, *16*, 1077–1088.
(7) Garcia, V.; Bibes, M. *Nat. Commun.* **2014**, *5*, 4289.
(8) Fong, D. D.; Stephenson, G. B.; Streiffer, S. K.; Eastman, J. A.; Auciello, O.; Fuoss, P. H.; Thompson, C. *Science* **2004**, *304*, 1650.
(9) Fong, D. D.; Kolpak, A. M.; Eastman, J. A.; Streiffer, S. K.; Fuoss, P. H.; Stephenson, G. B.; Thompson, C.; Kim, D. M.; Choi, K. J.; Eom, C. B.; Grinberg, I.; Rappe, A. M. *Phys. Rev. Lett.* **2006**, *96*, 127601.
(10) Kornev, I.; Fu, H.; Bellaiche, L. *Phys. Rev. Lett.* **2004**, *93*, 196104.
(11) Tenne, D. A.; Turner, P.; Schmidt, J. D.; Biegalski, M.; Li, Y. L.; Chen, L. Q.; Soukiassian, A.; Trolier-McKinstry, S., Schlom, D. G.; Xi, X. X.; Fong, D. D.; Fuoss, P. H.; Eastman, J. A.; Stephenson, G. B.; Thompson, C.; Streiffer, S. K. *Phys. Rev. Lett.* **2009**, *103*, 177601.
(12) Dawber, M.; Rabe, K. M.; Scott, J. F. *Rev. Mod. Phys.* **2005**, *77*, 1083–1130.
(13) Junquera, J.; Ghosez, P. *Nature* **2003**, *422*, 506–509.
(14) Vasudevan, R. K.; Balke, N.; Maksymovych, P.; Jesse, S.; Kalinin, S. V. *Appl. Phys. Rev.* **2017**, *4*, 021302.
(15) Cui, C.; Xue, F.; Hu, W.-J.; Li, L.-J. *npj 2D Mater. Appl.* **2018**, *2*, 18.
(16) Wu, M.; Jena, P. *Rev. Comput. Mol. Sci.* **2018**, *8*, e1365.
(17) Shirodkar, S. N.; Waghmare, U. V. *Phys. Rev. Lett.* **2014**, *112*, 157601.
(18) Fei, R.; Kang, W.; Yang, L. *Phys. Rev. Lett.* **2016**, *117*, 097601.
(19) Guan, S.; Liu, C.; Lu, Y.; Yao, Y.; Yang, S. A. *Phys. Rev. B* **2018**, *97*, 144104.
(20) Liu, F.; You, L.; Seyler, K. L.; Li, X.; Yu, P.; Lin, J.; Wang, X.; Zhou, J.; Wang, H.; He, H.; Pantelides, S. T.; Zhou, W.; Sharma, P.; Xu, X.; Ajayan, P. M.; Wang J.; Liu Z. *Nat. Commun.* **2016**, *7*, 12357.
(21) Chang, K.; Liu, J.; Lin, H.; Wang, N.; Zhao, K.; Zhang, A.; Jin, F.; Zhong, Y.; Hu, X.; Duan, W.; Zhang, Q.; Fu, L.; Xue, Q. -K.; Chen, X.; Ji, S. -H. *Science* **2016**, *353*, 274.
(22) Xiao, J.; Zhu, H.; Wang, Y.; Feng, W.; Hu, Y.; Dasgupta, A.; Han, Y.; Wang, Y.; Muller, D. A.; Martin, L. W.; Hu, P.; Zhang, X. *Phys. Rev. Lett.* **2018**, *120*, 227601.
(23) Zhou, Y.; Wu, D.; Zhu, Y.; Cho, Y.; He, Q.; Yang, X.; Herrera, K.; Chu, Z.; Han, Y.; Downer, M. C.; Peng, H.; Lai, K. *Nano Lett.* **2017**, *17*, 5508–5513.
(24) Cui, C.; Hu, W. -J.; Yan, X.; Addiego, C.; Gao, W.; Wang, Y.; Wang, Z.; Li, L.; Cheng, Y.; Li, P.; Zhang, X.; Alshareef, H. N.; Wu, T.; Zhu, W.; Pan, X.; Li, L. -J. *Nano Lett.* **2018**, *18*, 1253–1258.
(25) Zheng, C.; Yu, L.; Zhu, L.; Collins, J. L.; Kim, D.; Lou, Y.; Xu, C.; Li, M.; Wei, Z.; Zhang, Y.; Edmonds, M. T.; Li, S.; Seidel, J.; Zhu, Y.; Liu, J. Z.; Tang, W. -X.; Fuhrer, M. S. *Sci. Adv.* **2018**, *4*, 7720.
(26) Yuan, S.; Luo, X.; Chan, H. L.; Xiao, C.; Dai, Y.; Xie, M.; Hao, J. *Nat. Commun.* **2019**, *10*, 1775.
(27) Anasori, B.; Lukatskaya, M. R.; Gogotsi, Y. *Nat. Rev. Mater.* **2017**, *2*, 16098.

(28) Chhowalla, M.; Shin, H. S.; Eda, G.; Li, L. -J.; Loh, K. P.; Zhang, H. *Nat. Chem.* **2013**, *5*, 263–275.
(29) Nicolosi, V.; Chhowalla, M.; Kanatzidis, M. G.; Strano, M. S.; Coleman, J. N. *Science* **2013**, *340*, 1226419.
(30) Mannix, A. J.; Kiraly, B.; Hersam, M. C.; Guisinger, N. P. *Nat. Rev. Chem.* **2017**, *1*, 0014.
(31) Tan, C.; Cao, X.; Wu, X. -J.; He, Q.; Yang, J.; Zhang, X.; Chen, J.; Zhao, W.; Han, S.; Nam, G. -H.; Sindoro, M.; Zhang, H. *Chem. Rev.* **2017**, *117*, 6225–6331.
(32) Geim, A. K.; Grigorieva, I. V. *Nature* **2013**, *499*, 419–425.
(33) Novoselov, K. S.; Mishchenko, A.; Carvalho, A.; Castro Neto, A. H. *Science* **2016**, *353*, aac9439.
(34) Chatterjee, A.; Biswas, K. *Angew. Chemie Int. Ed.* **2015**, *54*, 5623–5627.
(35) Banik, A.; Biswas, K. *Angew. Chemie* **2017**, *129*, 14753–14758.
(36) Wu, J.; Yuan, H.; Meng, M.; Chen, C.; Sun, Y.; Chen, Z.; Dang, W.; Tan, C.; Liu, Y.; Yin, J.; Zhou, Y.; Huang, S.; Xu, H. Q.; Cui, Y.; Hwang, H. Y.; Liu, Z.; Chen, Y.; Yan, B.; Peng H. *Nat. Nanotechnol.* **2017**, *12*, 530–534.
(37) Wu, J.; Tan, C.; Tan, Z.; Liu, Y.; Yin, J.; Dang, W.; Wang, M.; Peng, H. *Nano Lett.* **2017**, *17*, 3021–3026.
(38) Li, J.; Wang, Z.; Wen, Y.; Chu, J.; Yin, L.; Cheng, R.; Lei, L.; He, P.; Jiang, C.; Feng, L.; He, J. *Adv. Funct. Mater.* **2018**, *28*, 1706437.
(39) Yin, J.; Tan, Z.; Hong, H.; Wu, J.; Yuan, H.; Liu, Y.; Chen, C.; Tan, C.; Yao, F.; Li, T.; Chen, Y.; Liu, Z.; Liu, K.; Peng, H. *Nat. Commun.* **2018**, *9*, 3311.
(40) Tian, X.; Luo, H.; Wei, R.; Zhu, C.; Guo, Q.; Yang, D.; Wang, F.; Li, J.; Qiu, J. *Adv. Mater.* **2018**, *30*, 1801021.
(41) Fu, Q.; Zhu, C.; Zhao, X.; Wang, X.; Chaturvedi, A.; Zhu, C.; Wang, X.; Zeng, Q.; Zhou, J.; Liu, F.; Tay, B. K.; Zhang, H.; Pennycook, S. J.; Liu, Z. *Adv. Mater.* **2019**, *31*, 1804945.
(42) Wu, J.; Liu, Y.; Tan, Z.; Tan, C.; Yin, J.; Li, T.; Tu, T.; Peng, H. *Adv. Mater.* **2017**, *29*, 1704060.
(43) Wu, M.; Zeng, X. C. *Nano Lett.* **2017**, *17*, 6309–6314.
(44) Chen, C.; Wang, M.; Wu, J.; Fu, H.; Yang, H.; Tian, Z.; Tu, T.; Peng, H.; Sun, Y.; Xu, X.; Jiang, J.; Schröter, N. B. M.; Li, Y.; Pei, D.; Liu, S.; Ekahana, S. A.; Yuan, H.; Xue, J.; Li, G.; Jia, J.; Liu, Z.; Yan, B.; Peng, H.; Chen, Y. *Sci. Adv.* **2018**, *4*, eaat8355.
(45) Zubko, P.; Gariglio, S.; Gabay, M.; Ghosez, P.; Triscone, J.-M. *Annu. Rev. Condens. Matter Phys.* **2011**, *2*, 141–165.
(46) Jesse, S.; Baddorf, A. P.; Kalinin, S. V. *Appl. Phys. Lett.* **2006,** *88*, 062908.
(47) Jesse, S.; Mirman, B.; Kalinin, S. V. *Appl. Phys. Lett.* **2006**, *89*, 022906.
(48) Perdew, J. P.; Burke, K.; Ernzerhof, M. *Phys. Rev. Lett.* **1996**, *77*, 3865–3868.
(49) Kresse, G.; Furthmüller, J. *Phys. Rev. B* **1996**, *54*, 11169–11186.
(50) Kresse, G.; Joubert, D. *Phys. Rev. B* **1999**, *59*, 1758–1775.
(51) Heyd, J.; Scuseria, G. E.; Ernzerhof, M. *J. Chem. Phys.* **2003**, *118*, 8207–8215.
(52) Ruleova, P.; Drasar, C.; Lostak, P.; Li, C. -P.; Ballikaya, S.; Uher, C. *Mater. Chem. Phys.* **2010**, *119*, 299–302.
(53) Tan, C.; Tang, M.; Wu, J.; Liu, Y.; Li, T.; Liang, Y.; Deng, B.; Tan, Z.; Tu, T.; Zhang, Y.; Liu, C.; Chen, J. -H.; Wang, Y.; Peng, H. *Nano Lett.* **2019**, *19*, 2148-2153.

(54) Schlom, D. G.; Chen, L. -Q.; Eom, C. -B.; Rabe, K. M.; Streiffer, S. K.; Triscone, J. -M. *Annu. Rev. Mater. Res.* **2007**, *37*, 589–626.

(55) Cheng, T.; Tan, C.; Zhang, S.; Tu, T.; Peng, H.; Liu, Z. *J. Phys. Chem. C* **2018**, *122*, 19970-19980.

(56) Pereira, A. L. J.; Santamaría-Pérez, D.; Ruiz-Fuertes, J.; Manjón, F. J.; Cuenca-Gotor, V. P.; Vilaplana, R.; Gomis, O.; Popescu, C.; Muñoz, A. Rodríguez-Hernández, P.; Segura, A.; Gracia, L. Beltrán, A.; Ruleova, P. Drasar, C.; Sans, J. *J. Phys. Chem. C* **2018**, *122*, 8853-8867.

(57) Xu, Y. -D.; Wang, C.; Lv, Y. -Y.; Chen, Y. B.; Yao, S. -H.; Zhou, J. *RSC Adv.* **2019**, *9*, 18042-18049.

Chapter 2

Transport Properties of Ultrathin Few Layer Oxy-chalcogenide BiCuSeO Nanosheets

Chapter 2

Transport Properties of Ultrathin Few Layer Oxychalcogenide BiCuSeO Nanosheets†

Summary

Layered materials with intrinsically low thermal conductivity are promising candidates for thermoelectric waste heat to electrical energy conversion. Recently, bulk form BiCuSeO, a layered oxychalcogenide, has drawn attention for thermoelectric applications. However, synthesis of two dimensional nanosheets of BiCuSeO and study of its thermoelectric properties have not been explored yet. Here, we present a facile surfactant free low temperature solvothermal synthesis of few layered ultrathin BiCuSeO nanosheets for the first time. Nanosheets of BiCuSeO exhibit a semiconducting band gap of 0.9 eV and p-type conduction. A dense hot pressed pellet of BiCuSeO nanosheets exhibits a superior power factor and lower lattice thermal conductivity compared to that of the bulk sample in the temperature range of 300–723 K temperature.

---

†*A Paper based on this study has been published in Inorg. Chem. Front.* **2017,** *4*, 84-90.

2.1 Introduction

Narrow band gap semiconducting inorganic solids with layered structure have been established as potential candidates for thermal management and thermoelectric power generation due to presence of favorable electrical and phonon transport properties.[1–4] Layered materials, such as Bi_2Te_3, Sb_2Te_3 and SnSe, have truly revolutionized the thermoelectric research.[5–11] Strong in-plane and weak out-of-plane bonding in layered materials cause bonding heterogeneity, and the consequent lattice anharmonicity brings down the lattice thermal conductivity (κ_{lat}). Further, the presence of atomically thin layers with weak interlayer interactions results in many low-dimensional features in electronic transport, such as the quantum confinement of free charge carriers leading to enhanced Seebeck coefficient (S).[1–4]

Layered quaternary metal oxychalcogenides, MCuXO (M= La, Ce, Nd, Pr, Bi, and In; X= Te, Se and S) have been found to be important materials for thermoelectrics, superconductivity and interesting electronic transport.[12,13] The presence of covalent metal-chalcogen and ionic metal-oxygen units in the layered structure leads to an unique structural chemistry and exciting properties. Preferential bonding of chalocogen and oxygen with one of the particular types of cations results in low dimensional structures in MCuXO, which leads to anisotropic electronic structures and properties.

BiCuSeO is an interesting material from the oxychalcogenide family which recently gained attention for thermoelectric applications due to its low thermal conductivity.[14] BiCuSeO is a multiband semiconductor and crystallizes in a ZrCuSiAs type layered structure with tetragonal unit cell (space group *P4/nmm*).[12–17] The crystal structure of BiCuSeO is consists of insulating $(Bi_2O_2)^{2+}$ and conductive $(Cu_2Se_2)^{2-}$ layers, which are stacked along crystallographic c axis of tetragonal cell (Figure 2.1a). The $(Bi_2O_2)^{2+}$ layers consist of distorted Bi_4O tetrahedra (fluorite type structure), whereas $(Cu_2Se_2)^{2-}$ layers consist of distorted $CuSe_4$ tetrahedra (anti fluorite type structure).[14,15] The phonon-phonon umklapp processes originates from the scattering of phonons from the interface due to layer structure, soft bonding and lattice anharmonicity results in low thermal conductivity (κ) in BiCuSeO.[14] The thermoelectric properties of bulk BiCuSeO have been improved by carrier engineering strategy using metal ions (e.g. Mg^{2+}, Ca^{2+}, Sr^{2+}, Pb^{+2} and Ba^{2+}) doping or introducing single and dual vacancies.[15,16,18–23]

Bottom-up wet chemical synthesis of inorganic solids in the form 2D nanosheets/nanoplates is an effective strategy for tuning the thermoelectric properties of bulk layered materials.[24–26] The ultrathin 2D form of layered materials can lead to quantum confinement of carriers, which can cause enhancement in Seebeck coefficient. Effective phonon scattering from the interfaces of nanosheets may results in reduction of lattice thermal conductivity. The free standing single layered Bi_2Se_3 showed excellent thermoelectric properties compared to that of the bulk counterpart due to improved electronic transport and reduced thermal conductivity.[25–28] Kinetically synthesized few layered nanosheets of intergrowth $(MX)_m(E_2X_3)_n$ [where M = Pb,Sn; E = Bi; X= Te, Se] homologous compounds exhibit ultra-low thermal conductivity due to phonon scattering by heterostructure interface.[29–31] Recently, ultrathin nanosheets of SnSe and $SnSe_2$ were synthesized by soft chemical synthesis, which show high power factor and low thermal conductivity.[32,33] These motivated us to synthesize and study the thermoelectric properties of pristine BiCuSeO nanosheets.

Herein, we demonstrate a surfactant free soft chemical synthesis of ultrathin (~ 4 - 5 layers and 3 – 4 nm thick) BiCuSeO nanosheets for the first time. Large scale few layered BiCuSeO nanosheets were synthesised by the reaction of $Bi(NO_3)_2.5H_2O$, $Cu(NO_3)_2.3H_2O$ and selenourea in presence of KOH/NaOH in solvothermal condition. The transmission electron microscopy (TEM) and atomic force microscopy (AFM) characterizations indicate the 2D nanosheet morphology of the sample. Room temperature optical absorption study indicates that as-synthesized BiCuSeO nanosheets exhibits a band gap of ~ 0.9 eV. Significantly low lattice thermal conductivity in the range of 0.55-0.4 $Wm^{-1}K^{-1}$ was measured in hot pressed dense pellet of BiCuSeO nanosheets in 300-700 K range, which is lower than that of the bulk BiCuSeO. Extensive phonon scattering from the interfaces of layers, bond anharmonicity and nanoscale grain boundaries resulted in low thermal conductivity in BiCuSeO nanosheets. Undoped BiCuSeO nanosheets exhibit *p*-type conduction (carrier concentration ~3.8×10^{18} cm^{-3}) and higher average power factor value than that of the bulk sample.

2.2 Methods

2.2.1 Reagents. Bismuth nitrate – $Bi(NO_3)_3.5H_2O$ (Alfa Aesar, 99.9%), selenourea – $SeC(NH_2)_2$ (Alfa Aesar , 99%), copper nitrate - $Cu(NO_3)_2.3H_2O$ (Alfa Aesar, 99%), potassium hydroxide - KOH, sodium hydroxide - NaOH and ethanol were used without further purification.

2.2.2 Synthesis of BiCuSeO nanosheets. In order to synthesize BiCuSeO nanosheets, 100 mg of $Bi(NO_3)_3.5H_2O$ (0.206 mmol) is dissolved in a mixture of 5 ml water and 5 ml ethanol upon stirring, which resulted in a milky white solution. To the resulting solution, 25.4 mg of selenourea (0.206 mmol) is added with stirring, which produced an orange colour. Finally, 120 mg of KOH, 320 mg of NaOH and 49.8 mg $Cu(NO_3)_2.3H_2O$ (0.206 mmol) are subsequently added with continuous stirring. The resulting black solution is then transferred into a 50 ml Teflon lined stainless steel autoclave and kept in hot air oven at 180°C for 1 day. Obtained as synthesized black coloured product is then washed with distilled water and ethanol for 3 times and purified product is dried in ambient condition. The time dependent study of the reaction indicates that 24 hrs is the optimum time required for the formation of pure BiCuSeO nanosheets.

2.2.3 Power X-ray diffraction. Room temperature powder X-Ray diffraction of all the samples was carried out in Rigaku diffractometer using Cu- Kα radiation (λ = 2.54187 Å). Data were collected in the 2θ range of 20º to 80º by with a step of 1º per minute.

2.2.4 Band gap measurement. In order to probe the optical band gap of the powder sample, diffuse reflectance spectroscopy was carried using a Perkin Elmer Lambda 900, UV/VIS/NIR spectrometer in reflectance mode. Absorption (α/Λ) data were estimated from reflectance data using Kubelka-Munk equation: $\alpha/\Lambda = (1-R)^2/2R$, where R is reflectance. α and Λ are the absorption and scattering co-efficient respectively. The energy band gap was obtained from α/Λ (a.u.) *vs*. E_g (eV) plot.

2.2.5 Field effect scanning electron microscopy (FESEM). For FESEM imaging, a NOVA NANO SEM 600 (FEI, Germany) instrument, operated at 15 kV, was used and Energy dispersive spectroscopy (EDAX) analysis was performed with an EDAX Genesis instrument attached to the FESEM column. A drop of BiCuSeO nanosheets dispersed in toluene were taken in a silicon substrate and dried for FESEM imaging.

2.2.6 Transmission electron microscopy (TEM). The TEM experiment was performed using a JEOL (JEM3010) TEM operating at 300 kV accelerating voltage fitted with a Gatan CCD camera. Along with that, additional TEM images were taken using a FEI TECNAI G2 20 STWIN TEM operating at 200 kV and elemental mapping was performed in STEM imaging mode. For sample preparation for TEM imaging, one drop of BiCuSeO nanosheets dispersed in toluene was drop casted in a holey carbon coated Cu grid.

2.2.7 X-ray photoelectron spectroscopy (XPS). An Omicron Nanotechnology spectrometer with an Mg-Ka (1253.6 eV) X-ray source was used for XPS measurement.

2.2.8 Atomic force microscopy (AFM). AFM was performed on a Bruker Innova Microscope in tapping mode using an antimony doped silicon tip.

2.2.9 Thermoelectric properties measurement. In order to measure thermoelectric properties of BiCuSeO nanosheets, BiCuSeO nanosheets were hot pressed at 723 K in vacuum (10^{-3} Torr) in a graphite die with a pressure of 40 MPa for 30 min. The density of the hot pressed sample was ~8.2 g cm^{-3}, which is ~92% of the theoretical density (ρ = 8.9 g cm−3).[20] Electrical conductivity (σ) and Seebeck coefficients (S) of the hot-pressed sample of the dimension, 2 mm ×3 mm ×8 mm, were measured using ULVAC-RIKO ZEM-3 instrument under helium gas from room temperature to ~723 K.

Thermal diffusivity, D, of the hot pressed sample of dimension of 10 mm diameter and 2 mm thickness was measured in the range of 300 – 723 K by using laser flash diffusivity method in a Netzsch LFA-457 instrument. Temperature dependent heat capacity, C_p, was obtained using standard sample (pyroceram) in LFA-457, which is slightly higher than the Dulong–Petit C_p value of BiCuSeO. The total thermal conductivity, κ, was calculated using the equation, $\kappa = DC_p\rho$, where ρ is the density of the sample. Electrical and thermal transport were measured in similar direction of the pellet.

2.2.10 Hall measurement. Carrier concentration of hot pressed sample of BiCuSeO nanosheets was obtained by measuring Hall coefficient of the sample at room temperature using four-contact Hall-bar geometry by Excel instrument Hall measurement system. A variable magnetic field of in the range of 0.1 to 0.57 Tesla and a current of ~ 100 mA were applied during the measurements. At 300 K, the carrier concentration, p, of the sample was

calculated from the formula: $p = 1/e\ R_H$, where e is the electronic charge and R_H is hall coefficient.

2.3 Results & discussion

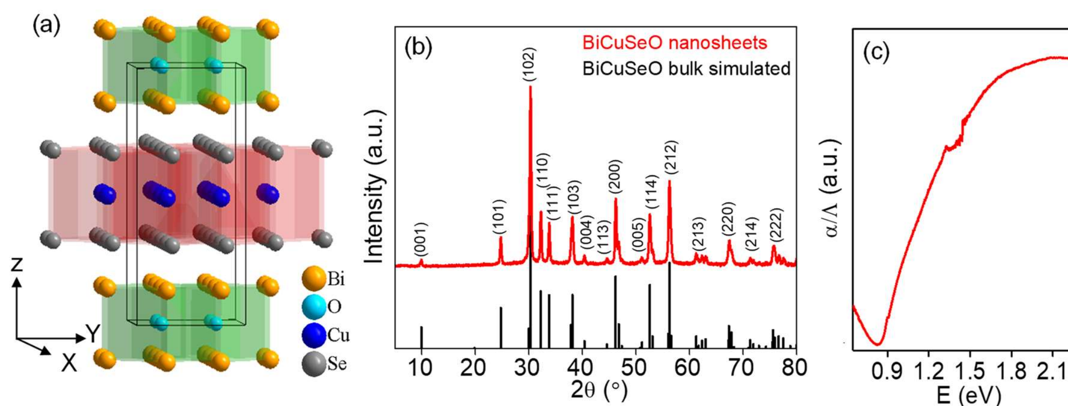

Figure 2.1. *(a) Crystal structure of BiCuSeO representing layered structure. (b) Powder XRD patterns of as synthesized BiCuSeO nanosheets. (c) Optical absorption spectra of as synthesized BiCuSeO nanosheets.*

Ultrathin ~ 4-5 layers thick BiCuSeO nanosheets were synthesized using easily available precursors: $Bi(NO_3)_3.5H_2O$, $Cu(NO_3)_2.3H_2O$, selenourea and green solvents: water and ethanol in presence of KOH/NaOH in solvothermal condition. KOH and NaOH were used as mineralizer agent[17] in order to increase the solubility of the reactant species. In the synthesis procedure, no surfactant was used as we were rather interested to measure the transport properties of the end product. Powder X-ray diffraction patterns (PXRD) of as synthesized BiCuSeO nanosheets could be indexed based on pure tetragonal BiCuSeO with *P4/nmm* space group, with no other impurity phase being observed within the detection limits of PXRD (Figure 2.1b). Optical absorption spectra of BiCuSeO nanosheets shows a well-defined band gap of ~ 0.9 eV (Figure 2.1c)., which is higher compare to bulk BiCuSeO (~0.8 eV).[14]

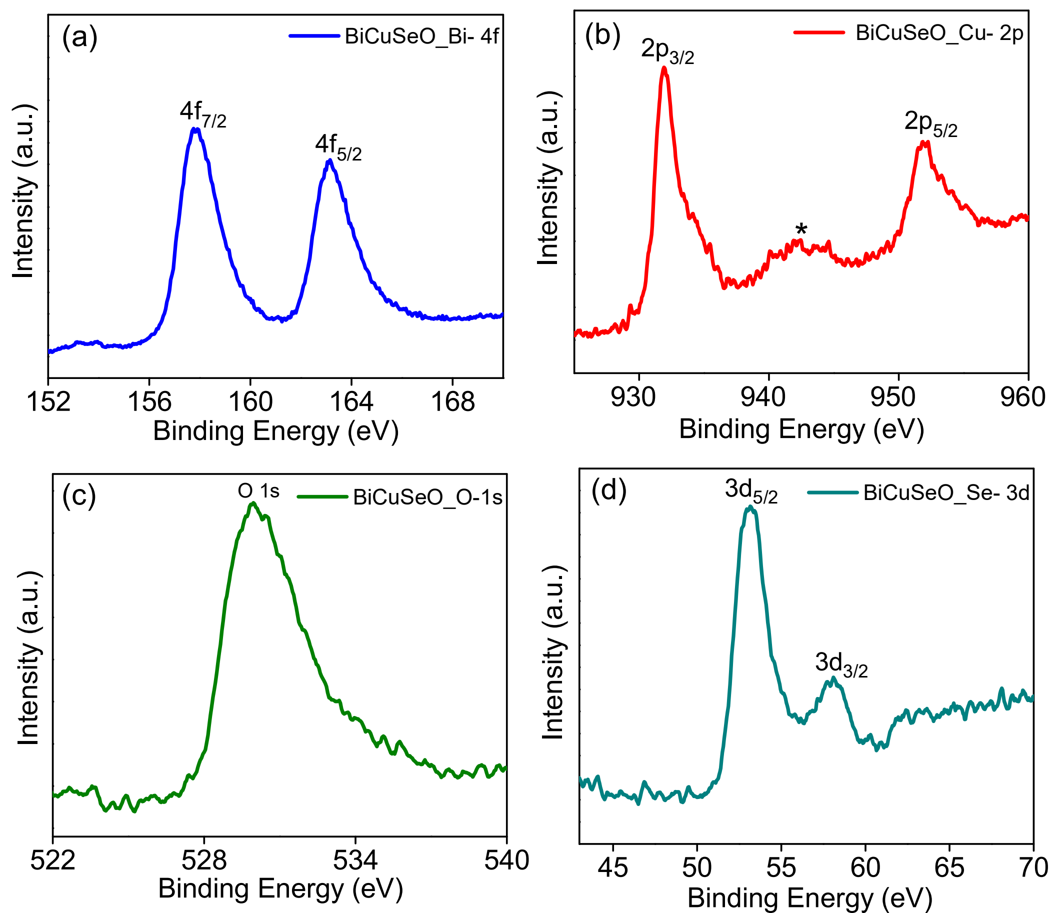

Figure 2.2. *X-ray photoelectron spectra of BiCuSeO nanosheets showing the (a) Bi 4f, (b) Cu 2p, (c) O 1s and (d) Se 3d peaks. An additional peak (* marked) in Cu 2p XPS spectra is attributed to the presence of small amount of Cu(II) at the surface.*

In order to confirm the presence of Bi, Cu, Se and O elements and their oxidation states, XPS of as synthesized BiCuSeO nanosheets was performed (Figure 2.2). Two strong peaks at 157.8 eV and 163.2 eV with a peak splitting of 5.4 eV can be best assigned to Bi $4f_{7/2}$ and Bi $4f_{5/2}$ respectively, which is in good agreement with the value of Bi(III). The doublet peaks at 932 eV and 952 eV correspond to Cu(I) $2p_{3/2}$ and $2p_{1/2}$, respectively. An additional small intensity peak located at 942.4 eV is due to presence of minor amount of Cu(II).The reason of presence of minor amount of Cu(II) is because of surface oxidation of Cu(I) to more stable Cu(II).[34] The peak at 529.9 eV arises due to O 1s. Peaks due to Se $3d_{5/2}$ and $3d_{3/2}$ are observed at 53.1 eV and 58.1 eV respectively.

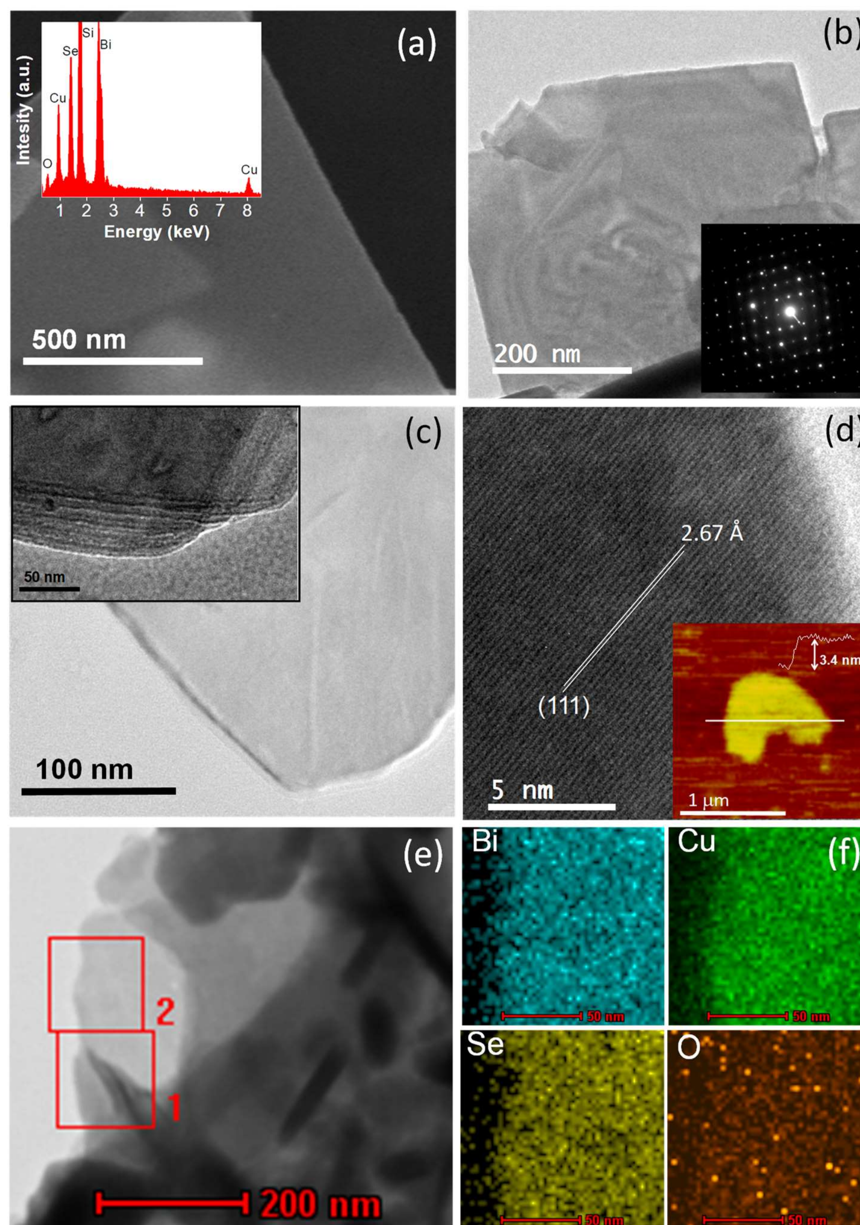

Figure 2.3. *(a) FESEM image of BiCuSeO nanosheets. The inset of (a) shows EDAX of BiCuSeO nanosheets. b) TEM image of BiCuSeO nanosheets. Inset of (b) shows SAED pattern of a single nanosheet. (c) Another TEM image of BiCuSeO nanosheets. Inset of (c) shows bent edges of several BiCuSeO nanosheets which are stacked one over another. (d) HRTEM image BiCuSeO nanosheets showing crystalline nature and spacing between (111) planes. Inset of (d) represents AFM image of BiCuSeO nanosheets and the height profile showing a thickness of ~3.4 nm. (e) STEM image of BiCuSeO nanosheets. (f) EDAX color mapping for Bi, Cu, Se and O in the BiCuSeO nanosheets during STEM imaging (from the highlighted portion, numbered as 2 in the STEM image).*

FESEM, TEM and AFM microscopy studies have been performed to understand the nanoscale morphology and the structure of the synthesized BiCuSeO sample. FESEM image reveals the 2D nanosheets morphology of the sample (Figure 2.3a). EDAX analysis of BiCuSeO sample indicates the presence of Bi, Cu, Se and O (inset of Figure 2.3a). Weight percentage (Wt%) and atomic percentage (At%) of all the elements present in BiCuSeO, calculated from EDAX analysis, are given in Table 2.1. TEM micrograph further confirms the thin nanosheet morphology of synthesised BiCuSeO (Figure 2.3b-c). The lateral dimensions of the nanosheets is ranging from 0.5 to 1 μm. The selected-area electron diffraction (SAED) pattern taken from a single sheet region depicts single crystalline nature of BiCuSeO nanosheets (inset of Figure 2.3b). The inset of Figure 2.3c shows TEM image of bent edges of BiCuSeO, which indicate stacking of few nanosheets one over another. High resolution TEM (HRTEM) image (Figure 2.3d) of the BiCuSeO nanosheets shows a clear lattice spacing of 2.67 Å, which corresponds to the (111) interplanar distance of tetragonal BiCuSeO. The ultra-thin nature of the nanosheets was further confirmed by AFM (inset of Figure 2.3d). The height profile obtained from a typical AFM micrograph indicate a thickness ~ 3.4 nm corresponds to 4 - layers of BiCuSeO with a lateral dimension of ~ 1 μm. Figure 2.3e shows the scanning transmission electron microscopy (STEM) image of BiCuSeO nanosheet. Additionally, EDAX elemental mapping analysis on selected area of BiCuSeO nanosheet (Figure 2.3e), which is presented in Figure 2.3f, point out the homogeneous distribution of all the elements in BiCuSeO nanosheets.

Table 2.1. *Wt% and At% of all the elements present in BiCuSeO obtained by EDAX analysis (Figure 2.3a).*

Element	Weight %	Atomic %
O K	4.23	23.16
Se L	26.75	29.65
Bi M	49.96	20.93
Cu K	19.06	26.26
Total	100	100

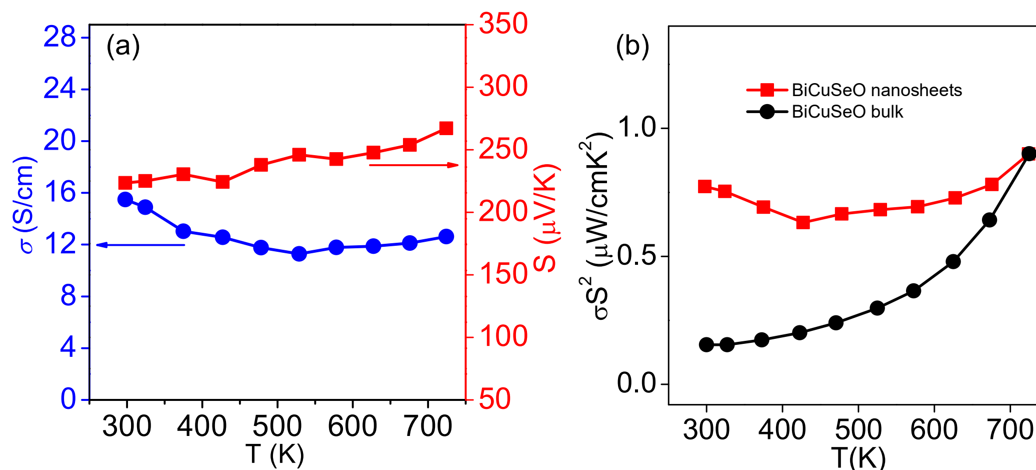

Figure 2.4. *(a) Temperature dependent Seebeck coefficient (S) and electrical conductivity (σ) of BiCuSeO nanosheets. (b Temperature dependent power factor (σS^2) of BiCuSeO nanosheets and bulk BiCuSeO.*[14]

Layered structure and low thermal conductivity of bulk BiCuSeO motivate us to measure the thermoelectric properties of BiCuSeO nanosheets. In order to measure thermoelectric properties, pellets of BiCuSeO nanosheets was made by hot pressing of as synthesized nanosheet powder sample. Figure 2.4 represents temperature dependent electronic transport properties of BiCuSeO nanosheets. Temperature dependent electrical conductivity (σ) and Seebeck coefficient (*S*) of BiCuSeO nanosheets are shown in Figure 2.4a. BiCuSeO nanosheets show superior σ value throughout the measured temperature range than that of bulk sample.[14] We have measured the *p*-type carrier in BiCuSeO to be ~3.8 × 10^{18} cm^{-3} at room temperature, which is higher than that of the bulk BiCuSeO.[14] We have estimated the carrier mobility (μ) in BiCuSeO nanosheets using the formula $\sigma = ne\mu$, where e is the electronic charge and n is the carrier concentrtaion. The estimated carrier mobility value is ~25 $cm^2V^{-1}s^{-1}$, which is slightly higher than that of the bulk pristine BiCuSeO (22 $cm^2V^{-1}s^{-1}$).[14] This attributes to the increase in electrical conductivity in nanosheet sample compared to that of bulk.[14] At room temperature, a σ value of ~ 15 S/cm was measured for BiCuSeO nanosheets, which remain almost flat and shows a value of ~ 13 S/cm at 722 K. The positive value of *S* depicts *p*-type conduction in BiCuSeO nanosheets. An *S* value of ~ 223 μV/K was measured at room temperature which increases to ~ 267 μV/K at 722 K (Figure 2.4a). Although, *S* value for nanosheets is lower than that of the bulk sample (due to increase in carrier concentration in nanosheet sample), large

increase in σ value resulted in significant improvement of the average power factor (σS^2) in nanosheet sample compared to bulk counterpart (Figure 2.4b).[14]

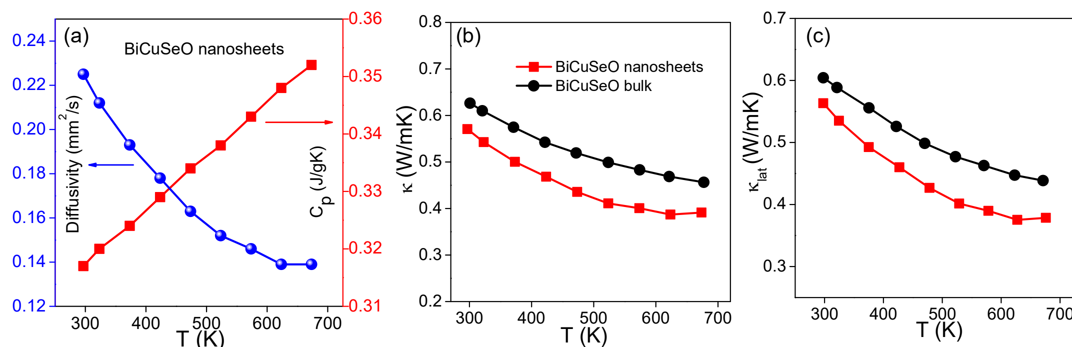

Figure 2.5. *(a) Temperature dependent thermal diffusivity (D) and heat capacity (C_p) of BiCuSeO nanosheets. Temperature dependent (b) total thermal conductivity (κ) and (c) lattice thermal conductivity (κ_{lat}) of BiCuSeO nanosheets and bulk BiCuSeO.*[14]

The total thermal conductivity (*κ*) of nanosheet BiCuSeO sample in the range of 300 – 700 K along with κ of the previously reported bulk sample[14] are presented in Figure 2.5b, whereas thermal diffusivity (*D*) and C_p values of BiCuSeO nanosheets are presented in Figure 2.5a. We found BiCuSeO nanosheets exhibit lower κ value throughout the measured temperature range compared to bulk counterpart. A *κ* value of ~ 0.56 W/mK was measured at room temperature, which further decreases to 0.4 W/mK at 675 K. The large decrease in temperature dependent *κ* compared to bulk sample is attributed due to significant reduction of the lattice thermal conductivity (κ_{lat}) in BiCuSeO nanosheets (Figure 2.5c). The κ_{lat} of BiCuSeO nanosheets are obtained by subtracting electrical thermal conductivity (κ_{el}) from total thermal conductivity (*κ*), whereas κ_{el} is calculated using the Wiedemann-Franz law, $\kappa_{el} = \sigma LT$, where L is the Lorenz number. L is derived by fitting of the respective Seebeck coefficients which estimate the reduced chemical potential assuming a single parabolic band which is described elsewhere.[35] Such low κ_{lat} in nanosheet sample originates due to phonon scattering by nano/meso scale interfaces and grains in hot pressed samples in addition to the interfaces of layers and bond anharmonicity in bulk BiCuSeO. A thermoelectric figure of merit (zT) value estimated to be 0.2 at 722 K for BiCuSeO nanosheet, which is higher than that of bulk sample[14] at that temperature.

2.4 Conclusions

In conclusion, we have synthesized few layered ultrathin (3 - 4 nm thick and ~1 μm long) nanosheets of BiCuSeO for the first time using a simple, high yield and surfactant free soft chemical method. BiCuSeO nanosheets exhibits an optical band gap ~0.9 eV and *p*-type conduction. Nanosheet sample exhibits superior electronic transport and low lattice thermal conductivity compared to that of the bulk sample in the measured temperature range. BiCuSeO nanosheet shows higher average σS^2 in the 300-723 K range than that of the bulk sample due to higher electronic conductivity compared to bulk BiCuSeO. Furthermore, low lattice thermal conductivity in BiCuSeO nanosheets originates form extensive phonon scattering from the nano/meso scale interfaces and grain boundaries in addition to interfaces of layers and bond anharmonicity of bulk BiCuSeO. Thus, pristine nanosheets of BiCuSeO extend a promise for its potential application in thermoelectric energy harvesting. We would like to note that the nanosheets sample used in the present study is not doped and hence the performance of nanosheets could be further improved by aliovalent chemical doping in future.

2.5 References

(1) Mao, J.; Liu, Z.; Ren, Z. *npj Quantum Mater.* **2016**, *1*, 16028.
(2) Zhou, Y.; Zhao, L. D. *Adv. Mater.* **2017**, *29*, 1702676.
(3) Wu, J.; Chen, Y.; Wu, J.; Hippalgaonkar, K. *Adv. Electron. Mater.***2018**, *4*, 1800248.
(4) Dresselhaus, M. S.; Chen, G.; Tang, M. Y.; Yang, R.; Lee, H.; Wang, D.; Ren, Z.; Fleurial, J. P.; Gogna, P. *Adv. Mater.* **2007**, *19*, 1043–1053.
(5) Poudel, B.; Hao, Q.; Ma, Y.; Lan, Y.; Minnich, A.; Yu, B.; Yan, X.; Wang, D.; Muto, A.; Vashaee, D.; Chen, X.; Liu, J.; Dresselaus; Chen, G.; Ren, Z. *Science* **2008**, *320*, 634–638.
(6) Kim, S. Il; Lee, K. H.; Mun, H. A.; Kim, H. S.; Hwang, S. W.; Roh, J. W.; Yang, D. J.; Shin, W. H.; Li, X. S.; Lee, Y. H.; Snyder, G. J.; Kim, S. W. *Science* **2015**, *348*, 109–114.
(7) Heremans, J. P.; Cava, R. J.; Samarth, N. *Nat. Rev. Mater.* **2017**, *2*, 17049.
(8) Roychowdhury, S.; Samanta, M.; Banik, A.; Biswas, K. *J. Solid State Chem.* **2019**, *275*, 103–123.
(9) Zhao, L.-D.; Chang, C.; Tan, G.; Kanatzidis, M. G. *Energy Environ. Sci.* **2016**, *9*, 3044–3060.
(10) Lee, Y. K.; Luo, Z.; Cho, S. P.; Kanatzidis, M. G.; Chung, I. *Joule* **2019**, *3*, 719–731.
(11) Chang, C.; Wu, M.; He, D.; Pei, Y.; Wu, C. F.; Wu, X.; Yu, H.; Zhu, F.; Wang, K.; Chen, Y.; Huang, L.; Li, J. F.; He, J.; Zhao, L. D. *Science* **2018**, *360*, 778–783.

(12) Luu, S. D. N.; Vaqueiro, P. *J. Materiomics* **2016**, *2*, 131–140.
(13) Kusainova, A. M.; Berdonosov, P. S.; Akselrud, L. G.; Kholodkovskaya, L. N.; Dolgikh, V. A.; Popovkin, B. A. *J. Solid State Chem.* **1994**, *112*, 189–191.
(14) Zhao, L.-D.; He, J.; Berardan, D.; Lin, Y.; Li, J.-F.; Nan, C.; Dragoe, N. *Energy Environ. Sci.* **2014**, *7*, 2900–2924.
(15) Liu, Y.; Zhao, L.-D.; Liu, Y.; Lan, J.; Xu, W.; Li, F.; Zhang, B.-P.; Berardan, D.; Dragoe, N.; Lin, Y.-H.; Nan, C.-W.; Li, J.-F.; Zhu, H. *J. Am. Chem. Soc.* **2011**, *133*, 20112–20115.
(16) Li, Z.; Xiao, C.; Fan, S.; Deng, Y.; Zhang, W.; Ye, B.; Xie, Y. *J. Am. Chem. Soc.* **2015**, *137*, 6587–6593.
(17) Stampler, E. S.; Sheets, W. C.; Bertoni, M. I.; Prellier, W.; Mason, T. O.; Poeppelmeier, K. R. *Inorg. Chem.* **2008**, *47*, 10009–10016.
(18) Li, J.; Sui, J.; Barreteau, C.; Berardan, D.; Dragoe, N.; Cai, W.; Pei, Y.; Zhao, L. *J. Alloys Compd.* **2013**, *551*, 649–653.
(19) Pei, Y.-L.; He, J.; Li, J.-F.; Li, F.; Liu, Q.; Pan, W.; Barreteau, C.; Berardan, D.; Dragoe, N.; Zhao, *NPG Asia Mater.* **2013**, *5*, e47.
(20) Barreteau, C.; Beardan, D.; Amzallag, E.; Zhao, L.; Dragoe, N. *Chem. Mater.* **2012**, *24*, 3168–3178.
(21) Lan, J.-L.; Liu, Y.-C.; Zhan, B.; Lin, Y.-H.; Zhang, B.; Yuan, X.; Zhang, W.; Xu, W.; Nan, C.-W. *Adv. Mater.* **2013**, *25*, 5086–5090.
(22) Yang, D.; Su, X.; Yan, Y.; Hu, T.; Xie, H.; He, J.; Uher, C.; Kanatzidis, M. G.; Tang, X. *Chem. Mater.* **2016**, *28*, 4628–4640.
(23) Li, J.; Sui, J.; Pei, Y.; Barreteau, C.; Berardan, D.; Dragoe, N.; Cai, W.; He, J.; Zhao, L.-D. *Energy Environ. Sci.* **2012**, *5*, 8543.
(24) Mehta, R. J.; Zhang, Y.; Karthik, C.; Singh, B.; Siegel, R. W.; Borca-Tasciuc, T.; Ramanath, G. *Nat. Mater.* **2012**, *11*, 233–240.
(25) Son, J. S.; Choi, M. K.; Han, M.-K.; Park, K.; Kim, J.-Y.; Lim, S. J.; Oh, M.; Kuk, Y.; Park, C.; Kim, S.-J.; Hyeon, T. *Nano Lett.* **2012**, *12*, 640–647.
(26) Sun, Y.; Cheng, H.; Gao, S.; Liu, Q.; Sun, Z.; Xiao, C.; Wu, C.; Wei, S.; Xie, Y. *J. Am. Chem. Soc.* **2012**, *134*, 20294–20297.
(27) Jana, M. K.; Biswas, K.; Rao, C. N. R. *Chem. - A Eur. J.* **2013**, *19*, 9110–9113.
(28) Zhao, Y.; Hughes, R. W.; Su, Z.; Zhou, W.; Gregory, D. H. *Angew. Chemie Int. Ed.* **2011**, *50*, 10397–10401.
(29) Chatterjee, A.; Biswas, K. *Angew. Chem. Int. Ed.* **2015**, *54*, 5623–5627.
(30) Chatterjee, A.; Guin, S. N.; Biswas, K. *Phys.Chem.Chem.Phys.* **2014**, *16*, 14635.
(31) Banik, A.; Biswas, K. *Angew. Chem. Int. Ed.* **2017**, *56*, 14561–14566.
(32) Luo, Y.; Zheng, Y.; Luo, Z.; Hao, S.; Du, C.; Liang, Q.; Li, Z.; Khor, K. A.; Hippalgaonkar, K.; Xu, J.; Yan, Q.; Wolverton, C.; Kanatzidis, M. G. *Adv. Energy Mater.* **2018**, *8*, 1702167.
(33) Chandra, S.; Biswas, K. *J. Am. Chem. Soc.* **2019**, *141*, 6141–6145.
(34) Guin, S. N.; Sanyal, D.; Biswas, K. *Chem. Sci.* **2016**, *7*, 534–543.
(35) Biswas, K.; He, J.; Zhang, Q.; Wang, G.; Uher, C.; Dravid, V. P.; Kanatzidis, M. G. *Nat. Chem.* **2011**, *3*, 160–166.

List of Publications

- **Included in thesis**

Articles

1. **M. Samanta**, K. Pal, U. V. Waghmare, and K. Biswas, Intrinsically Low Thermal Conductivity and High Carrier Mobility in Dual Topological Quantum Material, *n*-type BiTe. *Angew. Chem. Int. Ed.,* **2020,** 59**,** 4822 (***VIP research article***).
2. **M. Samanta**, T. Ghosh, R. Arora, Umesh V. Waghmare, and K. Biswas, Realization of both *n*- and *p*-type GeTe Thermoelectrics: Electronic Structure Modulation by $AgBiSe_2$ Alloying. *J. Am. Chem. Soc.,* **2019**, 141, 19505.
3. **M. Samanta**, K. Pal, P. Pal, U. V. Waghmare, and K. Biswas, Localized Vibrations of Bi Bilayer Leading to Ultralow Lattice Thermal Conductivity and High Thermoelectric Performance in Weak Topological Insulator *n*-type BiSe, *J. Am. Chem. Soc.,* **2018**, 140, 5866 (***spotlight and cover page***).
4. **M. Samanta**, and K Biswas, Low Thermal Conductivity and High Thermoelectric Performance in $(GeTe)_{1-2x}(GeSe)_x(GeS)_x$: Competition between Solid Solution and Phase Separation, *J. Am. Chem. Soc.,* **2017***,* 139, 9382.
5. S. Perumal,[#] **M. Samanta**,[#] T. Ghosh, U. Sandhya Shenoy, A. K. Bohra, S. Bhattacharya, A. Singh, U. V. Waghmare, and K. Biswas, Realization of High Thermoelectric Figure of Merit in GeTe by Complementary Co-doping of Bi and In. *Joule*, **2019**, 3, 2565. (# - Equal Contribution).
6. T. Ghosh, **M. Samanta,** A. Vasdev, K. Dolui, J. Ghatak, T. Das, G. Sheet, and K. Biswas, Ultrathin Free-standing Nanosheets of Bi_2O_2Se: Room Temperature Ferroelectricity in Self-assembled Charged Layered Heterostructure. *Nano Lett.,* **2019,** 19, 5703.
7. **M. Samanta**, S. Roychowdhury, J. Ghatak, S. Perumal, and K Biswas, Ultrahigh Average Thermoelectric Figure of Merit, Low Lattice Thermal Conductivity and Enhanced Microhardness in Nanostructured $(GeTe)_x(AgSbSe_2)_{100-x}$, *Chem. Eur. J.,* **2017**, 23, 7438.
8. **M. Samanta**, S. N. Guin and K. Biswas, Ultrathin Few Layer Oxy chalcogenide BiCuSeO Nanosheets, *Inorg. Chem. Front.,* **2017,** 4, 84.
9. **M. Samanta**, and K Biswas, 2D Nanosheets of Topological Quantum Materials from Homologous $(Bi_2)_m(Bi_2Se_3)_n$ Heterostructures: Synthesis and Ultralow Thermal Conductivity, *Submitted.*
10. S. Roychowdhury, **M. Samanta,** S. Perumal, and K. Biswas, Germanium Chalcogenide Thermoelectrics: Electronic Structure Modulation and Low Lattice Thermal Conductivity, *Chem. Mater.,* **2018**, 30, 17, 5799.
11. S. Roychowdhury, **M. Samanta,** A. Banik and K. Biswas, Thermoelectric energy conversion and topological materials based on heavy metal chalcogenides. *J. Solid State Chem.***,** **2019,** 275, 103.
12. **M. Samanta**, T. Ghosh, S. Chandra and K. Biswas, Layered Materials with 2D Connectivity for Thermoelectric Energy Conversion, *J. Mater. Chemistry A,* **2020,** *Under review.*

Book Chapter

- **M. Samanta,** M. Dutta and K. Biswas, "Thermoelectric Energy Conversion" in the book "Advances in the Chemistry and Physics of Materials", Eds. S. J George, C. Narayana and C. N. R. Rao, *World Scientific Publications*, **2019,** 350-375.

Patent

- **M. Samanta** and K. Biswas, "A tellurium-free *n*-type material and implementations", **2018**, *Indian Provisional Patent* (201841034822).

- **Not included in thesis**

1. B. B. Singh, S. K. Jena, **M. Samanta**, K. Biswas, B. Satpati, and S. Bedanta, Inverse Spin Hall Effect in Electron Beam Evaporated Topological Insulator Bi_2Se_3 Thin Film, *Phys. Status Solidi RRL,* **2018**, 1800492.
2. B. Srinivasan, C.Boussard-Pledel, V. Dorcet, **M. Samanta**, K Biswas, R. Lefèvre, F.Gascoin, F. Cheviré, S. Tricot, M. Reece, and B. Bureau,* Thermoelectric Properties of Highly-Crystallized Ge-Te-Se Glasses Doped with Cu/Bi, *Materials,* **2017**, 10, 328.

Biography

Manisha Samanta obtained her B.Sc. (2013) degree in chemistry from University of Burdwan, India and M.Sc. (2015) degree in chemical sciences from Indian Institute of Technology (IIT) Chennai, India. She is currently pursuing her Ph. D. under the guidance of Prof. Kanishka Biswas at New Chemistry Unit, Jawaharlal Nehru Centre for Advanced Scientific Research (JNCASR), Bangalore, India. Her research areas focus on investigations of thermoelectric and ferroelectric properties of metal chalcogenides, oxy-chalcogenides and topological quantum materials. She is the recipient of the best-poster awards at the "ICONSAT (2018), Indian Institute of science, India", "Indo-UK Thermoelectric Workshop (2018), JNCASR, India", "Annual In-House Symposium (2016), JNCASR, India" and "14th JNC research conference on Chemistry of Materials (2018), Thiruvananthapuram, India".